J. Astrophys. Astr. (1994) **15,** 1

Preface

This year the Indian Academy of Sciences celebrates its **Diamond Jubilee.** To commemorate this we plan to reproduce in these issues some classic papers by distinguished Fellows of the Academy that pertain to Astronomy. This year also marks the Birth Centenary of S. N. Bose. In this issue we reproduce his seminal paper of 1924 in which he put forward the statistics obeyed by photons. This profound discovery marked the birth of Quantum Statistics. Bose sent his paper to the *Philosophical Magazine* for publication, but extraordinarily they turned it down. This inspired Bose to send his paper to Einstein in Berlin with a request to have it translated into German and to have it published in the *Zeitschrift für Physik.* The rest is history. Einstein translated Bose's paper into German and had it published. A re-translation into English of this fundamental paper appeared in the *American Journal of Physics*, Vol. 44, No. 11, November 1976. We have reproduced this with the kind permission of the Editors of the *American Journal of Physics.*

One of the most radical ideas in observational astronomy in this century is the Intensity Interferometer invented by R. Hanbury Brown, Fellow of the Indian Academy of Sciences, and R. Q. Twiss. This novel idea exploited the fact that photons obeyed Bose statistics, and in a sense marked the birth of Quantum Optics. We have also reproduced their famous paper. It may be recalled that this idea of Hanbury Brown and Twiss stirred up a great controversy in the physics community. In a historic paper published in *Nature* the same year, E. M. Purcell gave an elegant exposition of this idea in which he showed that the brilliant "idea of Hanbury Brown and Twiss, far from requiring a revision of quantum mechanics, is an instructive illustration of its elementary principles". With the kind permission of the Editors of *Nature* we have reproduced this·beautiful paper by Purcell.

J. Astrophys. Astr. (1994) **15**, 3–7

Reproduced from *American Journal of Physics*
Vol.**44** No.**11**, November 1976

PLANCK'S LAW AND THE LIGHT QUANTUM HYPOTHESIS

By *[Satyendranath] Bose*
Dacca University, India
Received by Zeitschrift fur Physik on 2 July 1924

The phase space of a light quantum in a given volume is subdivided into "cells" of magnitude h^3. The number of possible distributions of the light quanta of a macroscopically defined radiation over these cells gives the entropy and with it all thermodynamic properties of the radiation.

Planck's formula for the distribution of energy in blackbody radiation forms the starting point for the quantum theory which has been developed during the past twenty years and has yielded rich harvests in all fields of physics. Since its publication in the year 1901 many types of derivations of this law have been suggested. It is acknowledged that the fundamental assumptions of the quantum theory are inconsistent with the laws of classical electrodynamics. All existing derivations make use of the relation

$$\rho_\nu d\nu = \left(8\pi\nu^2 d\nu/c^3\right) E.$$

representing the relation between the radiation density and the mean energy of an oscillator, and they make assumptions concerning the number of degrees of freedoms of the ether as exemplified in the above equation (the first factor on the right-hand side). This factor, however, could be deduced only from the classical theory. This is the unsatisfactory point in all derivations, and it is not

surprising that again and again efforts are made which try to give a derivation free of this logical deficiency.

A remarkably elegant derivation has been given by Einstein. Recognizing the logical defect in the existing derivations, he attempted to deduce the formula independently of any classical the ory. Starting with very simple assumptions about the energy exchange between molecules and the radiation field, he finds the relation

$$\rho_\nu = \frac{\alpha_{mn}}{\exp\left[(\epsilon_m - \epsilon_n)/kT\right] - 1}$$

However, in order to make this formula agree with that of Planck, he has to make use of Wien's displacement law and Bohr's correspondence principle. Wien's law is based on the classical theory; the correspondence principle assumes that the quantum theory agrees asymptotically with the classical theory in certain limiting cases.

In all cases it appears to me that the derivations have insufficient logical foundation. In contrast, the combining of the light quanta hypothesis with statistical mechanics in the form adjusted by Planck to the needs of the quantum theory does appear to be sufficient for the derivation of the law, independent of any classical theory. In the following I wish to sketch briefly the new method.

Let the radiation be enclosed in a volume V and its total energy be E. Let there be different species of quanta each characterized by the number N, and energy $h\nu_s$(s = 0 to s = ∞). The total energy E is then

$$E = \sum_s N_s h\nu_s = V \int \rho_\nu d\nu \tag{1}$$

The solution of our problem requires then the determination of the numbers N_s which determine ρ_ν. If we can state the probability for any distribution characterized by an arbitrary set of N_s, then the solution is determined by the requirement that the probability be a maximum provided the auxiliary condition (1) is satisfied. It is this probability which we now intend to find.

The quantum has a moment of magnitude $h\nu_s /c$ in the direction of its forward motion. The instantaneous stateof the quantum is characterized by its coordinates $x,y,z,$ and the associated momenta p_x,p_y,p_z. These six quantities can be interpreted as point coordinates in a six-dimensional space; they satisfy the relation

$$p_x^2 + p_y^2 + p_z^2 = h^2\nu^2/c^2$$

by virtue of which the above-mentioned point is forced to remain on a cylindrical surface which is determined by the frequency of the quantum. In this sense the frequency domain $d\nu_s$ is associated with the phase space domain

$$\begin{aligned}\int dx\, dy\, dz\, dp_x\, dp_y\, dp_z &= V 4\pi (h\nu/c)^2 h d\nu/c \\ &= 4\pi \left(h^3\nu^2/c^3\right) V d\nu\end{aligned}$$

If we subdivide the total phase space volume into cells of magnitude h^3 , then the number of cells belonging to the frequency domain $d\nu$ is $4\pi V$ (ν^2/c^3) $d\nu$. Concerning the kind of subdivision of this type, nothing definitive can be said. However, the total number of cells must be interpreted as the number of the possible arrangements of one quantum in the given volume. In order to take into account the polarization, it appears mandatory to multiply this number by the factor 2 so that the number of cells belonging to an interval $d\nu$ becomes $8\pi V$ $(\nu^2 d\nu/c^3)$.

It is now very simple to calculate the thermodynamic probability of a macroscopically defined state. Let N^s be the number of quanta belonging to the frequency domain $d\nu^s$. In how many different ways can we distribute these quanta over those cells which belong to the frequency interval $d\nu^s$? Let p_0^s be the number of vacant cells, P_1^s the number of those cells which contain one quantum, p_2^s the number of cells containing two quanta, etc.; then the number of different distributions is

$$\frac{A^s!}{p_0^s! p_1^s! \ldots}$$

where

$$A^s = \left(8\pi\nu^2/c^3\right) d\nu^s,$$

and

$$N^s = 0p_0^s + 1p_1^s + 2p_2^s + \ldots$$

is the number of quanta belonging to the interval $d\nu^s$. The probability of the state which is defined by all the p_r^s is obviously

$$\prod_s \frac{A^s!}{p_0^s! p_1^s! \ldots}$$

In view of the fact that we can look at the p_r^s as large numbers, we have

$$\ln W = \sum_s A^s \ln A^s - \sum_s \sum_r p_r^s \ln p_r^s,$$

where

$$A^s = \sum_r p_r^s.$$

This expression should be maximum satisfying the auxiliary condition

$$E = \sum_s N^s h\nu^s; \quad N^s = \sum_r r p_r^s.$$

Carrying out the variation gives the condition

$$\sum_s \sum_r \delta p_r^s (1 + \ln p_r^s) = 0, \quad \sum_s \delta N^s h\nu^s = 0,$$

$$\sum_r \delta p_r^s = 0, \quad \delta N^s = \sum_r r \delta p_r^s$$

It follows that

$$\sum_s \sum_r \delta p_r^s (1 + \ln p_r^s + \lambda^s) + \frac{1}{\beta} \sum_s h\nu^s \sum_r r \delta p_r^s = 0$$

From this we get as the next step

$$p_r^s = B^s \exp\left(-rh\nu^s/\beta\right).$$

However, since

$$A^s = \sum_r B^s \exp\left(-\frac{rh\nu^s}{\beta}\right) = B^s\left[1-\exp\left(-\frac{h\nu^s}{\beta}\right)\right]^{-1},$$

We have

$$B_s = A^s\left[1-\exp\left(-h\nu^s/\beta\right)\right].$$

Furthermore, we have the relation

$$N^s = \sum_r rp_r^s = \sum_r rA^s\left[1-\exp\left(-\frac{h\nu^s}{\beta}\right)\right]\exp\left(-\frac{rh\nu_s}{\beta}\right) = \frac{A^s\exp\left(-h\nu^s/\beta\right)}{1-\exp\left(-h\nu^s/\beta\right)}$$

Because of the above stated value of A^s, it is also true that

$$E = \sum_s \frac{8\pi h{\nu^s}^3\,d\nu^s}{c^3}\,V\,\frac{\exp\left(-h\nu^s/\beta\right)}{1-\exp\left(-h\nu^s/\beta\right)}$$

Using the preceding results, one finds also that

$$S = k\left\{\frac{E}{\beta}-\sum_s A^s\ln\left[1-\exp\left(\frac{h\nu^s}{\beta}\right)\right]\right\};$$

from this it follows that $\beta = kT$, because of the condition $\partial S/\partial E = 1/T$. Substituting kT for β in the above equation for E, one obtains

$$E = \sum_s \frac{8\pi h{\nu^s}^3}{c^3}V\left[\exp\left(\frac{h\nu^s}{kT}\right)-1\right]^{-1}d\nu^s.$$

which is equivalent to Planck's formula.

J. Astrophys. Astr. (1994) **15,** 13–19

Reproduced from *Nature (London)* (1956) **177**, 27-32

CORRELATION BETWEEN PHOTONS IN TWO COHERENT BEAMS OF LIGHT

By *R.Hanbury Brown*
University of Manchester, Jodrell Bank Experimental Station
and
R.Q.Twiss
Services Electronics Research Laboratory, Baidock

In an earlier paper[1], we have described a new type of interferometer which has been used to measure the angular diameter of radio stars[2]. In this instrument the signals from two aerials A_1 and A_2 (Fig.la) are detected independently and the correlation between the low-frequency outputs of the detectors is recorded. The relative phases of the two radio signals are therefore lost, and only the correlation in their intensity fluctuations is measured; so that the principle differs radically from that of the familiar Michelson interferometer where the signals are combined before detection and where their relative phase must be preserved.

This new system was developed for use with vey long baselines, and experimentally it has proved to be largely free of the effects of ionospheric scintillation[2]. These advantages led us to suggest[1] that the principle might be applied to the measurement of the angular diameter of visual stars. Thus one could replace the two aerials by two mirrors M_1, M_2 (Fig.lb), and the radio-frequency detectors by photoelectric-cells C_1 C_2, and measure, as a function of the separation of the mirrors, the correlation between the fluctuations in the currents from the cells when illuminated by a star.

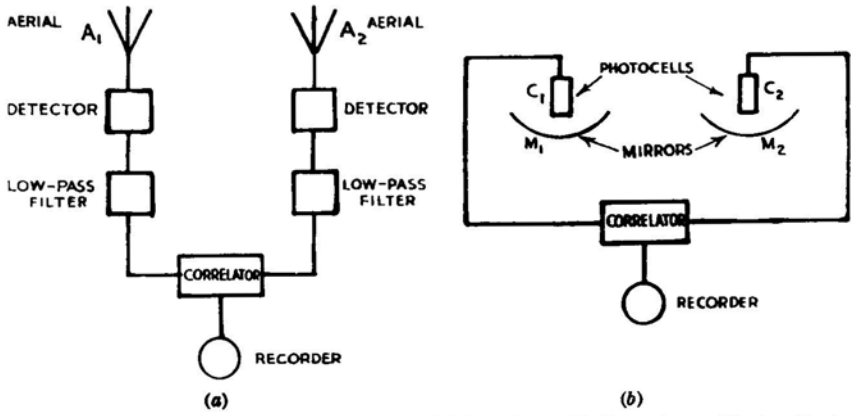

Fig. 1. A new type of radio interferometer (*a*), together with its analogue (*b*) at optical wave-lengths

It is, of course, essential to the operation of such a system that the time of arrival of photons at the two photocathod.es should be correlated when the light beams incident upon the two mirrors are coherent. However, so far as we know, this fundamental effect has never been directly observed with light, and indeed its very existence has been questioned. Furthermore, it was by no means certain that the correlation would be fully preserved in the process of photoelectric emission. For these reasons a laboratory experiment was carried out as described below.

The apparatus is shown in outline in Fig.2. A light source was formed by a small rectangular aperture, 0.13 mm × 0.15 mm in cross-section, on which the image of a high-pressure mercury arc was focussed. The 4358 Å line was isolated by a system of filters, and the beam was divided by the half-silvered mirror M to illuminate the cathodes of the photomultipliers C_1, C_2. The two cathodes were at a distance of 2.65 m from the source and their areas were limited by identical rectangular apertures O_1, O_2, 9.0 mm × 8.5 mm in crosssection. (It can be shown that for this type of instrument the two cathodes need not be located at precisely

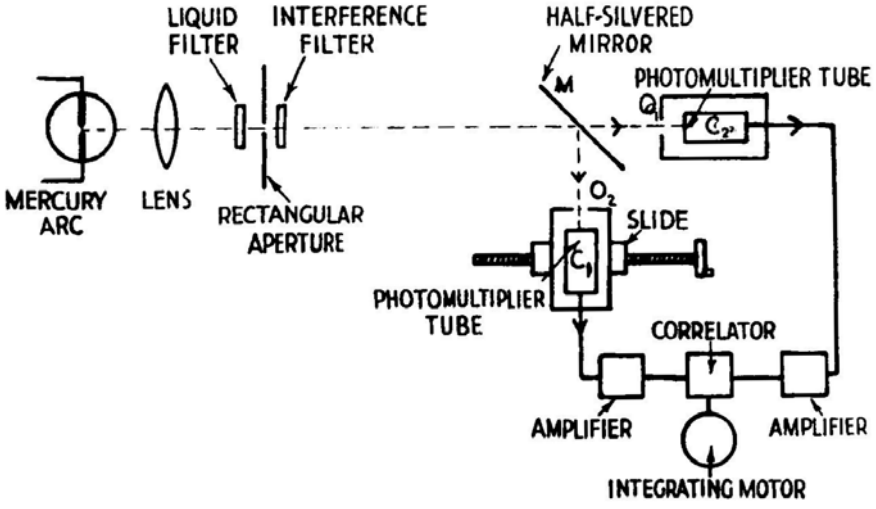

Fig. 2. Simplified diagram of the apparatus

equal distances from the source. In the present case their distances were adjusted to be roughly equal to an accuracy of about 1 cm.) In order that the degree of coherence of the two light beams might be varied at will, the photomultiplier C_1 was mounted on a horizontal slide which could be traversed normal to the incident light. The two cathode apertures, as viewed from the source, could thus be superimposed or separated by any amount up to about three times their own width. The fluctuations in the output currents from the photomultipliers were amplified over the band 3-27 Mc./s. and multiplied together in a linear mixer. The average value of the product, which was recorded on the revolution counter of an integrating motor, gave a measure of the correlation in the fluctuations. To obtain a significant result it was necessary to integrate for periods of the order of one hour, so very great care had to be taken in the design of the electronic equipment to eliminate the effects of drift, of interference and of amplifier noise.

Assuming that the probability of emission of a photoelectron is proportional to the square of the amplitude of the incident light, one can use classical electromagnetic wave theory to calculate the correlation between the fluctuations in the current from the two cathodes. On this assumption it can be shown that, with the two cathodes superimposed, the correlation $S(0)$ is given by:

$$S(0) = A.T.b_\nu.f\left(\frac{a_1\theta_1\pi}{\lambda_0}\right).f\left(\frac{a_2\theta_2\pi}{\lambda_0}\right)\int \alpha^2(\nu).n_0^2(\nu).d\nu \qquad (1)$$

It can also be shown that the associated root-mean-square fluctuations N are given by:

$$N = A.T.\frac{2m}{m-1}b_\nu(b_\nu T)^{-\frac{1}{2}}\int \alpha(\nu).n_0(\nu).d\nu \qquad (2)$$

where A is a constant of proportionality depending on the amplifier gain, etc.; T is the time of observation; $\alpha(\nu)$ is the quantum efficiency of the photocathodes at a frequency ν; $n_0(\nu)$ is the number of quanta incident on a photocathode per second, per cycle bandwidth; b_ν is the bandwidth of the amplifiers; $m/(m-1)$ is the familiar excess noise introduced by secondary multiplication; a_1, a_2 are the horizontal and vertical dimensions of the photocathode apertures; θ_1, θ_2 are the angular dimensions of the source as viewed from the photocathodes; and λ_0 is the mean wave-length of the light. The integrals are taken over the complete optical spectrum and the phototubes are assumed to be identical. The factor $f\left(\frac{a\theta\pi}{\lambda_0}\right)$ is determined by the dimensionless parameter η defined by

$$\eta = a\theta / \lambda_0 \qquad (3)$$

which is a measure of the degree to which the light is coherent over a photocathode. When $\eta \geq 1$, as for a point source, $f(\eta)$ is effectively unity; however, in the laboratory experiment it proved convenient to make η_1, η_2 of the order of unity in order to increase the light incident on the cathodes and thereby improve the ratio of signal to noise. The corresponding values of $f(\eta_1)$, $f(\eta_2)$ were 0.62 and 0.69 respectively.

When the centres of the cathodes, as viewed from the source, are displaced horizontally by a distance d, the theoretical value of the correlation decreases in a manner dependent upon the dimensionless parameters, η_1 and d / a_1. In the simple case where $\eta_1 \ll 1$, which would apply to an experiment on a visual star, it can be shown that $S(d)$, the correlation as a function of d, is proportional to the square of the Fourier transform of the intensity distribution across the equivalent line source. However, when $\eta \geq 1$, as in the present experiment, the correlation is determined effectively by the apparent overlap of the cathodes and does not depend critically on the actual width of the source. For this reason no attempt was made in the present experiment to measure the apparent angular size of the source.

The initial observations were taken with the photocathodes effectively superimposed ($d = 0$) and with varying intensities of illumination. In all cases a positive correlation was observed which completely disappeared, as expected, when the separation of the photocathodes was large. In these first experiments the quantum efficiency of the photocathodes was too low to give a satisfactory ratio of signal to noise. However, when an improved type of photomultiplier became available with an appreciably higher quantum efficiency, it was possible to make a quantitative test of the theory.

A set of four runs, each of 90 min. duration, was made with the cathodes superimposed ($d = 0$), the counter readings being recorded at 5-min. intervals. From these readings an estimate was made of N_e the root mean square deviation in the final reading $S(0)$ of the counter, and the observed values of $S_e(0)/N_e$ are shown in column 2 of Table 1. The results are given as a ratio in order to eliminate the factor A in equations (1) and (2), which is affected by changes in the gain of the equipment. For each run the factor

$$\frac{m-1}{m} \int \alpha^2(\nu) n_0^2(\nu) d\nu \; / \; \int \alpha(\nu) n_0(\nu) d\nu \qquad (4)$$

was determined from measurements of the spectrum of the incident light and of the d.c. current, gain and output noise of the photomultipliers; the corresponding theoretical values of $S(0)/N$

are shown in the second column of Table 1. In a typical case, the photomultiplier gain was 3×10^5, the output current was 140μ amp., the quantum efficiency $\alpha(\nu_0)$ was of the order of 15 per cent and $n_0(\nu_0)$ was of the order of 3×10^{-3}. After each run a comparison run was taken with the centres of the photocathodes, as viewed from the source, separated by twice the width ($d = 2a$), in which position the theoretical correlation is virtually zero. The ratio of $S_e(d)$, the counter reading after 90 minutes, to N_e, the root mean square deviation, is shown in the third column of Table 1.

Table 1. COMPARISON BETWEEN THE THEORETICAL AND EXPERIMENTAL VALUES OF THE CORRELATION

	Cathodes superimposed ($d = 0$)		Cathodes separated ($d = 2\alpha = 1.8$cm)	
	Experimental ratio of correlation to r.m.s. deviation $S_e(0)/N_e$	Theoretical ratio of correlation to r.m.s. deviation $S(0)/N$	Experimental ratio of correlation to r.m.s. deviation $S_e(d)/N_e$	Theoretical ratio of correlation to r.m.s. deviation $S(d)/N$
1	+ 7.4	+8.4	−0.4	~ 0
2	+ 6.6	+8.0	+0.5	~ 0
3	+ 7.6	+8.4	+1.7	~ 0
4	+ 4.2	+5.2	−0.3	~ 0

The results shown in Table 1 confirm that correlation is observed when the cathodes are superimposed but not when they are widely separated. However, it may be noted that the correlations observed with $d = 0$ are consistently lower than those predicted theoretically. The discrepancy may not be significant but, if it is real, it was possibly caused by defects in the optical system. In

particular, the image of the arc showed striations due to imperfections in the glass bulb of the lamp; this implies that unwanted differential phase-shifts were being introduced which would tend to reduce the observed correlation.

This experiment shows beyond question that the photons in two coherent beams of light are correlated, and that this correlation is preserved in the process of photoelectric emission. Furthermore, the quantitative results are in fair agreement with those predicted by classical electromagnetic wave theory and the correspondence principle. It follows that the fundamental principle of the interferometer represented by Fig.lb is sound, and it is proposed to examine in further detail its application to visual astronomy. The basic mathematical theory together with a description of the electronic apparatus used in the laboratory experiment will be given later.

We thank the Director of Jodrell Bank for making available the necessary facilities, the Superintendent of the Services Electronics Research Laboratory for the loan of equipment, and Mr.J.Rodda, of the Ediswan Co., for the use of two experimental phototubes. One of us wishes to thank the Admiralty for permission to submit this communication for publication.

1. Hanbury Brown, R., and Twiss, R.Q., *Phil.Mag.*, **45**, 663 (1954).
2. Jennison, R.C., and Das Gupta, M.K., *Phil.Mag* (in the press)

J. Astrophys. Astr. (1994) **15,** 27–32

Reproduced from *Nature* (1956) **17 8,** 1449-50

Brannen and Ferguson[1] have reported experimental results which they believe to be incompatible with the observation by Hanbury Brown and Twiss[2] of correlation in the fluctuations of two photoelectric currents evoked by coherent beams of light Brannen and Ferguson suggest that the existence of such a correlation would call for a revision of quantum theory. It is the purpose of this communication to show that the results of the two investigations are not in conflict, the upper limit set by Brannen and Ferguson being in fact vastly greater than the effect to be expected under the conditions of their experiment. Moreover, the Brown-Twiss effect, far from requiring a revision of quantum mechanics, is an instructive illustration of its elementary principles. There is nothing in the argument below that is not implicit in the discussion of Brown and Twiss, but perhaps I may clarify matters by taking a different approach.

Consider first an experiment which is simpler in concept than either of those that have been performed, but which contains the essence of the problem. Let *one* beam of light fall on *one* photo-multiplier, and examine the statistical fluctuations in the counting-rate. Let the source be nearly monochromatic and arrange the optics so that, as in the experiments already mentioned, the difference in the length of the two light-paths from a point *A* in the photocathode to two points *B* and *C* in the source remains constant, to within a small fraction of a wavelength, as *A* is moved over the pohotocathode surface. (This difference need not be small, nor need the path-lengths themselves remain constant.) Now it will be found, even with the steadiest source possible, that the fluctuations in the counting-rate are slightly greater than one would expect in a random sequence of independent events occurring at the same average rate. There is a tendency for the counts

to ‘clump’. From the quantum point of view this is not surprising. It is typical of fluctuations in a system of bosons. I shall show presently that this extra fluctuation in the single-channel rate necessarily implies the cross-correlation found by Brown and Twiss. But first I propose to examine its origin and calculate its magnitude.

Let P denote the square of the electric field in the light at the cathode surface in one polarization, averaged over a few cycles. P is substantially constant over the photocathode at any instant, but as time goes on it fluctuates in a manner determined by the spectrum of the disturbance, that is, by the ‘line shape’. Supposing that the light contains frequencies around ν_0, we describe the line shape by the normalized spectral density $g(\nu - \nu_0)$. The width of the distribution g, whether it be set by circumstances in the source itself or by a filter, determines the rate at which P fluctuates. For our purpose, the stochastic behaviour of P can be described by the correlation function $\overline{P(t)\ P(t+\ )}$, which is related in turn to $g(\nu - \nu_0)$ by[3]

$$\overline{P(t)P(t+\tau)} = \overline{P}^2(1+|\rho|^2), \quad \text{where } \rho = \int_{-\infty}^{\infty} g(x)\ \exp\ 2\pi i\tau x\ dx \qquad (1)$$

For the probability that a photoelectron will be ejected in time dt, we must write αPdt, where α is constant throughout the experiment. It makes no difference whether we think of P as the square of an electric field-strength or as a photon probability density. (In this connection the experiment of Forrester, Gudmundsen and Johnson[4] on the photoelectric mixing of incoherent light is interesting.) Assuming one polarization only, and one count for every photoelectron, we look at the number of counts n_T in a fixed interval T, and at the fluctuations in n_T over a sequence of such intervals. From the above relations, the following is readily derived:

$$\overline{n_T^2} - \bar{n}_T^2 = \bar{n}_T(1 + \alpha \bar{P} \tau_0) \tag{2}$$

Where$_0$ = τ_0 $\int_{-\infty}^{\infty} |\rho|^2 d\tau$ and it has been assumed in deriving (2) that $T \gg \tau_0$. Now $\alpha \bar{P}$ is just the average counting-rate and τ_0, a correlation time determined by the light spectrum, is approximately the reciprocal of the spectral bandwidth $\Delta\nu$; in particular, if $\Delta\nu$ is the full width at half intensity of a Lorentzian density function, $\tau_0 = (\pi\Delta\nu)^{-1}$, while if $\Delta\nu$ is the width of a rectangular density functon, $\tau_0 = \Delta\nu^{-1}$. We see that the fractional increase in mean-square fluctuation over the 'normal' amount is independent of T, and is about equal to the number of counts expected in an interval $1/\Delta V$. This number will ordinarily be very much smaller than one. The result, expressed in this way, does not depend on the counting efficiency.

If one insists on representing photons by wave packets and demands an explanation in those terms of the extra fluctuation, such an explanation can be given. But I shall have to use language which ought, as a rule, to be used warily. Think, then, of a stream of wave packets, each about $c/\Delta\nu$ long, in a random sequence. There is a certain probability that two such trains accidentally overlap. When this occurs they interfere and one may find (to speak rather loosely) four photons, or none, or something in between as a result. It is proper to speak of interference in this situation because the conditions of the experiment are just such as will ensure that these photons are in the same quantum state. To such interference one may ascribe the 'abnormal' density fluctuations in any assemblage of bosons.

Were we to carry out a similar experiment with a beam of electrons, we should, of course, find a slight suppression of the normal fluctuations instead of a slight enhancement; the accidentally overlapping wave trains are precisely the configurations excluded by the Pauli principle. Nor would we be entitled in that case to treat the wave function as a classical field.

Turning now to the splitbeam experiment, let n_1 be the number of counts of one photomultiplier in an interval T, and let n_2 be the number of counts in the other in the same interval. As regards the fluctuations in n_1, alone, from interval to interval, we face the situation already analysed, except that we shall now assume both polarizations present. The fluctuations in orthogonal polarizations are independent, and we have, instead of (2),

$$\overline{\Delta n_1^2} = \overline{n_1^2} - \overline{n}_1^2 = \overline{n}_1 \left(1 + \frac{1}{2}\overline{n}_1 \tau_0 / T\right) \tag{3}$$

where n_1/T has been written for the average counting-rate in channel 1. A similar relation holds for n_2. Now if we should connect the two photomultiplier outputs together, we would clearly revert to a single-channel experiment with a count $n = n_1 + n_2$. We must then find:

$$\overline{\Delta n^2} = \overline{n} \left(1 + \frac{1}{2}\overline{n}\tau_0 / T\right) \tag{4}$$

But $\overline{\Delta n^2} = \overline{(\Delta n_1 + \Delta n_2)^2}$

$$= \overline{n}_1 \left(1 + \frac{1}{2}\overline{n}_1 \tau_0 / T\right) + \overline{n}_2 \left(1 + \frac{1}{2}\overline{n}_2 \tau_0 / T\right) + \overline{2\Delta n_1 \Delta n_2} \tag{5}$$

From (4) and (5) it follows that:

$$\overline{\Delta n_1 \Delta n_2} = \frac{1}{2}\overline{n}_1^2 \tau_0 / T \tag{6}$$

This is the positive cross-correlation effect of Brown and Twiss, although they express it in a slightly different way. It is merely another consequence of the 'clumping' of the photons. Note that if we had separated the branches by a polarizing filter, rather than a half-silvered mirror, the factor 1/2 would be lacking in (4), and (5) would have led to $\overline{\Delta n_1 \Delta n_2} = 0$, which is as it should be.

If we were to split a beam of electrons by a non-polarizing mirror, allowing the beams to fall on separate electron multipliers, the outputs of the latter would show a negative cross-correlation. A split beam of classical particles would, of course, show zero cross-correlation. As usual in fluctuation phenomena, the behaviour of fermions and the behaviour of bosons deviate in opposite directions from that of classical particles. The Brown-Twiss effect is, thus, from a *particle* point of view, a characterstic quantum effect.

It remains to show why Brannen and Ferguson did not find the effect. They looked for an increase in coincidence-rate over the 'normal' accidental rate, the latter being established by inserting a delay in one channel. Their single-channel rate was 5×10^4 counts per sec., their accidental coincidence rate about 20 per sec., and their resolving time about 10^{-8} sec. To analyse their experiment one may conveniently take the duration T of an interval of observation to be equal to the resolving time. One then finds that the coincidence-rate should be enhanced, in consequence of the cross-correlation, by the factor $(1 + \tau_0/2T)$. Unfortunately, Brannen and Ferguson do not specify their optical band-width; but it seems unlikely, judging from their description of their source, that it was much less than 10^{11} cycles/sec., which corresponds to a spread in wavelength of rather less than 1 Å at 4358 Å. Adopting this figure for illustration, we have $\tau_0 = 10^{-11}$ sec., so that the expected fractional change in coincidence-rate is 0.0005. This is much less than the statistical uncertainty in the coincidence-rate in the Brannen and Feguson experiment, which was about 0.01. Brown and Twiss did not count individual photo-electrons and coincidences, and were able to work with a primary photoelectric current some 10^4 times greater than that of Brannen and Ferguson. It ought to be possible to detect the correlation effect by the method of Brannen and Ferguson. Setting counting efficiency aside, the observing time required is proportional to the resolving time and inversely proportional to the square of the light flux per unit optical band-width. Without a substantial increase in the latter quantity, counting periods of the order of years would be

needed to demonstrate the effect with the apparatus of Brannen and Ferguson. This only adds lustre to the notable achievement of Brown and Twiss.

E.M.PURCELL

Lyman Laboratory of Physics
Harvard University
Cambridge, Massachusetts

1. Brannen, E., and Ferguson, H.I.S., *Nature*, **178**, 481 (1956)
2. Brown, H.R., and Twiss, R.Q., *Nature*, **177**, 27 (1956)
3. Lawson, J.L., and Uhlenbeck, G.E., "Threshold Signals", p.61 (McGraw-Hill, New York, 1950).
4. Forrester, A.I., Gudmundsen, R.A., and Johnson, P.O., *Phys.Rev.*, **99**, 1691 (1955).

J. Astrophys. Astr. (1994) **15,** 39–45

Bose Statistics and the Stars

R. Hanbury Brown *White Cottage, Penton Mewsey, Andover, Hants, SP11 ORQ,England.*

Received 1994 January 14.

Abstract. A brief account is given of the early development of a new technique, intensity interferometry, to measure the angular size of radio sources. Following the chance discovery that it was unaffected by scintillation it was proposed to apply the same principle to measuring visible stars. This proposal met with vigorous opposition from physicists when it was realised that it implied that the time of arrival of photons in two mutually coherent beams of light must be correlated. Two laboratory experiments were done to demonstrate that this correlation does in fact take place. Then, after a pilot model had measured the angular size of Sirius, a full scale stellar intensity interferometer was built and installed at Narrabri in Australia. In a programme lasting 12 years it measured the angular diameters of 32 single stars in the spectral range O to F and established the first wholly empirical temperature scale for stars in that range. For the last 10 years the work has been continued by the construction of the larger and more sensitive Sydney University Stellar Interferometer called SUSI.

Key words: Instrumentation: interferometers—stars: fundamental parameters.

Most of the work which I am going to talk about was done rather a long time ago; indeed it was started in 1949 at the Jodrell Bank Experimental Station of the University of Manchester. At that time the most exciting problem in radio-astronomy was the nature of the so-called ‘radio stars’ – the bright points of radio emission which had been discovered in the sky. What were they – galaxies, stars, or nebulae? We didn’t know. Most of us thought they were some sort of invisible stars and, as it turned out later, most of us were wrong.

I decided to measure their angular size –at least that would tell us if they were stars or galaxies. An obvious way of doing this was to make a radio analogue of Michelson’s stellar interferometer using spaced radio antennas instead of spaced mirrors; but if it should turn out that these ‘radio stars’ were really stars, as we suspected, then to measure angles of the order of 1/l00th of a second of arc or less, the two antennas would have to be thousands of kilometres apart. In 1949 I could see no way of doing this; the principal technical difficulties were to provide independent local oscillators with sufficient stability, and to equalise the very large and variable delay in the two channels. Nowadays all this can be done.

Talk given at the Raman Research Institute, Bangalore on 13th January 1994.

I worried over this problem for weeks until late one night I saw a possible way of making an interferometer which might work with a baseline of thousands of kilometres. In my mind I saw two people with identical radio receivers sitting in a field looking at cathode-ray tubes on which were displayed the noise from the same radio star; would they, I wondered, both see the same picture? If so, maybe I could find the angular size of the star by comparing their two pictures? To cut a long story short the answer was 'yes', and with the help of a friendly mathematician Richard Twiss, I developed the theory (Brown & Twiss 1954) of a radically new type of instrument which we were certain could be made to work with very long baselines, the intensity interferometer.

In due course an intensity interferometer working on a wavelength of 2 metres was built by R. C. Jennison and M. K. Das Gupta (1956); with it they measured the angular size of the two principal radio sources in the sky (Cygnus A and Cassiopeia A). Neither of these sources proved to be a star–one was a galaxy, the other a supernova remnant – to my disappointment there was no need for a very long baseline – it would have been much easier to use a radio version of Michelson's interferometer!

But all was not lost. One day while Richard Twiss and I were watching this radio interferometer actually working we realised, to our complete surprise, that we had overlooked one of the most valuable properties of an intensity interferometer–its measurements are totally unaffected by twinkling. It dawned on us that the same principle might, perhaps, be used to crack the ancient and difficult problem of measuring the angular size of the visible stars.

Michelson's stellar interferometer was limited by its size (20 ft) to measuring only six stars. Efforts to enlarge it to 50 ft were made by Hale and others, but they failed and the work was discontinued in 1930. The major difficulties were, firstly, that the two paths of the light inside the instrument had to be held equal to a few microns and that proved too difficult mechanically; secondly, the effects of twinkling in the atmosphere were disastrous. What we now realised was that an intensity interferometer working with visible light would overcome both these difficulties; we decided to carry on where Michelson had left off.

It was at this point that we ran into trouble. We had worked out the mathematics of the intensity interferometer for radio waves and now we had to do it for light, and that meant that we must think about photons. So far the principle of our new instrument had been accepted without question, in those days radio engineers didn't worry about photons; but when we decided to apply it to light, physicists became interested and did worry about photons. Indeed they were very unhappy about what we proposed to do.

The trouble was that, when seen in terms of photons, our scheme looked like Fig. 1. Individual photons from the star produce a pulse of current in the output of two separated phototubes and these pulses are fed to a coincidence counter. We showed theoretically that when the spacing between the two phototubes is large and the light on them is mutually incoherent then the coincidence rate is – obviously – that for two random streams of pulses. However, when the spacing is small and the light is mutually coherent, we showed that the times at which photons arrive at the two phototubes must be correlated; photons tend to arrive simultaneously at the two phototubes and the output of the coincidence counter is therefore increased. Furthermore we showed that this 'excess' coincidence rate is a measure of the mutual coherence of the light

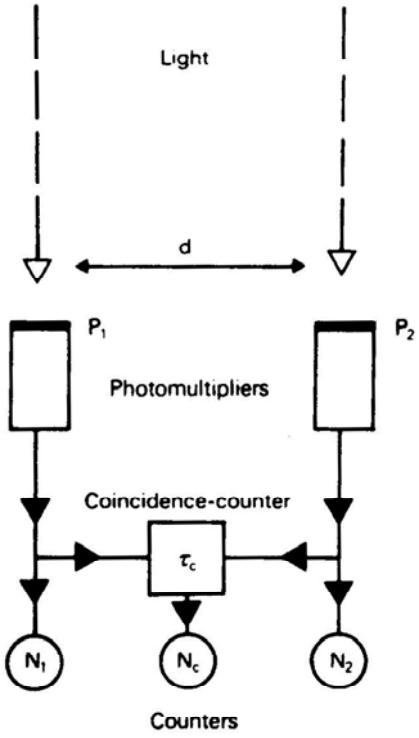

Figure 1. A coincidence-counting intensity interferometer.

at the two phototubes and so, by measuring it at different spacings, it is possible to find the angular (diameter of the star.

To most physicists our ideas were laughable. Their simplest argument, among many more highbrow ones, was that because photons are generated at random times and travel with the velocity of light, they must therefore arrive at random times. conceivable way, we were told, in which they can arrive in pairs; to arrive hand in hand they would have to hang about waiting for each other! Obviously our proposal would not work.

Furthermore on page 18 of one of the holy books of physics, 'Quantum Mechanics', Dirac had written "interference between different photons can never occur"–and yet our theory involved the coordinated behaviour of different photons. Every time I stuck my nose inside Manchester University, I was waylaid by a physicist brandishing some sacred text, Heitler or Dirac, showing that the behaviour of photons could never be correlated. They told me this in person, in letters and in print. Even after the publication of our first experiment, which I shall describe in a minute, laboratory experiments were carried out in Hungary and Canada which claimed to show that there was no correlation between photons. We analysed both these experiments in detail and published a paper pointing out that, with their experimental set-up, it would have taken the Canadians at least 1000 years to demonstrate the phenomenon and with their equipment the Hungarians would have had to observe for a time considerably longer than the age of the Earth! Neither of them had managed to work

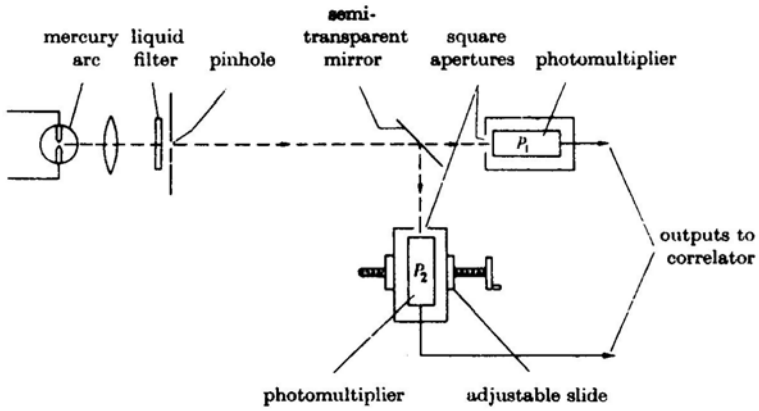

Figure 2. Optical system of first correlation experiment.

out the theoretical signal to noise ratio of their experiments – I couldn't do it either, but my colleague Richard Twiss could!

The difficulty which many physicists had in accepting that the arrival of photons can be correlated was that most of them were particle physicists who thought of a photon as a real thing with its own properties, like a cricket ball, whereas it is better to think of it as an *event* not as a *thing*–something which happens when light is generated or detected. They hadn't grasped that 'photon' and 'wave' are both metaphors which describe the behaviour of light only in a limited context; outside that context these metaphors can be very misleading.

To build a stellar intensity interferometer to measure visible stars we needed lots of money and to convince the people who might give us that money, and to reassure ourselves that our ideas were sound, we did some experiments.

As a first experiment (Brown 1974) we built an optical analogue of our radio interferometer (Fig. 2). We made an artificial star by focussing the light from a high pressure mercury arc through a narrow band optical filter on to a pinhole. The light was then divided by a half-silvered mirror into two beams which were detected by identical phototubes. To vary the spacing between the detectors, as seen from the pinhole, one phototube could be translated sideways. In this experiment the number of photons was so great that the individual pulses in the output of a phototube were superimposed and formed a continuous waveform of noise which was fed to an electronic correlator with a bandwidth of about 50 MHz. The correlation between the two noise outputs was measured as a function of the spacing between the detectors. The total observing time was 9 hours; the results are shown by the points in Fig. 3.

By assuming that the probability of emission of a photoelectron is proportional to the intensity of the light, we showed that there are two components of noise in the output current of a phototube, the classical 'particle' or 'shot' noise in a stream of electrons and the 'wave' noise due to the fluctuations in the intensity of the light itself. Obviously the particle noises from the two phototubes are uncorrelated; but if the light on their photocathodes is mutually coherent then the wave noises will be correlated. I will not go through the rather cumbersome expressions for the correlation which are given in the literature, but simply point to the solid line in Fig. 3 which shows the theoretical correlation for this experiment.

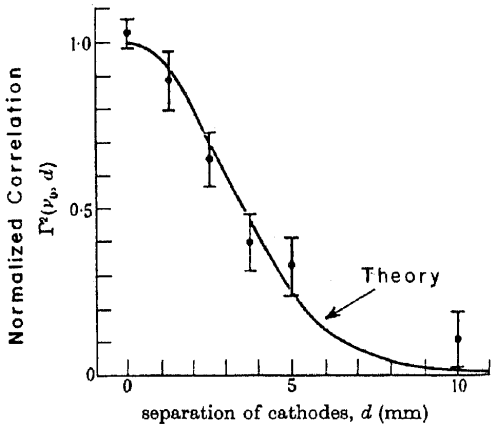

Figure 3. Results of first correlation experiment.

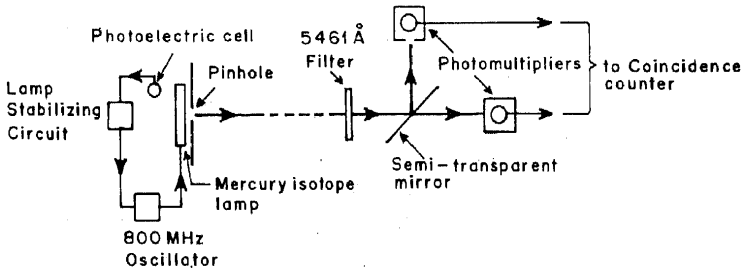

Figure 4. Optical system of second correlation experiment.

As you can see the experimental results agreed well with theory and any residual doubts which we had about our proposal for an optical interferometer were laid to rest.

All the same, Twiss and I thought it would be interesting, and good for our public relations, to demonstrate more clearly that the arrival time of individual photons is actually correlated; we therefore set up the experiment shown by Fig. 4. The optical layout was similar to the first experiment but to achieve a workable signal noise ratio with individual photons the light source must have a very high specific intensity; we used an electrodeless mercury isotope lamp excited by radio-frequency. The output of each phototube was taken through wide-band amplifiers to a coincidence counter with a resolving time of about 3.5×10^{-9} s.

The rate of arrival of photoelectrons in each channel (N_1 , N_2) and the number of coincident pulses (N_c) was measured for two minutes, first with the two photocathodes superimposed, as seen from the pinhole, and then with them sufficiently far apart to resolve the pinhole. In a total exposure time of eight hours we measured the ratio of the 'excess' of correlated coincidences ($N_c - N_r$) to the random coincidences (N_r) to be,

$$(N_c - N_r) / N_r = 0.0193 \pm 0.0016 \text{ (p.e.)}. \qquad \text{experimental}$$

Theory showed us that the coincidence rate should be,

$$N_c = N_1 N_2 2T_c[1 + \tfrac{1}{2}|\gamma_{12}|^2 T_0/2T_c] \quad (1)$$

where N_1 N_2 are the counting rates in the two channels, T_c is the resolving time of the coincidence counter, T_0 is the coherence time of the light, $|\gamma_{12}|$ is the modulus of the mutual coherence of the light on the two photocathodes and it is assumed that in practice $T_c \gg T_0$.

The first term in equation (1) corresponds to the inevitable random coincidences between two streams of photoelectrons; the second term corresponds to the 'bunching' of particles which obey Bose statistics and it increases the coincidence rate when the light is mutually coherent on the two photocathodes.

The expected value of $(N_c - N_r)/N_r$, calculated from equation (1) after allowing for the partial resolution of the pinhole by the photocathodes and a small loss of correlation due to polarisation in the half-silvered mirror, was

$$(N_c - N_r)/N_r = 0.020 \quad \text{(with an uncertainty of about 0.002)}$$

Within the rather wide limits of error, the observed correlation agreed with theory.

Thus, although this second experiment was not as precise as the first, it was a clear demonstration that the time of arrival of individual photons in mutually coherent beams of light is actually correlated.

So far so good, but to raise money for a new interferometer we still had to show that we could actually measure a star. To do this I borrowed two very large searchlights from the Army, removed their arc lamps and put phototubes at the focus of their mirrors. With this equipment I measured the angular diameter of Sirius in 1956, the first time the angular size of a main sequence star had ever been measured. The whole thing worked perfectly; there was no need for high mechanical precision; furthermore Sirius twinkled violently most of the time but that didn't affect the measurements.

The stage was now set to build a full-scale instrument which we did in partnership with the University of Sydney. In 1962 it was installed in the Australian bush at Narrabri some 350 miles north west of Sydney.

It was a very striking instrument – the light from the star was received by two 260 inch mosaic glass mirrors which ran on a circular railway track 200 metres in diameter. At the focus of each mirror there was a photomultiplier whose output current was carried by a catenary cable to a laboratory in the centre of the track. The correlation between the electrical 'noise' in the two currents was measured by an electronic correlator with an electrical bandwidth of 100 Hz, The angular size of the star was measured by recording this correlation as a function of the spacing between the two mirrors.

It worked perfectly for 12 years during which time we measured the angular sizes of 32 of the brightest single stars in the southern sky in the spectral range O to F. measurements were the first ever to be made of main sequence stars. In fact Thosethey established the first wholly empirical temperature scale for stars; all previous scales had been based on theory. We did lots of other experiments, on double stars, spinning and emission-line stars and the Cerenkov radiation from gamma rays, but I won't bother you with all that.

The Stellar Intensity Interferometer was designed to measure stars brighter than magnitude + 2.5 and when that was done I shut it down and sold it for scrap, leaving the foundations of its great circular track for future archaeologists to interpret.

The work I started at Narrabri goes on. To measure fainter stars we decided to go back to square one and find out if the original difficulties of enlarging Michelson's stellar interferometer could be overcome using all the latest gadgets which weren't around in his day–lasers, narrow-band filters, phototubes, computers, active optics and all that sort of thing. We believe that this will yield a cheaper and more sensitive instrument than a larger intensity interferometer.

Let me show you how far we've got. The new instrument at Culgoora near Narrabri is called SUSI (Sydney University Stellar Interferometer) and is run by Professor John Davis. SUSI has 12 small mirrors–coelostats–in a line 640 metres long; they reflect the light from a star into an evacuated pipe which carries it to a central laboratory where there is a very impressive optical system. By selecting different pairs of mirrors it is possible to work with baselines in the range 5 to 640 metres.

The faintest star which SUSI can reach is expected to have a magnitude of + 8 or + 9, over 100 times fainter than the original instrument at Narrabri could reach, and the angular size range will be from 0.02 to 0.00005 seconds of arc. It has already worked with baselines of up to 80 m and in the near future I think we can look forward to great things.

References

Brown Hanbury, R.,Twiss, R. Q. 1954, A new type of interferometer for use in radio-astronomy, *Phil Mag*., **45**, 663–682.

Brown Hanbury, R. 1974, *The Intensity Interferometer*, (London: Taylor and Francis).

Jennison, R. C, Das Gupta, M. K. 1956, The measurement of the angular diameter of two intense radio sources, Phil Mag. Ser. (8), **1,** 55.

J. Astrophys. Astr. (1994) **15,** 47–67

The R Coronae Borealis Stars – A Few Mere Facts

David L. Lambert, *Department of Astronomy, University of Texas, Austin, TX, USA*
N. Kameswara Rao *Indian Institute of Astrophysics, Bangalore 560 034*

Received 1994 January 6; accepted 1994 January 29

Abstract. This review presents a selection of recent highlights of observations of R Coronae Borealis variables. Emphasis is placed on an abundance analysis of a complete sample (18 stars) of the warm galactic RCBs. It is shown that 14 of the 18 have very similar compositions: the iron mass fraction ranges about a factor of 3 around the solar value (assuming C/He = 3%) but abundance ratios X/Fe for elements from Na to Ba show little variation. By contrast, the other 4 stars are deficient in iron but not in Na, Si, S and some other elements. With for example, [Si/Fe] $\simeq$ 2, the quartet is indeed 'peculiar'. One of the quartet, V854 Cen shows depletions of elements (other than CNO) similar to the depletions seen in interstellar medium corresponding to average log $n(H_{tot})$ = – 1.5. Scenarios for creating RCB from normal single and double stars are summarised.

Key words: Hydrogen deficient stars—irregular variables—abundances—evolution.

1. Introduction

This modest essay attempts to introduce a fascinating class of rare variable stars – the R Coronae Borealis (RCB) stars and to provide a few highlights from our continuing collaboration into their structure, composition, and origins. The collaboration grew out of the Mysore meeting in 1985 on 'Hydrogen Deficient Stars and Related Objects'. There, our review (Lambert 1986) of the chemical compositions of RCBs concluded with Samuel Taylor Coleridge's exclamation: "how mean a thing a mere fact is except as seen in the light of some comprehensive truth". The English essayist and poet's remark taken from an essay 'A Prefatory Observation on Modern Biography' was uncovered just prior to the Mysore meeting. Our pursuit of RCB stars is, of course, aimed at establishing the 'comprehensive truth', namely placing the stars correctly in the context of stellar evolution. But in 1985 the lack of 'mere facts' – the abundances of the chemical elements – could be seen as limiting the search for the comprehensive truth. This limitation led us to begin a collaboration on a thorough spectroscopic examination of the RCBs beginning with determinations of the chemical compositions

Invited review talk presented at the Asia-Pacific regional IAU meeting held at Pune from 16–20 August 1993.

of the warmer members of the class, i.e., the stars with the more tractable spectra. Here, we summarize the progress in the context of a general discussion of the class.

R Coronae Borealis stars, as a class, are defined by two main characteristics:

- First, the spectrum of a RCB star suggests that the atmosphere is hydrogen deficient: the Balmer lines are weaker than expected for a supergiant and may even be absent. The lines of C I are strong and for the cooler stars the C_2 Swan bands are prominent in the visual spectrum. The combination of H-deficiency and C-enrichment has suggested that the atmospheres consist primarily of material exposed to He burning.
- Second, the variability portrayed by the class *is* unique. At irregular intervals the stars decline rapidly by up to 5–8 magnitudes and may remain faint for extended periods. The dimming is attributed to obscuration of the star by a cloud of carbon dust grains.

2. Some basic data

Before discussing the chemical compositions of the RCB stars, we shall summarize the stars' known properties. Emphasis is placed on the more recent findings. The chemical compositions are discussed later.

Catalogue: Drilling & Hill (1986) provide a list of 20 'cool' and 3 'hot' RCBs. One star (LR Sco) listed by Drilling & Hill is not a RCB (Giridhar, Rao & Lambert 1991). To the 1986 list of 'cool' RCBs should be added: UX Ant (Herbig 1990; Kilkenny & Westerhuys 1990), V854 Cen (McNaught & Dawes 1986), and V739 Sgr, V1159 Sgr, V1783 Sgr (Lloyd Evans, Kilkenny & van Wyk 1991), V1860 Sgr, V4017 Sgr (Herbig 1990), V517 Oph (Kilkenny *et al.* 1992) and FH Sct. At present, then there are 32 known galactic RCBs.

Spectrum at maximum light: The stars span a range in effective temperature from about 20000K (DY Cen, early B-type, and V348 Sgr, WC11-like) to cool carbon stars resembling the R stars (WX CrA and S Aps with $T_{\rm eff}$ = 4000 K). A majority of the RCBs spectroscopically resemble the F–G Ib supergiants with $T_{\rm eff}$ = 7000 ± 1000 K. Of course, the Balmer lines and the CH bands are weaker and the CI lines and C_2 bands are stronger in the RCBs than in normal supergiants. It could be noted that the H deficiency may not always take extreme values. In particular, the recently discovered RCB V854 Cen shows Balmer lines with pronounced Stark broadened wings indicative of a substantial H abundance.

Absolute luminosities: Estimates of luminosity are difficult to obtain for the galactic RCBs. Most probably, the best estimates are provided from the three RCBs identified in the Large Magellanic cloud: M_v = – 4 to – 5 (Feast 1979). Estimates for galactic RCBs are generally consistent with this range (e.g. Rao & Lambert 1993a).

Galactic distribution and kinematics: Arilling (1986) reviewed the galactic distribution and kinematics. The RCBs are concentrated towards the galactic center. The distribution of radial velocities (referred to the local standard of rest) shows that the majority of the RCBs follow the galactic rotation curve appropriate to a galactocentric distance of about 4 kpc. About 5 or 6 of the RCBs are high velocity objects. Several are to be found at quite large distances (about 2 kpc) from the galactic plane.

Light variations – Irregular declines: As noted above, these declines which may reach – 8magnitudes are a defining characteristic of the class. RCB stars, in general, spend

most of their time at or near maximum brightness and suddenly undergo declines with an initial phase lasting a few days to a few weeks. The decline to minimum may not be smooth: 'halts' are sometimes reported. Minima generally last several weeks to months with some variations in brightness. Recovery to maximum brightness often takes much longer than the decline. The frequency of declines varies from star to star. XX Cam has apparently experienced but one shallow decline in the last 100 years (Rao, Ashok & Kulkarni 1980). By contrast, V854 Cen, the third brightest RCB at maximum light, is more often found in decline than at maximum light which presumably explains why this RCB was not recognised until 1986. In those cases where observations are extensive, statistical analysis shows that declines occur at random intervals (Sterne 1935; Howarth 1976, 1977).

Light Variations – Pulsations: In addition to the dramatic declines, RCBs show minor variations in visual light of 0.1 to 0.5 mag. in amplitude and with pseudoperiods averaging about 40 days (Feast 1990; Lawson *et al.*).1990). Only in the case of RY Sgr these variations may be said to be regular and due to atmospheric pulsations. RY Sgr's period of 38.6 days is not constant but according to Kilkenny (1982) and Marraco & Milesi (1982) decreases at the rate of 0.15 day/cycle – see also Lawson & Cottrell (1990). There is evidence that declines of RCBs occur at maximum light in the pulsational cycle (Lawson *et al.* 1992) but quite obviously many maxima may pass before a decline is initiated or, in the words of Lawson *et al.* "it is possible to predict when a decline *might* happen, although not when it will *occur".*

Infrared excesses: Circumstellar dust is betrayed by infrared excesses in the near-infrared (< 12 μm). In several cases and notably for the eponymous star RCrB infrared excesses are detected at wavelengths as long as 100. μm.mFor reviews of the infrared excesses and the circumstellar dust see Feast (1986) and Walker (1986). A representation of the near-infrared fluxes by a blackbody results in dust temperatures of 600–900 K. The infrared flux from RY Sgr has been shown to vary at the photospheric pulsation period showing that the dust is heated by photospheric radiation (Feast *et al.* 1977; Feast 1986). In a decline, however, the infrared flux remains approximately unchanged despite the several magnitudes dimming in visible light. If the decline is caused by the onset of dust formation above the visible photosphere, the dust resident in the shell prior to the decline must subtend a solid angle at the star greater than that initially subtended by the new cloud. In addition to the warm (700 K) dust, much cooler and more extended dust shells have been detected around RCrB and SU Tau (Rao & Nandy 1986; Gillett *et al.* 1986; Walker 1986). RCrB's cool shell which extends 18' on the sky corresponding to a linear size of about 8pc has been interpreted as a hydrogen rich shell ejected earlier.

Polarimetric observations. A few stars have been observed for polarization at visual wavelengths near maximum light. Observations of linear polarization for RCrB suggest that the dust formation and ejection occurs in a preferred plane (Stanford *et al.* 1988). A similar preference has been suggested for V854 Cen (Rao & Raveendran 1993). Few observations of polarization have been reported for stars near minimum light. One key observation by Whitney *et al.* (1992) of V854 Cen in a deep minimum showed the emission lines (see below) were unpolarized but the continuum was quite strongly polarized; hence, the emission lines come from regions not obscured by dust.

Nebulae around RCB stars: Several RCBs are associated with low density low excitation nebulae. RCrB's nebula was revealed by Herbig's (1949, 1968) detection of the [O II] 3727 Å lines at minimum light. Spectra of the hotter RCBs – DY Cen,

MV Sgr, V348 Sgr – show nebular forbidden emission lines (Rao, Giridhar & Lambert 1993; Rao, Houziaux & Giridhar 1990; Pandey, Rao & Lambert 1993; Herbig 1958). Extended nebulosity of 30" diameter has been detected around V348 Sgr by Pollacco, Tadhunter & Hill (1990). A reflection nebulosity around UW Cen was reported by Pollacco *et al.* (1991). Broad emission lines of [N II],[O I] and [S II] in the spectrum of V854 Cen in a deep minimum were reported by Rao & Lambert (1993b) and interpreted as coming from a bipolar nebula with an orthogonal thick dusty accretion disk. V605 Aql which at maximum light in 1919 seems to have had the spectrum of a cool RCB (Bidelman 1973) is now a faint stellar object (V = 22.3) surrounded by the planetary nebula A58 which has helium enriched knots (Pollacco *et al.* 1992) and so resembles the planetary nebulae A30 and A78 (Hazard *et al.* 1980; Jacoby & Ford 1983). FG Sge, the most enigmatic of peculiar supergiants, has long been known to be associated with a planetary nebula. In its recent RCB-like decline, FG Sge showed strong C_2 bands and has been advanced for membership in the RCB class (Kipper & Kipper 1993; Juresik 1993).

Spectrum at minimum light: The spectrum in the decline to minimum light has been well documented for RCrB (Payne-Gaposchkin 1963; Cottrell, Lawson & Buchhorn 1990), and RY Sgr (Alexander *et al.* 1972). The reader is referred to these papers for descriptions of the 'chromospheric' emission lines which are generally sharp and blue-shifted by about 10 km s^{-1} to the photosphere. The photospheric lines remain visible during the decline with an enhancement of low excitation lines such as the C_2 Swan bands (Lambert, Rao & Giridhar 1990). Very few spectra have been reported for stars in deep minima; the reader may surmise the logistical reasons for this lacuna in our knowledge of RCBs. Rao & Lambert (1993b) discuss a high resolution spectrum of V854 Cen showing sharp 'chromosphere' lines and broad emission lines **(**FWHM = 200–300 km s^{-1}) of Ca II H and K, Na D, Hα the C_2 Swan bands as well as the forbidden lines listed above. Old reports speak of the absorption lines as 'veiled' (i.e., present but weakened) in spectra of RCrB at minimum but in V854 Cen the continuum was unaccompanied by absorption lines and even the very strongest photospheric lines were absent. A set of unidentified broad emission lines may be linked to the carriers of interstellar diffuse bands (Rao & Lambert 1993c).

Evolutionary sequence?: Putative relatives of the RCBs are recognizable on both the low and high temperature boundaries of the RCB domain from about 20000 K to 4000 K. The hydrogen deficient carbon (HdC) stars are likely relatives with effective temperatures ranging up to the low temperature boundary of the RCBs. This linkage was first drawn by Bidelman (1953) who noted that four non-variable stars were "apparently hydrogen-deficient stars which appear also to be rich in carbon" The prototype is HD182040. Five galactic examples are now known. The classic (and only) abundance analysis is by Warner (1967); we comment below on whether the results of Warner's analysis of the HdC and our new analysis of the RCBs would encourage promotion of an evolutionary link. At the high effective temperature limit for RCBs, the extreme helium stars are probable relatives; the similarities in composition between the RCBs and EHes is noted later. The HdC, RCB and EHe stars form a sequence of approximately constant luminosity running in the (log g, log $T_{\rm eff}$) plane from about (0.5, 3.8) to (3.0, 4.5). We do not include spectroscopic binaries like v Sgr in our definition of an EHe.

The existence of this sequence suggests but does not demand an evolutionary connection between the three classes. Additional information is needed to discern the direction of an evolutionary sequence. A further question is suggested by the rarity

of these hydrogen deficient stars: Do few single or binary stars become RCBs or is the RCB phase a very short-lived event in the life of many single or double stars?

In an attempt to answer these questions we began our study of the chemical compositions of RCBs with an initial emphasis on the warmer stars –18 in all – whose spectra are dominated by atomic lines rather the forbidding rich spectra of the C_2 and CN molecules. In the following section we sketch the preliminary results of our analysis.

3. Chemical compositions

Our 1986 review of the chemical compositions of RGBs drew upon detailed analyses of three stars (RCrB, XX Cam, RY Sgr) and less complete and curve of growth analyses of 3 additional stars (U Aqr, UV Cas, SU Tau). Presently, we have results for 18 stars including 5 of the above 6 with U Aqr considered too cool for present consideration. The hot RCB DY Cen was analysed recently by Jeffery & Heber (1993). We also analysed 2 EHes which with 4 discussed in Heber's (1986) review provide a useful sample for comparison with the RCBs. Knowledge of the HdCs' compositions is restricted to that provided by Warner (1967).

Spectra for our analysis were gathered primarily at the Cerro Tololo Inter-American Observatory with the Cassegrain echelle at the 4 m telescope. The spectral resolution is 0.2 to 0.3 Å. The wavelength coverage is 5000–7000 Å. The S/N ratio is generally 100 or better. Similar spectra were obtained at the McDonald Observatory for several northern RCBs. Sample spectra are shown in Figs. 1 and 2.

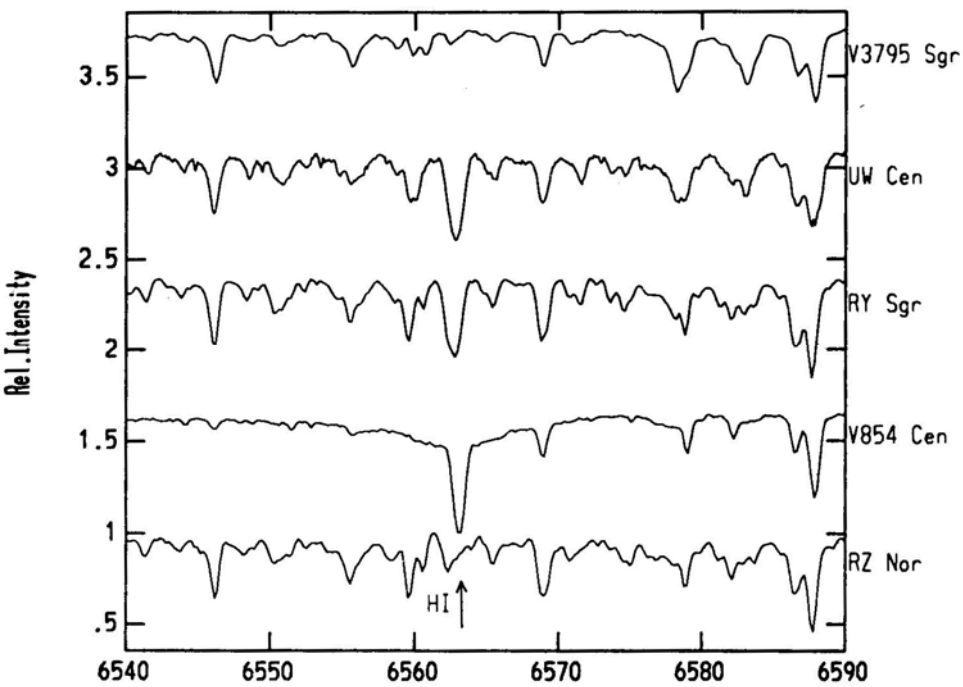

Figure 1. Spectra of V3795 Sgr, UW Cen, RY Sgr, RZ Nor, and V854 Cen near the Hα line at 6563Å. Note the broad wings of Hα for V854 Cen and the absence of Hα from V3795 Sgr.

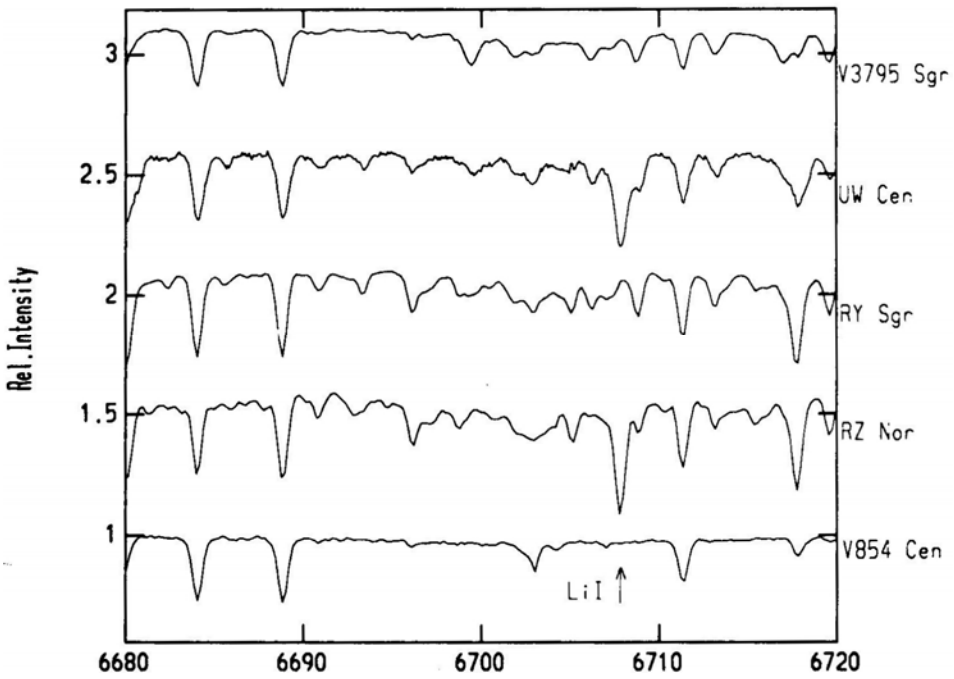

Figure 2. Spectra of V3795 Sgr, UW Cen, RY Sgr, RZ Nor, and V854 Cen near the Li I resonance doublet at 6707 A. The Li I doublet is present in RZ Nor and UW Cen but absent from the other three spectra.

For the analysis of the spectra, we have used a family of model atmospheres kindly provided by D. Schönberner– see Schönberner (1975). We are grateful to U. Heber for supplying models of hotter stars. Model atmospheres were available for C/He ratios of 1 and 3% by number at a H abundance too low for H to contribute to the continuous opacity and with a solar mix of elements other than H, He and C. A computer program originally written by Sneden (1973) was adapted to meet the special requirements of RCB atmospheres by adding several sources of continuous opacity. The model atmospheres and the analysis assumes local thermodynamic equilibrium.

In discussing the compositions of the RCBs it is essential to define clearly what is meant by 'the abundance of an element'. Abundance of an element E, as determined by spectroscopic analysis, is commonly taken to identify the number density ratio $n(E)/(H)$ which we may write as E/H. This is a natural definition because the continuous opacity in normal stellar atmospheres in spectral regions usually used for abundance analyses is controlled by hydrogen atoms or the negative H ions. For the RCB atmospheres, however, carbon atoms probably control the continuous opacity unless either the C/He ratio is extremely small or the H/C is quite large. If carbon dominates the continuous opacity, the equivalent width of a C I line in a RCB spectrum is expected to be almost independent of the C/He ratio. Furthermore, the equivalent width is expected to be insensitive to the atmosphere's effective temperature and gravity because the continuous opacity which arises from photoionization of neutral carbon atoms is contributed by C I energy levels of only slightly higher

excitation energies than the levels providing the observed C I lines. Our spectra show that the equivalent width of a given C I line is almost unchanged across the sample of stars despite their obvious differences in effective temperature, gravity and H content.This isevidence that carbon(or an element correlated with carbon) dominates the continuous opacity. It is not evidence that carbon is the most abundant element; helium is the most abundant element (Schönberner 1975).

On the assumption that carbon dominates the continuous opacity, the 'spectroscopic' abundance is $S(E) = E/C$. The more fundamental quantity is $Z(E)$, the mass fraction of the element E, where

$$Z(E) = \frac{\mu_E}{\mu_C} Z(\mathrm{C}) S(E) \tag{1}$$

and

$$Z(\mathrm{C}) = \frac{3\mathrm{C/He}}{(1 + 3\mathrm{C/He} + \ldots)} \tag{2}$$

and μ_E is the atomic mass ofelement E. Since C/He $\ll$ 1 wefindfrom(1) and (2)that

$$Z(E) \simeq 3 \frac{\mu_E}{\mu_C} \frac{\mathrm{C}}{\mathrm{He}} S(E) \tag{3}$$

Interpretation of the abundances is based in large part on the ratios of abundances but fortunately $Z(E_1)/Z(E_2) = S(E_1)/S(E_2)$ so that the possibly unknown factor C/He cancels.

The He I 5876 Å triplet is present in spectra of RCBs (Keenan & Greenstein 1963), but it is not an accurate indicator of the C/He ratio. Abundances given here are based largely on the model atmosphere grid computed for C/He = 3%. For the EHes and the hot RCB DY Cen, Heber and colleagues are able to derive the C/He ratio from helium and carbon lines (Heber 1986; Jeffery & Heber 1993): the mean ratio from 5 stars including DY Cen is C/He = 0.83% with a range of just 1.0 to 0.66% (Jeffery *et al.* (1988) derived a remarkably low C/He (= 0.02%) ratio for the hot RCB MV Sgr.) We comment as appropriate on the effect on our abundances of a change from 3 to 1% in the adopted C/He ratio.

Our abundance analysis included whenever possible the following elements: H, Li, C, N, O, Na, Al, Si, S, Ca, Fe, Ni, Y, and Ba. Additional elements were measured in some of the 18 RCBs (e.g., Ne, P, Zr, and Nd). A summary of the results appears in Table 1. Perhaps, the most significant finding is that the majority of the RCBs have an essentially common composition.Fourteen of the 18 RCBs comprise this majority. They are UX Ant, XX Cam, UV Cas, UW Cen, R CrB, V482 Cyg, Y Mus, RT Nor, RZ Nor, FH Set, RY Sgr, GU Sgr, SU Tau, and RS Tel. We discuss next the composition of this majority.

Our analysis uses the model atmosphere grid constructed for a carbon to helium ratio of3% and the abundances are normalized to log $\Sigma N_i \varepsilon_i$ = 12.15, i.e., log ε(He) = 11.51 and log ε (C) = 10.0. Analysis of a selection of C I lines returns a mean carbon abundance of log ε (C) = 9.8 ± 0.2, which is slightly less than the adopted abundance but this difference could be erased in several acceptable ways; e.g., adopt an alternative choice of the source for the C I f-values. Unless otherwise stated all abundance are quoted for analyses based on C/He = 3% and normalized as above.

Table 1. Chemical compositions of R Coronae Borealis stars.

Elements	log ε					
	Sun[a]	Majority	Minority			
			V854 Cen	VCrA	VZSgr	V3795 Sgr
H	12.00	…[b]	11.2	9.8	7.2	< 4.3
Li	3.31	…[b]	< 1.9	< 1.3	< 2.3	< 3.1
C	8.55	9.8 ± 0.2	9.7	9.6	9.7	9.2
N	7.97	9.7 ± 0.3	8.4	10.0	8.7	8.3
O	8.87	9.1 ± 0.5	9.2	9.9	9.5	8.0
Na	6.32	7.1 ± 0.3	6.5	6.6	6.8	6.2
Al	6.48	6.9 ± 0.2	5.5	6.0	6.4	6.3
Si	7.55	8.0 ± 0.3	7.3	8.7	8.3	8.0
S	7.23	7.8 ± 0.4	6.7	8.2	7.9	7.9
Ca	6.34	6.2 ± 0.2	5.2	6.4	6.0	5.3
Fe	7.51	7.5 ± 0.3	6.3	6.2	6.9	6.0
Ni	6.25	6.8 ± 0.4	6.0	6.2	6.3	6.3
Y	2.24	2.7 ± 0.6	2.3	1.2	3.7	2.0
Ba	2.21	1.9 ± 0.5	1.1	0.4	2.1	0.0

[a]Meteoritic/Solar abundances from Grevesse & Noels (1993) for C, N, O and Fe, and Anders & Grevesse (1989) for other elements. Based on He/H = 0.1 from Grevesse & Noels (1993) and, hence, $\log(\sum \mu_i \varepsilon_i) = 12.15$.
[b]See text.

The iron abundances (metallicity) of the majority span the range log ε(Fe) = 6.9 (UX Ant) to log e(Fe) = 8.0 (XX Cam, UV Cas). The mean Fe abundance is the solar abundance. With our choice of C/He = 3% the most metal rich stars correspond to [Fe/H] $\simeq$ + 0.5 which might appear unusually high except that many of the RCBs are located towards the galactic centre where metallicities may be higher on average than in the solar vicinity. Recall from Equation 3 that mass fraction of iron depends on the assumed C/He ratio. If C/He = 1%, as analyses of the EHes and the hot RCB DY Cen (see above) suggest, the mass fractions of Fe are reduced by about 0.5 dex. Then the most Fe-rich RCBs have about the solar metallicity and the most metal-poor of this majority correspond to a metallicity of [Fe/H] $\simeq -$ 1. The assumption of C/He = 1% does seem to be preferable. Without a direct estimate of the C/He ratio for individual RCBs we cannot determine how to apportion the evident spread in the apparent metallicities between a real spread in the C/He ratio and a spread in the iron mass fractions. Our measurement errors should not exceed ± 0.2 to ± 0.3 dex.

A defining characteristic of the majority is the similarity of their elemental abundances, especially the abundance ratios with respect to Fe. Hydrogen and lithium are exceptions in this regard. The hydrogen abundances range from a maximum of log ε (H) = 8.3 (SU Tau) to a minimum of log ε (H) < 4.9 (XX Cam). The mean value of log ε (H) = 7.1 ± 0.8 (including the upper limit for (XX Cam) corresponds to a hydrogen deficiency of 10^5. Four stars show a strong Li *T* 6707 Å resonance doublet. Lithium was first detected in RCBs by Keenan & Greenstein (1963) from spectra of the eponymous star. The Li-rich quartet are UW Cen, R CrB, RZ Nor, and SU Tau with a mean Li abundance of log ε (Li) = 4.3 ± 0.3. (The abundance is log ε (Li) ~ 3.8 for C/He = 1%.) Lithium appears overabundant with respect to the stars' initial Li

abundance; the local abundance is now log ε (Li) = 3.3. Scenarios purporting to describe the origin of RCBs must, therefore, account for lithium production in some RCBs. The Lirich stars seem to be a subclass of the majority because the upper limits on Li in the other 10 stars range from log ε (Li) < 2.6 to loge (Li) < 1.6 in the coolest stars. The subclass have similar H abundances. (This abundance of Li is similar to that seen in super Li-rich luminous AGB stars in LMC (Smith & Lambert 1989, 1990) – could these Li rich RCBs be the luminous counterparts of the RCB population).

Inspection of Table 1 shows that nitrogen is greatly overabundant in this LTE analysis. The N abundance exceeds that attainable by the complete conversion of initial (solar) C, N, and O to N by the H-burning CNO-cycles; if C/He= 1% is assumed, the N abundance (log ε (N) = 9.2) is close to the upper limit provided by solar C, N, and O. The RCBs apparently contain material in which carbon synthesized in He-burning was partially converted to nitrogen on exposure to warm protons. This conclusion is reinforced by the observation that oxygen has a normal abundance in RCBs.

Sodium is overabundant: [Na/Fe] $\simeq$ + 1. Aluminium is slightly overabundant but calcium with a sensitivity to the model atmospheres similar to that of Na and Al has a normal abundance. One surmises that Na and Al have been synthesised prior to the formation of the RCBs. Synthesis of Na and Al necessarily accompanies the burning of H by the ON-cycles.

Mass fractions of silicon and sulphur exceed solar values by about 0.4 and 0.6 dex respectively. Although these excesses would vanish if we adopted C/He = 1%, the abundances relative to Fe would remain about 0.5 dex larger than the solar ratios. The Si and S abundances are not necessarily indicative of production of these elements. It is a well known feature of chemical compositions of stars that Si and S (relative to Fe) increase in abundance in metal-poor stars. Edvardsson *et al.* (1993) also show that the increase is more pronounced for stars originating from the inner regions of the Galaxy. We suppose that the Si and S enrichments may reflect an enrichment present at the birth of the RCBs. A difficulty with this claim is that Ca is seen to follow Si and S in normal stars but not in the RCBs.

There is a suggestion in our analyses that there is a real spread in the Y and Ba abundances across the sample of 14 RCBs. On average, yttrium is overabundant by about 0.5 dex but barium has a normal or slightly subnormal abundance.

Four of the 18 RCBs have compositions that set them apart from the majority. The four are V854 Cen, V CrA, VZ Sgr, and V3795 Sgr. Put in the simplest way possible, the quartet are distinguished by having a low metallicity (Fe) but 'normal' abundances of Si (and some other elements): log ε (Fe) = 6.0 to 6.9 and log ε (Si) = 7.3 to 8.7 for the quartet but log ε (Fe) = 6.9 to 8.0 and log ε (Si) = 7.4 to 8.4 for the majority of 14. We comment on the elemental abundances from H to Ba in the quartet relative to the abundances of the majority. Abundances are given in Table 1.

Hydrogen: A myth that *all* RCBs are extremely deficient in hydrogen is exploded by our analyses. Significantly, the two most hydrogenrich RCBs are members of the minority quartet: V854 Cen (see Fig. 1) and V CrA with H deficiencies of a factor of 10 and a factor of 100 respectively. The quartet also includes the most H-poor RCB of the entire sample of 18: V3795 Sgr with a deficiency of at least a factor of 18[8].

Nitrogen and oxygen: The abundances of N and O for the sample of 18 RCBs are compared in Fig. 3. A 'low' N abundance is found for 3 of the quartet of 'unusual'

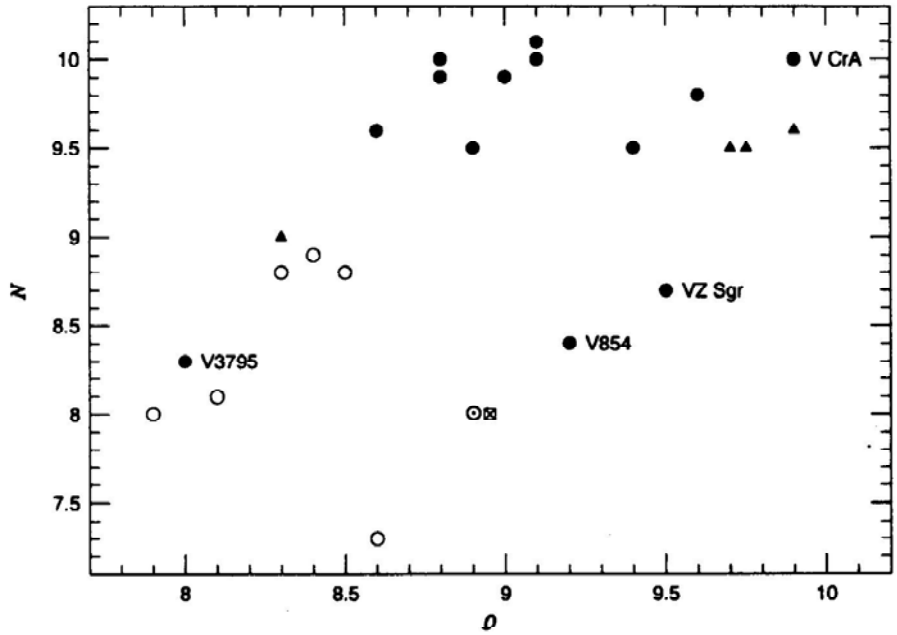

Figure 3. Nitrogen and oxygen abundances of the RCB and EHe stars. The 18 RCBs of our samples are represented by the filled symbols with the Li-rich stars by filled triangles. EHes are represented by open circles and the hot RCB DY Cen by the cross. The solar composition is denoted by the usual symbol. The points representing the peculiar RCBs are labelled. Location of solar N and O abundance is marked by the usual symbol.

RCBs but V CrA is one of the most N-rich and O-rich of all the RCBs. In Fig. 3, there appears to be a separation between the RCBs and the EHes and the hot RCB DY Cen. In part, this is a result of our assumption that C/He = 3%. If C/He = 1%, as analyses of the EHes and DY, Cen indicate, the N and Oabundances would be reduced by about 0.5 dcx but this revision would not bring the mean N and O abundances of the RCBs to the level of the EHes.

Sodium through Calcium: The quartet is distinguished by the fact that Na, Al, Si, and S are not, as is Fe, underabundant (except V854 Cen). In other words, the stars display remarkably high abundance ratios of these elements relative to Fe. Fig. 4 illustrates this point. Calcium is overabundant relative to Fe in 2 of the 4 stars. (Note too the small scatter in ratios such as Si/Fe and Na/Fe among the majority sample of 14 RCBs.) Si and S are well correlated – see Fig. 5.

Iron and Nickel: A distinctive feature of the quartet is that the Ni/Fe ratio is much larger than for the majority and distinctly non-solar.

Yttrium and Barium: Figs. 6 and 7 show Y and Ba as a function of the Fe abundances for the sample of 18 RCBs and the members of the quartet are individually labelled. With the exception of VZ Sgr, the entire sample is distributed with a marked scatter about a line of constant Y/Fe ratio which is offset from the solar ratio by about 0.8 dcx. The barium abundances (Fig. 7) show that the Ba/Fe ratio is approximately constant and solar for the RCBs with VZ Sgr having a Ba/Fe ratio only slightly above the average for RCBs. The scatter in Y/Fe at a given Fe abundance exceeds that in Ba/Fe and for both ratios the scatter exceeds that readily attributed to errors

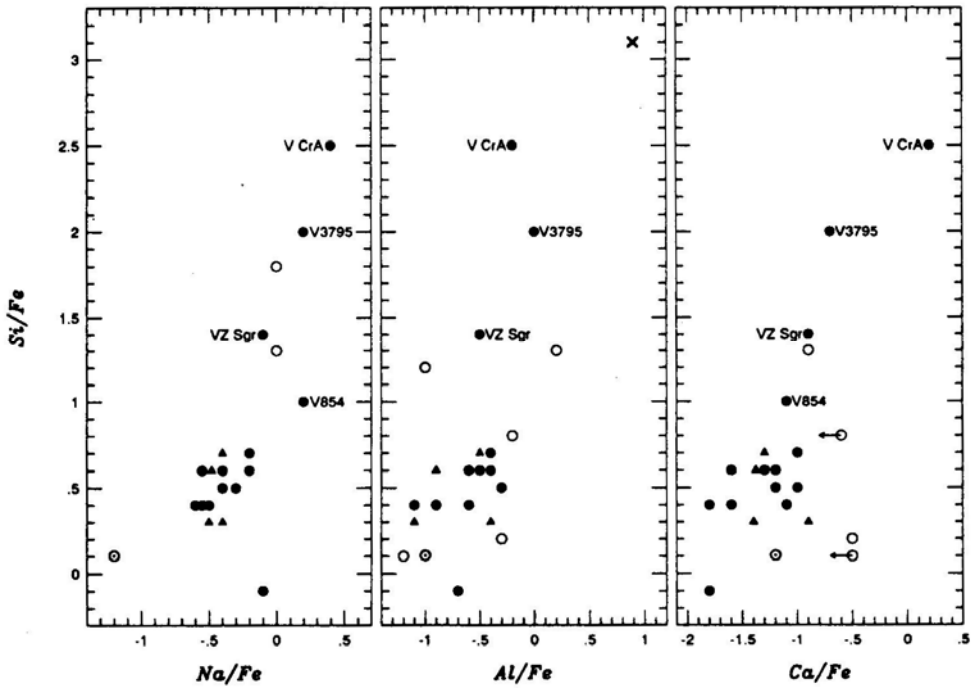

Figure 4. The ratio Si/Fe vs. Na/Fe, Al/Fe, and Ca/Fe. See the caption to Fig. 3 for the key to the symbols.

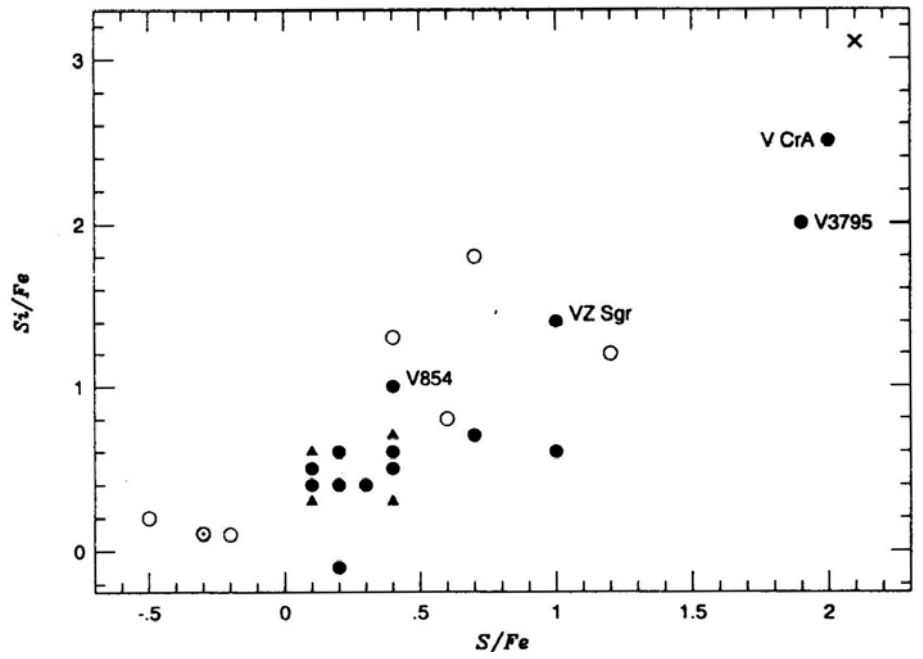

Figure 5. The ratio Si/Fe vs. S/Fe. See the caption of Fig. 3 for the key to the symbols.

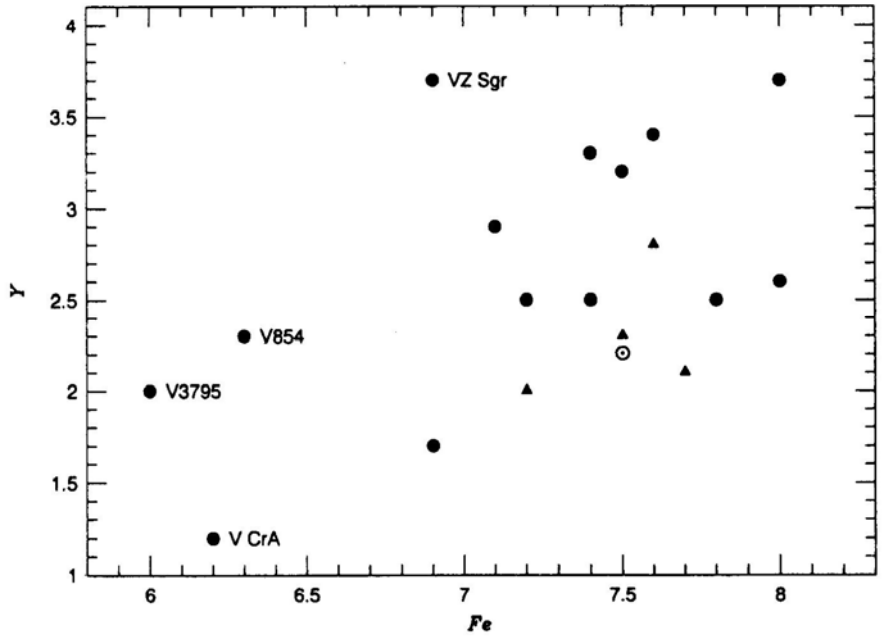

Figure 6. Yttrium and iron abundances of the RCB and EHe stars.See the caption to Fig.3 for the key to the symbols.

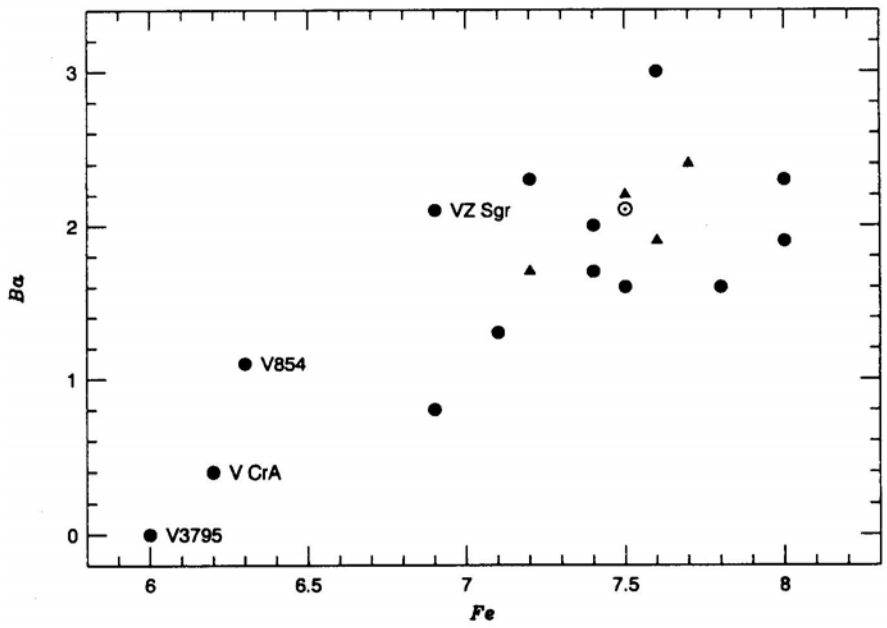

Figure 7. Barium and iron abundances of the RCB and EHe stars.See the caption to Fig.3 for the key to the symbols.

of measurement. There is a hint that the Y/Ba ratio, which also shows a large scatter, declines with increasing metallicity. Unless a systematic error vitiates the analyses, the result that theY/Ba is higher than the solar ratio implies that *s*-processing products in RCBs have been more mildly exposed to the *s*-process than material comprising the solar system.

As putative relatives of the RCBs, it is of interest to note how the compositions of the EHes and the hot RCB DY Cen relate to those of the RCBs.. Where available, the abundances of the EHes and DY Cen have been shown in Figs. 3 through 7. It is apparent that the EHes and DY Cen span the same range in compositions as the RCBs – see, for example, Fig. 5. One striking fact is that none of the 6 EHes appear to have the composition of the majority sample of 14 RCBs. DY Cen, the hot RCB, is the most metal-poor of the combined sample of EHes and RCBs with log ε (Fe) = 5.0 but with abundances of Ne, Mg, Al, Si, P, S, and Ar that are near or above the solar abundances: e.g., [Fe/H] = – 2.5 but [X/H] = + 1.5 (Ne), + 0.6 (Si), and – 0.1 (S). DY Cen may be regarded as an extreme member of the peculiar minority of RCBs.

4. Composition and origins of RCBs

4.1 *Boundary Conditions*

At the beginning of our endeavours, we supposed that a comprehensive abundance analysis (‘mere facts’) would surely lead to novel and thorough insights into the evolutionary history of RCBs (‘the comprehensive truth’).A reading of this section will show that we are far from recognising the comprehensive truth but, perhaps, other minds will discern this truth among our enlarged collection of mere facts.

Prerequisites to our jottings on the origins of the RCBs should be the succinct discussions by Schönberner (1986) and Renzini (1990). Schönberner establishes that He giants such as the RCB and HdCs may be either low mass stars ($0.7 \lesssim M / M_{\odot} \lesssim 2$) burning He in a shell around a C – O electron degenerate core or more massive stars ($2 \lesssim M/M_{\odot} \lesssim 2.7$) burning C in the core or a shell. The latter identification is most probably not a satisfactory one for a majority of RCBs because it implies that the original star was quite massive, a requirement in conflict with the galactic distribution and kinematics of the RCBs. We suppose that most of the RCBs are low mass He/C–O stars.

It is not known whether these low mass stars were created as He main sequence stars or as He-rich supergiants. The former evolve on exhaustion of He in their cores into He-rich supergiants. The supergiants, if the electron-degenerate core has a mass less than $1.4M_{\odot}$, evolve through a phase as an EHe to the top of the white dwarf cooling track. It is as yet impossible to decide observationally whether the RCBs were formed as supergiants or evolved from EHes – see Schönberner (1986). He-rich supergiants with a core mass exceeding the Chandrasekhar mass will explode as a supernova.

Scenarios for the formation of RCBs and EHes must meet two conditions set by observations (Schönberner 1986; Renzini 1990):

- The progenitors must belong to a rather old galactic population, i.e., if the progenitor is a single star, it must be of low mass or if the progenitor is a double star, a slow process of production is required;

- The conversion of the progenitor to a Hdeficient star must provide an envelope that

(α) – retains (or accretes) a small amount of the envelope(s) of the original star(s);
(β) – contains material exposed heavily to the H-burning CN-cycle and possibly the ON-cycles;
(γ) – contains substantial amounts of material exposed to He-burning.

These three conditions (α, β, γ) are based on the results of the abundance analyses conducted prior to our survey. Condition (a) recognizes that H is present in trace amounts in most RCB (and EHes). Condition (β) is imposed because the N abundance is high; N is produced during Hburning, but converted to Ne during He-burning. Condition (γ) is needed to account for the relatively high observed abundance of ^{12}C. Amplification and extension of these conditions is now suggested by our survey. First, Li production must be possible in a proposed evolutionary scenario. Second, a scenario must be devised to account for Fe-poor RCBs and EHes with near-normal abundances of other lighter elements (e.g. Ne, Al, Si, S) commonly lumped with Fe as 'metals': the Si/Fe and S/Fe ratios recorded for the extreme RCBs (i.e., [Si/Fe] $\simeq$ [S/Fe] $\simeq$ 2) have no precedents among H-rich stars of low (or high) metallicity.

4.2 *Is Iron a Metallicity Indicator?*

Metallicity of a star is most commonly identified with the iron abundance which is taken to be Fe/H for a normal star. In the case of the RCBs, it has usually been assumed that the mass fraction of iron is unaltered as normal stars are transformed to RCBs. In the light of the very peculiar elemental abundances of some RCBs and EHes, it seems timely to question whether the low Fe abundances of some stars are indeed the initial Fe abundances of these stars.

Three simple possibilities deserve consideration:

(i) the low Fe abundances result from an underestimate of the C/He ratio;
(ii) the atmospheric compositions have been altered by a diffusive or chemical separation (fractionation) of elements;·
(iii) the atmospheric compositions are primarily the result of the changes wrought by nucleosynthesis.

Hypothesis (i) is surely untenable for two reasons. First, the low Fe abundance of several EHes and the hot RCB DY Cen cannot be attributed to the assumed low C/He ratio because in these cases the C/He ratio is measured explicitly from C II, C III, and He I lines. Second, although the C/He ratio adopted for our analyses of the RCBs could be raised to increase the inferred Fe abundance (see Equation 3), ratios such as Si/Fe would remain highly anomalous and require explanation. Moreover, a very high C/He ratio would be demanded.

Under the umbrella of possibilities represented by (ii), the current favourite is a separation of dust and gas such that present photospheres consist of gas from which condensable elements have been removed in the form of dust grains. This hypothesis was invoked by Venn & Lambert (1990) to explain the unusual compositions of λ Bootis stars (young main sequence stars of type A) and post-AGB stars. (As we discuss below the RCBs are quite possibly a. variety of postAGB stars.) In their discussion

of DY Cen, Jeffery & Heber (1993) allude to removal of iron in the form of dust grains. Unfortunately, the pattern of the elemental abundances is not easily reconciled with that of gas from which dust has removed condensable elements (except in V854 Cen – see below). Certainly, the RCBs are factories for dust grains but one imagines carbon grains and silicon carbide to be the dominant material along with MgS (Sedlmayr 1989 – however the 11.3μm feature attributed to SiC is not present in any RCB spectrum obtained so far). If this is correct and there is exchange of material between the atmosphere and the site of dust formation, silicon will be removed from the atmosphere as the grains are driven out by radiation pressure. But the 'peculiar' RCBs (except V854 Cen) are Si-rich and Fe-poor! If the site of dust-gas separation is made the oxygen-rich atmosphere of an earlier evolutionary stage of the RCB (say, the immediate post-AGB phase), one expects the abundances to reflect the pattern of depletions of elements in interstellar gas (Jenkins 1987,1989) and in very metal-poor post-AGB stars (Bond 1991).

The abundance pattern indicated by one of the stars of the metal poor quartet, V854 Cen does show this aspect of fractionation. The differential abundances with respect to sun (depletions) are shown in Fig. 8 along with the average depletions seen in interstellar medium for hydrogen density of log $n(H_{\rm tot})= -1.5$ (Jenkins 1987). Except for CNO elements, the match of V854 Cen depletions to the ISM depletions is surprisingly good. Sulphur is relatively more depleted (may be locked up in MgS) and Ni is less depleted in V854 Cen than in ISM. Thus there is a strong possibility that the Fe poorness in V854 Cen is due to the grain depletion as seen in some post-AGB stars. However there is little similarity in the remaining three stars of the quartet for such a pattern: for example, the post-AGB stars have a low Si/S ratio and Si and Fe are rather similarly depleted.

By elimination, hypothesis (iii) (or an as-yet unidentified alternative) stands. The most outstanding puzzle in explaining the anomalous abundances of the peculiar RCBs and EHes in terms of nucleosynthesis does not, of course, concern C, N, and O, which may be attributed to H and He burning, but the unusual ratios such as Si/Fe, S/Fe and Ni/Fe. In this regard, we conceive of two extreme possibilities:

– the measured Fe abundance is or is quite similar to the initial abundance but the abundances of Si and other elements have been increased by nucleosynthesis;
– the measured abundances of Si and other elements are approximate indicators of the star's initial composition and the Fe abundance has been drastically lowered by nucleosynthesis.

In principle, iron may be transmuted into heavier elements by neutrons, as in the *s*-process. This seems unlikely to be applicable here because the Y and Ba abundances of the peculiar RCBs are approximately the values initially expected for a star of low Fe abundance not the much higher values expected if Si not Fe is a measure of the initial metallicity. Very severe exposures to neutrons would convert iron-group nuclei to nuclei (Tl, Pb, Bi) at the termination of the *s*process path. Exceptionally mild exposures would process the irongroup nuclei to slightly heavier nuclei (Cu–Br). Since we have as yet not measured the abundances of either these nuclei just above the iron-group or the very heavy nuclei, we cannot definitively eliminate these extreme exposures. But the fact that the Y/Si and Ba/Si ratios are distinctly non-solar would seem to exclude the possibility that a mild exposure has reduced the Fe abundance.

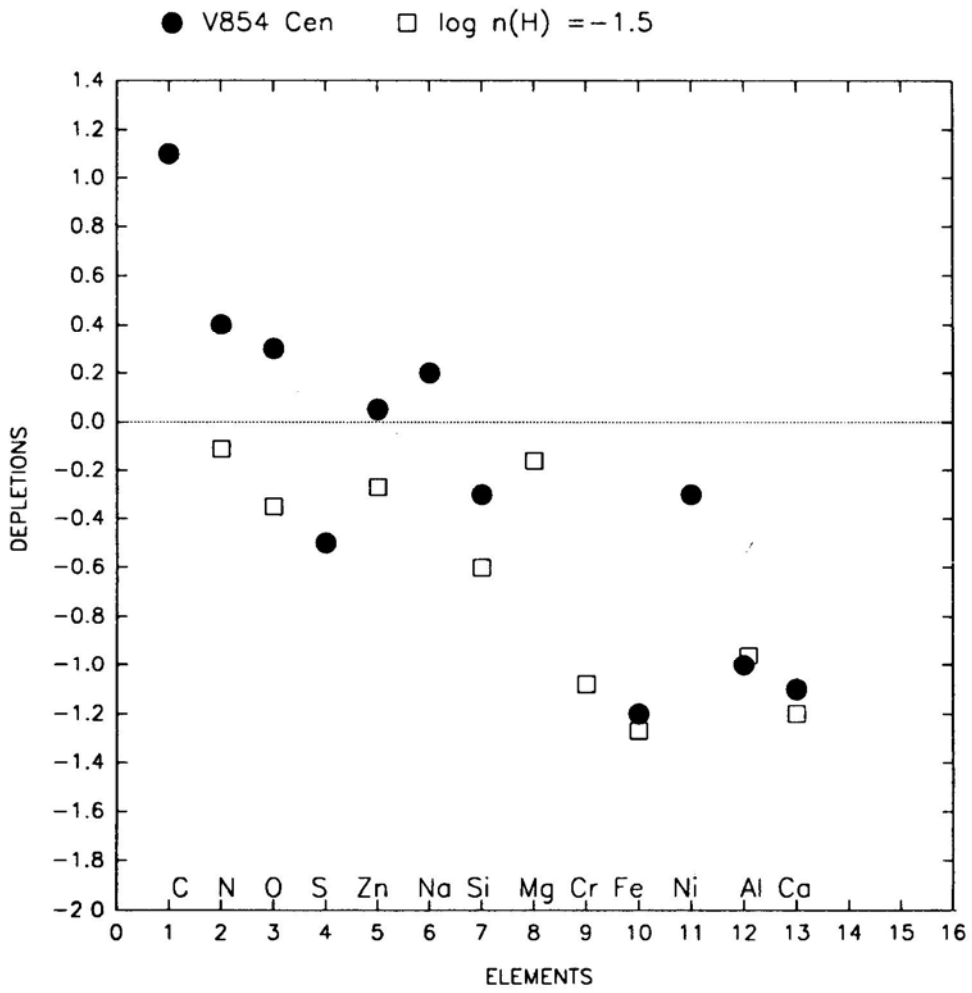

Figure 8. The depletions (w r.t solar abundances) of elements in V854 Cen (dots) are shown along with average ISM depletions for log $n(H_{tot})$ = – 1.5 (open squares). Elements are plotted with increasing amount of depletion from left to right.

4.3 *How Were RCBs Formed?*

Schönberner (1986) provides a concise review of the various proposals to account for these H-deficient stars. His preferred method of RCB production involves the merger of two white dwarfs, as advocated initially by Webbink (1984, see also Iben and Tutukov 1984,1985) and dubbed 'the double degenerate conjecture' (here, DD) by Renzini (1990). Renzini's assessment of evolutionary scenarios leading to RCBs leads him to reject the DD conjecture and to advocate the alternative proposal that the RCB are a class of post-AGB stars that, as white dwarfs, experience a final He-shell flash and are re-inflated briefly to supergiant dimensions (Renzini 1979, 1981; Iben *et al.* 1983). Renzini (1990) dubs this alternative 'the final helium shell flash conjecture' (here, FF). Schönberner (1986) discards the FF conjecture on the grounds that the predicted lifetimes of the RCBs are too short ($\tau \sim 10^2$ yr) with respect to the

inferred pulsational lifetimes of one (or two!) RCBs. Renzini (1990) tentatively discards the DD conjecture favoured by Schönberner because it appears unable to account for the compositions of the RCBs as known in 1990 from analyses of XX Cam, RCrB and RY Sgr; these three are members of our majority class of 14 RCBs. We comment briefly on the DD and FF conjectures. A third conjecture was discussed by Whitney, Soker & Clayton (1991) who devise a binary model leading to a RCB through two episodes of mass transfer and development of a common envelope for the two stars; this model may not be able to explain why the RCBs belong to a rather old galactic population. We should not preclude the possibility that two (or more) evolutionary paths may lead to RCBs. In particular, the majority and minority (peculiar RCBs) classes may be produced in different ways. Separate evolutionary paths from single and double stars to the RCBs could reasonably account for the two classes of RCBs.

Consideration of Table 1 suggests that evolutionary paths responsible for the majority of RCBs should provide for an atmosphere rich in the products of H and He burning with, perhaps, a contribution from the *s*-process. The DD and FF conjectures are broadly designed to meet this requirement. By sharp contrast, if the low Fe abundance of the peculiar RCBs is accepted as the initial abundance, the evolutionary paths must account for the synthesis of considerable amounts of intermediate elements Na–Ca (He, C or O burning?). Neither the DD nor the FF conjecture as presently sketched, account for production of intermediate elements.

The DD conjecture: This supposes that the immediate progenitor of a RCB is a close pair of white dwarfs: a He white dwarf and a C–O white dwarf. The pair is imagined to have evolved from a pair of main sequence stars via mass transfer and a common envelope phase. Emission of gravitational wave radiation forces a merger of the white dwarfs. Accretion of the Herich white dwarf by the C–O white dwarf produces a He-rich supergiant with a lifetime of 10^4–10^5yr. The basic features of the composition of the majority class of RCBs are explained qualitatively as follows:

- Accretion of the lighter He white dwarf by the C–O white dwarf provides an N-rich (also Na and Alrich) He atmosphere;
- A thin layer of unburnt layer of H may reside on the surface of the He white dwarf and this is transferred as an RCB is made;
- As accretion proceeds, shear mixing at the surface of the C–O white dwarf may add C and O to the envelope of the RCB.

Perhaps, it is more difficult to account for the Li-rich RCBs. The DD conjecture matches the observational constraint that RCBs may not be rich in ^{13}C; this constraint is strongest for the HdCs for which ^{12}C/ ^{13}C > 100 (Climenhaga 1960; Fujita & Tsuji 1977). Another problem which crops up for the DD conjecture is that of the metallicity of stars. As questioned by Hill (1986) the period of coalesence by gravitational wave radiation is expected to be long, about 10^{10} years, the stars thus are expected to be generally metal poor contrary to our present finding of solar metallicity to majority of stars. It is also not clear in DD conjecture how to account for the presence of nebulosities seen around several stars as described in section 2. It remains to be shown that the DD conjecture can account for the observed number of galactic RCBs.

The FF conjecture: After severe mass loss, a red giant leaves the AGB to evolve at constant luminosity to the white dwarf cooling track. If the post-AGB star burns H at the base of the thin H star, the H ash increases the mass of the He shell around the C–O core. Then, the He shell may ignite for a final flash when the star is on the

cooling track. Renzini (1990) sketches how this flash may convert the white dwarf to a RCB star. He enlivens his discussion with back-of-the-envelope calculations (and references). The following is a crude summary of the conversion:

- The convective He shell quickly ingests the thin H layer and H is burnt at a temperature of about 10^8 K;
- Energy released by H-burning inflates the mixed thin H–He layer on the white dwarf to a supergiant;
- The energy is stored as gravitational potential energy and subsequently radiated away to return the RCB to the white dwarf cooling track.

Since this supergiant's atmosphere contains products of severe H-burning and of He-burning, the scenario seems a viable way to create H-poor C-rich stars with a high N abundance and an enrichment of Na and Al. Renzini notes that Li production is possible too. The H layer will contain:

^{3}He produced by the main sequence star. Synthesis of ^{7}Li form ^{3}He may occur through the ^{7}Be-transport mechanism (Cameron & Fowler 1971): ^{3}He (α, γ) ^{7}Be(e^+ ν)^7 Li. On the scoreboard for the FF vs DD game, Renzini cites ^{7}Li synthesis as a point in favour of the FF conjecture; ^{7}Li may not be so easily produced by the DD conjecture.

A potential failure of the FF conjecture, according to Renzini, is that the H-burning results in a low ^{12}C/^{13}C ratio for the RCB star. This is in conflict with the observations of RCB and HdC stars. Renzini argues, however, that the ^{13}C nuclei may be largely burnt near the hot base of the He shell. The reaction ^{13}C(α, n)^{16}O destroys ^{13}C and releases neutrons. (The reader is referred to Renzini's discussion for an explanation of how ^{13}C may be destroyed but ^{14}N preserved). The neutrons run an *s*-process in the presence of the poison ^{14}N. If the neutron flux is not very high, Y but not Ba may be produced.

Recall that Schönberner (1986) discarded the FF conjecture on the grounds that the resulting RCB has a very short lifetime. Renzini (1990) argues that the lifetime is acceptably long provided that the post-AGB star has a sufficiently low mass. Potential tests of the FF conjecture are noted by Rerizini: "a large ^{15}N/^{14}N ratio may result" and "the less uncertain prediction of the FF conjecture is that a great deal of star-to-star variations in the surface abundances are instead to be expected". Since the RCBs with a quasi-solar Fe abundance, the majority of 14, show little variation in abundances, should we reject them as products of an FF? On the other hand the presence of nebulae can be easily accounted for (or even expected to be present) in FF conjecture.

As noted earlier, the DD and FF conjectures as presently conceived cannot account for the peculiar RCBs with their high Si/Fe and other ratios. (The majority of RCBs may be mildly enriched in intermediate elements Na–S.) One wonders if He, C or O burning can be made a part of the DD conjecture under some conditions: accretion of the He white dwarf heats the C–O white dwarf to the ignition point? Can ingestion of the H layer into the He shell drive a kind of *rp*-process to synthesis of Na–Ca?

It is to be hoped that more detailed calculations of the predicted compositions resulting from the DD and FF conjectures will be attempted soon.

5. Concluding remarks

A biography of Edgar Allan Poye by Silverman (1991) provided the first author of this review with enjoyment on the long flight to India this summer. In April 1841,

Poe published "a tale of ratiocination" titled 'The Murders in the Rue Morgue'. With this tale, Poe invented the murder mystery as a form of fiction. In earlier publications such as 'The Fall of the House of Usher' Poe had shown his mastery of tales of horror. Unravelling the compositions of the RCBs and tracing the genealogy of these dying stars could be considered the astrophysical equivalent of a murder mystery. We leave the reader to decide whether the story of the RCBs with their highly unusual chemical compositions should be classified as a 'murder mystery' or 'a tale of horror'! Whatever the classification, we hope that the inventory of 'mere facts' is now significantly more complete and that we are closer to 'the comprehensive truth' about these fascinating stars.

We thank our colleagues Dr. Sunetra Giridhar and Mr. Gajendra Pandey for their help with the abundance analyses. David L. Lambert acknowledges the support of the U.S. National Science Foundation (grant AST91–15090) and the Robert A. Welch Foundation. N. K. Rao would like to thank CSIR and NSF(US) for the Indo-US exchange scientist award which enabled his visit to UT, Austin, where part of this work was done.

References

Alexander, J. B., Andrews, P. J., Catchpole, R. M., Feast, M. W., Lloyd Evans, T., Menzies, J. W., Wisse, P. N. J., Wisse, M. 1992, *Mon. Not. R. astr. Soc*, **158**, 305.

Anders, E., Grevesse,N.1989, *Geochim. Cosmochim. Acta*,**53**,197.

Bidelman, W.P.1953, *Astrophys. J.*, **117**, 25.

Bidelman, W.P.1973, *Bull. Am. astr. Soc*, **5**, 442.

Bond, H. E. 1991 in *Evolution of Stars: The Photospheric Abundance Connection*, Ed. G. Michaud & A. Tutukov (Dordrecht: Kluwer) p. 341.

Cameron,A. G. W., Fowler, W.A.1971, *Astrophys. J.*, **164**, 111.

Climenhaga, J. L.1960, *Publ. Dom. astr. Obser.* (*Victoria*),**11**, 307.

Cottrell, R. L, Lawson, W. A., Buchhorn, M. 1990, *Mon. Not. R. astr. Soc*, **244**, 149.

Drilling, J.S.1986, in *Hydrogen Deficient Stars and Related Objects*, Ed. K. Hunger, D.Schönberner & N. K. Rao (Dordrecht: Reidel), p. 9.

Edvardsson, B., Andersen, J., Gustafsson, B., Lambert, D. L., Nissen, P. E., Tomkin, J. 1993, *Astr.Astrophys.*, **275**, 101.

Feast, M. W.1979, in Changing trends in variable star research, IAU Coll. **46**, Ed. F. M. Bateson p. 246.

Feast, M.W.1986, in *Hydrogen Deficient Stars and Related Objects*, Ed.K.Hunger, D.Schönberner & N. K. Rao (Dordrecht: Reidel), p. 151.

Feast, M. W.1990, *ASP Conf. Ser. 11.*, p. 538.

Feast, M. W., Catchpole, R. M., Lloyd Evans, T., Robertson, B. S. C, Dean, J. F., Bywater, R. A. 1977, *Mon. Not. R. astr. Soc*, **178**, 4117.

Fujita, Y.,Tsuji, T.1977, *Publ. astr. Soc. Japan*, **29**, 711.

Gillett, F. C, Backman, D. E., Beichman, C, Neugebauer, G. 1986, *Astrophys. J.*, **310**, 842.

Giridhar, S., Rao, N. K., Lambert, D. L.1990, *J. Astrophys. Astr.*, **13**, 307.

Grevesse, N., Noels, A. 1993 in *Origin and Evolution of the Elements* Ed. N. Prantzos, E. Vangioni-Flam & M. Casse (Cambridge Univ. Press) p. 15.

Hazard, C, Terlevich, R. J., Morton, D. C, Sargent, W. L. W., Ferland, G. 1980, *Nature*, **285**, 463.

Heber, U.1986, in *Hydrogen Deficient Stars and Related Objects*, Ed. K. Hunger, D. Schönberner & N. K. Rao (Dordrecht: Reidel), p. 33.

Herbig, G. H.1949, *Astrophys. J.*, **110**, 143.

Herbig, G. H.1958, *Astrophys. J.*, **127**, 312.

Herbig, G.H.1968, *Mem. Soc. R.Sci., Liege*, **17**, 353.

Herbig, G. H. 1990, (private communication).

Hill, P. W.1986, in *Hydrogen Deficient Stars and Related Objects*, Ed. K.Hunger, D.Schönberner & N. K. Rao (Dordrecht: Reidel) p. 481.

Howarth, I. D. 1976, *Publ. Var. Star Sec. R. astr. Soc. NZ.* No **44**.
Howarth, I. D. 1977, *Acta astr.*, **27**, 65.
Iben, I. Jr., Kaler, J. B., Truran, J. W., Renzini, A. 1983, *Astrophys. J.*, **264**, 605.
Iben, I. Jr., Tutukov, A. V. 1984, *Astrophys. J. Suppl.*, **54**, 335.
Iben, I. Jr., Tutukov, A. V. 1985 *Astrophys. J. Suppl.*, **58**, 661.
Jacoby, G. H., Ford, H. C. 1983, *Astrophys. J.*, **266**, 298.
Jeffery, C. S., Heber, U. 1993, *Astr. Astrophys.*, **270**, 167.
Jeffery, C. S., Heber, U., Hill, P. W., Pollacco, D. 1988, *Mon. Not. R. astr. Soc.*, 231, 175.
Jenkins, E. B. 1987, in *Interstellar Processes*, Ed. D. J. Hollenbach & H. A. Thronson, Jr. (Dordrecht: Reidel), p. 533.
Jenkins, E. B. 1989, in *Interstellar Dust*, Ed. L. J. Allamandola & A. G. G. M. Tielens (Dordrecht: Kluwer), p. 23.
Juresik, J. 1993, *Acta astr.*, (in press).
Keenan, P. C., Greenstein, J. L. 1963, *Contrib. Penkins Obs.*, **2**, 13.
Kilkenny, D. 1982, *Mon. Not. R. astr. Soc.*, **200** 1019.
Kilkenny, D., Lloyd Evans, T., Bateson, F. M., Jones, A. F., Lawson, W. A. 1992, *Observatory*, **112**, 158.
Kilkenny, D., Westerhuys, J. E. 1990, *Observatory*, **110,** 90.
Kipper, T., Kipper, M. 1993, *Astr. Astrophys.*, **276**, 389.
Lambert, D. L. 1986, in *Hydrogen Deficient Stars and Related Objects*, Ed. K. Hunger, D. Schönberner & N. K. Rao (Dordrecht: Reidel), p. 127.
Lambert, D. L., Rao, N. K., Giridhar, S. 1990 *J. Astrophys. Astr.*, **11,** 475.
Lawson, W. A., Cottrell, P. L. 1990, *ASP Conf. Ser. 11*, p. 566.
Lawson, W. A., Cottrell, P. L., Gilmore, A. C., Kilmartin, P. M. 1992 *Mon. Not. R. astr. Soc.*, **256**, 339.
Lawson, W. A., Cottrell, P. L., Kilmartin, P. M., Gilmore, A. C. 1990, *Mon. Not. R. astr. Soc.*, **247**, 91.
Lloyd Evans, T., Kilkenny, D., van Wyk, F. 1991, *Observatory*, **111,** 244.
Marraco, H. G., Milesi, G. E. 1982, *Astr. J.* **87**, 1775.
McNaught, R. H., Dawes, G. 1986, *IAU Circ.*, 4233.
Pandey, G., Rao, N. K., Lambert, D. L. 1993, *Proc. Asia Pacific regional IAU meeting*, (in press).
Payne-Gaposchkin, C. 1963, *Astrophys. J.*, **138**, 320.
Pollacco, D. L., Hill, P. W., Houziaux, L., Manfroid, J. 1991, *Mon. Not. R. astr. Soc.*, **248**, 1p
Pollacco, D. L., Lawson, W. A., Clegg, R. E. S., Hill, P. W. 1992, *Mon. Not. R. astr. Soc.*, **257,** p. 33.
Pollacco, D. L., Tadhunter, C. N., Hill, P. W. 1990, *Mon. Not. R. astr. Soc.*, **245,** 204.
Rao, N. K., Ashok, N. M., Kulkarni, P. V. 1980, *J. Astrophys. Astr.*, **1,** 71.
Rao, N. K., Giridhar, S., Lambert, D. L. 1993, *Astr. Astrophys.*, **280,** 201.
Rao, N. K., Houziaux, L., Giridhar, S. 1990, *J. Astrophys. Astr.*, **10,** 89.
Rao, N. K., Lambert, D. L. 1993a, *Publ. astr. Soc. Pacific*, **105,** 574.
Rao, N. K., Lambert, D. L. 1993b, *Astr. J.*, **105,** 1915.
Rao, N. K., Lambert, D. L. 1993c, *Mon. Not. R. astr. Soc.*, **263,** L27.
Rao, N. K., Nandy, K. 1986, *Mon. Not. R. astr. Soc.*, **222**, 357.
Rao, N. K., Raveendran, A. V. 1993, *Astr. Astrophys.*, **274,** 330.
Renzini, A. 1979, in *Stars and* Star *Systems*, Ed. B. E. Westerlund (Dordrecht: Reidel), p. 155.
Renzini, A. 1981, in *Effects of Mass Loss on Stellar Evolution*, Ed. C. Chiosi & R. Stalio (Dordrecht: Reidel), p. 319.
Renzini, A. 1990, *ASP Conf. Ser. 11*, p. 549.
Schönberner, D. 1975, *Astr. Astrophys.*, **44**, 381.
Schönberner, D. 1986, in *Hydrogen Deficient Stars and Related Objects*, Ed. K. Hunger, D. Schönberner & N. K. Rao (Dordrecht: Reidel), p. 33.
Sedlmayr, E. 1989, in *Interstellar Dust*, Ed. L. J. Allamandala & A. G. G. M. Tielens (Dordrecht: Kluwer), p. 467.
Silverman, K. 1991, Edgar A. Poe: *Mournful and Never-ending Remembrance* (New York: Harper-Collins).
Smith, V. V., Lambert, D. L. 1989, *Astrophys. J.*, **345,** L75.
Smith, V. V., Lambert, D. L. 1990, *Astrophys. J.*, **361,** L59.
Sneden, C. 1973, *Ph. D. Dissertation*, Univ. of Texas.

Stanford, S. A., Clayton, G. C, Mead, M. R., Nordsieck, K. H., Whitney, B. A., Murison, M. A., Nook, M. A., Anderson, C. M. 1988, *Astrophys. J.*, **325**, L9.
Sterne, T, E. 1935, *Harvard Bull*., **896**, 17.
Venn, K., Lambert, D. L. 1990, *Astrophys. J.*, **363**, 234.
Walker, H. J. 1986, in *Hydrogen Deficient Stars and Related Objects*, Ed. K. Hunger, D. Schönberner & N. K. Rao (Dordrecht: Reidel), p. 407.
Warner, B. 1967, *Mon. Not R. astr. Soc*, **137**, 119.
Webbink, R. F. 1984, *Astrophys. J.*, **277**, 355.
Whitney, B. A., Clayton, G. C, Schulte-Ladbeck, R. E., Mead, M. R. 1992, *Astr. J.*, **103**,1652.
Whitney, B. A., Soker, N., Clayton, G. C. 1991, *Astr. J.* **102,** 284.

J. Astrophys. Astr. (1994) **15,** 69–83

The Spatial Distribution of Pulsars and the Spiral Structure of the Galaxy

R. Ramachandran & A. A. Deshpande *Raman Research Institute, Bangalore 560 080*

Received 1993 November 23; accepted 1994 February 22

Abstract. We have looked for and found a possible spatial correlation between the present pulsar distribution and the estimated locations of the spiral arms at earlier epochs. Through a detailed statistical analysis we find a significant correlation between the present distribution of pulsars and the mass distribution (in the spiral arms) expected about 60 Myr ago for a corotation resonance radius of 14kpc. We discuss the implications of this correlation for the minimum mass of the progenitors of pulsars. Interpreting the spread in the locations of pulsars with respect to the past locations of the spiral arms as predominantly due to their space velocities, we derive an average velocity for the pulsar population.

Key words: Pulsars: velocities—galaxy: structure, dynamics—stars: end states.

Introduction

Ever since their discovery, pulsars have been the subject of many statistical studies. However, the importance of the connection between their birth places and the locations of spiral arms was not emphasized until the work of Blaauw (1985). From a detailed consideration Blaauw argued that the local birthrate of pulsars should equal the local deathrate of massive stars. He found that the regions of active star formation, the OB associations, contribute only a small fraction (~ 15%) of the local birthrate of pulsars; most of the pulsars come from the field population of 6–10$M_{\odot}$ stars. Hence, one of his conclusions was that *pulsars are*, *on the Galactic scale*, *tracers of regions of past spiral structure* (*20–50 Myr ago*) *rather than of 'active' spiral structure.* If this is true, one should find a spatial correlation between the global distribution of pulsars and the location of spiral arms in the past. Such a correlation may be reduced considerably if their progenitors and later pulsars move from their birth places by distances comparable to the interarm spacing. But if a correlation is found despite these effects, then it can provide a significant constraint on the velocity distribution of pulsars. In this paper, we have attempted to look for a possible spatial correlation of the 'global' pulsar distribution with the expected locations of the spiral arms at different epochs. A recent model of electron density distribution due to Taylor & Cordes (1993) is used to obtain more reliable distance estimates to pulsars from their dispersion measures. Fig. 1 shows the 'observed' pulsar distribution based on this model superimposed on the model electron density distribution. The true dis-

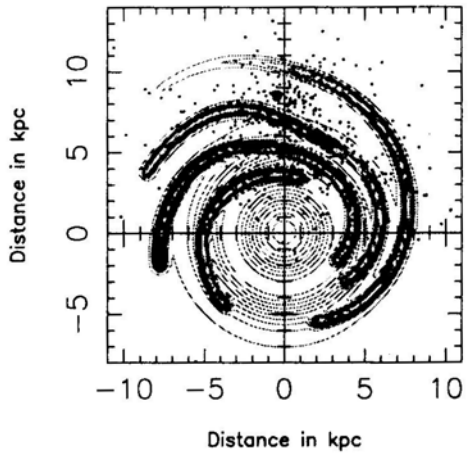

Figure 1. The new electron density distribution model of Taylor & Cordes (1993). Projected locations of all known pulsars are plotted as dots. Sun is at (0,8.5).

tribution can be obtained from this after accounting for the selection effects. Section 2 describes the method we have adopted to estimate the selection factors *as a function of position in the Galaxy*. The method of evaluating the correlation between the Galactic distribution of pulsars and the spiral pattern is discussed in section 3. We use a value of 14 kpc for the Galactic *corotation resonance radius* (following Burton 1971); this is needed to define the angular velocity of the spiral pattern. We argue that the present Galactic pulsar distribution of pulsars can be well correlated with the mass distribution in the spiral pattern about 60 Myr ago. In this section we also discuss the implications of this result for the minimum mass of pulsar progenitors. Our analysis shows that the minimum mass of the progenitors of pulsars may be as low as 7 $M_{\odot}$.

In section 4 we examine the *spread* in the locations of pulsars with respect to the past locations of the spiral arms and discuss possible explanations for it. By attributing this spread primarily to pulsar velocities and after allowing for the distance uncertainties, we obtain an estimate for the average velocity of pulsars.

2. Selection effects

The observed distribution of pulsars shown in Fig. 1 is expected to deviate systematically from the real distribution due to various selection effects which make detection of radio pulsars difficult. The detectability is affected by both the luminosity of the pulsar and the pulsed nature of the emission. The interstellar scattering and dispersion result in the broadening of the observed pulses reducing the peak pulsed flux. The effect of such factors can be readily seen in Fig. 2, where the distribution of minimum distances ($d_{\rm min}$) from the nearest arm to the pulsars is plotted. The value of $d_{\rm min}$ is taken to be positive when it is from that side of the arm which is nearer to the sun and as negative otherwise. One would expect this distribution to be roughly symmetric if the probability of detection were uniform over the Galaxy. In reality, the probability of detection reduces with increasing distance from the Sun. Hence, pulsars closer to the Sun (which are assigned + ve $d_{\rm min}$ values) tend to skew the distribution of minimum

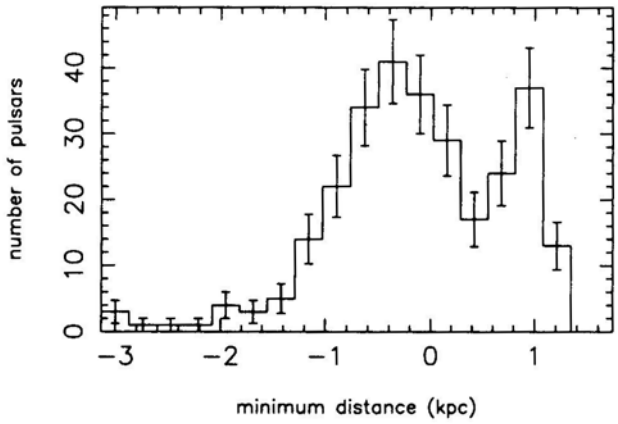

Figure 2. Distribution of minimum distances ($d_{\min}$) of pulsars to the nearest spiral arms. The value of $d_{\min}$ is taken as positive when it is from that side of an arm which is nearer to the sun and as negative otherwise. The peak at 0.9 kpc is identified to be due to the pulsars in the solar neighbourhood. Error bars indicate 1σ deviation on either side.

distances. The feature at $d_{\min} \approx 0{\cdot}9$ kpc can be attributed to the bias caused by the pulsars close to the Sun. The asymmetry seen in the observed distribution of $d_{\min}$ clearly stresses the need for compensation of selection effects. We give below the procedure we have adopted to compute the scale factors $S(R, z, \phi)$ (ratio of the total number to the number observed) to compensate for the selection effects as a function of the position in the Galaxy.

In the discussion to follow, our sample of pulsars is restricted only to those which in principle could have been detected by any one of eight of the major pulsar surveys namely, (1) Jodrell, (2) U. Mass–Arecibo, (3) Second Molonglo, (4) U. Mass–NRAO, (5) Princeton–NRAO phase 1, (6) Princeton–NRAO phase 2, (7) Princeton–Arecibo and (8) Jodrell-1400 MHz. Of the 570 pulsars known to data, only 325 pulsars satisfy the above mentioned selection criterion. The globular cluster pulsars, extragalactic pulsars and the millisecond pulsars are not included in this analysis.

2.1 *Scale Factors as a Function of the Position in the Galaxy*

A complete treatment of modelling various selection effects is given in Narayan (1987) (see also Bhattacharya *et al.* 1992 and Lorimer *et al.* 1993). The parameters which go into the determination of selection effects are (1) regions covered by the pulsar surveys, (2) their sampling rates and sensitivities, (3) scattering and dispersion smearing of the pulse profiles, and (4) the luminosity function of pulsars. The procedure we have used to determine the scale factors as a function of position in the Galaxy may be described as follows.

First, the scale factor as a function of pulsar period and luminosity $S(P, L)$ are estimated as (Narayan 1987),

$$S(P, L) \equiv \frac{\int\int \rho_R(R)\rho_z(z) R \, \mathrm{d}R \, \mathrm{d}\phi \, \mathrm{d}z}{\int\int_{\mathrm{obs}} \rho_R(R)\rho_z(z) R \, \mathrm{d}R \, \mathrm{d}\phi \, \mathrm{d}z} \tag{1}$$

here R is the galactocentric radius, z is the distance from the Galactic plane, P is the rotation period of the pulsar and $\dot{P}$ is its time derivative and L is the luminosity of the pulsar. The function ρ describes the distribution of pulsars with respect to the corresponding variable in the bracket. Here, the integral in the numerator is over the whole Galaxy and the integral in the denominator is over only those parts of the Galaxy where a pulsar of period P and luminosity L can be detected by at least one of the eight surveys included in our analysis. We have computed this scale factor as a function of P and L by doing a Monte Carlo simulation. A detailed description of the estimation of such scale factors can be found in Narayan (1987). For the computation of dispersion and scattering smearing we used the new electron density distribution model of Taylor & Cordes (1993).

A luminosity relation as a function of P and B then enables one to evaluate S (P, B) from S (P, L) where B is the magnetic field of the pulsar (see Narayan & Ostriker 1990; Prozynski & Przybycien, 1984 for the luminosity relation). We also take into account the dispersion of luminosity around the model luminosity as suggested by Narayan & Ostriker (1990).

Since the scale factor is the ratio of the *'true'* number of pulsars to the number of known pulsars, the true number of pulsars in a bin of width ΔP around the period P and ΔB around the field B can be given by

$$N_{\rm real}(P,B) = \sum_{i=1}^{n_{\rm psr}} S_i(P,B) \tag{2}$$

where $n_{\rm psr}$ is the number of known pulsars in that bin. We have used the usual relation $B^2 \propto P\dot{P}$. Although we have defined the number distribution as a function of (P, B),one could also define it as a function of (P, $\dot{P}$) (see Srinivasan 1991; Deshpande *et al.* 1994). Fig. 3 shows the expected distribution of the 'true' number of pulsars as a function of P and B, which we use to compute the scale factor $S(R, \phi, z)$ as a function of the location in the Galaxy (where R, ϕ and z are galactocentric radius, azimuth

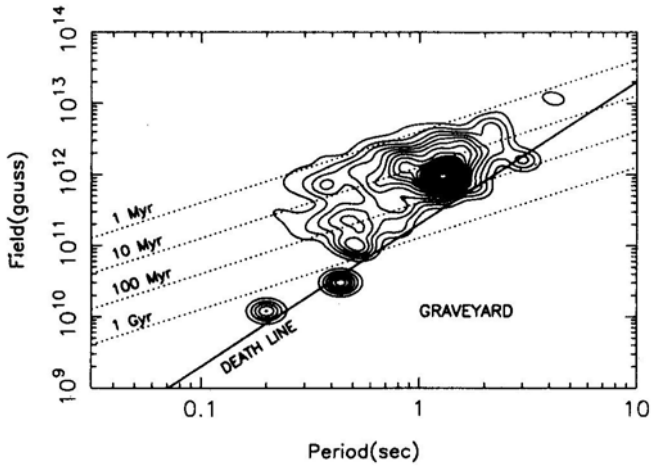

Figure 3. A contour representation of the distribution of 'true' number of pulsars as a function of pulsar period and magnetic field.The constant characteristic age lines corresponding to 1 Myr, l0 Myr, 100 Myr,and 1 Gyr are also plotted.(From Deshpande *et al*. 1994. Reproduced by permission).

angle and the height from the plane, respectively) in the Galaxy. Given the location of a pulsar in the Galaxy (from the selected sample) we populate that location with pulsars of various periods and magnetic fields with weightage given by equation (2). Then the ratio of the total number of pulsars projected to be at that location and the number of pulsars detectable by at least one of the eight surveys used in our analysis can be taken as the *scale factor corresponding to that location.* In our case, because we are primarily interested in the projected distribution in the Galactic plane, the z dependence was averaged over as given below.

$$S(R,\phi) = \alpha\left[\int_{-Z_{max}}^{Z_{max}} \frac{\exp(-|z|/Z_0)}{S(R,z,\phi)}\mathrm{d}z\right]^{-1} \tag{3}$$

where, $\alpha = \int_{-Z_{max}}^{Z_{max}} \exp(-|z|/Z_0)\mathrm{d}z$, Z_{max} and Z_0 are taken to be 2·5 kpc and 0·45 kpc, respectively. The scale factors, $S(R,\mathrm{f})$, computed for our sample range between 1 and ~ 6000 with 90% of the sample having scale factors less than 500. The large values of the scale factors can be in error by a large factor as in such cases the pulsars are situated most often in the inner region of the Galaxy where modelling of the selection effects is not very satisfactory. Also, if only a small fraction of the sample has a very wide tail in the scale factor distribution, then that fraction would dominate in the analysis and result in poor statistics. Hence, we have excluded about 10% of our sample of pulsars (those with scale factors > 500) from the sample used for rest of the analysis presented in this paper. This automatically excludes the pulsars within a radius of 4 kpc from the Galactic centre, this is also the region where the spiral arms are poorly defined.

3. Correlation between the pulsar distribution and the spiral arms

The relative galactocentric angular motion between the matter in the Galaxy and the spiral density wave pattern in a given time t can be given by (see Lin *et al.* 1969),

$$\beta(t,R) = V_{rot}\left(\frac{1}{R} - \frac{1}{R_c}\right)t \tag{4}$$

where V_{rot} is the velocity in the model of the Galaxy with a flat rotation curve (we assume the IAU recommended value of 225 km/sec. See Kerr & Lynden-Bell 1986) and R_c is the corotation resonance radius of the Galaxy. At this radius, circular velocity of the spiral pattern and the circular velocity of the matter around the centre of the Galaxy are equal. Matter leads the spiral pattern inside the corotation radius, and will lag behind outside. This relation enables us to find out the distribution of the pulsar population relative to the spiral arms at any given epoch (present epoch being taken as the reference). If pulsars had no space velocities, then their present positions should correlate with the mass distribution at the epoch of the formation of their progenitors. This correlation is, however, expected to be smeared due to: (1) The spread of the birth places of the progenitors, and (2) The velocity of the progenitors. But the star forming regions are expected to be confined within a belt along the spiral arms of width ≈ 100 pc. As the progenitors have typical velocities of about 15 km/sec (see Gies & Bolton 1986; Lequeux 1979), this would cause a

smearing of few hundreds of parsecs in space. Indeed, if one can establish that the present distribution traces the location of the spiral arms at a past epoch, then it should give us useful constraints on the parameters related to the above effects.

Before proceeding further, for convenience we make a provisional assumption that the mass distribution in the spiral pattern is adequately described by the 'arm component' of the electron distribution model of Taylor & Cordes (1993). As this electron density model is based on the observations of Giant HII regions (see Taylor & Cordes 1993; Georgelin & Georgelin 1976; Caswell & Haynes 1987 for details), we consider our assumption reasonable. Our second assumption is about the value of the corotation radius (R_c) which gives a normalization for the rotation rate of the spiral pattern. We have assumed a value of 14 kpc for the R_c since this seems to fit the HI data rather well (Burton 1971). As we will see in one of the following sections (section 3.2), this value for the corotation radius is quite reasonable. Given these assumptions, we define $C(t)$ a measure of the correlation between the pulsar distribution in the Galaxy and the spiral pattern by,

$$C(t) = \frac{\sum_{i=1}^{N_{psr}} S(R_i, \phi_i) n(R_i, \phi_i - \beta(t, R_i))}{\sum_{i=1}^{N_{psr}} S(R_i, \phi_i)} \tag{5}$$

where, n is the mass density at the extrapolated location of i^{th} pulsar and $S(R_i, \phi_i)$ is the corresponding scale factor. The mass distribution perpendicular to the arm in this model is gaussian with σ = 0·3 kpc and the width of the arm is restricted to 3σ on either side. This correlation is computed for a given relative epoch and corotation resonance radius, by rotating the pulsar distribution relative to the spiral pattern as per equation (4). The variation of the correlation as a function of the relative epoch for an assumed value of 14 kpc for the corotation resonance radius is shown in Fig. 4. *This plot shows a peak correlation at an epoch corresponding to about 60 Myr ago* accompanied by another peak around the present epoch. It is the correlation at

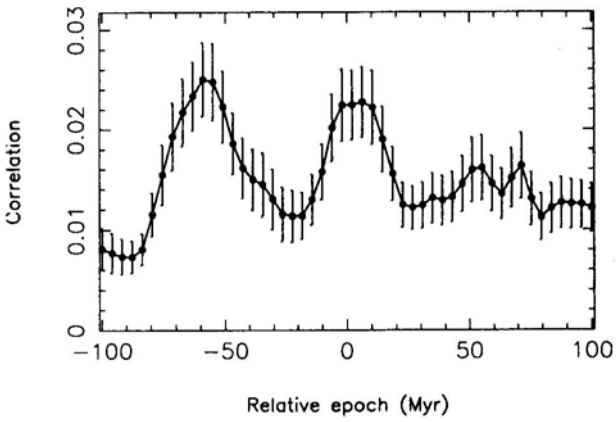

Figure 4. Plot of the correlation of the mass distribution in the spiral pattern at various epochs with the present pulsar distribution.This plot corresponds to a corotation resonance radius of 14kps.The error bars indicate 1σ derivation on either side.The locations of the peaks of the correlation correspond to an epoch which is 60 Myr ago and the present epoch.

– 60 Myr that we wish to identify as being associated with the past positions of the spiral pattern traced by the present distribution of the pulsars. We will discuss in section 5 some possible causes for the secondary peak in the correlation at the present epoch.

We have excluded from the above analysis pulsars with magnetic fields in the range $10^{10} < B < 10^{11.5}$ gauss as they have been tentatively identified as a separate population of recycled pulsars from intermediate mass binary systems (Deshpande *et al.* 1994). The correlation peaks seen in Fig. 4 are not affected even if these pulsars are included.

3.1 *Significance of the Correlation Maximum*

To test the significance of the above mentioned correlation maxima we adopted the following procedure: (1) Every pulsar was randomly assigned the longitude of some other pulsar, keeping their original distances the same, (2) Scale factors corresponding to their new positions in the Galaxy were computed, (3) This new set of parameters were used to compute the correlation as a function, of the relative epoch (using equation 5) and the value of the maximum correlation was noted.

The above mentioned procedure (step (1) to step (3)) was repeated thirty thousand times. Then, from the distribution of maxima of correlations, we find that the maximum found at the relative epoch of – 60 Myr with the original data (in Fig. 4) has a significance of 99·95%.

After scrambling the longitudes, a further test was made by also varying the distances by about 30% (rms), which showed an even higher significance for the correlation maximum found at – 60 Myr.

The significance of the correlation feature around the present epoch (0 Myr) was also tested in a similar manner but with maxima searched over an epoch range of – 25 Myr to 25 Myr. The significance of this feature is found to be only 93·3% which is rather poor.

3.2 *Resonance Radii of the Galaxy*

As mentioned earlier, Fig. 4 shows a peak correlation for a corotation radius (R_c) of 14 kpc and an epoch corresponding to about 60 Myr ago. We have repeated the correlation analysis for various values of the corotation radius. We find that our sample being mostly confined within a radius of 13 kpc from the Galactic centre is, naturally, not very sensitive to variations in the corotation radius beyond about 12 kpc. However, when the value of R_c is reduced below 12 kpc, the correlation peak (at – 60 Myr) broadens and shifts rapidly to earlier epochs disappearing completely for R_c below about l0 kpc. This is consistent with the observations of external galaxies where in all cases the pattern is found to be trailing the gas as far as the matter can be seen.

The resonance radii (Inner and Outer Lindblad resonance radii and the corotation resonance radius) play a central role in the study of spiral patterns and bars in galaxies. The relation between the resonance radii is as given below (see Binney & Tremaine 1987).

$$\omega_{\mathrm{ILR}} = \omega_p + \kappa/2; \qquad \omega_{\mathrm{OLR}} = \omega_p - \kappa/2 \tag{6}$$

Here, ω_p is the spiral pattern angular velocity, κ is the epicyclic frequency, $\omega_{\rm ILR}$ is the angular velocity corresponding to the inner Lindblad resonance and $\omega_{\rm OLR}$ is the angular velocity corresponding to the outer Lindblad resonance. For a flat rotation curve, ($\kappa = \sqrt{2}\omega$). Thus, for a given value of the corotation radius R_c, the inner and the outer Lindblad resonance radii would be about 0.3 R_c, and 1.7 R_c, respectively. Since there is clear evidence of spiral arms beyond ~ 4 kpc, the inner Lindblad resonance radius is unlikely to be larger than this. This would suggest a value for the corotation radius $\leqslant$ 13 kpc, consistent with what we find from our analysis viz. $12 \leqslant R_c \leqslant 15$ kpc. Thus, our estimate for the inner and outer Lindblad resonance radii are in the range 3.5–4.5 kpc, and 21–25 kpc, respectively. (We wish to mention in passing that Mulder & Liem (1986) estimate R_c, to be ~ 8.5 kpc from their global gas dynamical model.)

3.3 *Minimum Mass for Neutron Star Formation*

In his paper Blaauw (1985) restricted himself to the observed sample of pulsars whose distances from the sun projected on to the plane of the Galaxy are within 0.5 kpc. After calculating the deathrate of massive OB stars in the OB associations in the solar neighbourhood, he arrived at the conclusion that the local pulsar population cannot be replenished by the OB associations alone. The field stars must therefore make significant contribution. While trying to match the local pulsar birthrate with the local deathrate of massive stars, he concludes that the overwhelming majority of the pulsar progenitors should correspond to relatively less massive stars (in the range 6–10 $M_\odot$). Based on more limited data Gunn & Ostriker (1970) had also come to the conclusion that the estimated pulsar birthrate implied relatively low mass for their progenitors. If this is true, then since the less massive stars live longer, an equally important corollary is that 'pulsars, on the Galactic scale, are tracers of past spiral structure (20–50 Myr ago) rather than of active spiral structure' (Blaauw 1985).

Our correlation analysis confirms this prescient conjecture. As can be seen from our correlation curve in Fig. 4, the correlation peaks at ≈ -60 Myr. This means that the epoch of the formation of stars which gave birth to most of the present population of pulsars was $\approx$ 60 Myr ago. To a first approximation this timescale is the sum of the lifetime of the progenitors of pulsars and the average age of the present population of pulsars. We estimate the average age of pulsars in the present sample as follows,

$$\langle \tau \rangle = \frac{\sum_{i=1}^{N'_{\rm psr}} S_i(R,\phi)\tau_i}{\sum_{i=1}^{N'_{\rm psr}} S_i(R,\phi)} \qquad (7)$$

Here, τ_i is the characteristic age (defined as $P/2\dot{P}$) of i^{th} pulsar and $S_i(R,\phi)$ is the corresponding scale factor. $N'_{\rm psr}$ is the number of pulsars confined to the regions where the model mass density is non-zero at the relative epoch of – 60 Myr. This average age($\langle \tau \rangle$) turns out to be 10 ± 2 Myr. Therefore, the average lifetime of the progenitors is about 50 Myr, which would correspond to an 7 $M_\odot$ star (see Schaller *et al.* 1992). So, all stars with masses greater than about 7 $M_\odot$ should end up as neutron stars. We will discuss this conclusion in greater detail in section 5.

It is worth mentioning here that when we selected pulsars in different average age

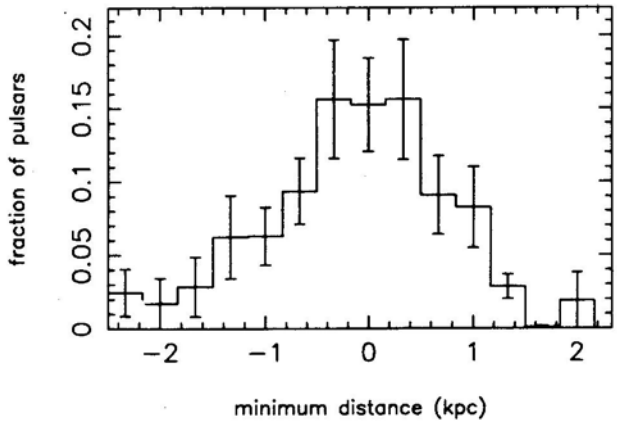

Figure 5. Distribution of $d_{\min}$ after compensating for the selection effects. Y-axis gives the *true* number of pulsars (after scaling the observed number of pulsars by appropriate scale factors as a function of position in the Galaxy). This distribution is produced after *rotating* the Galaxy by – 60Myr. The error bars indicate 1s deviation on either side.

ranges, the correlation peak (corresponding to the past epoch) was seen to shift systematically implying a roughly constant value for the lifetime of the progenitor stars.

3.4 *Modified* $d_{\min}$ *Distribution*

As mentioned earlier, the scale factor is the ratio of the *true* number of pulsars in the Galaxy to the observed number. If the Galaxy is rotated back to the epoch (– 60Myr) where the correlation is maximum, one expects to find the distribution of $d_{\min}$ with respect to the scale factors S (R,ϕ) symmetric and centred around zero $d_{\min}$. This is one of the necessary conditions to check the estimation of scale factors. Fig. 5 shows this distribution after rotating the Galaxy back in time corresponding to – 60Myr. This distribution is reasonably symmetric in contrast to Fig. 2. We have also confirmed that this modified $d_{\min}$ distribution is more compact and symmetric than similar distributions computed for various other epochs.

4. Space velocities of pulsars

As explained in the last section, after correcting for the selection effects we get a symmetric compact number distribution as a function of $d_{\min}$. If we assume the space velocities of pulsars as the prime factor causing the spread seen in the $d_{\min}$ distribution, it is possible to estimate some useful quantities related to these velocities.

For this purpose, we selected a subset of our sample that contributes to the peak of the correlation in Fig. 4. This subset therefore confines $|d_{\min}|$ to $\leqslant 0{\cdot}9$ kpc (as only in this $d_{\min}$ range the model mass density is assumed to be non-zero), and characteristic age τ_{ch} less than l0Myr. Also, while deriving the velocity distribution, we have neglected the pulsars with log B < 11.5 as they would introduce a systematic bias towards low velocities. It can be argued that most of the pulsars with fields in the

range $10^{10-11.5}$ are recycled pulsars from wide binaries which are expected to have low velocities (Bailes 1989; Deshpande et al. 1994). For each pulsar thus selected, a *projected velocity* can be computed by dividing its $d_{\min,}$ value by its characteristic age.

The connection between the *projected velocity* distribution and the real velocity distribution involves the following arguments. If pulsars are distributed following a real velocity distribution $P(v)$ and evolved for a fixed age τ, the number of pulsars in a unit volume at a distance $(v\tau)$ is simply proportional to $P(v)/(v\tau)^2$. Pulsars in a shell of radius $(v_0\tau)$ contribute uniformly to all *projected velocities in* the range zero to $v_{0.}$ In general, the distribution of *projected velocities* (v_p) *can* be expressed as,

$$P_p(v_p) \propto \int_{v_p}^{\infty} \frac{P(v)}{v} dv \tag{8}$$

It is worth noting that as v_p is defined in the plane of the Galaxy, the above procedure is unaffected by the height of the birth places above the plane and by accelerations normal to the plane.

4.1 *Accounting for Distance Uncertainties*

Before one uses the $d_{\min,}$ distribution to deduce a velocity distribution it is important to assess the effect of uncertainties in the assumed distances to pulsars on the estimation of $d_{\min}$. Taylor & Cordes (1993), whose electron density model forms the basis of our distance estimation, have shown that in most cases the uncertainty in distance is < 25%. If the range of $d_{\min}$ values is comparable to the errors in the distance to pulsars from the sun, then the conclusions derived regarding the velocities of pulsars would be seriously affected (we thank J. P. Ostriker for pointing this out).

In order to independently assess the magnitude of the distance uncertainties relevant to the samples used in the present analysis, we have used the following procedure.

We add x% error to the distances and compute a distribution of maximum correlation (C) by a Monte Carlo simulation. For x small compared to the intrinsic error x_0, this should make little difference and the computed distribution will be highly peaked around C_0 (the maximum correlation in Fig. 4). For x large compared to the intrinsic error x_0, our ensemble will behave like the one in which the *true* distances have errors $x \gg x_{0.}$ In this case the correlations C will be typically smaller than C_0 implying a higher significance for C_0. We estimate x_0, the intrinsic error in the model, by that value of x for which this significance saturates. We found that the significance level increased from about 40% when negligible extra error was introduced in distances, to about 80% when the extra error in distances was about 20%. Although this indicates that the probable distance error in our data is likely to be $\leqslant$ 20%, to be conservative we have used the value of 20% error for further analysis. Incidentally, the estimated error in the distance derived by us from the model due to Taylor & Cordes (1993) agrees quite well with their estimate.

For every pulsar in our sample set we varied the distance by 20% (rms) and computed the resulting variance $.\sigma^2_{d_{\min}}$ of $d_{\min.}$ The implied error in the *projected velocity* is then $\Delta v = \sigma_{d_{\min}}/\tau_{ch}$.To reduce the contribution from pulsars with large values of Δv, we have weighted their contributions in the estimation by the following function.

$$w_d = \exp\left[-\left(\frac{\sigma_{d_{\min}}}{\tau_{ch} \Delta v_{max}} \right)^2 \right] \tag{9}$$

Here,Δv_{max} is arbitrarily chosen to be 40km/sec. We also estimated the resultant spread in the velocity distribution caused merely due to the distance uncertainties as a function of the tolerance level (Δv_{max}). For arbitrarily large Δv_{max} (which is the case where w_d is more or less the same for all pulsars), this resultant rms spread turns out to be about 500 km/sec (for about 20% error in distances), emphasising the need for the explicit weighting by w_d with a realistic tolerance level. With the choice of 40 km/sec for the tolerance level, the spread comes down to about 42 km/sec. Hence we believe that the *mean velocity* estimated using the above weighting function will not be seriously affected by the distance uncertainties, provided it is of the order of or greater than ≈ 80 km/sec.

4.2 *Aliasing due to Finite Interarm Spacing*

It should be remembered that the contributions from velocities greater than ($D/2\tau$), where D is the interarm spacing, get *aliased* with the contributions in the range zero to ($D/2\tau$). This effect is naturally more serious in the regions where the interarm spacing is small and can lead to underestimation of the mean velocity. We have tried to overcome this difficulty by appropriately weighting down the contributions from regions of severe aliasing by using the following weighting function,

$$w = \left[\frac{D}{D_0}\right]^a, \quad D < D_0$$
$$w = 1 \qquad D \geqslant D_0 \tag{10}$$

Here, D is the interarm spacing at the location of a given pulsar and a is a weighting exponent. We have used D_0 of 4 kpc and a weighting exponent of unity. In our sample, most of the pulsars which would be seriously affected by *aliasing* are also the ones that are weighted down while accounting for the distance uncertainties. Therefore, our results werefound notto be verysensitive to the parameters of this weighting function.

4.3 *Estimation of Average Velocity*

We have estimated a *projected velocity distribution* as well as the mean value of d_{min} (0.3 ± 0.07) and the mean age (2.8 ± 0.7) of pulsars whose contributions have been weighted appropriately to minimize the effect of distance uncertainties and possible aliasing as described above. Using the above average values, a simple minded estimation of the mean *projected velocity* turns out to be (105 ± 35) km/sec. If we assume a Maxwellian type distribution for the speed, then this implies a mean velocity of about (200 ± 70) km/sec. We have also estimated an average value of the *projected velocity* implied by the d_{min} and characteristic age combination considered for each pulsar contributing to the correlation. This average *projected velocity* is (80 ± 20)km/sec implying a mean velocity of about (160 ± 40) km/sec. In principle one should be able to do a detailed fit on the *projected velocity* distribution. However, in the present case, because of high statistical noise we are not in a position to carry out this exercise. Also, because we have chosen a set of pulsars which are within ± 0.9 kpc from the arms (see the beginning of section 4), the present analysis is not sensitive to high velocities (v > 400km/sec).

5.Conclusions and discussions

As described in the earlier sections, an examination of the correlation between the location of the spiral arm at different epochs and the present pulsar distribution has enabled us to estimate three important parameters: (1) The corotation resonance radius of the Galaxy, (2) The minimum mass of pulsar progenitors, and (3) The distribution of pulsar velocities.

The steps and assumptions involved in inferring the minimum mass of pulsar progenitors from our correlation analysis need a careful discussion. The Initial Mass Function of stars is believed to be steep ($N(M) = M^{-2.35}$, Salpeter 1955). Hence, it is reasonable to assume that the majority of pulsars come from progenitors with masses just above the cutoff mass for the formation of neutron stars. As we do not expect any particular correlation of the lifetime of pulsars with the mass of the progenitors, the above assumption should hold good. Therefore, the epoch of maximum correlation (Fig. 4) should correspond to the formation of progenitors close to the cutoff mass. Reduced correlations are expected from pulsars formed from more massive progenitors which should show up at more recent epochs (than the epoch corresponding to correlation maximum) consistent with the evolution timescales of the progenitors and the average age of the corresponding pulsars. A significant tail corresponding to such more recent epochs is clearly seen in Fig. 4.

While associating the inferred evolution timescale ($\approx$ 50 Myr) with a mass of the progenitor $\sim 7\ M_{\odot}$, we make an implicit assumption that the progenitors are *single stars*. If the progenitors with the above evolution timescales were to be in binaries, the progenitors need to be more massive. This is because we expect the time interval between the star formation and the release of an 'observable' pulsar to be longer by as much as a factor of two or more (depending on the mass ratio) compared to the evolution timescales of the progenitors if they were single stars. Conversely, the single star fraction of the progenitors of a given mass will contribute collectively to the correlation over a narrow range of epochs (typically over the average age of pulsars), while the remainder will contribute to the correlation at epochs spread over a large range depending on the mass of the companion. Therefore, the fact that the correlation seems to be peaking over a narrow range of epochs should necessarily be interpreted as due to the contribution from 'single' progenitors.

A formal uncertainty in the epoch of maximum correlation can be estimated from the statistical errors in the correlation (shown in Fig. 4). This uncertainty is estimated to be about ± l0Myr. However, most of it can be attributed to a genuine width of a correlation function that one would obtain for a fixed mass of progenitors (for example, if stars of the limiting mass are born over a region of width $\approx$ 100 pc along the spiral arms, one would see the correlation width to be 16 Myr). Hence, we believe that the uncertainty in estimating the epoch of maximum correlation is small enough to take seriously our conclusion that all stars above $7M$ must produce pulsars.

The correlation between the pulsar distribution and the spiral pattern as a function of azimuthal rotation is sensitive in the regions where the arms are not azimuthal and in the regions away from corotation. The pulsars in the region of corotation and the regions where the spiral arms are predominantly azimuthal, contribute to a non-varying component of the correlation as can be clearly seen in Fig. 4. We have confirmed this behaviour by excluding the contribution from such regions.

While computing the correlations at various epochs we have used only the azimuthal

shifts appropriate to the *present* galactocentric radius of pulsars as their galactocentric distances at earlier epochs cannot in general be guessed. However, the error introduced due to this should get averaged out as our sample is sufficiently large.

The origin of the feature at the present epoch (see Fig. 4) is not entirely clear. Such a feature, however, is expected to appear if the electron density model used for estimating the dispersion measure distances to pulsars somehow on the average tends to artificially cluster pulsars in the spiral arms. One possible way this can happen is if the ratio of electron density in the *arm component* to that in the *smooth component* has been overestimated in the electron density model. Another possibility is that the arm pattern in the model deviates in some systematic way from the *true* pattern. In such a case the artificial clustering of pulsars in the arms should be more pronounced in the inner regions of the Galaxy where the model is likely to be inadequately constrained. We have looked at the correlation function from pulsars confined to the inner part of the Galaxy (galactocentric radius less than 7 kpc) and find the 0 Myr feature more pronounced. As a preliminary test we varied the model electron density in the arm by factors on either side of unity, recomputed the pulsar distances and found that the relative strength of the 0 Myr feature (with respect to the – 60 Myr feature) *dropped* when the arm density was reduced by about 10%, and *increased* when the arm density was increased by about 10%. The real explanation for the origin of the 0 Myr feature may, however, involve a combination of the above mentioned possibilities in addition to some others that we have not considered here. We wish to emphasize that the – 60 Myr feature is seen clearly in all the subsets of the data (e.g. in different ranges of the galactocentric radii; with different scale factor cutoffs; different characteristic age groups; etc.). This and the high statistical significance associated with the correlation peak at – 60 Myr (as discussed in section 3.1) suggests that the validity of the correlation maximum found at – 60 Myr is not affected seriously by the possible causes for the 0 Myr feature.

While estimating the average pulsar velocity, we have ignored the spread in the $d_{\min}$ distribution due to the width of the spiral arms (over which star formation occurs) and the progenitor velocities. Since pulsar velocities are quite large compared to the expected velocities of their progenitors (see Lyne *et al.* 1982; Bailes *et al.* 1990; Harrison *et al.* 1993), we expect the former to dominate the spread in the $d_{\min}$ distribution. Also, while deriving the velocity distribution, we have neglected the pulsars with $\log B < 11.5$ as they would introduce a systematic bias towards low velocities. This is because most of these pulsars with fields in the range $10^{10} - 10^{11.5}$ gauss have been identified as recycled pulsars and have been shown to have very low velocities (Bailes 1989; Deshpande *et al.* 1994) due to their binary history.

The velocities inferred from VLBI proper motion measurements are on the average much higher than the mean velocity of 160–200 km/sec as estimated by us in section 4. If the large proper motions are considered as part of the tail of our velocity distribution then there should be a large number of low velocity pulsars for which such proper motion measurements are yet to be done. This is not very surprising since the proper motion measurement techniques tend to select against low velocity and far away pulsars.

From an independent analysis of the pulsar population, Narayan & Ostriker (1990) have argued for two distributions for the pulsar velocities. They estimate 50 and 150km/s as the mean one-dimensional velocities for their low and high velocity distributions respectively with roughly half of the pulsar population in each distribution.

This would imply a mean velocity of the population that is in agreement with our estimate (≈ 160–200 km/sec).

Summary

The main results of this paper can be summarized as follows:

1. The corotation resonance radius of the Galaxy is estimated to be (13.5 ± 1.5) kpc. Assuming a flat rotation curve for the Galaxy, the other two resonance radii (the inner and outer Lindblad radii) are estimated to be in the range 3.6–4.5 kpc and 21.4–25.5 kpc, respectively.
2. The correlation between the present position of pulsars and the location of the spiral pattern in the past suggests a mean lifetime of their progenitors ≈ 50 Myr. This would imply that all stars more massive than approximately 7 $M_{\odot}$ must leave behind neutron stars.
3. The global mean of pulsar velocities is estimated to be in the range ≈ 160–200 km/sec.

Acknowledgements

We wish to thank J. P. Ostriker, A. Blaauw, G. Srinivasan, R. Nityananda and D. Bhattacharya for several critical comments. We are particularly indebted to J. P. Ostriker for several suggestions that have strengthened the arguments and conclusions presented in this paper. We also wish to thank V. Radhakrishnan and C. S. Shukre for their comments on the manuscript.

References

Bailes, M. 1989, *Ph. D. thesis*, Australian National University.
Bailes, M., Manchester, R. N., Kasteven, M. J., Norris, R. P., Raynold, J. E. 1990, *Mon. Not. R. astr. Soc.*, **247,** 322.
Bhattacharya, D., Ralph, A. M., Wijers, Jan Willem Hartman, Frank Verbunt 1992, *Astr. Astrophys.*, **254,** 198.
Binney, J**.,** Tremaine, S. 1987, *Galactic Dynamics*, Princeton, N.J.: Princeton University Press.
Blaauw, A. 1985, in *Birth and Evolution of Massive Stars and Stellar Groups*, Eds. W. Boland & H. Van Woerden (Dordrecht: D. Reidel), p. 211.
Burton, W. B. 1971, *Astrophys. J.*, **10**, 76
Caswell, J. L., Haynes, R. F. 1987, *Astr. Astrophys.*, **171,** 261.
Deshpande, A. A., Ramachandran, **R.,** Srinivasan, G. 1994 (to be submitted to *J. Astrophys. Astr.*).
Georgelin, Y. M., Georgelin, Y. P. 1976, *Astr. Astrophys.*, **49,** 57.
Gies, D. R**.,** Bolton, C. T**.** 1986, *Astrophys. J.*, **61, 419.**
Gunn, J. E., Ostriker, J. P. 1970, *Astrophys. J.*, **160,** 979.
Harrison, P. A., Lyne, A. G., Anderson, B. 1993, *Mon. Not. R. astr. Soc.*, **261,** 113.
Kerr, F. J., Lynden-Bell 1986, *Mon. Not. R. astr. Soc.*, **221,** 1023.
Lequeux, J. 1979, *Astr. Astrophys.*, **80,** 35.
Lin, C. C., Yuan, C., Shu, F. H. 1969, *Astrophys. J.*, **155,** 721.
Lorimer, D. R., Bailes, M., Dewey, R. J., Harrison, P. A. 1993, *Mon. Not. R. astr. Soc.*, **263,** 403.
Lyne, A. G., Anderson, B., Salter, M. J. 1982, *Mon. Not. R. astr. Soc.*, **201,** 503
Mulder, W. A., Liem, B. T. 1986, *Astr. Astrophys.*, **157, 148.**

Narayan, R. 1987, *Astrophys. J.*, **319,** 162.
Narayan, R., Ostriker, J. P. 1990, *Astrophys. J.*, **352,** 222.
Prozynski, M., Przybycien, D.1984, in *Millisecond Pulsars*, Eds. S.P.Reynolds &D.R.Stinebring, *NRAO*, p. 151
Salpeter, E. E. 1955, *Astrophys. J.*, **121,** 161.
Schaller, G., Schaerer, D., Meynet, G., Maeder, A. 1992, *Astr. Astrophys. Suppl*, **96**, 269.
Srinivasan, G. 1986, in *The Origin and Evolution of Neutron Stars*, *IAU symposium No. 125*, Eds. D. J. Helfand & J. H. Huang, (Dordrecht: Reidel) p. 109.
Srinivasan, G. 1991, in *Texas/ESO-CERN Symposium on Relativistic Astrophysics*, *Cosmology and Fundamental Physics*, Annals of the New York Academy of Sciences, **647,** 538.
Taylor, J. H., Cordes, J. M. 1993, *Astrophys. J.*, **411,** 674.

J. Astrophys. Astr. (1994) **15,** 85–94

Observations of Enhanced Sub-Iron (Sc–Cr) to Iron Abundance Ratios in the Low Energy Galactic Cosmic Rays in Spacelab-3 and their Implications

S. Biswas, N. Durgaprasad, R. K. Singh, M. N. Vahia & J. S. Yadav *Tata Institute of Fundamental Research, Bombay 400 005*

A. Dutta & J. N. Goswami *Physical Research Laboratory, Ahmedabad 380 009*

Received 1993 October 26; accepted 1994 January 29

Abstract. The Anuradha cosmic ray experiment in Spacelab-3, flown in the orbit at 350 km with an inclination of 57° for about six days, was used to measure the low energy galactic cosmic ray (GCR) heavy ions using a specially designed CR-39 detector module incorporating the arrival time information of the particles. The abundances of sub-iron (Sc–Cr) and iron particles in the low energy interval of 30–300 MeV/N were determined from the measurements made in four different depths of the CR-39 detector module of 150 layers. From these studies we obtained sub-iron (Sc–Cr) to iron abundance ratios of 0·8 to 1·2 in 30–300 MeV/N energy range. It is found that these ratios are enhanced by a factor of two as compared to interplanetary ratios of about 0·5. It is shown that the enhancement of the ratio inside the earth's magnetosphere is probably due to the degree of ionization of low energy Sc to Cr and Fe ions in the galactic cosmic rays and to the rigidity filtering effects of the geomagnetic field. Further studies are needed to understand fully the phenomena and their implications.

Key words: Cosmic ray abundances—subiron and iron nuclei—space lab-3—Anuradha experiment

1. Introduction

For over two decades, there have been studies on the abundance ratios of sub-iron (Sc–Cr) to iron nuclei in the galactic cosmic rays, as it is well known that the sub-Fe nuclei are produced by the fragmentation of iron nuclei in collision with interstellar matter and hence the ratios of (Sc–Cr)/Fe are sensitive indicators of the amount of matter traversed by the galactic cosmic rays in the interstellar medium (see e.g. Shapiro & Silberberg 1970). These abundance ratios have also been used to determine the shape of the path length distributions in interstellar medium. The results obtained in the energy range > 500 MeV/N showed that path lengths and their distributions, which give best fit to the secondary to primary ratios of boron to carbon, do not exactly fit the (Sc–Cr)/Fe ratios. Hence, one invokes the hypothesis of truncation of path length distributions at short path lengths, that implies more than one confinement

volume for cosmic ray heavy ions. These problems have been discussed by several authors (e.g. Garcia-Munoz *et al*. 1984; Soutoul *et al*. 1985; Guzik & Wefel 1984 and Ferrando *et al*. 1991).

When the measurement of the sub-iron to iron abundance ratio was extended to lower energies ($E \leqslant 300$ MeV/N) in the Skylab cosmic ray experiment, it was found for the first time that the abundance ratio at low energy of 35–250 MeV/N was significantly higher than that at high energies (Biswas *et al.* 1975; and Durgaprasad & Biswas 1988). It was, therefore, necessary to conduct such an experiment with higher statistical accuracy. The Anuradha cosmic ray experiment in the Spacelab-3 Mission was specially suitable for such studies. Initial results on the (Sc–Cr)/Fe abundance ratio measured in the lowest energy range in the Spacelab-3 also showed enhanced values and these were reported in international conferences (Biswas *et al.* 1987, 1989; Durgaprasad et *al.* 1990a, b). Since then additional measurements were carried out and the sub-iron (Sc–Cr) to iron abundance ratios were measured at four different depths of the detector. From these, the abundance ratios were obtained in four energy intervals, from 30 to 300 MeV/N. These final results and interpretations are presented in this paper.

The experiment conducted in the Soyuz-6 mission by USSR group (Gagarin *et al.* 1990) also reported enhanced values of the ratios at low energies, confirming the data from the Skylab and Spacelab-3 experiments. Thus it is established that inside the earth's magnetosphere, the sub-iron (Sc–Cr) to iron abundance ratio is about 1.0 in the 30–300 MeV/N energy region, which is about a factor of two enhanced as compared to the interplanetary values measured in IMP-8, ISEE-3 and Voyager-2 spacecrafts (Garcia-Munoz *et al.* 1987; Leske & Widenbeck 1990; Ferrando *et al.* 1991). The reasons for the enhancements were not understood earlier and this has been a puzzling problem.

In this paper, after presenting the experimental procedure and results, we discuss the implication of the results and show that the enhancements of the ratios inside the magnetosphere can be understood in terms of the new findings in the Spacelab-3 cosmic ray experiment. It is found by Biswas *et al.* 1990, Singh *et al.* 1991 and Dutta *et al.* 1993, that about 25% of low energy (30–130 MeV/N) sub-iron (Sc–Cr) and Fe particles in galactic cosmic rays are in partially ionized states. These observations together with the rigidity filtering process of the earth's magnetic field are used to explain the enhancement effects, as discussed in this work.

2. Experimental procedure and results

The Anuradha cosmic ray experiment in Spacelab-3 of NASA was flown in space at an altitude of 350 km in a circular orbit at an inclination of 57° to the equator in a six-day mission during April 29–May 6, 1985. The detector module consisted of (a) a top fixed stack of a single sheet of CR-39 of diameter about 40 cm and of thickness 0.33 mm and (b) a movable stack of 149 CR-39 sheets each of nominal thickness of about 0.25 mm. The two stacks were separated from each other by a fixed gap of 0.5 mm. The bottom stack was rotated with respect to the fixed top stack at a slow uniform rate in steps of 40 sec of arc once in 10 sec. By identifying the track segments in the upper fixed and the lower movable stack and measuring their displacements,

the arrival time of the cosmic ray heavy ions were determined. This information, together with other measured properties of the particles, was used to determine the ionization states of the anomalous and low energy GCR heavy ions. The details of the instrument, experimental method and procedure for analysis have been reported earlier (Biswas *et al.* 1986; Biswas *et al.* 1990; Singh 1990; Singh *et al.* 1991; Dutta *et al.* 1993). Here we briefly present the relevant aspects of the procedure for the analysis of subiron and iron abundance ratios and the results obtained.

The shielding above the detector consisted of 25 mg cm $^{-2}$ of aluminium alloy and 0.5 mil of aluminised mylar (Kapton) so that GCR iron ions, of energy 25 MeV/N and above, could be detected. The topmost detector sheet was numbered as 1–0 and subsequent sheets as 1–1 to 1–150. For sub-iron and iron abundances ratios, the scanning and measurements of GCR heavy ions were carried out in four different depths of the detector. A pair of plates were scanned at a time. These were plates of numbers (1) 1–0 and 1–1, (2) 1–2 and 1–3, (3) 1–14 and 1–15, (4) 2–50 and 2–51. Each pair of CR-39 plates were scanned for double cones in each plate so that, in general, four cones of each of the particles were seen in the pair of plates. The selected cones are followed through successive plates till the particles were brought to rest in the stack. Using cone length vs residual range, the identification of the atomic number of the particles were made. With the track selection procedure used, cosmic ray particles of $Z > 10$ were identified, and the particles of $Z > 20$ were used in the analysis. It may be noted, that in our etching conditions, maximum etched length was about 0.3 mm for Mg ions which increased rapidly to about 3 mm for Fe particles. Hence the Fe-group particles could be followed in as many as about 15 plates and a large number of independent measurements of nuclear charge could be made for the GCR particles of $Z = 21$ to 28 in the detector and their identity could be well established. The detailed analysis of the charge resolution of the particles obtained in the experiment, was made by Yadav & Singh (1990), who showed that the standard deviation of the charge determination for a single cone measurement obtained by the deconvolution method is given by the equation $\sigma(z) = 0.285 + 0.03Z$, where Z is the atomic number and $\sigma(z)$ the standard deviation of the charge value. For Fe nuclei $\sigma(z) \approx 1$ charge unit for a single cone observation. On the average about nine cones were measured for Fe ions in this experiment. Hence the charge resolution is obtained as 0.3 charge units for Fe-ions. Thus the atomic number of the particles of Sc to Ni could be unambiguously determined. Fig. 1 shows the observed histogram of the mean fractional charges of Ti to Ni events in this study. It is pointed out that the response function in CR-39 of cosmic ray heavy ions increases rapidly with the atomic number Z and hence the respective response functions are to be used to determine their relative abundances.

In Table 1, we show the results of the abundance ratios of (Sc–Cr)/Fe from the present work, carried out at four different depths in the detector module. The energies of particles given in Table 1 refer to those at the top of the detector module. When measured fluxes of sub-iron (Sc–Cr) and of Fe are in slightly different energy intervals, corrections for the relative response functions are made to obtain the corrected abundance ratio. For measurements made in the lower depths of stacks in plates 2–50 and 2–51, the measured fluxes and (Sc–Cr)/Fe ratios are corrected for loss of particles due to nuclear interactions in the stack and also for the contribution to Sc–Cr fluxes by the fragmentation of Fe nuclei in the stack. For this purpose diffusion

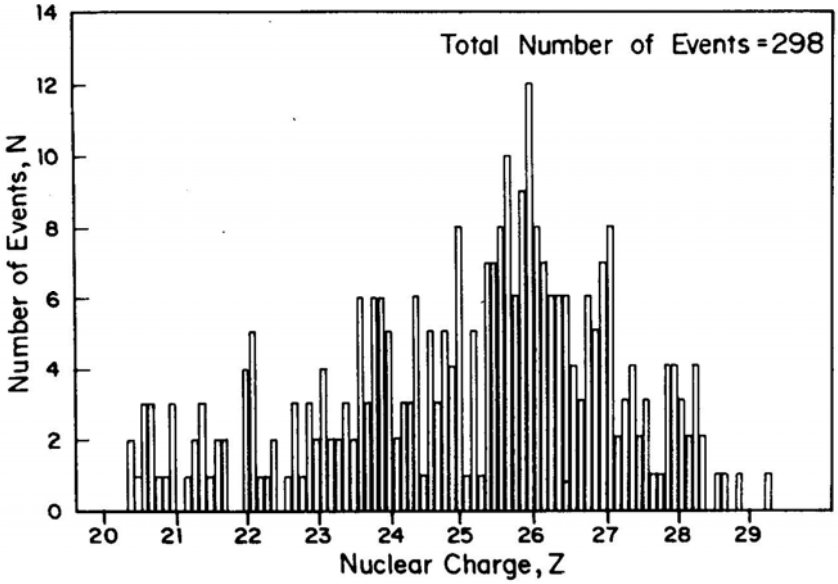

Figure 1. Observed histogram of sub-Fe and Fe ions.

Table 1. Sub-iron (Sc–Cr) to Fe abundance ratios in Spacelab-3.

Scan plates and area scanned	Event type and exposure time (hrs)	No. of events measured and used[a]	Energy interval MeV/N	Mean energy MeV/N	Measured (Sc–Cr)/Fe ratio	Extrapolated (Sc–Cr)/Fe ratio
(1–0)(1–1)	T.A.E.[b]	70				
400 cm^2	64	44	22–80	51	1.02 ± 0.30	1.02 ± 0.30
(1–0)(1–1)	S.S.E.[c]	52				
400 cm^2	72	46	30–120	75	0.59 ± 0.18	0.59 ± 0.18
(1–2)(1–3)	T.T.E.[d]	97				
	120	50	54–80	67	1.17 ± 0.28	1.17 ± 0.28
(1–14)(1–15)	T.T.E.	23				
	120	21	90–170	130	1.18 ± 0.52	1.15 ± 0.51
(2–50)(2–51)	T.T.E.	70				
	120	39	190–280	235	1.05 ± 0.33	0.97 ± 0.31

[a] No. of events 'used' is given by the lower number in the column and refers to those in selected overlapping energy intervals.
[b] Time annotated events.
[c] Stationary state events.
[d] Total time events.

equation with partial fragmentation cross sections are used.As depth in stack is small and amounts to only about 2.5 g cm^{-2},the correction is small and amounts to only ~10%

The results obtained on (Sc–Cr)/Fe rations in the four energy intervals are shown in Fig. 2 together with those of other investigators measured in spacecrafts inside the

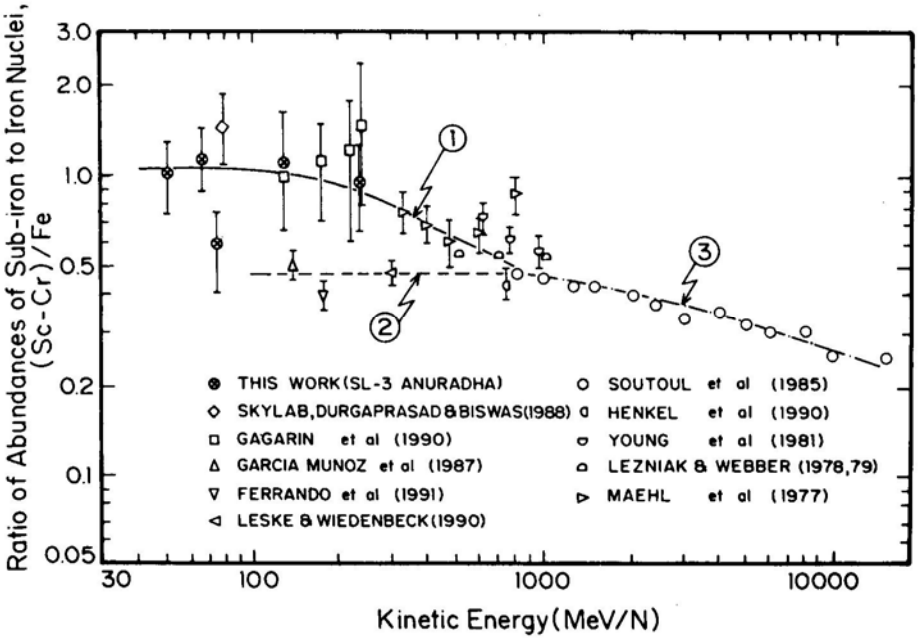

Figure 2. The ratio of abundances of (Sc–Cr) to Fe ions vs kinetic energy in 30 MeV/N to ~ 10 GeV/N. The eyefit line denoted by 1 represents approximate curve for the ratio measured inside the magnetosphere in Skylab,Spacelab-3 and Soyuz-6,whereas the eyefit line 2 shows the value of the ratio measured in the interplanetary space. The line 3 shows the variation of the ratio in the high energy region in 1–l0G eV/N measured in HEAO-3 spacecraft.

magnetosphere and outside of it. It is seen that the present results of Spacelab-3 are in good agreement with those of Skylab (Durgaprasad & Biswas 1988) and Soyuz-6 (Gagarin *et al.* 1990). An eye fit line drawn through these data is marked as 1. The HEAO-3 results of $E \sim 1$–10 GeV/N are shown in this figure. In the same figure, it is seen that the interplanetary measurements of the ratio in IMP-8 (Garcia-Munoz *et al.* 1987), ISEE-3 (Leske & Widenbeck 1990) and Voyager-2 (Ferrando *et al.* 1990) are in good agreement with one another and these can be represented by a flat dashed line marked 2 which joins smoothly with the high energy HEAO-3 data marked as 3. It is seen that the ratios, measured at low energies (30–300 MeV/N) inside the magnetosphere are enhanced by a factor of about two, as compared to the interplanetary value of ~ 0.5.

3. Discussions

3.1 *Enhanced Abundance Ratios and Solar Modulation*

In this experiment the charge resolution is adequate to identify individual charges, as noted earlier. The energy determinations are made from the range measurements of stopping particles and hence these are accurately known. Hence the enhanced (Sc–Cr)/Fe ratios in the Spacelab-3 experiment can not be due to uncertainties of

nuclear charge and energy determinations. Although individual data points have fairly large statistical errors, all the low energy measurements of the ratios inside the magnetosphere, taken together, clearly establish that the abundance ratios inside the magnetosphere are enhanced by a factor of about two as compared to the interplanetary ratio.

The sub-iron to iron ratios measured inside the magnetosphere are only weakly dependent on solar modulation. The Skylab measurements were made in 1973–74 which were close to climax neutron monitor maxima of 1976 and the Spacelab-3 Anuradha experiment was conducted in 1985 at low level of solar activity, about two years prior to neutron monitor maximum of 1987. The Soyuz data refer to 1978–79, when neutron monitor rate was close to that of Spacelab-3 of 1985. Hence the solar modulation effects should be small and somewhat similar for the three results. Also, these effects can be neglected in the present data, where statistical errors are fairly large

It is seen in Fig. 2, that the eye fit line through the low energy (30–300 MeV/N) data smoothly joins the HEAO-3 data at high energies (1 to 15 GeV/N). In the intermediate energy range of 300–500 MeV/N, the balloon data of the ratios are consistent with the line (1) and the data of 500–1000 MeV/N are consistent with the lines (1) and (2) as these are close to each other. In discussing the enhanced (Sc–Cr)/Fe ratios at low energy observed in Spacelab-3, Skylab and Soyuz-6, Wefel (1991) has questioned whether some of these sub-iron and iron particles could be due to the following process. An iron ion just above cut-off energy, travels to the mirror point in the upper atmosphere, where it loses energy and undergoes fragmentation and electron capture process, and thus enters the detector as a partially ionized particle. This process is not possible for two important reasons. Firsly, the amount of material traversed by an iron particle in the upper atmosphere is typically $\leqslant 0.1$ g cm^{-2}, whereas interaction length in air is about 10 g cm^{-2}. Hence fragmentation in upper atmosphere is not possible. Secondly, the sub-iron and iron ions measured by us are mostly in 50–100 MeV/N. At these energies, it is impossible for these particles to capture electrons, as the electron stripping cross section greatly exceeds the capture cross section. Hence the above suggestion can be completely ruled out. The electron capture near mirror point may be possible for Fe particles in the range of energy of 1–10 MeV/N, which are not considered in any of the present space experiments.

3.2 *Flux of Low Energy Fe-Nuclei and their Ionization States*

We discuss here the flux of iron nuclei and their ionization states which can be deduced from the measured data. It is now established (Biswas *et al.* 1988; Adams *et al.* 1991) that the fluxes and energy spectra of low energy GCR nuclei, measured both inside and outside the magnetosphere at the same time, together with the geomagnetic transmission factors, could be used to determine their mean ionization states. Here, we first compute the orbit average flux of Fe-nuclei in the 22–80 MeV/N interval for the time annotated events (as given in Table 1). The sample is selected, because these time-annotated Fe events were also used to determine the ionization states of individual ions by the trajectory computation method (Biswas *et al.* 1990; Singh *et al.* 1991; Dutta *et al.* 1993), and the results from both the methods could be compared. The orbit average flux for the 64 hr exposure was obtained as 2.47 ± 0.64 p/(M^2 Sr Sec MeV/N) for Fe-ions of 22–80 MeV/N. We derived the interplanetary Fe flux in the following

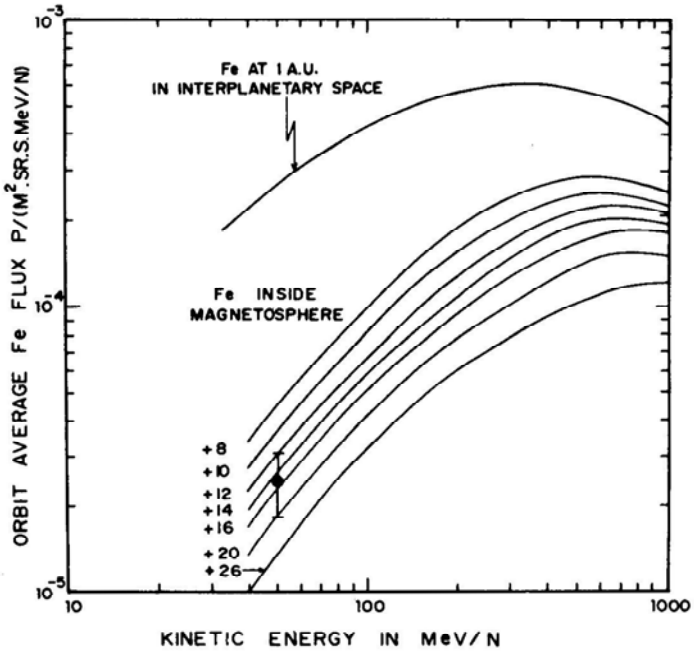

Figure 3. Fe-flux vs 1 AU outside the magnetosphere is shown in the uppermost curve, and the calculated orbit average Fe fluxes inside the magnetosphere are shown by the lower set of curves for assumed mean ionization states of Fe^{+8} to Fe^{+26}. The measured orbit average flux in SL-3 at 50 MeV/N is shown which indicates that the ionization state of these Fe particles is +15.

manner. We used the GCR oxygen flux measured in 45–300 MeV/N by Dutta (1991) in Spacelab-3 within the magnetosphere and as these GCR particles were fully stripped nuclei, their interplanetary flux at 1 AU could be determined. This determined flux agrees well with the demodulated spectrum of oxygen at 1 AU in 1985 and with the ISEE-3 data. Next we used the well known abundance ratio of Fe/O in GCR as 0.129 (Biswas & Durgaprasad 1980), to derive the Fe-energy spectrum at 1 AU in 1985, which is shown in Fig. 3. Then using geomagnetic transmission factors for Spacelab-3 orbit as given by Biswas *et al.* (1988), we calculate the expected orbit average fluxes of Fe-ions for different ionization states (Z^*) of + 8 to + 26. Thus from the measured orbit-averaged flux at 45 MeV/N, the mean ionization state of Fe-ions of 22–80 MeV/N is determined as $Z^* = 15$, as shown in Fig. 3. The measurements of the ionization states of the individual particles of the same sample of events by trajectory computation method was done by Biswas *et al.* (1990) and Dutta *et al.* (1993) and the upper limit of mean Z^* is obtained as + 20. Both these results are in agreement with each other.

3.3 *Ionizations States and the Abundance Ratios*

We now discuss and compute the enhancement of the abundance ratios by the rigidity filtering effect of the geomagnetic field. The partially ionized particles of Fe-group

Table 2. Calculated and measured ratios of (Sc-Cr)/Fe.

Ion	Mean degree of ionization Z^*/Z	Average A/Z^*	Average momentum/N Pc GeV	(A/Z^*) Pc = cut-off rigidity GV	Effective exposure factor	Calc. enhancement factor	Measured enhancement factor
Sc–Cr	0.71	3.1	0.37	1.14	> 0.091	> 1.2	2.2
Fe	0.80	2.7	0.37	0.99	0.079	1	1

will have higher magnetic rigidities and hence these will have higher exposure factors. The detailed computation of the effective exposure factors as a function of threshold rigidity for the Spacelab-3 Anuradha exposure is given by Biswas *et al.* 1988. We use these to calculate the effective exposure factors for sub-iron (Sc–Cr) and Fe ions. From the measurements of ionization states of cosmic ray ions in Spacelab-3 (Biswas *et al.* 1990; Singh *et al.* 1991; Dutta *et al.* 1993), we calculate the relevant parameters as shown in Table 2. It is seen that mean Z^*/Z of (Sc–Cr) is 0.71 as compared to 0.80 of Fe. These are based on 16 events of Sc to Cr and 22 events of Fe. This is indicative of the trend and further studies are needed to confirm this. In column 5 we show the mean values of $(A/Z^*) \times$ pc which is equal to rigidity. It is seen that effective cut-off rigidity for Sc–Cr is 1.14 which is about 14% higher than 1.0 of Fe. The effective exposure factors 0.091 and 0.079 are then obtained using the computation of effective exposure factor vs threshold rigidity (as given in figure 4 of Biswas *et al.* 1988). The calculated enhancement factor is then determined as (0.091/0.079) = 1.2. As Z^* is the upper limit, exposure factor can be larger; hence calculated enhancement factor may be > 1.2. This can be compared with the measured enhancement of 2.2.

3.4 *Ionization States and Interstellar Propagation of GCR Particles*

In order to understand the enhancements of the low energy (Sc–Cr)/Fe abundance ratios, we suggest the following scenario which is consistent with the standard model of cosmic ray origin and propagation. GCR heavy ions such as Fe originate from some galactic sources, e.g. SN, SNR, etc. and after being mixed with the ions of interstellar medium (ISM), they are injected with some initial acceleration into the ISM through which they propagate. In the GCR propagation in the galaxy, the following characteristic processes may occur:

(a) Interactions of GCR iron ions can take place with matter in ISM and could undergo fragmentation to sub-iron particles, e.g. Sc, V, Ti, Cr and Mn. Thus the well measured parameters of sub-iron to iron abundance ratios, together with the well-determined interaction and fragmentation cross sections, are used to determine the amount of material traversed by GCR particles in the ISM and in source region. This procedure yields at low and intermediate energy ($\geqslant$ 300 MeV/N) a path length of about 8 to 10 g cm^{-2} of interstellar matter (see e.g. Shapiro & Silberberg 1970; Garcia-Munoz *et al.* 1984, 1987; Ferrando *et al.* 1991).

(b) Energy loss of GCR heavy ions: Subiron and iron particles of low energy galactic cosmic rays (E ~ 50–200 MeV/N) suffer ionization loss while traversing ISM, and a fraction of these are reduced to energies of 1–10 MeV/N. At these energies Fe and Sc–Cr ions readily capture orbital electrons while traversing ISM or interstellar gas clouds, and a population of GCR ions of $Z > 20$ with various ionization states are produced. This is so because electron capture cross sections exceed the electron stripping cross sections by a few orders of magnitude (Biswas *et al.* 1990).

In the course of interstellar propagation a fraction of the particles in partially ionized state and with the equilibrium charge distribution, are expected to intercept the supernova remnant shock fronts in the interstellar medium. In some of these encounters, the acceleration of these heavy ions may take place. Thus, after several encounters, we expect to have a GCR population of heavy ions with equilibrium energy spectrum and with equilibrium charge distribution. These propagate in the interplanetary medium where they maintain their charged state.

4. Summary and conclusions

1. Spacelab-3 cosmic ray experiment, supported by other experiments, conclusively established that sub-iron (Sc–Cr) to iron abundance ratios in the low energy (30–300 MeV/N) galactic cosmic rays measured inside the magnetosphere are enhanced by a factor of about two as compared to their interplanetary ratios.
2. It is found that the abundance enhancement is wholly or partly due to the rigidity filtering effects of the geomagnetic field. Further experiments with higher statistical accuracy are needed to determine the degree of ionization of Sc–Cr and Fe particles in the low energy cosmic rays and these will help in understanding the details of the phenomena.
3. We suggest that in future cosmic ray detectors for sub-iron and Fe particles at low energies be flown in spacecrafts inside the magnetosphere and in the interplanetary space at the same period of time and the results therefrom can provide information on the mean ionization of the elements $Z = 21$ to 28. These, in turn, will help in understanding their propagation effects in the interplanetary medium and in the magnetosphere.

Acknowledgements

The authors are thankful to National Aeronautics and Space Administration, USA; Indian Space Research Organization; Tata Institute of Fundamental Research; Physical Research Laboratory and Bhabha Atomic Research Centre for their excellent support in various phases of the Anuradha Cosmic Ray experiment in the Space Shuttle Spacelab-3 mission. The authors are grateful to the members.of the Anuradha team for their contributions for the successful experiment and data analysis. One of the authors, S. Biswas, is thankful to the Council of Scientific and Industrial Research, Government of India, for the support provided by the ES Research Scheme No. 21 (156)/89-EMRII.

References

Adams, Jr. J. H., Beahm, L. P., Tylka, A. J. 1991, *Astrophys. J.*, **377**, 292.

Biswas, S., Nevatia, J., Durgaprasad, N., Venkatavaradan, V. S. 1975, *Nature*, **258**, 409.

Biswas, S., Durgaprasad, N. 1980, *Space Sci. Rev.*, **25**, 285.

Biswas, S., Chakrabarti, R., Cowsik, R., Durgaprasad, N., Kajarekar, P. J., Singh, R. K., Vahia, M. N., Yadav, J. S., Dutt, N., Goswami, J. N., Lal, D., Mazumdar, H. S., Subhedar, D. V., Padmanabhan, M. K. 1986, *Pramana – J. Phys.*, **27**, 89.

Biswas, S., Durgaprasad, N., Dutt, N., Goswami, J. N., Lal, D., Singh, R. K., Vahia, M. N., Yadav, J. S. 1987, *Proc. 20th ICRC, Moscow,* **3**, 451.

Biswas, S., Durgaprasad, N., Mitra, B., Singh, R. K., Vahia, **M.** N., Yadav, J. S., Dutta, A., Goswami, J. N. 1988, *Astrophys. Space Sci.,* **149**, 357.

Biswas, S., Durgaprasad, N., Mitra, B., Singh, R. K., Vahia, M**.** N., Dutta, A., Goswami, J. N. 1989, *Adv. Space Res.,* **9**, 12, 25.

Biswas, S., Durgaprasad, N., Mitra, B., Singh, R. K., Dutta, A., Goswami, J. N. 1990, *Astrophys. J. Lett.*, **359**, L5.

Durgaprasad, N., Biswas, S. 1988, *Astrophys. Space Sci.* **149,** 163.

Durgaprasad, N., Mitra, B., Singh, R. K., Biswas, S., Dutta, A., Goswami, J. N. 1990a, *Proc. 21st ICRC*, *Adelaide*, **3**, 389.

Durgaprasad, N., Biswas, S., Mitra, B., Singh, R. K., Vahia, M. N., Dutta, A., Goswami, J. N. 1990b, *Indian J. Phys.*, **64A**, 175.

Dutta, A. 1991, *Ph. D. Thesis,* Gujarat University, India.

Dutta, A., Goswami, J. N., Biswas, S., Durgaprasad, N., Mitra, B., Singh, R. K. 1993, *Astrophys. J.,* **411,** 418.

Ferrando, P., La, N., McDonald, F. B., Webber, W. R. 1990, *Proc. 21st ICRC*, *Adelaide*, **3**, 41.

Ferrando, P., La, N., McDonald, F. B., Webber, W. R. 1991, *Astr. Astrophys.,* **247,** 163.

Gagarin, Yu. F., Dvoryanchikov, Ya. V., Lyaguchin, V. I., Ovchinnikova, A. Yu., Solovyev, A. V., Khilyuta, I. G. 1990, *Proc. 21st ICRC*, *Adelaide*, **3**, 11.

Garcia-Munoz, M., Guzik, T. G., Simpson, J. A., Wefel, J. P. 1984, *Astrophys. J.*, **280,** L13.

Garcia-Munoz, M., Simpson, J. A., Guzik, T. G., Wefel, J. P., Margolis, S. H. 1987, *Astrophys. J. Suppl.*, **64,** 269.

Guzik, T. G., Wefel, J. P. 1984, *Adv. Space Res.*, **4**, 215.

Henkel, M., Acharya, B. S., Heinbach, U., Heinrich, W., Hesse, A., Koch, Ch., Luziett, B., Noll, A., Simon, A., Tittel, H. O., Esposito, J. A., Streitmatter, R. E., Ormes, J. F., Balasubramanyan, V. K., Christian, E. R., Barbier, L. M. 1990, *Proc. 21st ICRC*, *Adelaide*, **3**, 15.

Leske, R. A., Wiedenbeck, M. E. 1990, *Proc. 21st CRC, Adelaide,* **3**, 57.

Lezniak, J. A., Webber, W. R. 1978, *Astrophys. J.*, **223**, 69.

Lezniak, J. A., Webber, W. R. 1979, *Astrophys. Space Sci.*, **63**, 35.

Maehl, R. C., Ormes, J. F., Fisher, A. J., Hagen, F. A. 1977, *Astrophys. Space Sci.*, **47**, 163.

Shapiro, M. M., Silberberg, **R.** 1970, *Annual Reviews of Nuclear Science*, Annual Review Inc., USA, **20**, 323.

Singh, R. K. 1990, *Ph. D. Thesis,* University of Bombay, India.

Singh, R. K., Mitra, B., Durgaprasad, N., Biswas, S., Vahia, M. N., Yadav, J. S., Dutta, A., Goswami, J. N. 1991, *Astrophys. J.*, **374**, 753.

Soutoul, A., Englemann, J. J., Ferrando, P. H., Koch-Miramond, L., Masse, P., Webber, W. R. 1985, *Proc. 19th ICRC, Denver,* **2**, 8.

Yadav, J. S., Singh, R. K. 1990, *Nucl. Inst. Methods,* **B51,** 63.

Young, J. S., Freier, S. P., Waddington, C. **J.,** Brewster, N. C., Fickle, **R. K.** 1981, *Astrophys. J.*, **246**, 1014.

Webber, W. R. 1982, *Astrophys. J.*, **252**, 386.

Wefel, J. P. 1991, in *Cosmic Rays, Supernova and the Interstellar Medium*, Ed. M. M. Shapiro *et al.* (Kluwer Academic Publishers) NATO ASI Series C, **337**, 29.

J. Astrophys. Astr. (1994) **15,** 95–102

Application of INSAT Satellite Cloud-Imagery Data for Site Evaluation Work of Proposed GRACE Observatory

R. K. Kaul, C. L. Bhat, M. L. Sapru & M. K. Kaul *Bhabha Atomic Research Centre, Nuclear Research Laboratory, Trombay, Bombay 400 085*

Received 1993 July 23; accepted 1994 January 29

Abstract. The weather-imageries from the INSAT group of satellites provide reliable and concurrent multistation cloud-cover data – an important input for a proper selection of an observatory site for optical, infra-red and γ-ray astronomy work. Using these data, it is shown that Gurushikar, Mt. Abu, promises to be an excellent site for setting up the proposed GRACE facility for high-sensitivity Gamma-Ray Astrophysics Cerenkov Experiments.

Key words: INSAT-satellites—cloud-imageries—observatory site-selection—groundbased gray astronomy.

1. Introduction

Our group has been actively involved, for over 2 decades now, in a variety of investigations related to the field of gamma-ray astronomy. These studies, based mainly on the use of ground-based atmospheric fluorescence and Cerenkov techniques (Bhat 1982), have covered a wide range of photon energies from ~ 100 keV to a few PeV, and time-scales from a few nanoseconds to around a second. In the initial phase, a series of exploratory experiments were carried out at Gulmarg and Srinagar for detecting short time-scale cosmic gamma-ray bursts expected to accompany Supernova outbursts and the explosive evaporation phase of primordial black-holes (Bhat *et al.* 1980). Successful searches were made for PeV γ-ray signals from cosmic sources like Cyg X-3 and AM-Her binary systems (Bhat *et al.* 1986; Bhat *et al.* 1991a). More recently, a TeV γ-ray telescope (Koul *et al.* 1989) was developed and operated at Gulmarg between 1985 and 1989 to detect cosmic gamma-ray sources and study their emission characteristics on a variety of time-scales (see Razdan 1989; Bhat 1993 and references therein). We have plans to consolidate these activities further in the next decade. Accordingly, under a new project GRACE (Gamma Ray Astrophysics Cerenkov Experiments), two high-sensitivity telescopes, TACTIC and MYSTIQUE, both based on the atmospheric Cerenkov technique, are being developed to undertake comprehensive temporal and spectral studies of cosmic gamma-ray sources over the energy range 0·2 TeV – 10 PeV. While we refer the reader to Bhat *et al.* (1991b, 1993) for a discussion on the design philosophies and other technical details of the experiments, we limit ourselves here to pointing put that an essential pre-requisite

for their successful execution is a proper observatory site. The main qualifications for such a site are:

1. Cloud-Free nights, as far as possible, during a calendar year.
2. Dark site, with a negligible contribution to the background light level from artificial sources.
3. Atmosphere free from haze, dust and anthropogenic pollution.
4. Operational ease, good logistics and mild climate.
5. Reasonably flat terrain of upto 0.25 km^2 in area – a requirement for MYSTIQUE mainly.

Unlike in optical astronomy, a high order of atmospheric 'seeing' (< a few areseconds) is not particularly required in the context of atmospheric Cerenkov work. On the other hand, it is of paramount significance here that the night-sky is as cloud-free as possible for the sake of maximizing possible observation time (T_0) per source per calendar (or sidereal) year (Bhat *et al*. 1993). This need is perhaps far more acute here than for optical and infra-red astronomies because the typical source flux that one is dealing with in the very high energy (VHE) and ultra high energy (UHE) gamma-ray regions is extremely small, both in absolute terms as also in relation to the cosmic-ray-generated background events (Weekes 1988; Bhat 1993). This renders the experimental scene in gamma-ray astronomy analogous to searching for the proverbial 'needle-in-a-haystack' situation. Several techniques have been developed, in the last few years for retrieving the extremely weak γ-ray signals from the far-excessive cosmic-ray background in these energy domains and thereby helping to boost the sensitivities of telescopes like TACTIC and MYSTIQUE (Weekes 1992). Nevertheless, the importance of maximizing T_0 continues to remain valid, in order that the full potential of these systems is exploited for making a real dent in this still-fledgling, *albeit* promising, field (Lamb 1989).

In view of this importance, we have embarked on a search for a proper observatory site in India, which, in addition to satisfying pre-requisites (2) to (5) listed above, can also offer the maximum number of cloud-free nights per year. This search need not remain confined to the already established observatory sites only (for which some information on annual cloud-cover is available in literature), but can extend to some other places in the country, which may be more viable from other points of view, including some of the above-listed requirements. In addition, it is also desirable to have more recent and preferably concurrently-recorded cloud-cover data on all these candidate sites in order that more reliable inferences can be drawn regarding the suitability of a site. In the present communication, we first show that the cloud-imagery data, recently obtained by the INSAT series of satellites, is quite suitable for meeting these specifications. Based on these results, we then go on to establish that, among the nine locations investigated in this work, Gurushikar, Mount Abu, is the best astronomical site in India in respect of the availability of clear nights per year.

2. Data analysis and results

Nine candidate sites, listed in Table 1 alongwith their geographical coordinates and altitudes, were chosen for the present study, keeping in mind the overall implementa-

Table 1. A list of 9 potentially-promising locations for the proposed GRACE observatory.

Location	Longitude	Latitude	Altitude (m)
Leh	77°34′E	34°09′N	4100
Gulmarg	74°24′E	34°05′N	2743
Jammu	74°24′E	32°24′N	330
Solan	77°05′E	30°33′N	1000
Nainital	79°42′E	29°21′N	1927
Gurushikar	72°43′E	24°36′N	1700
Pachmahri	78°12′E	22°18′N	1350
Rangapur	78°43′E	19°49′N	554
Kavalur	78°49′E	12°34′N	725

tion strategy for the project GRACE. The cloud-imagery data used in the present analysis belongs to the 5-year period 1987–1991. These data have been generated and transmitted to ground by the Very High Resolution Radiometer (VHRR) onboard the INSAT-IB satellite for the period 1986 –July 1990 and thereafter via INSAT-ID satellite. The processed images are available from the Satellite Meteorological Unit, Indian Meteorological Department, in the form of black and white photographs taken at three-hour intervals in the visible band (550–750 nm) and in the infra-red (IR) band (10500–12500 nm).

For the present work, we have studied the IR cloud-imagery pictures taken at 21, 00, 03, 09 hrs (1ST). Fig. 1 shows a typical cloud photograph recorded in the IR-band and superimposed on a map of India, which is shown fitted inside a grid pattern formed by the parallels of longitude and latitude. Each individual cell in the grid pattern has dimensions of 5° (long.) × 5° (lat), corresponding to linear dimensions of 500 km × 500 km for a representative latitude of ~ 20°N. As the actual position of a location of interest can be fixed on the image-plane with an uncertainty of ~ 50 km, we have associated a ‘circle of influence’ of ~ 150 km around it. Next, each location has been graded on a scale of 1–4 on a daily basis at the abovereferred 4–epochs, depending on whether its corresponding ‘circle of influence’ is completely cloud-free (grade 1),or,is under a thick cloud-cover(white-patch;grade 4). The two intermediate grades, 2 and 3, refer to hazy sky conditions and partially (broken) cloudy-sky, in that order. Depending upon the grading obtained at each epoch, a particular night is classified as ‘excellent’ if all the four epochs have a grade of 1. Such a night is regarded as having 10 hrs of ‘clear-sky’. Similarly, if only the 3 consecutive night-epochs are graded as 1, the night is classified as ‘good’ and allotted a clear-sky time of eight hrs. Again, if only two consecutive epochs during the night turn out to have the grade 1, the night is termed as ‘fair’, with 4.5 hrs of clear-sky. Lastly, if only one epoch of two non-contiguous epochs turn out to have the grade 1, the night is referred to as ‘poor’, with no observation time possible.

We would like to invite attention to one ‘limitation’ of the procedure adopted here. While the (generally-encountered) large scale cloud complexes, overlapping partially or fully a given ‘circle of influence’, can be readily identified through the present technique, localized cloud-formations lying within this circle may be missed with the spatial resolution used here. In that sense, the results obtained here on clear-sky conditions are more likely to refer to combined photometric and spectroscopic sky

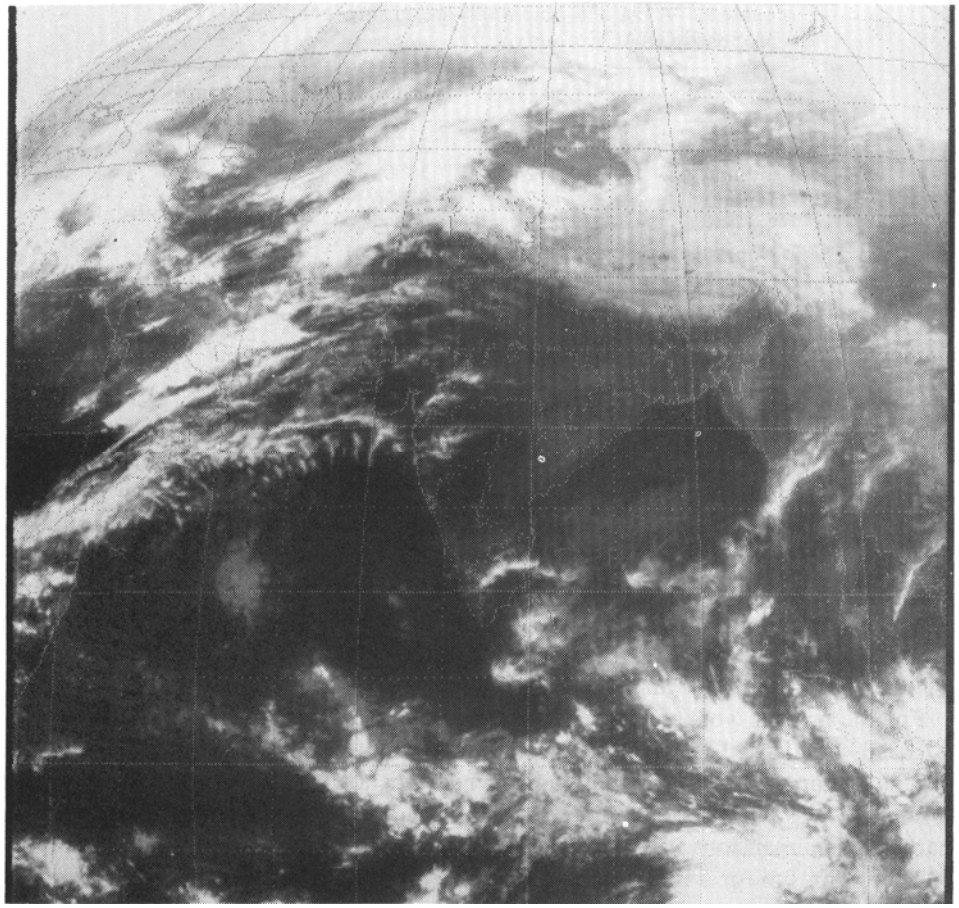

Figure 1. An INSAT cloud-imagery photograph recorded on 3 Dec. 1991 at 1200 hrs. in the IR band.

conditions and not to strictly photometric-skies only (Bhatnagar & Gandhi 1991). It will be shown later, from a comparison of the results obtained here with the reference data available for some established observatory locations like Nainital, Gurushikar and Kavalur, that this indeed seems to be the case. Another practical limitation of the technique also became evident during this work: while scanning the cloud imageries, it was difficult to distinguish between cloud features and snow-covered areas in the high-Himalayas. Because of this ambiguity, the analysis for Leh could not be completed with enough reliability. This has forced us to preclude this station from any further discussions here. In case of all other locations, the only ambiguity resulted by way of discrimination between a clear day and a hazy day, especially when the picture had a poor contrast. In all such doubtful cases, the location was graded as 2 or 3, so that the number of clear sky hours quoted here for that night may have been somewhat under-estimated (< 10%).

Figure 2 summarizes the results in the form of average number of clear, night-time hours per year (period: 1987–1991) for the other eight locations listed in Table 2. Taking the typical lunar cycle into account, only ~ 48% of this time would be

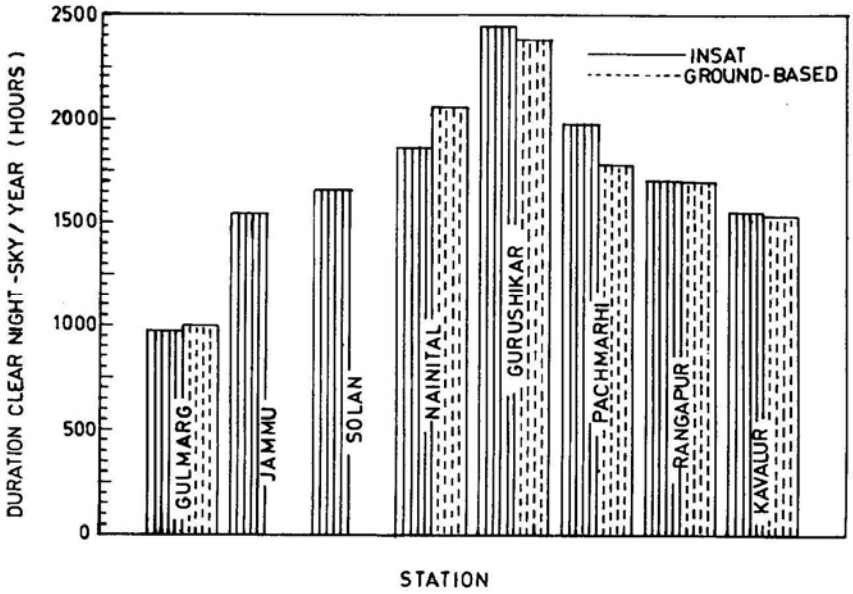

Figure 2. Number of 'clear night-sky' hours (spectroscopic sky) inferred from INSAT cloud-cover data are compared with results of some ground-based observations.

Table 2. Possible observation time per year for a given location inferred from INSAT cloud-cover data, is compared with the corresponding value quoted in literature from ground-based studies.

Site	Clear Night-sky (Hours)			
	Photometric	Spectroscopic		INSAT
	(a)	(a)	(b)	(c)
Leh	740	1760	1600	—
Gulmarg	—	—	1000*	975
Jammu	—	—	—	1543
Solan	—	—	—	1658
Nainital	1025	2060	1900	1862
Udaipur	1440	2250	—	—
Gurushikar	1760	2385	—	2453
Pachmarhi	915	1782	—	1977
Rangapur	—	—	1700	1704
Kavalur	245	1429	1535	1554

(a) Bhattacharya 1989.
(b) Bhatnagar & Gandhi 1991.
(c) Present work.
* Bhat 1982.

sufficiently dark for atmospheric Cerenkov work in the optical region. This correction factor applies more or less uniformly to all the stations referred to in this work. In view of the remarks made above that the present procedure should relate better with the combined photometric and spectroscopic skies rather than with the photometric skies only, we have also plotted in Fig. 2 the average number of spectroscopic hours

per year published in literature for some well known observatory sites, viz. Gulmarg, Nainital, Gurushikar, Pachmarhi, Rangapur and Kavalur (Bhat 1982, Bhattacharya 1989 and Bhatnagar & Gandhi 1991; see also Table 2). The values quoted for Kavalur and Gulmarg are based on the actual ground-based cloud-cover measurements for the period 1972 to 1978. Those for the other stations have been derived from the climatological tables and refer to the pre-1967 period (Bhattacharya 1989). It is reassuring to note that the results obtained here from an examination of INSAT cloud-imagery data for the other four stations are in excellent agreement with the values quoted by Bhattacharya (1989) and Bhatnagar & Gandhi (1991), and this vindicates the reliability of the approach followed here, at least in a statistical sense.

The following important conclusion immediately follows from an examination of Fig. 2: Gurushikar offers the maximum number of clear nights per year among the Indian stations considered here, corresponding to approximately 2450 hrs of clear night-sky annually (hereonwards referred to as 'spectroscopic hours'). This may be compared with the annual average of (spectroscopic) observation time quoted for some of the best observatories in the world: 2800 hrs at Mauna Kea, 2600 hrs at Cerro Tololo, La Silla and Las Campanas, 2200 hrs at Mount Palmor and Kitt Peak and 2000 hrs at Siding Spring and Lick Observatory. Thus, aurushikar is found to compare reasonably well with these observatories in respect of this important parameter. In view of the lunar cycle referred to above, the total effective time per year for optical Cerenkov observations works out to be 2450 × 0 48 hrs, or, 1176 hrs at Gurushikar.

AnotAnother advantage of working at Gurushikar becomes evident from Fig. 3, which shows the monthly distribution of 'spectroscopic' hours averaged over the 5-year period 1987-91, at the eight Indian stations of interest to this work. It is seen that,

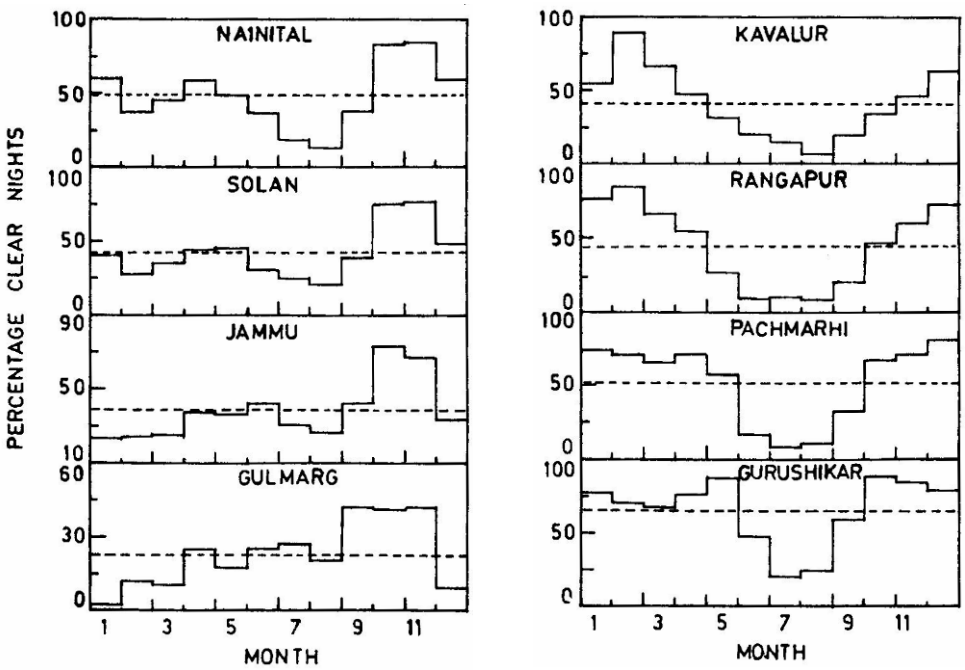

Figure 3. Monthly distribution of clear-nights for eight Indian locations. The dashed-line represents the annual average value.

in the case of the 4 sub-Himalayan stations, the average percentage of clear nights is < 40% per month at Gulmarg, < 50% at Jammu and Solan and < 60% at Nainital for almost 10 months in a year, the only two exceptions being the post-monsoon months of October and November. As can be expected, it is also evident from Fig. 3 that the effect of summer-monsoons becomes progressively more extensive in the monthly distribution of spectroscopic nights as one proceeds southwards from Gurushikar to Pachmarhi, Rangapur and Kavalur. As a result, the percentage of clear nights turns out to be maximum, between 60–90% for nine months at Gurushikar, with the monsoon affected period here being mainly limited to the months of July and August. This feature is an added attraction at Gurushikar, for, in principle, this gives a more uniform sky coverage and brings a wider range of candidate cosmic sources within the scope of meaningful investigations at this place (Sapru *et al.* 1993).

Figure 4 gives the yearly distribution of clear nights at the eight Indian stations for the period 1987–1991. The annual percentage of clear nights at each station is found to remain within ± 10% of the corresponding mean value. A closer examination of the figure suggests a systematic increase in the percentage of clear night-sky at most of the stations in 1989 (particularly so for non-Himalayan stations, responding mainly to summer monsoons) and a comparable decrease below the corresponding average level in 1991. The fact that these two deviations from the average behaviour are observed at most of the stations implies that they have a physical origin and are not due to statistical fluctuations. It is also an indication of the good sensitivity of the present technique.

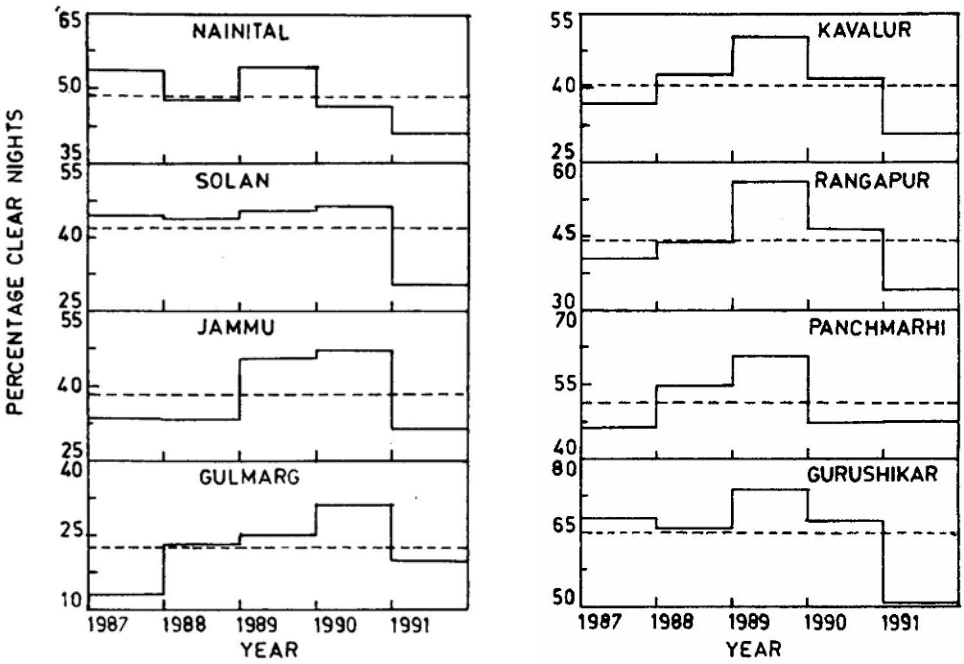

Figure 4. Yearly distribution of clear-nights for eight Indian locations. The dashed-line gives the average percentage of clear-nights for the period 1987-1991.

3. Conclusions

From an analysis of the INSAT satellite cloud-imagery data, collected for the 5-year period 1987–1991, it is shown that, from the point of view of cloud-free nights, Gurushikar is the best astronomical site in India yielding upto ~ 2400 spectroscopic hours of observations per calendar year. This time is distributed more or less uniformly over 9 months (September-May) of a year, thereby making it possible in principle, to study a wide range of interesting cosmic objects located in different parts of the sky in a purposeful manner through the optical atmospheric Cerenkov technique. In view of this encouraging trend, some in situ site-evaluation studies have been initiated at Gurushikar, within the premises of the existing Infrared Astronomy Observatory of the Physical Research Laboratory, Ahmedabad, with the main aim of seeking answers to conditions (2–5) listed in section 1. These studies include measurements of the daily dust-load (total particulate matter) and wind velocity, (both these factors can potentially constrain total observation time as also its monthly distribution), atmospheric extinction coefficient and the night sky light level. The results of this supplementary study, which are also quite promising, are being presented separately (Sapru *et al*. 1993).

Acknowledgements

The authors would like to thank Dr. A. V. R. Krishna Rao, Director Satellite Meteorological Unit of the Indian Meteorological Department, New Delhi, for helpful discussions and for making available the data used in this work.

References

Bhat, C. L., Razdan, H., Sapru, M. L. 1980, *Astrophys. Space Sci.* **73**, 513.
Bhat, C. L. 1982, Phd. Thesis, Kashmir University.
Bhat, C. L., Sapru, M. L., Razdan, H. 1986, *Astrophys. J*., **306**, 587.
Bhat, C. L., Kaul, R. K., Rawat, H. S., Senecha, V. K., Rannot, R. C., Sapru, M. L., Tickoo, A. K., Razdan, H. 1991a, *Astrophys. J*., **369**, 475.
Bhat, C. L., Kaul, R. K., Koul, R., Sapru, M. L., Kaul, C. L., Tickoo, A. K., Rannot, R. C., Senecha, V. K., Razdan, H. 1991b, NRL *Technical Report No. 2*, p. 1.
Bhat, C. L., Koul, R., Tickoo, A. K., Kaul, I. K., Kaul, S. K., Kaul, S. R. 1993, *Proc. Natl. Symp. Advanced Instr. for Nucl. Res.* p. 16.
Bhat, C. L. 1993, *Bull. astr. Soc. India,* (to be published).
Bhatnagar, A., Gandhi, S. L. 1991, *Tech. Report on DST Project,* p. 23.
Bhattacharya J. C. 1989, *IIA Newsletter,* **4,** 18.
Koul, R., Bhat, C. L., Tickoo, A. K., Kaul, I. K., Kaul, S. K., Gazi, R. A., Kaul, R. K., Rawat, H. S.,Senecha, V. K., Rannot, R. C., Sapru, M. L., Razdan, H. 1989, *J. Phys. E*: *Sci. Inst*., **22**, 47.
Lamb, R. C. 1989, *Proc. Int. Workshop VHE Gamma-ray Astronomy*, Crimea, p. 1.
Razdan, H. 1989, *Indian J. Pure Appal. Phys*., **27**, 355.
Sapru, M. L., Bhat, C. L., Kaul, M. K., Dhar, V. K., Kaul, R. K., Rannot, R. C., Tickoo, A. K. 1993, *Bull. astr. Soc. India*, (to be published).
Weekes, T. C. 1988, *Phys. Rev*., **160,** 1.
Weekes, T. C. 1992, *Space Sci. Rev*., **59**, 315.

J. Astrophys. Astr. (1994) **15,** 103

Preface

As mentioned in the March issue, we are reproducing some classic papers by distinguished Fellows of the Indian Academy of Sciences as part of the **Diamond Jubilee** celebrations. In this issue we reproduce four historic papers by **Subrahmanyan Chandrasekhar ,** one of the **Foundation Fellows** of the Academy. To select four papers from Chandrasekhar's publications over the last six decades is a daunting task for any Editor! Faced with this difficulty we decided to reproduce four papers from the earliest period – after all these are some of his most famous and fundamental papers.

The first paper, reproduced from the *Philosophical Magazine,* was inspired by the seminal paper by R.H.Fowler in which the newly discovered Fermi-Dirac statistics was invoked to explain the stability of white dwarfs. Chandrasekhar wrote this paper when he was still an undergraduate student at the Presidency College in Madras. As he has stated on a number of occasions, his interest in the possible role of electron degeneracy to the structure of white darfs was stimulated by his meeting with Arnold Sommerfeld in Madras in the late fall of 1928.

The second paper reproduced from the *Astrophysical Journal* deals with the effect of relativistic degeneracy. It is in this celebrated paper that he derived the upper limit to the mass of an ideal white dwarf.

One of the profound results obtained by Chandrasekhar in his early years is contained in the third paper reproduced from the *Zeitschrifl für Astrophysik.* In this prescient paper a rigorous criterion for degeneracy to set in is derived, and the fundamental result established that for all centrally condensed stars of mass greater than a critical mass *"the perfect gas equation of state does not break down, however high the density may become, and the matter does not become degenerate. An appeal to the Fermi-Dirac statistics to avoid α central singularity cannot be made".* Since this is one of his most famous papers from this period the following paragraph from Chandrasekhar's own 'Preface' to his **Selected Papers** published by the University of Chicago Press might be of interest: *"Perhaps an additional historical remark may be made regarding the concluding sentence of paper 8 [Zeitschrift für Astrophysik,* 5 *No. 5, 1932, 321-27], which has been quoted in various accounts. This paper was written in 1931 very soon after the publication of paper 6 [MNRAS,* **91** *No.5, (1931), 456- 66] , but I withheld publication because of E.A.Milne's dissent. A year later, when I joined the Institut For Teoretisk Fysik in Copenhagen, I discussed the paper with Leon Rosenfeld, who strongly urged me to publish it. To avoid additional discussions with Milne, I sent it to the Zeitschrift für Astrophysik, with editorial offices at the Astrophysikalisches Observatorium in Potsdam. But Professor Milne happened to be visiting Potsdam at that time and he was asked to referee the paper; and in a letter directly written to me, he stated, "Unfortunately I have been unable to recommend acceptance, as the paper contains a mistake in principle, and in any case it would only do your reputation harm if it were published." Again I discussed the matter with Rosenfeld, and at his urging I returned the paper to the editor (W.Grotrian) with some pro forma changes."*

The fourth paper deals with the then controversial subject of stellar configurations with degenerate cores and is reproduced from *The Observatory.* Since this paper is so often quoted — particularly the prophetic last paragraph — but seldom read(!) we felt that it would be appropriate to reproduce this also.

The Academy is most grateful to the Editors of the *Philosophical Magazine, The Astrophysical Journal, Astronomy and Astrophysics,* and *The Observatory* for very kindly granting us permission to reproduce these papers.

J. Astrophys. Astr. (1994) **15,** 105–109

Reproduced from *Philosophical Magazine,* **11** (Suppl.Feb.1931), 592-596

XLVIII. *The Density of White Dwarf Stars.*

By S. CHANDRASEKHAR *.

1. THE first application of the Fermi-Dirac statistics to stellar problems was by Fowler † in connexion with the well-known problem of the companion of Sirius. This idea has lately been taken up by Stoner ‡ and others to calculate the limiting density of white dwarf stars. In this paper another way of arriving at the order of magnitude of the density of white dwarfs from different considerations is given.

2. Let p_r denote the radiation pressure and p_G the gas pressure, and the total pressure P is then given by

$$P = p_r + p_G. \quad . \quad . \quad . \quad . \quad . \quad . \quad (1)$$

We introduce the constant β, such that

$$\left.\begin{aligned} p_r &= (1-\beta)P, \\ p_G &= \beta P. \end{aligned}\right\} \quad . \quad . \quad . \quad . \quad . \quad . \quad (2)$$

We will make the assumption that β = 1 approximately, *i.e.,* we leave the radiation pressure out of account. We are dealing therefore with *ideal* conditions which can perhaps exist only in stars which are much higher in the white dwarf stage than even $O_{2,}$ Eridani B.

* Communicated by R. H. Fowler, F.R.S.

† R. H. Fowler. Month. Not. Roy. A. S. lxxxvii. p. 114 (1926)

‡ E. C. Stoner, Phil. Mag. vii. p. 63 (1929): ix. p. 944 (1930).

Reproduced from *Philosophical Magazine,* **11** (Suppl.Feb.1931), 592–596

Now for a fully degenerate electron gas (in the Sommerfeld sense) the pressure is given by

$$p_e = \frac{\pi}{60}\frac{h^2}{m}\left(\frac{3n}{\pi}\right)^{5/3} \quad . \quad . \quad . \quad . \quad . \quad . \quad (3)$$

We assume that it is this electron pressure which is by far the greatest contribution to the gas pressure, und therefore to the total pressure. Further, if ρ is the density of the stellar material, the number of electrons is given by

$$n = \frac{\rho}{\mu \mathrm{H}(1+f)}, \quad . \quad . \quad . \quad . \quad . \quad . \quad (4)$$

where f is the ratio of the number of ions to the number of electrons (we can in practice neglect f), H the mass of the hydrogen atom, and μ the molecular weight. For a fully ionized material of the type we are dealing with μ = 2·5 nearly. We will use this value Later. We have therefore

$$p_G = \frac{\pi}{60}\frac{h^2}{m}\left(\frac{3}{\pi \mathrm{H}}\right)^{5/3}\frac{\rho^{5/3}}{\mu^{5/3}(1+f)^{5/3}}$$

$$= 9{\cdot}845 \times 10^{12}\left[\frac{\rho}{\mu(1+f)}\right]^{5/3}, \quad . \quad . \quad . \quad (5)$$

(The values used for h, m, etc. are those given in. A. S. Eddington's 'Internal Constitution of Stars,' Appendix (1).)

Putting

$$\mathrm{K} = \frac{9{\cdot}845 \times 10^{12}}{\mu^{5/3}(1+f)^{5\cdot 3}}, \quad . \quad . \quad . \quad . \quad . \quad (6)$$

we have for the total pressure

$$\mathrm{P} = \mathrm{K}\rho^{5/3}. \quad . \quad . \quad . \quad . \quad . \quad (7)$$

We can now straightway apply the theory of the polytropic gas spheres, where for the exponent γ we have

$$\gamma = 5/3 \text{ or } 1 + \frac{1}{n} = 5/3,$$

giving $n = 3/2$. . . . . (8)

We have therefore*

$$\left(\frac{\mathrm{GM}}{\mathrm{M}'}\right)^{+1/2}\left(\frac{\mathrm{R}'}{\mathrm{R}}\right)^{-3/2} = \frac{[5/2\mathrm{K}]^{3/2}}{4\pi \mathrm{G}}, \quad . \quad . \quad . \quad (9)$$

* A. S. Eddington, 'Internal Constitution of Stars,' p. 83 *et seq*. The notation is the same as that used in his book and now generally adopted. The particular equation (9) follows from the second of the equations (57.3)

Reproduced from *Philosophical Magazine,* **11** (Suppl.Feb.1931), 592-596

Or $$\frac{GM}{M'} = \frac{125 \times 9{\cdot}845^3 \times 10^{36}}{128\pi^2 G^2} \cdot \frac{1}{\mu^5(1+f)^5}\left(\frac{R'}{R}\right)^3 \quad . \quad . \quad (10)$$

The values o£ R' and M' can be obtained from the extensive tables given by Emden in his 'Gas-Kugeln,' and are (page 79, tabbelle 4)

$$\left.\begin{aligned} R' &= 3{\cdot}6571, \\ M' &= 2{\cdot}7176. \end{aligned}\right\} \quad . \quad . \quad . \quad . \quad . \quad . \quad (11)$$

Using these values in (10), and expressing the mass in terms of that of the Sun (= $1{\cdot}985 \times 10^{33}$ grams), we get the result

$$(M/\odot)R^3 = \frac{2{\cdot}14 \times 10^{28}}{\mu^5} (= 2{\cdot}192 \times 10^{26}). \quad . \quad (12)$$

The second value for $(M/\odot)\ R^3$, given in brackets, we get by using the value 2·5 for μ. We can express (12) differently, as follows:

$$R^6\rho = \frac{1{\cdot}014 \times 10^{61}}{\mu^5} (= 1{\cdot}039 \times 10^{59}), \quad . \quad . \quad (13)$$

$$\rho = 2{\cdot}162 \times 10^6 (M/\odot)^2. \quad . \quad . \quad . \quad . \quad . \quad (14)$$

We will apply the above equations to the case of the companion of Sirius. The mass of it, as determined from the double star orbit, is trustworthy, and equals ·85⊙· The computed radius = $1{\cdot}8 \times 10^7$. (But we cannot use this value in (13) to calculate the density, as it is based on formulae which may not be applicable to this case.) From the mass we can derive the radius und equals $6{\cdot}361 \times 10^8$ (about thirty times the accepted value). For the density of the companion of Sirius we get from (14), *provided* it were completely degenerate (which, however, is extremely unlikely),

$$\rho_{\text{c. Sirius}} = 1{\cdot}562 \times 10^6 \text{ grams per cm.}^3 \quad . \quad (15)$$

The mean density assumed is $\cdot 5 \times 10^5$, being thus thirty times smaller than that given by (15). We can, however, take the value given by (15) as indicating the *maximum* density which a stellar material having a mass equal to that of the companion of Sirius can have. A similar calculation can be made for O_2 Eridani B and Procyon B, and the calculated values are collected in a table below. The calculations for the *limiting density* on Stoner's theory give different values, and they are also given for comparison. We discuss the cause of the difference below.

We further note (i.) that the radius of a white dwarf is inversely proportional to the cube root of the radius, (ii.) the density is proportional to the square of the mass, (iii.) the central density would be six times the mean density ρ.

Reproduced from *Philosophical Magazine,* **11** (Suppl.Feb.1931), 592-596

3. Stoner (*loc. cit.*) arrives at a formula for the *limiting* density for a material composed of completely ionized atoms on the following argument:—

The density increases as the sphere shrinks, and the limit is reached when the gravitational energy released just supplies the "energy required to squeeze the electrons closer together." The limiting condition would then be given by

$$\frac{d}{dn}(E_G + E_K) = 0, \quad . \quad . \quad . \quad . \quad . \quad (16)$$

E_G being the gravitational energy and E_K the kinetic energy, for which, of course, the Fermi formula is used. The formula he gets is (without his latter relativity-mass correction)

$$\rho_{max.} = 3{\cdot}977 \times 10^6 (M/\odot)^2, \quad . \quad . \quad . \quad . \quad (17)$$

which is exactly the same as our (14) with a difference in the

Star.	Mass.	Radius.	Density.		
			As calc. by (14).	Accepted value.	By Stoner's formula (17).
O_2 Eridani B.	·44 ⊙	$7{\cdot}927 \times 10^8$	$4{\cdot}186 \times 10^5$	$·98 \times 10^5$	$7{\cdot}8 \times 10^5$
Procyon B.	·37 ⊙	$8{\cdot}399 \times 10^8$	$2{\cdot}960 \times 10^5$	—	$5{\cdot}445 \times 10^5$
Companion of Sirius.	·85 ⊙	$6{\cdot}361 \times 10^8$	$1{\cdot}562 \times 10^6$	$·5 \times 10^5$	$2{\cdot}872 \times 10^6$

numerical factor only, the discrepancy being about 1:2. The difference in the two is obviously due to the fact that our value for ρ is not the " limiting density" in the sense in which Stoner uses the term ; but our calculation gives us a much nearer approximation to the conditions actually existent in white dwarfs than Stoner's calculation does. At any rate, it brings out clearly that the *order of magnitude* of the density which one can on purely theoretical considerations attribute to a white dwarf is the same.

Our results (see table) agree with Stoner's in showing that O_2 Eridani B is much nearer the ideal dwarf-star stage than the companion of Sirius, but indicate also that neither of them is so far from the ideal stage as Stoner's calculation would seem to indicate.

Reproduced from *Philosophical Magazine,* **11** (Suppl.Feb.1931), 592-596

Summary.

The density of the white dwarf stars is reconsidered from the point of view of the theory of the poly tropic gas spheres, and gives for the *mean density* of a white dwarf (under ideal conditions) the formula

$$\rho = 2{\cdot}162 \times 10^6 \times (\mathrm{M}/\odot)^2.$$

The above formula is derived on considerations which are a much nearer approximation to the conditions *actually existent* in a white dwarf than the previous calculations of Stoner based on uniform density distribution in the star and which gave for the limiting density the formula

$$\rho = 3{\cdot}977 \times 10^6 \times (\mathrm{M}/\odot)^2.$$

J. Astrophys. Astr. (1994) **15,** 115–116

Reproduced from *The Astrophysical Journal,* **74** (1), (1931), 81-82

THE MAXIMUM MASS OF IDEAL WHITE DWARFS

BY S. CHANDRASEKHAR

ABSTRACT

The theory of the *polytropic gas spheres* in conjunction with the equation of state of a *relativislically degenerate electron-gas* leads to a *unique value for the mass of a star* built on this model. This mass (= $_{0}{}_{9}\mathrm{I}\odot$) is interpreted as representing the upper limit to the mass of an ideal white dwarf.

In a paper appearing in the *Philosophical Magazine*,[I] the author has considered the density of white dwarfs from the point of view of the theory of the polytropic gas spheres, in conjunction with the degenerate non-relativistic form of the Fermi-Dirac statistics. The expression obtained for the density was

$$\rho = 2.162 \times 10^{6} \times \left(\frac{M}{\odot}\right)^{2}, \tag{I}$$

where $M/\odot$ equals the mass of the star in units of the sun. This formula was found to give a much better agreement with facts than the theory of E. C. Stoner,[2] based also on Fermi-Dirac statistics but on uniform distribution of density in the star which is not quite justifiable.

In this note it is proposed to inquire as to what we are able to get when we use the relativistic form of the Fermi-Dirac statistics for the degenerate case (an approximation applicable if the number of electrons per cubic centimeter is $> 6\times10^{29}$). The pressure of such a gas is given by (which can be shown to be rigorously true)

$$P = \tfrac{1}{8}\left(\frac{3}{\pi}\right)^{\frac{1}{3}} \cdot hc \cdot n^{4/3}, \tag{2}$$

where h equals Planck's constant, c equals velocity of light; and as

$$n = \frac{\rho}{\mu H(1+f)}, \tag{3}$$

[I] II, No. 70, 592, I93I.

[2] *Philosophical Magazine,* **7**, 63, I929.

Reproduced from *The Astrophysical Journal,* **74** (1), (1931), 81-82

μ equals the molecular weight, 2.5, for a fully ionized material, H equals the mass of hydrogen atom, and f equals the ratio of number of ions to number of electrons, a factor usually negligible. Or, putting in the numerical values,

$$P = K\rho^{4/3}, \tag{4}$$

where K equals 3.619×10^{14}. We can now immediately apply the theory of polytropic gas spheres for the equation of state given by (4), where for the exponent γ we have

$$\gamma = \frac{4}{3} \text{ or } 1+\frac{1}{n} = \frac{4}{3} \text{ or } n = 3 .$$

We have therefore the relation[1]

$$\left(\frac{GM}{M'}\right)^2 = \frac{(4K)^3}{4\pi G},$$

or

$$\begin{aligned} M &= 1.822 \times 10^{33} \\ &= .91\odot \text{ (nearly)} \end{aligned} \tag{5}$$

As we have derived this mass for the star under ideal conditions of extreme degeneracy, we can regard 1.822×10^{33} as the maximum mass of an ideal white dwarf. This can be compared with the earlier estimate of Stoner[2]

$$M_{\max} = 2.2 \times 10^{33}, \tag{6}$$

based again on uniform density distribution. The "agreement" between the accurate working out, based on the theory of the polytropes, and the cruder form of the theory is rather surprising in view of the fact that in the corresponding non-relativistic case the deviations were rather serious.

TRINITY COLLEGE
CAMBRIDGE
November 12, 1930

[1] A. S. Eddington, *Internal Constitution of Stars,* p. 83, eq. (57.3.)

[2] *Philosophical Magazine,* **9**, 944, 1930.

J. Astrophys. Astr. (1994) **15,** 119–125

Reproduced from *Zeitschrift für Astrophysik,* **5** (5), (1932), 321-327

Some Remarks on the State of Matter in the Interior of Stars.

By **S. Chandrasekhar** (Copenhagen).

With 3 figures. (Received September 28, 1932.)

It is shown that for *all* stars for which the radiation-pressure is greater than a tenth of the total pressure, an appeal to the FEBMI-DIRAC statistics to avoid the central singularity which arises in the discussions of the centrally condensed and the collapsed stars cannot be made. The bearing of this result on the possible state of matter in the interior of stars is indicated.

Since the publication of MILNE'S memoir on the "Analysis of Stellar Structure" in the Monthly Notices for November 1980[1]) a great deal of Work has been done to consider "composite" stellar models. But the following simple considerations seem to have escaped notice and it seems worth while to state them explicitly.

§ 1. The Surfaces of Demarcation. As we approach the centre of a centrally-condensed or a collapsed star, we change over to the equation of state $P = K_1 \varrho^{5/3}$ if the perfect gas law breaks down. If the perfect gas-law breaks down at all, the actual transition from the perfect-gas envelope to the degenerate core must occupy a certain zone, but we could for the sake of convenience consider a definite surface of demarcation defined as the surface at which the two equations of state give the same gas-pressure.

Now in the perfect gas envelope the *total* pressure is given by

$$P = \left[\left(\frac{k}{\mu}\right)^4 \frac{3}{a}\left(\frac{1-\beta}{\beta^4}\right)\right]^{1/3} \varrho^{4/3}, \tag{1}$$

where

$$\beta = 1 - \frac{\varkappa L}{4\pi c G M}, \tag{2}$$

x = the opacity coefficient, L = luminosity in ergs cm^{-3}, M = mass in grams, k = BOLTZMANN'S Constant, μ. = molecular weight = αm_{H} (say), m_{H} = mass of the hydrogen atom. Since for the standard model the gas pressure p is given by

we have

$$p = \beta P, \tag{3}$$

where

$$p = C \varrho^{4/3}, \tag{4}$$

$$C = \left[\left(\frac{k}{\mu}\right)^4 \frac{3}{a} \frac{1-\beta}{\beta}\right]^{1/3} = \frac{2.632 \cdot 10^{15}}{\alpha^{4/3}} \left[\frac{1-\beta}{\beta}\right]^{1/3}. \tag{4'}$$

[1]) Refered to as 1. c.

The equation of state in the degenerate zone is

$$p = K_1 \varrho^{5/3}, \tag{5}$$

where

$$K_1 = \frac{1}{20}\left(\frac{3}{\pi}\right)^{2/3} \frac{h^2}{m\,\mu^{5/3}} = \frac{9.890 \cdot 10^{12}}{\alpha^{5/3}}. \tag{6}$$

At the first surface of demarcation which we will call S_1, the density ϱ_1 is given by

$$C\,\varrho_1^{4/3} = K_1\,\varrho_1^{5/3},$$

or

$$\varrho_1 = \left(\frac{C}{K_1}\right)^3. \tag{7}$$

Now, it is well known that the equation of state (5) changes over again into the relativistic-degenerate-equation of state

$$p = K_2 \varrho^{4/3}, \tag{8}$$

$$K_2 = \frac{hc}{8\,\mu^{4/3}}\left(\frac{3}{\pi}\right)^{1/3} = \frac{1.228 \cdot 10^{15}}{\alpha^{4/3}}. \tag{8'}$$

Hence if *circumstances* permit we have to consider a second surface of demarcation, S_2, where the density ϱ_2 is given by

$$\varrho_2 = \left(\frac{K_2}{K_1}\right)^3. \tag{9}$$

Hence we have *two* surfaces of demarcation if and only if

$$\varrho_2 > \varrho_1,$$

or

$$\left(\frac{K_2}{K_1}\right)^3 > \left(\frac{C}{K_1}\right)^3, \tag{10}$$

i. e. only when [cf. equations (4'), (6), (8')]

$$\frac{1-\beta}{\beta} < \frac{h^3 c^3 a}{512\,\pi\,k^4} = 0.1015,$$

or

$$\beta > 0{,}9079. \tag{11}$$

It may be remarked in passing that the above value for β is independent of the assumed molecular weight. *It depends only on the mass, luminosity and opacity in the gaseous envelope.* It is also independent of whether we consider the same opacity for the degenerate zone and the gaseous envelope, or different opacities in the two regions.

§ 2. The meaning of the fundamental inequality (11) is made clear by the following.

In the following graph I plot log p against log ϱ.

For numerical calculations I use $\alpha = 2$. The straight line *ABK* represents the equation of state $p = K_1 \varrho^{5/3}$ and *BC* the equation of state $p = K_2 \varrho^{4/3}$. These two intersect at *B* where the density is that which corresponds to the *second* surface of demarcation, namely ϱ_2. *ABC* gives roughly the equation of state of a degenerate gas.

Let us consider a star for which $\beta = 0.98$. By (4) we get

$$\log p = 14.455 + {}^4/_3 \log \varrho. \tag{12}$$

DE represents this equation. It intersects the degenerate equation of state *AB, C at E.* The point *E* corresponds to the first surface of demarcation S_1. Hence for all stars for which $\beta = 0.98$, we first traverse a perfect gas envelope with an equation of state represented by *DE.* Then we traverse a degenerate zone corresponding to *E B* and finally (if we have not yet reached the centre) a relativistically degenerate zone.

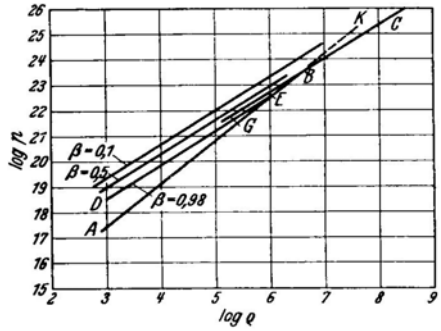

Fig. 1.

Now, if $\beta = 0.9079$, then *GB* represents the perfect gas equation of state and the degenerate zone reduces to a single layer, and the relativistically degenerate zone is described equally well by the perfect gas equation.

Now if $\beta < 0.9079$[1]) the perfect gas equation of state has *no* intersections with *ABC* and this means that however high the density may become the temperature rises sufficiently rapidly to prevent the matter from becoming degenerate.

In this connection it will have to be remembered that considerations of relativity do not affect the equation of state of a perfect gas. $p = N k T$, *is true independent of relativity.*

§3. Centrally-Condensed Stars. Now, for each mass M there is a unique luminosity L_0 — the "EDDINGTON luminosity" which makes the star

[1]) The radiation pressure is *greater* than a tenth of the total pressure if $\beta < 0.9079$.

a perfect gas sphere, with a polytropic index 3. This L_0 characteristizes a unique β_0 which is in fact related to M by means of EDDINGTON'S quartic equation:

$$1 - \beta = 0.003\,09 \left(\frac{M}{\odot}\right)^2 \alpha^4 \beta^4. \tag{13}$$

Now from the definition of a centrally-condensed and a collapsed star, it is clear that

$$\left.\begin{aligned} \beta_{c.c} &< \beta_0 \\ \beta_{\text{col.}} &> \beta_0. \end{aligned}\right\} \tag{14}$$

Consider first the mass $\mathfrak{M}$ for which $\beta_0 = 0.9079$. By (13) we have

$$\mathfrak{M}/\odot = 6{,}623\,\alpha^{-2}. \tag{15}$$

If we assume $\alpha = 2$,

$$\mathfrak{M}/\odot = 1.656. \tag{15'}$$

Now consider a centrally-condensed star of mass *M greater* than (or equal to) $\mathfrak{M}$. Then we obviously have

$$\left.\begin{aligned} {}_M\beta_0 &< {}_{\mathfrak{M}}\beta_0 = 0.908. \\ {}_M\beta_{c.c} &< {}_{\mathfrak{M}}\beta_0 < 0{,}908. \end{aligned}\right\} \tag{16}$$

Hence, we have the result that for *all centrally condensed stars of mass greater than* $\mathfrak{M}$, *the perfect gas equation of state does not break down, however high the density may become, and the matter does not become degenerate. An appeal to the Fermi-Dirac statistics to avoid the central singularity cannot be made.*

Since however we cannot allow the infinite density which the centrally condensed solution of EMDEN'S differential equation — index 8 — allows at the centre and in the absence of our knowledge of any equation of state governing the perfect gas other than that of degenerate matter, our only way out of the singularity is to assume that there exists a maximum density $\varrho_{\max}$ which matter is capable of. We have therefore to consider the "fit" of a gaseous envelope of the centrally condensed type on to a homogeneous core at the maximum density of matter. *If we insist on the density to be continuous at the interface* the equation of "fit" is found to be[1])

$$\frac{1}{3}\,\xi'\,\Theta'^3 = -\left(\frac{d\Theta}{d\xi}\right)_{\xi=\xi'}, \tag{17}$$

[1]) S. CHANDRASEKHAR, M. N. **91**, 456, 1931, equation (47).

where the polytropic equation describing the gaseous part of the star is

$$\frac{1}{\xi^2}\frac{d}{d\xi}\left(\xi^2\frac{d\Theta}{d\xi}\right) = -\Theta^3, \tag{17'}$$

where ξ is the value of ξ at which $\varrho_{\max}$ begins. In (17') the meaning of Θ and ξ are the following:

$$\varrho = \lambda_3\Theta^3, \quad r = \xi\left[\frac{C}{\pi G\beta}\right]^{-1/3}\lambda_3^{-1/3}. \tag{17''}$$

(λ_3 is a *homology, constant*). But (17) has *no* solutions if Θ is of the EMDEN'S or of the centrally-condensed type. Hence the acceptance of a $\varrho_{\max}$ does not

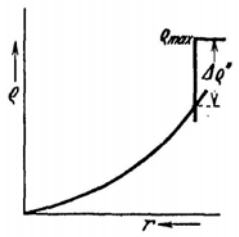

Fig. 2.

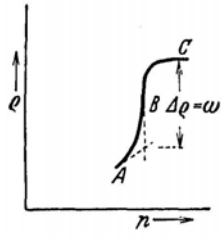

Fig. 3.

help us out of the difficulty if we insist on the density to be continuous at the interface. The procedure then to construct an equilibrium configuration would be to proceed along the centrally condensed solution until the mean density ϱ_m (r) of the *surviving mass* M (r) equals $\varrho_{\max}$ which will occur at a determinate $r = r''$ (say) where

$$M(r'') = {}^4/_3\pi r''^3\varrho_{\max}; \tag{18}$$

we then replace the material inside $r = r''$ by a sphere of incompressible matter at the density $\varrho_{\max}$. At r'' there will be a discontinuity of density (see Fig. 2).

Now the form of Θ as $\xi \to 0$ for a centrally condensed solution is (MILNE, l. c) :

$$\Theta \sim \frac{1/\sqrt{2}}{\xi\,[\log(D/\xi)]^{1/2}}, \tag{19}$$

where D is a constant. D is *fixed* by the condition that the analytic continuation of (19) passes through $\xi = 1$ and $\Theta = 0$ and satisfies here the requisite boundary condition, namely

$$M = -\frac{4}{\pi^{1/2}}\left(\frac{C}{G\beta}\right)^{3/2}\left(\xi^2\frac{d\Theta}{d\xi}\right)_0. \tag{20 [1]}$$

[1]) C is given by equation (4').

Hence we get the result that D is a function of L, M and x only and hence fixed. Since D is fixed by the boundary condition, it follows that the value of ξ'' at which Θ (ξ'') becomes equal to $\Theta_{\max}$ (where cf. equation (17″))

$$\Theta_{\max} = \varrho_{\max}^{1/3} \lambda_3^{-1/3}, \tag{21}$$

is fixed as a function of λ_3. In other words the discontinuity in Θ, $\Delta\Theta''$ at the interface ξ'' is a single-valued function of L, M, x and λ or

$$\Delta\Theta'' = F(L, M, \varkappa; \lambda_3) \tag{21'}$$

or by (21)

$$\Delta\varrho'' = f(L, M, \varkappa; \lambda_3) \tag{22}$$

where $\Delta\varrho''$ is the discontinuity of density at the interface.

But it has been suggested by LANDAU[1]) (among others) that the maximum density of matter will arise *after* some kind of *overcompressibility, the incompressibility setting in later* (see Fig. 8).

Further it has been suggested that 1) the pressure at which the overcompressibility sets in must be a physical property of the atomic nuclei and the electrons in the enclosure, and 2) the form of the curve *A B C is* again an intrinsic physical property of matter. If we idealise the situation of Fig. 8, we see that $\Delta\varrho$ *ought to be a physical property of matter.* Let this $\Delta\varrho$ be ω. Then by (22) we have to so choose the homology constant λ_3, that $\Delta\varrho''$ equals ω:

$$f(L, M, \varkappa; \lambda_3) = \omega. \tag{23}$$

This fixes λ_3 and hence by (17″) fixes r_0 – the radius of the configuration. Hence *we are able to obtain equilibrium configurations for arbitrary mass, and arbitrary luminosity, the radius however bieng determinate in each case.*

§ 4. In the above section we have tried to construct the equilibrium configurations for all centrally-condensed stars of mass greater than $\mathfrak{M}$[2]), and found that the introduction of a homogeneous core at the maximum density of matter ($\varrho_{\max}$) with a discontinuity of density at the interface was necessary. We may now ask about the equilibrium configurations for centrally condensed stars with $\beta > 0.908$. Now the star has clearly a degenerate zone (see Fig. 1). A little consideration shows that if we come along a centrally-condensed solution in the perfect gas part of the star then at the interface S_1 (cf. § 1) we are compelled to choose a centrally-condensed solution for the polytropic equation of index "$^3/_2$"

[1]) I am indebted to Dr. STRÖMGREN for advice on these matters.

[2]) Or more generally, centrally-condensed stars with $\beta < 0.908$.

to describe the non-relativistic degenerate part of the star[1]); also at the second surface demarcation S_2 we are again forced to choose a centrally-condensed solution for the potytropic equation of index "3". Hence in this case also we are unable to avoid the central singularity by appealing to the FERMI-DIRAC statistics alone. The star must have a homogeneous core with a discontinuity of density at the interface. The considerations of the previous section apply and we see that the centrally-condensed stars $\beta > 0.908$ differ from the centrally-condensed stars with $\beta < 0.908$ only in this, that while in the former type of stars we have to traverse a degenerate zone before reaching the homogeneous core, in the latter type, the stellar material continues to be a perfect gas till we reach the homogeneous core. Thus we find that *all centrally-condensed stars (on the standard model) must have a homogeneous core at the centre with a discontinuity of density at the interface.*

§ 5. Collapsed-Stars. Just a few remarks about collapsed stars may be permitted. A detailed analysis of *highly-collapsed* stars has been given elsewhere (CHANDRASEKHAR, 1. c).

Consider a collapsed star of mass greater than $\mathfrak{M}$ and let further $\beta_0 < \beta_{\text{col.}} < 0.9078$. In other words the collapse" has not proceeded sufficiently far to increase β beyond 0.9078. In such a case the collapse can occur only on a homogeneous core. But if the collapse proceeds sufficiently far, such that $\beta_{\text{col}} > 0.9078$ in spite of β_0 being less than 0,9078, the star will then possess a degenerate zone as well.

Conclusion: We may conclude that great progress in the analysis of stellar structure is not possible before we can answer the following fundamental question:

Given an enclosure containing electrons and atomic nuclei, (total charge zero) what happens if we go on compressing the material indefinitely?

[1]) This is also true if we ascribe different opacities to the gaseous and the degenerate part of the star.

Reproduced from *Zeitschrift für Astrophysik,* **5** (5), (1932), 321-327

J. Astrophys. Astr. (1994) **15,** 133–137

Reproduced from *The Observatory,* **57**(727), (1934), 373-377

Stellar Configurations with degenerate Cores.

IN an article published in the March number of *The Observatory* the new orientation towards the general problem of Stellar Structure resulting from the use of degenerate statistics was discussed. A result obtained in that article and which is of importance in our present discussion can be recalled in the following terms :— For stellar material at a specified temperature T and density ρ we can define abstractly a quantity β denoting the ratio between the gas pressure ρ and the total pressure P (which is the sum of the gas kinetic and radiation pressure). Then if

$$\frac{960\,(1-\beta)}{\pi^4\,\beta^2} > 1, \quad \ldots\ldots \quad (1)$$

the material at density ρ and temperature T will be a perfect gas in the classical sense. If β_ω be such that relation (I) is an *equality* then in stellar configurations in which $(1-\beta)$ is always greater than $(1-\beta_\omega)$ the stellar material continues to be a perfect gas however high the density may become. On the standard model this means that if the mass be greater than a certain critical mass (say $\mathfrak{M}$) then finiteness of central density restricts us to consider only the nonsingular solutions of Emden's equation with index 3. This means that if we plot $(1-\beta)$ against the radius R then the curves of constant mass ($M>\mathfrak{M}$) are lines parallel to the R-axis. For $(1-\beta)>(1-\beta_\omega)$ these lines (which I shall refer to as " Eddington lines ") are not distorted by the introduction of degenerate states. The question of using degenerate states for these configurations does not arise at all. If, however $(1-\beta)<(1-\beta_\omega)$, the curves of constant mass are no longer fully represented by the Eddington lines, and in this region we have a nontrivial solution to Milne's fundamental problem, which for our purposes can be formulated as follows :—" For a star to be wholly gaseous the mass is a function of β only. Call the appropriate β, β_M. Has the star equilibrium configurations for $\beta\neq\beta_M$?" This problem is important, for it is precisely by formulating the problem of stellar structure in this way that we can fully analyse the structure of stars of mass less than $\mathfrak{M}$ $(=6{\cdot}623\,\mu^{-2}\odot)$ *.

***** *Cf.* S. Chandrasokhar, *Zs. f. Astrophysik,* **5.** 321 (1932), equation (15).

Reproduced from *The Observatory,* **57**(727), (1934), 373-377

To answer Milne's problem for (I —β)<(I—β_ω) it is essential to take the equation of state for the degenerate matter in the exact form. We cannot neglect relativistic degeneracy since we have seen already that precisely because of the relativistic effects the Eddington lines are undistorted in the greater part of the (I—β, R) diagram. I shall refer to such a plot as a *Milne diagram.*

Now the equation of state for the degenerate state can be written parametrically as follows :—

$$p = \frac{\pi m^4 c^5}{3h^3} f(x) \; ; \; \rho = \frac{8\pi m^3 c^3 \mu m_H}{3h^3} x^3 = \mathrm{B}x^3 \text{ (say)}, \quad . \quad (2)$$

where

$$f(x) = [x(x^2+1)^{1/2}(2x^2-3)+3 \sinh^{-1} x], \quad . \quad . \quad (3)$$

the other symbols having their usual meaning. It may be noticed here that with the same definition for ρ as in (2) the pressure for a classical gas can be written as

$$p = \frac{\pi m^4 c^5}{3h^3}\left(\frac{960}{\pi^4}\frac{1-\beta_1}{\beta_1}\right)^{1/3} . \, 2x^4. \quad . \quad . \quad . \quad (4)$$

As a preliminary to the study of composite configurations with degenerate cores we firstly consider the structure of *completely* collapsed configurations with β=I. In this case the radiation pressure p' is zero and the total pressure p is given by (2). If one introduces the function ϕ defined as

$$\rho = \frac{\rho_c}{\left(1-\frac{1}{y_0^2}\right)^{3/2}}\left(\phi^2-\frac{1}{y_0^2}\right)^{3/2}, \quad . \quad . \quad . \quad (5)$$

where

$$y_0^2 = x_0^2+1 \; ; \; \rho_c = \rho_{\text{central}} = \mathrm{B}x_0^3, \quad . \quad . \quad (5')$$

then one can prove that the structure of the configurations is completely specified by the solution of the differential equation

$$\frac{1}{\eta^2}\frac{d}{d\eta}\left(\eta^2\frac{d\phi}{d\eta}\right) = -\left(\phi^2-\frac{1}{y_0^2}\right)^{3/2}, \quad . \quad (6)$$

with

$\phi = 1$ at $\eta = 0$; $\phi(\eta_1) = \frac{1}{y_0}$, η_1 referring to the boundry,

. . . (7)

where η measures the radius vector in a suitable scale. (6) is an *exact* equation, and it is surprising that it has

Reproduced from *The Observatory*, **57**(727), (1934), 373-377

not been isolated before. The derivation of this exact equation has led to a considerable simplification in the analysis of the problem of stellar structure. For a specified y_0, *i. e.* for a specified central density, the structure is completely determined and in particular its mass. We see from (6) that as $y_0 \to \infty$, $\phi \to$ the Emden-function with index 3. The mass of these configurations therefore tends to a unique limit as $y_0 \to \infty$. This mass is naturally M_3 (which was first obtained by the writer (*M. N.* **91**. p. 456, 1931)). Configurations with mass less than M_3 have finite radii. On the Milne diagram we can therefore plot on the radius-axis a series of points corresponding to the radii of different masses of these configurations. M_3 in particular is at the origin of the two axes (r —β, R).

With this necessary preliminary analysis of these configurations with β=1 we can now see how the Eddington lines should be distorted in the region of the Milne diagram (1—β)<(1—β_ω) If we consider a star of mass M less than an and contract it from infinite extension the star continues to be wholly gaseous till the central density is such that (*cf.* equations (z) and (4))

$$\left(\frac{960}{\pi^4}\frac{1-\beta_M}{\beta_M}\right)^{1/3} = \frac{f(x_0)}{2x_0^4}\ ;\ \rho_c = Bx_0^3 \ldots \quad (8)$$

The radius R_0 of this configuration (with $\rho_c = Bx_0^3$) can now be determined. We can therefore draw the curve (R_0, I—β_M) in the Milne diagram. This curve naturally intersects the (I—β) axis, where $\beta_M = \beta_\omega$ corresponding to M=.$\mathfrak{M}$. Hence the curves of constant mass are vertical lines parallel to the R-axis until they intersect the (R_0, I—β_M) curve. Below this curve the Eddington lines are distorted, and to study the curves of constant mass inside this region we have to consider composite configurations where the structure of the degenerate core is governed by the differential equation (6) and the outer envelope by Emden's equation with index 3. In considering these configurations it would be natural to work the generalized-standard-model in which " $\kappa\eta$ " takes different values in the envelope and in the core. We will, however, first consider the usual standard model where " $\kappa\eta$ " has the same constant value throughout the star.

The composite configurations can now be studied

Reproduced from *The Observatory,* **57**(727), (1934), 373-377

by writing down the " equations of fit " and solving them. It may be stated that for solving the equations of fit one can with some modifications adopt here the methods developed by Milne in a rather different connection. One can first prove that when β_1 has the same value in the envelope as in the core then *only collapsed configurations are possible,* i. e., a composite configuration has a " I—β " which is always less than the value (I—β_M) which it has in the wholly gaseous state. The nature of the curves of constant mass can at once be predicted. If the mass is less than M_3 then in the completely collapsed state (β_1=I) it has a unique radius already determined from our analysis of these configurations. For each mass M' we can calculate β_M . The vertical line through (I—β_M′) cuts the (I—β_M, R_o) curve at the point (I—β_M′, R_0(M′)). When the star contracts further it goes along some smooth curve joining the point (I—β_M′, R_0(M′)) with a point on the R-axis corresponding to the radius which this M' has in the completely collapsed state. In particular, the curve of constant mass for M_3 passes through the origin. One finds that β_{M_3} is specified by

$$\frac{960\,\mathrm{I}-\beta_{M_3}}{\pi^4\ \beta^4_{M_3}}=\mathrm{I}, \quad . \quad . \quad . \quad . \quad . \quad . \quad . \quad (9)$$

Let $\beta_{M3} = \beta_0$. Clearly (I–β_ω)>(I–β_0).

The question arises what happens for stars with $M_3<M\leq\mathfrak{M}$. Now when (I—β)<(I—β_ω) then the configuration has a mass $M_3\beta^{-3/2}$ as $y_0\to\infty$. (This result was obtained in my paper in *M. N.* already referred to.) Hence when $M_3<M\leq\mathfrak{M}$ the curves of constant mass intersect the (I —β) axis at a point β^* such that

$$\mathbf{M}=\mathbf{M}_3\beta^{*-3/2}. \quad . \quad . \quad . \quad . \quad . \quad . \quad (10)$$

One can show that β^* is related to $\beta\dagger$— the value it has in the wholly gaseous state—by the relation

$$\beta^*=\left(\frac{\pi^4\ \beta\dagger^4}{960\,\mathrm{I}-\beta\dagger}\right)^{1/3} \quad . \quad . \quad . \quad . \quad . \quad . \quad (11)$$

We notice that $\beta^*=\beta\dagger=\beta_\omega$ is a solution. Also β^*=I when $\beta\dagger=\beta_0$. These results are of course necessary for consistency. We should further have

$$\mathfrak{M}=\mathbf{M}_3\beta_\omega^{-3/2}. \quad . \quad . \quad . \quad . \quad . \quad . \quad (12)$$

Reproduced from *The Observatory,* **57**(727), (1934), 373-377

Relation (I2) can in fact be shown to be true. Hence Milne's problem admits of a solution (consistent with our present knowledge of the equations of state for ionized material) for $(I-\beta)<(I-\beta_\omega)$, and in this region only collapsed configurations are possible on the standard model. We have also seen how the curves of constant mass run in this region.

The treatment of the generalized standard model ("β_2" of the core different from " β_1" of the envelope) can be carried out in a similar way, though the analysis is very much more complicated. If we consider $\beta_2=I$ as an extreme case, then one can prove for instance that *composite configurations with* $M>M_3$ *are necessarily centrally condensed.* When $M\leq M_3$, but greater than another critical mass, " quasi-diffuse" and centrally-condensed configurations make their appearance in addition to the usual collapsed configurations. It is clearly impossible to describe these results in this short communication, which is intended primarily as a preliminary statement of some of the results of the author's recent studies. The detailed investigations with full tables of solutions will be published elsewhere, but the purpose of writing this article was to show how the setting up of an exact differential equation to describe the degenerate state has led to an almost complete solution of the general problem of stellar structure along the lines indicated above.

Finally, it is necessary to emphasize one major result of the whole investigation, namely, that it must be taken as well established that the life-history of a star of small mass must be essentially different from the life-history of a star of large mass. For a star of small mass the natural white-dwarf stage is an initial towards complete extinction. A star of large mass (>𝔐) cannot pass into the white-dwarf stage, and one is left speculating on other possibilities.

Trinity College, Cambridge.
1934 October 24.

S. CHANDRASEKHAR.

J. Astrophys. Astr. (1994) **15,** 143–156

Seismology of the Solar Convection Zone

Sarbani Basu & H. M. Antia *Tata Institute of Fundamental Research, Homi Bhabha Road, Bombay 400 005*

Received 1993 October 5; accepted 1994 April 15

Abstract. An attempt is made to infer the structure of the solar convection zone from observed *p*-mode frequencies of solar oscillations. The differential asymptotic inversion technique is used to find the sound speed in the solar envelope. It is found that envelope models which use the Canuto-Mazzitelli (CM) formulation for calculating the convective flux give significantly better agreement with observations than models constructed using the mixing length formalism. This inference can be drawn from both the scaled frequency differences and the sound speed difference. The sound speed in the CM envelope model is within 0.2% of that in the Sun except in the region with $r > 0.99R_\odot$. The envelope models are extended below the convection zone, to find some evidence for the gravitational settling of helium beneath the base of the convection zone. It turns out that for models with a steep composition gradient below the convection zone, the convection zone depth has to be increased by about 6 Mm in order to get agreement with helioseismic observations.

Key words: Sun: oscillations—convection.

1. Introduction

Helioseismology has provided us with a tool to probe the interior of the Sun using the observed frequencies of solar oscillations. Although a lot of effort has been directed towards studying the deeper layers of the Sun, very little attention appears to have been paid to the envelope region below the solar surface. The structure of the surface layers is predominantly determined by convective heat transport. Although, there is no accepted theory of stellar convection, most stellar models are traditionally constructed using the mixing length theory (MLT), which is based on essentially *ad hoc* simplifying assumptions regarding turbulent convection. Recently, Canuto & Mazzitelli (1991) have proposed an alternative prescription of stellar convection based on a more detailed study of turbulence, which considers the full spectrum of turbulent eddies. In this paper we would like to examine if the available helioseismic data can distinguish between the MLT models and models constructed using the Canuto-Mazzitelli (CM) formulation. By comparing the frequencies of different solar models constructed using MLT and CM prescriptions with the observed frequencies, Paterno *et al.* (1993) conclude that the model constructed with the CM formulation gives better agreement with observations. However, in that work, they compared models obtained using stellar evolution codes, and as such, the results are liable to be affected

by uncertainties in the theory of stellar evolution. In order to avoid this uncertainty, we use solar envelope models to study the difference between the CM and MLT formalisms. Further, we have used inversion techniques to identify the differences.

For most part of the solar convection zone, the temperature gradient is very close to the adiabatic gradient. Below the ionization zones of hydrogen and helium the adiabatic index is known reliably, and as a result, the uncertainties in the structure of this region are small. Beneath the convection zone, the temperature gradient depends on the opacity which is uncertain to some extent. Apart from the opacity there is a possibility of a composition gradient due to the gravitational settling of helium and metals (Cox, Guzik & Kidman 1989; Bahcall & Pinsonneault 1992; Christensen-Dalsgaard, Proffitt & Thompson 1993). The hope is that if we can reliably determine the structure of the solar convection zone using helioseismic techniques, it may be possible to infer uncertainties in opacity as well as in the composition gradient below the convection zone. Of course, it may not be possible to separate out the effect of composition gradient from that of the uncertainties in opacity and the depth of the convection zone.

In this work we use the differential asymptotic technique of sound speed inversion (Christensen-Dalsgaard, Gough & Thompson 1989) to determine the relative difference in the sound speed between the Sun and solar envelope models. From the sound speed difference we should be able to determine which model is closer to the Sun. We use envelope models in our analysis because a) they are relatively easy to construct, b) they are less affected by uncertainties in the theory of stellar evolution, c) it is possible to construct models with essentially arbitrary helium abundance and depth of the convection zone. In any case, the helium abundance and the depth of convection zone in the Sun can be independently determined from helioseismology. Although the depth of convection zone is known very reliably (Christensen-Dalsgaard, Gough & Thompson 1991), there is some uncertainty in the helium abundance (Vorontsov, Baturin & Pamyatnykh 1992; Kosovichev *et al.* 1992; Antia & Basu 1994 and references therein). Once the parameters of the envelope model are fixed, we can extend the model inwards towards the center. However, the composition gradient in the interior cannot be determined without constructing an evolutionary model, and hence the inward extension of the envelope model is uncertain. Nevertheless, it may be possible to distinguish between various models of helium diffusion using extended envelope models. It may be argued that the envelope model may not represent the Sun, since the boundary condition at the center may not be satisfied when the models are extended to the center. However, a small discrepancy in the central boundary condition can be attributed to uncertainties in the opacities, nuclear reaction rates and the composition profile.

2. The inversion technique

We have constructed several solar envelope models using different prescriptions for calculating the convective flux. Basically the envelope models depend on two parameters: the helium abundance Y, and the mixing length parameter, α. In conformity with the usual practice, in the models using MLT, we use the mixing length $L = \alpha H_p$, while for models with the CM formulation, we use $L = \alpha + z$, where z is the depth measured from the radius where the optical depth, $\tau = 1$. In the mixing

length formalism, the convective flux is given by

$$F_C^{\mathrm{MLT}} = \frac{8\sigma T^4(\nabla - \nabla_{\mathrm{ad}})}{3\kappa\rho H_p} a_0 \Sigma^{-1}[(1+\Sigma)^{1/2} - 1]^3, \tag{1}$$

where a_0 = 9/4, and Σ is a quantity which depends on the superadiabatic gradient and is defined by equation (5) of Canuto & Mazzitelli (1991). In the CM formulation, the corresponding convective flux is expressed as

$$F_C^{\mathrm{CM}} = \frac{16\sigma T^4(\nabla - \nabla_{\mathrm{ad}})}{3\kappa\rho H_p} a_1 \Sigma^m[(1+a_2\Sigma)^n - 1]^p, \tag{2}$$

where, the coefficients a_1 = 24·868, a_2 = 0·097666, m = 0·14972, n = 0·18931, and p = 1·8503. This expression has been obtained by fitting the results of detailed numerical calculations of the spectrum of turbulent eddies and includes the contribution from eddies of all sizes. The main difference between the two formalisms occurs at the subsurface layer near the top of the convection zone where the CM formulation gives a steeper temperature gradient leading to the density inversion in a thin layer in that region. In the deeper layers, the superadiabatic gradient in CM models is much less than that in MLT models, however since the degree of super-adiabaticity is very small in both models, the temperature gradient is effectively adiabatic. Consequently, there is no measurable difference between the two models in the deeper layers of the convection zone.

It should be stressed that both sets of models are constructed using the same procedure, except for the expressions for convective flux and mixing length. The parameter α is adjusted to give a convection zone depth d_{cz} , of approximately 200 Mm. The helium abundance in the convection zone is taken to be between 0·24 and 0·26 which is the estimated value of Y from helioseismic data (Antia & Basu 1994). All the models have a uniform metal abundance of Z = 0·02. Below the convection zone we have used different composition profiles as given by various models of gravitational settling of helium. We have however, not included the gravitational settling of metals. In particular, we have used the composition profile as given by Bahcall &Pinsonneault (1992) (henceforth BP) and the models TD1 and TD2 using turbulent mixing from Christensen-Dalsgaard, Proffitt & Thompson (1993) (henceforth CDPT). The BP model has a sharp composition gradient just below the convection zone, while in the model TD2 which includes turbulent mixing, the composition profile is smooth.

All the envelope models use the MHD equation of state (Hummer & Mihalas 1988; Mihalas, Däppen & Hummer 1988; Däppen *et al.* 1988) since this equation of state is found to be close to that of the solar material (Vorontsov, Baturin & Pamyatnykh 1992; Antia & Basu 1994). Most models use OPAL opacities (Rogers & Iglesias 1992), however, we have also constructed models with opacities from Cox & Tabor (1976) to test the effect of uncertainties arising from opacity values. All the models used in this study extend up to a depth of 500 Mm, and their properties are summarized in table 1.

We use the differential asymptotic method for sound speed inversion (Christensen-Dalsgaard, Gough & Thompson 1989) to find the relative difference in sound speed between the Sun and envelope models. In this method, the difference between the frequencies of a solar model and the observed solar frequencies provides the basic

Table 1. Properties of solar envelope models.

Model	Y	d_{cz} (Mm)	Convection theory	Composition profile	Opacity
M1	0.24	200	MLT	Uniform	OPAL
M2	0.26	200	MLT	Uniform	OPAL
M3	0.24	200	CM	Uniform	OPAL
M4	0.26	200	CM	Uniform	OPAL
M5	0.25	200	CM	Uniform	OPAL
M6	0.25	198	CM	BP	OPAL
M7	0.25	200	CM	TD2	OPAL
M8	0.25	198	CM	TD2	OPAL
M9	0.25	200	CM	TD1	OPAL
M10	0.25	204	CM	BP	OPAL
M11	0.25	200	CM	Uniform	CT

input to find the corresponding sound speed difference between the solar model and the Sun. Following Christensen-Dalsgaard, Gough & Thompson (1989) we express the frequency difference in the form

$$S(w)\frac{\delta\omega}{\omega} = S(w)\frac{\omega_0 - \omega}{\omega_0} = H_1(w) + H_2(\omega), \tag{3}$$

where

$$S(w) = \int_{r_t}^{R_\odot} \left(1 - \frac{c_0^2}{w^2 r^2}\right)^{-1/2} \frac{\mathrm{d}r}{c_0}, \tag{4}$$

and

$$H_1(w) = \int_{r_t}^{R_\odot} \left(1 - \frac{a^2}{w^2}\right)^{-1/2} \frac{c_0 - c}{c_0} \frac{1}{a} \frac{\mathrm{d}r}{r}. \tag{5}$$

Here $r_t = c_0/w$ is the lower turning point, c_0 is the sound speed in the reference model and c is the sound speed in the Sun, $a = c_0/r$, ω_0 is the frequency of p-mode in the reference model, while ω is the observed frequency for the same mode and $w = \omega/(l + 1/2)$. Thus, the frequency difference depends asymptotically on the interior sound speed difference through a function of w, and on differences in the surface layers through a function of ω. Using the known frequency differences between a large number of modes, we can obtain the functions $H_1(w)$ and $H_2(\omega)$ by a least squares solution of equation (3). For this purpose we expand $H_1(\omega)$ in terms of B-spline basis functions in log w and likewise expand $H_2(\omega)$ using B-splines in w. For $H_1(w)$ we use 25 knots uniformly spaced in log w, while for $H_2(\omega)$ we use 20 uniformly spaced knots in ω. We have done experiments to find that the final results are not sensitive to the number of knots used. Since in this work we are interested in envelope models, we consider only those modes for which $1.0 < \omega < 5.5$ mHz and $w < 0.25$ mHz. Further, we restrict the sample of modes to those listed in the tables of Libbrecht, Woodard & Kaufman (1990) and weigh each point according to the quoted standard deviation in the frequencies. Since the asymptotic relation cannot be expected to hold for the f-mode, we do not include the f-mode ($n = 0$) in the set of modes used for inversion. After applying these cut-offs we are left with about 2530 eigenmodes to calculate

$H_1(w)$ and $H_2(\omega)$. For obtaining the least squares solution of equation (3), we use singular value decomposition (SVD) (refer Antia 1991) which directly gives the coefficients of both sets of B-splines.

With the help of the function $H_1(w)$ determined as above, we can obtain the difference in sound speeds between the model and that in the Sun using the relation,

$$\frac{\delta c}{c} = \frac{c_0 - c}{c_0} = -\frac{2r}{\pi}\frac{da}{dr}\int_{a_s}^{a} \frac{\frac{dH_1}{dw}w\,dw}{(a^2 - w^2)^{1/2}}, \tag{6}$$

where $a_s = a(R_\odot)$. Note that, equation (6) is slightly different from the corresponding equation in Christensen-Dalsgaard, Gough & Thompson (1989), but it can be readily shown that the two expressions are equivalent.

3. Comparison of convection theories

We have computed the relative sound speed difference between the various models and the Sun using the technique outlined in the previous section. Fig. 1 shows the relative sound speed difference between models Ml , M2, M3, M4 and the Sun. Models Ml and M2 are constructed using the mixing length formulation while models M3

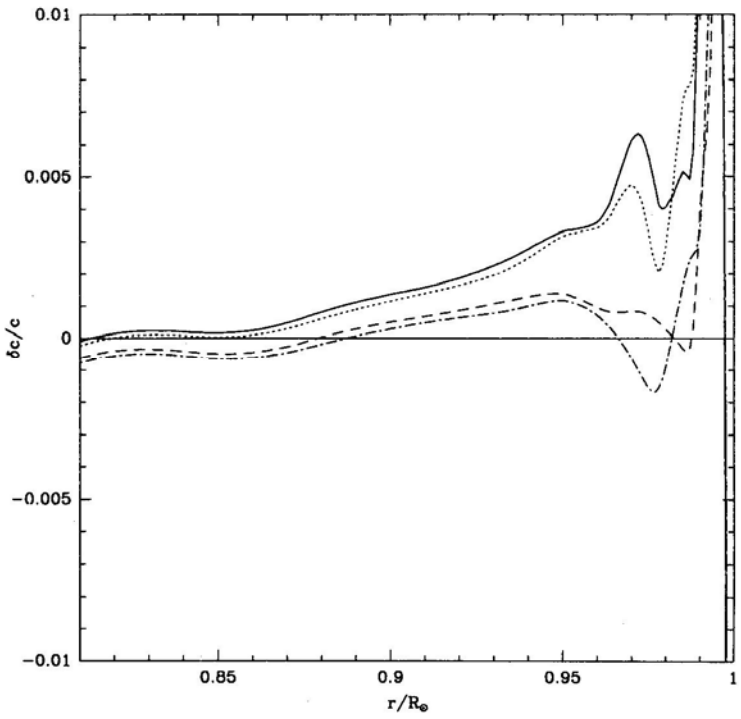

Figure 1. The relative sound speed difference between different envelope models and the Sun as a function of the fractional solar radius. The solid line represents model Ml, the dotted M2, dashed M3, and dot-dashed M4. Models Ml and M2 are MLT models and M3 and M4 are CM models.

and M4 use the CM prescription. We notice that for all the models the sound speed difference is fairly small (< 0.4%) in most of the convection zone. The main differences arise close to the surface (for $r > 0.95R_\odot$). It is clear that the sound speed in the CM models is distinctly closer to that in the Sun as compared to that in the MLT models. For $r > 0.985R_\odot$ there appears to be significant difference between the sound speed in the Sun and the models. However, in this region the applicability of the asymptotic inversion technique used in the present work is questionable.

In order to estimate the error due to the uncertainties in the observed frequencies, we have simulated 25 sets of frequencies where random errors with standard deviation quoted by the observers are added to the model frequencies. For each of the 25 sets of frequencies we have determined the relative sound speed difference. Using these 25 sets of simulations we can find the mean and variance of $\delta c/c$ at each radius. It is found that the error on the whole is very small, with the maximum variance being of the order of 0.01% for $r < 0.98R_\odot$. Thus we see that the difference between $\delta c/c$ obtained from CM and MLT models is more than the errors expected due to uncertainties in the frequencies.

Evidently, the sound speed very close to the solar surface cannot be reliably determined using the asymptotic technique. In this region, the basic assumption underlying the asymptotic theory will break down, since the vertical wavelength of the *p*-modes is not small as compared to the local scale heights. Apart from this,

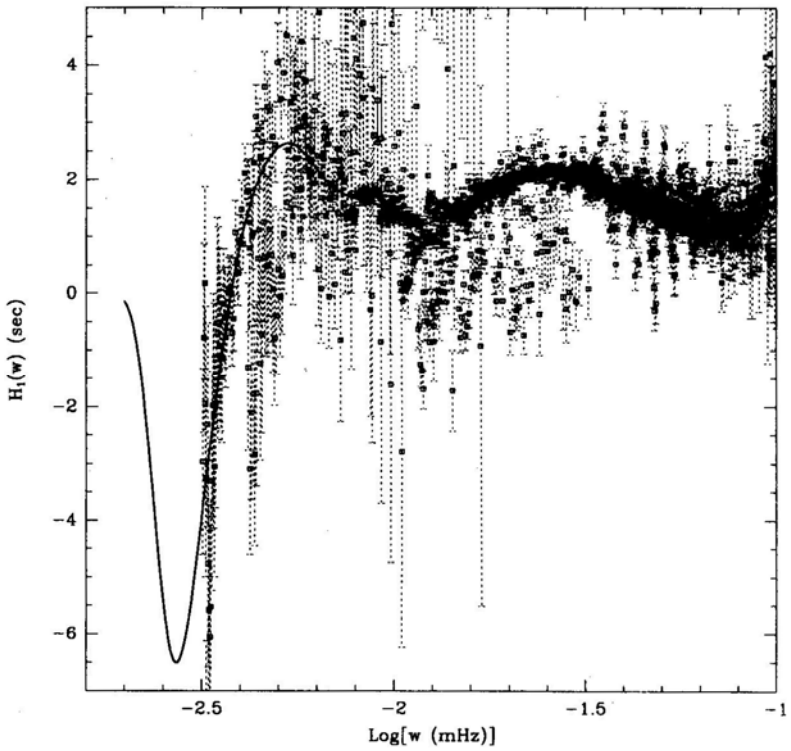

Figure 2. The function $H_1(w)$ for the Sun with model M5 as the reference model. The points mark $S(w)(\delta\omega/\omega) - H_2(\omega)$ against log w.

there is an additional difficulty because of the fact that there are no trapped modes with arbitrarily shallow turning points. For example, in the set of modes used in the present work, there is no mode with w < 0.0031 mHz, which corresponds to the lower turning point at a radius of $\approx 0.997R_\odot$. The function $H_1(w)$ for smaller value of w has then to be determined by extrapolation, which introduces uncertainties in the sound speed inversion close to the solar surface. Fig. 2 shows $H_1(w)$ for the Sun with respect to model M5. The points corresponding to the different modes are also marked in the figure. Each point shows ($log\ w$, $S(w)(\delta\omega/\omega) - H_2(\omega)$) for the modes used in the present study. It is clear from the figure that the dip in the points towards the low w gets magnified in the function $H_1(w)$ because of the extrapolation. It is this dip in $H_1(w)$ that gives rise to the fairly large peak in $\delta c/c$ at $r > 0.99R_\odot$ for all models. Since it is not obvious how to extrapolate the function in this range, we have chosen the last knot for the *B*-spline basis functions at log[w(mHz)] = – 2.5, and the knot spacing is chosen such that $H_1(w) \rightarrow 0$ at the surface. In order to estimate the effect of the uncertainty in extrapolation, we have performed inversions by adding an arbitrary constant to dH_1/d log w for log[w(mHz)] < – 2.5 as in Christensen-Dalsgaard, Gough and Thompson (1989). Fig. 3 shows the result obtained by adding an extreme value of ± 50 sec. to dH_1/d log w. The difference between these curves should give an upper limit to the error caused by extrapolation. Clearly, there may be a significant uncertainty in the relative sound speed difference for $r > 0.97R_\odot$.

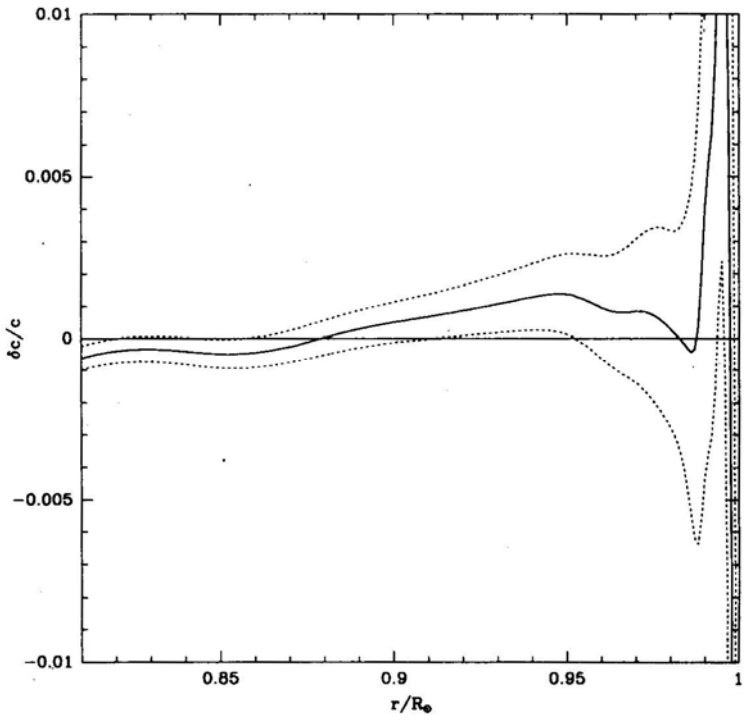

Figure 3. The effect of extrapolation of $H_1(w)$ at log w on the derived sound speed. The solid line is the relative sound speed difference between the model M3 and the Sun derived using the function $H_1(w)$ obtained directly from the least squares solution. The dotted lines are $\delta c/c$ obtained after adding a constant value of ± 50 sec. to $dH_1\ (w)/d$ log w for log[w(mHz)] < – 2.5.

This technique can be tested by using the frequency differences between two known solar models to estimate the corresponding difference in the sound speeds. From such tests also, we find that the relative sound speed difference has significant errors for $r > 0.97R_{\odot}$. However, the extrapolated $H_1(w)$ for $\log[w(\mathrm{mHz})] < -2.5$ is similar for all the models considered here, and hence the uncertainty due to extrapolation may give similar errors in $\delta c/c$ relative to the Sun for each model. We therefore expect the difference between the CM and MLT models to be relatively unaffected by this uncertainty.

Another measure of the difference between the models and the Sun is provided by the function $H_1(w)$ which is a measure of the sound speed difference. The advantage of using the function $H_1(w)$ instead of $\delta c/c$ is that $H_1(w)$, for $\log [w(\mathrm{mHz})] > -2.5$, is obviously unaffected by the extrapolation at smaller values. The function $H_1(w)$ between models M1–M4 and the Sun is shown in Fig. **4.** We see that for the CM models, the systematic trend in $H_1(w)$ for $\log[w(\mathrm{mHz})] > -2.3$ is much less than that for the MLT models. It must be noted that $H_1(w)$ between similar models shows no systematic trend with w. The fact that CM models show a much flatter $H_1(w)$ indicates that they are probably closer to the Sun than the models constructed using MLT.

Apart from $H_1(w)$, the function $H_2(\omega)$ can also be used as a measure of the difference between models and the Sun. Since, $H_2(\omega)$ is supposed to reflect the differences in the surface layers, it may be better suited to see the difference between the two

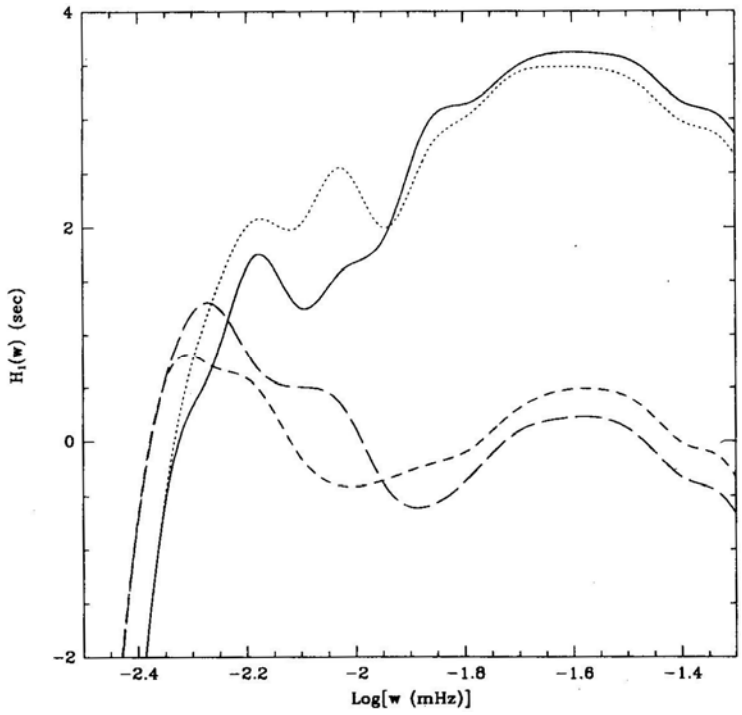

Figure 4. The function $H_1(w)$ between the Sun and different envelop models. The solid line represents model Ml, dotted line is for model M2, dashed line for model M3 and dot-dashed line for model M4.

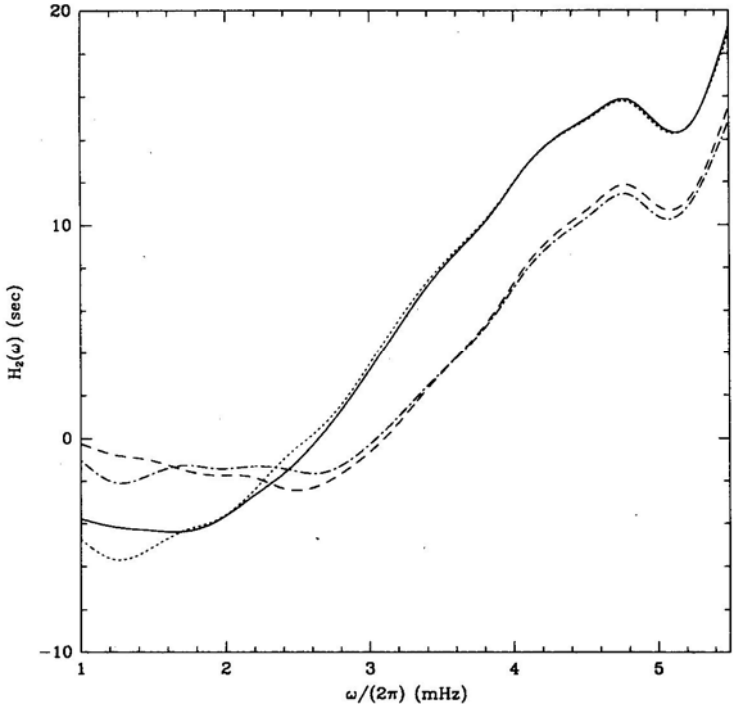

Figure 5. The function $H_2(\omega)$ between the Sun and different envelop models. The solid line represents model Ml, dotted line is for model M2, dashed line for model M3 and dot-dashed line for model M4.

formulations of stellar convection, which predominantly affects the surface layers. Fig. 5 shows $H_2(\omega)$ plotted for models M1–M4. We can see that the MLT models Ml and M2 have a much larger variation in $H_2(\omega)$ than do the CM models M3 and M4. In particular, $H_2(\omega)$ for the CM models is practically flat for $\omega < 3$ mHz. At higher frequencies the uncertainties in the treatment of atmosphere and the non-adiabatic effects may influence the frequencies of *p*-modes significantly.

With a view to provide an independent criterion to determine which of the two convection theories gives better results, we have considered the scaled frequency differences between the models and the Sun. We define the scaled frequency difference $\Delta_{n,l} = Q_{n,l}\delta\omega$, where $Q_{n,l} = E_{n,l} / \bar{E}_0(\omega_{n,l})$,

$$E_{n,l} = \frac{4\pi \int_0^{R_\odot} [|\xi_r(r)|^2 + l(l+1)|\xi_t(r)|^2]\rho r^2 \mathrm{d}r}{M_\odot [|\xi_r(R_\odot)|^2 + l(l+1)|\xi_t(R_\odot)|^2]}, \tag{7}$$

where, ξ_r and ξ_t are the radial and tangential components of the displacement for the given mode, ρ is the equilibrium value of the density; and $\bar{E}_0(\omega_{n,l})$ is the value of $E_{n,l}$ for $l = 0$ interpolated to the frequency $\omega_{n,l}$.

In Fig. 6 we have plotted the scaled frequency differences between the observed solar frequencies and those computed for models M2 and M4 as a function of *w*. It is clear that for $\log[w(\mathrm{mHz})] > -2.2$ the scaled frequency differences for the CM model are smaller by a factor of approximately 1.5 as compared to those for the

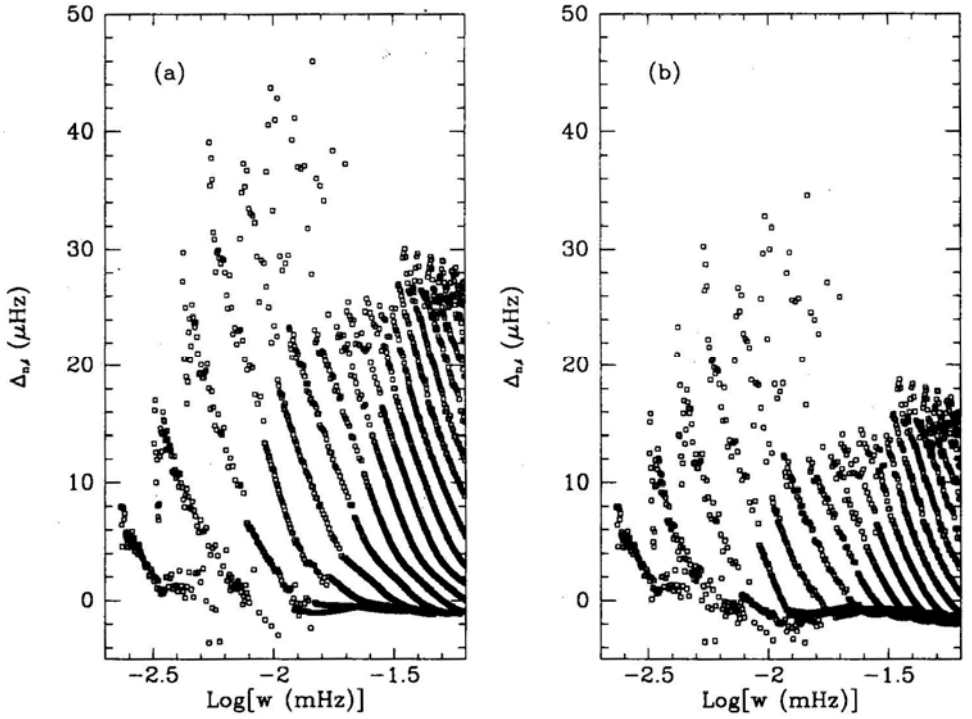

Figure 6. The scaled frequency difference between the Sun and (a) model M2, and (b) model M4. This figure also includes the frequency differences for the *f*-mode even though those are not used in inversion.

MLT model. These frequency differences are not very sensitive to small changes in helium abundance or the convection zone depth. Thus the scaled frequency differences should reflect the effect of the underlying convection theory: This difference can be attributed to the differences in $H_2(\omega)$ for the models.

Thus, on the basis of both the sound speed difference and the scaled frequency difference between the models and the Sun, we are led to the conclusion that the CM models give better agreement with observations than the MLT models.

4. Test for helium diffusion

Gravitational settling of helium and heavy elements introduces a composition gradient below the base of solar convection zone, which can be detected helioseismically. Unfortunately, the composition profile is not unique but depends on the adopted treatment of turbulence (Christensen-Dalsgaard, Proffitt & Thompson 1993). In the absence of turbulence, diffusion leads to a sharp increase in Y just below the base of the convection zone. Such a composition profile should give a clear signature in the sound speed profile, since the increase in the mean molecular weight will decrease the sound speed.

Guzik & Cox (1993) studied the effects of diffusion on solar oscillations and found

that models with helium diffusion without turbulent mixing appear to give better agreement with the observed frequencies than either models without diffusion or models which have diffusion with turbulent mixing. They rely on simple comparison between the observed and calculated frequencies, hence it is difficult to separate the effect of diffusion from other uncertainties. Using evolutionary solar models CDPT found that the models using helium diffusion yield better agreement with helioseismic data. However, in their models the dominant contribution to the sound speed difference appears to be due to difference in the convection zone depth. The model without helium diffusion yields a rather shallow convection zone and hence the sound speed does not agree very well with observations. While it is true that models with helium diffusion give nearly correct convection zone depth, we cannot draw any definite conclusions from these results since the convection zone depth could depend on other uncertainties in the stellar evolution theory. In order to provide an independent test for the gravitational settling of helium, in this work, we have attempted to detect signatures of helium diffusion using envelope models, where the convection zone depth can be adjusted independently. Thus our work can supplement the conclusions of CDPT obtained using evolutionary models, which include the inner core.

Once the parameters of the envelope model are determined reliably, we can extend the model inwards assuming different profiles of δX, the change in chemical composition. The results are displayed in Fig. 7 which shows the relative difference

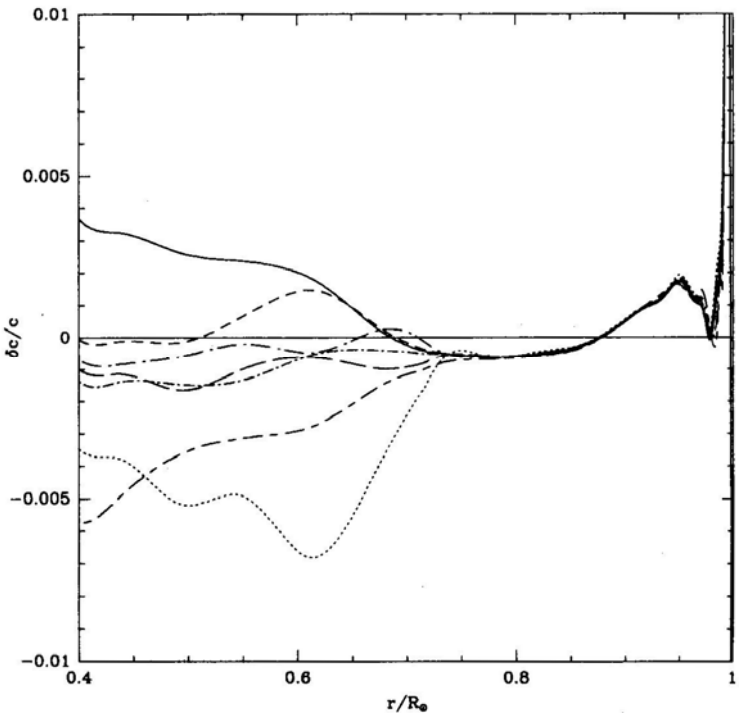

Figure 7. Relative sound speed difference between the Sun and models M5 (solid line), M6 (dotted line), M7 (short dashed line), M8 (long dashed line), M9 (dot short-dashed line), M10 (dot long-dashed line), and M11 (long dash-short dashed line).

in sound speed between the models and the Sun. If we consider the model M5 which has uniform composition, no sharp change is seen in $\delta c/c$ near the base of the convection zone. In this case $\delta c/c$ increases gradually below the convection zone. This increase could be attributed to either a lack of increase of helium abundance or an overestimation of opacity in these layers. Model M6, which uses the composition profile of BP, shows a sharp decline in $\delta c/c$ as compared to the Sun. From these results it is tempting to conclude that sharp changes in the composition profile of the form assumed in the BP model are unlikely to occur inside the Sun. However, uncertainties in opacities and the depth of the convection zone may mask the sharp change in $\delta c/c$ below the convection zone.

The model M7, which has the composition profile as given by CDPT (their model labelled TD2) shows a small hump in $\delta c/c$ near the base of the convection zone. This hump could be due to a small difference in the depth of the convection zone of the order of 2 Mm or due to a steep X gradient. In principle, uncertainty in the depth of the convection zone or overshoot layer could mask the changes due to composition profile. Alternatively, a sharp change in the composition profile could lead to some uncertainty in determination of the depth of the convection zone or the thickness of the overshoot layer. Using the oscillatory signal in the frequencies as a function of the radial order η arising from sharp changes in the temperature gradient below the base of the convection zone, Monteiro, Christensen-Dalsgaard & Thompson (1993); and Basu, Antia & Narasimha (1994) concluded that the observed solar frequencies are consistent with a no overshoot model. Further, an upper limit of $0.1H_p$ on the extent of overshoot was given. This result may be affected if there is a composition gradient, since that may also give rise to an abrupt change in the sound speed gradient.

In order to identify the origin of the hump in $\delta c/c$ for model M7, we have constructed models with slightly different convection zone depth and with small overshoot layer. For model M8 with a convection zone depth of 198 Mm, there is no hump, but $\delta c/c$ is systematically lower than that for model M7. Similarly, model M9 which has a convection zone depth of 200 Mm, but has the composition profile of the model TD1 of CDPT also gives a smooth $\delta c/c$. In this manner, a small increase in the depth of the convection zone appears to compensate for the somewhat sharp composition gradient in the model. In case of the composition profile given by the diffusion model of BP, the convection zone depth has to be increased to 204 Mm (model M10), in order to compensate for the change in sound speed due to the steep composition gradient. This depth is slightly larger than that estimated by Christensen-Dalsgaard, Gough, & Thompson (1991). The exact relative sound speed difference between this model and model M8, however, shows a small kink at the base of the convection zone which is not resolved by the inversion technique. Thus we can see that helium diffusion introduces an uncertainty in the depth of the convection zone as determined from the observed frequencies.

It is found that inclusion of overshoot below the convection zone does not change the sound speed substantially. It only gives rise to a small kink in $\delta c/c$ near the base of the convection zone. If the extent of overshoot in the models is less than the upper limit given by Basu, Antia & Narasimha (1994), we find that the kink in $\delta c/c$ is not noticeable in the inverted $\delta c/c$ profile. This result is consistent with the upper limit on the extent of overshoot.

In order to estimate the effect of uncertainties in opacity on $\delta c/c$, we have constructed one model (model M11) using Cox-Tabor opacities (Cox & Tabor 1976),

the result of which is shown in Fig. 7. In this case, $\delta c/c$ decreases below the convection zone and since the inclusion of diffusion can only lead to a further reduction of $\delta c/c$, we may conclude that the opacity of solar material is higher than that given by Cox & Tabor (1976). This is consistent with the conclusion drawn by Christensen-Dalsgaard *et al.* (1985). On the other hand, for model M5 which uses the OPAL opacities, there is a gradual increase in $\delta c/c$ below the convection zone. As emphasized earlier this increase could be due to the absence of helium diffusion or due to an overestimate of the opacity.

From the sound speed profile of the envelope model with constant composition gradient, we can conclude that helium abundance increases below the solar convection zone, provided that the opacity of the solar material at the base of the convection zone is not less than that given by the OPAL tables. This result supports the hypothesis of gravitational settling of helium in the Sun. Nevertheless, considering the uncertainty in the depth of the convection zone, it is not possible to distinguish between different models of gravitational settling. Conversely, helium diffusion introduces an uncertainty in the depth of the convection zone of about 6 Mm.

5. Conclusions

We have attempted in the present study, to construct a solar envelope model which is close to the Sun as inferred from helioseismic observations. Apart from the usual mixing length formulation, we have tried the CM prescription for convective energy transport in the solar convection zone. Applying the differential inversion technique to the difference in frequencies of solar models and the observed frequencies, we find that the CM models appear to give a significantly better agreement with observations. This result follows from the relative difference in the sound speed $\delta c/c$, the functions $H_1(w)$ and $H_2(\omega)$, as well as from the scaled frequency differences between the models and the Sun. Thus, it appears that the CM formulation which gives a significantly steeper temperature gradient in the surface layers, is closer to reality as compared to the mixing length theory. The remaining difference in $\delta c/c$ around $r \approx 0.98 R_\odot$could be due to uncertainties in the equation of state or due to the limitations of the asymptotic inversion technique.

By considering $\delta c/c$ just below the convection zone we can test different models with helium diffusion. The models with gravitational settling of helium which ignore turbulent diffusion, tend to give a composition profile with a sharp gradient just below the convection zone. Since $\delta c/c$ for model M5, which has a uniform composition, increases steadily below the convection zone, we surmise that the helium abundance should increase with depth. Uncertainties in the opacity will also affect the sound speed profile, but if OPAL tables do not overestimate the opacity of solar material below the convection zone, then indeed there is a need to invoke helium diffusion. Apart from the opacity, uncertainties in the depth of the convection zone will also affect the sound speed in this region. This uncertainty makes it difficult to choose between the different composition profiles that we have tested. If the envelope model has the composition profile given by BP, a convection zone depth of 204 Mm is required to obtain a sound speed close to that in the Sun. This depth is somewhat larger than the value obtained by Christensen-Dalsgaard, Gough & Thompson (1991). Models with the composition profile given by the model TD1 of CDPT require a

convection zone depth of 200 Mm, while models with a smooth composition profile (TD2) need a depth of only 198 Mm.

A limitation of the present work is that we have used solar envelope models. If these models are extended to the center it is unlikely that the required boundary conditions on the mass and luminosity at the center will be satisfied. By adjusting the composition profile, opacities and nuclear reaction rates within reasonable limits, it may be possible to satisfy the boundary conditions. However, such calculations are unlikely to yield any information about the uncertainties in these quantities. On the other hand, it should be noted that we have considered inversion for sound speed only, which is essentially determined by the temperature profile. Thus even though the temperature profile in our models may be close to that in the Sun, the density may be somewhat different. In which case, the inward extension of the model may not be expected to yield a proper solar model. Thus it would be interesting to perform the inversion for density also to provide additional constraints on these envelope models. We plan to carry out the density inversion in future calculations.

Acknowledgement

We thank V. M. Canuto, I. Mazzitelli and L. Paterno for useful communications regarding the CM formulation for convective flux.

References

Antia, H. M. 1991, *Numerical Methods for Scientists and Engineers* (New Delhi: Tata McGraw-Hill) p. 87.

Antia, H. M., Basu, S. 1994, *Astrophys. J.*, (in press).

Bahcall, J. N., Pinsonneault, M. H. 1992, *Rev. Mod. Phys.,* **64**, 885 (BP).

Basu, S, Antia, H. M., Narasimha, D.1994, *Mon. Not. R. astr. Soc,* **267**, 209.

Canuto, V. M., Mazzitelli, I. 1991, *Astrophys. J.,* **370**, 295 (CM).

Christensen-Dalsgaard, J., Gough, D. O., Thompson, M. J. 1989, *Mon. Not. R. astr. Soc,* **238**, 481.

Christensen-Dalsgaard, J., Gough, D. O., Thompson, M. J. 1991, *Astrophys. J.,* **378**, 413.

Christensen-Dalsgaard, J., Proffitt, C. R., Thompson; M.J. 1993, *Astrophys. J.,* **403**, L75 (CDPT).

Christensen-Dalsgaard, J., Duvall, T. L. Jr., Gough, D. O., Harvey, J. W., Rhodes, E. J. Jr. 1985, *Nature,* **315**, 378.

Cox, A. N., Tabor, J. E. 1976, *Astrophys. J. Suppl.,* **31**, 271.

Cox, A. N, Guzik, J. A., Kidman, R. B. 1989, *Astrophys. J.,* **342**, 1187.

Däppen, W., Mihalas, D., Hummer, D. G., Mihalas, B. W. 1988, *Astrophys. J.*, **332,** 261.

Guzik, J. A., Cox, A. N. 1993, *Astrophys. J.,* **411**, 394.

Hummer, D. G., Mihalas, D.1988, *Astrophys. J.,***331**, 794.

Kosovichev, A. G., Christensen-Dalsgaard, J., Däppen, W., Dziembowski, W. A., Gough, D. O., Thompson, M. J. 1992, *Mon. Not. R. astr. Soc,* **259**, 536.

Libbrecht, K. G., Woodard, M. F., Kaufman, J. M. 1990, *Astrophys. J. Suppl.,* **74**, 1129.

Mihalas, D., Däppen, W., Hummer, D. G. 1988, *Astrophys. J.,* **331,** 815.

Monteiro, M. J. P. F. G., Christensen-Dalsgaard, J., Thompson, M. J. 1993, in *Proc. GONG 1992: Seismic Investigation of the Sun and Stars,* Ed. T. M. Brown (San Francisco: PASPC) **42**, 253.

Paterno, L., Ventura, R., Canuto, V. M., Mazzitelli, I. 1993, *Astrophys.* J., **412**, 733.

Rogers, F. J, Iglesias, C A . 1992, *Astrophys. J. Suppl.,* **79**, 507.

Vorontsov, S. V., Baturin, V. A., Pamyatnykh, A. A. 1992, *Mon. Not. R. astr.* Soc, **257**, 32.

J. Astrophys. Astr. (1994) **15,** 157–163

Observations of the Bright-rimmed Molecular Clouds near the Cepheus OB2 Association

C. Indrani & T. K. Sridharan *Raman Research Institute, Bangalore 560 080*

Received 1994 March 31; accepted 1994 April 18

Abstract. Massive stars have significant influence on the evolution of the interstellar medium. Bright rims, cometary morphology of clouds, as well as their motion are some examples of the influence of massive stars on nearby molecular clouds. The cometary clouds in the Gum-Vela region are very good examples. In an attempt to understand the kinematics of the clouds in such regions we have carried out CO line observations towards bright-rimmed clouds near the OB Association Cep OB2. The radial velocities of the clouds are consistent with an expansion of the system at $\approx$ 4kms^{-1} away from the dominant O6.5V star in the association, HD206267. We find the rocket mechanism to be the most likely cause for expansion as found for both the Gum-Vela and the Rosette globules. We conclude that such expanding motions are quite common in regions near massive stars and make a brief comparison of the Cepheus system with the Gum-Vela system.

Key words: Bright-rimmed clouds—OB associations.

1. Introduction

Bright-rimmed clouds are typically found in the vicinity of massive stars. They are seen as patches of obscuration with bright rims on the side facing the stars and sometimes a tail like extension on the other side. Their peculiar morphology is believed to be caused by the effects of UV radiation and stellar winds from young stars. Some of these clouds show evidence for on-going low mass star formation. Sizeable populations of such clouds exist in the Gum-Vela region (Zealey *et al.* 1983; Reipurth 1983), the Rosette Nebula (Block 1990, 1992; see also Schneps, Ho & Barret 1980), the Cep OB2 region (containing IC 1396) (Gyulbudagyan 1985), and the Orion region (Bally *et al.* 1991). Catalogs of bright rimmed clouds have been compiled by Sugitani, Fukui & Ogura (1991) and Gyulbudagyan (1985). Studies of the clouds in the Gum-Vela region have shown that they are expanding at $\approx$ 12kms^{-1} about a common central region containing massive stars (Sridharan 1992). Motion away from the central stars has also been seen in the Rosette globules at $\approx$ 6kms^{-1} (Patel, Xie & Goldsmith 1993). In both these cases the *rocket effect* arising from the anisotropic illumination of the clouds appears to be the mechanism accelerating the clouds away from the stars. These observations are in agreement with the theory of Bertoldi and McKee (1990) for such clouds. In order to find out if such motions are prevalent in other regions with massive stars, and to develop, an evolutionary scenario for

comparison with theory, it is necessary to study many regions near OB associations. As a step in this direction we studied the bright-rimmed clouds near the OB association Cep OB2.

The Cep OB2 association is at a distance of 750 pc, with the dominant member being the O6.5 V star HD206267 (SAO36266) which excites the HII region IC 1396. This region is rich in bright-rimmed clouds (globules) which are distributed over an area of diameter 3°. The lack of well developed tail like extensions possibly indicates an earlier stage of evolution compared to the Gum-Vela region. Gyulbudagyan (1985) has identified and classified the globules here into four radial systems based on their orientation and morphology. The clouds with bright rims (category a) all have their rims perpendicular to the line joining them to the star HD206267 with extensions pointing away from it. From CO observations of these clouds it was found that clouds classified into different groups also had different radial velocity ranges (Gyulbudagyan, Rodriguez & Canto 1986). The clouds in this region were also observed by Heske & Wendker (1985) in H_2CO absorption. Based on a coarse survey of the molecular clouds in this region, Leisawitz, Bash & Thaddeus (1989) suggested that these clouds may be receding from the central star. Evidence for on-going star formation in these clouds has been found from IRAS data and from the presence of bipolar outflows (Sugitani *et al.* 1989; Sugitani, Fukui & Ogura 1991; Schwartz, Gyulbudagyan & Wilking 1991; Duvert *et al.* 1990).

In this paper we report additional CO observations and a new analysis of the radial velocities of the clouds using data both from our own observations and the previous studies. The next section describes the observations. In section 3 we analyse the radial velocities of the clouds and show that the system is expanding. Section 4 deals with the possible causes for this expansion.

2. Observations

We observed 21 clouds in the $J = 1 \rightarrow 0$ transition of CO at 115.271 GHz using the 10.4 m millimeter-wave radio telescope at the Raman Research Institute during 1993. Their coordinates were obtained from the POSS plates. An acousto-optic spectrometer with a resolution of 100 kHz and coverage of 30 MHz was used giving a velocity resolution of $0.26 \mathrm{kms}^{-1}$. An ambient temperature chopper was used for calibration. All the observations were done in the frequency switched mode. Line center velocities were obtained by fitting gaussians to the lines. Table 1 lists the positions observed along with the parameters of the detected lines. Observations of a few locations behind the bright rims show similar velocities. Using repeated observations of one of the clouds we estimate the error on the velocities obtained to be $0.05 \mathrm{kms}^{-1}$.

3. Analysis of the radial velocities

A comparison of our velocities with those of Gyulbudagyan, Rodriguez & Canto (1986) and Heske and Wendker (1985) shows good agreement. Cloud 11 shows two components, as was also found by Gyulbudagyan, Rodriguez & Canto (1986). This is interpreted as due to material belonging to different categories of globules (of Gyulbudagyan 1985) falling along the same line of sight. We assume a distance of

Table 1. Summary of observations.

	Co-ordinates (1950.0)									
	ra			dec			T_a^*	v_{LSR}	v_{fwhm}	T_{rms}
No.	h	m	s	°	′	″	*K*	kms^{-1}	kms^{-1}	*K*
1	21	34	11	57	12	36	1.67	−8.9	2.1	0.30
2	21	38	44	57	42	12	2.97	−0.7	1.3	0.32
3	21	36	53	57	44	10	4.27	0.1	1.6	0.39
4	21	36	19	57	34	22	2.29	0.3	2.3	0.27
5	21	39	1	58	2	42	2.13	0.4	3.2	0.27
6	21	31	29	57	43	54	1.41	−6.6	1.1	0.25
7	21	34	25	58	22	43	1.46	−3.7	0.9	0.28
8	21	31	14	57	38	13	2.90	−4.3	1.6	0.25
9	21	31	46	57	17	21	4.79	−5.6	1.6	0.28
10	21	44	46	57	9	25	4.50	−2.4	2.1	0.12
11	21	38	52	56	21	54	1.73	1.1	1.6	0.16
							1.39	6.6	1.0	0.16
12	21	31	41	57	16	12	4.62	−5.8	1.4	0.36
13	21	32	2	57	50	5	3.73	−5.3	1.7	0.24
14	21	34	35	58	18	9	4.42	−4.0	1.8	0.24
15	21	34	40	57	14	3	6.32	−8.4	2.2	0.24
16	21	38	53	56	22	16	1.38	0.7	2.8	0.27
17	21	39	10	58	2	28	2.25	1.0	5.9	0.23
18	21	44	30	57	12	28	2.90	−2.0	1.9	0.17
19	21	44	38	56	55	4	7.10	−2.4	2.3	0.36
20	21	44	52	57	4	44	3.30	−2.2	2.9	0.25
21	21	45	0	56	58	28	3.91	−2.3	2.0	0.19

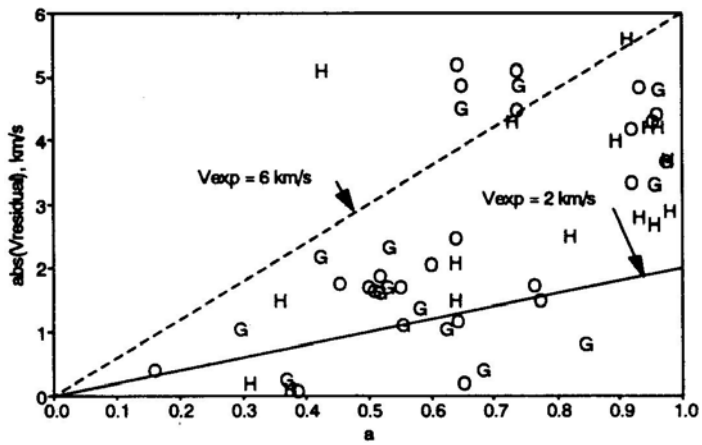

Figure 1. Absolute value of the residual velocities plotted against $(1 - \sin^2\theta/\sin^2\theta_{max})^{1/2} (\equiv a)$. The symbols G, H and O indicate data from Gyulbudagyan, Rodriguez & Canto (1986), Heske & Wendker (1985) and our measurements respectively. The straight lines shown represent shells expanding uniformly at 2 and $6 kms^{-1}$.

750 pc and remove the galactic rotation component using a value of 14.5kms^{-1} kpc^{-1} for Oort's constant A. We now look for evidence for systematic expansion in the *residual velocities.*

For a uniformly expanding shell of bright-rimmed clouds the residual radial velocities after removing the contribution due to galactic rotation are given by the expression (Sridharan 1992)

$$|v_{res}| = v_{exp}(1 - \sin^2\theta/\sin^2\theta_{max})^{1/2} \quad (1)$$

where v_{exp} is the expansion velocity, θ the angular distance of a cloud from the center of the distribution and θ_{max} the maximum value of θ (radius of the shell). We take the location of the star HD206267 to be the center and θ_{max} is 1.2°. In Fig. 1 we have plotted the absolute value of the residual velocities against $a = (1 - \sin^2\theta/\sin^2\theta_{max})^{1/2}$. Clearly the velocities increase at higher a (center) as expected in the case of expansion. The straight lines shown given by equation 1, correspond to expansion velocities of 2 and 6kms^{-1}. We conclude that the system of bright rimmed clouds in this region is expanding away from the star HD206267 at ≈ 4kms^{-1}. The expansion age of the system works out to be 4 Myr.

4. Discussion

In this section we consider possible causes for this expansion such as stellar wind, radiation pressure and rocket acceleration. We also estimate the age of the HD206267 and make a brief comparison between the cometary clouds in the Gum-Vela region and the Cepheus region. We first estimate the energy and momentum of a typical cloud due to expansion. Reliable mass estimates are not available for all except one cloud. We use this single cloud mapped in CO by Duvert *et al.* (1990) as a guide to estimate masses for the other clouds. The size of this cloud is 1′ and the estimated mass is 18$M_\odot$. The average size of the clouds in our sample is 1.6', ignoring the largest cloud with size 11′. Assuming the average densities for all the clouds to be the same we estimate the mass of a typical cloud to be 70$M_\odot$ and its momentum and energy (due to expansion) are 6×10^{40} gm cm s^{-1} and 1×10^{46} ergs respectively. In the rest of this section we make rough estimates for the momentum and energy available from the previously mentioned processes. We will take the average current distance between the clouds and the star HD206267 to be 10.4 pc corresponding to an angular separation of 0.8°. We will also assume that the effects of the processes have remained constant at the current level over the expansion age of the system.

4.1. *Stellar wind*

Direct data for stellar wind from HD206267 are not available. Therefore we assume a terminal velocity of 2900 kms^{-1} and a mass loss rate of $3 \times 1\ 0^{-6}\ M_\odot$ yr $^{-1}$ believed to be appropriate for this star (the mass loss rate is likely to be considerably less than the assumed value: Drake 1990; Bieging, Abbot & Churchwell 1989). We find the total momentum intercepted by a globule over the expansion age of the system

to be 6×10^{38} gm cm s^{-1} , which is less than the required momentum by a factor of 100, leading to the conclusion that stellar wind could not have caused the expansion.

4.2. *Radiation pressure*

The luminosity of an O6.5V star is 3×10^5 $L_\odot$giving a maximum available momentum due to radiation pressure of $L/c = 4 \times 10^{28}$ gm cm s^{-1}. We estimate that a typical globule will acquire, over the expansion age of the system, a total momentum of 4×10^{38} gm cm s^{-1} which falls short of the required momentum by two orders of magnitude. We therefore conclude that the radiation pressure cannot be responsible for the observed expansion.

4.3. *Rocket effect*

We finally consider the rocket effect caused by anisotropic ablation of the clouds caused by ionising radiation impinging on the sides of the clouds facing the star (Oort & Spitzer 1955). Taking the mass loss velocity to be the same as the sound speed in the ionised bright rim (l3kms^{-1}; $T \approx 10^4$K), and the measured density of 100cm^{-3} (Duvert *et al.* 1990), we estimate the total mass lost over the expansion age to be $11M_\odot$. With the mass loss occurring at 13kms^{-1}, the momentum imparted to the cloud is then $3 \times l0^{40}$ gm cm s^{-1} compared to the required momentum of 6×10^{40} gm cm s^{-1}. Taking into account the fact that the clouds would have lost mass at a higher rate when they were closer to the star, it appears reasonable to conclude that the clouds have been accelerated to their present velocities by the rocket mechanism.

4.4. *Age of HD206267*

Using available photometry and stellar evolution models we make a rough estimate of the age of the star HD206267, classified as O6.5V. Using data from Humphreys (1978) we estimate the bolometric luminosity of the star to be – 8.83. As extinction for this star itself is not available, we have used the average of the values for HD206267C & D (A_v = 1.55). The extinction values for the other stars in the region (Ceph OB2) are similar. We used a distance of 750 pc and a bolometric correction of – 3.5 corresponding to the spectral type O6.5. Now using the stellar evolution models of Schaller *et al.* (1992) for z = 0.02, we estimate that the ZAMS mass of HD206267 to be $\approx 40M_\odot$ and its age to be a few million years. This age is in reasonable agreement with the dynamical age of the expanding system of globules. There is no estimate available for age of the HII region IC1396. Observations and modelling in this direction will be useful.

4.5. *Comparison with the Gum-Vela region*

We list below the characteristics of the cometary clouds in the Gum-Vela and the

Cepheus regions, derived from our previous study (Sridharan 1992) and the present results.

	Gum-Vela	Cepheus
Morphology	Well developed tails	Only broad extensions
Size of the distribution	140 pc	40 pc
Expansion	12 kms^{-1}	4 kms^{-1}
Expansion age	6 Myrs	4 Myrs
Energy source	O4f star (ζ Pup) + massive stars in the recent past + SNe	Single O6.5f star

The first three points indicate that the Gum-Vela cometary clouds are in a later stage of development compared to those in Cepheus. In spite of the similar dynamical ages the differences in the evolutionary stages are possibly due to the stronger sources of energy in the Gum-Vela region. In addition to the massive star ζ Pup, the Gum-Vela region may have had a more massive star near its center about half a million years ago which exploded as a supernova (Sridharan, Srinivasan & Ramachandran 1994), and the progenitor of the Vela SNR. A more detailed analysis of the two environments using the theory of Bertoldi & McKee (1990) may help clarify the matter.

5. Conclusions

Our study of the radial velocities of the bright-rimmed clouds in the Cep OB2 has given evidence for expansion of the system away from the star HD206267 at $\approx$ 4kms^{-1}. The expansion age is 4 Myrs. This implies that such expanding motions are prevalent in regions surrounding high mass stars. Rocket effect appears to be the most likely operative mechanism in these regions. In spite of their similar ages, there are differences between the Gum-Vela region and the Cepheus region which can possibly be understood in terms of the differences in their energising sources.

References

Bally, J., Langer, W. D., Wilson, R. W., Stark, A. A., Pound, M. W. 1991 in *Fragmentation of Molecular Clouds and Star Formation,* Ed. G. Falgarone, F. Boulanger & G Duvert, (Dordrecht: Kluwer) p. 11.

Bertoldi, F., McKee, C. F. 1990, *Astrophys. J.,* **354**, 529.

Bieging, J. H., Abbot, D. C, Churchweli, E. B. 1989, *Astrophys. J.,* **340**, 518.

Block, D. L. 1990, *Nature,* **347**,452.

Block, D. L. 1992, *Astrophys. J.* (*Lett.*), **390**, L13.

Drake, S. A. 1990, *Astr. J.,* **100**, 572.

Duvert, G., Cernicharo, J., Bachiller, R., Gomez–Gonzalez, J. 1990, *Astr. Astrophys.,* **233**, 190.

Gyulbudagyan, A. L. 1985, *Astrofizica,* **23**, 295.

Gyulbudagyan, A. L., Rodriguez, L. F., Canto, J. 1986, *Astrofizica,* **24**, 201.

Heske, A., Wendker, H. J. 1985, *Astr. Astrophys.,* **149**, 199.

Humphreys, R. M. 1978, *Astrophys. J. Suppl.,* **38**, 309.
Leisawitz, D., Bash, F. N., Thaddeus, P. 1989, *Astrophys. J. Suppl.,* **70**, 731.
Oort, J. H., Spitzer, L. 1955, *Astrophys. J.,* **121**, 6.
Patel, N. A., Xie, T., Goldsmith, P. F. 1993, *Astrophys. J.,* **413**, 593.
Reipurth, B.1983, *Astr. Astrophys.,***117**, 183.
Schaller, G., Scharer, D., Meynet, G., Maeder, A. 1992, *Astr. Astrophys. Suppl.,* **96**, 269.
Schneps, M. H., Ho, P. T. P., Barret, A. H. 1980, *Astrophys. J.,* **240**, 84.
Schwartz, R. D., Gyulbudagyan, A. L., Wilking, B. A. 1991, *Astrophys. J.,* **370**, 263.
Sridharan, T. K. 1992, *J. Astrophys. Astr.,* **13,** 217.
Sridharan, T. K., Srinivasan, G., Ramachandran, R. 1994, *J. Astrophys. Astr.* (to be submitted).
Sugitani, K., Fukui, Y., Mizuno, A., Ohashi, N. 1989, *Astrophys. J.* (*Lett.*)*,* **342**, L87.
Sugitani, K., Fukui, Y., Ogura, K. 1991, *Astrophys. J. Suppl.,* **77,** 59.
Zealey, W. J., Ninkov, Z., Rice, E., Hartley, M, Tritton, S. B. 1983, *Astrophys. Lett.,* **23**, 119.

J. Astrophys. Astr. (1994) **15,** 165–178

Orbital Elements and Evolutionary Nature of the Long Period RS CVn Type Eclipsing Binary RZ Eridani

P. Vivekananda Rao, M. B. K. Sarma & B. V. N. S. Prakash Rao *Centre for Advanced Study in Astronomy, Osmania University, Hyderabad 500 007*

Received 1993 May 20; accepted 1994 March 31

Abstract. Light curves of the long period RS CVn type eclipsing binary RZ Eri, obtained during the period 1976–1979 with the 1.2 m telescope of the Japal–Rangapur Observatory are analysed, using Wilson–Devinney method, by fixing the two parameters T_h (7400°K) and q(0.963), resulting in the following absolute elements: A = 72.5 ± 1.4$R_\odot$, R_h = 2.84 ± 0.12$R_\odot$, R_c = 6.94 ± 0.20$R_\odot$, $M_{\rm bol,\ h}$ = 1.35 ± 0.28, $M_{\rm bol\ ,c}$= 1.41 ± 0.28, m_h = 1.69 ± 0.06$m_\odot$ and m_c= 1.63 ± 0.13$m_\odot$. The presence of humps and dips of varying amplitudes at a few phases in the normal UBV light curves is explained as due to residual distortion wave. The derived (B-V) and (U-B) colours of both the components appear to have been reddened to an extent of $0^m.20$ in (B-V) and $0^m.16$ in (U-B) colours. This reddening is attributed to the presence of an envelope around the system, the material of which might have come from the loss of mass experienced by the evolving cooler component. Taking into consideration the dereddened colours and temperatures of the components, spectral types of *F*0 IV for the primary and G 5–8 III–IV for the secondary component were derived. The fractional radii of 0.039 and 0.096 of the two components, when compared with the radii of their critical Roche lobes of 0.378 and 0.372 suggest that these components are well within their critical sizes. From the position of the components on the. isochrones and the evolutionary tracks of stars of Pop I composition computed by Maeder & Meynet, it is concluded that the evolution of the components of RZ Eri is abnormal. This system is found to be situated at a distance of 185 pc, with an age of about 2.5 × 10^9yrs.

Key words: Eclipsing binaries, orbital elements, evolution—long period RS CVn stars—stars, individual.

1. Introduction

RZ Eridani (RZ Eri) (BD-10°993, HD 30050) is a relatively bright (m_v = 7.7) Algol type binary with a long period of $39^d.3$. Cesco & Sahade (1945) found Ca II *H* and *K* emission lines in the spectrum of the secondary component. This was confirmed by Joy & Wilson (1949) and Bidelman (1954). Later, Popper (1962), Gronbech (1975) and Eggen (1978) classified the primary component of this system to be an *A*5-*F*5 or Am type star and the secondary to be either a *G*8 or a *K* type giant. Popper (1976,

1982) obtained spectra of this system and improved the spectroscopic orbital elements of Cesco & Sahade (1945).

Based on its known characteristics, Hall (1976) included RZ Eri in the long-period RS CVn group. Caton & Oliver (1979) obtained the photoelectric light curve of the system and observed the following features:

(a) Absence of secondary minimum.
(b) No significant distortion wave.
(c) No significant change in period.

The light curves obtained later by Caton (1986) showed a distortion wave of a few hundredth of a magnitude in total amplitude. According to him, there was a possible presence of secondary eclipse near phase 0.67. Popper (1988) and Burki *et al.* (1992) confirmed the presence of the secondary eclipse at this phase.

Studies of RZ Eri in X-rays were reported by Walter & Bowyer (1981) and in radio radiation by Gibson (1979), Hjellming & Gibson (1979) and Paredes *et al.* (1987).

In order to improve our knowledge of this system, its absolute elements and evolutionary nature, we observed RZ Eri during 1976–1979 observing seasons. The preliminary results were already reported by Vivekananda Rao *et al.* (1988). In the following we give a detailed report on the results of our study of this system.

2. Observations

We observed the system RZ Eri in UBV passbands (Johnson system) during 1976–1979 observing seasons. The stars BD – $10^0$999 and – $10^0$994 were used as comparison and check stars respectively. These observations were made using an unrefrigerated EMI 6256B photomultiplier attached to the 1.2 m reflecting telescope of the Japal–Rangapur Observatory. The photocurrent was amplified by means of a GR 1230A DC amplifier and was recorded on a Honeywell Brown chart recorder. The observations of the comparison star were used for determining the nightly extinction coefficients. The rms error Δm (check-comparison) was found to be $\pm\ 0^m.01$ in V and $\pm\ 0^m.02$ in B and U, which indicated that the comparison star was constant in brightness within these errors during the period of our observations. All the observations were corrected for atmospheric extinction. The instrumental differential magnitudes Δm (variable comparison) were transformed to the Johnson and Morgan standard UBV system using the transformation coefficients obtained from the observations of an adequate number of standard stars, in each season on two nights. The transformation relations given by Hardie (1962) were used. The average standard magnitudes of the comparison star, during 19761979, were found to be $V = 9^m.08 \pm 0.01$, $B = 9^m.74 \pm 0.02$ and $U = 9^m.83 \pm 0.02$. The individual standardised observations in the form HJD versus ΔV, ΔB, and ΔU were published elsewhere (Vivekananda Rao & Sarma 1986).

3. Solution of the light curves

3.1 *Period fixation and formation of normal points*

From our observations, the following two primary minimal times were obtained:

HJD(Pri. Min) = 2443574.0830 and 2443888.3618.

Fitting these times and the other times of minima available in the literature up to 1979 to a linear relation, we obtained the following improved ephemeris:

$$\text{HJD(Pri. Min)} = 244{,}3888.3618 + 39^d.2824660 \quad (1)$$

and used this for calculating the phases of all our observations. From an (O-C) diagram we found that the period of the system remained constant during 1906 to 1979. Using the observations available upto 1989, Burki *et al.* (1992) derived a slightly longer period of $39^d.28254$, but this will not affect the phases of our observations calculated from the ephemeris at (1).

The light curves of RS CVn systems are usually affected by a distortion wave and its effect has to be removed before solving them for elements. The nature of the wave in RZ Eri is not well established. Caton & Oliver (1979) did not find any distortion wave in their 1977–1978 observations. However, a distortion wave of a few hundredth of a magnitude in total amplitude was found by Caton (1986) in his observations of 1978–1979. Burki *et al.* (1992) reported that out of all their observations between November 1977 and April 1989 they could find a well described variability for a safe removal of the effects of the spots only in their 1987–1988 observations. They had also stated that the nature of the spots, whether bright or dark, was also not known. Thus our knowledge about the nature of the distortion wave in RZ Eri is very limited.

Since the period of RZ Eri is quite long ($39^d.3$) we could not observe a complete light curve in any one observing season during 1976–1979, thus making it difficult for us to find the nature of the wave and correct our light curves, before solving them for elements. However, assuming that by combining the observations of the three seasons, the wave effects, if any, will be averaged out and that the solution of these curves will give average elements of the secondary component which is found to be responsible for the wave (Burki *et al.* 1992). Accordingly, we formed normal points by combining all our observations according to their phases.

As the slope of the light curves, Δm versus phase, varied rapidly during the primary eclipse, to represent the observations faithfully, as far as possible, we grouped together points within a phase range of about $0^P.001$ (0°.5) to form a normal point in the eclipse region whereas outside the eclipses, points within a phase range of about $0^p.003$ (1°) were grouped together. About 155 normal points were formed in this manner for each of the U, B, V pass bands. These normal points are plotted in Figs. 1a and 1b as filled circles.

3.2 *Light curve solution by Wilson—Devinney method*

3.2.a *Methodology and initial solution*: Out of the presently existing synthetic binary light curve methods Wilson-Devinney (1971) method (hereafter referred to as W-D method) is regarded as more reliable and is widely used. Hence we used this method for obtaining the elements of RZ Eri. Initially, from a preliminary analysis of UBV light curves of this system by Kopal's method (1959), we ascertained that the primary eclipse is an occultation and the system is detached. This conclusion is in conformity with the findings of Popper (1988) and Burki *et al.* (1992).

For initiating the W-D method, one needs reliable preliminary elements. As Kopal's

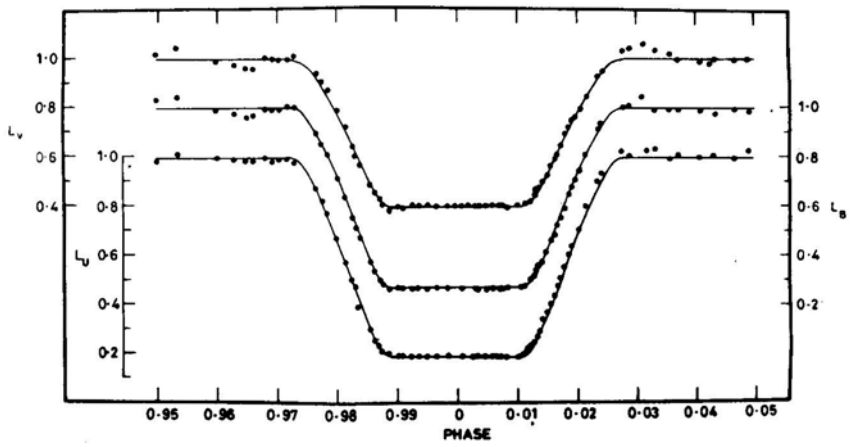

Figure 1a. RZ Eri: Light curves in V, B and U passbands during $0_P.95$ to $0_P.05$. Filled circles represent observations (normals) and solid lines represent the theoretical curves obtained from WD solution with fixed parameters of T_h (7400°K) and q (0.963).

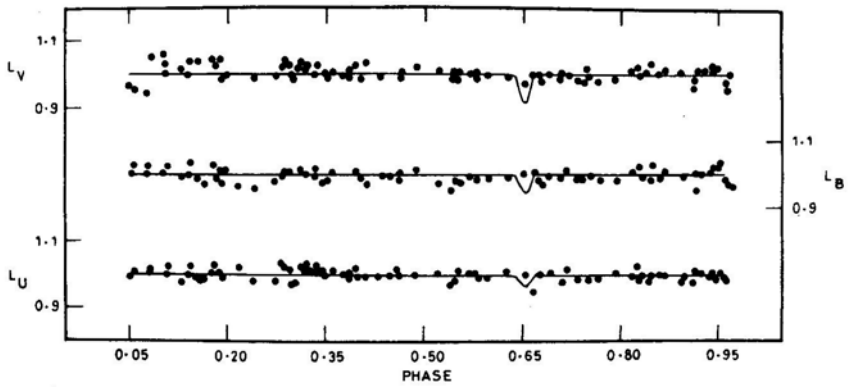

Figure 1b. RZ Eri: Same as Fig. la for $0^p.05$ to $0^p.95$.

method gave discordant parameters in U passband compared to those of B and V, we used the elements given by Popper (1988) and Burki *et al.* (1992) as initial parameters for the WD method and these are given in column 2 of Table 1. A plot of the preliminary theoretical light curves obtained with WD method showed a phase shift of about 0.09 with respect to the observed curve and hence a correction was applied to this effect. According to the principles of WD method, initially we adjusted the following parameters: the inclination i, the surface potentials Ω_h and Ω_c, the mass ratio q, the relative monochromatic luminosity L_h, the temperatures $T_{e,h}$ and $T_{e,c}$ and the third light, l_3. The limb darkening coefficients x_h and x_c, and gravity darkening exponents G_h and G_c were also adjusted but the choice of these coefficients seemed to have negligible effect on the derived elements of RZ Eri. Sufficient number of runs of the DC programme (code 2 for detached systems) was made till the sum of the residuals $\Sigma w(O\text{-}C)^2$ showed a minimum and the corrections to the parameters became smaller than their probable errors. In order to check the internal consistency of the

Table 1. RZ Eri: Elements derived from the combined solution (all parameters varied).

Element	Initial parameters	Combined UBV solution
1	2	3
e	0.352	0.3496 ± 0.0236
ω	312°.1	$312°.11 \pm 3°.0$
P shift	0.0914	0.0914
$T_{e,h}$(°K)	7400	8530 ± 87
$T_{e,c}$(°K)	4790	4970 ± 62
Ω_h	26.6968	26.6508 ± 0.0130
Ω_c	12.4647	12.4350 ± 0.0171
q	0.9643	1.05924 ± 0.00157
i^0	89.3	89.280 ± 0.07
$L_h/L_h + L_c$	V = 0.5952	0.6029 ± 0.0190
	B = 0.7356	0.7204 ± 0.0200
	U = 0.8388	0.7970 ± 0.0230
$L_c/L_h + L_c$	V	0.3971 ± 0.0200
	B	0.2796 ± 0.0200
	U	0.1780 ± 0.0220
$l_3/L_h + L_c + l_3$	0	0.0250 ± 0.0004
r_h(pole)		0.0400 ± 0.0009
r_h(point)	.0385	0.0400 ± 0.0010
r_h(side)		0.0400 ± 0.0010
r_h(back)		0.0400 ± 0.0010
r_c(pole)		0.0965 ± 0.0010
r_c(point)		0.0971 ± 0.0012
r_c(side)	0.0939	0.0966 ± 0.0012
r_c(back)		0.0970 ± 0.0014
x_h	V = 0.60	0.582 ± 0.02
	B = 0.54	0.557 ± 0.02
	U = 0.50	0.530 ± 0.03
x_c	V = 0.80	0.778 ± 0.03
	B = 0.96	0.931 ± 0.03
	U = 0.99	0.990 ± 0.04
$A_h = A_c$	1.0	1.0
$G_h = G_c$	1.0	1.0

results (Popper 1984) separate solutions were made for each of the U, B and V light curves and for the combined set, by keeping all parameters as unknown. These solutions were found to be in close agreement. In column 3 of Table 1, we give the results of the combined solution only.

3.2.b *Reddening of the colours*: Using the derived luminosities (Table 1, column 3) and the differential magnitudes of $\Delta V = -\ 1^m.312$, $\Delta B = -\ 1^m.308$ and $\Delta U = -\ 1^m.112$,

corresponding to unit luminosity at maximum light at quadrature, we derived the magnitudes and colours of the individual components. These values are:

	Hot component	Cool component
V	8.317	8.771
B-V	0.471	1.045
U-B	0.176	0.776

The values of V = 9^m.08, B = 9^m.74 and U = 9^m.83 for the comparison star were used in these calculations (section 2). Assuming no interstellar reddening (r = 185 pc and b = – 33°) the above derived value of (B-V) for the hotter star corresponds to spectral type of *F*7 (Allen 1976). However, the (U-B) colour for such a star should be about 0.04 (Allen 1976). Hence its derived (U-B) value of 0.18 suggests a reddening of 0.14 in this colour. Similarly, the (B-V) colour of 1.04 of the secondary component should correspond to a (U-B) of 0.84. Hence its derived (U-B) value of 0.78 suggests it to be 'bluer'. A similar conclusion was arrived at by Popper (1988). As interstellar reddening seems to be negligible, this reddening in the colours might have arisen from gases existing around the system probably in the form of an envelope. From the studies of RZ Eri in Geneva colour system, Burki *et al.* (1992) suggested the presence of an envelope around this system which contributed a colour excess, E(B-V) of 0^m.20 for both the components. If we assume the nature of the material in the envelope to be similar to that of the interstellar matter, E(B-V) = 0^m.20 should correspond to E(U-B) = 0^m.16 (Allen 1976). Adopting these values to the colours of both the components of RZ Eri, one gets the following unreddened colours:

	Hot component	Cool component
$(B-V)_0$	0.271	0.845
$(U-B)_0$	0.016	0.616

The above corrected $(B-V)_0$ colour of the primary corresponds to a temperature of 7400° (*F*0*V*) (Allen 1976), while $(U-B)_0$ colour gives a temperature of 6600°. However, since the primary component was found to have metallic line characteristics (Morgan in Cesco & Sahade 1945), one cannot give much weight to the (U-B) colour in fixing the temperature or spectral type as the (U-B) in such stars is a function of both temperature and metallicity. Hence giving full weight to the corrected (B-V) colour of 0.27, the temperature of the primary is fixed as 7400°K.

As discussed above, since our U, B, V observations were reddened due to the circum-stellar envelope, they should first be corrected for this effect before analysing them for elements. In order to achieve this, we reanalysed the normal light curves, assumed to be free of the distortion wave, by keeping the parameter ' T_h' as fixed at a value of 7400°K instead of treating it as an unknown parameter.

3.2.C *Fixation of mass-ratio for the analysis:* A reanalysis of the yellow light curve with the parameter 'T_h' fixed at 7400°K and with the remaining parameters as unknown, yielded again a mass-ratio of 1.06, the same as that obtained from the analysis where all the parameters were treated as unknown (column 3, Table 1). This indicates that $m_2 > m_1$. Popper (1988) published radial velocity curves of both the components and spectroscopic elements of RZ Eri. From these studies, a mass-ratio of 0.963 was derived, indicating that $m_2 < m_1$. According to Burki *et al.* (1992) the possibility that the most evolved component of RZ Eri, in reality, to be also the most massive i.e., $m_2 > m_1$, by at least one-tenth of a solar mass, does exist.

In order to see how best the spectroscopic data of Popper (1988) fit the theoretical RV curves with the mass ratio 1.06, we computed theoretical radial velocity curves with WD method for the mass-ratios of 1.06 and 0.963 using V_0 = 43.2 km/sec and $A/R_\odot$ =72.5 as given by Popper (1988) and e = 0.3496, ω = 312°.11 and i = 89°.28 derived from light curve analysis (Table 1). A plot of these curves is shown in Fig. 2. Here the dashed lines represent the theoretical radial velocity curves of RZ Eri for a mass ratio of 1.06 and those with continuous lines represent the same for a mass ratio of 0.963. The As represent the observations of Popper (1988) for the primary, hot component and the points represent his observations obtained from absorption lines for the secondary, cool component. The circled points represent the radial velocities of the Ca II emission lines. The phases are the same as those of the light curves. It is clear from Fig. 2 that the observations fit the radial velocity curves with m_2/m_1 =0.963 much better than they fit the curves with m_2/m_1 = 1.06.

As is evident from the above, since the spectroscopic mass-ratio of 0.963 is a better value compared to the derived photometric mass-ratio of 1.06, we reanalysed the

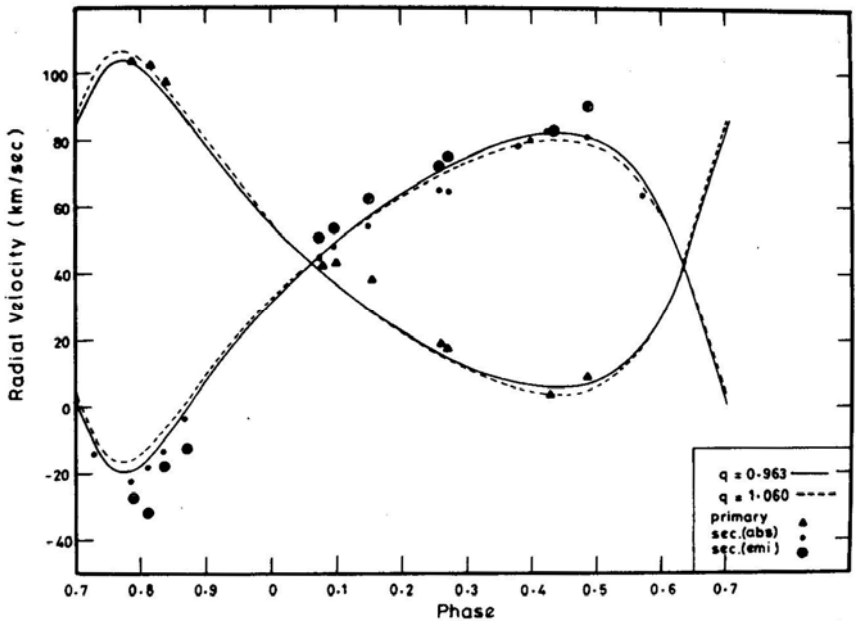

Figure 2. RZ Eri: A plot of phase versus theoretical radial velocities computed by the W-D synthetic method using V_0 = 43.2 km/sec, A = 72.5$R_\odot$, e = 0.3496, ω = 312°.11 and i = 89^0.28. The phases are according to the ephemeris at equation (1) section 3.1.

Table 2. RZ Eri: Summary of elements derived from W-D method (T_h and q fixed).

Element	V Solution	B Solution	U Solution	Combined UBV solution
1	2	3	4	5
e	0.3496 ± 0.0236	0.3496 ± 0.0236	0.3496 ± 0.0236	0.3496 ± 0.0236
ω	312.11 ± 3.00	312.11 ± 3.00	312.11 ± 3.00	312.11 ± 3.00
P shift	0.0914	0.0914	0.0914	0.0914
$*T_{e,h}$(°K)	7400	7400	7400	7400
$T_{e,c}$(°K)	4663 ± 52	4585 ± 50	4745 ± 60	4670 ± 60
$*q$	0.963	0.963	0.963	0.963
i°	89.70 ± 0.06	89.50 ± 0.07	89.58 ± 0.07	89.61 ± 0.07
$\frac{L_h}{L_h + L_c}$	0.5993 ± 0.0200	0.7231 ± 0.0200	0.8075 ± 0.0230	V = 0.6040 ± 0.0190 B = 0.7177 ± 0.0200 U = 0.8132 ± 0.0230
$\frac{L_c}{L_h + L_c}$	0.4007 ± 0.0200	0.2769 ± 0.0200	0.1925 ± 0.0220	V = 0.3960 ± 0.0200 B = 0.2823 ± 0.0200 U = 0.1868 ± 0.0220
l_3	0	0	0	0
r_h(pole)	0.0393 ± 0.0010	0.0388 ± 0.0010	0.0393 ± 0.0022	0.0391 ± 0.0009
r_h(point)	0.0393 ± 0.0010	0.0389 ± 0.0010	0.0393 ± 0.0023	0.0391 ± 0.0010
r_h(side)	0.0393 ± 0.0011	0.0388 ± 0.0011	0.0393 ± 0.0026	0.0391 ± 0.0010
r_h(back)	0.0393 ± 0.0011	0.0389 ± 0.0011	0.0393 ± 0.0025	0.0391 ± 0.0010
r_c(pole)	0.0950 ± 0.0010	0.0958 ± 0.0009	0.0957 ± 0.0017	0.0955 ± 0.0010
r_c(point)	0.0956 ± 0.0012	0.0965 ± 0.0011	0.0963 ± 0.0020	0.0962 ± 0.0012
r_c(side)	0.0951 ± 0.0014	0.0959 ± 0.0012	0.0957 ± 0.0022	0.0956 ± 0.0012
r_c(back)	0.0955 ± 0.0019	0.0964 ± 0.0014	0.0962 ± 0.0026	0.0961 ± 0.0014
x_h	0.600 ± 0.020	0.535 ± 0.020	0.501 ± 0.030	V = 0.600 ± 0.02 B = 0.535 ± 0.02 U = 0.501 ± 0.03
x_c	0.810 ± 0.030	0.960 ± 0.030	0.990 ± 0.040	V = 0.810 ± 0.03 B = 0.960 ± 0.03 U = 0.990 ± 0.04
$*A_h = A_c$	1.0	1.0	1.0	1.0
$*G_h = G_c$	1.0	1.0	1.0	1.0

* Fixed parameters.

light curves by keeping the parameter $q(m_2/m_1 = 0.963)$ also as fixed parameter along with T_h (7400°K). It is expected that analysis of the light curves with fixed T_h and q at known values should yield most reliable elements.

3.2.d *Results of the reanalysis of the light curves with T_h and q fixed:* As discussed above, we reanalysed the normal UBV light curves by keeping T_h (7400°K) and q(0.963) as fixed parameters in the W-D method. These results, for individual as well as for the combined set, are given in Table 2. It is interesting to note that the third light, l_3, which is present only in the U pass band of the solution of the combined

set given in column 3, Table 1, is not present in Table 2 in any of the solutions. The theoretical light curves computed with the elements derived from the combined solution (Table 2, column 5) are shown as solid lines in Figs, la and 1b. The fit of the theoretical curves to the observed normal points is quite satisfactory.

4. Absolute elements

4.1. *Spectral classification*

From the derived luminosities of the combined solution (Table 2) and using the corresponding differential magnitudes for unit luminosity (section 3.2b), the magnitudes and colours of the individual components are derived. These are:

	Hot component	Cool component
V	8.315	8.774
(B-V)	0.477	1.031
(U-B)	0.150	0.735

After applying the reddening correction (section 3.2b), we get

	Hot component	Cool component
$(B-V)_0$	0.28	0.83
$(U-B)_0$	− 0.01	0.58

The $(B-V)_0$ colour of the primary, now corresponds to a spectral type of *F*0 with a temperature of 7400°K (Allen 1976) and is the same as the fixed parameter T_h. This confirms that our analysis with fixed T_h (7400°K) and q (0.963) yielded results akin to the reddening free data. The $(B-V)_0$ colour of the secondary component corresponds to a spectral type of *G*8 V or *G*5 III whereas its $(U-B)_0$ colour corresponds to *K*1 V or *G*6 III. A temperature of 4670°K derived for the secondary (Table 2) corresponds to a spectral type of *K*1 V or *G*8 III. Both the colours and temperature yield consistent results. Keeping in view the sizes of the components (section 43), we have adopted *F*0IV and *G*5-*G*8 III-IV as the spectral types of the primary and secondary components respectively. From an earlier preliminary study, Sarma (1985) concluded that this system consisted of an *F*6 V primary and *K*2 IV secondary. Popper (1988) classified the components to be of *F*5 V and *K*2 III or *K*5 V spectral types. Burki *et al.* (1992) classified them as A8–*F*0 IV and *G*8–*K*2 III–IV. Morgan's tentative classification (in Cesco & Sahade 1945) for the primary was *F*5 IV, with a weak *K* line corresponding to type *A*5. In the same paper, Morgan suggested that the spectral type of the secondary was probably a sub-giant class *G*8. Thus our adopted spectral

Table 3. RZ Eri: Element of RZ Eri obtained from different studies.

Parameter method	Popper (1988) (a)	Burki *et al.* (1992) (b)	Present studies (c)
1	2	3	4
Primary radius (r_h)	$0.039 \pm .003$	$0.0385 \pm .0006$	0.0391 ± 0.0010
Secondary radius (r_c)	$0.097 \pm .003$	$0.0938 \pm .0009$	0.0957 ± 0.0013
e	$0.352 \pm .024$	$0.377 \pm .008$	0.3496 ± 0.0236
ω	312°.1	$312°.7 \pm 1.2$	$312°.11 \pm 3.00$
$i°$	89.0 ± 1.0	89.31 ± 0.13	89.61 ± 0.07
$q = m_c/m_h$	0.963	0.96*	0.963*
$R_h/R_\odot$	2.83	2.79	2.84 ± 0.12
$R_c/R_\odot$	$7.00 \pm .30$	$6.80 \pm .23$	6.94 ± 0.20
$T_{e,h}$(°K)	—	7390 ± 80	7400*
$T_{e,c}$(°K)	—	4790 ± 100	4670 ± 60
Log $L_h/L_\odot$	$1.10 \pm .80$	$1.34 \pm .60$	1.33 ± 0.11
Log $L_c/L_\odot$	$1.26 \pm .50$	$1.32 \pm .07$	1.31 ± 0.11
$m_h/m_\odot$	$1.68 \pm .10$	$1.69 \pm .06$	1.69 ± 0.06
$m_c/m_\odot$	$1.62 \pm .20$	$1.63 \pm .13$	1.63 ± 0.13
$M_{bol,h}$	—	$1.40 \pm .15$	1.35 ± 0.28
$M_{bol,c}$	—	$1.45 \pm .17$	1.41 ± 0.28
$M_{v,h}$	$1.92 \pm .20$	$1.41 \pm .15$	1.36 ± 0.28
$M_{v,c}$	$2.10 \pm .20$	$1.85 \pm .17$	1.82 ± 0.28
Log g_h	$3.75 \pm .09$	—	3.76 ± 0.10
Log g_c	$2.97 \pm .05$	—	2.97 ± 0.06
Spectral type (primary)	*F5*	*A8-F0* IV	*F0* IV
Spectral type (secondary)	*K2* III or *K5* V	*G8-K2* IV–III	*G5-8* III–IV
Distance (pc)	200	180	185
Age (yr)	—	3.3×10^9	2.5×10^9

(a) – Nelson-Davis-Etzel Programme.
(b) – EBOP Programme (v, b and ⟨m⟩ mean).
(c) – Wilson & Devinney Programme.
* – Assumed.

types of the components of RZ Eri are, in good agreement with those reported from various other studies.

4.2. *Masses of the components*

For any eclipsing system, one can get reliable absolute elements provided it presents total eclipses with both the eclipses present. Also the system should be a double-lined

spectroscopic binary whose radial velocity amplitudes are large enough to get an accurate mass-ratio. In the case of RZ Eri, even though the primary eclipse is total and very deep, the secondary eclipse is not present in any of our light curves. As discussed in section 3.2c, the mass-ratio of the system, as derived by Popper (1988) and adopted in the present analysis is 0.963. Combining the values of K_1 and K_2 from Popper with the other required parameters from Table 2 and using relevant equations, we obtained $A/R_\odot$ = 72.50 ± 1.4 and $m_1/m_\odot$ = 1.69 ± 0.06 and $m_2/m_\odot$ = 1.63 ± 0.13.

4.3. *Sizes and luminosities*

Using the values of A, r_h, r_c, T_h and T_c (Table 2) for the primary and secondary components we obtained their sizes, luminosities, bolometric and visual absolute magnitudes. These values, with their errors, are:

	Hot component	Cool component
Radius $R/R_\odot$	2.84 ± 0.12	6.94 ± 0.20
Log $L/L_\odot$	1.33 ± 0.11	1.31 ± 0.11
M_{bol}	1.35 ± 0.28	1.41 ± 0.28
M_v	1.36 ± 0.28	1.82 ± 0.28

The bolometric corrections are from Popper (1980). For comparison, the elements of RZ Eri as derived by us, Popper (1988) and Burki *et al.* (1992) are given in Table 3.

Assuming an absorption of $A_v = 0^m.6$ for the material of the envelope and with negligible space absorption, the distance of RZ Eri is found to be 185 ± 0.5 pc.

5. Evolutionary nature

With a view of studying the evolutionary status of the components of RZ Eri, we used the evolutionary tracks computed by Maeder & Meynet (1988) for stars of Pop I composition. These evolutionary tracks for stars of initial mass of 1.7 and 2.0 in solar units are shown as solid lines in Fig. 3 which is a plot of log $L/L_\odot$versus log T_e. In the same diagram, the dashed lines represent the isochrones for ages of 2.5 and 3.0 billion years. These isochrones were obtained by interpolation between the evolutionary tracks of Maeder & Meynet (1988) based on points of corresponding evolutionary status. It can be seen that the evolutionary nature of the primary and the secondary are different. The secondary component which is of smaller mass is in an advanced phase of evolution (sub-giant) and is presently on its way to a rapid expansion. The primary component with a slightly higher mass is still in the main sequence phase. The secondary component with a mass of 1.63 ± 0.13$m_\odot$, fits the evolutionary path of a star of mass 1.7 $m_\odot$, whereas the primary component with a mass of 1.69 ± 0.06 $m_\odot$ fits the evolutionary track of a star of mass 2.0$m_\odot$. Comparing the general properties of 22 RS CVn binaries, Montesinos *et al.* (1988) separated them into three groups, of which the third group consisted of binaries with abnormal evolution. Systems like SS Boo, CG Cyg, WW Dra, Z Her, AR Lac, TY

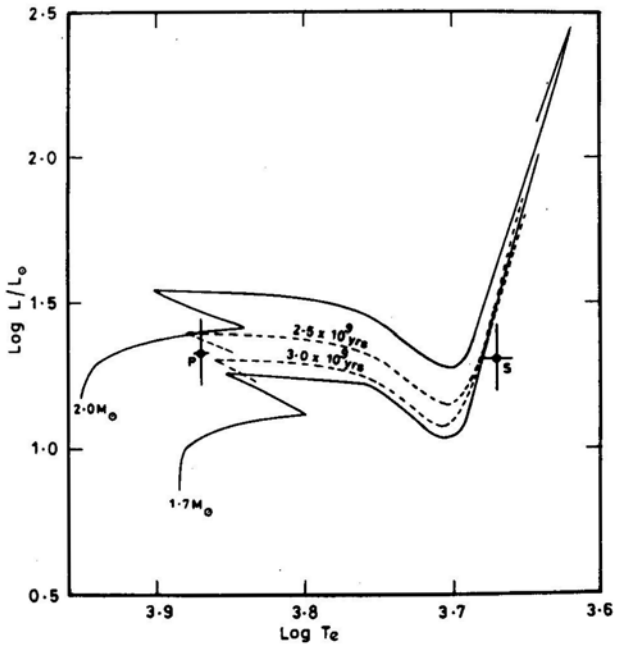

Figure 3. RZ Eri: Location of the primary (P) and secondary (S) components in the log $L/L_{\odot}$ vs. log T_e diagram. The evolutionary tracks (continuous line) are by Maeder & Meynet (1988). The lines (dotted) of equal ages are also noted.

Pyx, RZ Cnc, AR Mon and RZ Eri were placed in this group. The last three members were further noted to be more conspicuous than the remaining ones. The evolution of these systems is abnormal in the sense that either the more massive stars of the system have the smallest radii or, components with similar masses show a large difference between their radii. In addition to this abnormality, we now find that in RZ Eri the primary component appears to follow an evolutionary track of a slightly higher mass. For a clear understanding of this phenomenon, high quality spectroscopic and photometric studies in as many pass-bands as possible are desirable. Theoretical studies based on computations of stellar evolution including mass transfer in binaries having components with equal masses and dissimilar composition (e.g. metallicity) are needed.

From Fig. 3 one can notice that both the primary and secondary components fit the isochrone of 2.5×10^9 years. Hence it is concluded that the age of RZ Eri is about $2.5 \pm 0.1 \times 10^9$ years.

6. Discussion

One can notice several humps and dips, with differing amplitudes, at a few phases, in UBV light curves of RZ Eri (Figs. la and lb). These may be the effects of the residual waves that may not have been completely nullified in the process of combining the observations of all the seasons, as expected. However, observed reddening of the (B-V) and (U-B) colours of the components of RZ Eri are explained as due to the

presence of an envelope around the system. The material in the envelope might have been expelled from the secondary component of RZ Eri during evolution to its present sub-giant stage. Comparing the observed fractional radii of 0.039 and 0.096 of the primary and secondary components with their radius of the critical Roche lobes of 0.378 and 0.372 respectively, for a mass-ratio of 0.963 (Plavec & Kratochvil 1964), it is found that the components are well within their critical sizes (filling only 10% and 25% respectively). The position of either of the components on the evolutionary tracks (section 5) does not indicate any possibility of a 'Case B' type evolution. However, as the secondary, cooler and bigger component is in an advanced stage of evolution, there may be a mild exchange ($< 5 \times 10^{-11} m_{\odot}$/yr) of mass and mass loss when this component was crossing the H–R gap (Popper & Ulrich 1977) and may be responsible for the envelope detected in the system. The IR excess detected in this system by Busso *et al.* (1990) is a confirmation of a circumstellar shell or envelope around RZ Eri. A similar circumstellar envelope has been detected by Glebocki *et al.* (1986) around λ And. It is interesting to note that both RZ Eri and λ And belong to the long-period group of the RS CVn systems.

Acknowledgements

Our thanks are due to Prof. K. D. Abhyankar for many helpful discussions. Our thanks are also due to the unknown referee for his valuable suggestions. M.B.K.S. wishes to thank the Council of Scientific and Industrial Research, New Delhi, for financial assistance under the Emeritus Scientists Scheme.

References

Allen, C. W. 1976, *Astrophysical Quantities, 3rd edn.,* (London: The Athlone Press) p. 206.
Bidelmann, W. P. 1954, *Astrophys. J. Suppl. Ser.,* **1**, 175.
Burki, G., Kviz, Z., North, P. 1992, *Astr. Astrophys.,* **256**, 463.
Busso, M., Scaltriti, F., Ferrari-Toriolo, M., Origlia, L., Persi, P., Robberto, M., Silvestro, G. 1990, *Mem. Soc. astr. Ital.***,61**, 77.
Caton, D. B., Oliver, J. P. 1979, *Inf. Bull. Var. Stars,* No. 1665.
Caton, D. B., 1986, *Astr. J.,* **91**, 132.
Cesco, C. U., Sahade, J. 1945, *Aρ. J.*, **101**, 370.
Eggen, O, J. 1978, *Inf. Bull. Var. Stars,* No. 1426.
Gibson, D. M. 1979, in *IAU Symp. 88: Close Binary Stars: Observations and Interpretation,* Eds. M. J. Plavec, D. M. Popper & R. K. Ulrich (Dordrecht: D. Reidel) p. 31.
Glebocki, R., Sikorski, J., Bielicz, E., Krogulec, M. 1986, *Astr. Astrophys.,* **158**, 392.
Gronbech, B. 1975, *Inf. Bull Var. Stars,* No. 1956.
Hall, D. S. 1976, in *IAU Coll. 29: Multiple Periodic Variable Stars, Part I,* Ed. W. S. Fitch, (Dordrecht: D. Reidel).
Hardie, R. H. 1962, in *Astronomical Techniques,* Ed. W. A. Hiltner (University of Chicago Press) p. 178.
Hjellming, R. M., Gibson, G. M. 1979, in *IAU Symp. 88*: *Close Binary Stars: Observations and Interpretation,* Eds M. J. Plavec, D. M. Popper & R. K. Uhich, (Dordrecht: D. Reidel) p. 209.
Joy, A. H., Wilson, R. E. 1949, *Astrophys. J.,* **109**, 231.
Kopal, Z. 1959, *Close Binary Systems* (Chapman and Hall Ltd).
Maeder, A., Meynet, G. 1988, *Astr. Astrophys. Suppl. Ser.,* **76,** 411.

Montesinos, B., Gimenez, A., Fernandez-Figneroa, M. J. 1988, *Mon. Not. R. astr. Soc.*, **232**, 361.
Paredes, J. M., Estalella, R. Rius, A. 1987, *Astr. Astrophys.*, **186,** 178.
Plavec, M., Kratochvil, P. 1964, *Bull. astr. Inst. Csl.*, **15**, 165.
Popper, D. M. 1962, *Publ. astr. Soc. Pacific*, **74,** 129.
Popper, D. M. 1976, *Inf. Bull. Var. Stars*, No. 1083.
Popper, D. M., Ulrich, R. K. 1977, *Astrophys. J.*, **212,** L131.
Popper, D. M. 1980, *A. Rev. astr. Astrophys.*, **18,** 115.
Popper, D. M. 1982, *Publ. astr. Soc. Pacific*, **94,** 945.
Popper, D. M. 1984, *Astr. J.*, **89,** 132.
Popper, D. M. 1988, *Astr. J.*, **96,** 1040.
Sarma, M. B. K. 1985, in *Highlights of Astronomy*, Ed. J. P. Swings, **7,** 443 (Dordrecht: D. Reidel).
Vivekananda Rao, P., Sarma, M. B. K. 1986, *Contr. Nizamiah & Japal-Rangapur Obs.*, No. 18.
Vivekananda Rao, P., Sarma, M. B. K., Prakash Rao, B**.** V. N. S., 1988, in *IAU Coll. 107: Algols*, Ed. A. H. Batten, (Kluwer Academic Publishers), p. 357.
Walter, F. M., Bowyer, S. 1981, *Astrophys. J.*, **245,** 671.
Wilson, R. E., Devinney, E. J. 1971, *Astrophys. J.*, **166,** 605.

J. Astrophys. Astr. (1994) **15,** 179–186

Probable Spectral Steepening of UHE γ-rays of Nuclear Origin and its Consequences

Abhas Mitra *Nuclear Research Laboratory, Bhabha Atomic Research Centre, Bombay 400 085*

Received 1993 June 9; accepted 1994 March 31

Abstract. Recent accelerator data based parameterization of the inclusive cross section ($c - s$) for π_0 production in hadronic collisions and an explicit incorporation of the finiteness of the relevant projectile hadron spectrum suggest a significant steepening in the spectrum (by as much as 0.4 in the spectral index) of the secondary γ-ray towards the end of the spectrum. We emphasize here that this spectral steepening in conjunction with the possibility that in the bright X-ray binaries the maximum energy to which the γ-ray producing progenitor protons may be accelerated is only ~ l0 PeV, may imply an effective efficiency for γ-ray production, ε, as reckoned by the PeV arrays, one or two orders smaller than the previous estimates. To explain the genesis of a given PeV photon flux from an X-ray binary, one, therefore, has to. accordingly consider a much higher value of the progenitor proton beam luminosity, L_p. This requirement may raise further questions regarding the actual genesis of PeV γ-rays in X-ray binaries, or alternatively, on the veracity of the high values of the PeV photon fluxes reported by earlier experiments.

Key words: Gamma rays: general—particle acceleration—radiation mechanisms—cosmic rays: general.

1. Introduction

Over the last decade or two, detection of TeV-PeV γ-rays has been reported from various kinds of discrete sources (Weekes 1988; Chadwick *et al.* 1990). The strongest emitters, initially, seemed to be the various bright X-ray binaries like Cygnus X-3, Her X-l, Vela X-l and Sco X-l. Nevertheless, there was always room for scepticism for the genuineness of some of these findings (Bonnet-Bidaud & Chadrin 1988). In general, there appears to be a clear trend that most of the more recent experiments with higher sensitivity (and followed by more careful data-analysis), are failing to record any positive signal from such sources. Significantly, a similar trend is seen in the much lower TeV region too, yielding corresponding upper-limits on the TeV-PeV γ-ray fluxes which are often one or two orders smaller than the initially reported values. However, new generation highly sensitive telescopes are expected to rewrite this chapter with a definitive note whether it is a case of actual detection or fixing an upper-limit. In particular, as far as very high energy region is concerned, imaging Cerenkov telescopes have already established two discrete sources, namely, the Crab nebula and the AGN Mk 421 as sources of TeV γ-rays at a high significance level.

In this context, it may be worthwhile to look back on some of the theoretical aspects in a more definitive fashion. We note that, for the discrete sources of the X-ray binary variety as well as for the diffused component (Berezinsky & Kudryavtsev 1990), one of the most pertinent mechanisms responsible for the production of ultra high energy grays is believed to be the nuclear process. One important question in γ-ray astronomy would therefore be, given a progenitor high energy differential proton (or neutron) spectrum $\sim E^{-\alpha}$, what would be the spectral nature of the resultant secondary nuclear γ-rays, $E^{-\beta}$, where both α and β are assumed to be energy independent. Another associated question, which is vital for appreciating the competing production mechanisms and models, would be, given a certain source particle luminosity, L_p, integrated over all bands, what would be the efficiency for γ-ray production $\varepsilon(> E_\gamma)$ as seen by a given detector with a threshold E_γ? In fact most of the estimates of L_p made so far have been based on some sort of general idea where one typically assumes $\beta = \alpha$ and $\varepsilon_\gamma = 0.1$.

We would see that this idea remains approximately correct as long as $E_\gamma < 10^{-2} E_*$, where E_* is the maximum proton energy. First we emphasize here that in the context of the supposed production of PeV γ-rays in the bright X-ray binaries this foregoing condition is unlikely to be satisfied in view of the fact that it is extremely difficult to conceive of any efficient acceleration mechanism operating in the X-ray binaries which can lead to a value of E_* in excess of 10 PeV (Hillas 1984; Mitra 1991). This happens because in the binary environment, the PeV protons undergo strong synchrotron and photomeson energy losses. And in case, the ambient magnetic field (B) is considered weak enough to avoid the synchrotron losses (though the photomeson losses alone can quench the acceleration process), it can be seen that the basic acceleration rate goes down (which is generally proportional to B) and also the test particles cannot be confined to the acceleration site for sufficient duration. We are of the opinion that as long as the particle acceleration is believed to be taking place in the magnetosphere, a generous value of E_* is $\sim$ 10 PeV, and thus the lowest value of $x \equiv E_\gamma / E_*$ to which the PeV arrays may operate should be $x \sim 0.1$. And the corresponding lowest value for the ultra high energy (UHE) arrays should be $x \sim 0.01$. By extending the relevant works of previous authors, we intend to study the secondary nuclear γ-ray spectrum in the region $x > 0.01$ in order to see some of its consequences on the nuclear-orbital TeV-PeV γ-ray production models (Vestrand & Eichler 1982).

The crucial factor in determining the emissivity of the γ-ray source function in a phenomenological approach is the assumption regarding the form of the effective π^0 production cross section (which tantamounts to assumption about the inclusive cross section). Stecker (1970, 1971) used a phenomenological form of the effective pion production cross section:

$$\sigma(E_\pi | E_p) \sim E_p^a \delta(E_\pi - \chi_0 E_p^b) \tag{1}$$

where a, b, and χ_0 are suitable parameters. In the isobaric-fireball model of particle production of Stecker in which the isobars carry 50–60% of the available energy, one obtains a secondary γ-ray spectral index:

$$\beta = \frac{\alpha - 2a}{1 - a} \tag{2}$$

which leads to $\beta \geqslant \alpha$, for $\alpha \geqslant 2.0$. In the pre-scaling era, a particular simplification of the above scheme assumed $\alpha = 0.25$ and $b = 0.75$ leading to $\beta = 4/3\ (\alpha - 0.5)$. In fact one can obtain this value of β by assuming a simplified pion multiplicity law $\sim s^{0.25}$ and an equitable distribution of the available energy amongst the secondary pions. In a much more rigourous exercise, by using accelerator data upto ~ 1 TeV, Ganguli & Sreekantan (1979) made quite accurate numerical parameterization of the pion production cross section through the observed rapidity distribution function. Then they proceeded to numerically evaluate the γ-ray spectrum which showed $\beta \approx \alpha$. At a later stage Stecker (1979) considered an extreme form of scaling where the 'fireball' carries the whole of the available energy to give rise to a single 'leading pion' implying $a \rightarrow 0$ and $b \rightarrow 1$. Obviously equation (2) then yields $\beta \approx \alpha$. Here we consider only high energy regimes $E_p > 10$ GeV, as at lower energies, there may be additional complicacies because of the presence of resonances and the absence of any scaling behaviour (Dermer 1986).

We note here that in most of such earlier works the value of E_* was considered much higher than the region of interest. Or in other words, it was assumed that $E_* \rightarrow \infty$, or $x_\pi \equiv E_\pi/E_* \rightarrow 0$. On the other hand, several authors have tried to find the secondary γ-ray spectrum in a completely numerical and exact manner. In particular, the secondary γ-ray spectrum has recently been derived quite accurately (Harding & Gaisser 1990, henceforth HG), and this work is partly based on the previous work by Berezinsky and his coworkers (for instance Berezinsky & Kudryavtsev (1990)). For the sake of completeness, we briefly summarize their work below to arrive at formal definitions of ε which would enable one to quickly calculate the value of L_p for a given value of PeV photon flux.

2. Formulation

For a certain thin target with optical depth τ, the γ-ray emissivity in $p - p$ reactions can be obtained by a convolution of the differential spectrum of the accelerated hadrons with the target density, the π^0 production $c - s$ and the π^0 decay spectrum. The crucial parameter here is the differential $c - s$ for π^0 production:

$$\mathrm{d}\sigma^{\mathrm{in}}(E_\pi | E_p)/\mathrm{d}E_\pi = \sigma_\pi^{\mathrm{in}}(E_p) f(x_\pi)/E_\pi \tag{3}$$

Following the recent accelerator based data parameterization by Berezinsky and Kudryavtsev (1990), one can use

$$\sigma_{pp}^{\mathrm{in}}(E_p) = \{31 + 0{\cdot}37 \ln^2(E_p/50\,\mathrm{GeV})\}\,mb; \quad \text{and} \tag{4}$$

$$f(x_\pi) = 0.61(1 - x_\pi)^{3.5} + 0.46\exp(-18x_\pi). \tag{5}$$

With some further mathematical manipulation (HG), one can express the γ-ray yield function as

$$Y_\gamma(>E_\gamma) = \tau \frac{2}{\alpha(\alpha-1)} \frac{Z_{p\pi^0}(x)}{E_\gamma^{(\alpha-1)}} \left[\int_{E_0}^{E_*} \frac{\mathrm{d}E_p}{E_p^{(\alpha-1)}} \right]^{-1} L_p \tag{6}$$

where $Z_{p\pi^0}(x)$ is the spectrum weighted moment of the inclusive $c - s$ as reckoned

Table 1. Total effective inclusive gamma ray production cross-section for various values of α.

α	2.0	2.1	2.2	2.3	2.4	2.5	2.6	2.7	2.8
$Z_{p\pi^0}(0)$	0.16	0.11	0.092	0.08	0.066	0.056	0.048	0.04	0.036

by the detector with a finite threshold:

$$Z_{p\pi^0}(x) = \int_x^1 \left\{ \left[z^\alpha + (\alpha - 1)x^\alpha \right] - z\alpha(x)^{\alpha-1} \right\} f(z) \frac{dz}{z^2} \tag{7}$$

For a gray detector which records the entire γ-ray spectrum (i.e. $E_\gamma = 0$) or alternatively if $E_* \to \infty$ for a finite E_γ (as has been implicitly assumed in several earlier works), the γ-ray yield function is simply determined by the total spectrum weighted moment of the inclusive $c - s$:

$$Z_{p\pi^0}(0) = \int_0^1 x^{\alpha-2} f(x) dx \tag{8}$$

Both $Z_{p\pi^0}(x)$ and $Z_{\rho\pi^0}(0)$ can be evaluated numerically. Table 1 shows the values of $Z_{p\pi^0}(0)$ for various values of α . Fig. 1 shows the plot of quantity $Z_{\rho\pi^0}(x)/Z_{\rho\pi^0}(0)$ (HG). It may be noted here that although HG calculated the spectrum in terms of $Z_{p\pi^0}(x)$ by incorporating the parameterization of Berezinsky & Kudryavtsev, they did not explicitly discuss the steepening aspect and its consequences. We note that for $x > 10^{-3}$, one may crudely parameterize $Z_{\rho\pi^0}(x) \sim x^{-n}$, where n itself is a weakly dependent function of x and α. However, we may assign an approximate mean value of $n \approx 0.4$ for $\alpha \geq 2.0$, and ≈ 0.3 for $\alpha \approx 2.8$. Thus, we see that the shape of the high energy γ-ray spectrum depends on the value of E_γ and E_* .

For a stationary material target with a grammage of Δx, we can write the optical thickness as $\tau = \Delta x/\lambda$, where λ is the nuclear interaction length. And in case the

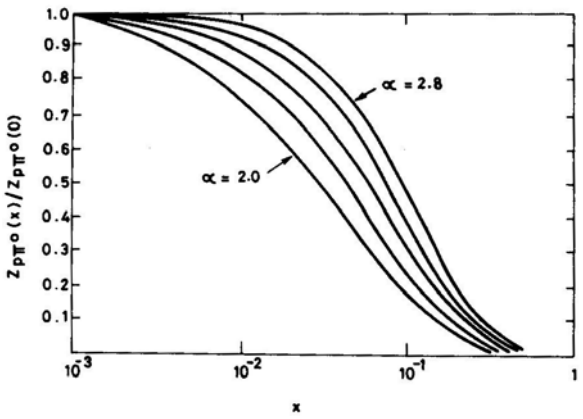

Figure 1. Ratio of the apparent effective inclusive cross section for γ-ray production and the total effective value of the same for a γ-detector with an energy threshold E_γ . Successive values of α considered are 2.2, 2.4, 2.6, and 2.8.

projectile protons are trapped in the target itself (say for *in situ* acceleration and γ-ray production in a shock-front), we may write $\tau = t_{trap}/t_{p-p}$, where t_{trap} is the trapping time scales of the protons and t_{p-p} , is the nuclear cooling time scale of the protons. In case of large optical depths, we must replace the factor τ in equation (6) with $(1 - e^{-\tau})$. In the latter form of origin of optical depth, because of the probable small value of Δx, it might be possible to have a maximum value of $(1 - e^{-\tau}) \rightarrow 1.0$. But, in the former case, a thick target would imply self absorption of the produced γ-rays in the source, and without going into the details of cascading, one can have a generous estimate about the maximum optical value of $(1 - e^{-\tau}) \approx 0.5$.

Further, in the case of a non-in *situ* orbital γ-ray production scenario, like the one conceived by Vestrand and Eichler (1982) where protons emanating from a distant point source in a solid angle Ω impinge on a suitable material target for a fraction of binary duty cycle $\Delta\phi$, following the initial illustrations by Hillas (1985), one can write

$$N_\gamma(E_\gamma) = \frac{4\pi}{\Omega}\frac{1}{4\pi d^2}\Delta\phi \quad Y_\gamma(>E_\gamma) \tag{9}$$

where $N_\gamma(>E_\gamma)$ is the photon flux recorded at Earth from a source at a distance d. The probable attenuation of the γ-rays in the course of their propagation (say due to cosmic background radiation) will further modify the foregoing equation – but here we will not divert our attention to such effects.

3. Effective efficiency of a detector

The efficiency for γ-ray production as seen by a detector with a threshold E_γ, could be defined as the quantity linking the inferred γ-ray luminosity $L_\gamma(>E_\gamma)$ with the progenitor particle beam luminosity. To this effect, let us recall that for $\beta = 2.0$, we can write

$$L_\gamma(>E_\gamma) \equiv E_\gamma\, Y_\gamma(>E_\gamma)(1 - E_\gamma/E_\gamma^*)^{-1}\log(E_\gamma^*/E_\gamma) \tag{10}$$

and for $\beta > 2.0$, we have

$$L_\gamma(>E_\gamma) \equiv \frac{\beta-1}{\beta-2}E_\gamma\left[\frac{1-(E_\gamma^*/E_\gamma)^{2-\beta}}{1-(E_\gamma^*/E_\gamma)^{1-\beta}}\right] Y_\gamma(E_\gamma) \tag{11}$$

where any probable energy dependence of β has been neglected as a first order approximation. Since the maximum pion elasticity ≈ 0.5, we may assume a value of the maximum γ-ray photon $E_\gamma^* = 0.5E_*$. Then by ignoring the optical depth factor, and combining equations (6) and (11), we may define the efficiency as

$$\varepsilon(x) = \frac{\log(1/2x)}{\log(E_*/E_0)} \quad (1-2x)^{-1}\, Z_{p\pi^0}(x); \quad \alpha = \beta = 2.0, \tag{12a}$$

$$\varepsilon(x) = \frac{\beta-1}{\beta-2}\frac{1-(2x)^{\beta-2}}{1-(2x)^{\beta-1}}\frac{Z_{p\pi^0}(x)}{\log(E_*/E_0)}; \quad \alpha = 2.0, \quad \beta > 2.0, \tag{12b}$$

$$\varepsilon(x) = \frac{2}{\alpha}\frac{\beta-1}{\beta-2}\frac{\alpha-2}{\alpha-1}\frac{1-(2x)^{\beta-2}}{1-(2x)^{\beta-1}}\frac{(E_\gamma/E_0)^{2-\alpha}}{1-(E_*/E_0)^{2-\alpha}} Z_{p\pi^0}(x); \quad \text{both } \alpha,\ \beta > 2.0, \tag{12c}$$

where E_0 is the lower cutoff of the particle spectrum. Note that the apparent efficiency of a detector with a finite threshold is naturally reduced for $E_0 \ll E_\gamma$, because the portion of the γ-ray spectrum below E_γ is simply not reckoned. This obvious cause apart, in the range of $x \sim 0.1$, there is equally or more significant reduction of the efficiency owing to the spectral steepening associated with $Z_{p\pi^0}(x)$.

For the sake of illustration, we consider a specific case previously considered by Hillas (1985) where, he took, $\alpha = 2.0$, $E_* = 100$ PeV, $E_\gamma = 1$ PeV (i.e. $x = 0.01$) and also, presumably, considered $E_0 = 1$ PeV. The corresponding value of ε considered by him was 0.16. However, for this value of x, we find from Table 1, a value of $Z_{p\pi^0}(0) = 0.16$ with $Z_{p\pi^0}(0.01) \approx 0.12$. It may be noted here that as per previous discussion, the spectral index of the secondary gamma-ray spectrum, β, is, on the average, larger by an amount ~ 0.4 ($\alpha \sim 2.0$). By considering an appropriate value of $\beta \sim 2.4$, from the equation 12b, we find $\varepsilon(0.01) \approx 0.07$. On the other hand, by assigning $E_* = 10$ PeV (i.e. $x = 0.1$) and repeating this exercise, we find a value of $\varepsilon(0.1) = 0.013$. For an expected smaller value of E_0 the value of ε goes down in a logarithmic fashion. For instance, by assigning $E_0 = 1$ TeV, we find $\varepsilon(0.1) = 0.008$.

For further illustration, let us estimate $\varepsilon(0.1)$ for a case with $\alpha = 2.2$, $\beta \approx 2.6$, $E_o = 1$ TeV and with other parameters remaining unchanged. From equation (12c), we come out with a value of $\varepsilon(0.1) = 0.24.10^{-2}$ which is substantially smaller than the usually considered value of $\varepsilon \sim 0.1$. And remember here that an incorporation of the optical depth factor would further reduce these estimates at least by a factor of 2.

Does this efficiency increase in case of a monoenergetic proton source? For a range of monoenergetic values of E_p, the differential π^0 production spectrum has been computed by Cheng *et al.* (1990) by considering pure scaling as well as certain kind of violation of the same. It is seen that the scaling violation gives steeper fall of the cross section, and in general, the cross section falls off drastically at the end ($x > 10^{-3}$ — 10^{-2}) even when no cascading is considered. In particular, they have specifically calculated the γ-ray yield funcion for $E_p = 2$ PeV under the assumption of scaling violation. This shows a drastic steepening of the spectrum for $x > 10^{-3}$ and the spectrum practically terminates at $x \approx 0.1$. Thus, it may be expected that, for monoenergetic cases too, $\varepsilon(x)$ would be equally low for sufficient large values of $x > 10^{-2}$.

4. Reestimation of proton beam power

One may also directly relate the value of the inferred photon flux $N_\gamma(> E_\gamma)$ (vis-a-vis the L_γ) and L_p to find a modified definition of the γ-ray production efficiency:

$$\varepsilon'(x) = \frac{Z_{p\pi^0}(x)}{\log(E_*/E_0)}; \quad \alpha = 2.0, \tag{13a}$$

$$\varepsilon'(x) = \frac{2(\alpha-2)}{\alpha(\alpha-1)} \frac{(E_\gamma/E_0)^{2-\alpha}}{1-(E_*/E_0)^{2-\alpha}} Z_{p\pi^0}(x); \quad \alpha > 2.0 \tag{13b}$$

It is trivial to find that the value of ε' also falls appreciably with the rise in the value of x. In terms of the modified definition of ε', we can rewrite

$$L_p = E_\gamma N_\gamma(> E_\gamma)(1-e^{-\tau})^{-1} 4\pi d^2 \frac{\Omega}{4\pi} \frac{1}{\Delta\phi} \frac{1}{\varepsilon'_\gamma(x)} \tag{14}$$

Specifically, let us consider here the most discussed source Cygnus X-3 and we note that, so far, the most careful estimate of the value of L_p is that due to Berezinsky (1987), where it was assumed that E_0 = 1 GeV. E_* =10^8 GeV , α = 2.1, $\Delta\phi$ = 0.1 (actually for most of the PeV observations $\Delta\phi \sim 210^{-2}$ i.e. 2%). To explain an integral flux of $N_\gamma(>1\ \text{PeV}) = 1.6\ 10^{-13}\ \text{cm}^{-2}\,\text{s}^{-1}$, he required

$$L_p \approx 10^{41}\,\text{erg s}^{-1}\,\frac{N_\gamma(>1\,\text{PeV})}{1.6\,10^{-13}\,\text{cm}^{-2}\,\text{s}^{-1}}\,\frac{\Omega}{4\pi}\,\frac{2\%}{\Delta\phi}\left(\frac{d}{12\,\text{kpc}}\right)^2\tau \tag{15}$$

To compare our result with that obtained by Berezinsky, we find from equation (13b), a value of $\varepsilon'(0.01) \approx 0.002$ which leads to a value of $L \approx 5.10^{40}$ erg s^{-1} provided all other relevant parameters remain unchanged. Thus there is some discrepancy between these two results. Now if we have x = 0.1 (E_* = 10 PeV), we find $\varepsilon'(0.1) = 2.7.\ 10^{-4}$. In such a case, we can write

$$L_p \approx 7.4\,10^{41}\,\text{erg s}^{-1}\,\frac{N_\gamma(>1\,\text{PeV})}{1.6\,10^{-13}\,\text{cm}^{-2}\,\text{s}^{-1}}\,\frac{\Omega}{4\pi}\,\frac{2\%}{\Delta\phi}\left(\frac{d}{12\,\text{kpc}}\right)^2\tau \tag{16}$$

Finally, for a typical value of the recent upper limit of the UHE (0.1 PeV) photon flux (muon poor) from the direction of Cyg X-3 (Aglietta *et al.* 1993), the corresponding value of the $L_p(x = 0.01)$ would be

$$L_p \approx 2.4\,10^{39}\,\text{erg s}^{-1}\,\frac{N_\gamma(>0.1\,\text{PeV})}{3.10^{-14}\,\text{cm}^{-2}\,\text{s}^{-1}}\,\frac{\Omega}{4\pi}\,\frac{2\%}{\Delta\phi}\left(\frac{d}{12\,\text{kpc}}\right)^2\tau \tag{17}$$

5. Conclusion

The steepening in the spectrum of the secondary γ-rays of nuclear origin resulted from an explicit consideration of the finiteness of the progenitor particle spectrum and a use of reasonable accelerator based data parameterization. This exercise presented above was a logical extension of the relevant works carried out by some previous authors as mentioned here. For a finite value of E_*, the high energy regime of the secondary spectrum is gradually depleted of secondary photons, and in the absence of still higher energy particles this depletion never gets adequately replenished giving rise to a steepening. This kind of steepening may be absent in the low energy regimes (inspite of a finite cutoff) $E_* \sim 10$ GeV, because of the small pion multiplicities involved in such cases. Here the leading γ-rays may indeed share considerable and almost similar fraction of the available energy. This would mean roughly a one-to-one correspondence between a primary proton and a leading secondary γ-ray which may lead to $\beta \approx \alpha$ except for the resonance regions. If one uses the Vestrand and Eichler (1982) type model to understand the probable origin of UHE/PeV γ-rays in the X-ray binaries, in view of the fact that a generous upper-limit on the value of E_* is only 10 PeV, it follows that the value of L_p might have been underestimated by at least. one order of magnitude in the past.

By turning around this finding, and by recalling that the value L_p is often limited by sound physical constraints (for instance for the X-ray binaries L_p may be limited by accretion power) one has some extra room for scepticism for the genuineness of

the earlier reported high values of PeV photon flux from Cygnus X-3 ($N_\gamma \sim 10^{-13}$ photon c m^{-2} s^{-1}) . In fact most of the subsequent and probably more accurate experiments have often failed to detect any UHE/PeV signal from Cygnus X-3 (or from any other point source) yielding upper limit of N_γ (> 0.1 PeV) < 3.10^{-14} photons cm^{-2} s^{-1} . In view of such difficulties, the present author has proposed an entirely new class of models for UHE γ-ray production in Cyg X-3 (Mitra 1994). In this case, the γ-rays are produced close to the compact object and are therefore subject to the intense magnetic pair production a possibility which Was initially overlooked (Mitra 1990). However, if the magnetopause indeed considerably shields the neutron star magnetosphere, it may be possible for this model to explain the above referred UHE upper limit by starting from a modest value of $L_p \sim 1.75.10^{37}$ erg s^{-1} which is well within the Eddington luminosity of the source.

References

Aglietta, M. *et al.* 1993, *Proc. 23rd Int. Cos, Ray Conf.* (Calgary), **1**, 216.
Berezinsky, V. S. 1987, *Proc. 20th Int. Cos, Ray Conf.* (Moscow), **9**, 39.
Berezinsky, V. S., Kudryavtsev, V. A. 1990, *Astrophys. J.,* **349**, 620.
Bonnet-Bidaud, J. M., Chadrin, G. 1988, *Phys. Rep.,* **170**, 325.
Chadwick, P. M., McMomb, T. J. L, Turver, K. E. 1990, *J. Phys. G.,* **16**, 1773.
Cheng, K. S. *et al.* 1990, *J. Phys. G.,* **16**, 115.
Dermer, C. D. 1986, *Astr. Astrophys.,* **22**, 425.
Ganguli, S. N., Sreekantan, B. V. 1979, *J. Phys.,* A9, 311.
Harding, A. K., Gaisser, T. K. 1990, *Astrophys. J.,* **358**, 561 (HG).
Hillas, A. M. 1984, *A. Rev. Astr. Astrophys,,* **22**, 425.
Hillas A. M. 1985, *Proc. 19th Int. Cos. Ray. Conf.* (LaJolla), **2**, 296.
Mitra, A. 1990, *Astr. Astrophys.,* **234**, L5.
Mitra, A. 1991, *Astrophys. J.,* **370**, 345.
Mitra, A. 1994, *Astrophys. J.,* **425**, 720.
Stecker, F. W. 1970, *Ap. S&S,* **6**, 377.
Stecker, F. W. 1971, in *Cosmic Gamma Rays* (Baltimore: Mono Book Corp.) p. 118.
Stecker, F. W. 1979, *Astrophys. J.,* **228**, 919.
Vestrand, W. T. Eichler, D. 1982, *Astrophys. J.,* **261**, 251.
Weekes, T. C. 1988, *Phys. Rep.,* **160**, 1.

J. Astrophys. Astr. (1994) **15,** 187–192

Test of Evolutionary Models for Stellar Population Studies

N. Srivastva, R. K. Gulati & N. C. Rana *Inter-University Centre for Astronomy and Astrophysics, Post Bag 4, Ganeshkhind, Pune 411 007*

Received 1993 December 4; accepted 1994 March 31

Abstract. Using the Andersen (1991) data on the mass, absolute visual magnitude, the effective surface temperature and the bolometric corrections, new calibrations for the mass vs. absolute visual magnitude and for the bolometric correction vs. effective surface temperature have been derived. Comparison between the latest evolutionary models with the empirical data has been made to test the evolutionary models for the purpose of stellar population studies.

Key words: Mass-luminosity relation—evolutionary models—bolometric correction.

1. Introduction

A well-known empirical relationship exists between the absolute visual magnitude M_v and the colour or the photospheric effective temperature $T_{\rm eff}$ for the populous main sequence stars. Relationship between mass m of a star and its M_v could not be derived in absence of the direct knowledge of the mass of a star. Only when we have a binary system of stars, the orbit of individual component stars around their common centre of mass can be measured which can reveal mass of the individual components. By 1980, Popper had determined mass and the visual luminosity of nearly a hundred stars which could have been used for the mass luminosity calibration of the main sequence stars in the solar neighbourhood. Cester *et al.* (1983) and Grenier *et al.* (1985) enlarged this catalogue which was used by Rana (1987) for deriving the initial mass function of stars, IMF in short. Basu & Rana (1992) included Liebert & Drobst (1987) for their latest revision of the IMF. More recently, Andersen (1991), hereafter referred to as A91, has compiled the masses, radii, surface temperature and absolute visual magnitude for 45 binary systems (90 single stars). Because the A91 data is primarily concerned with the intermediate and high mass stars, we complement the low mass stars from Basu & Rana (1992) in order to cover the whole range of stellar masses.

On the theoretical side, there is a tremendous improvement in the treatment of opacity in computation of stellar evolutionary models. For instance, Claret & Gimenez (1992) and Maeder and his coworkers (refer Schaller *et al.* 1992, hereafter referred to as SSMM) have computed new theoretical grid of evolutionary stellar models which take into account the updated opacity tables due to Rogers & Iglesias (1992) and Kurucz (1992).

The calibration between observed quantities has been discussed in section 2. We also compare the empirical data with theoretical evolutionary models in order to

evaluate the evolutionary status of stars in A91 and to test the consistency of evolutionary models with the observations.

2. Results and discussion

The input data in the current study comes from various sources in order to produce reliable empirical relationships between mass and absolute visual magnitude for the construction of IMF, and between bolometric corrections and effective temperature for the deduction of luminosity vs effective temperature (required for comparing the theoretical HR-diagram with the observational one).

The data for the first relationship were taken from Basu & Rana (1992) and Andersen (1991), where M_v's were binned according to M_v in steps of unity. A smooth relationship was derived by using the spline fitting with a constraint that solar values are reproduced by the modeled line. In Table 1 we provide M_v as a function of log m, use of this result for the construction of IMF will be discussed in a separate paper.

As we expect for the $M_v > 15$ the effective temperature of the stars falls considerably below 3000 K and therefore the visual band will allow very little light to come out as a result of which a small decrease in mass will tend to show a very large decrease in M_v . This is well demonstrated in Fig. 1. As compared to previous calibrations used by Scalo (1986), similarly on the high luminosity end the star would gradually approach the Eddington luminosity i.e. $L \propto m$ instead of $L \propto m^3$. This implies that fast flattening of the $M_v - m$ relationship beyond log $m > 1.5$, and this trend is also obvious in Fig. 1. However, in the mass range $0.1 <$ log $m < 10$ the slope of the M_v – log m relationship has several undulatory features which were not apparent in the semiempirical studies so far. This has got a direct bearing on the estimation of the present day mass function from the luminosity function. Though A91 data already use bolometric correction from Popper (1980) to convert absolute magnitude to luminosity of stars, here we trace back this parameter from the observed quantities,

Table 1. Mass-luminosity relationship.

log m	M_v	log m	M_v
− 1.2	17.50	0.2	2.69
− 1.1	15.90	0.3	1.85
− 1.0	14.73	0.4	1.11
− 0.9	13.93	0.5	0.41
− 0.8	13.32	0.6	− 0.29
− 0.7	12.71	0.7	− 0.98
− 0.6	11.96	0.8	− 1.65
− 0.5	11.05	0.9	− 2.28
− 0.4	10.00	1.0	− 2.86
− 0.3	8.84	1.1	− 3.38
− 0.2	7.57	1.2	− 3.83
− 0.1	6.22	1.3	− 4.24
0.0	4.85	1.4	− 4.62
0.1	3.67	1.5	− 4.97

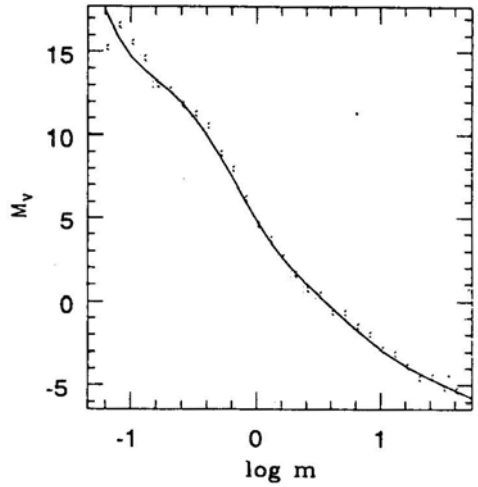

Figure 1. The absolute magnitudes of the binned data is shown as a function of the logarithm of the masses in A91. The solid line represents the calibration derived from the data (see text for detail).

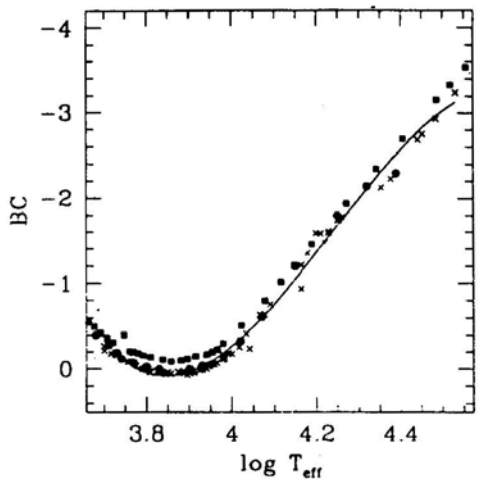

Figure 2. The bolometric corrections of stars in A91 is plotted against the logarithm of the effective temperatures. The solid line corresponds to the calibration derived. The filled squares and filled hexagons are the points from the calibrations of Schmidt–Kaler (1982) and Böhm–Vitense (1992) respectively.

luminosity and absolute magnitude (assuming $M_{\mathrm{bol},\odot}$ = 4.69). In Fig. 2 we plot BC as a function of log T_{eff} for stars in A91. A smooth relationship in the form of best fit polynomial of order five was followed to calibrate BC in terms of log T_{eff} . For comparison we plot also other existing calibrations from Schmidt–Kaler (1982) and Böhm–Vitense (1992) for main-sequence stars. In Table *2,* we provide the calibration of BC as a function of log T_{eff} together with other calibrations mapped into log T_{eff} in steps of 0.1.

Table 2. Bolometric correction in mag as a function of log T_{eff} for luminosity class V from three different sources.

log T_{eff}	BC[a]	BC[b]	BC[c]
3.70	– 0.39	– 0.31	– 0.33
3.75	– 0.35	– 0.08	– 0.09
3.80	– 0.15	– 0.03	– 0.04
3.85	– 0.09	0.00	– 0.08
3.90	– 0.13	0.00	– 0.03
3.95	– 0.19	– 0.07	– 0.08
4.00	– 0.41	– 0.23	– 0.26
4.05	– 0.65	– 0.49	– 0.49
4.10	– 0.93	– 0.82	– 0.76
4.15	– 1.23	– 1.20	– 1.05
4.20	– 1.53	– 1.52	– 1.36
4.25	– 1.82	– 1.80	– 1.68
4.30	– 2.11	– 2.07	– 1.99
4.35	– 2.40	– 2.23	– 2.29
4.40	– 2.67	– 2.31:	– 2.58
4.45	– 2.96	– 2.30:	– 2.82
4.50	– 3.23	– 2.46:	– 3.03

[a] Schmidt–Kaler 1982.
[b] Böhm–Vitense 1992.
[c] This paper.

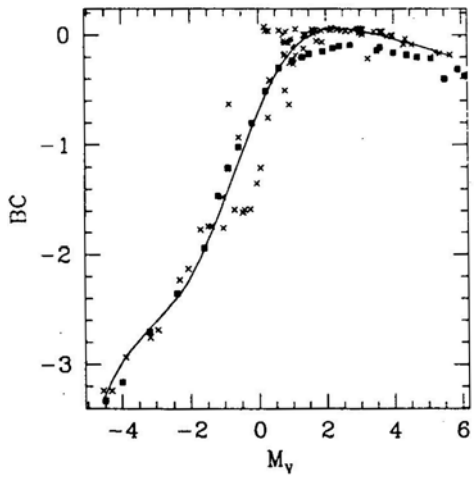

Figure 3. The bolometric corrections of the A91 is shown as a function of the absolute visual magnitude together with points from other calibrations as in Fig. 2. The solid line is the calibrated line from the A91 sample.

In Fig. 3 we plot BC as a function of *Mv,* the region $-1.5 < M_v < 2.2$ corresponding to log *m* on the other side of 0.8 ± 0.1 falls in the well-known Balmer discontinuity region, A very wide dispersion in this region is attributed to the presence of Balmer discontinuity.

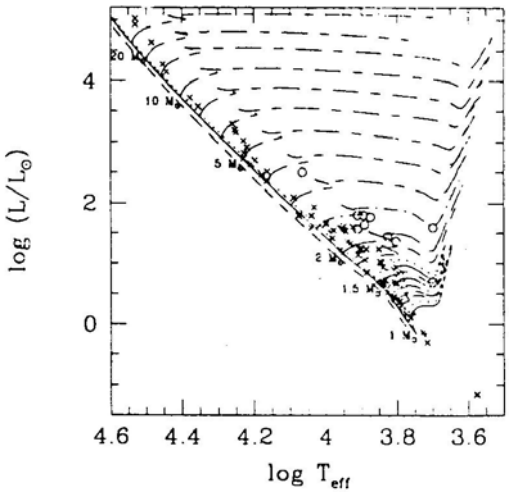

Figure 4a. Theoretical HR diagram of Claret, A., Gimenez, A. (1992) evolutionary models for solar metallicity with ZAMS for three metallicity (Z = 0.01, 0.02, and 0.03). Crosses indicate stars in A91 of luminosity classes V, while circles represent other luminosity classes.

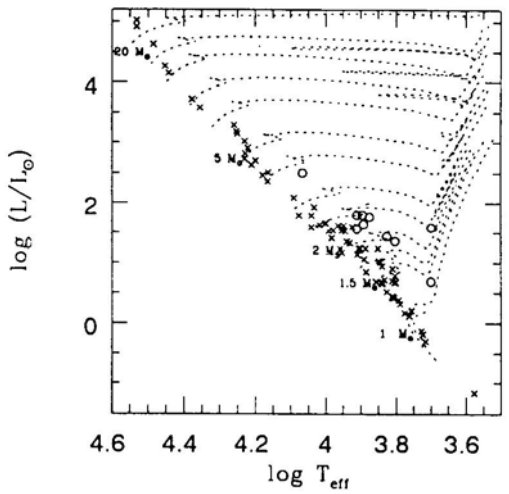

Figure 4b. Same as Fig. 4a, but for the SSMM models.

Fig. 4a essentially confirms the findings of Andersen (1992), who has shown that Claret models reproduce not only the masses of binary stars on the evolutionary frame, but also that $T_{\rm eff}$ of primary and secondary components are in agreement. However, here we have compared evolutionary models of Schaller *et al.* (1992) against the empirical data. There is not much difference in the distribution, as evidenced from Fig. 4a and 4b that most of A91 stars are distributed between zero age main sequence (ZAMS) and theoretical age main sequence (TAMS) which is further confirmed from luminosity classes of these stars. Those stars with luminosity classes

less than V (which are quite few) fall away from TAMS and are in the late stages of evolution. More observational data will be required to ascertain the consistency of evolutionary models in evolutionary phases not covered by the A91.

It is advantageous to use the latter SSMM models, since they are exhaustive in masses which are useful for population synthesis.

In conclusion, a reliable calibration of the mass and absolute visual magnitude of single stars (detached binaries), and bolometric correction as a function of effective temperature and visual magnitude are derived. A comparison has also been made between the absolute luminosity and effective temperature (HR diagram) between the observed data points with the latest evolutionary models justifying the consistency of SSMM models with correct identification of the luminosity class.

References

Andersen, J. 1992, in *Inside the Stars, IAU Coll. 137,* Ed. Werner W. Weiss & Annie Baglin, p. 347.

Andersen, J. 1991, *Astr. Astrophys. Rev.,* **3**, 91.

Basu, S., Rana, N. C. 1992, *Astrophys. J.,***393**, 373.

Böhm-Vitense 1992, *Stellar Astrophysics* (Cambridge: Cambridge University Press).

Cester, B., Ferluga, S., Boehm, C. 1983, *Astrophys. Space Sci.,* **96**, 125.

Claret, A., Girnenez, A. 1992, *Astr. Astrophys. Suppl. Ser.,* **96**, 225.

Grenier, S., Gomez, A. E., Jaschek, C, Jaschek, M., Heck, A.1985, *Astr. Astrophys.,* **145**, 331.

Kurucz, R. L. 1992, in *Stellar Atmosphere: Beyond classical model,* Ed. L. Crivelleeri, I. Hubeny & D. G. Hummer, NATO ASI Series (Dordrecht: Kluwer).

Liebert, J., Drobst, R. 1987, *A. Rev. Astr. Astrophys.,* **25**, 473.

Popper, D. M. 1980, *A. Rev. Astr. Astrophys.,* **18**, 115.

Rana, N. C. 1987, *Astr. Astrophys.,* **184**, 104.

Rogers, F. J., Iglesias, C. A. 1992, *Astrophys. J. Suppl. Ser.,* **79**, 507.

Scalo, J. M. 1986, *Fund. Cosmic Phys.* 11, 1.

Schalter, G., Schaerer, D., Menet, G., Maeder, A. 1992, *Astr. Astrophys. Suppl. Ser.,* **96**, 269.

Schmidt Kaler, T. H. 1982, Physical parameters of the stars, in *Landolt–Bornstein New Series, Vol 2b, astronomy and astrophysics Stars and star clusters* Eds. K Schaifers & H. H. Voigt, (New York: Springer–Verlag).

J. Astrophys. Astr. (1994) **15,** 193–196

Mass Luminosity Ratio of Nearby Stars and its Relation to Baryonic Dark Matter Problem

N. C. Rana & Mridula Chandola[†] *Inter-University Centre for Astronomy and Astrophysics, Post Bag 4, Ganeshkhind, Pune 411 007*

Received 1993 December 16; accepted 1994 March 31

Abstract. In view of the recent report on the discovery of low mass halo stars for the candidates of MACHOs, a calculation has been made for the possible enhancement of M/L ratio for populations of stars of varying mass domains taking the input data from the latest present day mass function (PDMF) of stars. It is seen that there is good scope for explaining dark matter problem where the dark matter is mostly in the form of low mass stars.

Key words: Baryonic dark matter—present day mass function and M/L ratio.

1. Introduction

It is seen that in the solar neighbourhood of the disc the mass to luminosity ratio in units of $M_\odot/L_\odot$ is fairly low, 0(2–3), but on the whole scale of the Galaxy there is a substantial contribution to mass by partially visible halo and therefore the mass to light ratio of the galaxy as a whole increases to a large extent ~ 10 or more. It is also observed that when we go to the larger scales of length, like including several galaxies in the cluster of galaxies, this problem of mass to light ratio becomes more acute, mainly values, that is, the ratio shoots up to ~ 30–100. When we consider superclusters of galaxies the M/L ratio is very large ~ 200–1000. This problem is canonically known as the dark matter problem.

Obviously for the sun the M/L ratio is defined to be as unity and in the solar neighbourhood more than 99% of stars are slightly less massive than the sun. Hence the stellar M/L ratio is not very much different from unity. But the fact remains that on the higher scales of distance the M/L ratio goes up.

In the present work, a study has been made using the latest input of the basic stellar parameters and the local spatial distribution of stars, namely the mass function of stars. We are trying to determine how M/L ratio could be affected by the imposition of a cut-off at the lower or the upper end of the mass function.

[†] A student of second year MSc (Physics), Fergusson College, Pune.

2. Methodology and the present work

The test input for this study consists as follows:

(i) Mass luminosity calibration using Anderson data has already been obtained by Srivastava *et al.* (1993).
(ii) For the construction of the PDMF and the IMF luminosity, function of the local stars given in Basu's thesis (1993) is used, and
(iii) M_v, that is, the visual magnitude and the bolometric correction to be used for the analysis were taken from Srivastava *et al.* (1993).

First we constructed PDMF ($\phi_{ms}\log m$) from the luminosity function of the stars and corrected for the multiple stellar component in the scheme presented by Basu & Rana (1992). We are more concerned about PDMF than IMF, even though we have calculated IMF in order to find out the average star formation rate in the solar neighbourhood.

We present the plot fox the luminosity function. This is, by definition, the number of stars per unit volume (pc) per unit interval of the visual magnitude M_v running from 17th magnitude on the fainter side to about – 6.5 on the brighter side. We calculate $\langle M/L\rangle$ as

$$\left\langle \frac{M}{L_v} \right\rangle = \frac{\int_{\log m_l}^{\log m_u} [m/L_v]\,\phi_{ms}(\log m)\,\mathrm{d}\log m}{\int_{\log m_l}^{\log m_u} \phi_{ms}(\log m)\,\mathrm{d}\log m}; \left\langle \frac{M}{L} \right\rangle = \frac{\int_{\log m_l}^{\log m_u} [m/L]\,\phi_{ms}(\log m)\,\mathrm{d}\log m}{\int_{\log m_l}^{\log m_u} \phi_{ms}(\log m)\,\mathrm{d}\log m}$$

We vary the lower limit (log m_l) keeping the upper limit (log m_u) fixed and see how the $\langle M/L_v\rangle$ is varying. Next we varied log m_u keeping log m_l fixed. The result is shown in Table 1 and a corresponding plot in Fig. 1, where $\langle M/L_v\rangle$ is given varying with

Table 1. *M/L* ratios for varying upper and lower limits of stellar mass in the PDMF (all in solar units).

Log m	Log(M/L_v) for fixed lowermost limit of log m	Log(M/L) for fixed lowermost limit of log m	Log(M/L_v) for fixed uppermost limit of log m	Log(M/L) for fixed uppermost limit of log m
– 1.2	4.62	3.62	– 2.45	– 4.45
– 1.0	3.51	2.07	– 2.52	– 4.35
– 0.8	2.66	1.76	– 2.53	– 4.30
– 0.6	2.45	1.43	– 2.46	– 3.94
– 0.4	2.05	1.24	– 2.14	– 3.39
– 0.2	1.38	0.99	– 1.64	– 2.56
0.0	0.74	0.60	– 0.90	– 1.50
0.2	0.49	0.40	– 0.38	– 0.75
0.4	0.42	0.37	– 0.13	– 0.48
0.6	0.40	0.28	0.00	– 0.35
0.8	0.39	0.23	0.08	– 0.27
1.0	0.38	0.17	0.14	– 0.21
1.2	0.37	0.12	0.21	– 0.15
1.4	0.37	0.08	0.27	– 0.13
1.6	0.37	0.04	0.31	– 0.11
1.8	0.36	0.02	0.32	– 0.10
2.0	0.36	– 0.08	0.36	– 0.08

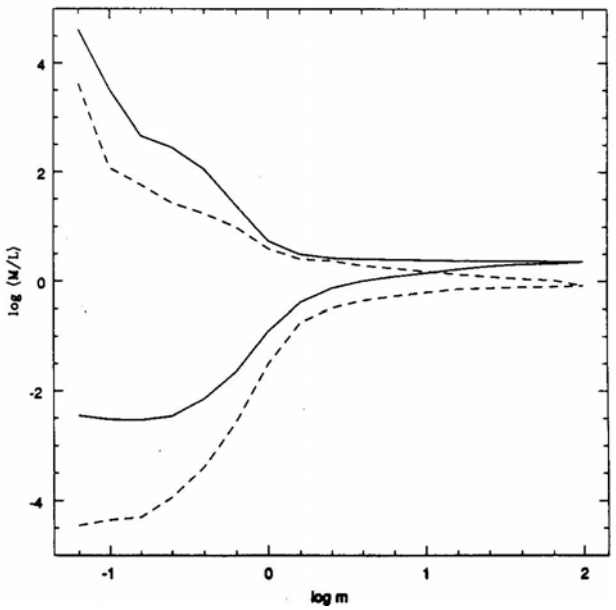

Figure 1. A plot for the ratios $\langle M/L_v \rangle$ and $\langle M/L \rangle$ vs increasing upper limit of stellar mass keeping the lower limit at the lowest end and vs decreasing lower limit of stellar mass keeping upper limit at the uppermost end, and suitably averaged over the observed PDMF of the main, sequence stars in the solar neighbourhood. Solid line corresponds to log $\langle M/L_v \rangle$ vs log m and the dashed line for log $\langle M/L \rangle$ vs log m. Only the upper sections of these two curves are relevant for the discussion of the present work.

the mass limits. After correcting for the bolometric correction (BC) we obtain true luminosity of each star and perform the same exercise once again. The idea has been to see whether large M/L ratio can be obtained at all, by introducing a cut-off at a different level of absolute magnitude or mass, that is, equivalently the mass of the star. It is always suspected that the halo of galaxy contains subluminous, subsolar stars of late spectral type, say *K*, or M dwarfs. This work is to test the viability of such a hypothesis.

3. Discussion and conclusion

It is seen that if any system of stars has got a large population of very low mass stars, the effective M/L ratio can go up to an order of 10^3 provided the average mass of the low mass stars is about 0.1 $M_\odot$ or so. If it so happens that under conditions of low metallicity, low turbulence and low magnetic field, the star formation, for example in the halo, had taken place with a substantial peak at low mass, particularly around 0.1 $M_\odot$, then the M/L ratio for the solar neighbourhood can remain at about 2.5 or lower while in the halo or the older populations could have a substantially higher M/L ratio due to stars only. Already direct indications for MACHOs have been reported in the recent TAUP '93 meeting at L'Aquila, Italy, September 22 1993, on behalf of EROS collaboration (A. Milsztajn *et al.*) and of Barkeley Australia

collaboration (D. Spergel *et al*.), for a possible large population of low mass stars (about 0.1 $M_{\odot}$) in the halo of the Galaxy. The present work justifies such a case as a viable one from the latest form of the present day mass function obtained by Basu & Rana (1992) and Basu (1993). As we move away from the plane of the disc, massive stars gradually drop out from the high mass end, and by the time we reach the value of $<0.5\ M_{\odot}$in the halo, $\langle M/L_v \rangle$ becomes as high as $\sim$ 100, even if the general form of the PDMF over the relevant range of mass is taken to be universal.

It should also be noted that the finite age of the disc brings in a natural cut-off in stellar mass at about 0.95 $M_{\odot}$ in the mass function, but we have gone further below this limit assuming halo stars had its own Wielen type of dip in mass function in the domain of low mass stars; it does not surely affect our result even if there existed another peak in the mass function on the high mass side for the halo stars.

References

Basu, S., Rana, N. C. 1992, *Astrophys. J.,* **393**, 373.
Basu, S. 1993, *Ph D. Thesis,* University of Bombay, India.
Srivastva, N., Gulati, R., Rana, N. C. 1994, *J. Astrophys. Astr.,* **15**, 187.

J. Astrophys. Astr.(1994) **15,** 197–200

Metallicity Distribution of F-dwarf Stars in the Solar Neighbourhood

N. C. Rana & Atish D. Jana* *Inter-University Centre for Astronomy and Astrophysics, Post Bag 4, Ganeshkhind, Pune 411 007*

Received 1993 November 30; accepted 1994 March 31

Abstract. A volume-limited sample of F-dwarfs is chosen from Knude (1989) with low radial velocity as well as distance from the sun and compared with the expected model metallicity [Fe/H] distributions, taking the possible chemical inhomogeneity into account. There is found to be an agreement between the two within the error limits of small sampling.

Key words: Metallicity distribution—F-dwarfs—star formation.

1. Introduction

The metallicity distribution of the G-dwarfs in the solar neighbourhood has played a central role in our understanding of the chemical evolution of the solar neighbourhood. Since the main-sequence life time of G-dwarfs is above 9 Gy, most of them, once formed, could not die during the evolution of the disc. This is obviously not true for F-dwarfs, whose main-sequence life time could be anything between 5.5 and 9 Gy. By now, we have a fairly consistent model of chemical evolution of the solar neighbourhood, which agrees with the age-metallicity relation, G-dwarf metallicity distribution, history of star formation, the initial mass function of stars, various proportions of the mass distribution in the form of gas, stars and dead stellar remnants to make up for the dynamical estimate of mass in the solar neighbourhood, the occurrence rates of supernova, etc.

The motivation for finding a reasonably volume-limited metallicity distribution of F-dwarfs are three-fold:

1. The observed distribution should be consistent with the known age-metallicity relation and history of the star formation rate (SFR).
2. We tacitly assume that the birth function of stars $C(m, t)$, which is a function of both stellar mass (say, m in units of solar mass $M_\odot$) and time of formation (say, t, with its origin at the epoch of the formation of the disc; assumed to be t_d= 13 Gy ago), can be written as a product of two functions, say $\Psi(t)$ and $\xi(m)$, thus allowing m and t to act as separable coordinates for the function $C(m,t)$. This assumption is justifiable only if the motivation number (1) is simultaneously justified.
3. There were several attempts in the past to obtain F-dwarf metallicity (in fact, [Fe/H]) distributions in the solar neighbourhood, but either they lacked completeness

*A summer school student from the Department of Physics, Vidyasagar University, Midnapore 721 101, India.

in a sample volume or solid angle, or no ambiguous criterion to distinguish a halo star from a disc star apart from the metallicity itself. Knude has recently measured the radial velocity W, [Fe/H] and the radial distance z from us for a complete magnitude limited sample of 183 dwarf stars covering the solid angle within the Galactic latitude $b \geqslant 70°$ and belonging to the spectral class A5–G0. If we do not discriminate the sample stars on the basis of radial velocity (which is in the present case a measure of the component of velocity perpendicular to the disc) and the distance, the metallicity distribution appears to be bimodal. A bimodal distribution was also obtained more than a decade ago by Marsakov & Suchkov (1980) for F-dwarfs. However, a single-peaked distribution was obtained by Rana & Basu (1990) from a sample of data compiled from various sources which was neither volume-limited nor magnitude-limited, and therefore, no firm conclusions could have been drawn apart from showing that the data reasonably satisfied the criteria (1) and (2) in the context of a chemically inhomogeneous model of stellar birth function. While the chemical inhomogeneity of the interstellar medium as well as of stars in open clusters and in open fields, even on length scales as short as 100 pc around the sun, cannot be ignored as the accuracy of the determinations of [Fe/H] has considerably improved in recent years, it can very well wash out the bimodality, which were not too far separated in the metallicity bins.

2. Criterion for data selection and results

We took the data set of Knude (1989) as the basis set, which considered a *uby*β photometric catalogue of 183 A5–G0 main sequence stars brighter than $V = 11.5$ mag and with the Galactic latitude $b > 70°$. The table listed the effective surface temperature, [Fe/H], radial velocities, age, distance and colour difference, for most of the stars. Knude had constructed the histograms for age, metallicity and radial velocity (which is essentially equivalent to the component of velocity perpendicular to the plane of the disc) for the entire sample. However, for the sake of having a completeness in volume (here solid angle) as well as assuring ourselves about the disc population I type of stars only, we restricted the sample to radial distance $\leqslant$ 100 pc, $-$ 0.75 dex $\leqslant$ [Fe/H] $\leqslant +$ 0.35 dex, and the magnitude of radial velocity not exceeding 40 km s^{-1}. The size of the sample reduced to 62 stars, of which we could choose only 54, because for the rest 8 stars no measured value of [Fe/H] was quoted. Fig. 1 shows the histogram of [Fe/H] distribution thus obtained, with the error bars reflecting only $\sqrt{N}$ for individual metallicity bins.

It is apparent from Fig. 1 that the metallicity distribution of the F-dwarfs (actually over A5–G0) in the solar neighbourhood does not appear to be bimodal.

The range of the main sequence spectral types A5 to GO implies the mass range of the stars to be 1.88 $M_\odot$ through 1.10 $M_\odot$ (Svechnikov & Taidakova 1984) and correspondingly their main-sequence life times between 4.2 and 8.7 Gy (Maeder & Meynet 1989), with an average life time of the sample stars being 7.0 Gy (say, $= t_m$). We then took a model of inhomogeneous chemical evolution as suggested in Rana & Basu (1990) (see equation (11) therein) and the evolution of SFR from (a) Rana & Basu (1992) and (b) Soderblom *et al.* (1991). For individual bins (say, the ith bin) of metallicity between say, z_1 and z_2, where $z \equiv$ [Fe/H], the number of stars at the

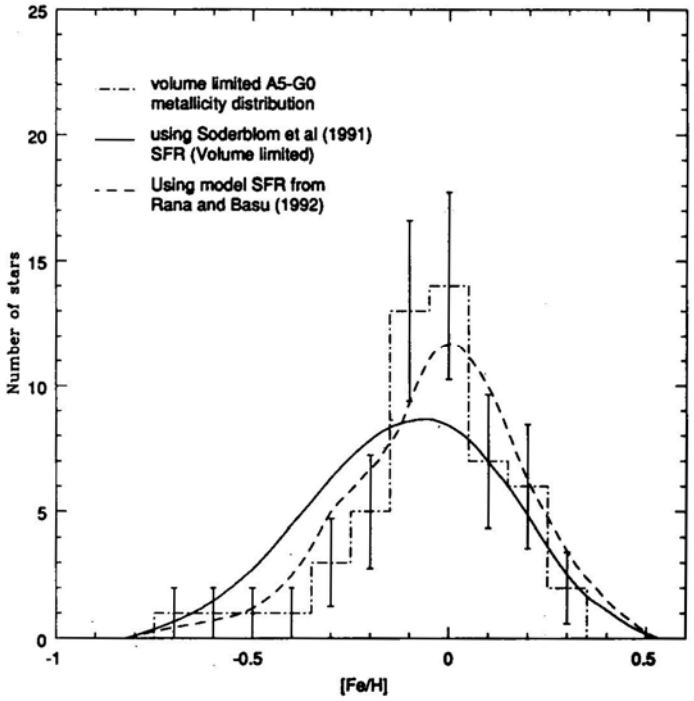

Figure 1. The [Fe/H] distribution of a volume limited sample of 54 A5–G0 stars in the solar neighbourhood of the disc, selected from Knude (1989), and compared with the expected model distributions of the same normalised to the same total of 54 stars.

present epoch are given by

$$N_i(z_1, z_2) = \frac{1}{\sigma_z \sqrt{2\pi}} \int_{z_1}^{z_2} \int_{\bar{z}(t_d)-\bar{z}(t_m)}^{\bar{z}(t_d)} C(\bar{z}) \exp\left[-\frac{1}{2} \frac{(z-\bar{z})^2}{\sigma_z^2} \right] d\bar{z}\, dz \qquad (1)$$

such that $\Sigma N_i = 54$, and the age metallicity relation (AMR) z(t) = [Fe/H] (t) is implicit in the stellar birth function $C(z)$. The AMR has also been taken from Rana & Basu (1992) for the sake of consistency. The value of σ_z is adopted to be 0.2 dex.

The solid curve (a) and the dashed curve (b) in Fig.. 1 were computed using equation (1) above and the two SFRs as stated in the above paragraph. The fit for the case (b) seems to be better than that for (a), even though both the fits were found to be agreeing with the data set chosen in the present work. The whole distribution could also be fitted with a single Gaussian form, but then the width of the distribution would be too large compared to errors of individual observation.

3. Conclusion

The metallicity distribution for the F-dwarfs derived from the sample of Knude (1989) with the extra conditions $|v_z| \leqslant 40$ kms^{-1}, distance $z \leqslant 100$ pc, and -0.75 dex $\leqslant$ [Fe/H] $\leqslant +0.35$ dex, is found to be unimodal and agreeing reasonably well with the

theoretical expectations from a chemically inhomogeneous model of evolution of the solar neighbourhood.

References

Knude, J. 1989, *Astr. Astrophys. Suppl. Ser.,* **81**, 215.
Maeder, A., Meynet, G. 1989, *Astr. Astrophys.* **210**, 155.
Marsakov, V. A., Suchkov, A. A. 1980, *Soviet Astr.,* **24**, 32.
Rana, N. C, Basu, S. 1990, *Astrophys. Space Sci.,* **168**, 317.
Rana, N. C, Basu, S. 1992, *Astr. Astrophys.,* in press.
Soderblom, D. R., Duncan, D. K., Johnson, D. R. H. 1991, *Astrophys. J.,* **375**, 722.
Svechnikov, M. A., Taidakova, T. A. 1984, *Soviet Astr.,* **28**, 84.

J. Astrophys. Astr. (1994) **15,** 201–202

Preface

The theory of ionization equilibrium based on statistical thermodynamics is now considered as a simple exercise in graduate text books. But when Saha published his paper entitled "**Ionization in the Solar Chromosphere"** [*Philosophical Magazine,* 40, 472,(1920)] it made a profound impact in the newly emerging field of theoretical astrophysics.Saha derived the famous "ionization formula" by extending well known ideas in physical chemistry pertaining to the dissociation of molecules to the ionization of atoms.It is appropriate to mention here that Lindemann at Oxford had independently derived an ionization formula for hydrogen and discussed the possibility of the complete ionization of hydrogen in the solar chromosphere. However, it was Saha who fully appreciated that a sufficiently generalized theory of thermal ionization, supplemented with accurate values for the ionization potentials of atoms obtained from spectroscopic data, constitutes the key to the interpretation of stellar spectra. This seminal paper triggered' a great deal of activity and inspired the subsequent development of the subject by R.H.Fowler, E.A.Milne, H.N.Russell and C.H.Payne.

A year later Saha published a paper in the *Proceedings of the Royal Society (Series A)* It appears that this paper was also.originally submitted to the *Philosophical Magazine* under the title "On the Harvard Classification of Stellar Spectra". Shortly after sending this paper Saha went to London, withdrew it from the *Philosophical Magazine* and completely re-wrote it in A.Fowler's Spectroscopic Laboratory in the Imperial College of Science and Technology in London. To quote Saha (from The Collected Works of Meghnad Saha, Edited by S Chatterjee, Orient Longman): *"I took about four months in rewriting this paper,and all the time I had the advantage of Professor Fowler's criticism, and access to his unrivalled stock of knowledge of spectroscopy and astrophysics. Though the main ideas and working of the paper remained unchanged, the substance matter was greatly improved on account of Fowler's kindness in placing at my disposal fresh data, and offering criticism wherever I went a little astray, out of mere enthusiasm."* It is this paper entitled**"On a Physical Theory of Stellar Spectra"** that we are reproducing in this issue with the permission of the Editors of the *Proceedings of the Royal Society.*

Saha's theory of thermal ionization was put on a more rigorous foundation by R.H fowler, who, along with C.G.Darwin, had just developed some new and powerful methods for discussing properties of matter in statistical equilibrium. A couple of years later,Fowler and Milne published two classic papers in the *Monthly Notices of the Royal Astronomical Society* entitled "**The Intensities of Absorption Lines in the Stellar Spectra and the Temperature and Pressures in the Reversing Layers "** [Vol.**83**, 403 (1923)] and " **On the Maxima of Absorption lines in Stellar Spectra"**. We have reproduced in this issue the second of these papers with the kind permission of the Editors of *the Monthly Notices.* To bring out the new ideas that were put forward in, the above mentioned two papers we wish to quote from S.Chandrasekhar's Obituary of R.H.Fowler published in *The AstroPhysical Journal* [Vol.**101**, 1, (1945)]: "*In Saha's investigations attention was focused on the relative intensities of absorption lines arising from the successive stages of ionization of an atom and this was correlated with the relative numbers of atom, in the various stages of ionizationin the reversing layers. However, in attempting to deduce the temperature of the reversing*

layers, the "first" and ihe last" (or the " marginal") appearances of a line along the spectral sequence were used as the principal criteria. But, as Fowler and Milne pointed out, the use of this notion of marginal appearance makes the precision of the early calculations doubtful, for we do not know, a priori, how small the "very small" fraction of the atoms must be at marginal appearance. Among other things, this will depend on the relative abundances of the various elements *giving rise to the lines. In view of these difficulties, Fowler and Milne start with the following assumption: "Other things being equal, the intensity of a given absorption line in α stellar atmosphere varies always in the same sense as the concentration of the atoms in the reversing layer capable of absorbing the line." With this formulation and with attention focused on the place along the spectral sequence at which a given line attains its* maximum intensity, *the vagueness associated with the concept of marginal appearance is avoided, for on the assumption which has been made, a line will attain its maximum intensity when the concentration of the atoms in the particular stage of ionization and excitation capable of absorbing the line reaches its maximum. Consequently, the position of the maximum will depend only on the temperature and the electron pressure and will be independent of the absolute abundance of the particular element under consideration. It is, moreover, apparent that the temperature at which, for a given electron pressure, a given line arising from a known stage of ionization and excitation will reach its maximum intensity can be readily derived from the properties of the equilibrium state. Thus, on this method each observed maximum of a line in the spectral sequence relates the temperature and the electron pressure of the reversing layer at the point of the sequence. This is the well-known "method of maxima" A major result of this investigation was to reveal, for the first time, the correct order of magnitude of the electron pressures which prevail in stellar atmospheres.*

The method of Fowler and Milne rapidly became the principal basis for analyzing stellar spectra in the twenties, and we can relive the enthusiasm which it inspired and the impetus which it gave to astrophysics during these years by reading again C.H. Payne's brilliant tract on "Stellar Atmospheres". It is remarkable how, in spite of the enormous progress which has been achieved in recent years on the mechanism of the formation of the absorption lines themselves, the original method of Fowler and Milne still retains its preeminence for a first analysis of complex stellar spectra; for by their simple assumption (though crude from a more advanced point of view) they sweep the problem of its inessentials and bring into relief the basic physical factors which are in operation."

J. Astrophys. Astr. (1994) **15,** 203–221

Reproduced from the *Proceedings of the Royal Society (Series A)*
XCIX, 135-153, (1921)

On a Physical Theory of Stellar Spectra.

By M. N. SAHA, D. Sc, Lecturer in Physics and Applied Mathematics,
Calcutta University.

(Communicated by Prof. A. Fowler, F.E.S. Received January 18,1921.)

1. *Introduction.*

The present paper embodies an attempt towards a physical explanation of the ordered gradation in the spectra of stars—a subject in which pioneering work was done by the late Sir Norman Lockyer, but which was worked up with systematic thoroughness at the Harvard College Observatory, under the lead of the late Prof. E. C. Pickering and Miss A. J. Cannon.* During this interval the spectra of more than 100,000 stars have been photographed, classified, and published with full details in the Henry Draper Memorial Catalogue. The most noteworthy facts which have been brought to light from these monumental studies have thus been summarised by H. N. Russell.†

" The spectra of the stars show remarkably few radical differences in type. More than 99 per cent of them fall into one or the other of the six great groups which during the classic work of the Harvard College Observatory were recognised as of fundamental importance, and received as designations, by the process of the survival of the fittest, the rather arbitrary letters B, A, F, G, K, M. That there should be so few types is noteworthy, but much more remarkable is the fact that they form a continuous series. Every degree of gradation between the typical spectra denoted by B and A may be found in different stars, and the same is true to the end of the series, a fact recognised in the familiar decimal classification, in which B5A, for example, denotes a spectrum half-way between the typical examples B and A. The series is not merely continuous, it is linear. There exists slight difference between the spectra of different stars of the same spectral class, such as Ao, but these relate to minor details. Almost all the stars of the small outstanding minority fall into three other, classes (or rather four), denoted by the letters P, O, N, R. Of these, O undoubtedly precedes B at the head of the series, while R and N, which grade one into the other, come probably at its other end, though in this case the transition stages are not clearly worked out."

Russell is of opinion that the principal differences in the stellar spectra arise in the main from variations in a single physical variable in the stellar

* Harvard, ' Annals,' vol. 28, Parts I and II ; vols. 56, 76, and 91.

† ' Nature,' vol. 93, pp. 227, 252, 281.

atmosphere, and many converging lines of argument show that this variable is the temperature of the stellar atmosphere. Table I shows these facts diagrammatically with provisional values of the temperature.

Table I.

Stellar class.	Typical star.	Secchi's classification.	Temperature.*		Remarks.
			Wilsing and Scheiner.	Saha.	
Pb	The Great Orion Nebula	—	15,000 K†		
Pc	I.C., 4997	—	30,000 K	—	Gaseous nebulæ with bright lines.
Oa	B.D. + 35°, 4013...	Type V, including Wolf-Rayet stars.	23,000	23,000–24,000	
Ob	B.D. + 35°, 4001...		—	22,000	
Od	ζPuppis				
Oe	29 Canis Majoris				Henceforth all lines are dark.
Oe5	τCanis Majoris ...				
Bo	εOrionis	—	20,000	18,000	
B5A	γTauri.....	Type I, Helium and hydrogen stars.	14,000	14,000	
Ao	αCanis Majoris ...		11,000	12,000	
A5F	βTrianguli		9,000		
Fo	αCarinæ	Type II, Yellow-red stars.	7,500	9,000	
F5A	αCanis Minor.....		6,000		
Go	αAurigæ		5,000	7,000	The sun is a dwarf star of this class.
G5K	αReticuli.....		4,500		
Ko	αBootis		4,200		
K5M	αTauri		3,200		
Ma	αOrionis	Type III, Red stars.	3,100	5,000	
Md	0Ceti		2,950	4,000	
N	—	Type IV	2,300		
R	—				

* (Compiled from the Harvard ' Annals,' vo.l. 91, p. 5, and Russell's paper, *loc. oit*. Temperatures given under the heading Saha are calculated from the method given in the present paper.)

† Buisson and Fabry, ' Journal de Physique, ' 1912, p. 472 (calculated according to the limit of interference method).

It is necessary to dwell a little on the physical basis of stellar classification.The earliest astrophysicists classified the stars acoording to colour; thus Secchi's type I denoted white stars, type II stood for yellow stars, type III for yellow-reddish stars, and type IV for deep red stars. But Lockyer and Pickering found that the varying intensity of particular groups of absorption-lines in stellar spectra was a far better criterion of stellar Classification. Table II, compiled from the Harvard ' Annals,' illustrates the principle.

[For the methods by means of which the intensity of a particular line in different stars has been estimated, reference should be made to Harvard ' Annals,' vol. 27, p. 234; vol 56, p. 56; vol. 91, p. 5. The following is added for the sake of general explanation :—

Numbers which are underlined denote that the liue is bright; otherwise

the lines are dark. Lines which are barely visible have the number 1 assigned to them. Faint lines are labelled 2. ⊕ denotes a line of which the intensity cannot be obtained from the Harvard ‘ Annals.’ (?) denotes that the intensity is not stated in numbers in the Harvard ‘ Annals,’ but is compiled from descriptions scattered here and there. The symbol M^+ denotes that the line is due to the ionised atom of the element M, *i.e.,* the atom which has lost one electron. Lockyer called them “proto” elements, and the lines were known as " enhanced lines." We shall subsequently show that they are due to the atom which has lost one electron as the result of the high temperature prevailing in the stars, and acquired a net positive charge.

Table II.—Intensity of Stellar Lines.

Element	Helium.		Parhe	He^+	He^+	He^+*	H*	Ca	Ca^+	Mg^+
Line	4471	4713	4388	4686	4542	4860	4860	4227 (*g*)	3934 (*k*)	4481
Series description	*2p–4d*	*2p–4s*	*2p–5d*	*3d–4f*	*4f–9k*	*4f–8k*	*2p–4d*	1S–2P	*1s–2p*	*3d–4f*
Stellar class.										
Pe	—	—	—	⊕	⊕					
Pf	—	—	—	⊕	⊕	⊕				
Oa	0	—	—	⊕	⊕	⊕				
Ob	0	—	—	*100*	*12*	*10*	0			
Oc	1	—	—	*40*	*3*	*3*	0	—	—	faint
Od	1	—	—	*20*	10	20*	10*	—	2	faint
Oe	15	2	3	*8*	5	25	10	—	2	1
Oe5	15	4	5	5	4	25	20	—	5	1
Bo	15	5	6	2	2	25	25	—	3	2
B2	22	6	10	1	0	35	35	—	4	3
B3	22	6	10	0	0	40	40	—	4	4
B5	10	3	7	—	—	—	60	—	8	7
B8	5	1	3	—	—	—	80	faint	⊕	7 (?)
B9	4	0	1	—	—	—	90	faint	⊕	7
Ao	0	—	0	—	—	—	100	2	10	10
A2	—	—	—	—	—	—	100	4	40	15
A3	—	—	—	—	—	—	90	⊕	70	⊕
A5	—	—	—	—	—	—	70	⊕	80	⊕
Fo	—	—	—	—	—	—	50	⊕	120	⊕
F5	—	—	—	—	—	—	40	15	150 (?)	faint
Go	—	—	—	—	—	—	20	20	200	faint
G5	—	—	—	—	—	—	15	⊕	200 (?)	0
Ko	—	—	—	—	—	—	10	60	150 (?)	0
K5	—	—	—	—	—	—	5	⊕	⊕	
Ma	—	—	—	—	—	—	2	⊕	⊕	
Mb	—	—	—	—	—	—	—	100	faint	
Mc	—	—	—	—	—	—	0	strong	faint	
Md	—	—	—	—	—	—	—	strong	0	

*The line 4860, generally known as H_β, has been shown in the Table both as a hydrogen and a He^+ line. For reasons see footnote to Table VII, and the concluding paragraphs of §6.

The Tables show that the lines of an element just appear at a certain stage, rise step by step to a maximum, and disappear at the other end. Thus the He lines just appear at the Ao class, rise to a maximum intensity at the

B3 class, and go out at the Ob class. Similarly for lines of Ca, Mg, H, and groups of nitrogen and oxygen lines not treated here, because their series formulae are not known.

2. *Physical Processes at High Temperatures.*

The explanation of these phenomena follows from the theory of " Thermal Ionisation and Thermal Radiation" of gaseous elements developed by the author in a number of papers published elsewhere. The following is a summary.*

Up to this time thermodynamics has been confined to the treatment of physical processes like liquefaction and vaporisation, or chemical processes like decomposition or dissociation of molecules into atoms. It has thus carried us up to the stage where all substances are broken up into constituent atoms. But what takes place if a gaseous mass consisting of atoms only be continued to be heated ? Hitherto, the ideas on this point have not been very clear. In his interesting theory of internal constitution of stars, Eddington† indeed suggested that in the interior of stars atoms may be, for the most part, broken up into positive nuclei and free electrons—a view which was also supported by Jeans.‡ Following a suggestion by Nernst,§ Eggert || tried to calculate the temperature required for tearing off the outer ring of eight electrons from the Fe-atom; he was the first to apply Nernst's theorem of the reaction-isochore (which enables us to calculate the chemical equilibrium of a dissociating system from the vapour-pressure data of the products of decomposition), to the above mentioned process of the breaking up of the Fe-atom. But not only is the supposed process a hypothetical one, but also the energy evolved in the process, which is essential for the calculation, was obtained in a rather artificial manner. Lindemann¶ calculated the breaking up of the H-atom into the nucleus and the electron in the solar atmosphere by using a method almost identical with that of the author, and taking the ionization-potential = 13·6 volts in accordance with Bohr's theory.

The author has shown that the first effect of increasing temperature will be

* M. N. Saha, " Ionisation in the Solar Chromosphere" (A), ' Phil. Mag.,' October, 1920; " Elements in the Sun" (B), December, 1920 ; " On the Temperature Radiation of Gases" (C), February, 1921; " On Electron-Chemistry and its Application to Problems of Radiation and Astrophysics" (D), ' Journ. Ind. Ast. Soc.,' July, 1920.

† Eddington, 'M.N.R.A.S.,' vol. 77, pp. 16 and 596 ; vol. 79, p. 2.

‡ Jeans, ' M.N.R.A.S.,' vol. 79, p. 319.

§ Nernst, ' Die Theoretische und Experimentellen' Grundlagen des Neuen Wärmesatzes,' 1918, p. 154, Chap. 13, concluding paragraph.

|| Eggert, ' Phys. Zeit.,' December, 1919, p. 570.

¶ Lindemann, ' Phil. Mag.,' December, 1919.

to tear off the outermost electron from the atomic system, as represented in the equation,

$$Ca = Ca^{+} + e - U_1 \quad (1)$$

The energy of ionisation for a gm.-atom can be exactly calculated (*i.e.,* in a way free from any hypothesis about the arrangement of electrons about the nucleus), from the ionization-potential V_i, with the aid of the formula,

$$U_1 = \frac{eV_iN}{300J} \text{ calories.} \quad (2)$$

[N = Avogadro-number, J = mechanical equivalent of heat.]

In cases where the ionization-potential is not known from direct experi mental work, it can be calculated from the convergence-frequency, 1*s*, of the principal series of the element with the aid of the quantum relation*

$$V_i = \frac{h(1s)}{e} \cdot 300 \text{ (in. volts).} \quad (3)$$

There is now very little doubt that the relation is exact. In certain cases the l*s*-term is very large, and, as the principal series lie beyond the Schumann region, it has not been obtained at all. In such cases the 2*s*-term is often mistaken for the l*s*-term. Helium is a well-known example. What are usually called the principal series of helium and the so-called par-helium are not 1*s-mp* series at all, but 2*s-mp* series.† That this is so clear from the associated property that ordinary cool vapour of helium does not absorb the so-called principal series at all, but is quite transparent to them. If these were the true principal series, helium would have absorbed these lines (λ = 20587, 10830, etc.), just as sodium-vapour absorbs the D_1 and D_2 lines.

Another good example is thallium, discussed by Foote and Mohler ‘ Phil. Mag.,’ vol. 37, p. 33.

At a given temperature and concentration, a definite equilibrium will be established between the proportions of Ca, Ca^{+}, and *e,* as represented by the Van’t Hoff formula of reversible chemical reaction,

$$Ca \rightleftarrows Ca^{+} + e. \quad (4)$$

* This relation, which is fundamental in the theory of the ionization-potential, has now been definitely established for a number of elements. For a comprehensive account see McLennan, ′ Proc. Phys. Soc. Lond.,′ December, 1918. Franck and Hertz, ‘ Phys. Zeit.,’ vol. 20, p. 132 (1919). The relation has been definitely established for:— Hg, Franck and Hertz, Davis and Goucher, ‘Phys. Rev.,’ vol. 10, p. 101 (1917); Na, Cd, Rb, Zn, Tate and Foote, ‘ Phil. Mag.,’ vol. 36, p. 64 (1918); Mg, Tl, Foote and Mohler,’ ‘Phil. Mag.,’ vol. 37, p. 33 ; Rb, As, Cs, Foote, Rognley, Mohler, ‘ Phys. Rev.,’ vol. 10, p. 59 ; Pb, Ca, Mohler, Foote, Stimson, ' Phil. Mag.,' vol. 40, p. 73 ; Cs, Foote and Meggers, ‘ Phil. Mag.,’ vol. 40, p. 80.

† *Vide* Franck and Reiche, ‘ Zeits. f. Physik,’ vol. 1, p. 154 (1920).

The equation of the reaction-isochore for calculating the equilibrium is*

$$\log \frac{x^2}{1-x^2} P = -\frac{U_1}{2{\cdot}3\,RT} + \frac{5}{2} \log T - 6{\cdot}5. \quad (5)$$

Where x = fraction ionised, P = total pressure.

Calculations for the ionisation of Ca, Sr, Ba, Mg, Na, K, Rb, CS, H, He, will be found in the papers A and B.

The next point in question is the identification of the ionised elements in the physical systems in which they may occur. Spectroscopically,† it is quite an easy matter, for the ionised elements show a system of lines which is quite different from the lines of the neutral atom. They are generally known as "enhanced lines." The line-system of the neutral atoms, when classified into series, have the Rydberg number N = $(2\pi^2 e^4 m/h^3)$, but the enhanced lines can be grouped into series only with the Rydberg number 4N. This fact has been very satisfactorily established for He^+, and the alkaline earths by Fowler‡ and Lorenser.§ It is an easy corollary from Bohr's theory of spectral emission that such lines should be due to the ionised atom.

For Zn, Cd, and Hg, Paschen and Wolff || have discovered a number of lines in the extreme ultra-violet, which are analogous to the lines of the alkaline earths.¶ Fues shows that these lines are due to the ionised atoms of the elements. For other elements, some lines are supposed to be due to the ionised atom, but these have not yet been grouped into series or critically investigated.**

At the end of § 5, a Table of the chief lines of the neutral and ionised elements are given, with their series-position.

3. *Physical Processes Leading to Ionisation– Radiation of the Characteristic Lines of the Neutral Atom.*††

The process of ionisation cannot be an abrupt one, for the electron, in the course of passing off to infinity, can take up an infinite number of stable

* For the deduction of this formula, see Paper A, *loc. cit,*

† For a *résumé* of the early works to detect ionisation in heated gases, see McLennan, ' Roy. Soc. Proc.,' A, vol. 92, p. 691. McLennan's own experiments with Hg, Zn, Cd, Tl - vapour seems to be quite inconclusive.

‡ Fowler, "Bakerian Lecture," ' Phil. Trans.,'vol. 214.

§ Lorenser,' Inaug. Dissertation,' Tübingen, 1913.

|| Paschen,'Ann. der Physik,' vol. 35 ; Wolff, *loc. cit.,* vol. 42, pp. 825-839.

¶ Fues,' Ann. der Physik,' vol. 63, No. 17 (1920).

** For example, the Grund-Spektra of Alkalies, discussed by Goldstein, 'Ann. Der Physik,' vol. 27, p. 773 ; Schillinger, ' Wien. Ber.,' p. 608,1909, and Nelthorpe, 'Astro-physical Journal,' January, 1915; also the enhanced lines discussed by Lockyer and others.

†† See Saha, ' Phil. Mag.,' February, 1921, " On the Temperature Radiation of Gases" (C).

orbits characterised by the rotational quantum-number n, and the radial quantum number n' [n = 1, 2, 3, ..., n' = 0,1, 2, ...], according to the Bohr-Sommerfeld* theory of spectral emission. The various quasi-stationary orbits are represented in the following diagram, which is a slightly modified form of one given by Bohr.†

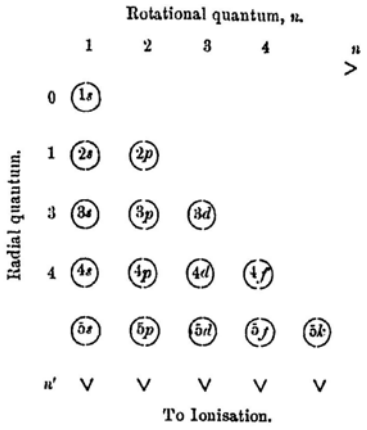

In a mass of atoms, comparatively cool, and not subject to any stimulus, the atoms have their vibrating electron in the 1*s*-orbit. This orbit is circular, corresponding to $n = 1$, $n' = 0$, and has the energy A-h (1*s*). This mass of gas does not emit any light, and when traversed by a continuous beam, can absorb only lines of the principal series, ν = l*s*-*mp*.‡ It cannot absorb lines of the diffuse, sharp or fundamental series. But if we continue to heat up the mass, atoms will progress towards ionisation through the quasi-stationary stages represented in the above diagram, and radiation will follow as a result of the mutual interchange of orbits.§ First of all we shall have emission of 1*s*-2p line or lines (fundamental lines), to be followed by the emission of the 1*s*-*mp* series. When the mass of gas emits the line l*s*-2*p* rather strongly it can absorb lines of the sharp or diffuse series.‖ At a

* Sommerfeld, "Atombau und Spektral-Analyse."

† Bohr, 'Zeitschrift für Physik,' vol. 2, p. 434 (1920).

‡ This fact, which comes out as a necessary corollary of the Bohr-Sommerfeld theory, has been experimentally established for Na-vapour (Wood, ' Astr.Jour.,' vol. 29, p. 97; vol. 43, p. 73); for the other alkalies (Bevan, 'Roy. Soc. Proc,' A, vol. 83, pp. 821-828 ; vol. 84, pp. 209-225; vol. 85, pp. 54-76), and Hg (Wood, ' Phys. Zeit.,' vol 14, pp. 191-195 (1913)), for cadmium (Wood,' Astr. Jour.,' vol. 29, p. 211).

§ For attempts to apply the quantum-theory to these cases, see the following papers:— Einstein,' Phys. Zeit.,' 1918, p. 124 ; Planck, 'Ann. der Physik,' vol. 50 ; 'Berliner Sitz. Ber., 1916; · Verh. D. Physik. G.,' vol. 17 (1915).

‖ As a matter of fact, the 2*p*-*ms* lines, as well as the *2p-md* lines, have not been reversed at all in the laboratory for any element, when the light is passed through

further stage the 2*p*-*md*, or 2*p*-*ms* lines will begin to be emitted. The gas will now be able to absorb the fundamental series. The whole process can thus be symbolically written :—

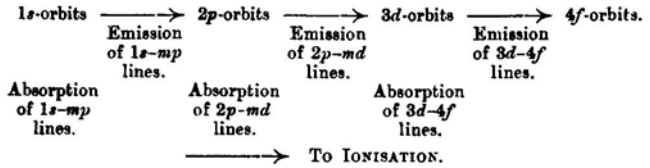

The theory is not yet sufficiently perfect to enable us to calculate the proportion of atoms in the quasi-stationary orbits characterised by the quantum numbers *n* and *n′,* but some general statements can be made.* The ″ radiation temperature " (*i.e.,* the temperature at which the fundamental line 1*s*-2*p* is emitted, and 2*p*-orbits are just commencing to form) will be higher, the higher is the ionization-potential of the element. Other orbits will be formed at temperatures intermediate between this and the temperature at which ionisation is completed. At any stage, the proportion of atoms distinguished by the quantum numbers (*n, n′*) will be smaller, the larger are the values of *n* and *n′.* So that we see that the 1*s*-2*p* line (and l*s*-*mp* series) will be the first to come out, the last to go, the least amount of element will show then† and will be the most intense line all the while. The 2*p*-*md,* 2*p*-*ms,* 2*s*– *mp* lines will come out later, go out earlier, and will be increasingly fainter. The disappearance of 1*s*-2*p* line may be taken as marking the completion of ionisation.

cool vapour (J. J. Thomson, ‘ Phil. Mag.,’ April, 1919). The Balmer series of hydrogen, which may be regarded as the combined sharp and diffuse series of that element, are not reversed when continuous light is passed through ordinary H_2-vapour ; but Ladenburg and Loria (‘ Verh. der D. Physik. G.,’ vol. 10, p. 858 (1908)) showed that they can be obtained as reversed lines when the absorbing column of H_2-vapour is traversed by an electric current. Similarly, Paschen obtained the reversal of the so-called principal series lines of He and Parhe (λ = 10830, 20587) by passing an electric current through the absorbing column of helium-gas ; ordinary helium-gas is quite transparent to these lines. This shows that the lines are not really principal lines.

* Based partly on the works of Planck and Einstein (*loc. cit.*) Planck tries to calculate the distribution of atoms in the different orbits, and Einstein considers the emission and absorption of radiant energy from the standpoint of quantum-statistics. See also Epstein, “ Zur Theorie des Starkeffektes,” ‘Ann. der Physik,’ vol. 50, p. 489, who considers the relative probability of passing to the quasi-stationary orbits characterized by the quantum numbers *n* and *n′.*

† *Cf.* the experiments of Du Gramont on the “ Raies Ultimes” of elements, which are either the l*s*-2*p* line or such lines of 1*s*-*mp* series as lie in the visible region. Du Gramount, ‘ Bull. Soc. franc, de Phys.,’ 1911, No. 14.

4. *Theory of Second-step Ionisation.*

Let us now consider what takes place when the first-step ionisation is completed. Suppose that we have a gaseous mass consisting wholly of Ca^+-atoms, and we continue to heat it up. It is clear that we shall have the emission of the ionised elements, *i.e.,* of the enhanced lines, followed by the commencement of a second-step ionisation, in which Ca^+ loses another electron, and acquires a net double positive charge.

The second-step ionisation is represented by the formula

$$M^+ . \rightleftarrows M^{++} + e - U_2. \qquad (6)$$

The value of U_2 is generally very large, and have not been at all experimentally investigated. But, in the case of helium and the alkaline earths, the enhanced lines have been completely studied and grouped into series. From this we can calculate the energy of second-step ionisation by applying formula (2).

Second-Step Ionisation.*

Element.	1*s*.	Ionisation-potential.	U_2 in calories.
He	4N	53·4 volts.	$12·3 \times 10^5$
Mg	121,270	15·02 ,,	$3·46 \times 10^5$
Ca	95,740	11·86 ,,	$2·70 \times 10^5$
Sr	88,840	10·70 ,,	$2·50 \times 10^5$
Ba	80,575	9·86 ,,	$2·30 \times 10^5$
Zn	147,544	18·20 ,,	$4·18 \times 10^5$
Cd	140,226	17·80 ,,	$3·98 \times 10^5$
Hg	161,800 (?)	19·95 ,,	$4·60 \times 10^5$

Let us suppose that the fractions x and y of the total Ca-atoms are dissociated to Ca^+ and Ca^{++}-atoms respectively. Then it can be easily shown that the equation of chemical equilibrium is of the form

$$\log P \frac{x^2}{(1-x-y)(1+x+2y)} = -\frac{U_1}{2·3\,RT} + \frac{5}{2}\log T - 6·5, \qquad (7)$$

$$\log P \frac{y^2}{x(1+x+2y)} = -\frac{U_2}{2·3\,RT} + \frac{5}{2}\log T - 6·5. \qquad (8)$$

Since we are confining ourselves to the range where the proportion of

* Fowler, ‘ Phil. Trans.,’ A, vol. 214 ; and new calculations not yet published ; Fues, 'Ann. d. Physik,' vol. 63, No. 17 ; Fues’s figures for the l*s*-terms of Zn^+ and Cd^+ are 159,000 and 155,000. The above figures are due to Fowler. The figure for Hg^+ has been calculated by me by using the interesting relation that the l*s*-term of the enhanced series is roughly 17/9 times the l*s*-term of the neutral line system in the case of the alkaline earths, and Zn and Cd. *Vide* Fues, *loc. cit.*

neutral Ca-atoms is vauishingly small, we can put $x+y = 1-\varepsilon$, where ε is a small fraction. The equation (8) then takes the form

$$\log \frac{Py^2}{(1-y)(2+y)} = -\frac{U_2}{2{\cdot}3\,RT} + \frac{5}{2}\log T - 6{\cdot}5. \qquad (8)$$

It is no longer necessary to consider equation (7). The following Table shows the percentage of second-step ionisation of the alkaline earths at pressures of 1 and 10^{-1} atms. Percentage of the first-step ionisation is also shown for the sake of comparison.

Table III.

Element temp.	Mg.	Mg^+.	Ca.	Ca^+.	Sr.	Sr^+.	Ba.	Ba^+.
10,000	56–90	—	85–99	8–26	90–100	14–40	94–100	23–56
11,000	75–96	—	93	18–44	95	26–64	—	40–78
12,000	86–98	—	97	31–70	98	49–89	—	59–91
13,000	93–99	10–35	99	47–86	—	61–92	—	75–96
14,000	96	21–54	—	64–93	—	76–96	—	86
15,000	98	32–72	—	81–97	—	88	—	92
16,000	99	46–85	—	87	—	92	—	96
17,000	—	61–92	—	92	—	96	—	98
18,000	—	74–96	—	95	—	98		
19,000	—	83–98	—	99				
20,000	—	89–99	—	99				
21,000	—	93						
22,000	—	96						
23,000	—	98						

In each pair of columns, the first gives the percentage of ionisation under a pressure of 1 atm., the second under a pressure of 10^{-1} atms.

The following Table gives the ionisation of helium (both first-step and second-step) at temperatures higher than 16,000° K.

Table IV.—First-Step Ionisation of Helium.

Pressure temperature.	1	10^{-1}	10^{-2}	10^{-3}	10^{-4}	Atm.
17,000	9	28	66	94	99	
18,000	14	41	81	97	—	
19,000	21	57	90	99		
20,000	31	71	95	—		
21,000	41	81	98			
22,000	53	89	99			
23,000	64	93	—			Complete.
24,000	73	96				
25,000	81	98				
26,000	87					
27,000	91					
30,000	98					

Table V.—Second-Step Ionisation of Helium.

Pressure temperature.	10^{-3}.	10^{-4}.	10^{-5}.	10^{-6}.
24,000	—	10	24	60
25,000	—	14	39	78
26,000	—	23	57	90
27,000	10	33	72	98
28,000	17	47	86	98
29,000	26	63	95	Complete.
30.000	35	77	97	„

The second-step ionisation of helium is too small even in stars having the highest temperature. Consequently, He^+ lines should be observed even when the temperature reaches 40,000° K., but actually they disappear from the Pc-class of gaseous nebula, the temperature of which is not probably so high. Probably this is an effect of low pressure. According to Emden,* $P = 10^{-5}$ atm. in nebulae. This brings the temperature of the completion of the ionisation of He^+ to 29,000°30,000° K., which is not improbable.

Table VI given the ionisation of hydrogen. It will appear from the Tables that hydrogen should definitely disappear when the temperature reaches the value 22,000° K., but this is not the case, for, according to the 'Harvard Annals,' the Balmer lines occur not only up to the Oa-class, but also in the Pa-class of nebulse, the temperature of which is probably very large.

Table VI.—Ionisation of Hydrogen.

Pressure temperature.	1-atm.	10^{-1}.	10^{-2}.	10^{-3}.	10^{-4}.	10^{-5}.
7,000	—	—	—	1	4	1·5
7,500	—	—	1	3	8	12
8,000	—	—	2	5	18	26
9,000	—	2	6	20	55	44
10,000	2	5	18	49	86	89
11,000	4	13	39	80	97	
12,000	9	28	68	94		
13,000	16	45	84	98	—	Complete ionisation.
14,000	27	65	98			
15,000	40	81	97			
16,000	55	90				
17,000	69	94				
18,000	80	97				
19,000	87					
20,000	92					
21,000	95					
22,000	97					
23,000	—					

* Emden, 'Gaskugein,' p. 282.

5, *Characterstic Lines of Neutral and Ionised Elements.*

In § 3 we remarked that the ionised elements have a system of characteristic lines which are quite different from the line-system of the neutral element. Table VII shows the chief lines of both systems side by side for a few elements. Here 1*s* - *mp,* 2*p-md,* 2*p-ms,* 3*d-mf* respectively stand for the principal, the diffuse, the sharp, and the fundamental series. The 1*s* term is generally single, but the other terms are double, treble, or sometimes quadruple. In the principal series *m* begins with 2, in the diffuse with 3, in the sharp with 2, and in the fundamental with 4. Generally the headline of the series, and in some cases the next one or two, are given.

Table VII.

Element.	Principal 1*s–mp.*	Diffuse 2*p–md.*	Sharp 2*p–ms.*	Fundamental 3*d–4f.*	Remarks.
H	1215·3 (etc.).	H_α 6562·8 H_β 4861·3 (etc.).	—	18,751	The sharp series coincides with the diffuse series.
He	570–480 (?)	5875	7065	?	Helium.
		4471	4713	?	
		6678	7281	—	So-called parhelium.
		4922	5047		
He^+	304-278 (?)	1640 1215 1087 (etc.).	—	4686	The sharp series coincides with the diffuse series as in H.
Mg	2852·11	3838·29	5183·62		
	4571·88	32·31	72·70		
		29·86	67·38		
Mg^+	2795·52	2797·99	2936·50	4481	The 4481 line is also double.
	2802·70	2790·77	2928·68		
Ca	g 4226·78				
	6572·78				
Ca^+	K 3933·66	—	3736·90		
	H 3968·47	—	06·02		
Sr	4607·34				
Sr^+	4077·88	—	4305·60		
	4215·66	—	4161·95		
Ba	5535·69				
Ba^+	4554·21				
	4934·24				
Zn	2139·33				
	3075·99				
Zn^+	2025·57	—	2558·03		
	2061·98	—	2502·11		
Cd	2288·79				
	3261·17				
Cd^+	2144·45	—	2748·68		
	2265·13	—	2573·12		
Hg	1849·0				
	2536·72				
Hg^+	?	—	2847·85		
			2224·70		

The principal series of hydrogen is given by the formula $v = N (l/1^{2-} 1/m^2)$, the combined sharp and diffuse series by $v = N(l/2^2—1/m^2)$, and the fundamental series by $v = N (l/3^2—1/m^2)$. They are usually named after Lyman, Balmer, and Paschen respectively.

The classification given for helium lines is somewhat different from that usually given. The lines 20857, 5016... and 10830, 3889..., which are usually regarded as the principal series of parhelium and helium, are here regarded as 2*s*-*mp* series; for reasons see § 2. The l*s*-term is, as Franck remarks,* probably single, and is calculated from the ionization-potential 25·4 volts, as experimentally obtained. The head-lines are calulated by taking 2*p* from the parhelium terms.† Probably 570-480 may be the lines detected photo-electrically by Richardson and Bazonni.‡

The figures for the principal series of He^+ are calculated from the series formula $v = 4 N (l/ l^2—1/m^2)$; the lines, of course, have not been identified. The combined sharp and diffuse series lines $v = 4 N (1 / l^2—l/m^2)$ have been obtained by Lyman. The 4686 is the headline of the Bergmann or ″fundamental″ combination $v = 4 N (1/3^2—l/m^2)$. The next series combination, 4*f*-*mk*-..., is represented by the formula $v = 4N(1/4^2— l/m^2)$ and include the Pickering lines $v = N [l / 2^2—l/(m+\frac{1}{2})^2]$ as its odd members, while the even members reduce to the Balmer formula for hydrogen, $v = N(l/2^2—l / m^2)$. Their wave-lengths are, however, slightly different, owing to slightly different value of N for He^+. The intensity of these lines is also very small.§ The series $v = 4N (l /3^2–l /m^2)$ and $4N(l/4^2—1/m^2)$ were first obtained in the laboratory by Fowler.‖

For the neutral atom of the alkaline earth group and Zn, Cd, Hg the principal lines given are those corresponding to the series combination 1S-2P, $lS–2p_2$.¶ These are the most important lines, for experiments on ionization-potential show that these are the first to come out when the gas is bombarded by electrons possessing the proper quantum-voltage. The ionised atoms show a system of doublets like the alkalies.

The interest of the above Table lies in the fact that it affords a possibility of spectroscopically testing the ionisation produced by a high temperature. For example, let us take a small quantity of calcium, sealed within a quartz tube which is fitted with plane ends, and then begin to heat the tube, and allow a beam of continuous light to pass through the tube. Then as soon as

* ′Zeits. f. Physik,′ vol. 1, p. 154.
† Franck, *loc. cit.*
‡ ' Phil. Mag.,' vol. 34, p. 285 (1917).
§ Evans, ′Phil. Mag.,′ vol. 29, p. 284 (1913).
‖ ′Phil. Trana.,' vol. 214.
¶ *Vide* Fowler, *loc. cit.*

calcium vapour is formed, the spectrum of the transmitted beam will, on spectroscopic examination, be found to be crossed with the dark absorption lines $\lambda = 4227$, $\lambda = 6573$, and other associated lines of the lS-*m*P, lS-mp_2 series. The H, K lines will not be reversed; but if we go on increasing the temperature, then provided that the tube does not collapse, we shall find absorption lines of the diffuse and sharp series lines. Ultimately we shall find the H, K lines as reversal lines. The appearance of these lines may be taken as an indication that a good proportion of Ca atoms has become ionised.

On account of the high value of the ionization-potential of Ca and the elements given above, it is very doubtful, however, whether experiments described above can succeed with quartz tubes or tubes of similar refractory substances known up to the present time. Experiments with the alkali elements Cs, Rb, K are more likely to succeed, for these have very low ionization-potentials, but the knowledge of their enhanced lines is very meagre.

In view of the total lack of laboratory data to test our hypothesis, we have to turn to the stellar data given in § 1. This is done in the next section.

6. *Physical Processes taking place in Stars; Temperature of Emission of the Stellar Atmospheres.*

The physical meaning of the appearance and disappearance of lines given in § 1, Table II, now becomes apparent. Let us start with the calcium " g" and Ca^+– K lines.

The " g " line appears in maximum intensity from the very stage when the star begins its effective life. There is no trace of the K line at the lowest stages. This just begins to appear at the Mc-stage, showing that calcium has just begun to be ionised. As we go higher up, the ionisation increases (g is fading off, K becoming more intense). The ″ g ″ line completely disappears at the B8-stage, showing that here all calcium has been ionised to Ca^+. The K line reaches a maximum intensity at the G5-stage, then steadily diminishes, showing that a second step ionisation has begun. It disappears completely at the Oc-stage showing that all Ca^+ has been further ionised to Ca^{++}, from above this stage.

Now referring back to Table III, we can assign the following temperatures to the points of completion of ionisation,

B8 ……Ca completely ionized ……. 13,000° (Ca 1·5 p.c.).
Oc ……Ca^+ completely ionised to Ca^{++} ……20,000° (Ca^+ 1 p.c.).

and we have also at the stages

Me …… Ca just begins to be ionized …… 4,000° (Ca+ just traces).
Go ……. Maximum proportion of Ca-atoms 70,00°.

Both Ca and Ca^+ can be identified with the aid of their fundamental lines 1*s*–2*p*. But such is not the case with any other element excepting Sr, Sr^+, Ba, and Ba^+, for which we have no satisfactory data. It is well known that owing to atmospheric absorption, observations have to be confined to the spectral region $\lambda = 3600$ to about $\lambda = 6000$. It seems to be generally recognised, but nowhere clearly stated, that this fact alone tends to give decided preference to certain elements to the exclusion of others.

For example, let us take hydrogen. In the stars, it can be identified by the 2*p*-*md* lines, the l*s*-*mp* lines falling within the region of atmospheric absorption. But according to § 2, the 2*p*–*md* lines cannot be absorbed by the ordinary H-atoms, but by such H-atoms of which the electron is in the 2*p* orbit. We can have such orbits only at high temperatures. Hence we find the Balmer lines gradually disappearing in the lower stages. We have at the stage

Mb …… 2*p*-orbits of H just appearing …… T = 4500°.

On the other side of the scale we find the Balmer lines of hydrogen disappearing at the Ob stage. This is an effect of complete ionisation. We have, therefore, at the stage

Ob ……. Complete ionisation of H..... 22,000° C. (Table VI).

But if some day we can overcome the limitations imposed by the atmospheric absorbing layer, and examine stellar spectra up to 1000 Å.U., it is very probable that we shall get the Lyman lines (1*s*-*mp*) even at the lowest stage at which a star begins its life,* just like Calcium ″ g.″

The disappearance of Balmer lines from a certain class therefore does not mean that hydrogen is absent from this class, but rather that the stimulus is not sufficiently great to bring out the lines lying within the range of observation.

The position of helium is quite similar. It cannot be identified by its l*s*-*mp* lines, but by the 2*p*-*md* lines (*vide* Table VII). This can take place only when a sufficient proportion of He-atoms have been converted to the 2*p* state. Owing to the higher value of ionisation-potential of helium, this takes place, as Table II shows, at a much higher stage than that of hydrogen, viz., at the Ao stage. We have, therefore, at the stage

Ao …… 2*p*-orbits of He just appearing ……. T = 12,000° K.

The helium lines are very persistent, as Table II shows. They occur faintly in the Ob and Oa classes, and even in the gaseous nebula† up to the P*d* stage.

* Provided, of course, the continuous spectrum from the stellar nucleus extends up to $\lambda = 1000$ Å.U., and is not wholly absorbed by the stellar atmosphere itself,

† Harvard ‘ Annals,’ vol 91, p. 5.

Here the transition stages have not been satisfactorily worked out. Now a glance at Table IV shows that if we take the pressure 1 atm., helium does not become completely ionised even at a temperature of 30000°. For a pressure of 10^{-1} atm., the temperature of complete ionisation is 25000° K

The ionisation of helium becomes marked from the B2-stage, as is shown from the appearance of the 4686 line. According to Fowler, this is the 3*d*-4*f* line of He^+, and according to our theory, this requires for its absorption, not only a rather greater stimulus than that which suffices for mere ionisation, but also a greater concentration of the He^+-atoms. We can, therefore, assign to the stage

B2A ... Ionisation of He considerably advanced ... T = 17,000°.

I have sought in vain for satisfactory data for Mg, which can be detected by the $2p$–$3d_j$ lines only (*vide* Table VII). Mg^+ is detected by the line 4481, which, according to Fowler, has the series-combination 3*d*-4*f*. A glance at Table II shows that, at the Go-stage, the ionisation of Mg has been considerably advanced, reaching its completion at the Oastage. We have, therefore, at the stage

Oa ……Mg^+ Completely ionised ……. T = 23,000° K.

Unfortunately, we have no data of the exact stellar classes from which the Sodium, D_1, and D_2 lines, the Sr line 4607, the Ba line 5543, and the Mg triplet 3838, 3832, 3829, the Sr^+ 4215, 4077, and Ba 4554, 4904, ... just disappear. If these were available, they would have served as good landmarks for determining the temperature of emission of the stellar atmospheres at their various stages of evolution. If these arguments are correct, we are not justified in speaking of a star as a Hydrogen, Helium, or Carbon star, thereby suggesting that these elements form the chief ingredients in the chemical composition of the star. The proper conclusion would be that under the stimulus prevailing in the star, the particular element or elements are excited to radiation of their characteristic lines, while other elements are either ionised, or the stimulus is too weak to excite the lines by which we can detect the elements. This strikes at the root of the prevailing conception of primordial elements.

Table VIII shows the above results at a glance.

A serious discrepancy is shown by hydrogen, which, as shown by the presence of the Balmer lines, is present even beyond the Oa-stage (*vide* Table II, He^+, 4860; we called it an He^+ line there in anticipation of the arguments which follow). But modern spectroscopic work has shown that the lines represented by the Balmer formula $\nu = N(1/2^2 — 1/m^2)$ cannot only be due to hydrogen, but may be due to He^+ and to Li^{++}. If the

Table VIII.

Phenomena.	Stellar class.	Temperature.	Remarks.
Appearance of the K line	Mc	4,000 K	Beginning of the ionisation of Ca.
Disappearance of the "g" line.....	B8A	13,000	Ca completely ionised.
Appearance of Mg^+ 4481	Go	7,000	Mg considerably ionised.
Disappearance of the K line	Oc	20,000	Ca^+ completely ionised.
Mg^+ 4481 disappears	Oa	23,000	Mg^+ completely ionised.
Appearance of 4686	B2A	17,000	He considerably ionised.
Disappearance of 4471	Oa	24,000 (10^{-1} atm.)	He completely ionised.
Appearance of Balmer lines	Mb	4,500	Appearance of the $2p$-orbits of H.
Appearance of He lines	Ao	12,000	Appearance of $2p$-orbits of He.
Maximum absorption of hydrogen lines	Ao	12,000	Maximum concentration of $2p$-orbits of H.
Maximum absorption of helium lines	B2A	17,000	Maximum concentration of $2p$-orbits of He.
Disappearance of 4295	B8A	14,000 (10^{-1} atm.)	Sr^+ completely ionised.
Disappearance of Balmer-hydrogen lines	Ob	22,000	H completely ionised.
Disappearance of 4686	Pe	25,000°–30,000°	He^+ completely ionised.

lines be due to He^+, they should have the same intensity as the Pickering lines $\nu = 4N [1/4^2 — 1/(2m + 1^2)]$, for they form the even members of the $4f$-mk series of He^+. Now, if we look back at Table II, we find that this is actually the case from the Oa- to the Oc-clase, but in Od and Oe, while the Pickering lines are fading away, the Balmer lines are gaming in intensity.

This fact, taken along with the result that at 20,000° K, 10^{-1} atm. Pressure hydrogen is completely ionised, leads us to the conclusion. The Balmer lines due to hydrogen disappear from the Ob-class; those occurring in the Oa-, Ob-class, are due to He^+. In the Oc-, Od-, and Oe-class, there are blends of H and He^+ lines, but below B2A they are entirely due to hydrogen.

The question can be settled by accurately measuring the wave-lengths of the Balmer lines in the different spectral classes, for, owing to slightly different values of N in the case of hydrogen and helium, the wave-lengths are slightly different, as the following Table shows:—*

Hydrogen Lines. $\nu = N_H[1/2^2 - 1/m^2]$,		He$^+$ Lines. $\nu = 4N_{He}[1/4^2 - 1/(2m)^2]$.	
M = 1 Hα,	λ = 6562·8,	M = 1,	λ = 6560·1.
M = 2 Hβ,	λ = 4861·3,	M = 2,	λ = 4859·3.
M = 3 Hγ,	λ = 4340·5,	M = 3,	λ = 4338·7.
M = 4 Hδ,	λ = 4101·7,	M = 4,	λ = 4100·0.

* Fowler, " Bakerian Lecture," ' Phil. Trans.,' A, vol. 214 ; Paschen, 'Ann. d. Physik,' vol. 49.

The lines $\nu = N\,[1/2^2 - 1/m^2]$ also occur in the highest class of gaseous nebulae, Pa, which is far higher up than the class from which He^+ disappears. There is thus a certain anomaly attached to the Balmer lines.

7. *Concluding Remarks.*

The work thus corroborates Russell's view that the continuous variation of stellar spectral types is mainly due to the varying values of the temperature of the stellar atmosphere, and the classification B, A, F, G, K, M, which has been adopted by the Harvard Astrophysicists, as the result of long years of study and observation, are therefore seen to acquire a new physical significance.

Some minor differences may be noted here. It appears that the temperatures assigned by Wilsing and Scheiner to stellar classes below G_0 are rather too low. Wilsing and Scheiner assign a temperature of 5000° K. to stars of the G_0-class, of which the sun is a typical example. But Biscoe* has shown in a comprehensive work that the black-body temperature of the sun is in the neighbourhood of 7500° K. Wilsing and Scheiner's value is therefore too low. The temperatures assigned to the K5, Ma, Md classes (3200°, 3100°, 2950° K.) are too close to each other to explain the large difference in the spectra of these types. Moreover, if these were the true temperatures, the dwarf stars of these classes would possess liquid or solid crusts consisting of carbon, tungsten, tantalum, and probably of some compounds.†

From the fact that Ca^+ first comes out in considerable quantities in the Mc class, we are probably right in assigning to this class a temperature of 4000° K. But more work is required in the spectral classification of the red stars before we can come to any definite conclusion on this point.

Adams and Kohlschütter‡ have recently shown that there exists considerable difference in the spectra of the giant and the dwarf stars of the same spectral class, when the intensity of certain groups of lines are compared. It will be seen from Sections 2 and 3 that the nature of the spectra is decided not only by the temperature, but also by the concentration of atoms in the stellar atmosphere. Probably the mass of the star and the average density act differently on elements of different atomic weight, so

* Biscoe, 'Astrophysical Journal,' vol. 46 (1917).

† The melting points of tungsten and tantalum are 3800° K. and 3200° K. Carbon is a volatile substance, *i.e.,* has its boiling point lower than the melting point. But Lummer claims to have succeeded in melting carbon by running the arc in an enclosed space under its own vapour pressure. He estimates the melting point to be 4200° K. under a pressure of 1 atm. of its own vapour.

‡ Adams,' Communications from Mount Wilson Solar Observatory,' No. 23, 1916.

far as the concentration in the effective layer from which the absorption lines originate is concerned. The problem, however, awaits further investigation.

In spite of the uncertainty in choosing the proper concentration for a given element, it will be admitted from what has gone before that the temperature plays the leading *role* in determining the nature of the stellar spectrum. Too much importance must not be attached to the figures given, for the theory is only a first attempt for quantitatively estimating the physical processes taking place at high temperature. We have practically no laboratory data to guide us, but the stellar spectra may be regarded as unfolding to us, in an unbroken sequence, the physical processes succeeding each other as the temperature is continually varied from 3000° K. to 40,000° K.

In conclusion, it is my great pleasure to record my best thanks to Prof. A. Fowler for the interest he has taken in the work, and the many valuable items of information, advice, and criticism with which he has helped me. I also wish to express my thanks to Mr. S. K. Ghosh, M.Sc, of the Calcutta University, for much useful help in the preparation of this paper.

J. Astrophys. Astr. (1994) **15,** 241–257

Reproduced from the *Monthly Notices of the Royal Astronomical Society* **84** No.7, 499-515, (1924)

The Maxima of Absorption Lines in Stellar Spectra (*Second Paper*).

By R. H. Fowler and E. A. Milne.

(*Commnunicated by the Director of the Solar Physics Observatory.*)

§ 1. In a previous paper† we have applied the theory of high-temperature ionisation, first developed by Saha, to the positions of maximum intensity of absorption lines in the stellar sequence of spectra. During the past year the series relationship of lines belonging to trebly-ionised silicon and to ionised carbon, which are important in the spectra of the hotter stars, have been discovered by A. Fowler. ‡ It is the object of the present paper to use A. Fowler's results to calculate by the method of maxima the temperatures and pressures in the reversing layers of the hotter stars. We can supplement these results by provisional estimates for certain other spectra. We deal also with a number of other points which arise in applications of the theory.

§ 2. *Résumé of the Method.*—We use the terms " principal series " or " principal lines" to denoto series or lines which are absorbed in transitions from the normal state of a neutral, singly-ionised, or multiply-ionised atom to an excited state, or state of higher energy. We use the

* *Monthly Notices,* **84**, No. 5, 367, 1924 March.
† *M. N.,* **83**, 403(1923).
‡ *Proc. Roy. S*oc, A, **103**, 413 (1923); A, 105, 299 (1924).

terms " subordinate series " or " subordinate lines " to denote series or lines which are absorbed in transitions from one excited state to another excited state. In the usual spectroscopic terminology a principal series is one in which the constant term is derived from an orbit which is most conveniently described as having the azimuthal quantum number unity. Subordinate series are those whose constant terms are derived from orbits of higher azimuthal quantum numbers. It frequently happens that the state of lowest energy is one of azimuthal quantum number unity, and the two terminologies more or less coincide; this was in fact the case with all the atoms whose spectra were considered in our previous paper. But for ionised carbon, for example, the states of lowest energy are the pair $^1\pi_{1,2}$, which give rise to the sharp and diffuse series, whilst the first σ state, which gives rise to the "principal series" of optics and has the azimuthal quantum number unity, is one of greater energy. In stellar applications we require a special name for lines derived from the state of lowest energy, and we shall therefore use the word principal in the sense stated above. When we wish to refer to a "principal series" in the optical sense, we shall call it a "first principal series," a "second principal series," etc., as the case may be. A second principal series is necessarily a subordinate series in our terminology, since it is derived from the *second* level of azimuthal quantum number unity.

In a mass of gas in statistical equilibrium, the number of neutral atoms in the normal state steadily decreases as the temperature rises, owing to increasing ionisation. The number of neutral atoms in a given excited state increases to a maximum and then decreases. It follows that if the gas is producing absorption lines, the intensity of a principal line will steadily decrease as the temperature increases, but the intensity of a subordinate line will rise to a maximum and then decrease.

We showed in our previous paper that if χ_1 is the ionisation potential of the atom, $\chi_1^{(r)}$ the (negative) energy of a given excited state, then for a given partial pressure P_e of free electrons, the temperature T of maximum concentration of atoms in the given excited state $\chi_1^{(r)}$ is given by

$$P_e = \frac{\chi_1^{(r)} + \frac{5}{2}kT}{\chi_1 - \chi_1^{(r)}} \cdot \frac{(2\pi m)^{\frac{3}{2}}(kT)^{\frac{5}{2}}\sigma_1}{h^3 b_1(T)} \cdot e^{-\chi_1/kT} . \quad . \quad . \quad (1)$$

In (1) m is the mass of the electron, k is Boltzmann's constant, h is Planck's constant, σ_1 is the symmetry number of the neutral atom, and $b_1(T)$ is the partition function, given by

$$b_1(T) = q_1 + q_1^{(2)} e^{-(\chi_1 - \chi_1^{(2)})/kT} + q_1^{(3)} e^{-(\chi_1 - \chi_1^{(3)})/kT} + \ldots \quad . \quad (2)$$

In (2) the q's are the weights of the corresponding stationary states, and the summation is extended over all the stationary states of which the given atom, in its neutral state, is capable. Equation (1) is an equation in T whose root is T_{max}, but we found it convenient to assume values of T_{max} and calculate from (1) the corresponding values of P_e. A certain difficulty connected with the convergence of the series in (2) has recently been removed by the work of H. C. Urey.* We return to this in § 9.

* *Astrophys. Journ.,* 59, 1 (1924).

The principal lines of the singly-ionised atom will also have a maximum as the temperature increases. We showed that the temperature at which the concentration of singly-ionised atoms reaches a maximum is given by

$$P_e = \left[\frac{\sigma_1\sigma_2}{b_1(T)b_2(T)}\right]^{\frac{1}{2}}\left[\frac{\chi_2+\frac{5}{2}kT}{\chi_1+\frac{5}{2}kT}\right]^{\frac{1}{2}}\frac{(2\pi m)^{\frac{3}{2}}(kT)^{\frac{5}{2}}}{h^3}e^{-\frac{1}{2}(\chi_1+\chi_2)/kT} \quad . \qquad (3)$$

Where χ_2 is the second-stage ionisation potential and σ_2 and $b_2(T)$ refer to the singly-ionised atom.

The subordinate lines of the singly-ionised atom will have a maximum which arises in the same way as the maximum of those of the neutral atom. Provided that the first-, second-, and third-stage ionization potentials are sufficiently well separated, so that only two stages of ionisation are simultaneously present in appreciable proportions, the maximum for subordinate lines of the singly-ionised atom is given by (1), when χ_1 and $\chi_1^{(r)}$ are replaced by the corresponding quantities χ_2 and $\chi_2^{(s)}$

Similar formulae hold for multiply-ionised atoms under the same conditions. If, however, an atom possesses a pair of consecutive ionisation potentials which are close together, more than two stages of ionisation may be present simultaneously, and a correction may be required. This is worked out in § 8, since at one time it was thought probable that it would be required for the discussion of trebly-ionised silicon.

We made the assumption, in our previous paper, that the maximum intensity of a line in the stellar sequence of spectra occurred when the concentration of atoms in the state capable of absorbing the line, calculated thermodynamically, had a maximum for given P_e. We assumed implicitly, therefore, that the reversing layer of a star could be regarded as in thermodynamic equilibrium, and that the state of affairs could be represented by introducing a partial electron-pressure P_e and a temperature T. These quantities must be taken to represent the mean values of the actual temperature and partial electron-pressure throughout the thickness of the layer in which the absorption line originates. It will be noted that we assumed P_e constant for different temperatures. To determine T_{max} from (1) the value of P_e must be known. We assumed the value $P_e = 1{\cdot}31 \times 10^{-4}$ atmos., this being the value which gave $T_{max} = 10{,}000°$ for the Balmer lines, which are observed to have their maximum in stars of type A_0. The significance of these assumptions will be discussed further in §§ 6, 7.

§ 3. *The Observed Maxima in Early-Type Stars.*—The following table shows the absorption-line maxima which occur in stars of type A_0 and earlier. It has been compiled from information supplied by Mr. Baxandall, supplemented by H. H. Plaskett's chart of intensities in his memoir* on "Three O-Type Stars." The horizontal rows correspond to the spectral types, the vertical columns to the different elements. Against each maximum is inserted the ionisation potential for the removal of the next electron from the corresponding atom, when known. Thus "Si IV $44{\cdot}9$" means that here lines of the spectrum Si IV, due to the

* *Pub. Domin. Astrophys. Obs.*, **1**, 356 (1922).

Si^{+++} atom,* reach a maximum, and that the ionisation potential for the removal of the electron is 44·9 volts. An ionisation potential enclosed in brackets denotes a value somewhat less exactly known.

TABLE I.

Absorption–line Maxima in early Type Stars

Element. / Type	Hydrogen.	Magnesium.	Helium.	Carbon.	Silicon.	Nitrogen.	Oxygen.	Sulphur.
?				C IV (64)				
O5			He II 54·2					
O7						N III		
O9							O III	
O9–Bo				C III	Si IV 44·9			
B1					Si III		O II	S III
B2			He I 24·5	C II 24·3		N II		
B8					Si II			S II
Ao	H 13·5	Mg II 15·0						

One or two comments on the table may be made. Plaskett's chart of intensities shows the Pickering lines of the atom He^{+} (part of the spectrum He II) to be still increasing in intensity at type O_5. However, the intensities are · estimated with reference to hydrogen, which is decreasing, so that it seems reasonable to put the maximum of He II at O_5. Plaskett himself appears to place the maximum not far beyond O_5, as he defines the hypothetical class Oo by the *disappearance* of the Pickering lines. The lines of Si IV are shown as having a maximum in type Bo in Plaskett's chart, though in the text he gives O_9. The lines of Si IV and C III appear to have maxima approximately simultaneously. Bright lines probably belonging to C IV have been found by Merton † and identified with emission lines in the spectra of Wolf-Rayet stars, and we have therefore left a possible place for an absorption-line maximum for lines of C IV. Plaskett gives a maximum ‡ for N III in type O_7, and, according to the Harvard observers, § the lines rise to a great intensity in the star 29 Canis Majoris, of type Oe. The relative behaviour of nitrogen and oxygen thus appears anomalous if the assignment of lines to spectra is correct.

For the estimate of the ionisation potential of C IV and for other provisional data, in particular for C III and Si III, we are indebted to some unpublished investigations kindly put at our disposal by Mr. D. R. Hartree, of St. John's College, Cambridge.

Since this paper was written, Miss Payne || has published a reinvestigation of the intensity curves of lines of Si I, II, III, and IV as a function of spectral type. Her curves show maxima of Si I in G_5,

* It appears most suitable to speak of a *spectrum* as ZI, ZII , etc., and of the corresponding *atom* which emits it as Z, Z+, etc. We attempt to do so consistently here.

† *Proc. Roy. Soc.,* A, **91**, 498 (1915).

‡ He allots the doubtlet λλ4097, 4103, to N^{+}, but A. Fowler in his " Report on Series in Line Spectra " gives reasons for allotting it to N^{++}, *i.e.* N III.

§ *H.A.,* **28**, pt. II., 233. || *Harvard Coll. Obs.,* Circ. No. 252.

Si II in Ao, Si III in B_2 – B_1, and. Si IV in Oe_5 (or beyond). The resulting changes in Table I., if made, lead to obvious slight modifications in the deductions of this paper, which we have thought unnecessary to incorporate at this stage. The general agreement between theory and observation is hardly affected . if anything, it is improved. This paper contains certain results which may prove of considerable interest in future, for the observed and theoretical decay of the lines on the high-temperature side of their maxima seem to agree better than we had anticipated. It is to be hoped that these investigations will be extended to the C, N, and O lines of high-temperature stars.

§ 4. *Calculated Maxima.*—The calculation of the position of a maximum. requires a knowledge of the appropriate ionisation potential χ and the energy level $\chi^{(r)}$ from which the given subordinate series is derived. But a glance at formula (1) shows that the *order of magnitude* of P_e for given $T_{max,}$ or of T_{max} for given P_e, is fixed almost entirely by the ionisation potential χ; provided we are sure the lines in question belong to a subordinate series, *i.e.* provided we know that $\chi^{(r)}$ does not coincide with χ, it is immaterial as regards order of magnitude what value we select for $\chi^{(r)}$. It is therefore possible to make rough calculations of maxima in certain cases even if the lines have not been fully classified, given an estimate of χ. We can thus first give the precise calculations for C II and Si IV based on A. Fowler's work. We can also legitimately use Table I., in view of the dominant effect of χ and the agreement in the values of χ in each row both here and at lower temperatures, to make estimates of χ for spectra as yet incompletely known. In this way we may possibly be able to make stellar observations help in the exact elucidation of these spectra, and complete our knowledge of the temperature scale for hot stars.

We arrange the data and calculations in the same way as in our previous paper. It may be recalled that $(2\pi m)^{\frac{3}{2}}h^{-5}h^{-3}=0\,332$;that kT is 0 860 volts when T = 10,0000; that wave numbers are converted into volts by multiplying by $1\,234 \times 10^{-4}$; and that pressures in dynes/cm.^{2} (as given by (I) and (3)) are converted into atmospheres by multiplying by 10^{-6} More precisely we should say that we define our " atmosphere" to be 10^{6} dynes/cm.^{2}.

(i.) *C II* (C^+) *Fundamental Series.* $\lambda\lambda 4267\,3$, $4267\,0$ $(2\delta_2 - 3\phi)$ $1\pi_2 = 196670$, $\chi_2 = 24{\cdot}28$; $2\delta = 51108$, $\chi_{2}^{(2\delta)} = 6{\cdot}31$ b_2 (T) = 2, σ_2 = 1. – We take b_2(T)= 2 because the $1\pi_1$-state is so close to the state of lowest energy $1\pi_2$ that they contribute equally to b_2(T) near T_{max} We take σ = 1 because the series electron is a single electron with a normal 2_2 orbit. (The other electrons are 2 in 1_1 and 2 in 2_1 orbits.) The doublet 4267 is precisely analogous to λ4481 Mg II, and is observed to have a maximum in stars of type B_2 simultaneously with the spectrum He I. It should be noted that the ionisation potentials of the atoms He and C^+ (24·5, 24·3) are almost identical. We find

$T_{max} = 14{,}000^\circ$, $P_e = 3{\cdot}58 \times 10^{-6}$ atmos.
$T_{max} = 15{,}000^\circ$, $P_e = 1{\cdot}71 \times 10^{-5}$ atmos.
$T_{max} = 16{,}000^\circ$, $P_e = 6{\cdot}47 \times 10^{-5}$ atmos.
$T_{max} = 17{,}000^\circ$, $P_e = 2{\cdot}23 \times 10^{-4}$ atmos.

(ii.) *Si IV* (Si^{+++}). *Second Principal Doublets.* λλ4088, 4116 ($2\sigma - 2\pi_{1,2}$). $I\sigma = 364117$, $x_1 = 44{\cdot}94$; $2\sigma = 170105$, $\chi_1^{(2\sigma)} = 20{\cdot}98$; $b_4(T)=1$, $\sigma_4 = 1$.—The electronic structure is that of Na. This well known doublet has been classified by A. Fowler. It is observed to have a maximum at Bo or O_9 simultaneously with the C III triplet λλ4647, 4650, 4652. Assuming that χ_3 and χ_4 are sufficiently far apart for no correction (§ 8) to be required (this is not yet completely certain), we find from (I)

$$T_{max} = 23.000^\circ, \qquad P_e = 3{\cdot}92 \times 10^{-6} \text{ atmos.}$$
$$T_{max} = 25{,}000^\circ, \qquad P_e = 3{\cdot}03 \times 10^{-5} \text{ atmos.}$$
$$T_{max} = 27{,}000^\circ, \qquad P_e = 1{\cdot}75 \times 10^{-4} \text{ atmos.}$$

(iii.) *Speculations on C III and Si III.*— If we may so far trust our theory, we must expect that the ionisation potential of C^{++} will be about 45 volts. We may also rely on the value 64 volts for C^{+++}, though this has not yet been fixed exactly. From these values and the known value 45 volts for Si^{+++}, we can derive a rough value for Si^{++}. The argument is that, as a matter of empirical fact, the ratios of two consecutive ionisation potentials for the removal of two electrons in equivalent orbits are roughly the same for all atoms of the same external structure. This ratio is known for Mg, Ca, Sr, Ba, Zn, Cd. We find the values 0508, 0·5115, 0·5115, 0·5120, 0·5114, 0·5116. These are all atoms with two equivalent series electrons in n_1-quantum orbits. We may therefore expect the same equality of the pairs C^{++} C^{+++} and Si^{++} Si^{+++}, though not necessarily the same ratio (·51) owing to the different net charge. Since 45/64 = 0·7033, we expect that $\chi_3 = (0{\cdot}7033)45 = 31{\cdot}6$ for Si^{++}. If the slight increase of the ratio with atomic number is significant, χ_3 should lie between 32 and 33.

We could confirm this estimate if we could estimate χ_2 for O^+. Now χ_1 for O has recently been properly determined.* Presumably O has 2 equivalent series electrons in 2_2 (circular) orbits. The only atom, of similar structure which we might legitimately use for comparison is He, for which the ratio $\chi_1 / \chi_2 = 0{\cdot}4512$. This gives $\chi_2 = 30$ for O^+. Very little weight can be attached to these calculations for O, but so far as they go they confirm the ostimate that the ionisation potential typical of maxima in B_I stars is about 32 volts.

The lines observed in stars are λλ4647, 4650, 4652 C III, and λλ4552, 4567, 4574 Si III. They are almost certainly homologous lines, type $2S-2P_{1,2,3}$. For provisional calculations one may take the rough values $\chi_3^{(2S)} = 18$ (C III), 15 (Si III); b_3 (T) = 1, $\sigma_3 = 2$. This indicates that for $P_e = 131 \times 10^{-4}$ atmos., the maximum of the lines Si III, $\chi_3 = 32$, should occur at about 19,000 °.

We put forward these speculations leading to 32 volts for the ionisation potential of Si^{++} for what they are worth. We had been informed by A. Fowler that the IS term for Si III was still somewhat uncertain, but that a value near 256,000 (31·6 volts) was perhaps to be expected. The independent line of argument here presented seems to us to point quite strongly to some such value.

* Birge, *Journ. Opt. SOC.Amer.*, **8**, 233 (1924), and Hopfield, *Phys. Rev.*, **21**, 710 (1923),assign the ionisation potentials 13·55 and 10·31 volts to O and S.

We are also informed by Mr. D. R. Hartree that an extrapolation by his method from Mg and Al^{+} leads to about 31 volts for Si^{++}.

§ 5. *The Temperatures and Pressures in the Reversing Layers of the Hotter Stars.*—Logarithmic interpolation amongst the values of P_e calculated in the preceding section gives the following values of T_{max} for P_e—$1{\cdot}31 \times 10^{-4}$ atmos. These form a continuation of the table on p. 420 of our previous paper. The value for He I has been repeated for

TABLE II.

Temperatures of Early-Type Stars.

$T_{max.}$	Type.	Maximum of
16,000°	B2	He I ; 1π–$m\delta$, etc.
16,560°	B2	C II ; 2δ–$m\phi$.
(19,000°	B1	Si III ; O II.)
26,600°	Bo–O9	Si IV ; 2σ–2π.
35,200°	? O5	He II ; "4686" and Pickering series.

convenience, recalculated for the correct ionisation potential 24·5 volts, and that for He II has been added also. The value in brackets is based on a provisional estimate only. C III is omitted, as its observed coincidence with Si IV has been used to derive the value for Si III.

We noted in our previous paper that the method of maxima indicates a temperature-scale which agrees with the observed temperatures for the late-type stars, but gives much higher temperatures for early-type stars than those commonly attributed to them. It is at once apparent that this indication is continued by the results for carbon and silicon. Indeed, the maximum of Si IV in stars of type $B0$-O_9 assigns to them a temperature of 26,600° ", far higher than had been anticipated. A change of temperature of 10,000° between stars of types B_2 and B_0-O_9 seems at first sight unlikely. It is therefore desirable to examine in detail the exact meaning of our determinations.

A glance at Table I., wherever the ionisation potentials are known, shows that the spectra of atoms with about the same ionisation potential have simultaneous maxima. As examples we have H and Mg II in Ao, and He I and C II in B_2. This is in accord with theory, since, as we have seen, the position of a maximum for a given P_e depends mainly on χ and comparatively little on $\chi^{(r)}$, b(T), and σ. Now the ionization potentials in the row B_2 are 24 volts and in the row B0–O9 are 45 volts. It is improbable that any small change of temperature could be responsible for such a large change of excitation as is implied by a change of relevant ionisation potential from 24 volts to 45 volts. Quite apart from the details of our method, therefore, A, Fowler's determination of the ionisation potential of Si^{+++} as 45 volts, combined with the observed maximum of the Si IV doublet in stars of type O_9–Bo, would have suggested that the temperature-step from B_2 to B_0 must be a large one. The same argument can be applied to the jump of 6000° from Ao to B_2. Roughly speaking, the paramount circumstance is the value of the ionisation potential, and the temperature of the maximum is

approximately proportional to the ionisation potential in the absence of any other alteration of circumstances.

We have already made one fundamental application of the observed maxima of Table 1. on this basis, in assigning 45 volts to C III. It is possible to use Table I. to estimate roughly other unknown ionisation potentials. For example, by itself it strongly suggests that the ionisation potentials of Si^{+} and S^{+} are I8–I9 volts, that of N^{+} 24. volts, that of S^{++} 32 volts, and those of O^{++} and N^{++} between 48 and 53 volts. The circumstance that the ionisation potentials (and calculated temperatures) increase apparently erratically with spectral type need cause us no concern, for the steps of the subdivisions of spectral type are purely arbitrary.

The temperatures given in Table II. depend on the assumed partial electron pressure P_e = $1{\cdot}31 \times 10^{-4}$ atmos. Though the large increase in ionisation potential from He and C^{+} to C^{++} and Si^{+++} necessarily implies a considerable step in temperature from B2 to B0, the actual amount of the step will be smaller if a smaller value of P_e is required for the maxima of C III and Si IV than we have assumed, Thus for Si IV,P_e =$3{\cdot}9 \times 10^{-6}$ atmos. gives T_{max} = 23,000°. T_{max} = 20,000° requires a value of P_e near 8×10^{-8} atmos.

For ε Orionis, the typical star of type Bo, Coblentz* found a temperature of 13,000°–14,000° from thermocouple observations. For ε Persci, also of type Bo, H. H. Plaskett † has given the provisional temperature of 15,000° as determined by the wedge method. For γ Cassiopeise, of type Bop, Plaskett has found 15,000° and Sampson ‡ 16,900. The temperatures determined by the method of maxima can only be reconciled with these spectrophotometric temperatures by taking values of P_e 10^6 times smaller than those indicated by the observed maxima in types M to A0.

Plaskett § has directed attention to certain anomalies in the intensity-distribution in the spectra of O-type stars. The Victoria observers find that the O-type stars as a class are white. They appear almost as white as stars of type A0, whilst they would be expected to be bluer than the B-stars. It is possible, therefore, as Plaskett suggests, that the intensity-distributions in the spectra of the hotter stars fail to give an indication of their temperatures; in other words, that owing to departure from the black body distribution the colour-temperature has no relation to the true temperature. If this is so, the objections to the high temperatures determined by the method of maxima disappear.

It must, however, be repeated that the adoption of a constant value for P_e is a pure assumption, made provisionally as a working hypothesis. The adopted value P_e= $1{\cdot}31 \times 10^{-4}$ atmos. gives a temperature-scale from M to A0, and probably to B_2, which is in agreement with the spectrophotometric scales. It may be that for high ionisation potentials smaller values of P_e are required.

It should be observed in passing that the spectrophotometric scales give the effective temperature of the star. The reversing layer should be at a lower temperature—its average temperature should be in the

* *Pop. Astron.,* **81**, 113 (1923).
† *Pub. Domin. Astrophys. Obs.,* 2, 258 (1923).
‡ *M.N*, **88**, 174 (1923). § *Loc. cit,*

neighbourhood of, or somewhat lower than, the Schwarzschild boundary temperature, which is some 15–20 per cent. lower than the effective temperature. Perhaps we ought to adopt 90000 for the reversing-layer temperature of stars of type A0. This would require a value of P_e, in the neighbourhood of 10^{-5} atmos. We do not propose, however, to consider this modification further in this paper.

§ 6. *The Meaning of P_e.*—The physical significance of the value found by the method of maxima for the partial electron pressure P_e has already been briefly described by one of us elsewhere.* The value found corresponds to the level in the stellar atmosphere at which a strong subordinate-series line originates. The greater the absorption coefficient of the gas as a whole, in the frequency concerned, the less far can we see into it, and the nearer the surface must be the level in which the emergent radiation originates, and so the lower the pressure. Now the absorption coefficient of a gas like hydrogen, for example for the Balmer lines, is proportional to the product of the concentration of atoms in the 2-quantum state and the atomic absorption coefficient. The method of maxima ascertains when the concentration of atoms in the 2-quantum state is a maxirmim for given P_e, but it is clear that the greater the atomic absorption coofficient the smaller will be the appropriate value of P_e. If the atomic absorption coefficients for different atoms are different, the corresponding pressures will be different. If atoms with high ionisation potentials have large atomic absorption coefficients for certain lines, we should be entitled to take lower values of P_e for these lines in the hotter stars, and the calculated temperatures would be lower. It would be out of place to enter into details, but it may be mentioned that though the theory of atom-structure suggests the possibility of some such effect, the actual amount appears to be too small to have any serious influence on the value of P_e.

The next point is the ratio of the number of atoms of the kind concerned, at any level, to the number of free electrons. An element less abundant relative to free electrons will yield lines orginating at greater depths, and so at higher electron pressures, than an element more abundant. This does not invalidate our previous statement that the method of maxima avoids certain difficulties in Saha's method of marginal appearances introduced by the question of the relative abundance of the elements. In the method of marginal appearances, the relative abundance of the elements comes in even if the partial electron pressure is regarded as known—the lines of a more abundant element will appear earlier and linger longer than those of a less abundant one. In the method of maxima, the question of relative abundance does not enter if P_e can be regarded as known. We are simply pointing out here that the proper value of P_e must be a function of the abundance of the atom in question relative to free electrons.

For the hotter stars, where owing to greater ionisation free electrons will be more abundant relative to atoms·, we should expect to require larger electron pressures than for the cooler stars. The effect would only give rise to a small numerical factor. Such as it is, however, it would lead to higher values of T_{max} than we have calculated.

Milne, *Phil. Mag.,* **47**, 2I I (1924); *Proc. London Phys. Soc,* **36**, 109 (1924).

A third point is the dependence of P_e on g, the surface value of gravity. For the same " optical depth," P_e would be expected to vary roughly proportionally to g. The argument is too well known to repeat. Dwarf stars should therefore require larger values of P_e than giants, and maxima in dwarfs should occur at higher temperatures than in giants. This is in agreement with observation, though the fact is usually expressed in the form that for given spectral type giants have lower effective temperatures than dwarfs. If g_1 , g_2 are the values of gravity for a giant and dwarf of the same spectral type, T_1 and T_2 their temperatures, then assuming simultaneous maxima we have roughly

$$\frac{T_1^{\frac{5}{2}} e^{-\chi/kT_1}}{g_1} = \frac{T_2^{\frac{5}{2}} e^{-\chi/kT_2}}{g_2} \quad . \quad . \quad . \quad . \quad (4)$$

where χ is the mean effective ionisation potential for the lines whose maxima fix the type. Consider as an example the Sun (dwarf) and the brighter component of Capella (giant). We have $g_1 = 0{\cdot}067 \times 10^4$, $g_2 = 2{\cdot}73 \times 10^4$, $g_2/g_1 = 40{\cdot}7$. Let us take $T_2 = 6000°$, and use (4) to calculate T_1. From the data and calculations of our previous paper, a maximum of a subordinate line at a temperature of 6000° corresponds to about $\chi = 8$ volts, assuming P_e to be about 10^{-4} atmos. for the dwarf. We then find from (4), $T_1 = 5000°$. This should be the temperature of the reversing layer in Capella. The Mount Wilson colour-indices * would appear to indicate a temperature between 5000° and 5500°; Eddington † adopts 5500°. The calculated difference of temperature between giants and dwarfs is thus of the same order as that observed, and the theoretical dependence of P_e on g is therefore confirmed, ‡

A fourth point is the dependence of P_e on the excitation potential $\chi - \chi^{(r)}$ which represents the energy that has to be communicated to the atom in order to tranesfer it from the normal state to the state in which it can absorb the given subordinate series. We have seen that for given P_e, the value of T_{max} depends principally on χ, the ionisation potential, and hardly at all on $\chi^{(r)}$. But the bigger the excitation potential $\chi - \chi^{(r)}$, the smaller is the concentration of excited atoms, and so the smaller the absorption coefficient of the gas as a whole. Hence the greater is the depth at which the line originates, and the larger is P_e. Thus lines for which $\chi^{(r)}$ is relatively small compared with χ would be expected to require greater values of P_e.

It is of interest in this connection to tabulate the fraction of atoms in given excited states at maxima. We showed in our previous paper § that if x_1 is the fraction of neutral atoms, then at the maximum of a given subordinate series ($\chi^{(r)}$) of the neutral atom the value of x_1 is given by

$$[x_1]_{max} = \frac{\chi_1^{(r)} + \frac{5}{2}kT_{max}}{\chi_1 + \frac{5}{2}kT_{max}},$$

---

* Seares, *Astrophy. Journ., 55*, 198 (1922).

† *M.N,* **84**, 109 (1924).

‡ Similar calculation has been made by J. Q. Stewart, *Pop. Astron.,* **81**, 88 (1923).

§ The notation has been changed slightly. What was called $(1 - x)$ in the previous paper is here called x_1

and the fraction of atoms in the given excited state $\chi^{(r)}$ at this maximum is $n_1^{(r)}$, given by

$$[n_1^{(r)}]_{max} = x_1 \frac{g_1^{(r)} e^{-(\chi_1 - \chi_1^{(r)})/kT_{max}}}{b_1(T_{max})}.$$

Similar relations hold for maxima belonging to the singly -or multiply-ionised atom, on replacing the suffix 1 by 2, 3 . . ., provided the ionisation potentials are well separated. The following table gives the values of x and $n^{(r)}$ for the various maxima discussed in this and the previous paper, assuming $P_e = 1{\cdot}31 \times 10^{-4}$ atmos.

TABLE III.

Fractional Concentrations at Maxima

Atom.	χ.	$\chi^{(r)}$.	T_{max}.	x_{max}.	$n^{(r)}{}_{max}$.
Na	5·12	3·03	3,900°	0·65	$1{\cdot}3 \times 10^{-3}$
Ca	6·08	4·20	4,270°	0·73	$4{\cdot}4 \times 10^{-3}$
Ca	6·08	3·16	4,420°	0·58	$2{\cdot}7 \times 10^{-4}$
Mn	7·39	5·29	5,020°	0·75	$6{\cdot}0 \times 10^{-3}$
Mg	7·61	4·92	5,250°	0·69	$1{\cdot}8 \times 10^{-3}$
Mg	7·61	3·29	5,440°	0·51	$4{\cdot}9 \times 10^{-5}$
H	13·54	3·39	10,000°	0·35	$7{\cdot}7 \times 10^{-6}$
Mg+	15·00	6·15	10,220°	0·49	$2{\cdot}1 \times 10^{-5}$
He	24·5	3·61	16,000°	0·25	$6{\cdot}4 \times 10^{-8}$
C+	24·28	6·32	16,560°	0·36	$5{\cdot}9 \times 10^{-7}$
[Si++	32	15	19,000°	0·53	$1{\cdot}6 \times 10^{-5}$]
Si+++	44·94	20·98	26,600°	0·53	$1{\cdot}5 \times 10^{-5}$
[C++	45	18	26,600°	0·47	$3{\cdot}5 \times 10^{-6}$]
He+	54·18	3·39	35,200°	0·18	$9{\cdot}1 \times 10^{-8}$

[ ] Provisional.

We commented on the small values of $n^{(r)}$ at maxima in discussing the peaks of the curves plotted in our previous paper.That only one atom in 10^5, for example, should be capable of absorbing a Balmer-line frequency, even at the maximum of these lines, seemed difficult to reconcile with the great intensity of the Balmer lines. Pannekoek * has called attention to the same point. But it is now known that atomic absorption coefficients are very large,† and these small values of $n^{(r)}$ at maxima no longer cause any difficulty.

Here we wish to draw attention to the variation in values of $n^{(r)}{}_{max}$ from atom to atom. From what has been said, other things being equal, we should expect to require bigger values of P_e the smaller the values of $n^{(r)}{}_{max}$. Increasing P_e increases T_{max}, and so increases

* *Physica,* **2**, 293 (1922).

† Milne, *Phil. Mag.,* **47**, 209 (1924).

$n^{(r)}_{\max}$. Now there is no reason to expect that the values of $n^{(r)}_{\max}$ for different atoms should be all equal, but a glance at the table shows that exceptionally low values are given by He and He^+. This arises because for He and He^+ $\chi^{(r)}$ is exceptionally small compared with χ—a very high degree of excitation is necessary for these atoms before they are capable of absorbing the are lines of helium and the Pickering lines respectively. This suggests that higher pressures should be adopted for He and He^+, thereby increasing the temperature of maxima. Type B_2 would then have a temperature nearer to that found from Si IV for Bo ; and the temperature of maximum development of the Pickering lines would be increased to above 35,000°, thus giving more room for types O_9 to O_5.

We may summarise the results of this discussion by saying that the partial electron pressure at a maximum, which is the mean electron pressure at which the line originates, should increase with increasing values of gravity, and with increasing excitation potential $\chi - \chi^{(r)}$, and should decrease with increasing abundance of the element relative to free electrons, and with increasing atomic absorption coefficient. The mathematical formulation of the problem * depends on the structure assumed for the stellar atmosphere, but ultimately it should be possible to use the observed maxima to furnish information concerning atomic absorption coefficients, values of gravity, and relative abundances. As regards the hotter stars, the discussion gives no basis for suspecting serious errors in the high temperatures found by the method of maxima. Indeed, it suggests rather that the temperatures of maxima of He I and He II should be somewhat increased.

§ 7. *The Value of P_e for Principal Lines.*—For an intense principal line of a neutral atom, or for the maximum of a principal line of an ionised atom, the fraction of atoms in the required state is almost unity ; for the required state is here the normal state. On the other hand, we have just seen that at the maxima of subordinate lines the fraction of atoms in the required state is from 10^{-3} to 10^{-5}, at least for the lower ionisation potentials. Thus atoms in the required state are 10^3 to 10^5 times as abundant for intense principal lines as for intense subordinate lines. It follows that principal lines must originate at much higher levels in the stellar atmosphere than subordinate lines, and consequently at much smaller pressures. In the absence of precise calculations, it is reasonable to conjecture that the value of P_e for a principal line is from 10^{-3} to 10^{-5} of the value for a subordinate line.

This appears to be the explanation of the fact noted in our previous paper, that the observed maxima of the lines of Ca^+, Sr^+, and to some extent Ba^+, which are all principal lines, demanded lower values of P_e than 10^{-4} atmos. The maximum of a principal line of an ionised atom is necessarily much blunter than that for a subordinate line, and the spectral type for the maximum is correspondingly difficult to determine. But it is of interest to use the observed maxima as far as possible. We therefore give a recalculation of the results for Ca^+, Sr^+, and Ba^+. The values of P e are calculated from formula (3).

* A preliminary result has been given in *Phil. Mag.,* **47**, 227 (1924).

TABLE IV.

Values of P_e (in Atmospheres) for Maxima of Principal Lines of Ionised Atoms.

$T_{max.}$	Ca^+. $\chi_1 = 6{\cdot}08$ $\chi_2 = 11{\cdot}82$	Sr^+. $\chi_1 = 5{\cdot}663$ $\chi_2 = 10{\cdot}97$	Ba^+. $\chi_1 = 5{\cdot}18$ $\chi_2 = 9{\cdot}95$
3500		$4{\cdot}6 \times 10^{-10}$	$5{\cdot}6 \times 10^{-9}$
4000	$3{\cdot}24 \times 10^{-9}$	$2{\cdot}03 \times 10^{-8}$	$1{\cdot}79 \times 10^{-7}$
4500	$7{\cdot}8 \times 10^{-8}$	$4{\cdot}0 \times 10^{-7}$	$2{\cdot}73 \times 10^{-6}$
5000	$1{\cdot}02 \times 10^{-6}$	$4{\cdot}4 \times 10^{-6}$	$2{\cdot}52 \times 10^{-5}$
5500	$8{\cdot}5 \times 10^{-6}$	$2{\cdot}62 \times 10^{-5}$	$1{\cdot}58 \times 10^{-4}$

If the H and K lines of Ca^+ are taken to have a maximum in stars of type K0, of temperature 4500°, then from the table $P_e = 7{\cdot}8 \times 10^{-8}$ atmos. This is about 6×10^{-4} times the value for subordinate lines, $P_e = 1{\cdot}3 \times 10^{-4}$ atmos., in agreement with the above conjecture. The same pressure fits the observed maxima for Sr^+ and Ba^+, these having slightly lower temperatures.

The maximum of a principal line of an ionised atom thus appears to originate at a partial electron pressure of 10^{-7} atmos. to 10^{-8} atmos. Optically and thermodynamically the principal lines of a neutral atom should behave in the same way. The intensity of a principal line of a neutral atom increases steadily with decreasing temperature in the range of stellar temperatures and so has no maximum there. We may still conclude, however, that when its intensity is great it also originates at a partial electron pressure of 10^{-7} atmos. to 10^{-8} atmos.

We should mention here that there is no theoretical discontinuity between principal lines and subordinate lines, but that there is a practical one, since we do not actually find examples in stellar spectra of subordinate lines for which $\chi - \chi^{(r)}$ is very small compared with χ. Just as, however, exceptionally large values of $\chi - \chi^{(r)}$ lead to very small concentrations at maximum and so may require values of P_e *larger* than normal, exceptionally small values of $\chi - \chi^{(r)}$ mean large concentrations at maximum and values of P *smaller* than normal. If $\chi - \chi^{(r)}$ is very small, the concentrations and values of P_e approximate to those of a principal line. In Table III. values of $\chi - \chi^{(r)}$, somewhat small compared with χ, are found for Mn, Ca, Mg, and Na. It is probable that these lines require pressures smaller than $1{\cdot}31 \times 10^{-4}$ atmos. and correspondingly smaller T_{max}, but we shall not enter into details here.

§ 8. *Determination of Maxima with two Close Ionisation Potentials.* —When two ionisation potentials, χ_1 and χ_2 say, are close together, which means in practice that they have a *ratio* nearly 1, the analysis of our previous paper must be supplemented as follows. The work is written out for the first and second stages, and applies of course unchanged to any consecutive stages when the suffixes 1, 2, and 3 are replaced throughout by *s*, *s* + 1, and *s* + 2.

Let x_1, x_2, x_3 be the fractions of neutral, singly- and doubly-ionised atoms. Then *

$$\frac{x_2}{x_1} P_e = \frac{(2\pi m)^{\frac{3}{2}}(kT)^{\frac{5}{2}}\sigma_1 e^{-\chi_1/kT}}{b_1(T)h^3}, \quad . \quad . \quad . \quad (5)$$

$$\frac{x_3}{x_2} P_e = \frac{(2\pi m)^{\frac{3}{2}}(kT)^{\frac{5}{2}}\sigma_2 e^{-\chi_2/kT}}{b_2(T)h^3}, \quad . \quad . \quad . \quad (6)$$

$$x_1 + x_2 + x_3 = 1. \quad . \quad . \quad . \quad . \quad (7)$$

(i.) To determine the maximum of a subordinate line of the neutral *atom we* have to make $dn_1^{(r)} / dT = 0$, where

$$n_1^{(r)} = x_1 q_1^{(r)} e^{-(\chi_1 - \chi_1^{(r)})/kT}/b_1(T),$$

and x_1 is calculated from (5), (6), and (7). Variations of b_1 (T) and b_2(T) with temperature are ignored. The resulting equation is most conveniently written in the form

$$P_e = \frac{\chi_1^{(r)} + \frac{5}{2}kT}{\chi_1 - \chi_1^{(r)}} \frac{(2\pi m)^{\frac{3}{2}}(kT)^{\frac{5}{2}}\sigma_1 e^{-\chi_1/kT}}{b_1(T)h^3} + \frac{1}{P_e} \frac{\chi_2 + \chi_1^{(r)} + 5kT}{\chi_1 - \chi_1^{(r)}} \frac{(2\pi m)^3 (kT)^5 \sigma_1 \sigma_2 e^{-(\chi_1+\chi_2)/kT}}{b_1(T) b_2(T) h^6} \quad . \quad (8)$$

The second term if small enough may be treated simply as a correcting *term* to P_e as calculated by (1). In other cases equation (8), a quadratic in P_e, must be solved directly. This equation must be used to calculate P_e, whenever the ionisation potential of the stage in question is closely *followed* by the ionisation potential of the succeeding stage.

(ii.) To determine the maximum of a subordinate line of the ionised atom we have to make $dn_2^{(r)}/dT = 0$, where

$$n_2^{(r)} = x_2 q_2^{(r)} e^{-(\chi_2 - \chi_2^{(r)})/kT}/b_2(T),$$

and x_2 is calculated from (5),. (6), and (7). We find here

$$P_e = \frac{\chi_2^{(r)} + \frac{5}{2}kT}{\chi_2 - \chi_2^{(r)}} \frac{(2\pi m)^{\frac{3}{2}}(kT)^{\frac{5}{2}}\sigma_2 e^{-\chi_2/kT}}{b_2(T)h^3} - P_e^2 \frac{\chi_1 + \chi_2 - \chi_2^{(r)} + \frac{5}{2}kT}{\chi_2 - \chi_2^{(r)}} \frac{b_1(T)h^3}{(2\pi m)^{\frac{3}{2}}(kT)^{\frac{5}{2}}\sigma_1} e^{\chi_1/kT} \quad (9)$$

Equation (9) must be used whenever the ionisation potential of the stage in question is closely *preceded* by the ionisation potential of the preceding stage.

The corrections in (8) and (9) result in making the maxima for the lines of the two stages occur further apart in the temperature scale.

If we express the correction in the form of a factor $(1 + \alpha)$, multiplying the P_e given by (1), then α is of the order $e^{-(\chi_2 - \chi_1)/kT_{max}}$ Since

* These are equations (7) and (8) of our previous paper in the present more systematic notation.

kT_{max} varies roughly as χ_1 or χ_2, we see that the importance of the correction is determined by the closeness of x_1/x_2 to 1.

§ 9. *The Exact Form of b*(T).—In our work hitherto we have ignored all questions as to the convergence of the series for *b*(T), and have deliberately assumed that its numerical value in all cases of interest in reversing layer problems is that of its first term (but see also § 4, C II). The explicit form (2) is derived on the assumption that atoms in any stationary state behave practically like a perfect gas, and does not fulfil the assumed conditions unless the series really terminates for some reason after a finite (but possibly large) number of terms. Our assumption has recently been shown to be correct for reversing layer problems by an investigation due to H. C. Urey ;* he resolves the difficulty in a manner which, in outline at least, we believe to be essentially correct.

Urey points out that atoms in any state, normal or excited, should probably be assigned a "volume" comparable to the volume swept by the orbit of their series electron. This is equivalent to assuming that in the ordinary collisions of statistical equilibrium the electronic orbits of two distinct atoms (or molecules) cannot in general interpenetrate. When these orbits are the quickly-traversed space-filling orbits of the normal atom, we have every reason to believe this assumption to be true. It must be just this non-mechanical impenetrability of the quantised orbits of two different atoms or molecules which gives to atoms and molecules (in fact to matter) the familiar property of extension. At first sight it is somewhat surprising that this property is to hold also for the large nearly degenerate orbits of highly excited atoms and even for the almost perfectly degenerate orbits of the excited hydrogen atom. But it must be borne in mind that the only necessary part of Urey's assumption is : *The orbits of the electrons of two distinct atoms can never interpenetrate in any collision which leads to no change in the quantum state of either atom,* When we are to consider any question of statistical (or thermodynamic) equilibrium, we may (and in fact must) properly exclude from consideration all actual processes of exchange, provided we retain merely the hypothesis that the necessary processes of exchange can occur occasionally. For the purpose of determining the equilibrium state, the " volume" of any atom, excited or not, is that region of space into which on the average, no other body may come without causing a change of quantum state. To a first rough approximation this may very reasonably be taken to be the volume swept out by the orbit of the series electron, or, as Urey does, a sphere of radius equal to the semi-axis major of this orbit. . Such " volumes " are then strictly comparable to the volumes of van der Waals' theory.

On this basis Urey has shown by thermodynamic arguments, which we need not repeat, that the weights $q^{(r)}$ in our formulæ must be replaced by functions $q^{(r)}/s^{(r)}$ where $s^{(r)}$ is a certain thermodynamic function depending on the " volume " of the atom in the r^{th} state. If for simplicity we assume that such atoms form a gas obeying van der Waals' equation,

$$P\,(v - b^{(r)}) = RT,$$

* *Loc. cit.*

It Follows thermodynamically that

$$s^{(r)} = e^{\beta^{(r)}P/kT} \quad . \quad . \quad . \quad . \quad . \quad (10)$$

In (10) $\beta^{(r)}$ is four times the "volume" of the atom in state r and P is the *total* pressure. It is thus shown that our $b(T)$ should correctly be replaced by

$$u(T) = \Sigma_r q^{(r)} e^{-\beta^{(r)}P/kT - (\chi - \chi^{(r)})/kT} \quad . \quad . \quad . \quad (11)$$

A numerical discussion for the hydrogen atom is at this stage sufficient to illustrate the numerical order of $u(T)$ for all atoms. Urey's assumptions in this case lead to $\beta^{(r)}/k = 1{\cdot}863 \times 10^{-8} r^6$. The early terms are then all identical with those for a perfect gas, but the terms later than a certain stage are rapidly cut out and the series converges. We tabulate some additional calculations.

TABLE V.

$\frac{1}{2}u(T)$, *the Corrected Value of* $\frac{1}{2}b(T)$.

P atmos. / T°	10^{-3}.	10^{-6}.	10^{-9}.
10,000	1·0007	1·017	1·55
20,000	3·0	62	1900

The order of magnitude of P and Pe will generally be the same. We see at once that, for calculations of T_{max} at reversing layer pressures, $b(T)$ and $u(T)$ reduce to their first term and are indistinguishable. Our previous calculations are unaltered. Further, even for calculation of $n^{(r)}$ as a function of T the difference between $b(T)$ and $u(T)$is of no account. The exact formula for $n^{(r)}$ reduces to

$$n^{(r)} = \frac{q^{(r)} e^{-\beta^{(r)}P/kT + \chi^{(r)}/kT}}{u(T) e^{\chi/kT} + 0{\cdot}332\, T^{\frac{5}{2}}/P_e} \quad . \quad . \quad . \quad (12)$$

If, for example, P, $P_e = 10^{-6}$ atmos., and T= 20,000°, $u(T)$ would have to be greater than 10^7 to affect $n_{(r)}$ appreciably. Thus the values 2 and 124 are indistinguishable. The values of $_s^{(r)}$ for the first few values of r do not differ appreciably from 1, so that the extra term in the numerator of (12) may also be discarded for ordinary absorption series.

§ 10. *Manganese.*—Since our previous paper the term values for the spectrum Mn I have become fully available.* Certain lines of this spectrum are well known in stars, and we record here the calculations of maxima as an addendum to our previous paper. The prominent narrow triplet Mn λλ4031, 4033, 4034·5 is a principal line of type $_1$S(mP +C), (Catalan), and its behaviour in the stars conforms to this, classification, for it has no maximum. Two other Mn lines of stellar importance are λλ4018, 4041. These are the most prominent

* Catalán, *Phil. Trans.*, A, **223**, 127 (1922).

lines of Multiplet VI. (Catalan), type D'–D". The complete multiplet consists of the 13-lines λλ4018, 36, 41, 49, 56, 60, 64, 68, 70, 79, 79, 83, 84. We have therefore

Mn. (D'D") *multiplet.* λλ4018, 4041 (*and others*). 1S = 59937, χ_1 =7·39; D_1' = 42885, $\chi_1^{(D_1')}$ = 5·29; b_1(T) = I, σ_1 *uncertain, assumed* 2. The maximum is difficult to determine, but is probably at K0. A more complete examination of this maximum is desirable. We find

$$T_{max} = 4{,}500^\circ, \quad P_e = 1{\cdot}38 \times 10^{-5} \text{ atmos.}$$
$$T_{max} = 5{,}000^\circ, \quad P_e = 1{\cdot}22 \times 10^{-4} \text{ atmos.}$$
$$T_{max} = 5{,}500^\circ, \quad P_e = 7{\cdot}45 \times 10^{-4} \text{ atmos.}$$

The chief interest of Mn consists in the very large value of $\chi_1^{(Di')}$ As a result, the value of $(n^{(r)})_{max}$ for Mn in Table III. is the largest we have yet found. The suggested T_{max} is high for type K0, unless P_e is smaller than normal. But as we saw in § 7 this smallness of P*e* is to be expected.

Other spectra are rapidly becoming available. The spectrum Cr I is now classified.* The only line whose stellar behaviour we have traced is λ4254 Cr, which is a principal line and shows no maximum.

§ 11. *Summary.*—As a result of the foregoing discussion we have found—

(i.) The temperature scale for early-type stars is roughly B_2, 16,500°; B_1, 19,000°; B0-O_9, 26,500; O_5, more than 35,000°.

(ii.) The partial electron pressure P_e at maximum is the mean electron pressure at which a line originates. It is fixed by fixing T_{max} for that line. For other lines and conditions P_e increases-with increasing values of gravity and increasing excitation potential χ—$X^{(r)}$, and decreases with increasing abundance of the element relative to free electrons and with increasing atomic absorption coefficient.

(iii.) The calculated temperature difference between giants and dwarfs of the same spectral type agrees with observation.

(iv.) The excitation potential χ–$\chi^{(r)}$ is exceptionally large compared with χ for both He and He^+. The fractional concentrations at maximum of atoms absorbing these lines is exceptionally small. Both P_e and T_{max} should probably be larger for these atoms than the values here assigned.

(v.) The concentration at maximum of normal ionised atoms capable of absorbing principal lines is exceptionally large (unity). For such lines probably $P_e = 10^{-7}$ atmos. – 10^{-8} atmos., and the observed maxima of the principal lines of Ca^+, Sr^+, and Ba^+ agree with these pressures.

In conclusion it is again a pleasure to thank Mr. Baxandall for the observational material which he has put at our disposal.

* Gieseler, *Zeit. f. Phys.,* **22**, 201 (1924); see also Laporte, *Zeit. f. Phys.,* **28**, **135** (1924), for a part at least of the spectrum Fe I; Goudsmit, *Nature,* **118**, 238 (1924).

J. Astrophys. Astr. (1994) **15,** 275–308

A VLA 20 and 90 centimetre Radio Survey of Distant A-bell Clusters with Central cD Galaxies

Joydeep Bagchi & Vijay K. Kapahi *National Centre for Radio Astrophysics, TIFR, Poona University Campus, Pune 411 007*

Received 1994 April 12; accepted 1994 May 27

Abstract. A radio survey, using the Very Large Array at 20 and 90 cm λ has been carried out in the direction of 46 distant Abell clusters ($0.1 \lesssim z \lesssim 0.3$) dominated by a cD galaxy (clusters classified to be Bautz-Morgan I type). A radio source coincident with the cD galaxy was detected in 16 clusters. We find that the radio luminosity function of the cD galaxies at 20cm λ, and below the luminosity $P_{1.4\mathrm{GHz}} \lesssim 10^{24.5}$ W Hz $^{-1}$, is similar to that of brightest ellipticals in less clustered environments. Above this luminosity, the cDs seem to have a higher probability of becoming radio sources. The effect of optical brightness on radio emission is shown to be the same for the two classes. No significantly large population of very-steep-spectrum sources with spectral index $\alpha > 1.2$ (flux density $\propto$ frequency $^{-\alpha}$) was found to be associated with cD galaxies. A significant negative correlation is found between the radio luminosity of the cD galaxy and the cooling-time of the intra cluster medium near the galaxy. We also present evidence that the probability of radio emission from first-ranked galaxies is dependent upon their location relative to the geometrical centres of clusters and thus related to the morphological class and the evolutionary state of the clusters. We argue that both these effects are primarily caused by the dynamical evolution of these distant clusters of galaxies.

Key words: Clusters of galaxies—cD galaxies—radio luminosity function—cooling flows.

1. Introduction

Great clusters are the richest agglomerates of galaxies known where the space density of galaxies can surpass the average galaxian density by a large factor. Rich clusters can therefore serve as laboratories for the study of the complex interplay of galaxies with their environment. A striking example of the influence of the cluster environment on galaxies is the evidence of their morphological segregation, first mentioned by Hubble (1936) and Zwicky (1938) and later studied in greater detail by Oemler (1974), Melnick & Sargent (1977) and Dressier (1980). These studies clearly demonstrated that the central regions of rich clusters are mostly populated by E and SO galaxies whereas their outlying and other low galaxy density regions are mainly spiral rich. Even more striking is the position of cD galaxies in

clusters. Mathew, Morgan & Schmidt (1964), while optically identifying the radio sources from early surveys, called attention to these extremely bright and massive galaxies of apparent elliptical morphology but with their associated amorphous and extensive stellar halos. The cD galaxies are almost always located near the densest and the innermost regions of rich clusters (Morgan & Lesh 1965; Leir & van Den Bergh 1977) although many relatively poor clusters are also known to contain these unique type of galaxies (Morgan *et al.* 1975; Albert *et al.* 1977). Despite these interesting observations, the physical mechanism causing their morphological segregation is not clearly known. The suggested mechanisms fall broadly under two categories. The first is the so called 'heredity' hypothesis according to which the morphologies of galaxies are decided at the time of their formation and remain unaltered subsequently. Thus ellipticals can and will form only in regions destined to become clusters. The second class of theories can be called the 'environment' theories which assume that all morphological types form in equal proportion everywhere and due to the influences of the local environment one galaxy type can evolve into another, eg. spiral galaxies may transform into SO galaxies if they lose their interstellar medium through ram-pressure ablations in intracluster gas (Gunn & Gott 1972). A basic difficulty with the heredity model is the implication that the galaxies must have known what their present surroundings would be like at the time of their formation. This introduces obvious problems in the hierarchical clustering model of structure formation but could arise naturally in the adiabatic theory, where galaxy formation is regulated by the evolution of largescale structures.

From the radio astronomical point of view, the observed morphological segregation of galaxies in clusters has significant relevance. The powerful cosmic radio sources (radio luminosity at 1.4 GHz, $P_{14} \gtrsim 10^{22}$ WHz $^{-1}$) are mostly found associated with galaxies of E, SO or cD types. The previous radio studies have indicated that amongst the clusters of all morphological types, the ones containing superbright elliptical galaxies near their cores (i.e. BM types I, II; Bautz & Morgan 1970) are significantly more likely to contain radio sources associated with the brightest cluster members (eg. McHardy 1979). The exact physical mechanism causing this phenomenon is not clear but is possibly related to evolution of clusters. The supergiant cD galaxies appear to be the special products of dense environments as they are found at the densest regions of already dense cluster environments. The special structural, positional and kinematical properties of cD galaxies suggest that they may have originated and be evolving due to dynamical processes in clusters. The radio emission phenomenon from central galaxies might then also be affected by the evolution of their host clusters. Studies of their space distribution have shown that radio galaxies and quasars have undergone strong cosmological evolution. It is believed that powerful radio sources were more numerous in the past (Schmidt 1968; Ryle 1968) and were also pronouncedly smaller in their linear dimensions (eg. Kapahi 1989). It is believed that these effects are caused by a possibly denser medium surrounding these high redshift objects (eg. GopalKrishna & Wiita 1991).

Yee & Green (1987) have found that many radio-loud quasars at redshifts $z \approx 0.6$ are associated with clusters of galaxies comparable in richness to Abell clusters. However, such quasars do not occur in similar nearby clusters, thereby implying a drastic fading of quasar population since $z \approx 0.6$. It is expected that 'relics' of this past phase of activity are surviving in the form of radio sources associated with E and cD galaxies in clusters. An important goal of observational cosmology is to

understand the physics governing the origin and evolution of optical and radio galaxies in the Universe. The evolution of galaxies in these wavebands may be intimately linked. Important clues to the understanding of physical mechanisms governing evolution can possibly be obtained by comparing the properties of clusters as a function of cosmological redshift. This requires a large-scale and complete catalogue of high redshift ($z \approx 1$) Abell type clusters which unfortunately is not yet available, though some clusters upto $z = 0.5$ are known (eg. Gunn *et al.* 1986). Very few systematic studies of the most distant A bell clusters ($z \approx 0.2$) have so far been attempted though these form the largest sample of distant clusters known as yet.The main aim of the present paper is to systematically study the radio properties of a fairly large and complete sample of most distant Abell clusters (Distance class D = 5,6 or $0.1 \lesssim z \lesssim 0.3$) known to contain cD galaxies in their central regions. No systematic radio survey of Abell clusters of such distances and morphology is available at present. Recently Ball *et al* (1993) have reported the results of a 6 centimeter VLA survey of about 90 Abell clusters of cDClass of a lower redshift range ($z < 0.10$).

In the present paper the results of our analysis of radio properties of central cD galaxies in distant Abell clusters are reported. The full catalogue and details of the nature of other radio sources in the direction of these clusters would be presented in a subsequent paper (under preparation). The section-wise division of the present paper is as follows. Section 2 contains the details of sample of clusters selected for study. Observations and the data reduction procedure are described in section 3. Section 4 presents the radio images, and the basic radio and optical data. The scientific results and their discussion are presented in sections 5,6,7, and 8, where we also discuss the possibility of further future work and in section 9, the main conclusions of this study are summarised. We have assumed an Einstein-de Sitter Cosmology ($\Omega = 1$, $q_0 = 0.5$) and 50km sec^{-1} Mpc^{-1} for the Hubble constant. Thus, 1 second of arc corresponds to 3.3 Kpc at the redshift $z = 0.15$.

2. Sample selection

We attempted to study a fairly large statistical sample of Abell clusters containing cD galaxies. All of the clusters observed were selected from amongst those in the largest distance classes ($D \geqslant 5$) of Abell's catalogue. The main reasons for this selection criterion were as follows. First, due to an intrinsic rarity of clusters dominated by a giant cD galaxy (Bautz-Morgan Class I), a large statistical sample can only be formed by going to the most distant clusters in Abell's catalogue. Secondly, the. angular size subtended by distant clusters is comparatively smaller, enabling us to map the whole cluster field without a large loss of detection sensitivity caused by the primary beam attenuation of radio dishes. The relatively smaller angular extents of distant clusters also imply a smaller probability of a chance coincidence of an unrelated source in the direction of the cluster at a constant flux density level. Lastly, the clusters selected should not be biased in any way towards their radio or X-ray properties. The only safe way of ensuring this is to select clusters from optical catalogues, as was done here. The clusters were selected from the listing of Leir & van Den Bergh (1977) who have classified all the clusters included in the original Abell's statistical sample into the Bautz-Morgan classes (see Bautz & Morgan 1970 for details). The clusters so selected are:

- Classified as BM type I or I**: (**i.e**.** contain a giant, first ranked cD galaxy).
- North of declination $\delta = -27°$ (the limit of Palomar Plates).
- Classified to have a distance class 5 or larger, corresponding to estimated redshift range $0.1 \lesssim z \lesssim 0.3$ (as derived by Leir & van Den Bergh 1977).
- Of a richness class $R \geqslant 0$.

The 49 clusters satisfying these criteria were selected for observations with the VLA at 20 cm and 90 cm wavelengths.

3. Observations and data reductions

The observations were carried out with the VLA radio telescope (Napier, Thompson & Ekers 1983). The array was in its C/D configuration during 20 cm observations (04 April 1988) and in the A/B configuration (17 February 1989) for the 90 cm observations. Due to constraints of available time and scheduling, 46 of the 49 clusters selected were actually observed at 20 λ cm 2. Only 34 of these could be observed also at 90 cm λ The observations were made with a bandwidth of 50 MHz at 20 cm (centre frequencies at 1452.4 MHz and 1502.4 MHz) and 3.13 MHz at 90 cm (centered at 333.0 MHz and 327.5 MHz**).** The centre of each cluster was tracked by the telescopes in the array, on the average for a total duration of about 15 minutes. During this interval visibilities on all baselines were averaged for 30 seconds to obtain $\approx 10^4$ visibilities for each cluster. Nearby strong point sources were observed roughly every half an hour to serve as phase calibrators.

The observations were bootstrapped to the flux density scale of Baars *et al.* (1977) using either 3C286 or 3C48 as the primary flux density calibrators. Subsequent to initial calibration, the u-v data were edited to remove any discrepant amplitude points. Data in the two IFs were then combined and the visibilities Fourier transformed and the point spread function deconvolved from the maps using the AIPS task MX. Two to three passes of phase self-calibration were performed to correct the visibility phases before the final images were produced. The final maps were of size 512 × 512 pixels (≈ 50 arcmin × 50 arcmin) at 20 cm and 1024 × 1024 pixels (≈ 3.4° × 3.4°) at 90 cm. These large map sizes were necessary to remove the effects of sidelobes of all the sources within the primary beam area. The final maps at 20 cm λ were made by convolving the clean components with circular Gaussian beams of 30″ × 30″ FWHM size (with 30% visibility tapering at longest baselines). The full resolution of 90 cm observations could not be achieved due to a lack of necessary computing power. Therefore, the final resolution of the 90 cm images was 60″ × 60″ FWHM, achieved after heavily tapering the measured visibilities. The list of clusters observed at the two frequencies is given in the first column of Table 1.

The observed r m.s noise fluctuation on the final 20 cm maps was generally between 0.05 and 0.15 mJy/beam which is close to the expected level of thermal noise. The 90 cm maps generally had r.m.s noise levels of about 1 to 2 mJy/beam, considerably higher than the expected thermal noise. This is mainly caused by the presence of many strong sources within the wide field of view and due to closure phase errors at 90 cms. We have adopted a conservative 12 σ signal requirement for 100% completion for unresolved radio sources near the image centres. This then implies that most 20 cm images are complete down to ~ 1 m.Ty whereas, most 90 cm images are

complete down to ~ 15–25 mJy. The detailed radio maps and the data on all the sources detected in each field will be presented in a separate paper. Here we concentrate on those radio sources that were found to be associated with cD galaxies. In order to find such sources the optical positions of the cD galaxies present in the clusters studied were measured on the POSS (Palomar Observatory Sky Survey) E-plates (red filter) using the digital X-Y measuring machine available with the IR/X-ray astronomy group at TIFR, Bombay. We used SAO standard stars near the fields of interest for astrometry. The accuracy of optical positional measurement has an r m.s (σ_0) error range of $\approx$ (0.5 — 4.0) arcsec. We consider a radio source to be identified with a cD galaxy if the radio-optical positional offset (Δ_{R-0}) is less than 2.5 times the combined errors from radio and optical positional measurements, i.e. $\Delta_{R-0} \leqslant 2.5 \times \sigma_{R-0}$

$$\text{where } \sigma_{R-O} = [(\sigma_0)^2 + (\sigma_R)^2]^{1/2}$$

Here σ_R denotes the r m.s error in radio position from the higher resolution 20 cm maps (generally about 1″ arc). Optical positions of the cD galaxies in 6 Abell clusters in this sample could not be measured as the corresponding sky survey prints were not available at Bombay. The optical data on one of these, viz. A1597 was however available from Huchra *et al.* (1990).

4. Radio and optical data on cD galaxies

Amongst the 41 clusters for which we had the optical data, 16 cD galaxies were detected at the wavelength of 20 cm λ Radio maps of the 11 resolved sources (LAS $\gtrsim$ 10 arcsec) at 1.4 GHz are presented in Fig. 1 which also contains maps of 4 cDs that were resolved at 330 MHz as well. Table 1 presents the radio and optical data on the 46 clusters that formed our sample. A blank in certain columns denotes non availability of data. The table is arranged as follows:

Col. 1: The Abell cluster number. An asterisk denotes the non availability of the optical position of the cD galaxy.

Col. 2 and 3: The optical R.A. and Dec. of the cD galaxy in the cluster (epoch 1950.0).

Col. 4 and 5: The flux density of the cD at 20 and 90 cm wavelengths respectively.

Col. 6: The distance of the cD galaxy from the cluster centre as listed in Abell's catalogue, measured in units of Abell radius (R_A).

Col. 7: Logarithm of the 1400 MHz radio luminosity of the cD galaxy in units of WHz^{-1}. If no spectral index information is available, a spectral index $\alpha = 0.75$ has been assumed.

Col. 8, 9,10 and 11: Morphological data on the parent clusters. The redshifts for 20 clusters are based on spectroscopic measurements,(Huchra, privatecommunication), for the other clusters we have used the redshifts estimated by Leir & Van Den Bergh (1977). These estimated values are enclosed in brackets. The BM classification, the distance class (D), and the richness class (R) were taken from the catalogue of Leir & Van Den Bergh (1977).

Table 1. Radio and optical data on cD galaxies.

Cluster designation	cD optical position (1950)						Flux density (mJy)		Distance from cluster center (r/R_A)	$\log(P_{1.4\,GHz})$ (W Hz^{-1})	Cluster data			
	h	m	s	o	$'$	$''$	at 20 cm	at 90 cm			Redshift z	BM type	D Cl.	R Cl.
A22	00	18	11.87	−25	59	16.0	21.4	71.5	0.017	24.29	0.1432	I	6	3
A42	00	26	06.61	−23	55	07.1	1.8	< 20.0	0.009	22.96	0.1087	I	5	3
A77	00	37	48.24	+29	16	53.4	13.3	15.0	0.084	23·45	0.0712	I:	5	1
A122	00	54	57.27	−26	33	04.1	—	—	0.033	< 22.75	0.1128	I:	5	1
A136	01	01	32.22	+24	48	58.5	—	—	0.132	< 23.34	0.1569	I	6	2
A146	01	04	46.48	−11	33	41.3	—	—	0.380	< 23.32	(0.215)	I	6	1
A192	01	21	42.78	+04	11	59.0	—	—	0.131	< 22.82	0.1219	I:	6	2
A214	01	32	02.33	−26	21	39.8	41.4	184.6	0.043	24.63	(0.150)	I	6	1
A261	01	48	54.63	−02	30	17.3	—	—	0.008	< 21.98	0.0467	I	5	1
A360	02	28	49.00	+06	45	40.5	9.3	19.8	0.218	24.42	(0.255)	I	6	2
A394	02	51	28.03	−14	52	00.9	13.6	42.0	0.106	24.54	(0.236)	I	6	1
A447*		—			—		—	—	—	—	(0.179)	I	6	1
A510	04	44	31.21	−21	07	11.2	1.0	< 20.0	0.112	23.00	(0.151)	I	6	1
A690	08	36	13.40	+29	01	17.0	808.0$^+$	1650.0$^+$	0.032	25.33	0.0788	I	5	1
A733	08	57	46.87	+55	51	03.5	32.2	236.6	0.070	24.31	0.1159	I:	6	1
A734	08	57	44.38	+16	26	11.8	53.1	< 20.6	0.122	24.52	(0.129)	I	6	1
A882	09	48	42.57	+08	33	22.0	—	—	0.220	< 22.95	0.1408	I	5	0
A994	10	20	25·27	+19	33	36.5	—	—	0.240	< 22.60	(0.094)	I:	6	1
A1027	10	27	52.36	+53	41	06.1	—	—	0.081	< 23.06	(0.160)	I	5	1

A1068	10	37	50.09	+40	12	50.6	20.1	19.4	0.083	24.19	0.1386	I	5	1
A1277	11	27	25.46	+13	12	49.0	—	—	0.083	< 23.42	(0.240)	I	6	1
A1391	11	47	12.78	−12	02	09.1	—	—	0.021	< 23.26	(0.200)	I	6	2
A1413	11	52	44.00	+23	41	11.0	1.8	< 15.0	0.156	23.22	0.1427	I	5	3
A1508	12	13	29.78	+17	45	39.0	—	—	0.090	< 23.44	(0.125)	I	5	1
A1576	12	34	45.82	+63	27	43.4	—	—	0.186	< 23.62	0.302	I	6	3
A1597**	12	39	16.30	+72	30	10.0	—	—	0.060	< 22.72	0.1096	I	6	1
A1602	12	40	57.36	+27	33	14.4	—	—	0.178	< 23.42	(0.241)	I:	6	1
A1654*		—			—		—	—	—	—	(0.133)	I	5	0
A1738	13	23	15.49	+57	51	36.7	96.6	484.2	0.033	24.76	0.1146	I:	5	2
A1839	13	59	56.15	−04	36	59.5	—	—	0.033	< 23.48	(0.131)	I	6	1
A1954*		—			—		—	—	—	—	0.1810	I:	6	2
A2025	15	04	43.90	+34	39	54.6	185.8	462.9	0.028	25.29	(0.154).	I:	5	1
A2058*		—			—		—	—	—	—	(0.227)	I	6	1
A2364	21	39	14.63	−20	33	45.1	—	—	0.059	< 23.04	(0.129)	I:	6	1
A2381	21	48	46.16	+20	04	01.5	—	—	0.273	< 22.63	(0.098)	I:	5	1
A2397	21	53	35.49	+01	09	10.0	—	—	0.248	< 23.36	0.2240	I	6	3
A2416	22	02	55.14	−25	27	41.6	—	—	0.347	< 23.34	(0.221)	I	6	1
A2420	22	07	37.97	−12	25	02.1	16.6	—	0.058	23.71	0.0838	I	5	2
A2456	22	32	33.62	−15	33	46.6	—	—	0.171	< 23.09	(0.165)	I	5	1
A2521	22	59	30.87	−22	17	32.4	—	—	0.122	< 22.91	0.1359	I	5	2
A2533	23	04	35.70	−15	29	41.7	3.5	—	0.049	23.57	(0.153)	I	5	1
A2575	23	17	23.14	−22	21	03.6	—	—	0.264	< 23.42	(0.242)	I	6	2
A2577	23	18	07.99	−23	15	58.0	—	—	0.078	< 22.85	(0.126)	I	6	1
A2579	23	18	36.95	−21	51	31.3	—	—	0.107	< 22.91	(0.135)	I:	5	1
A2667	23	49	05.11	−26	16	28.8	—	—	0.171	< 23.54	(0.276)	I	6	3
A2694*		—			—		—	—	—	—	0.0958	I:	5	3

*Optical position not available.

+ Due to a large angular size (~ 6 arcmin) of this radio source, our data did not provide accurate flux densities. The 20 cm flux is taken from Harris *et al.* (1980) and the 90 cm flux is estimated using $a = 0.5$ (Harris *et al.* 1980).

**Optical position from Huchra *et al.* (1990).

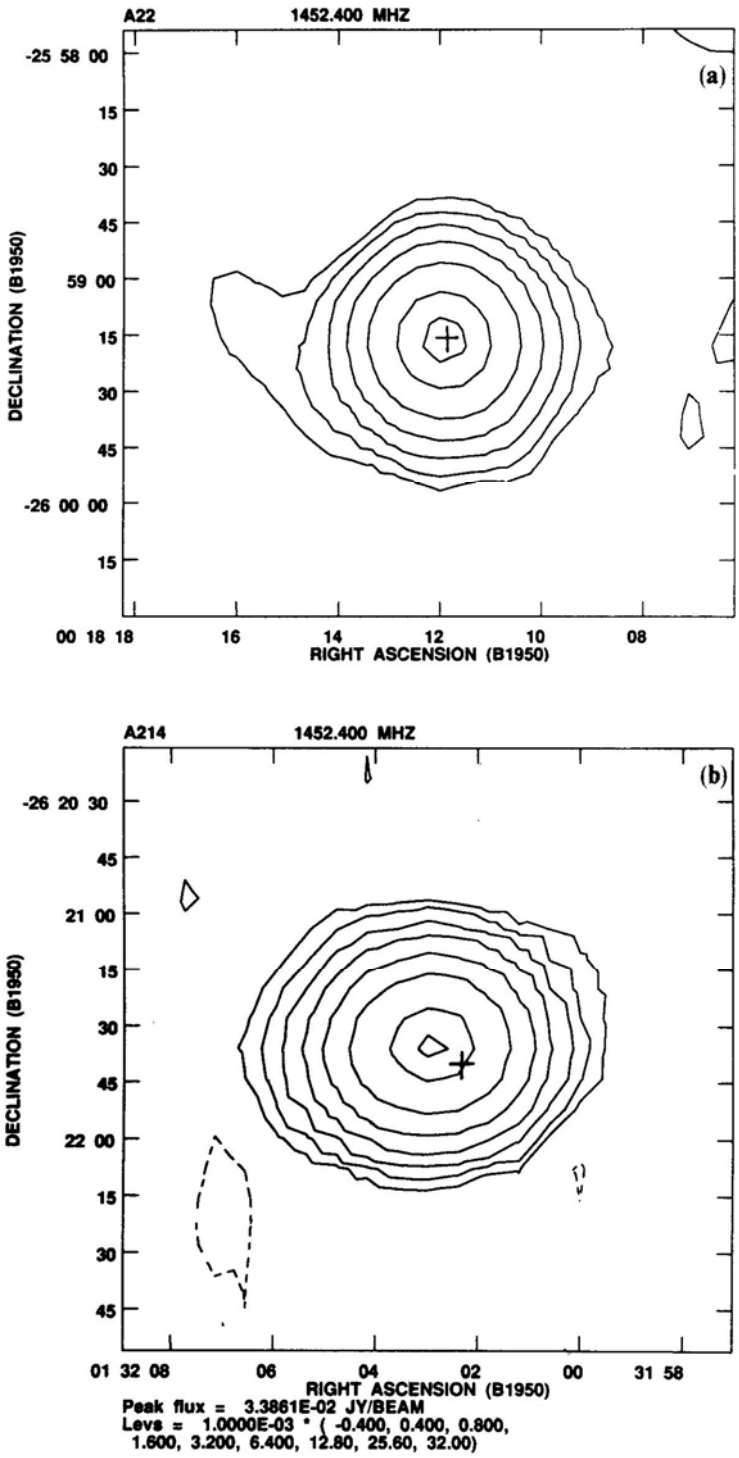
A22
1452.400 MHZ
(a)
-25 58 00
15
30
45
59 00
15
30
45
-26 00 00
15
DECLINATION (B1950)
00 18 18
16
14
12
10
08
RIGHT ASCENSION (B1950)
A214
1452.400 MHZ
(b)
-26 20 30
45
21 00
15
30
45
22 00
15
30
45
DECLINATION (B1950)
01 32 08
06
04
02
00
31 58
RIGHT ASCENSION (B1950)
Peak flux = 3.3861E-02 JY/BEAM
Levs = 1.0000E-03 * (-0.400, 0.400, 0.800,
1.600, 3.200, 6.400, 12.80, 25.60, 32.00)

Figure 1.(**a,b**).

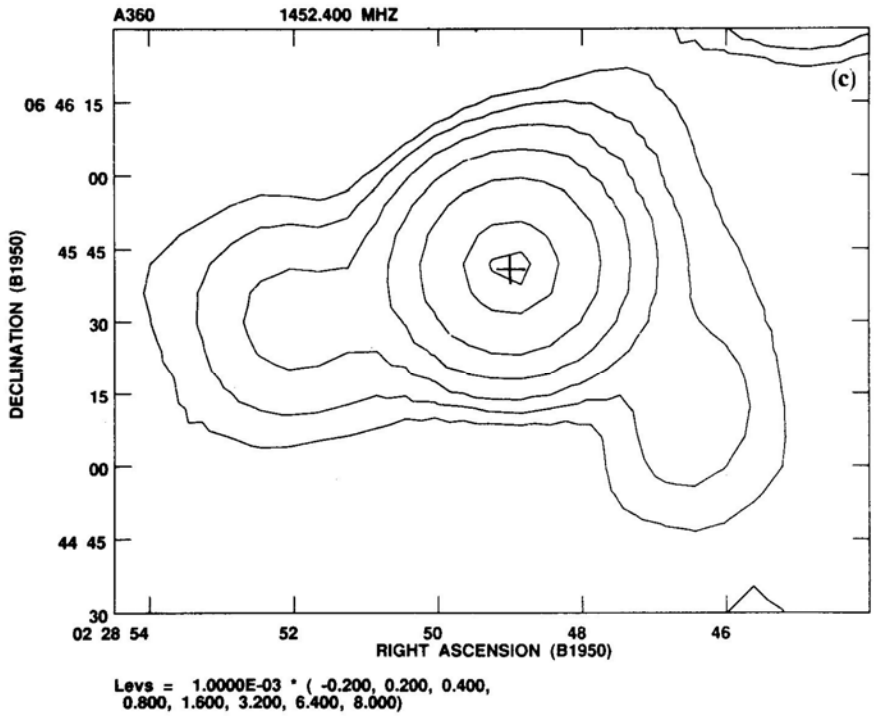
A360
1452.400 MHZ
(c)
06 46 15
00
45 45
30
15
00
44 45
30
DECLINATION (B1950)
02 28 54
52
50
48
46
RIGHT ASCENSION (B1950)
Levs = 1.0000E-03 * (-0.200, 0.200, 0.400,
0.800, 1.600, 3.200, 6.400, 8.000)

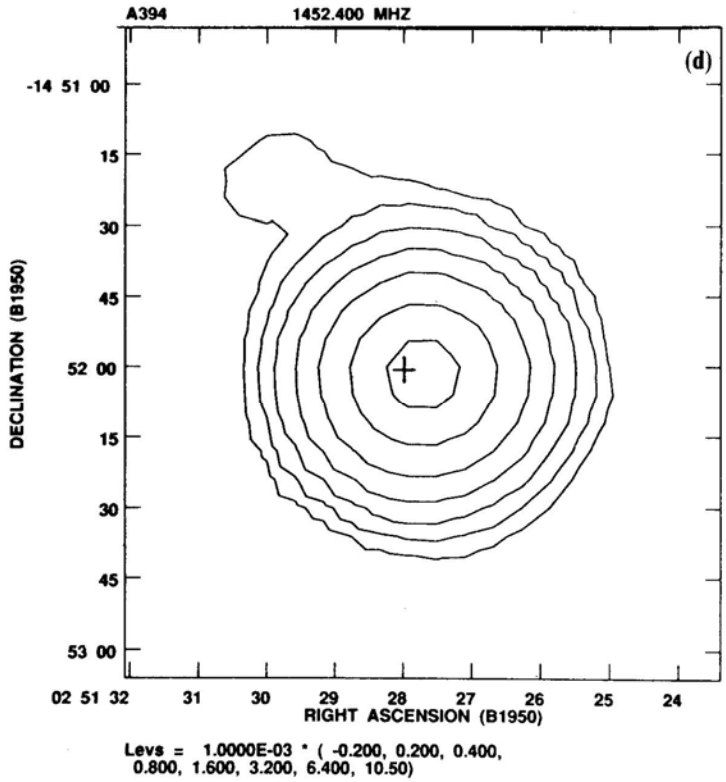
A394
1452.400 MHZ
(d)
-14 51 00
15
30
45
52 00
15
30
45
53 00
DECLINATION (B1950)
02 51 32
31
30
29
28
27
26
25
24
RIGHT ASCENSION (B1950)
Levs = 1.0000E-03 * (-0.200, 0.200, 0.400,
0.800, 1.600, 3.200, 6.400, 10.50)

Figure 1 (c,d).

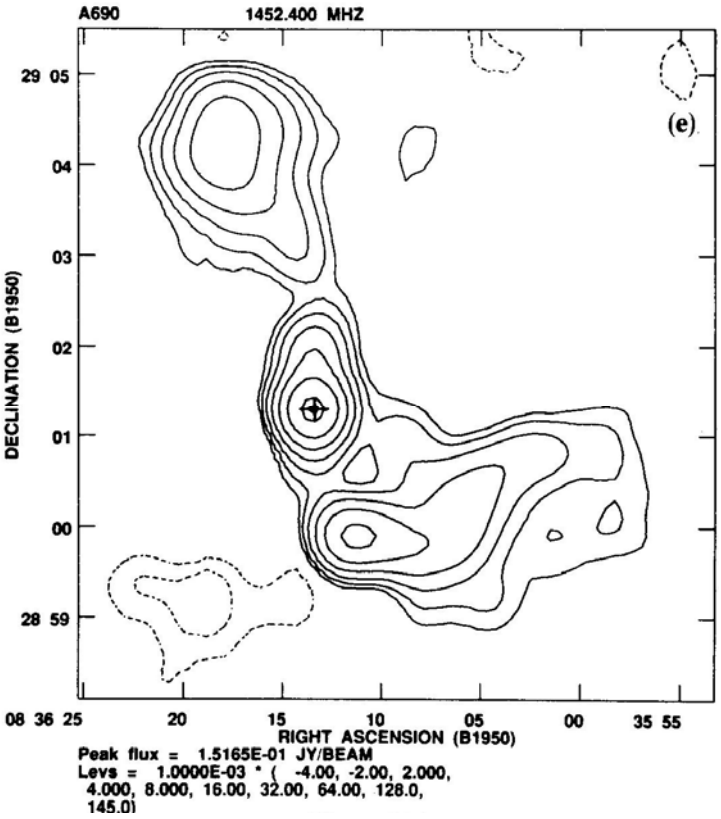

Figure 1 (e).

5. The radio luminosity function of cD galaxies

The radio luminosity function (RLF) of a class of objects is useful in estimating the probability of energy emission across a wide range of radio luminosities and can be used to study the effects of variable environmental factors on this probability. Here we construct the 1.4 GHz fractional RLF of cD galaxies, using the information given in Table 1. We use only the 41 clusters in which the optical positions of the cD galaxies were available. The estimated probability that a cD galaxy would be found to have a luminosity within the range P_{14} to P_{14} + d P_{14} (where P_{14} is the radio luminosity in units of WHz^{-1} at 1.4GHz) is the so called differential radio luminosity function (DRLF), denoted by $dF(P_{14})$. If the function dF (P_{14}) is integrated over all luminosities greater than a certain value P_{14} [here denoted by $F(> P_{14})$], obtain the integral radio luminosity function (IRLF). Our flux density detection limit of ~ 1 mJy in most of the clusters and the lower redshift limit of ~ 0.05 in our sample, essentially decide the weakest radio luminosity that can be reliably studied. This luminosity is in the range of (21.8 – 22.2) WHz^{-1} in log P_{14}. We construct the fractional DRLF by initially subdividing the radio luminosities into differential intervals of width Δ (log P_{14}) = 0.4. We then calculate, for each differential interval, the ratio of the number of cDs detected to the number that would have been detectable in our survey. This ratio is the DRLF for the given interval.

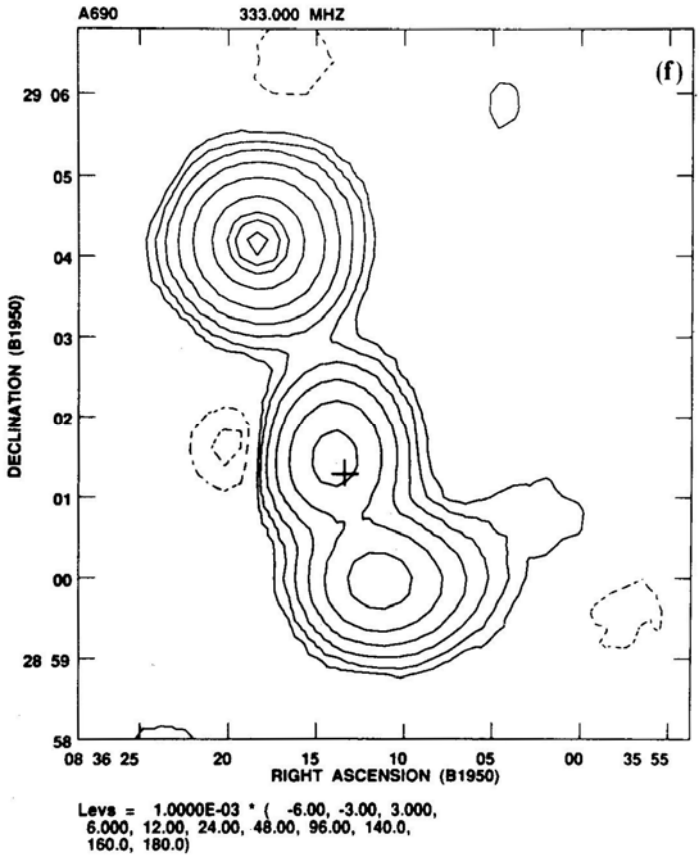

Figure 1 (f).

Table 2 summarises the information on the estimated DRLF and IRLF of cD galaxies observed by us. The graphical forms of these functions are shown in Fig. 2(a) and Fig. 2(b). The errors of estimating DRLF are assumed to be the Poissonian counting errors and the error bars on the IRLF values are obtained by quadratic combination of errors of DRLF. A fairly sharp change in the slope of the IRLF near log $P_{14} \approx$ 24.5 is visible in Fig. 2(b). This change in the slope of RLF at $\approx 10^{24.5}$ WHz^{-1} is also a general behaviour of radio sources associated with bright elliptical galaxies outside rich clusters (Colla *et al.* 1975; Auriemma *et al.* 1977). Auriemma *et al.* (1977) found that irrespective of the optical magnitude of the galaxy, a 'break' occurs at a luminosity between 10^{24-25} WHz^{-1}. A comparison of cD galaxy luminosity function with the local radio luminosity function of brightest ellipticals in absolute photographic magnitude ranges $-22 < Mp < -21$ and $-21 < Mp < -20$ (from Auriemma *et al.* 1977),shows that below.the 'break'at $\approx 10^{24.5}$ WHz^{-1} the cD galaxy function is quantitatively similar to the RLF of brighter ellipticals within errors (see Fig. 2b). However, above the 'break', the brighter elliptical galaxy function appears to be consistently below the RLF of cDs. We also find that the RLF of cDs, when compared with RLF of ellipticals in the magnitude range $-21 < Mp < -20$, clearly indicate a higher probability of radio.emission for all $P_{14} > 10^{22}$

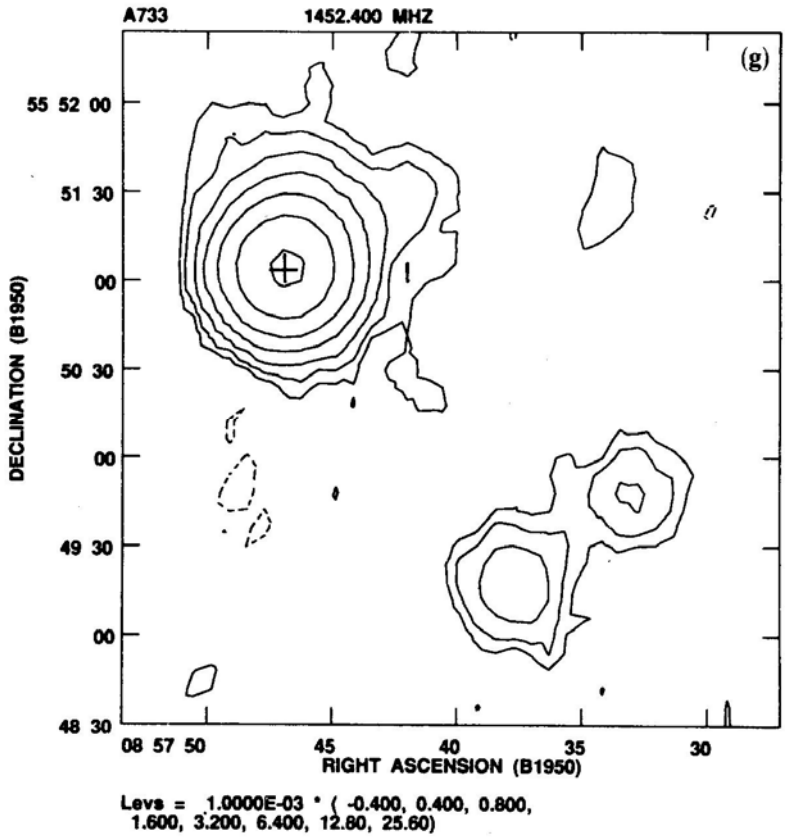

Figure 1 (g).

WHz^{-1} (Fig. 2b). For log $P_{14} > 24.8$ the estimated probability of radio emission is found to be $\approx$ 10 ± 5% for cD galaxies, whereas it is only $\approx$ 3 ± 1% and $\approx$ 0.8 ± 1% in the case of E galaxies in the two magnitude intervals shown in Fig. 2b. Thus it is possible that beyond the 'break' at $\approx 10^{24\cdot5}$ WHz^{-1}, cDs in rich clusters have a somewhat higher probability of being radio sources than that of brightest ellipticals in less-dense environments. Unfortunately, the number of detectable radio sources emitting above log $P_{14} > 25$, is quite small and hence this result needs to be checked using a larger sample of sources.

For giant E galaxies located outside rich cluster environments, a correlation between the probability of radio emission and the optical brightness of the parent galaxy is well known (Colla *et al* 1975; Auriemma *et al* 1977). We have investigated the possibility that the higher probability of radio emission in cDs is related to their larger optical luminosity. The mean absolute visual magnitude of cD galaxies, $< M_v >_{cD}$ was found to be – 23.71 by Sandage (1976). This is converted into mean photographic magnitude $< M_p >_{cD}$ using the relation used by Auriemma *et al* (1977) to obtain,

$$< M_p >_{cD} = < M_v >_{cD} + 1.15 = -22.56. \quad (1)$$

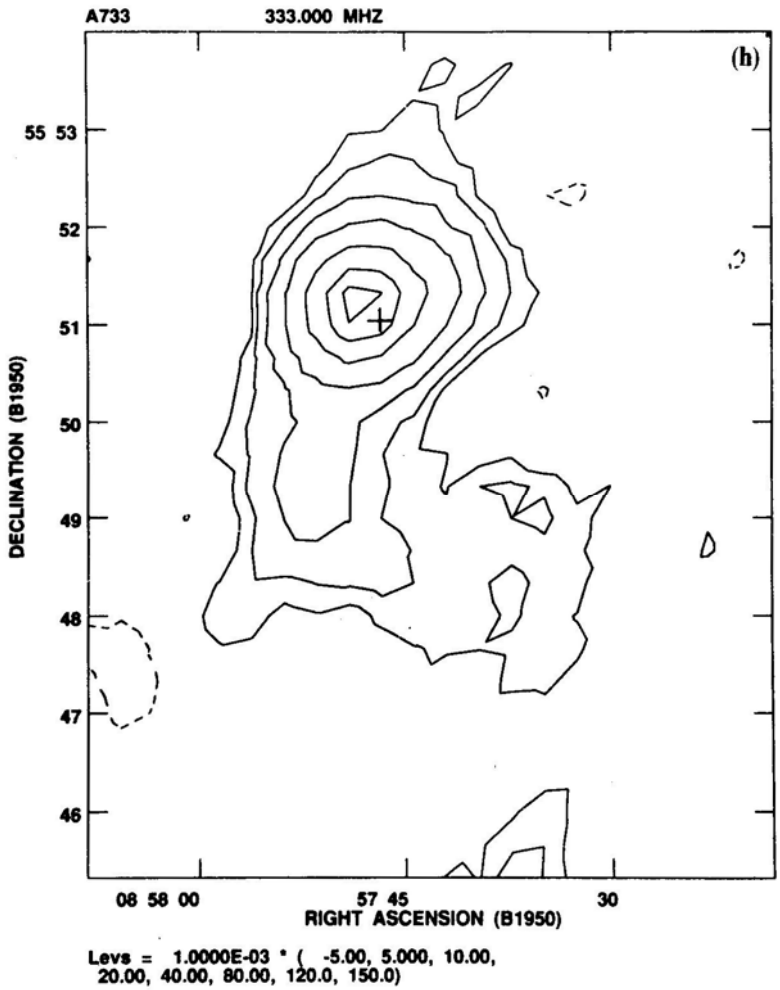

Figure 1 (h).

Now assuming that the bivariate nature of IRLF of brightest radio galaxies is expressible as,

$$\log(F > P_{1.4}) \propto M_p,$$

we derive, from a regression analysis of Auriemma *et al.* (1977) data, the following relationships,

$$\log(F > P_{1.4}) = -18.12 - 0.765(M_p) \text{ at } \log P_{1.4} = 25.0 \text{ and,} \tag{2}$$

$$\log(F > P_{1.4}) = -14.83 - 0.556(M_p) \text{ at } \log P_{1.4} = 25.8. \tag{3}$$

Both these equations have regression coefficient $r > 98\%$. Using these regression relations and using the mean visual magnitude $< M_p >_{cD}$ as calculated above (with an uncertainty of 0.25 magnitudes), we obtain the following estimates of

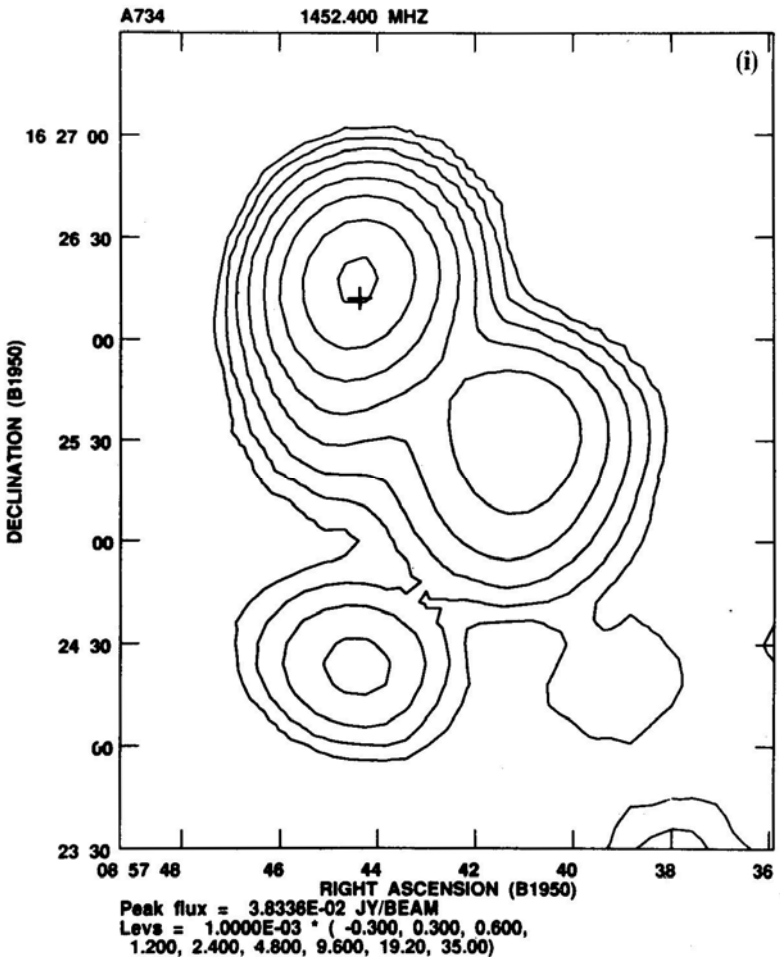

Figure 1 (i)

Probabilities for cD galaxies.

$$(F > P_{1.4}) = 0.138\,(^{+0.076}_{-0.050}),\ \text{at}\ \log P_{1.4} = 25.0\ \text{and},$$

$$(F > P_{1.4}) = 0.005\,(^{+0.002}_{-0.001}),\ \text{at}\ \log P_{1.4} = 25.8.$$

These predicted numerical values are consistent with the observed probabilities of 0.07 ± 0.04, and < 0.024 at same two values of P_{14} (Table 2, Fig. 2(b)). It thus appears that the physical effect that possibly causes the well known radio-optical correlation, also operates in the case of the cD galaxies in rich clusters. In a typical rich Abell cluster, the space density of galaxies at the location of the cD can be a factor of 100 or more larger compared to the density around field ellipticals (Dressler 1980). Despite this vast difference, it is striking to note that the RLFs behave identically. This in turn implies that instead of a global, large scale environmental effect, some physical factor dependent mainly upon the local conditions near a radio galaxy is more important in generating a powerful radio source. The local space

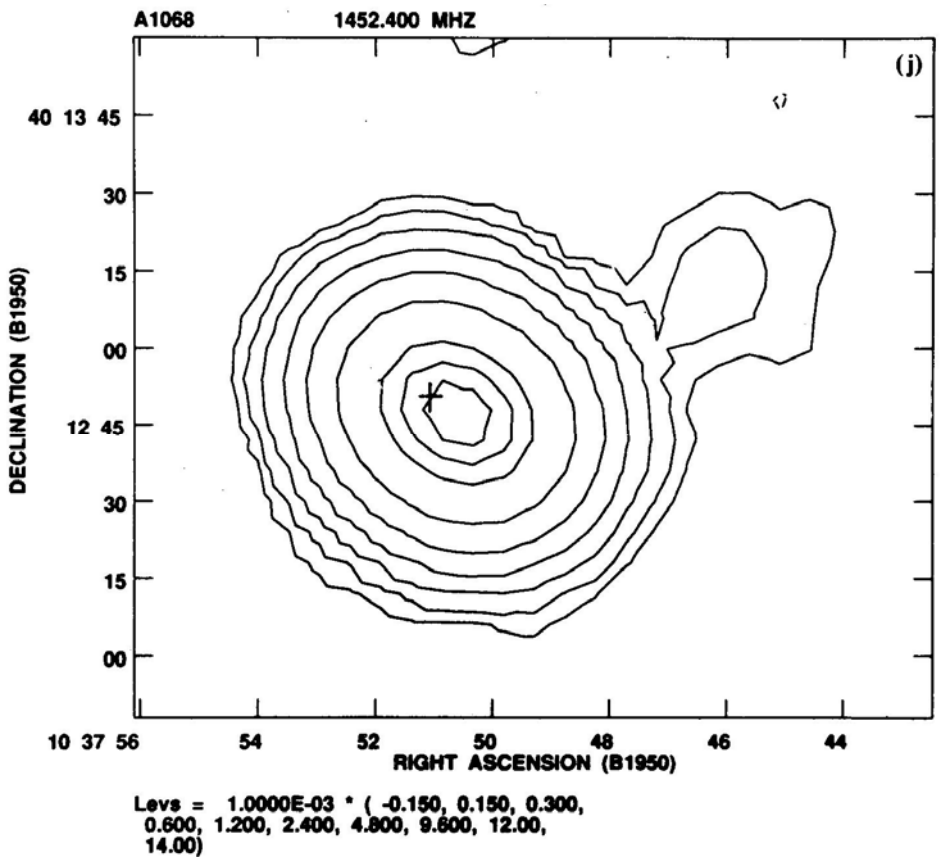

Figure 1 (j)

density of galaxies is unlikely to be this factor because comparison of RLF of ellipticals inside and outside rich clusters fails to indicate any detectable difference (eg. Auriemma *et al* 1977). Similarly, Valentijn & Bijleveld (1983) found that the radio luminosity function of cD galaxies occurring in many poor groups of galaxies is no different from that of elliptical radio galaxies of similar brightness but occurring in sparser regions.

A recent 6 cm wavelength study of a large number of lower redshift ($z < 0.1$) cD galaxies also fails to detect any influence of cluster richness on the radio detection probability (Ball *et al* 1993). This again implies that radio emission probability is more strongly dependent upon the optical brightness of the parent galaxy and less on its global environment. However, it seems clear that P_{14} – Mp correlation is unlikely to be a primary causal relation and is a manifestation of an underlying direct physical relation. The smooth scaling of the probability of radio emission with optical brightness in diverse environments points towards a unified mechanism for triggering of nuclear activity in giant ellipticals and cD galaxies. Our current understanding of the radio galaxies and quasars indicates that the observed rate of energy production is related to the mass of the central super massive object and to the rate at which gas can be fed to the potential well (Begelman *et al.* 1984). Thus, it is possible that the more massive and optically brighter galaxies like cDs that form only in clusters,

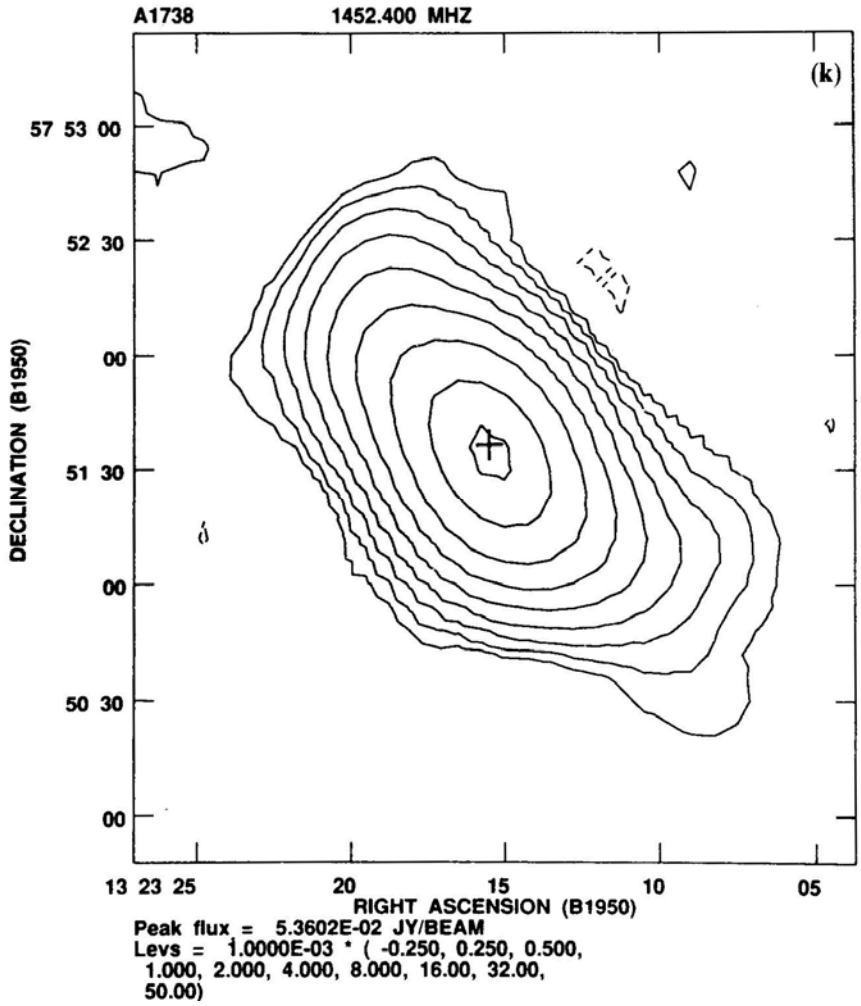

Figure 1 (k).

either harbour more massive central objects or have more efficient fuelling (or both of these), and can thus generate more powerful radio emission. It would be most informative if using high resolution spectroscopic methods, estimates of the masses of the central nuclear regions of these galaxies could be obtained. Some more important clues to the problem can be obtained from the direct study of the fuel for the activity i.e. the gaseous media within and surrounding the radio galaxies. A more detailed study directed towards this aspect is presented in the next section.

6. Radio emission from cD galaxies and cooling flows

As mentioned in the introduction, a strong cosmological evolution in the properties of cosmic radio sources is indicated by observations. It is possible that such effects arise due to dynamical evolution of groups and clusters where such sources are found.

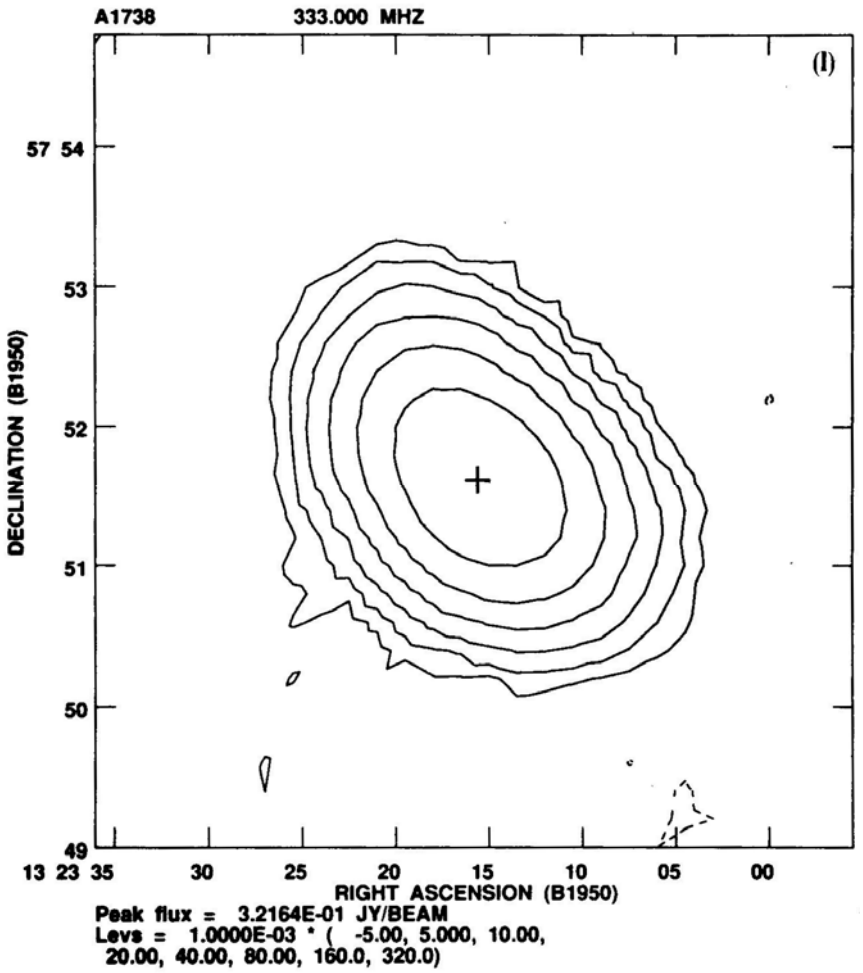

Figure 1 (l).

The quasi-steady flow of cooling gas (inferred from X-ray observations eg. Edge *et al.* 1992) towards cluster centres is a direct proof of the evolving intracluster medium (ICM). cD galaxies are invariably found at the 'focus' of all such 'cooling-flows' (Fabian 1987, and references therein). One of the models of active galactic nuclei invokes the accretion of gaseous medium as fuel for the nuclear source (Begelman *et al.* 1984). It is therefore of interest to investigate this possibility. Here we investigate the influence of the physical state of the ICM on radio emission from the central cD galaxies. Previously, a tendency for the occurrence of strong radio sources in X-ray luminous clusters has been noticed by Valentijn & Bijleveld (1983), and Burns (1990) has reported that cD radio sources are more probable in clusters with possible cooling flows. As yet no detailed X-ray data are available for the distant Abell clusters forming our sample. However, the radio and X-ray data already existing for the low-z cD clusters can provide a useful model of physical processes against which we can compare our radio results. Thus, from published literature we have formed a sample of clusters for which high sensitivity X-ray and radio data (mostly available at 4.8 GHz) are

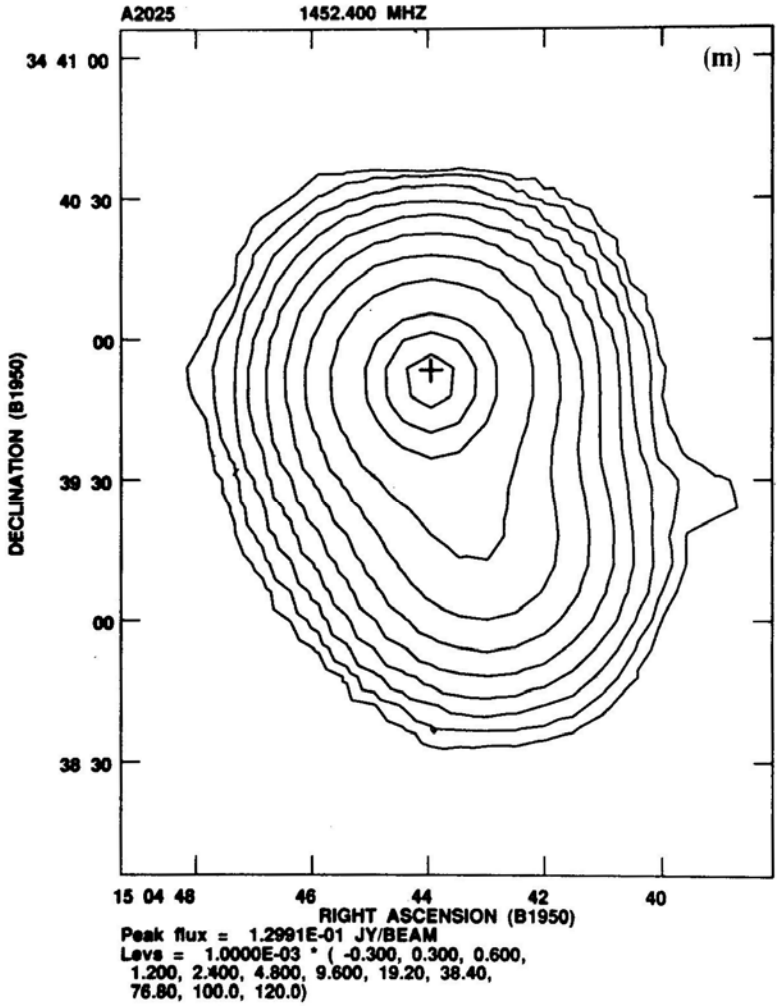

Figure 1 (m).

available. The main body of data comes from Burns (1990). The radio and X-ray data for cD galaxy PKS 2345–35 is from Schwartz *et al.* (1991) and radio data on the cD galaxy 3C318.1 in the poor cluster MKW3S is from our VLA observations of very steep spectrum radio sources (under preparation), and the X-ray data is from Kriss *et al.* (1983). The derived physical quantities pertaining to these clusters (cooling time, gas pressure etc.) are again taken from above references. Table 3 summarises this data which is organised as follows.

Col. 1: The cluster designation.
Col.2: The ratio of cooling time ($t_{\rm cool}$) to Hubble time ($t_{\rm Hubble}$ =H_0^{-1}) for the ICM in the cluster core.
Col. 3: The redshift of the cluster.
Col. 4: The 4.8 GHz radio luminosity of the cD galaxy or an upper limit.
Col. 5: The radio spectral index (α) of the cD between 4.8 GHz and 1.4 GHz (when available); here flux density $\propto$ (frequency)$^{-\alpha}$.

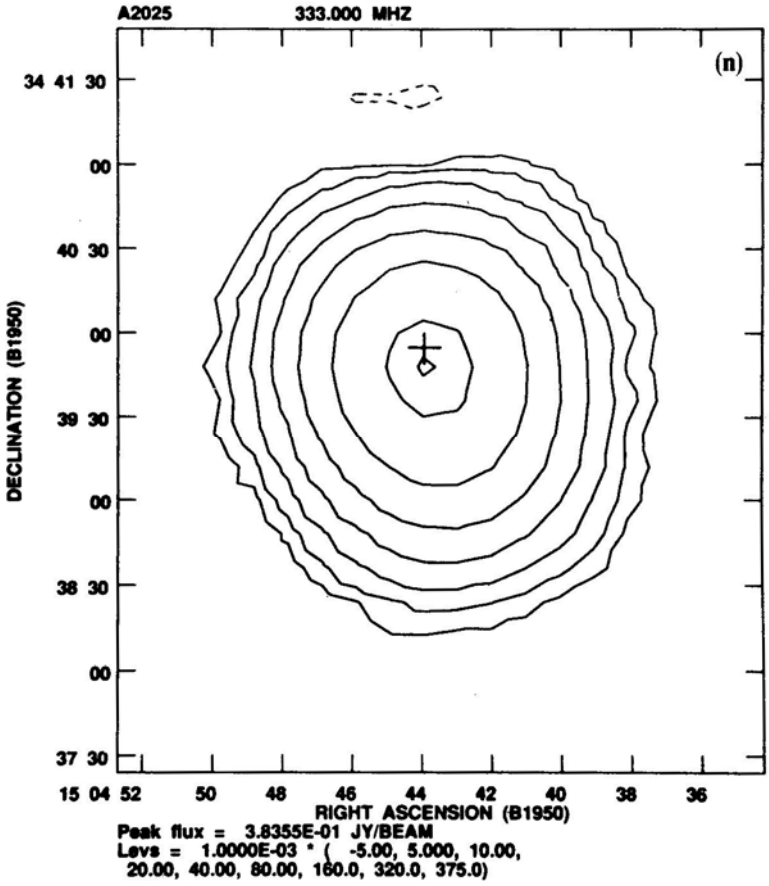

Figure 1 (n).

Col. 6: A code whether a cooling-flow exists $\left(\text{Y, if } \frac{t_{\text{cool}}}{t_{\text{Hubble}}} < 1\right)$ or not $\left(\text{N, if } \frac{t_{\text{cool}}}{t_{\text{Hubble}}} \geqslant 1\right)$.

Col. 7: The gas pressure of the ICM in the cluster core.

It is seen from Table 3 that the cooling time at the centres of many clusters is less than the Hubble time ($t_{\text{cool}} < t_{\text{Hubble}}>$ where $t_{\text{Hubble}} \approx 2 \times 10^{10}$ yr for H_0 = 50km sec $^{-1}$ Mpc $^{-1}$). These are the clusters in which there is a strong possibility of finding a cooling-flow in operation. The implied mass inflow rate generally is in the range of ($10M_{\odot} - 500M_{\odot}$) y $^{-1}$ (Fabian 1987). Can a massive flow of cool gas towards the cluster core influence the radio emission from cD and other galaxies? To investigate this, we plot the 4.8 GHz radio luminosity of cDs (P_{48} in WHz^{-1}) versus the normalised cooling time $\left(\frac{t_{\text{cool}}}{t_{\text{Hubble}}}\right)$ in Fig. 3. Clearly, despite a substantial scatter, There is an anti- correlation between log (P_{48}) and log $\left(\frac{t_{\text{cool}}}{t_{\text{Hubble}}}\right)$. A least square

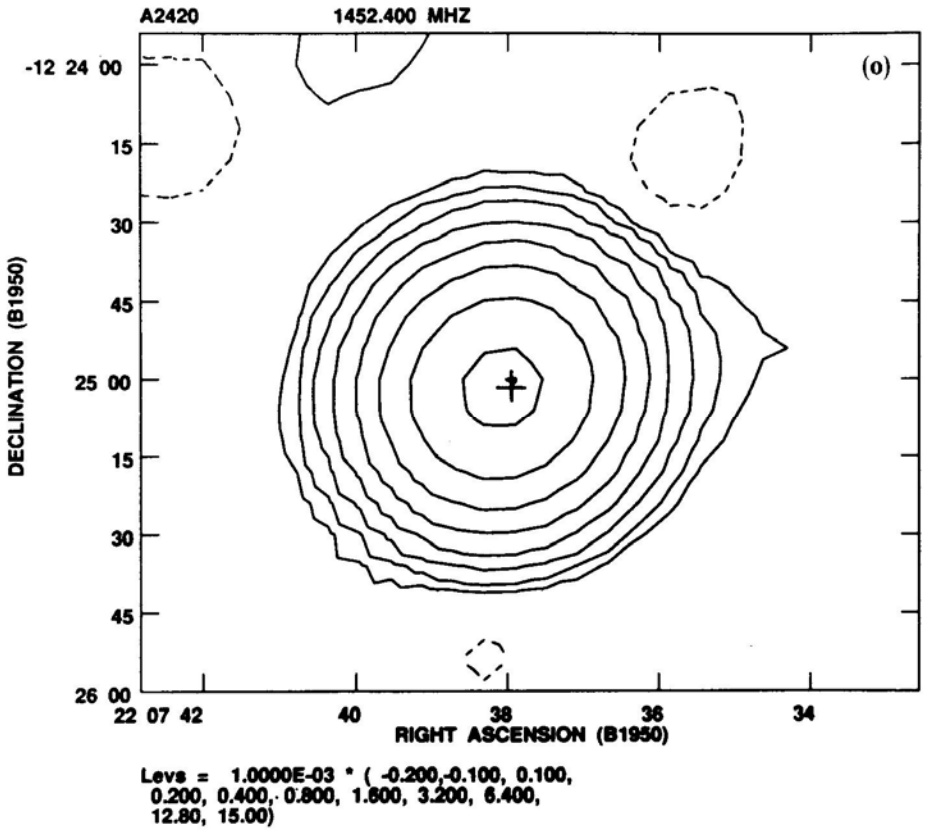

Figure 1 (o).

Figure 1 a-o. Radio maps of 11 resolved sources (LAS $\gtrsim$10 arcsec) at 1.4 GHz and 4 sources also resolved at 330 MHz. The FWHM sizes of the CLEAN beams are 30 arcsec × 30 arcsec at 1.4 GHz and 60 arcsec × 60 arcsec at 330 MHz. The optical position of the cD galaxy is marked by a + symbol and each map contains the cluster name at upper left corner. The peak of the flux density and the contour levels in Jy units are indicated at the bottom. The peak flux density in some maps (not listed at the bottom), in units of mJy/beam is as follows: A22:20.0mJy/beam; A360:8.4; A394:12.3; A690(0.33GHz): 189.7; A733(1.4GHz):28.8, (0.33 GHz) 159.6; A1068:15.4; A2420:15.1.

regression analysis of the data yields the following relation having a regression coefficient r = 0.78 (including the upper limits).

$$\log(P_{4.8}) = 22.31 - 1.69 \times \log\left(\frac{t_{\rm cool}}{t_{\rm Hubble}}\right) \quad (4)$$

It was noted by Owen *et al.* (1984) that wide-angle tailed (WAT) sources have large angular sizes and are radio luminous but tend to avoid cooling-flow clusters. The same is true for two WAT sources shown in Fig. 3. Burns (1990) also notes this feature and points out that these sources are morphologically distinct. The physical cause of this effect is not yet known but the mechanism responsible for the origin and the shape of these sources is separate from other cD radio sources. In view of this uncertainty, we have excluded two WAT sources and confined ourselves to the

Table 2. Differential and integral RLF of cD galaxies.

Log($P_{1.4}$) (Watt/Hz)	Number surveyed	Number detected	DRLF	(error)	IRLF	(error)
21.8 – 22.2	01	0	—	—	0.438	(0.113)
22.2 – 22.6	03	0	—	—	0.438	(0.113)
22.6 – 23.0	22	2	0.091	(0.064)	0.438	(0.113)
23.0 – 23.4	33	1	0.030	(0.030)	0.347	(0.093)
23.4 – 23.8	41	3	0.073	(0.042)	0.317	(0.088)
23.8 – 24.2	41	1	0.024	(0.024)	0.244	(0.077)
24.2 – 24.6	41	5	0.122	(0.055)	0.220	(0.073)
24.6 – 25.0	41	2	0.049	(0.034)	0.098	(0.048)
25.0 – 25.4	41	2	0.049	(0.034)	0.049	(0.034)
25.4 – 25.8	41	0	< 0.024		< 0.024	

Arrangement of Columns:

1. Log radio luminosity at 1.4 GHz in Watt/Hz.
2. Number of clusters surveyed.
3. Number of clusters detected.
4. Differential RLF with errors in brackets.
5. Integral RLF with errors in brackets.

'average' cD radio sources. From equation 4 above, it is implied that cD radio sources with $\log(P_{4.8}) \gtrsim 22.31$ WHz^{-1} occur more often ($\approx 65 \pm 20\%$) in clusters with $\left(\frac{t_{cool}}{t_{Hubble}}\right) < 1$, or those with cooling flows. The corresponding value of this radio luminosity at 1.4 GHz is $\log(P_{1.4}) = 22.7$ WHz^{-1} for a spectral index $\alpha = 0.75$. This is just about the weakest radio luminosity that can be detected in our more distant ($z > 0.1$) sample of cD clusters. From the derived RLF of these cDs (see Table 2, Fig. 2), we expect $\approx 40\% \pm 10\%$ of galaxies to have associated radio sources with $\log(P_{1.4}) > 22.7$ WHz^{-1}. Thus, it appears that the probability of radio emission from cDs in cooling flows is slightly higher than that of average cluster cDs. Valentijn & Bijleveld (1983) also present evidence for enhanced probability of radio emission from cDs in X-ray bright (an indirect evidence for a probable cooling flow) clusters of galaxies. The association of radio sources occurring in SO, E and cD galaxies with the cooling time of the ICM was investigated by Zhao *et al.* (1989) but they failed to find any significant correlation. It is quite likely that the cooling time versus radio power correlation holds only for cD galaxies which occupy a unique central position in cooling flow systems. Thus, we conclude that the physical state of the intracluster medium influences the probability of radio emission from cD galaxies. Powerful radio sources appear more likely to originate in clusters with cooling cores and the radio luminosity correlates inversely with the cooling time of the ICM. Two possible physical causes capable of producing such a correlation are: (i) the dense gas of a cooling-flow surrounding a cD galaxy leads to an efficient confinement of the radio plasma, rendering it visible due to prevention of adiabatic expansion losses; (ii) a fraction of the cool gas is accreted by the cD galaxy which then fuels the central engine of its active nucleus.

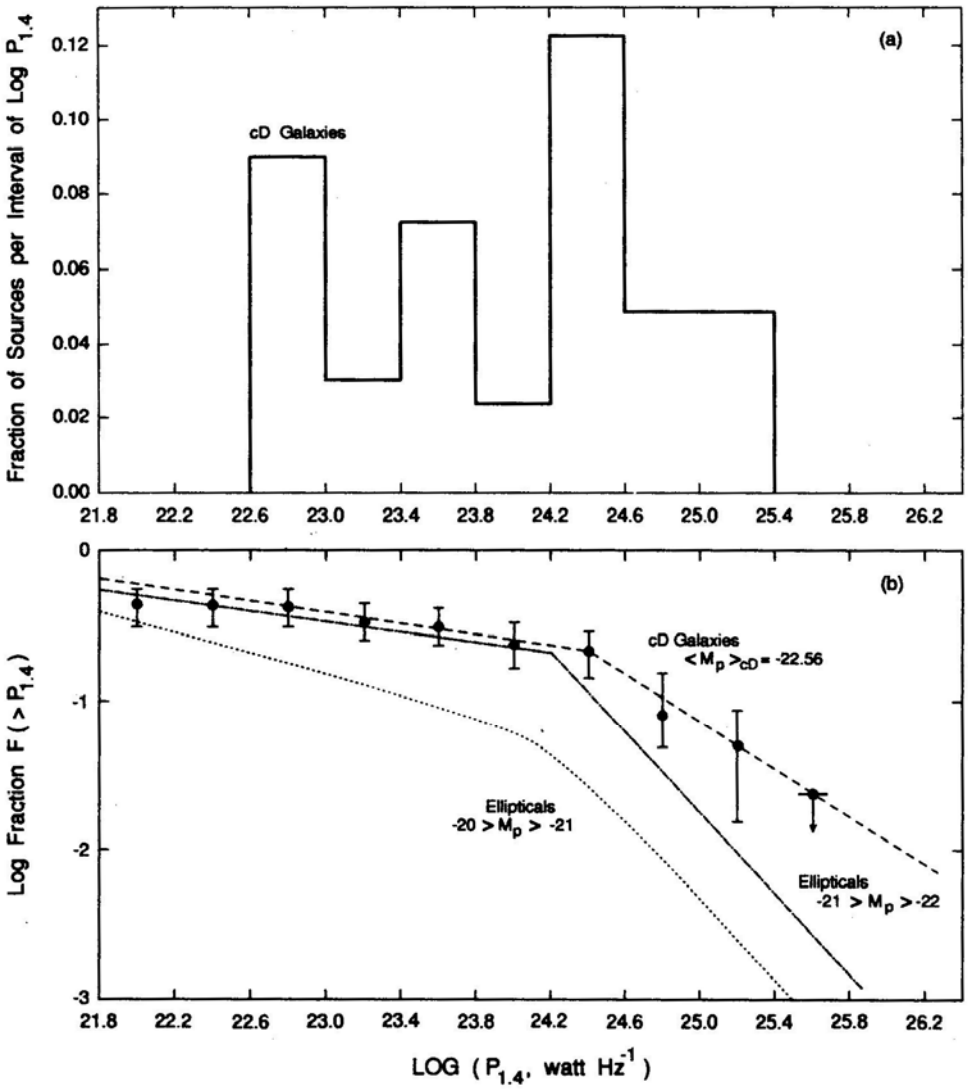

Figure 2. The differential **(a)** and integral (**b**) radio luminosity function for cD galaxies at 1.4 GHz. In Fig. 2(b) the dashed curve shows the best fitting function for the cD galaxies and the dot-dashed and dotted curves represent the functions for giant elliptical galaxies in the photographic magnitude ranges (– 22, – 21) and (– 21, – 20) obtained from the data of Auriemma *et al.* (1977).

We note that both the confinement and fuelling of a cD radio source can happen simultaneously by the ICM. The gas pressure of the ICM, $P_{gas} = n_e$ k T_g for electron density n_e and temperature T_g. The data on P_{gas} in Table 3 show that the average P_{gas} for cooling flow clusters is $\approx 4 \times 10^{-11}$ dyn cm $^{-2}$ as against $\approx 3 \times 10^{-11}$ dyn-cm^{-2} for non-cooling flow ones. Thus, given the uncertainties, the gas pressure is not much different in two types of clusters and is capable of confining all but the most luminous and compact of radio sources. This implies that thermal confinement

Table 3. Data on cD clusters with X-ray emission.

Cluster	$\frac{t_{cool}}{t_{Hubble}}$	Redshift (z)	Log radio lumin. P_6(W Hz^{-1})	Spectral index α	Cooling flow (Y/N)	Gas pressure $\times 10^{-11}$ dyn $-$ cm^{-2}
0745 – 191	0.1	0.1028	25.25	1.36	Y	19.3
MKW3S	0.4	0.0434	22.28	< 0.83	Y	1.1
PKS 2345 – 35	0.2	0.0480	23.99	—	Y	6.7
A85	0.4	0.0518	23.13	1.08	Y	5.1
A133	0.4	0.0570	22.99	2.82	Y	1.9
A399	4.8	0.0715	< 21.77	—	N	5.0
A401	1.0	0.0748	< 22.05	—	N	3.9
A496	0.1	0.0316	23.34	0.20	Y	1.4
A644	0.5	0.0781	< 21.78	—	Y	2.4
A671	1.7	0.0497	< 21.35	—	N	1.0
A1650	2.7	0.140	< 22.40	—	N	6.1
A1767	0.7	0.0756	< 21.74	—	Y	1.2
A1795	0.2	0.0621	24.59	1.07	Y	4.5
A1809	3.2	0.0788	< 21.90	—	N	1.4
A1890	> 1.0	0.0580	< 21.59	—	N	1.0
A2029	0.3	0.0767	24.38	1.31	Y	4.7
A2052	0.1	0.0345	24.68	1.23	Y	1.2
A2063	0.2	0.0337	21.86	2.28	Y	1.3
A2107	1.9	0.0421	< 21.24	—	N	2.0
A2124	2.0	0.0669	< 21.52	—	N	0.9
A2199	0.2	0.0305	24.32	1.35	Y	3.5
A2244	0.6	0.0997	< 21.82	—	Y	3.6
A2271	8.3	0.0616	< 21.48	—	N	1.4
A2319	1.8	0.0529	< 21.41	—	N	9.5
A2420	2.0	0.0838	23.21	—	N	2.5
A2593	2.8	0.0440	< 21.20	—	N	0.8
A2626	0.8	0.0562	23.03	1.37	Y	1.6
A2634	2.3	0.0322	25.10	0.70	N	0.6
A2670	2.0	0.0749	22.71	—	N	2.8

is unlikely to be a sufficient factor. However, confinement is necessary or else the lifetime of sources would be « 10^8 years due to adiabatic expansion losses. The fairly steep spectral indices ($\alpha \gtrsim 1.0$) for the cases where these are measured (Table 3) also indicate efficient confinement. In section 8 a more detailed analysis of observable effects of confinement is presented.

A definite proof for fuelling is difficult to obtain because once the gas cools below the X-ray emission temperature ~ 10^6 K, its fate is not clearly known (Fabian *et al.* 1984, 1991). The gas can eventually get accreted by the central galaxy as its virial temperature (~ 10^7 K) is of the same order as the cold gas of a cooling flow. As little as a few $M_\odot$ y^{-1} of gas supply is enough to fuel the active nuclei of most powerful radio sources. In order to accrete efficiently, the speed of the galaxy relative to cluster medium must be small ($\lesssim$ 100 km sec $^{-1}$) and thus cluster members located near the deepest regions of potential wells would be efficient accretors. The location of the cD galaxies and other giant ellipticals near the centre of cluster potential wells (Dressier 1980), and the observation that radio sources are also found most often

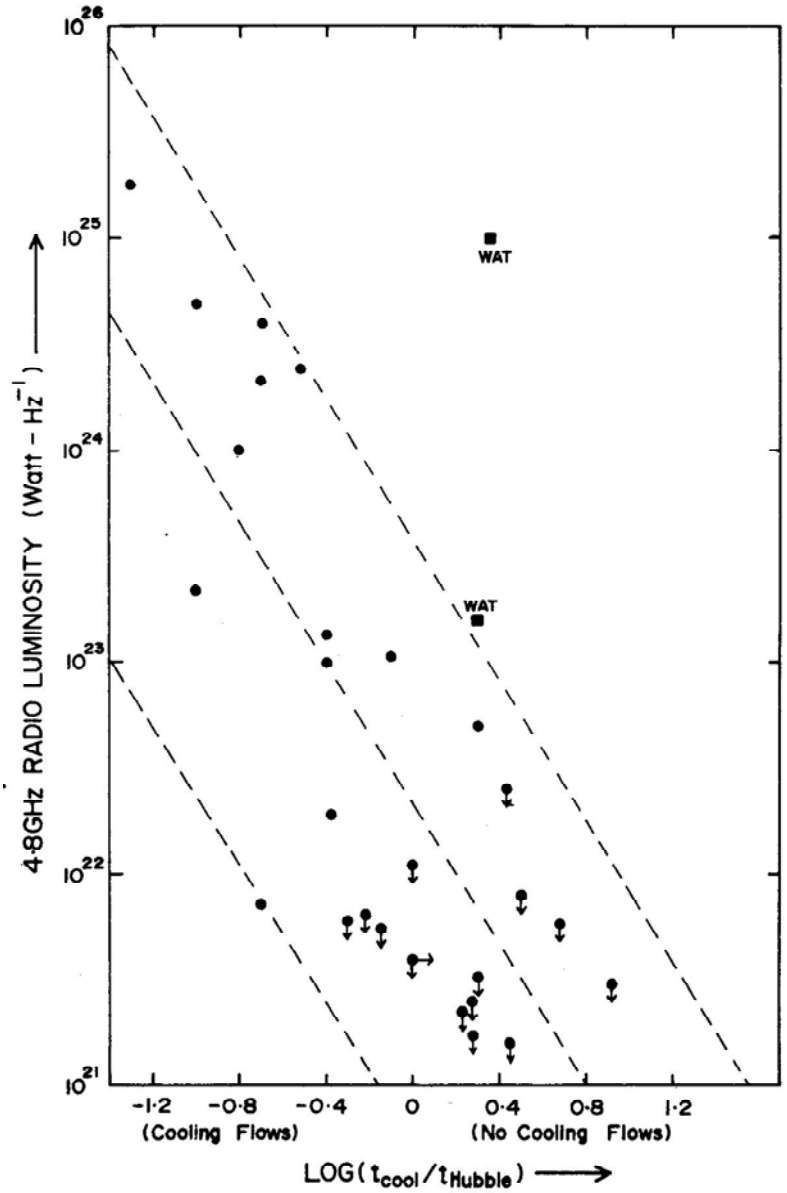

Figure 3. Plot of the radio luminosity of cD galaxies versus cooling time of the intracluster gas in the clusters. Radio luminosity at 4.8 GHz (in WHz^{-1}) is plotted against the log normalized cooling time (t_{cool}/t_{Hubbie}) for the intracluster medium in the cluster core. Upper limits on radio luminosities are indicated by arrows. The central dashed line is the best fitting regression line described in the text and the other two dashed lines represent the upper and lower envelopes. Two wide-angled-tailed (WAT) radio sources are shown by a filled square symbol.

near the cluster centres (McHardy 1979), are strong supportive evidences for the accretion hypothesis.

Optical observations of radio loud quasars indicate that their host galaxies havelight profiles of giant elliptical galaxies (eg. Hutchings *et al.* 1981) and for $z \gtrsim 0.5$,

they tend to lie in clusters of richness comparable to Abell clusters (Yee & Green 1987). The presence of massive cooling flows in the extranuclear regions of many of these quasars is indicated by the detection of extended emission line gas in pressure equilibrium with the external ICM (Crawford *et al.* 1988; Crawford & Fabian 1989). It has been suggested that the sudden fading of radio loud quasars since $z \lesssim 0.5$ is related to the disruption of gas supply available from massive cooling flow systems during the merger of subunits containing such quasars (Fabian & Crawford 1990). The final end products of such evolution in clusters are the massive cD like galaxies lying at the centres of more dynamically evolved clusters. Thus, the presence of massive cooling flows in low redshift clusters and the evidence of a correlation between the radio luminosity and cooling time strongly suggest that due to the revival of cooling flows in dynamically evolved clusters, the radio emission from the central regions of massive galaxies is also being revived. The evidence presently available to us is supportive of the accretion hypothesis. It would be quite useful if the link between the radio emission from central galaxies in clusters and the cooling flows could be further investigated by the radio and X-ray wavelength study of a larger sample of clusters spanning a wider range in redshift. A recent X-ray observation in this direction indicates a factor ~ 2 decline in number of cooling flows since $z = 0.3$, presumably due to subcluster mergers (Donahue *et al.* 1992). A further investigation of the relationship between the radio emission from cDs and the cluster dynamics is presented in the next section.

7. Link between cD galaxy location and radio emission

In this section we investigate, whether the location of a cD galaxy with respect to the centre of the cluster has any effect on its radio emission. This question is motivated by the fact that we are attempting to understand the nature of radio emissions from the optically brightest cluster members in rich clusters. X-ray data from the EINSTEIN satellite have already given the important clue that many of the brightest galaxies in clusters are uniquely placed at the centres of gravitational potential wells traced out by the hot intracluster gas (Jones & Forman 1984). Our study regarding the cooling flows in such clusters, presented in section 6, indicates a strong dependence of radio luminosity upon the cooling time of the intracluster medium, which is indicative of the dynamical state (virialized/irregular) of the central region of the cluster. Thus, it is of interest to study the related question of the effect of the position of the brightest cluster galaxies relative to the geometrical centres of cluster (again indicative of the dynamical state of the cluster), upon the radio emission from such galaxies. The geometrical centres of these clusters have already been determined using visual methods by Abell (1958) and Abell *et al.* (1989), and we have used these measurements. The range of uncertainty in these measurements is of the order of 1 to 3 arcmin. We divide the cD galaxies with optically measured coordinates (41 in number, Table 1) into two groups:

- *Radio Louds (13)*; those that have been detected as radio sources at 1.4 GHz, having a radio luminosity equal or above the limit $P_{\rm lim} = 10^{23.45}\mathrm{WHz}^{-1}$ and,
- *Radio Quiets (28)*; the ones that have their 1.4 GHz radio luminosities below this $P_{\rm lim}$

It needs to be mentioned here that the luminosity threshold $P_{\rm lim} = 10^{23\,45}$ WHz^{-1} corresponds to the minimum detectable radio luminosities from the clusters with largest redshifts ($z \approx 0.25$) in our sample. This choice of threshold radio luminosity was made in order to avoid a selection bias causing selection of less radio luminous sources from lowz clusters and viceversa. A K-S test shows that the redshift distributions of the cDs in the two groups are statistically indistinguishable. The distribution of the angular distances of the optical positions of the cD galaxies (r) as measured from their cluster centres is presented in Figs. 4(a) and (b) for radio-quiet and radio-loud cDs respectively. The displayed angular distances are normalised with respect to the Abell radius R_A (R_A = 3 Mpc). It is seen that the distribution of r/R_A for radio-quiet cDs is much wider compared to the radio-louds which are more centrally located. The median value of r/R_A for radio-quiet cDs is found to be $\approx$ 0.13 whereas, for the radio-loud group it is only $\approx$ 0.06. A Kolmogorov-Smirnov test performed

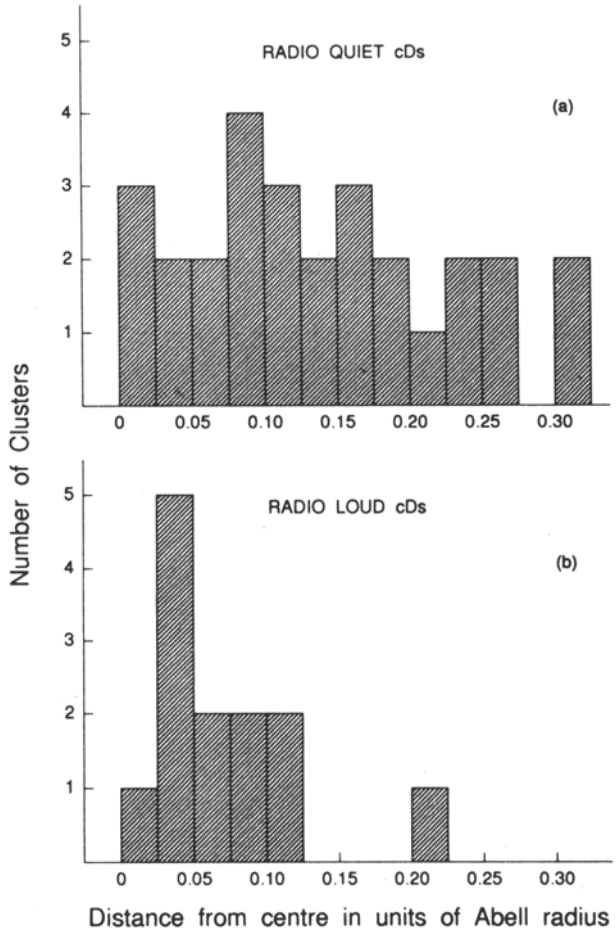

Figure 4. A histogram of the location of radio-quiet (**a**) and radio-loud (**b**) cD galaxies in Abell Clusters Plotted are the number of cDs in different radial bins from the cluster centres (in units of Abell radius R_A = 3 Mpc).

with null-hypothesis (the two distributions are identical) and test-hypothesis (that the radio-quiet sample is more extended), rejects the null hypothesis at a significance level of $\approx$ 0.03 (3%). Thus, we conclude that the radial distribution of radio-quiet cD galaxies is different and more extended compared to distribution of radio-loud cDs at $\approx$ 97% level of significance. As the cluster centres are determined only to an accuracy of 1 to 3 arcmin or so, the average error in cluster centre positions must be $\approx$ 0.16 in Abell radius units. We find that 12 out of 13 (92%) of the radio-loud cDs are situated within this range. It is therefore possible that the actual distribution of r/R_A of these is essentially a 'spike', the galaxies being located practically at the cluster centres. On the contrary, only ~ 56% of the radio-quiet cDs are located within this radius and thus, their intrinsic distributions are likely to be considerably wider.

Could the difference in the location of radio-loud and radio-quiet cDs be a selection effect? Two possible instrumental effects that can cause a loss in detection sensitivity away from cluster centres are, the primary beam attenuation of individual telescopes and, the effect of bandwidth smearing. Most of the 20 cm maps have a detection threshold for unresolved sources of $\approx$ 1 mJy at the cluster centres, which increases to $\approx$ 2mJy about 15 arcmin away from phase centres. For a mean redshift $< z > \approx$ 0.15, the Abell radius R_A is also $\approx$ 15 arcmin. Beam attenuation is therefore unlikely to have a significant effect as all of the radio-loud cDs are detected above the flux density of 2 mJy and the optical positions of all the cDs are within 5 arcmin from centres. Similarly, the effect of bandwidth smearing on radio detection within 5 arcmin from centres is quite small (about 10% loss in peak sensitivity with total flux density remaining unchanged) and is unlikely to have caused any systematic selection. Thus, the evidence for radio-emitting cDs to be more centrally located in clusters is very unlikely to be a selection effect.

We believe that the more central location of radio-loud cD galaxies is possibly related to the dynamical evolution of the clusters. In section 6 we have presented evidence for a strong correlation between radio emission from cDs and cooling-flows in their vicinity. All such cooling-flow clusters are known to have centrally peaked and spherically symmetric X-ray brightness distributions (Jones & Forman 1984). The distribution of galaxies in such clusters also shows a similar trend (Bahcall 1977; Oemler 1974) with higher than average velocity dispersions (Jones & Forman 1984). This suggests that the cooling-flow clusters are relatively more dynamically evolved with deeper central gravitational potential wells where a cD is almost always present. However, not all clusters could have relaxed during the Hubble time in a dynamical model where clusters are products of gravitational growth of small initial density perturbations. In the case of clusters of dimension $R_G \approx$ 1 Mpc (R_G, the gravitational radius), and of mass $\approx 10^{14} M_{\odot}$, the collapse time $t_{\rm coll} \approx 1.5 \times 19^9$ yr, whereas for a configuration with $R_A \approx$ 10 Mpc and the same mass, the collapse time is $\approx 4.7 \times 10^{10}$ yr (Sarazin 1988). This means that many of the clusters must be collapsing and merging at the present epoch. McGlynn & Fabian (1984) point out that during the merger of dense subclusters with each other, any cooling-flow if operating within subsclusters would be completely disrupted. The radio emission from a cD galaxy in the process of evolution in a merging subcluster should then be quenched. This mechanism provides a natural explanation to the phenomenon of radio emission from cD galaxy being influenced by its location in the cluster.

In order to further check the validity of our hypothesis of radio emission from dominant galaxies in clusters being influenced by the dynamical state of the cluster,

we have studied the optical morphology of the radio-loud and radio-quiet clusters. The morphological classes of the clusters used by us are obtained from the compilations of Struble & Rood (1991) who classified the Abell clusters into a 'double-tuning-fork' sequence (the Rood-Sastry or RS sequence) which runs from less evolved/irregular clusters (RS classes, I, F) to intermediate stage (RS classes L, C) and finally to more-evolved/relaxed clusters (RS classes B, cD). In Table 4 we present the data on the fraction of the radio-detected clusters from our sample in each of RS classes. Clearly, this fraction of radio detection is correlated with cluster morphology with 55%, 33%, 25% and 0% being detected among the classes cD, B, L + C and F +I respectively. It should be emphasized here that our cluster sample is selected only on the basis of optical brightness contrast of the brightest cluster member relative to less brighter members (BM types I, I:; Bautz & Morgan 1970) and thus should be more or less unbiased by the morphological state of the cluster. Despite this, the evidence favours an increasing probability of radio emission from the dominant members of more evolved clusters. This gives us confidence in concluding that, we are observing a real effect of cluster dynamical evolution on radio emission probability, and not an artefact of observational selection effects.

The presently popular cold dark matter theory requires that the clusters evolve towards dynamical relaxation by merging of pre-existing subcluster units. Computer simulations on a large scale appear to reproduce these structures (eg. Evrard 1990; Roettiger *et al.* 1993). However, the observational evidence for merging subclusters is controversial in optical studies (Geller 1990) but is quite strong in X-ray observations (eg. Jones & Forman 1984). A recent high sensitivity X-ray study of the Coma cluster with the ROSAT satellite in fact provides evidence for ongoing mergers of large subunits containing cD-like galaxies in their centres (White *et al.* 1993). It is also of

Table 4. Effect of cluster morphology on radio detection probability.

Revised Rood-Sastry morphological class		Abell number	Number surveyed	Percentage radio detection
	(cD)	77, 136, 146, 192, 261, 360, 510, 690, 733, 734, 1068, 1413, 1597, 1602, 1738, 2381, 2397, 2416, 2420, 2533	20	55%
Binary	(B)	22, 42, 122, 214, 394, 882, 1277, 1391, 1576, 2456, 2521, 2579	12	33%
Line and Core	(L) (C)	994, 1027, 1839, 2025	04	25%
Flat and Irregular	(F) (I)	1508, 2364, 2575, 2577, 2667	05	0%

interest to note that many of the best cluster candidates showing observational evidence for recent mergers (eg. A399-A401, A2634, A 2256 and Coma), show an absence of cooling flows (Edge *et al.* 1992) with weak or no detectable radio emission from their central galaxies (excluding WATs; see section 6). Thus, the available observations of nearby clusters support our hypothesis. Futher confirmation would be to show that the radioloud cDs are preferentially located at the focii of the well developed cooling flow systems and have small relative velocities with respect to the intracluster medium. The existence of subclusters in these clusters should also be rarer compared to radio-quiet ones. An observation of the dynamical states of the radio-loud and radio-quiet clusters (preferentially with an X-ray telescope) and a measurement of the shape and depth of their gravitational potential wells could thus provide a definite answer.

8. Spectral indices of cD radio galaxies

Out of the 41 clusters for which we measured the optical position of the cD galaxies, only 29 clusters have the radio data at both 20 cm and 90 cm wavelength. In these clusters, we have a sample of 14 radio sources either with definite spectral indices (10), or with upper limits (4). A plot of the distribution of $\alpha_{0\,3}^{1\,4}$ for the 14 sources is shown in Fig 5. Using only the actual detections the median value of $\alpha_{0\,3}^{1\,4}$ is derived to be $(\alpha_{0\,3}^{1\,4})_{med} = 0.70 \pm 0.13$ and the mean spectral index for this distribution is $(\alpha_{0\,3}^{1\,4})_{mean} = 0.66$. However, assuming the upper limits to represent the actual values, the median spectral index is derived to be$(\alpha_{0\,3}^{1\,4})_{med} = 0.83 \pm 0.13$. These fairly low values of the median spectral indices are somewhat surprising as it is generally believed that there is a significant population of very steep spectrum radio sources (with $\alpha_{0\,3}^{1\,4} > 1.0$) in rich clusters of galaxies. In fact, our estimated median value of ≈ 0.75

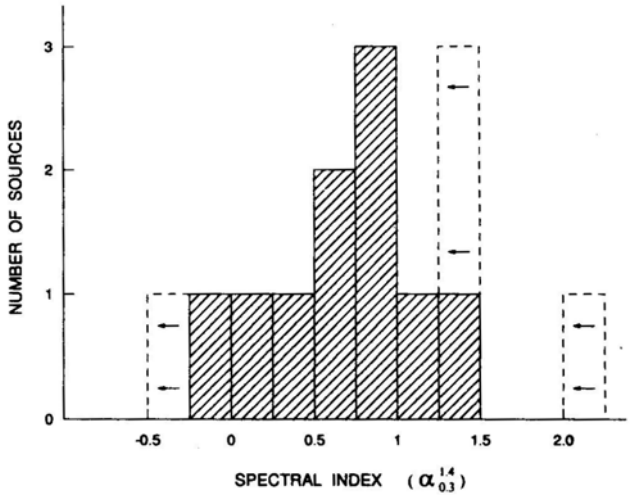

Figure 5. Histogram of the spectral index distribution for cD galaxies between the frequencies of 1.4 GHz and 330 MHz. The dotted sections represent upper limits to the spectral indices.

is similar to the median spectral index of canonical radio galaxies of similar radio uminosities but not necessarily in rich clusters of galaxies (Laing & Peacock 1980). An early study by McHardy (1979) reported that the mean radio spectral index of cD galaxies in BM type I clusters was 1.13 ± 0.24 (between 1400 MHz and 408 MHz). This spectrum was found by associating Abell clusters with radio sources selected from 4C survey and subsequently reobserving them at a higher resolution using Cambridge 1-Mile telescope (McHardy 1979). Although both the results, ours as well as McHardy's, are based on a rather small number of objects, the difference needs to be explained as spectral index is an important tool for understanding of the evolution of radio sources. Here we compare the two samples considering certain well known effects which might be responsible for the difference in spectral index distribution in the two samples.

■ *Spectral index vs selection frequency*: McHardy's (1979) sample was selected from a radio survey made at ν = 178 MHz which is much lower than the selection frequency of 1.4 GHz in our survey. It is well known that the median spectral index moves towards steeper values as one goes to lower selection frequencies.

■ *Luminosity vs spectral index correlation*: The limiting flux density of 2 Jy for. the 4C survey implies that from clusters with $z \approx 0.1$, no radio source with 178 MHz radio luminosity $< 8.6 \times 10^{25}$ WHz $^{-1}$ (or 1.4 GHz luminosity $< 1.8 \times 10^{25}$ WHz $^{-1}$ for $\alpha = 0.75$) can be detected. The RLF of cD galaxies detected by us, on the other hand extends down to $\approx 10^{22}$ WHz $^{-1}$ and we find that only $\sim$ 5% of the cDs emit a radio luminosity $> 10^{25}$ WHz $^{-1}$. The cluster sources of McHardy thus are of much higher luminosities (by a factor of $\gtrsim$ 100) than the typical sources associated with cDs in our survey. A positive correlation between radio luminosity and the spectral index is well known for radio sources in 3CR catalogue (Laing & Peacock 1980). This correlation could also be partly responsible for the steeper spectra found by McHardy.

In view of the small number of sources in both the samples, it is not clear if the entire discrepancy in the spectral index distributions can be explained by the above two effects. It is also possible that the occurrence of very steep spectrum sources in BM I clusters is confined only to the high end of the luminosity distribution. The presence of some extremely steep spectrum radio sources ($\alpha \gtrsim 1$) in clusters of galaxies is however well established (Baldwin & Scott 1973; Slingo 1974 a, b). Generally, these objects are of two types. The 'relic' radio plasmons of diffuse and extended morphology located near cluster centres but rarely coincident with any cluster member galaxy (eg. Slee & Reynolds 1984; Joshi *et al* 1986), and the so called head-tail radio galaxies (eg. O'Dea & Owen 1986). The underlying cause of the steep spectral indices for both the classes in the same, viz. 'ageing' of relativistic electrons due to radiation losses from a volume that no longer contains an active source of fresh particles: The value of $(\alpha_{0.3}^{1.4})_{\rm med} = 0.7$ found by us for cD galaxies on the other hand implies that this spectral ageing is not visible due to injection of fresh particles from the nuclear active regions into emitting volumes. We now apply the Kardashev (1962) theory in order to better understand the spectral evolution of such sources in the cluster medium.

The radio spectrum of a source evolves in two stages: during the first stage a radio plasmon receives a continuous supply of relativistic particles and expands till it comes to a pressure balance with the external medium. At this phase if α_0 be the spectral index of the radio spectrum at the time of injection, a 'break' in the spectrum, with index $\alpha_1 = \alpha_0 + 0.5$ beyond the break frequency develops. In the second stage if the supply of fresh particles ceases due to any reason, a second spectral break with

spectrum further steepening to index $\alpha_2 = (\frac{4}{3})\alpha_1 + 1$ beyond this break frequency develops. If we identify the average initial spectrum at the time of injection with α_0=0.7,then α_1=1.2 and α_2=2.6.Two of the cDs are detected with $\alpha_{0.3}^{1.4}$ =1 to 1.5 and none with $\alpha_{0.3}^{1.4}$> 1.5. Thus it can be safely concluded that the second spectral break is not yet visible in any of the sources and only a few may contain the first break. The location of the break in the spectrum is a diagnostic for the elapsed time since the two stages mentioned above. After a time t_1 the first break would be found at a frequency ν_1. given by the formula (Kardashev 1962, but modified to include inverse Compton losses)

$$\nu_1(\mathrm{Hz}) = \left(\frac{5.44 \times 10^9 \times B(\mathrm{Gauss}) \times t_1^{-2}(yr)}{[B^2(\mathrm{Gauss}) + B_{\mathrm{MBR}}^2(\mathrm{Gauss})]^2} \right), \tag{5}$$

where B is the internal magnetic field and $B_{\mathrm{MBR}} = 2.57 \times 10^{-6} \times (1 + z)^2$ Gauss is the effective magnetic field due to microwave background radiation field at the redshift z. We do not have the value for B and hence use the commonly found equipartition value of $\sim 10^{-6}$ Gauss. Using $B_{\mathrm{MBR}} = 3.4 \times 10^{-6}$ Gauss corresponding to average $< z > = 0.15$ for our sample and assuming the break frequency to lie above $\nu_1 = 1400$ MHz in the majority of cases, an upper limit for the probable spectral age, $t_1 < 1.6 \times 10^8$ yr, is then obtained. As majority of radio loud cDs are most probably located at. the centres of dense intracluster media of cooling-flow systems (section 6 above), it is possible that the radio emitting volumes do not expand to large sizes and consequently the internal magnetic fields $B < 10^{-6}$ Gauss. We can estimate the more probable value of the internal magnetic field if we assume pressure equilibrium with the external medium and the minimum energy condition. Under these assumptions,

$$B = \left[\frac{72.\pi}{13} . P_{gas} \right]^{1/2} \tag{6}$$

If we use the average value for the gas pressure $< P_{gas} > = 4 \times 10^{-11}$ dyn cm^{-2} obtained from the sample of clusters with cooling flows studied in section 6, we then obtain $B = 2.6 \times 10^{-5}$ Gauss and an even shorter spectral age of $t_1 < 1.5 \times 10^7$ yr. Higher resolution radio observations of the detected sources to actually detect active cores and X-ray data on the state of intracluster media is required to confirm these numbers.

In conclusion, our observations for the spectral indices of these cD galaxies indicate them to be relatively 'young' in terms of their spectral ages. The evidence favours an ongoing activity in the central regions of many of them and if located at the centres of dense cluster media of cooling flow systems, the spectral ages come out to be $< 2 \times 10^7$ yr for the majority of them.

9. Summary and conclusions

We have presented the results of a relatively deep radio survey at 20 cm and 90 cm λ of a Statistical sample of distant Abell clusters ($0.1 \lesssim z \lesssim 0.3$) containing dominant cD galaxies.The important results and conclusions from this study can be summarized as follows:

■ The radio luminosity function for the cD galaxies appears to agree quantitatively with the RLF of brightest giant elliptical galaxies (located in less rich galactic environments) for 1.4 GHz radio luminosity $\lesssim 10^{24.5}$ WHz^{-1} At higher luminosities the cD galaxies appear to be more likely to be radio sources. This behaviour of the RLF can be understood in terms of the correlation between the radio and optical luminosities of the giant elliptical systems, and suggests a unified mechanism for the triggering of the nuclear activity in radio galaxies in diverse environments.

■ We do not detect a significantly large population of very steep spectrum radio sources with $\alpha > 1.2$ (between 1.4 GHz and 0.3 GHz) to be associated with the cD galaxies. The median spectral index is found to be only 0.70, similar to that of typical radio galaxies not necessarily in rich clusters. The evidence favours ongoing activity in the central regions of many of the cD galaxies, and if they are located at the centres of the dense cluster media of cooling-flow systems, the spectral ages are likely to be $< 2 \times 10^7$ y for the majority of them.

■ An examination of the existing radio and X-ray data on the nearby ($0.03 < z < 0.15$) Abell clusters with cD galaxies has revealed a significant inverse correlation between the radio luminosity of the cD galaxy and the cooling time of the hot intra-cluster medium in its vicinity. As many as 70% of the radio emitting cD galaxies (with 1.4 GHz radio luminosity $\gtrsim 10^{22.7}$ WHz^{-1}**)** are found to be located at the focii of cooling flows and this suggests the presence of cooling flows in many of the distant Abell clusters containing radio-loud cD galaxies in our sample. In order to better understand the observed effect we have considered the physical models of confinement of the radio plasmas and the fuelling of the central energy sources by means of accretion. It is concluded that though confinement is necessary, it may not be a sufficient factor. The evidence currently available supports the idea that nuclear activity is triggered by the accretion of the cooler gas by the massive galaxies forming at the centres of cooling flows in dynamically evolving clusters of galaxies.

■ We have found evidence for the probability of radio emission from cDs to be related to their location within the cluster. The radio emitting cDs are located close to the centres of their host clusters, as against the radio-quiet ones, which are less centrally concentrated. That this could be related to the dynamical evolution of clusters is supported also by our observation that, even though all the clusters selected for our study had a first ranked giant elliptical galaxy, the probability of radio emission from this galaxy was found to be correlated with the evolutionary morphological class (the Rood-Sastry class) of the parent cluster. Dynamically more evolved classes of clusters (cD, B) are more likely to have radio sources associated with the brightest clusters members as against less evolved, irregular morphological classes (L, C, F, I). We have argued that this effect together with the correlation between the cooling time and the radio luminosity mentioned above indicates that the phenomenon of radio emission from the central galaxies in rich Abell clusters is mainly governed by the effects of the dynamical evolution of the clusters.

Acknowledgement

We gratefully acknowledge the support, help and advice from the late Prof. M. N. Joshi. We thank Dr. J. P. Huchra for providing us spectroscopic redshifts for many of the clusters in our sample. We have made extensive use of the computational and

other facilities at the Radio Astronomy Centre, Ootacamund and at TIFR Bombay. The Very Large Array is operated by Associated Universities Inc., under contract with the National Science Foundation, USA.

References

Abell, G. O. 1958, *Astrophys. J. Suppl.* **3**, 211.
Abell, G. O., Corwin, H. G., Olowin/R. P. 1989, *Astrophys. J. Suppl.* **70**, 1.
Albert, C. E., White, R. A., Morgan, W. W. 1977, *Astrophys. J.* **211**, 309.
Auriemma, C, Perola, G. C, Ekers, R., Fanti, R., Lari, C, Jaffe, W. J., Ulrich, M. H. 1977, *Astr. Astrophys.* **57**,41.
Baars, J. W. M., Genzel, R., Pauliny-Toth, I.I. K., Witzel, A. 1977, *Astr. Astrophys.* **61**, 99.
Bahcall, N. A. 1977, *A. Rev. Astr. Astrophys.,* **15**, 505.
Baldwin, J. E., Scott, P. F. 1973, *Mon. Not. R. astr. Soc.* **165,** 259.
Ball, R., Bums, J. O., Loken, C. 1993, *Astr. J.,* **105**, 53.
Bautz, L. P., Morgan, W. W. 1970, *Astrophys. J. Lett.,* **162**, L149.
Begelman, M. C, Blandford, R. D., Rees, M. J. 1984, *Rev. Mod. Phys.,* **56**, 255.
Burns, J. O. 1990, *Astr. J.,* **99**, 14.
Colla, G., Fanti, C, Gioia, I, Lari, C. 1975, *Astr. Astrophys.,* **38**, 209.
Crawford, C. S., Fabian, A. C, Johnstone, R. M. 1988, Mon. *Not. R. astr. Soc,* **235**, 183.
Crawford, C. S., Fabian, A. C. 1989, *Mon. Not. R. astr. Soc,* **239**, 219.
Donahue, M., Stocke, J. J., Gioia, I. M. 1992, *Astrophys. J.* **385**, 49.
Dressier, A. 1980, *Astrophys. J. Suppl.,* **42**, 565.
Edge, A. C, Stewart, G. C, Fabian, A. C. 1992, *Mon. Not. R. astr. Soc,* **258**, 177.
Evrard, A. E. 1990, *Astrophys. J.,* **363**, 349.
Fabian, A. C, Nulsen, P. E. J. Canizares, C. R. 1984, *Nature,* **310**, 733.
Fabian, A. C. (Ed) 1987, *Cooling Flows in Clusters and Galaxies* (Dordrecht: Kluwer Acad. Pub.).
Fabian, A. C, Crawford, C. S. 1990, Preprint.
Fabian, A. C, Nulsen, P. E. J., Canizares, C. R. 1991, *Astr. Astrophys. Rev.,* **2,** 191.
Geller, M. 1990, in *Proc. of Clusters of Galaxies Meeting* (Cambridge Univ. Press), pp. 25.
Gopal-Krishna, Wiita, P. J. 1991, *Astrophys. J.,* **373**, 325.
Gunn, J. E., Gott, J. R. 1972, *Astrophys. J.,* **176,** 1.
Gunn, J. E., Hoessel, J. G., Oke, J. B. 1986, *Astrophys. J.,* **306**, 30.
Harris, D. E., Lari, C, Valee, J. P., Wilson, A. S. 1980, *Astr. Astrophys. Suppl,* **42**, 319.
Hubble, E. P. 1936, in *The Realm of the Nebulae* (New Haven: Yale Univ. Press), pp. 210.
Huchra, J. P., Henry, J. P., Postman, M., Geller, M. J. 1990, *Astrophys. J.,* **365**, 66.
Hutchings, J. B., Crampton, D., Campbell, B. 1981, *Astrophys. J.,* **247**, 743.
Jones, C, Forman, W. 1984, in *Clusters and Groups of Galaxies* (Dordrecht: D. Reidel Pub Comp.), pp. 319.
Joshi, M. N., Kapahi, V. K., Bagchi, J. 1986, in *Proc. of the NRAO Workshop on 'Radio Continuum Processes in Clusters of Galaxies,* (Eds.) C. P. O, Dea & J. M. Uson, (NRAO) pp. 73.
Kardashev, N. S. 1962, *Astr. Zh,* **39**, 393.
Kapahi, V. K. 1989, *Astr. J.,* **97**, 1.
Kriss.G. A, Cioffi, D. F., Canizares, C. R. 1983, *Astrophys. J.,* **272**, 429.
Laing, R. A., Peacock, J. A. 1980, *Mon. Not. R. astr. Soc,* **190**, 903.
Leir, A. A., van Den Bergh, S. 1977. *Astrophys. J. Suppl,* **34,** 381.
Mathew, T. A., Morgan, W. W., Schmidt, M. 1964, *Astrophys. J.,* **140**, 35.
McGlynn, T. A., Fabian, A. C. 1984, *Mon. Not. R. astr. Soc,* **208**, 709.
McHardy, I. M. 1979, *Mon. Not. R. astr. Soc,* **188**, 495.
Melnick, J, Sargent, W. L. W. 1977, *Astrophys. J.,* **215**, 401.
Morgan, W. W., Lesh, J. 1965, *Astrophys. J.,* **142**, 1364.
Morgan, W. W., Kayser, S., While, R. A. 1975, *Astrophys. J.,* **199**, 545.
Napier, P. J., Thompson, A. R., Ekers, R. D. 1983, *Proc IEEE,* **71**,1295.
O' Dea, C. P., Owen, F. N. 1986, *Astrophys. J.,* **301**, 841.

Oemler, A. Jr. 1974, *Astrophys. J.,* **194,** 1.
Owen, F. N., Burns, J. O., White, R. A. 1984, in *Clusters and Groups of Galaxies* (Dordrecht: D. Reidel Pub. Comp.), pp. 295.
Roettiger, K., Burns, J., Loken, C. 1993, *Astrophys. J. Lett.,* **407**, L53.
Ryle, M. 1968, *A. Rev. Astr. Astrophys.,* **6**, 249.
Sandage, A. 1976, *Astrophys. J.,* **205**, 6.
Sarazin, C. L. 1988, in *X-ray Emissions from Clusters of Galaxies* (Cambridge Univ. Press) p. 33.
Schmidt, M. 1968, *Astrophys. J.,* **151,** 393.
Schwartz. D. A., Bradt, H. V., Remillard, R. A. 1991, *Astrophys. J.,* **376**, 424.
Slee, O. B., Reynolds, J. E. 1984, *Proc. astr. Soc. Australia,* **5**, 516.
Slingo, A. 1974(a), *Mon. Not. R. astr. Soc,* **166**, 101.
Slingo, A. 1974(b), *Mon. Not. R. astr. Soc,* **168**, 307.
Struble, M. F., Rood, H. J. 1991, *Astrophys. J. SuppL,* **77,** 363.
Valentijn, E. A., Bijleveld, W. 1983, *Astr. Astrophys.,* **125**, 223.
Yee, H. K. C, Green, R. F. 1987, *Astrophys. J.,* **319**, 28.
White, S. D. M, Briel, U. G., Henry, J. P. 1993, *Mon. Not. R. astr. Soc,* **261**, L8.
Zhao, J. H., Burns, J. O., Owen, F. N. 1989, *Astr. J.,* **98**, 64.
Zwicky, F. 1938, *Publ. astr. Soc. Pacific,* **50,** 218.

J. Astrophys.Astr.(1994) **15,** 309–319

Spectroscopy and Orbit Determination of the Chromospherically Active Double-Lined Binary System HD 163621 = V835 Herculis

R. F. Griffin* *The Observatories, Madingley Road, Cambridge CB3 0H A, England*
F. C. Fekel† & M. D. Morton *Department of Physics & Astronomy, Vanderbilt University, Nashville, Tennessee 37235; USA*
R. E.Fried *Braeside Observatory, P.O. Box 906, Flagstaff, Arizona 86002, USA*

Received 1994 May 17; accepted 1994 August 22

Abstract. HD 163621 is a double-lined spectroscopic binary in a circular orbit whose period is 3.3 days. Spectral classification of the components has proved difficult, but current results of K0 V and late K V are reasonably consistent with our best model of the system, which has spectral types of G8V and K7V. The object shows photometric variability and chromospheric activity and is therefore a member of the BY Draconis class of variables. The minimum masses are quite small, 0.10 and 0.07 $M_{\odot}$ for the primary and secondary, respectively, suggesting an orbital inclination of about 30°. The system is synchronously rotating. Its distance is estimated to be 31 pc, which makes it an excellent candidate for a trigonometric parallax determination.

Key words: Stars—spectra—spectroscopic binaries—radial velocities—orbits—stars, individual: HD 163621.

1. Introduction

HD 163621 is an eighth-magnitude object in the constellation Hercules, a little over one degree south—preceding the fourth-magnitude star θ Herculis. Its spectral type is given in the *Henry Draper Catalogue* (Cannon & Pickering 1922) as G5; apart from that, no astrophysical information concerning HD 163621 has existed until recently. What brought the object to our attention was its listing by Bidelman (1985) in a brief table of late-type stars exhibiting Ca II H and K emission, discovered in the course of a preliminary survey of objective-prism plates taken with the Burrell Schmidt telescope after its move to Kitt Peak. Bidelman characterized the emission strength as 'moderate', but that epithet has to be read in the context of the nature of the

*Guest Investigator, Palomar Observatory; Visiting Observer, Dominion Astrophysical Observatory, Victoria, and at the Geneva Observatory's 'Coravel' at Haute-Provence.
†Visiting Astronomer, Kitt Peak National Observatory, [U.S.] National Optical Astronomy Observatories, operated by AURA Inc. under contract with the [U.S.] National Science Foundation.

observational material: for the emission to be visible at all on objective-prism plates at the modest dispersion (108Å mm^{-1} at Hγ) offered by the Burrell Schmidt it had to be pretty strong.Two of the authors of the present paper (R.F.G. & F.C.F.) followed up Bidelman's discovery independently, and upon learning of one another's interest they decided to join forces in this description of their results. Finding their understanding of the composite spectrum seriously hampered by ignorance of the integrated colours,they commissioned photometry from R.E.F., while M.D.M. collaborated in the spectroscopic work.

Some information about HD 163621 has already appeared in print as a result of the new interest in it. Strassmeier *et al.* (1988) reported the object as being a double-lined spectroscopic binary. They suggested spectral types of F and G5 IV on the basis of some of the earliest of our spectra described below. Hooten & Hall (1990) found light variations amounting to $0^m.05$ in V, presumably due to rotational modulation caused by starspots. One of their possible periods is indistinguishable from the orbital period which we shall show to be 3.3 days. Strassmeier & Fekel (1990) found substantial difficulty in deriving spectral types for the components of HD 163621; their estimate was that the primary is type Kl IV and the secondary G6 V.

2. Observations

We have obtained three types of observations of HD 163621—photometry, spectroscopy and radial velocities.

The photometric data were obtained by R.E.F. at Braeside Observatory near Flagstaff, Arizona, with a photometer on a computer-controlled 16-inch Cassegrain reflector. Measurements were made in the *U, B* and *V* bands on six nights between 1990 August 8 and 1991 July 19. HD 163968 was used as the comparison star and HD 164251 as the check star for differential photometry; all-sky photometry was carried out on two nights against numerous Johnson and Landolt standards. The photometer employs a cooled Hamamatsu end-window photomultiplier and includes red-block filters. Seasonal values of the extinction were used; transformation coefficients were determined from the all-sky observations.

Spectroscopic observations were begun in the autumn of 1986 at Kitt Peak by F.C.F., who used a Texas Instruments CCD detector with the coudé spectrograph of the 84-inch telescope (Willmarth 1990); the observations were, however, made with the 38-inch coude auxiliary telescope rather than with the 84-inch itself. The majority of the spectra were centred at λ 6430 Å and covered a range of 84 Å, but one was taken in the violet, covering 56 Å centred on λ 4060 Å. In addition to providing information of a spectroscopic nature, the Kitt Peak observations have permitted the determination of radial velocities and have made a substantial contribution to the data discussed in sections 3 and 4 below.

Radial-velocity measurements were begun by R.F.G. at almost the same time as the Kitt Peak observations started. The instruments principally used were the original radial-velocity spectrometer at Cambridge (Griffin 1967) and the Geneva Observatory's 'Coravel' (Baranne, Mayor & Poncet 1979) at Haute-Provence; a few observations were also obtained with the instrument at the Dominion Astrophysical Observatory (Fletcher *et al* 1982), and one was made at Palomar with the spectrometer on the 200-inch telescope (Griffin & Gunn 1974).

3. Radial velocities

For radial-velocity purposes the Kitt Peak spectra have been measured by M.D.M. relative to the reference star μ Her A, spectral type G5 IV, whose radial velocity has been taken to be —16.4 km s $^{-1}$, as determined by Stockton & Fekel (1992) in comparison with β Oph, whose velocity has in turn been taken from the work of Scarfe, Batten & Fletcher (1990). We may say at once that the spectra reveal HD 163621 as double-lined, although the lines of the two components are of very disparate strengths and the velocities of the secondary star are therefore relatively ragged. The secondary is also detectable as a very weak feature, with a depth of only about 2 per cent of the 'continuum', on radial-velocity traces of sufficiently high S/N ratio; but it was only identified (or, in the case of the single Palomar trace, which did in fact show it, it was only believed) after the radial-velocity observer had been alerted to its existence by the spectroscopists.

After HD 163621 was found to exhibit rapid changes of radial velocity, an intensive observing campaign was undertaken by R.F.G. in the summer and autumn of 1987 and the period of 3.304 days was determined (Strassmeier & Fekel 1990). All the measurements of radial velocity that are now available, whether from spectra or otherwise, are collected in Table 1. There are 19 spectroscopic observations, all but three of which permit measurement of the velocity of the secondary as well as that of the primary; the number of measurements from radial-velocity spectrometers is 63,of which only six show the secondary as a measurable feature.

An effort has been made to place all the velocities onto the same zero-point (Griffin 1969) as the other photoelectric measurements that have been published from Cambridge in this journal; as far as HD 163621 is concerned, that zero-point depends almost wholly upon the adoption of the velocity of the reference star λ Lyr as – 16.9 km s^{-1}. There is a seemingly colour-dependent difference between the Coravel and Cambridge zero-points, similar to the DAO-Coravel discrepancy found by Scarfe, Batten & Fletcher (1990); in the present instance it has been removed by an empirical adjustment of + 1.0 km s^{-1} to the Coravel velocities, which were initially reduced, as is the usual procedure for that instrument, to the 'IAU faint standard' system (Mayor & Maurice 1985). The spectroscopically determined velocities, whose original zero-point depended on the chain of comparisons noted above, required an adjustment of + 0.5 km s^{-1} to place them on the Cambridge scale. No change was needed to the Palomar or DAO observations, which were made and standardized in the same way as the Cambridge ones.

4. Orbit

A preliminary orbit solution from all the data listed in Table 1 for the primary star showed that the 23 Cambridge observations have random errors that are about $\sqrt{3}$ times those of the other sources, so they were weighted 1/3 to equalize the variances in the final solution. The spectrometer velocities of the secondary are rather marginal and needed to be weighted 0.2 in comparison with those determined from spectra; additionally, the unit of weight for the secondary velocities had to be set at 0.06 of that of the primary in order to bring the weighted variances for the two stars into approximate equality. In the derivation of the orbit, velocities that were not explicitly

Table 1. Radial-velocity measurements of HD 163621.

Heliocentric date	HMJD	Velocity Prim. km s^{-1}	Velocity Sec. km s^{-1}	Phase	$(O-C)$ Prim. km s^{-1}	$(O-C)$ Sec. km s^{-1}	Source
1986 Oct 18.073	46721.073	+12.2	−67.9	0.986	−0.4	−1.3	KPNO
Nov 15.720	749.720	−37.9		9.655	+0.5		Camb.
26.106	760.106	−10.1	−37.6	12.798	+0.1	−3.6	Palomar
1987 Mar 12.514	46866.514	+12.0	−67.9	45.000	−0.7	−1.1	KPNO
14.487	868.487	−46.7	+18.7	45.597	+0.1	+0.4	KPNO
22.182	876.182	+9.3		47.926	0.0		Camb.
May 5.080	920.080	−11.1		61.211	+0.9		Camb.
June 1.030	947.030	−42.6		69.366	−0.7		Camb.
22.990	968.990	+12.3		76.012	−0.3		Camb.
24.347	970.347	−49.1	+19.7	.423	−0.1	−1.7	KPNO
24.971	970.971	−45.9		.612	−0.9		Camb.
26.319	972.319	+12.2	−65.8	77.019	−0.3	+0.6	KPNO
27.306	973.306	−33.1	0.0	.318	+0.5	+0.6	KPNO
28.370	974.370	−40.9	+7.3	.640	0.0	−2.5	KPNO
July 3.976	979.976	−36.8		79.337	+0.2		Camb.
4.948	980.948	−42.5		.631	−0.2		Camb.
5.982	981.982	+10.3		.944	−0.4		Camb.
6.094	982.094	+12.1		.978	−0.3		Camb.
Sept 14.848	47052.848	−45.4		101.390	−0.2		Camb.
24.863	062.863	−48.8		104.420	0.0		Camb.
26.927	064.927	+12.0		105.045	+0.6		Camb.
Oct 6.790	074.790	+11.4		108.030	−0.8		Camb.
6.898	074.898	+9.8		.063	−0.4		Camb.
12.777	080.777	−2.5		109.842	−0.3		OHP
12.925	080.925	+5.8		.886	+1.1		OHP
13.759	081.759	+1.0		110.139	0.0		OHP
13.821	081.821	−2.0		.158	+0.1		OHP
17.739	085.739	−38.8		111.343	−0.7		OHP
17.843	085.843	−43.3		.375	−0.2		OHP
18.794	086.794	−37.8		.663	−0.7		OHP
21.754	089.754	−52.0		112.558	−1.4		Camb.
22.758	090.758	+1.6		.862	+0.4		Camb.
24.787	092.787	−52.8		113.476	−0.4		Camb.
28.756	096.756	−34.3		114.677	+0.2		Camb.
28.856	096.856	−28.2		.708	+0.4		Camb.
Nov 20.716	119.716	−42.3		121.626	+0.8		Camb.
27.720	126.720	−19.4		123.745	+1.6		Camb.
Dec 7.698	136.698	−17.4		126.765	−0.4		Camb.
1988 Jan 23.600	47183.600	+11.5		140.959	−0.1		DAO
31.590	191.590	−43.2		143.377	+0.2		DAO
Feb 1.601	192.601	−33.4		.682	+0.1		DAO
Mar 11.205	231.205	−42.1		155.365	−0.4		OHP
12.197	232.197	−36.5		.665	+0.1		OHP
14.172	234.172	−22.5		156.263	+0.2		OHP
24.459	244.459	−43.3	+11.4	159.376	0.0	−1.9	KPNO
Nov 2.776	467.776	+11.1		226.958	−0.5		OHP
3.727	468.727	−18.6		227.245	+0.5		OHP
5.726	470.726	−0.5		.850	+0.2		OHP
6.742	471.742	−1.7		228.158	+0.4		OHP

(*Continued*)

Table 1. (*Continued*)

Heliocentric date	HMJD	Velocity Prim. km s^{-1}	Velocity Sec. km s^{-1}	Phase	$(O-C)$ Prim. km s^{-1}	$(O-C)$ Sec. km s^{-1}	Source
1989 Mar 25.162	47610.162	+11.2		270.047	−0.1		OHP
26.179	611.179	−40.2		.355	−0.1		OHP
27.141	612.141	−40.3		.646	−0.4		OHP
28.184	613.184	+11.7		.962	−0.1		OHP
30.186	615.186	−49.9		271.568	0.0		OHP
Apr 7.480	623.480	+9.0	−61.1	274.078	+0.1	+0.3	KPNO
10.396	626.396	+11.3	−66.7	.960	−0.4	−1.4	KPNO
28.110	644.110	−34.0		280.321	+0.1		OHP
30.148	646.148	+11.0		.937	+0.8		OHP
May 2.118	648.118	−52.3	+19.7	281.534	−0.3	−6.0	OHP
3.107	649.107	−4.0	−47.1	.833	−0.3	−3.8	OHP
Oct 10.128	809.128	−21.4		330.259	+0.6		KPNO
11.170	810.170	−49.4	+19.2	.575	−0.2	−2.5	KPNO
12.098	811.098	+0.7	−49.6	.856	+0.5	−0.8	KPNO
13.097	812.097	−1.9	−46.6	331.158	+0.2	−1.0	KPNO
14.090	813.090	−51.3	+26.9	.458	+0.4	+1.7	KPNO
15.091	814.091	−18.2		.761	−0.5		KPNO
16.072	815.072	+10.5	−63.5	332.058	−0.1	+0.2	KPNO
27.786	826.786	−46.1		335.603	0.0		OHP
Nov 1.744	831.744	+5.9		337.104	−0.1		OHP
1990 Jan 31.242	47922.242	−52.3		364.491	+0.4		OHP
1991 Jan 27.228	48283.228	−23.0		473.734	+0.2		OHP
28.239	284.239	+11.4	−62.6	474.040	−0.3	+2.7	OHP
29.234	285.234	−37.9		.341	−0.1		OHP
30.220	286.220	−40.8		.640	+0.1		OHP
Feb 3.220	290.220	−0.3	−48.5	475.850	+0.4	−0.9	OHP
4.235	291.235	−1.9		476.157	+0.1		OHP
5.238	292.238	−51.7		.461	+0.1		OHP
Oct 29.731	558.731	+5.4		557.109	0.0		OHP
Nov 1.752	561.752	+12.5		558.023	+0.1		OHP
1992 Apr 24.159	48736.159	−9.0	−32.8	610.803	+0.3	+2.5	OHP
1993 Apr 27.436	49104.436	−20.4		722.253	+0.2		KPNO
28.445	105.445	−50.3	+25.7	.558	+0.3	+2.0	KPNO

of the secondary have been regarded as being of the primary, even where they are close enough to the γ-velocity to have been blended, since 'dragging' of the blended velocities towards the γ-velocity is not obvious in the residuals. The final orbit is illustrated in Fig. 1 and has the following elements:

$P = 3.304412 \pm 0.000006$ days
$\gamma = -20.01 \pm 0.04$ km s^{-1}
$K_1 = 32.75 \pm 0.06$ km s^{-1}
$K_2 = 46.8 \pm 0.4$ km s^{-1}
$q = 1.429 \pm 0.014$ $(= m_1/m_2)$
$e \equiv 0$
ω is undefined

$T_0 = \text{MJD } 47451.3943 \pm 0.0011$
$a_1 \sin i = 1.488 \pm 0.003$ Gm
$a_2 \sin i = 2.126 \pm 0.017$ Gm
$f(m_1) = 0.01205 \pm 0.00007\, M_\odot$
$f(m_2) = 0.0351 \pm 0.0009\, M_\odot$
$m_1 \sin^3 i = 0.1015 \pm 0.0016\, M_\odot$
$m_2 \sin^3 i = 0.0711 \pm 0.0009\, M_\odot$

R.m.s residual (unit weight, primary star) = 0.36 km s^{-1}

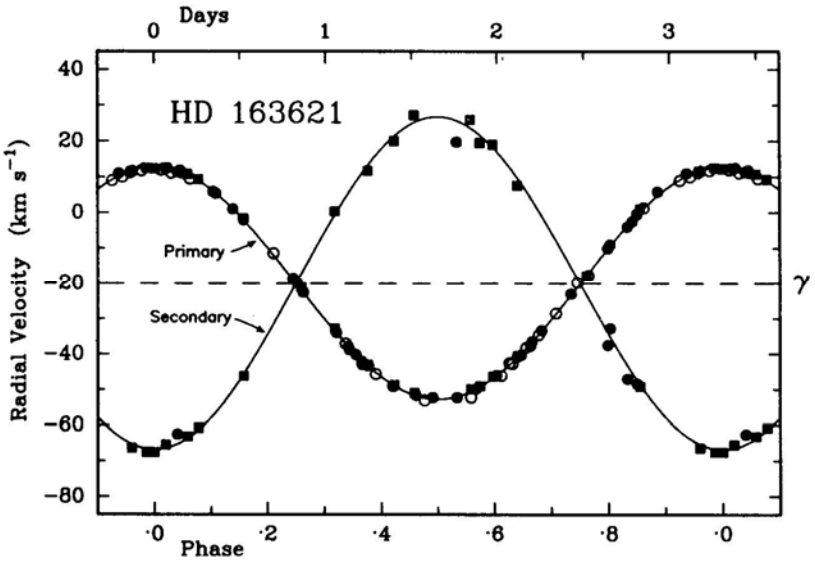

Figure 1. Orbital radial-velocity curves for the two components of HD 163621, with the measured velocities plotted. The measurements derived from Kitt Peak spectra are plotted as squares, while those obtained directly with radial-velocity spectrometers are shown as circles. The Cambridge observations, which are less accurate than the others and were attributed a weight of 1/3 in the orbital solution, are distinguished by the open circles.

The orbit has no eccentricity that is significant according to the tests given by Bassett (1978). The true period (in the rest frame of the system) is 3.304628 + 0.000006 days.

5. Photometry

The initial members of our consortium, R.F.G. and F.C.F., were not aware of any photometry of the object and found their ignorance of the colours to be a great handicap. They accordingly asked R.E.F. to observe HD 163621—which he did, as described in section 2. The mean magnitudes were found to be $V = 7^{m}.94$, $(B - V) = 0^{m},88$, $(U - B) = 0^{m}.41$. The colours are suggestive of a combined type (which would be nearly the type of the primary star, since that component is certainly the dominant contributor to the light of the system) of K0 V or a little earlier. There was evidence of brightness variations of the order of $0^{m}.1$, which was not altogether unexpected in view of the short orbital period and the consequent probability of starspots. Before R.E.F. could make a more comprehensive photometric investigation of HD 163621, it was learnt that Hall & Henry had had the object on the observing programme of the automatic photoelectric telescope (APT) on Mt. Hopkins since 1988. The APT observations, which are presented by their authors in the accompanying paper, are concerned with the variation of magnitude rather than the actual colours of the system, so we rely on the $(B - V)$ and $(U - B)$ values quoted above to guide us (in section 8 below) to our final model of HD 163621. In view of the small amplitudes

of the variations, it is unlikely that there are any colour changes large enough to be at all significant in relation to the choice of spectral types.

At the risk of appearing to use a circular argument, we remark that the comparative proximity of HD 163621 (31 pc according to the model put forward below) suggests that interstellar reddening will be practically negligible, so we assume the intrinsic colours of the system to be the same as the observed ones. The Galactic latitude is quite high, about + 26°, but since the whole of the light path between HD 163621 and ourselves is within the thickness of the Galactic disc the latitude makes little difference to its propensity for reddening.

6. Spectroscopy

All the spectra discussed here were obtained by F.C.F. at Kitt Peak, as noted in section 2 above. Spectra of HD 163621 in both the red and the violet have already been published by Strassmeier & Fekel (1990). Those authors have noted that the ratio of the observed line strengths of the primary and the secondary in the red region is 5.6 to 1. The crowding of lines in the blue prevents such a measurement spectroscopically, but the single Palomar radial-velocity trace gives a ratio of 7:1 (not very accurately determined) for the areas of the 'dips' given by the two components; that ratio has some bearing on the relative line strengths in the part of the spectrum (centred near λ 4600 Å) utilized by that radial-velocity spectrometer. The mean ratio found from Coravel traces, which utilize a wavelength band reaching much further shortward than the Palomar instrument, to λ 3600 Å, is as much as 13:1 (again none too accurate,owing to the·very weakness of the secondary 'dip').The apparent increase in disparity of the components towards shorter wavelengths is the reverse of what would be expected if the fainter component were also the bluer, as proposed by Strassmeier & Fekel (1990).

At our request Bidelman (private communication) examined his moderate-dispersion spectrograms of HD 163621. He classified it as K0V and found the spectrum to show no evidence for a composite nature. Pressed for additional constraints, he noted that the spectral type was not as late as K2 and the star might be at most a magnitude above the main sequence. The spectral type, in conjunction with the light variations of the system and its chromospheric activity, places it in the BY Draconis class of variables (Bopp & Fekel 1977).

One of the difficulties with the spectrum-addition method of Strassmeier & Fekel (1990) is that the fitting procedure is done by trial and error. The method works best when a starting spectral type for at least one of the components has been determined by a reliable classifier of spectra, or a photometric colour has been obtained. In their discussion Strassmeier & Fekel noted that no combination of reference stars gave an overall satisfactory fit to the spectrum of HD 163621. They found that the best fit to the primary was with a K0 V star while the best fit based on the total sum of the residuals was with a Kl IV primary and a G6V secondary. In retrospect, the problems encountered by Strassmeier & Fekel in determining the spectral types of HD 163621 were the result of the unusually strong lines of the primary combined with the assumption that the star had solar abundances, as well as the lack of either a reasonable estimate of the spectral type of the primary or a knowledge of the photometric colours.

Examination of the spectra of additional K-dwarf reference stars and several chromospherically active K-dwarf binaries shows that, along with the line ratios identified by Strassmeier & Fekel(1990), the strength of the line wings of the saturated lines in the λ 6430-Å region is a useful criterion for classifying K dwarfs. The luminosity-sensitive line ratios indicate that the primary of HD 163621 is indeed a dwarf. Therefore, the spectrum of the primary was compared with an appropriately weighted and broadened spectrum of each of three different reference stars: HR 511 (K0V; Morgan, Harris & Johnson 1953), ε Eri (K2V; Keenan & McNeil 1989) and HR 8832 (K3 V; Keenan & McNeil 1989). The spectrum of HR 511 (K0V) provided the best fit to the important line ratios and the wings of the saturated lines. According to the abundance catalogue of Cayrel de Strobel *et al.* (1992), the only abundance analysis of HR 511 is that of Hearnshaw (1974) who found [Fe/H] = + 0.36. The lines of the primary component in the composite spectrum of HD 163621 are fully as strong as those in the pure spectrum of HR 511, despite the high iron abundance in that star; the addition of another spectrum to fit the secondary will dilute the lines of the primary represented by HR 511, causing them to appear weaker than those in HD 163621. The lines of the secondary in the λ 6430-Å region are quite weak, suggesting that the secondary is a late-K or perhaps an early-M dwarf. Unfortunately, the reference stars that we have available in that range of spectral type (HD 156026, K5 V, and 61 Cyg B, K7 V) both appear to be metal-poor with respect to the Sun. Of the two stars, HD 156026 actually has the stronger lines. Thus, it is not possible to obtain a completely satisfactory fit to the spectrum of HD 163621 with the available reference stars.

With the above revised spectral type for the primary, a luminosity ratio was redetermined from the line ratios. The spectrum of HR 511 was shifted and broadened and then subtracted from a spectrum of HD 163621. That procedure approximately eliminated weak lines of the primary from contaminating and thus strengthening the weak secondary features. Because the lines are so weak, there is little difference between a comparison of this secondary spectrum and a weighted spectrum of HD 156026 or 61 Cyg B, and both provide acceptable fits. Little else can be said about the spectral type from this comparison. From five Fe I lines, the average line ratio is 7.8 ± 0.4 for the λ 6430-Å region, which is about 0.6 of the way between the central wavelengths of the Johnson *V* and *R* bandpasses. The new value of the line ratio is to be considered a more accurate estimate than the smaller one put forward by Strassmeier & Fekel (1990).

7. Luminosity ratio from line ratios

None of the intensity ratios mentioned in the first and last paragraphs of the preceding section represents the actual luminosity ratio of the components of HD 163621. The spectroscopically determined line ratio of 7.8 in the red part of the spectrum is smaller than would correspond to the difference of visual magnitude between the two stars, for two reasons, which we take in turn below.

One is that intrinsic line strengths in late-type stellar spectra steadily increase towards later types, so the relative strength observed for lines of the secondary star in this system is greater than the relative luminosity of the star in which they originate.

We can more or less quantify the effect by comparing directly the strengths, in σ Dra and in HD 156026,of the same set of iron lines as was used in the comparison described in the final paragraph of section 6: the mean factor is 1 to 1.08, so the line-strength ratio of 7.8 to 1 is to be interpreted as a luminosity ratio of 7.8 ×1.08, or 8.4 to 1—in magnitude terms a difference of $2^m.3$. We chose σ Dra instead of HR 511 as the K0V star to be compared with HD 156026 because its abundances are thought to be similar to those of the last-named star.

The second factor to be considered is that the comparison is made in the vicinity of λ 6430 Å, where the redder secondary star is relatively brighter than it is in the *V* band. Guided by (*V*—*R*) colours, we estimate that the luminosity difference found at λ 6430 Å should be increased by $0^m.2$ to refer to *V,* making the final value of the difference $2^m.5$.

The ratios found by radial-velocity spectrometers are even more indirect than line strengths as indicators of luminosity ratios, since they depend not only on intrinsic line strengths but also upon how well the line spectrum correlates with the radial-velocity mask. In both the relevant spectrometers the mask was made to correspond to the spectrum of Arcturus (K2 III); experience shows that the depth of the 'dip' in the cross-correlation function for main-sequence stars passes through a maximum in the K types and then falls off rather rapidly. In the present case, therefore, the ratios cannot be interpreted without rather exact advance knowledge of the spectral types involved, which is just what we might have hoped to determine *from* them, so that avenue of approach turns out to be a blind alley.

8. A model for HD 163621

At this point we are in possession of all the relevant facts needed to specify a model of the HD 163621 binary system. The orbit has provided an accurate mass ratio of 1.43; photometry has provided the integrated colours, as noted in section 5; and spectroscopy has provided a luminosity difference close to $2^m.5$, as well as giving estimates of the individual spectral types. All those data are fitted well by the model set out in Table 2, with components of types G8 V and K7 V. The colours adopted for the components have been taken from Allen (1973), p. 206, by rather cavalier linear interpolation between the spectral types directly tabulated there. The masses have been interpolated similarly from p. 209. The type of G8 V for the primary is slightly earlier than that suggested by direct spectroscopy of the composite spectrum, but is in keeping with the idea that the spectrum is metalrich; the intrinsic colours

Table 2. Model for HD 163621.

Spectral type	Absolute magnitude				Colour index		Mass	Mass ratio
	V	Δ*V*	*B*	*U*	(*B* − *V*)	(*U* − *B*)		
	m	*m*	*m*	*m*	*m*	*m*	$M_\odot$	
Model G8 V	5.58		6.39	6.75	0.81	0.36	0.84	
Model K7 V	7.98		9.27	10.44	1.29	1.17	0.59	
Model G8 V + K7 V	5.47	2.40	6.32	6.71	0.85	0.39	1.43	1.42
HD 163621 (observed)		2.5			0.87	0.41		1.43

of a KO V star, as given by Allen, are already redder than the observed colours of the HD 163621 system, which is itself necessarily redder than the primary star alone.

It is only the quantization of spectral types that created the slight discrepancies between the colours of the model in Table 2 and those of the actual binary system. If we cared to interpolate between G8 and G9 we could get the colours to agree almost exactly, but the apparent improvement would be illusory because in reality there is not a perfectly tight correspondence between spectral types and colour indices.

The combined absolute magnitude of the model stars is seen from Table 2 to be $5^{m}.47$, which may be compared with the observed mean apparent magnitude of $7^{m}.94$ to show that the distance modulus'is about $2^{m}.47$, corresponding to a distance of 31 pc. That distance ought to be capable of verification within an accuracy of about 6 per cent by the Hipparcos trigonometrical parallax determination; HD 163621 features in the *Hipparcos Input Catalogue* (Turon *et al.* 1992) as no. 87746.

9. Rotational velocities and orbital inclination

A worthwhile check can be made on the properties of our model of HD 163621 by seeing whether it correctly reproduces the observed rotational velocities of the component stars. Strassmeier *et al* (1988) reported $\upsilon \sin i$ values of 8 km s^{-1} for both components of HD 163621; in the subsequent catalogue by Strassmeier & Fekel (1990) those velocities were revised to 7 km s^{-1} for the primary and 6 km s^{-1} for the secondary. The mean value from the Coravel radial-velocity traces is 8.2 ± 0.3 kms $^{-1}$ for the primary, while the Palomar trace gives 9 km s^{-1} ; the traces leave the rotation of the very weak secondary indeterminate. The formal standard deviation of the Coravel value for the primary, derived from the interagreement of the results from all the individual traces, certainly understates the real uncertainty of the determination.

The orbital parameters yield masses multiplied by the factor $\sin^3 i$; the shortness of the orbital period and the lack of conspicuous interaction between the components reinforce the spectroscopic conclusion that the system consists of main-sequence stars; their masses are noted in Table 2. The radii of the model stars, according to the same source as the masses (Allen 1973, p. 209), are 0.87 and $0.70 R_{\odot}$. With the certainty that the primary star (at least, and in all probability the secondary too) rotates in synchronism with the orbital revolution, as discussed in the accompanying paper by Hall & Henry (1994), we obtain equatorial rotational velocities of 13.5 and 10.7 km s^{-1} .

The observed rotational velocities are expected to be smaller than the true ones by the factor sin *i,* which can be estimated by comparing the model masses with the quantities $m_{1,2} \sin^3 i$ found from the orbit. The masses quoted in Table 2 suggest that sin *i* is very close to 0.5, leading to expected values of $\upsilon \sin i$ of 6.7 and 5.3 k m s^{-1} , which we consider to be in fully satisfactory agreement with the observed ones. As a matter of fact, evidence has been accumulating that the masses of stars in the relevant range of spectral type are something like 15 per cent higher than the values given in our Table 2 (Griffin 1978; Griffin, Mayor & Gunn 1982; Fekel & Beavers 1984, Griffin *et al.* 1985). Owing to the cubic dependence of the mass function (and thus of sin *i*) on the adopted masses, however, a 15 per cent change in the masses would only imply a change of less than 5 per cent in the model values of the projected rotational velocities and would not significantly impair their correspondence with the observed quantities.

Acknowledgements

F.C.F. is very grateful to Kitt Peak National Observatory for the use of its equipment R.F.G is similarly grateful to the Geneva, Dominion Astrophysical and Palomar observatories, and is pleased to thank the UK SERC for defraying the costs of visiting those institutions for the 12 visits represented in Table 1. He is also glad to acknowledge the assistance of the late Dr. A. Duquennoy in performing the reductions of the Coravel radial-velocity observations, as well as the help of Dr. R. E. M. Griffin and of the late Mr. D. W. Beggs in connection with the orbit-solving computer programme. We thank Dr. D. S. Hall and Mr. G. W. Henry for sharing their results withus in advance of publication.

References

Allen, C. W. 1973, *Astrophysical Quantities* (third edition) (London: Athlone).
Baranne, A., Mayor, M., Poncet, J.-L. 1979, *Vistas Astr.,* **23**, 279.
Bassett, E. E. 1978, *Observatory,* **98,** 122.
Bidelman, W. P. 1985, *Astr.* J., **90**, 341.
Bopp, B. W., Fekel, F. 1977, *Astr. J.,* **82**, 490
Cannon, A. J., Pickering, E. C. 1922, *Ann. Harv. Coll. Obs.,* **97,** 109.
Cayrel de Strobel, G., Hauck, B., Francois, P., Thevenin, F., Friel, E., Mermilliod, M., Borde, S. 1992, *Astr. Astrophys. Suppl.,* **95**, 273.
Fekel, F. C, Beavers, W. I. 1984, *Astrophys. J.,* **267**, 682.
Fletcher, J. M., Harris, H. C, McClure, R. D., Scarfe, C. D. 1982, *Publ. astr. Soc. Pacific,* **94**, 1017.
Griffin, R. F. 1967, *Astrophys. J.,* **148**, 465.
Griffin, R. F. 1969, *Mon. Not. R. astr. Soc,* **145,** 163.
Griffin, R. F. 1978, *Observatory,* **98**, 257.
Griffin, R. F., Gunn, J. E. 1974, *Astrophys. J.,* **191**, 545.
Griffin, R. F., Mayor, M., Gunn, J. E. 1982, *Astr. Astrophys.,* **106**, 221.
Griffin, R. F., Gunn, J. E., Zimmerman, B. A., Griffin, R. E. M. 1985, *Astr. J.,* **90**, 609.
Hall, D. S., Henry, G. W. 1994, *J. Astrophys. Astr.,* **15,**. 000.
Hearnshaw, J. B. 1974, *Astron. Astrophys.,* **34**, 263.
Hooten, J. T., Hall, D. S. 1990, *Astrophys. J. Suppl.,* **74**, 225.
Keenan, P. C, McNeil, R. C. 1989, *Astrophys. J. Suppl.,* **71**, 245.
Mayor, M., Maurice, E. 1985, in *Stellar Radial Velocities* (IAU Colloquium 88), Eds. A. G. D. Philip & D. W. Latham (Schenectady: Davis), p. 299.
Morgan, W. W., Harris, D. L., Johnson, H. L. 1953, *Astrophys. J.,* **118**, 92.
Scarfe, C. D., Batten, A. H., Fletcher, J. M. 1990, *Publ. Dom. astrophys. Obs.,* Victoria, **18** 21.
Stockton, R. A, Fekel, F. C. 1992, *Mon. Not. R. astr. Soc,* **256**, 575.
Strassmeier, K. G., Hall, D. S., Zeilik, M., Nelson, E., Eker, Z., Fekel, F. C. 1988, *Astr. Astrophys Suppl,* **72**, 291.
Strassmeier, K. G., Fekel, F. C. 1990, *Astr. Astrophys.,* **230**, 389.
Turon, C. *et al* 1992, *The Hipparcos Input Catalogue* (esa SP-1136) (Noordwijk: ESA).
Willmarth, D. 1990, *Instrument Operation Manual of the coude Spectrograph* (Tucson: National Optical Astronomical Observatories).

J. Astrophys. Astr. (1994) **15,** 321–328

1988–1991 Photometry of the Chromospherically Active Double-Lined Binary System HD 163621 = V835 Herculis

Douglas S. Hall *Dyer Observatory, Vanderbilt University, Nashville, Tennessee 37235, U.S.A.*

Gregory W. Henry *Center of Excellence in Information Systems, Tennessee State University, Nashville, Tennessee 37203, U.S.A*

Received 1994 May 17; accepted 1994 August 23

Abstract. Photometry in V and B with a 16inch automatic telescope from 1988 to 1991 confirms the synchronous rotation suspected earlier and reveals variability up to $0^M.10$ in the B bandpass at one epoch. Five spots formed with lifetimes ranging from 0.15 to 0.77 years. As with other rapid rotators, the differential rotation coefficient ($k = 0.03$) is significantly smaller than that of the Sun ($k = 0.19$).

Key words. Photometry—individual stars–HD163621—V835Herculis–variable stars—binary stars—starspots—chromospheric activity.

1. Introduction

The reasonably bright ($V = 8^M.0$) star HD 163621 appeared in the Catalogue of Chromospherically Active Binaries (Strassmeier *et al.* 1988) as an SB2 with its orbital period not yet known, its expected photometric variability yet to be discovered, unremarkable rotational velocities of $V \sin i = 8$ km/sec for each component, and a crude spectral classification of G5 IV + F, with the former being the primary (more luminous) component. The 'moderate' Ca II H & K emission first noticed by Bidelman (1985) was what had drawn attention to HD 163621 as chromospherically active.

Strassmeier & Fekel (1990) refined the spectral classification of the primary and secondary components to K1IV + G6 V and their $V \sin i$ values to 7 km/sec and 6 km/sec, respectively. They also reported an orbital period of $3^d.304$, which had been communicated to them by R. F. Griffin.

Photometry covering a time span of 3.3 years and analyzed by Hooten & Hall (1990) showed light variations amounting to $0^M.05$ in the V bandpass. Of several periodicities they found in various of their data sets, the strongest was $3^d.35 \pm 0^d.02$, a value we see does not differ importantly from the recently reported orbital period. They had presumed the variability was due to rotational modulation caused by starspots. This is consistent with the finding by Hall (1991) that G5 or K0 dwarfs will be heavily spotted if their rotation periods are shorter than 18 or 23 days, respectively, and G5 or K0 subgiants if shorter than 36 or 47 days. Note that $3^d.3$ is much shorter.

Recently, in the 71st Name List of Variable Stars, HD 163621 was designated V835 Herculis.

In the paper by Griffin *et al.* (1994) in the same issue of this journal we learn the following information which is useful to us in interpreting the photometry. The revised orbital ephemeris is

$$\begin{array}{lll} \text{T(max.vel.)} = \text{JD(hel.)} & 2{,}447{,}451.8943 + 3^{d}.304412E & (1) \\ & \pm 11 \qquad\quad \pm 6 & \end{array}$$

where T(max. vel.) refers to the primary (more luminous) component. The two components, they conclude, are best understood to be G8 V and K7 V, with, the former more luminous by about $2^{M}.5$ in the *V* bandpass. Reasonable masses indicate a rather low orbital inclination, around $i = 30°$.

2. Photometry

HD 163621 was observed in 1988, 1989, 1990, and 1991 with the 16-inch automatic telescope described most recently by Henry & Hall (1994). The comparison star was HR 6711 = HD 164280 and the check star was 91 theta Her = HR 6695. The two bandpasses were *V* and *B* of the UBV system.

For analysis the data were grouped into the 14 sets shown in Table 1. The groupings were chosen, after trial and error, so that no set would include the disappearance of a starspot and/or the appearance of a new one. There were additional subdivisions wherever warranted by the density of observations. The first two sets and part of the third, from 1988, had been analyzed by Hooten & Hall (1990) in their initial finding that HD 163621 was photometrically variable.

3. Analysis of starspot variability

There are two late-type stars involved in the HD 163621 system, both of which are liable to exhibit variability associated with starspots. However, with the total range

Table 1. Data sets

Set number	Median date	Duration (days)
1	1988.35	26
2	1988.43	25
3	1988.78	57
4	1989.17	42
5	1989.28	27
6	1989.36	28
7	1989.44	28
8	1989.78	63
9	1990.19	67
10	1990.35	34
11	1990.44	28
12	1990.83	30
13	1991.15	43
14	1991.41	67

of magnitude variation only about $0^M.1$ and the primary star contributing about 90% of the light in the *V* bandpass, we probably incur little error by adopting a conceptual approximation in which all the magnitude variation is attributed to spottedness of the primary star alone.

Fourier analysis was used to search for periodicities which might reasonably be attributed to rotational modulation of the light by large dark regions on the surface of the primary star. Except in two cases (sets 10 and 12 in the *V* bandpass) a significant periodicity was found in the vicinity of the orbital period, and in most of the cases that periodicity was the one with the most power.

Table 2. Parameters of light curve fits.

Data set	λ	n	$\Delta m@1 = 1.0$	rms (mag)	Amplitude (mag)	JD(min.) (2440000 +)	O-C (days)
1	*V*	20	2.027 ± 0.005	0.021	0.065 ± 0.015	7288.86 ± 0.12	-0.02
1	*B*	21	1.950 ± 0.004	0.018	0.086 ± 0.013	7288.89 ± 0.07	$+0.02$
2	*V*	32	2.026 ± 0.003	0.020	0.034 ± 0.010	7318.85 ± 0.16	$+0.37$
2	*B*	25	1.958 ± 0.004	0.020	0.051 ± 0.013	7318.11 ± 0.12	-0.37
3	*V*	23	1.934 ± 0.004	0.019	0.020 ± 0.012	7446.85 ± 0.34	—
3	*B*	30	1.849 ± 0.004	0.021	0.035 ± 0.011	7446.94 ± 0.18	—
4	*V*	25	1.936 ± 0.003	0.014	0.034 ± 0.009	7591.43 ± 0.14	0.00
4	*B*	25	1.849 ± 0.004	0.021	0.046 ± 0.012	7591.63 ± 0.14	$+0.20$
5	*V*	25	1.926 ± 0.004	0.018	0.020 ± 0.011	7627.30 ± 0.30	-0.74
5	*B*	23	1.842 ± 0.004	0.018	0.012 ± 0.012	7628.62 ± 0.52	$+0.58$
6	*V*	25	1.923 ± 0.005	0.025	0.012 ± 0.017	7657.92 ± 0.64	-0.07
6	*B*	26	1.837 ± 0.004	0.021	0.039 ± 0.012	7658.12 ± 0.18	$+0.13$
7	*V*	18	1.920 ± 0.004	0.016	0.034 ± 0.012	7687.43 ± 0.24	-0.52
7	*B*	23	1.843 ± 0.005	0.022	0.029 ± 0.013	7688.29 ± 0.27	$+0.34$
8	*V*	27	1.906 ± 0.005	0.024	0.050 ± 0.014	7811.35 ± 0.15	$+0.25$
8	*B*	26	1.822 ± 0.004	0.021	0.055 ± 0.013	7810.94 ± 0.12	-0.16
9	*V*	17	1.931 ± 0.003	0.014	0.072 ± 0.010	7965.22 ± 0.08	$+0.04$
9	*B*	22	1.856 ± 0.005	0.023	0.062 ± 0.015	7965.19 ± 0.13	$+0.01$
10	*B*	12	1.861 ± 0.003	0.010	0.086 ± 0.009	8020.78 ± 0.06	-0.13
11	*V*	16	1.940 ± 0.006	0.021	0.071 ± 0.019	8053.84 ± 0.13	$+0.14$
11	*B*	16	1.865 ± 0.005	0.019	0.102 ± 0.016	8053.64 ± 0.08	-0.06
12	*B*	10	1.831 ± 0.005	0.014	0.096 ± 0.016	8193.75 ± 0.09	-0.16
13	*V*	10	1.931 ± 0.008	0.021	0.044 ± 0.024	8310.74 ± 0.29	$+0.38$
13	*B*	12	1.849 ± 0.003	0.008	0.018 ± 0.007	8310.35 ± 0.28	-0.02
14	*V*	38	1.923 ± 0.003	0.017	0.018 ± 0.008	8403.44 ± 0.24	-0.09
14	*B*	43	1.834 ± 0.003	0.021	0.020 ± 0.009	8403.42 ± 0.25	-0.11

The light curve in each data set was then fit with a sinusoid by least squares. The resulting parameters are given in Table 2. Column 1 is the data set number. Column 2 is the bandpass. Column 3 is the number of differential magnitudes included in the fit. Column 4 is the differential magnitude corresponding to unit light, i.e., the axis of the sine curve. Column 5 is the rms deviation of points from the fit. Column 6 is the amplitude of the light variation, the full amplitude of the sine curve. Column 7 is the Julian date of light minimum, the epoch when the starspot faced earth. The last column will be explained later.

There was no indication that one bandpass was statistically better than the other, nor that the two yielded significantly different parameters, except for the amplitudes. On the average, amplitudes were greater in *B* than in V by about 10% or 15%. Still, we remain puzzled why sets 10 and 12 showed strong periodicity and relatively large amplitudes in *B* but not in *V*.

With most power in the vicinity of the orbital period, not the half period, the variability must be dominated by rotational modulation of ONE relatively large dark area. Any spot covering significantly less than an entire hemisphere usually will produce a flat-topped light curve rather than a perfectly sinusoidal light curve. Therefore we experimented with the two-spot light curve fitting procedure devised

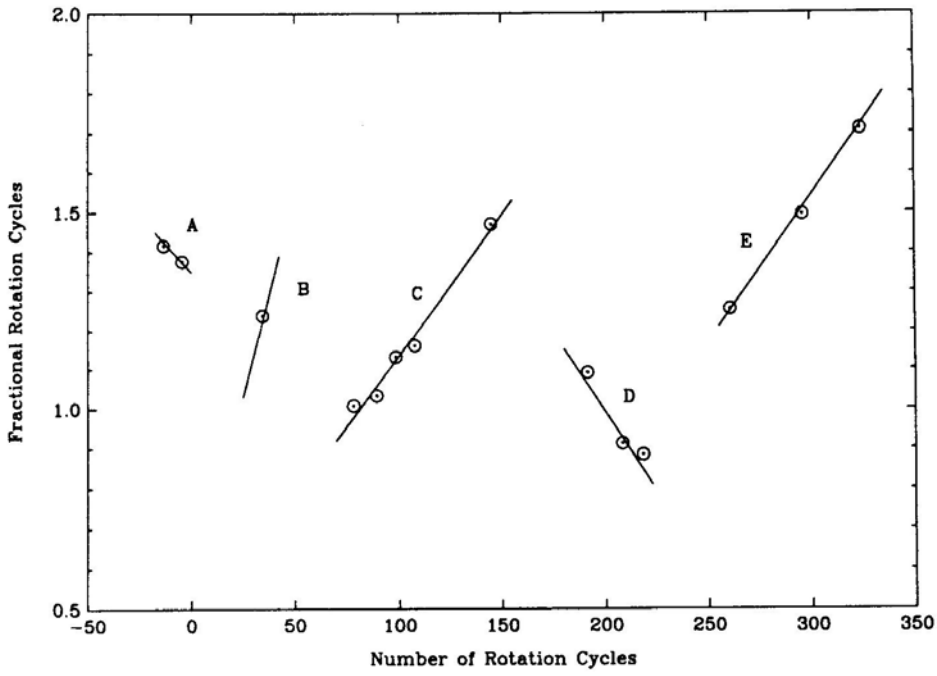

Figure 1. Migration curve for the spots in HD 163621. For every value of JD(min.) in Table 2, phase is computed with the ephemeris in equation (2), where the initial epoch is conjunction (primary star behind) and the period is the orbital period. The abscissa is time, in units of whole cycle numbers, and the ordinate is phase, in units of fractional cycles. Each point in Fig. 1 corresponds to a data set and is a mean of the JD(min.) estimates in *V* and *B*. Straight-line segments connect points judged to have belonged to the same spot. The five spots thus identified are designated A, B, C, D, E. Upward-sloping lines indicate rotation periods slightly longer than the orbital period used to compute the phases, vice versa for downward sloping. Note that even spot C lived less than one year.

by Hall, Henry & Sowell (1990), in a one-spot mode, but found it gave generally comparable best periods, Julian dates of light minimum, amplitudes, and rms deviations.

To understand the evolution of the starspots on HD 163621 we plotted the migration curve in Fig. 1. Phase was computed for each JD(min.) value in Table 2 with the ephemeris

$$T(\text{conj.}) = \text{JD(hel.)}2{,}447{,}333.7616 + 3^{d}.304412E, \quad (2)$$

gotten from equation (1) by adding a quarter cycle to the initial epoch to give us conjunction with the primary star behind (and subtracting 36 whole cycles, to facilitate plotting). The abscissa is time, in units of whole cycle numbers, and the ordinate is phase, in units of fractional cycles. Each point in Fig. 1 corresponds to a data set and is a mean of the JD(min.) estimates in *V* and *B*. Straight-line segments connect points judged to have belonged to the same spot. The five spots thus identified are designated A, B, C, D, E. Upward-sloping lines indicate rotation periods slightly longer than the orbital period used to compute the phases, vice versa for downward-sloping lines. The length of each line corresponds to the time span of the corresponding data set, from Table 1. The slope through the single spot *B* corresponds to the period in Table 3, explained in the next paragraph.

This was a difficult migration curve to interpret, not only because there are the unavoidable time gaps but also because the amplitudes are small (less than 5%) in many of the data sets and consequently the errors in the derived times of minimum are relatively large.

Ephemerides for these spots were determined in two ways. First we made sinusoidal fits which included all of the data sets belonging to each spot, separately in *V* and

Table 3. Spot ephemerides.

Spot	Sets included	Method	*n*	JD(min.) 2440000. +	Period (days)	ΔP/P (%)
A	1, 2	sin *V*	53	7305.50 ± 0.10	3.344 ± 0.020	
	1, 2	sin *B*	46	7305.13 ± 0.08	3.258 ± 0.016	
		linear	4	7305.32 ± 0.19	3.289 ± 0.041	− 0.5 ± 1.2
B	3	sin *V*	23	7446.85 ± 0.34	3.332 ± 0.065	
	3	sin *B*	30	7446.94 ± 0.18	3.414 ± 0.032	
		mean	—	7446.90 ± 0.16	3.373 ± 0.029	+ 2.1 ± 0.9
C	4, 5, 6, 7, 8	sin *V*	120	7687.89 ± 0.16	3.337 ± 0.006	
	4, 5, 6, 7, 8	sin *B*	123	7688.03 ± 0.11	3.325 ± 0.004	
		linear	10	7687.95 ± 0.14	3.328 ± 0.006	+ 0.7 ± 0.2
D	9, 11	sin *V*	33	8021.00 ± 0.09	3.289 ± 0.006	
	9, 10, 11	sin *B*	50	8020.88 ± 0.88	3.284 ± 0.008	
		linear	5	8020.91 ± 0.05	3.278 ± 0.004	− 0.8 ± 0.1
E	13, 14	sin *V*	76	8300.16 ± 0.17	3.329 ± 0.006	
	12, 13, 14	sin *B*	70	8299.86 ± 0.26	3.341 ± 0.012	
		linear	5	8300.38 ± 0.12	3.327 ± 0.005	+ 0.7 ± 0.2

B. Second, we made straight line fits to the JD(min.) values in Table 2. For spot *B*, which included only one data set, the linear fit could not be made. Results are given in Table 3. Column 1 identifies the spot. Column 2 indicates which data sets are included in each spot. Column 3 is the method used. Column 4 is either the number of differential magnitudes included in the sinusoidal fit or the number of JD(min.) values included in the linear fit. Column 5 is the epoch of minimum light. Column 6 is the effective rotation period. And Column 7 is the percentage difference between the rotation period and the orbital period.

Residuals in JD(min.), in the sense observed time minus time computed with the linear-fit rotation ephemerides in Table 3, are entered in the last column of Table 2 for comparison with the uncertainties in the individual observed JD(min.) values. It

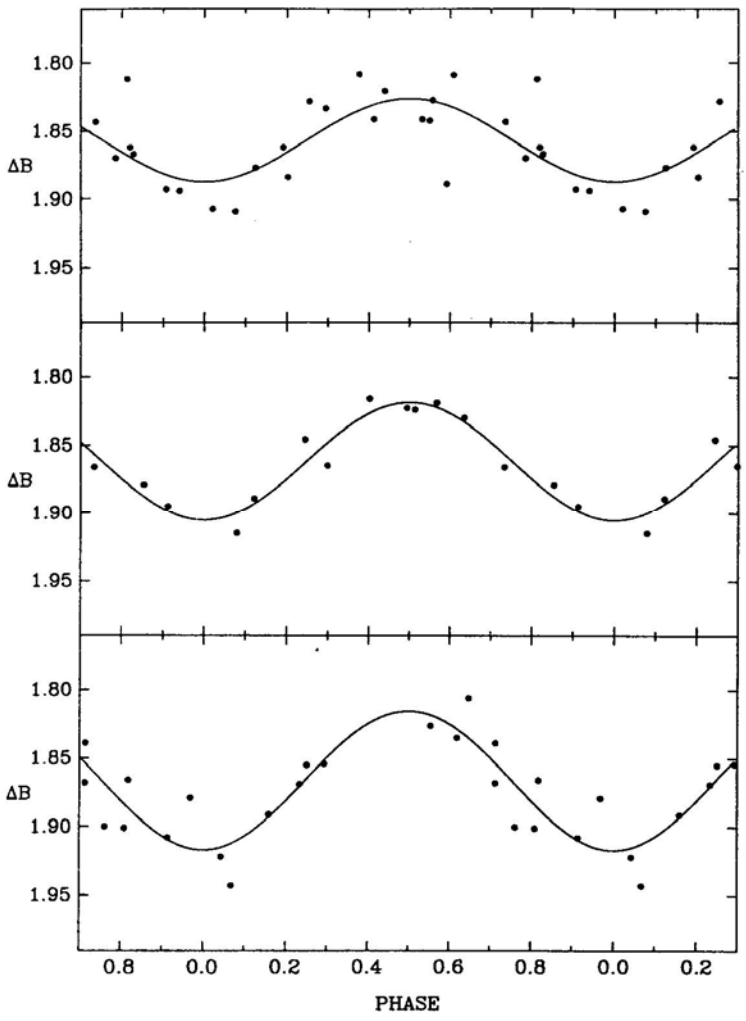

Figure 2. The light curve of one starspot, D, shown as an example. Data in the blue bandpass are illustrated and the three panels correspond to data sets 9,10, and 11. The solid curves represent the sinusoidal fits and zero phase in set at the corresponding values of JD(min.) in Table 2. Note that the amplitude increased monotonically from $0^M.06$ to $0^M.10$.

is gratifying that they are comparable in size. The respective averages are ± $0^d.20$ (column 7) and ± $0^d.21$ (column 8). This corresponds to only ± 0.06 phase units.

The observed lifetimes of these five spots can be estimated from Fig. 1. For spots A, B, C, D, and E, respectively, they were > 0.15, 0.15, 0.77, 0.36, and > 0.72 years. The light curve of one starspot, D, is shown as an example in Fig. 2. Data in the blue bandpass are illustrated and the three panels correspond to data sets 9, 10, and 11. The solid curves represent the sinusoidal fits and zero phase is set at the corresponding values of JD(min.) in Table 2. Note that the amplitude increased monotonically from $0^M.06$ to $0^M.10$.

4. Differential rotation

The last column in Table 3 shows that the five spot rotation periods range from 2.1% ±0.9% faster than synchronous to 0.8% ± 0.1% slower, the full range thus being Δ P/P = 0.029 ± 0.009. If we assume these five spots had latitudes covering nearly the full 90° range, as most heavily spotted dwarf stars are known to do (Gray 1988, table 7–1), then we can estimate that k = 0.029 ± 0.009 in the expression

$$P(\phi) = P(\text{eq}) / (1 - k \sin^2 \phi) \qquad (3)$$

commonly used to describe differential rotation as a function of stellar latitude, ϕ In such an expression k = 0.19 for the sun. This smaller value we have found for HD 163621 is in accord with results showing that more rapidly rotating stars have correspondingly smaller differential rotation coefficients (Hall 1991, Fig. 7). The physical reasonableness of that correlation between k and P (rot.) may be understood by realizing that the rate of angular shear between one latitude and another is holding constant for all stars.

5. Ellipticity effect? Eclipses?

A light curve was prepared in which the abscissa was orbital phase computed with the ephemeris in equation (2) and the ordinate was residuals from all of the sine-curve fits in Table 2. Fourier analysis failed to reveal a measurable ellipticity effect; the coefficient of the cos 2θ term was smaller than its uncertainty, in both V and B. Moreover, there was no significant light loss around phase 0.0 nor 0.5, where eclipses would occur. In view of the low inclination of the orbital plane, probably around i = 30°, eclipses are not to be expected.

Acknowledgement

This work was supported in large part by two research grants to Tennessee State University, one from N.A.S.A. (NAG 8–111) and one from the N.S.F. (HRD 9104484). We are also grateful to F. C. Fekel and R. F. Griffin for sharing information contained in their paper prior to publication and for making useful comments on earlier versions of our paper.

References

Bidelman, W. P. 1985, *Astr. J.* **90**, 341

Gray, D. F. 1988, *Lectures on Spectral Line Analysis: F, G, and K Stars* (Arva, Ontario: The Publisher).

Griffin,R.F.,Fekel, F.C,Morton,M.D.,Fried,R.E.1994, *J. Astrophys. Astr.* **15**,000-000.

Hall, D. S. 1991, in *Cool Stars and the Sun: Activity, Magnetism, and Dynamos,* Ed. I. Tuominen, D. Moss, & G. Rüdigen (Berlin: Springer-Verlag), p. 353.

Hall, D. S., Henry, G. W., Sowell, J. R. 1990, *Astr J.* **99**, 396.

Henry, G. W., Hall, D. S. 1994, *I.A.P.P.P. Comm.* No. **55**, 36.

Hooten, J. T., Hall, D. S. 1990, *Astrophys. J. Suppl.* **74,** 225.

Strassmeier, K. G., Fekel, F. C. 1990, *Astr. Astrophys.* **230**, 389.

Strassmeier, K.G.,Hall, D.S., Zeilik, M.,Nelson, E.,Eker, Z.,Fekel, F.C.1988, *Astr. Astrophys. Suppl.* **72**, 291.

J. Astrophys. Astr. (1994) **15,** 329–341

Pulsar Observations at Decametric Wavelengths using a Swept-frequency Dedisperser

A. A. Deshpande & V. Radhakrishnan *Raman Research Institute, Bangalore 560 080, India*

Received 1994 July 28; accepted 1994 August 30

Abstract. In this paper, we describe pulsar observations at decametric wavelengths using the Gauribidanur Radio Telescope made subsequent to our earlier measurements (Deshpande & Radhakrishnan 1992). To improve the time-resolution in our measurements of pulse profiles, we have used the 'swept-frequency dedispersion' method with some modifications to suit its application at such low radio frequencies. We also present a new scheme that simplifies the calibration of the receiver gain characteristics. We present average profiles on four pulsars from these improved measurements at 34.5 MHz.

Key words: Pulsars—average profiles—dispersion.

1. Introduction

The observations of pulsar signals are increasingly affected at lower radio frequencies by a variety of propagation effects occurring in the intervening medium. This limits pulsar studies at low radio frequencies to only nearby, i.e. low dispersion measure, pulsars. At these frequencies, observations of pulsars with high dispersion measures are in principle possible if the scatter broadening is not too severe. Using a single-spectral-channel receiver, we were able to detect 8 pulsars at 34.5 MHz (Deshpande 1987; Deshpande & Radhakrishnan 1992, hereafter referred to as DR92). However, the apparent profile widths were dominated by the dispersion effects over the 30 kHz bandwidth used. Hence, it was clear that to obtain high time-resolution profiles with sufficiently wide bandwidths, one needs some suitable dedispersion method. In this paper, we describe our pulsar observations at 34.5 MHz made using swept-frequency dedispersion (Deshpande 1987) with the Decameterwave Radio Telescope at Gauribidanur (GEETEE)*, India (Deshpande, Shevgaonkar & Sastry 1989). In the first part of this paper, the dedispersion method and the relevant observing setup is described. A new scheme for gain calibration, the procedures used for observation, data processing, and detection are also discussed. Average pulse profiles of four pulsars obtained from these observations are presented.

* This telescope is jointly operated by the Indian Institute of Astrophysics, Bangalore and the Raman Research Institute, Bangalore.

2. Swept-frequency dedispersion method

The pre-detection dedispersion method used by us involves a basic swept-frequency dedispersion procedure similar to that of Sutton *et al.* (1970) and McCulloch, Taylor & Weisberg (1979). In this method, the periodicity and the dispersed nature of the pulsar signals are used to our advantage. It can be shown, that due to the dispersion the pulsar signal at any instant in time gets mapped into the frequency domain. Therefore, a pulse profile over one full period could be obtained, if the intensity as a function of frequency can be measured over a finite bandwidth (Δf) given by,

$$\Delta f \sim kPf_0^3/\mathrm{DM} \tag{1}$$

where k = a constant, f_0 = center frequency of observation ($\gg \Delta f$), DM = Dispersion Measure, and P = Period of the pulsar.

However, such a spectral pattern sweeps across the frequency band at an approximate rate of ($-\Delta f/P$). In this scheme of dedispersion, the pattern is made to appear stationary in the frequency domain by also 'sweeping' the centre frequency of the receiver appropriately. The dispersed pulsar signal then results in a train of 'fixed' spectral features separated by Δf corresponding to the dedispersed pulse profiles. This requires that the centre frequency of observation be swept at a rate given by the dispersion relation, in practice the sweep being reset at intervals that are integral multiples of the pulsar period. Intensity patterns can be then measured with high spectral resolution using a suitable spectral line receiver. The maximum time-resolution obtained in this manner corresponds to the dispersion smearing over one spectral bin. This forms the basis of the method employed by us to dedisperse the pulsar signals and to enable observations with high time-resolution.

2.1 *The receiver setup*

Figure 1 shows a schematic for the receiver setup used for the present observations. There are two important components in such a setup, namely a sweeping local oscillator system and a high-resolution spectrometer. A suitable sweeping local oscillator system (SLOS) was specially built for this purpose. A detailed description of this system is given in Deshpande (1992), and we will briefly mention here only the main characteristic of the system relevant for this discussion.

This SLOS is given the dispersion measure and the period of a pulsar along with the choice of start frequency for the sweep. The maximum sweep bandwidth available is 1 MHz and is centred around 34·5 MHz. At these observing frequencies this SLOS is suitable for observations of pulsars with P/DM ratio smaller than 0.2 where P is in seconds and DM is in units of pc cm^{-3}. We have considered most of the pulsars detected at 102 MHz (Izvekova *et al.* 1979), as possible candidates for detection at 34.5 MHz, and find that the value of 1 MHz for the maximum sweep bandwidth is sufficient for most of them. The pulsars which need higher sweep bandwidths have either very low DMs or longer periods. Therefore, the effects of dispersion smearing are not very serious in their cases. The SLOS produces a staircase sweep matching closely with that described by the dispersion relation within an r m.s. of about 250 Hz. The r m.s. error in the sweep frequency produced should be less than the spectral resolution of the spectrometer used. The r.m.s. error in the present case results in an

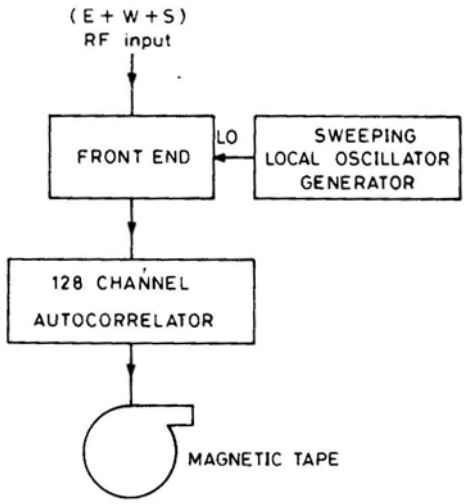

Figure 1. A simplified block diagram of the receiver setup.

additional smearing of about 8 milliseconds for DM= 100cm^{-3}pc. The staircase sweep has about 4000 steps of height 250 Hz on the average.

An existing 128 channel (complex) autocorrelation receiver provided high resolution intensity measurements in the frequency domain. (A detailed description of this receiver is given in Udayashankar & Ravishankar 1990). With a suitable choice of the baseband filter and appropriate sampling clock rate, the observing bandwidth (B) can be selected to give a spectral resolution of (B/256). A maximum sampling rate of 2MHz is possible with this receiver.

3. A new scheme for gain calibration

As discussed earlier, the intensity pattern in the spectral domain due to the pulsar signal can be made to appear stationary by the use of a suitable sweeping local oscillator system. Let us assume, that the SLOS frequency $f_{\text{out}}(t)$ is swept from f_s to f_e (such that $f_s > f_e$) in each interval equal to P starting from time $t = 0$ up to time $t = t_{on}$. The average intensity pattern at the output can be expressed in general as

$$\bar{I}(n) = \frac{1}{t_{on}} \int_0^{t_{on}} \left[\frac{1}{\delta f} \int_{-\delta f/2}^{+\delta f/2} |G_a(f_{RF})|^2 |G_b(f_{LF})|^2 [I_P(f_{RF}, t) + I_B(f_{RF}, t)] df \right] dt \qquad (2)$$

where n = bin index of the output intensity pattern, δf = resolution of the spectrum/ bin width, G_a = gain function of the telescope system upto the mixer stage, G_b = gain of the baseband filter, $I_P(f_{RF},t)$ = spectral power density of the pulsar signal at the input of the antenna, I_B (f_{RF}, t) = spectral power density of the background radiation, $f_{RF} = f_{out}(t) + n.\delta f + f, f_{LF} = n.\delta f + f,$ and $\delta f \ll (f_s - f_e) \ll f_{out}$.

If the interval (P') of each sweep is equal to the apparent period (P) of the pulsar and if the duration of observation, t_{on}, is an integral multiple of P, then the above

equation can be simplified to

$$\bar{I}(n) \simeq g(n)[\bar{I}_P(\phi_s(n)) + \bar{I}_B] \tag{3}$$

where

$$g(n) = \frac{1}{P}\int_0^P \left[\frac{1}{\delta f}\int_{-\delta f/2}^{+\delta f/2} |G_a(f_{\mathrm{RF}})|^2 |G_b(f_{\mathrm{LF}})|^2 \mathrm{d}f\right]\mathrm{d}t \tag{4}$$

and $\phi_s(n)$= longitude of the pulsar signal at the frequency (f_s + $n\delta f$) and at time t =0 $\bar{I}_p$ (ϕ_s (n))= time average of the intensity of the pulsar signal atlongitude $\phi_s(n)$,$\bar{I}_B$, = time average of the intensity of the background radiation.

We have assumed that over a small bandwidth δf all the above functions can be considered to be constant. It should be noted, that for obtaining the intensity profile corresponding to at least one period of the pulsar signal a total bandwidth of at least Δf (as in equation (1)) should be used. Further, to estimate the quantity [$\bar{I}_p$,($\phi_s(n)$), + $\bar{I}_n$], we need to know $g(n)$ to a sufficient accuracy. As the quantity $g(n)$ includes the antenna and the array component responses, it can be best measured by making observations *off* the source. In such a case, the measured intensities $\bar{I}_{\mathrm{off}}(n)$ are given by

$$\bar{I}_{\mathrm{off}}(n) \simeq \mathrm{g}(n)\,\bar{I}'_B \tag{5}$$

where $\bar{I}'_B$ = the background noise intensity *off* the source.

Thus the measured intensities can be treated as a scaled version of the function g(n). However, the accuracy to which $g(n)$ can be measured, i.e. $\Delta g(n)$, is given by

$$\Delta g(n) = \frac{\Delta I_{\mathrm{off}}(n)}{\bar{I}_{\mathrm{off}}(n)}\, g(n) \tag{6}$$

where

$$\Delta I_{\mathrm{off}}(n) = \frac{m\bar{I}_{\mathrm{off}}(n)}{\sqrt{\delta f\, t_{\mathrm{off}}}} \tag{7}$$

m= a receiver dependent constant and t_{off} = the duration of such an observation.

Noting that in practice $I_p \ll I_B$, the uncertainty in the estimation of $\bar{I}_p$,($\phi_s(n)$) can be shown to be

$$\Delta I_P \propto \frac{\bar{I}_B}{\sqrt{\delta f}}\left[\frac{1}{t_{\mathrm{on}}} + \frac{1}{t_{\mathrm{off}}}\right]^{1/2} \tag{8}$$

where $\bar{I}_B$ is assumed to be equal to $\bar{I}'_B$ for simplicity.

If the *off-source* measurements are made by switching the beam *on* and *off* the source at a fast rate, then t_{on} = t_{off} typically. The switching reduces the effective observing time on the source by a factor of 2. This will worsen the attainable sensitivity by a factor of 2, even if we ignore other problems associated with the fast beam switching. Another way is to make such *off-source* observations over a separate time span. Then the uncertainties in determining $g(n)$ *can* be considered negligible if $t_{\mathrm{off}} \gg t_{\mathrm{on}}$. Thus the *off-source* measurements need to be made over typically 3–4 hours. Apart from such large overheads in the observing time, it is also required that $g(n)$ does not change over the entire interval of observation. It should be noted that the function $g(n)$ will be different for different values of the period and the dispersion measure. These factors make such *off-source* measurements extremely time consuming.

Here, we suggest a different scheme for gain calibration, wherein we avoid the need for an accurate estimation of $g(n)$.

We have noted already that the spectral intensity pattern due to the pulsar signal is made to appear stationary if the appropriate LO sweep is reset only at invervals of the integral number (L) of the apparent period (P) of the pulsar. In our case,we will concentrate on the case when L= 1. Any deviation ΔP in such reset intervals causes the spectral intensity pattern to drift at a rate given by

$$\left(\frac{\mathrm{d}f_r}{\mathrm{d}t}\right)_d = \left(\frac{\Delta P}{P}\right)\cdot\left(\frac{\mathrm{d}f}{\mathrm{d}t}\right)_{sw} \tag{9}$$

(where $(\mathrm{d}f/\mathrm{d}t)_{sw}$ = the sweep rate of the SLOS and $\Delta P \ll P$.

If the intensity pattern is averaged for a long time without accounting for such a drift, the pulsar features would be smeared over the total drift. However, if the intensity patterns are sampled frequently enough and are averaged suitably by accounting for the drift, the average output intensity would have an equivalent gain $g'(n)$, given by

$$g'(n) = \frac{1}{t_{on}}\int_0^{t_{on}} g(n'(t))\,\mathrm{d}t \tag{10}$$

where

$$n'(t) = \mathrm{INT}\left[\mathrm{Frac}\left[\frac{(n+n_d(t))}{(\Delta f/\delta f)}\right]\cdot\left(\frac{\Delta f}{\delta f}\right)\right] \tag{11}$$

$n_d(t)$ is the number of bins by which the pattern drifts in time t and is given by

$$n_d(t) = \left(\frac{\mathrm{d}f}{\mathrm{d}t}\right)_d\cdot\left(\frac{t}{\delta f}\right) \tag{12}$$

It can be shown, that if

$$n_d(t_{on}) = N_d\left(\frac{\Delta f}{\delta f}\right) \tag{13}$$

where N_d = integer number of drift cycles (i.e. = 1,2,...) then the effective gain $g'(n)$ will have a constant value, say $\bar{g}$, irrespective of n. This condition implies that

$$t_{on} = \frac{N_d P^2}{\Delta P} \tag{14}$$

Thus, with suitable choices of t_{on}, ΔP and N_d, it is possible to obtain an average intensity pattern for the pulsar signal without needing an accurate measurement of $g(n)$. It should be pointed out at this stage, that if there exist large deviations within the gain function $g(n)$ from its means value, then the final signal-to-noise ratio attainable in the above scheme is reduced. In such a case, a crude estimate of $g(n)$ can be used to divide the individual intensity patterns before averaging, so as to reduce the deviations in the effective gain function drastically. The modified gain function is given by

$$g1(n) = \frac{g(n)}{g_0(n)} \tag{15}$$

where $g_0(n)$ = the crude estimate of $g(n)$.

The crude estimate $g_0(n)$ can be obtained by averaging the indivdual patterns without accounting for the del berate drift $(df/dt)_d$ and be used after suitable normalization Further, if should be noted, that the above solution is based on an assumption that to intensity pattern for the pulsar signal does not fluctuate during the observation However this a assumption does not strictly hold good in practice. Then, the final intensity pattern would correspond to the weighted (w.r.t. $g1(n)$) mean intensity pattern of the pulsar signal. The final profiles would be affected most due to this problem if N_d=1. Assuming that the fluctuations are random, this problem can be overcome to a great extent by choosing higher values of N_d. For given values of t_{on} and P,this would imply (from equation 14) higher values of ΔP. However any nonzero value of ΔP would cause additional smearing typically of the order of $\delta t = (\Delta P/P)\ T_s$; where T_s =the (read-out) sampling interval. This smearing should be as small as possible. If the sampling interval, T_s, is comparable to P, then this condition can be stated otherwise as $(\Delta P/P) \ll (\delta f/\Delta f)$. Therefore, the value of ΔP needs to be optimized with respect to N_d and δt

with a suitable choice of the above mentioned parameters, the output intensity pattern, $I(n)$, can be expressed as

$$\bar{I}(n) \simeq \bar{g}(\bar{I}_P(\phi_s(n)) + \bar{I}_B) \tag{16}$$

As $\bar{I}_p \ll \bar{I}_B$, a flux calibration could be obtained almost directly if an independent estimate of $\bar{I}_B$ is available. Apart from avoiding accurate measurements of the gain function g(n) on a routine basis, the above scheme has some more interesting and important advantages. In the conventional scheme, where $\Delta P = 0$, we need to observe over a bandwidth equal to or greater than Δf, to obtain the intensity pattern over one full period. It should be pointed out that the pulsar emission at low radio-frequencies may not be limited to the main pulse and the interpulse window alone (Bruck & Ustimenko 1976, 1977, 1979). This aspect makes it necessary to observe the intensity pattern corresponding to the full longitude range. The constraint in turn limits the resolution in time domain to P/N_{ch} in general, where N_{ch} is the number of spectral channels. However, our new calibration scheme readily provides a possibility of increasing the resolution beyond the above limit. In this scheme, if the observing bandwidth (B) is chosen smaller than Δf, then the time-resolution obtainable increases by factor $\gamma = \Delta f/B$. The observing band with can be decrease upto the limit when B/N_{ch}. becomes equal to the r m.s. error in the SLOS ouput frequency However, such an improvement in resolution is at the cost of reduction in the sensitivity by a factor of $1/.\sqrt{\gamma}$ The other advantage, which is quite important but implicit in this scheme, is that of not requiring absolute synchronization of the sweep with respect to the arrival time of the main pulse in the pulsar signal. Thus we note that the case when $\Delta P \neq 0$, has many important advantages compared to the conventional case when $\Delta P = 0$. We have used this new scheme for the observations described in this paper.

4. Observations and data acquisition

In this section, we describe the procedures adopted for the pulsar observations using the above discussed schemes. The basic receiver set-up is shown m Fig. 1. It should be noted, that the autocorrelation receiver (ACR) accepts only one input signal. The

antenna outputs are available from both the EW array and S array (of the Gauribidanur 'T' shaped array) separately. The possible single inputs to ACR are namely the (E+W),S or (E+W+S). The choice of (E+W+S)is obvious for the ACR input, due to the high effective aperture area corresponding to it. The beam pattern corresponding to this (E +W+S) mode is quite complex, and can be described as

$$R_{(E+W+S)} = R_{(E+W)} + R_{(S)} + 2 \cdot R_{((E+W)\times S)} \tag{17}$$

where $R_{('x')}$ = the beam pattern in, '*x*' mode.

The first two terms on the right hand side of the above equation correspond to two orthogonal fan beams, while the last term corresponds to a pencil beam due to the correlation. Thus the resultant beam has an equivalent resolution much poorer compared to that in the case of correlation. This aspect does not pose any serious problem in the case of pulsar observations, as the probability of encountering a 'confusing' pulsar, with its period and DM very close to that for the pulsar of interest, in the total field of view is very small. In this mode, the tracking facility (Deshpande, Shevgaonkar & Sastry 1989) can also be used to obtain longer observing time. The single input (E + W + S) is obtained by combining the (E + W) and S signals with equal phases. Amplitudes of the E + W and the S inputs are adjusted, such that all the basic array elements contribute equally at the combiner output. The SLOS is used with suitable settings. The relevant value of the Dispersion Measure (DM) is set accurate to ± 0.005 cm^{-3} pc. The sweep reset period is set different from the apparent pulsar period, such that $(\Delta P/P) \sim 2 \times 10^{-3}$ typically. The starting frequency for the sweep is chosen suitably to centre the sweep approximately at 34.5 MHz. Different observing bandwidths (B) can be employed by using appropriate base band filters and the sampling clock frequency. The choice of this bandwidth determines the signal-to-noise ratio and the time-resolution obtainable in the output profiles for given pulsar parameters. The online integration time (τ_{on}), to average the auto-correlations, can be selected in the range $(2^{12} \rightarrow 2^{19})/f_{clk}$ where f_{clk} is the sampling clock frequency. The averaged correlations available at the output of this receiver are recorded on a magnetic tape. The sampling time, T_s, is equal to the on-line integration time (τ_{on}). In order to recover the absolute amplitude information lost due to the one-bit processing in the receiver, it is required to measure the signal power at the input of the zero-cross detectors. Outputs of four threshold detectors/ integrators (Udayashankar & Ravishankar 1990) employed for this purpose are also recorded along with the autocorrelations.

5. Data processing and detection

The data recorded during these observations consist of the autocorrelation function measured using the autocorrelation receiver-SLOS combination. The autocorrelations available are *normalized one-bit autocorrelations* at positive delays. The processing involves the following steps.

5.1 *Estimation of the spectra*

The one-bit correlation values are translated to the corresponding analog correlations through the Van-vleck relation.

$$\rho_a = \mathrm{SIN}\left(\frac{\pi}{2}\rho_c\right) \tag{18}$$

where ρ_c is the normalized one-bit correlation and ρ_a is the corresponding normalized analog correlation. This computation is performed for both real and imaginary parts of the correlations separately As already noted, the absolute amplitude information is lost in one-bit processing. However, if estimates of the total Signal power at the input of the zero-cross detector are available, as in the present case it is possible to recover the absolute amplitude information. The available estimates of the total power are used to multiply the normalized correlations to obtain the amplitude calibrated (unnormalized) values of the autocorrelations. The amplitude calibrated (in-phase and quadrature) correlations obtained for positive delays are used to get a complex Hermitian symmetric autocorrelation function. The autocorrelation function and the power spectrum of the signal form a Fourier transform pair. We use a 256-point Fast Fourier Transform (FFT) routine to transform the autocorrelation function to a power spectrum. Thus, a power spectrum is obtained corresponding to each of the autocorrelation functions sampled at every interval of the on-line integration.

5.2 *Average band shape*

The power spectra obtained over the observing interval are averaged together to obtain a function representing the average gains of the spectral bins, i.e. the gain function $g_o(n)$ of the antenna-receiver combination. It should be noted that the band shape thus obtained is not expected to be affected by the presence of pulsar signals on the average, because of the deliberate slow drift of the spectral pattern due to the pulsar signal.

5.3 *Pulsar profiles*

Each of the power spectra contains a spectral pattern due to the observed pulsar signal. This pattern is weighted by the gain function of the receiver across the spectral band. We use the gain function $g_o(n)$ obtained earlier to divide each power spectrum so as to roughly equalize the receiver gain across the spectral pattern. The spectrum thus obtained ideally has a dc pedestal on which the pulsar pattern buried in the background noise is placed. The value of the dc pedestal corresponds to the average power due to the background noise (say, P_{noise}). Using an appropriate dispersion law, the spectral pattern is converted to a time domain pattern where the sampling becorncs, in general, non-uniform. This procedure is repeated for all power spectra obtained at regular intervals of the on-line integration. The final apparent time series obtained over the total observing interval (t_{on}) is then averaged synchronous to the apparent period of the pulsar. The bin-width in the time domain is chosen as close as possible to the dispersion smearing over one spectral bin, such that the apparent period is divktei into integral number of bins. Using similar procedure as described in DR92, an average profile over a two-period stretch is obtained and is tested for significant detction of two pulses which should be separated by exactly one period. The threshold for significant detection is chosen to be equal to three times the r.m.s.

deviations due to the noise in the two-period stretch. The value for the r.m.s. noise deviations (σ) is computed as

$$\sigma = \frac{mP_{\text{noise}}}{\sqrt{\bar{C}\tau_{\text{on}}\delta f}}, \tag{19}$$

where $\bar{C}$ is the mean number of samples averaged per bin. In case of a successful detection, the final average profile is obtained by combining the two halves of the corresponding two-period stretches. In an ideal case, the final profile has a flat baseline corresponding to the average noise power per bin (P_{noise}). However, in practice, the baselines are generally not flat. Such baselines can result from any low level broadcast interference within the observing band when swept across the band over Δf, and cannot be expected to have any systematic shape in general. For the purpose of baseline estimation the data in the off-pulse region of the profile was used and a lower order polynomial was fitted. The smooth baseline then was subtracted from the raw profile.

6. Results and discussion

Using the observational and the data processing procedures described in this paper, observations were attempted in the directions of more than 20 pulsars. The dispersion measures for these pulsars are in the range 12.4to 79 cm^{-3} pc. An observing band width (B) of 333 KHz and a sampling interval (read-out interval, T_s) of 1.57 second were used in all cases. In the cases of only four pulsars, namely PSRs 0628 — 28,0834 + 06, 0943 + 10 and 1919 + 21, was it possible to satisfy the detection criterion. For these pulsars, average pulse profiles were obtained with good signal-to-noise ratio.

As the values of Δf for three out of the four pulsars are larger than 333 KHz, it was possible to improve the time-resolution beyond (P/256) in these cases. The results obtained demonstrate the usefulness of the method employed to detect highly dispersed pulsar signals with high time-resolution.

The profiles obtained from these observations are shown in Fig. 2. The profiles presented are smoothened additionally over 3 bins for PSR 1919 + 21 and over 10 bins in other cases. The, error bars correspond to five times the standard deviations due to noise.

6.1 *PSR 0628 28* (*Fig. 2a*)

This pulsar with a dispersion measure of 34.56 cm^{-3} pc was detected at such a low frequency in our earlier observations (DR92). Note the weak emission feature at about 185° longitude, which can be easily distinguished from the rest of the off-pulse baseline (Fig. 2a). If this feature is due to interpulse emission, then the ratio of the energy of the interpulse to that of the main pulse is about 0.15. However, more observations made to confirm the possible interpulse emission did not show this feature. Therefore, at best, it suggests sporadic interpulse emission. The observed width at half-maximum of the main pulse is about 125 milliseconds.

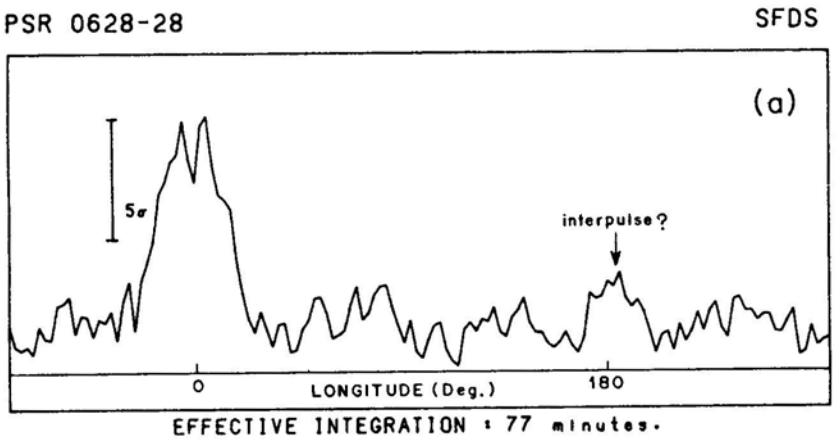
PSR 0628-28
SFDS
(a)
5σ
interpulse?
0
LONGITUDE (Deg.)
180
EFFECTIVE INTEGRATION : 77 minutes.

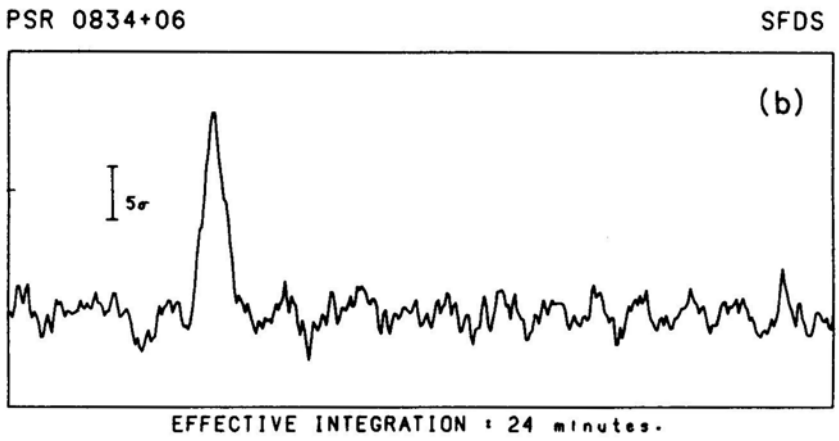
PSR 0834+06
SFDS
(b)
5σ
EFFECTIVE INTEGRATION : 24 minutes.

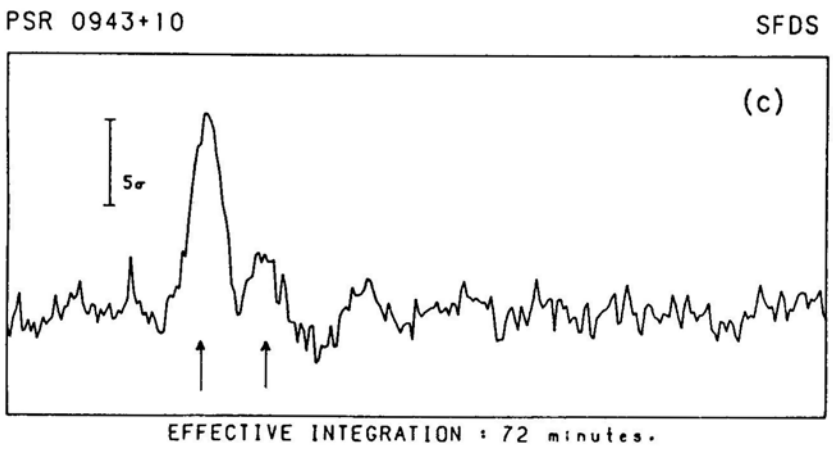
PSR 0943+10
SFDS
(c)
5σ
EFFECTIVE INTEGRATION : 72 minutes.

Figure2 (a,b,c).

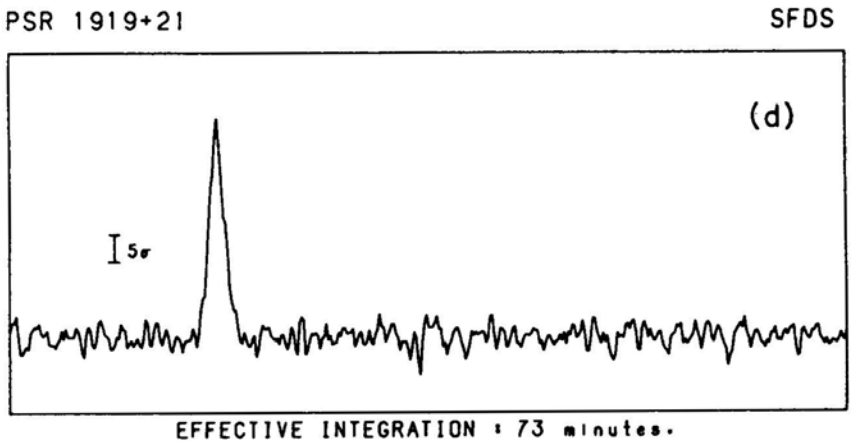

Figure2(d).

Figure 2. The average pulse profiles for (**a**)**:** PSR 0628 –28; (**b**)**:** PSR 0834 + 06; (**c**)**:** PSR 0943 + 10 and (**d**)**:** PSR 1919 + 21 observed at 34.5 MHz using the swept-frequency dedisperser.

6.2 *PSR 0834 + 06* (*Fig. 2b*)

A high time-resolution profile obtained in the present observations (on one day) is shown in Fig. 2b. The improvement in the time-resolution due to the SFDS in comparison with our earlier measurements (DR92) is quite striking. The observed width in this case is approximately 36 milliseconds. The average profile does not show any significant interpulse emission contrary to that reported at 25 MHz (Bruck & Ustimenko 1976, 1979), but is consistent with the observations by us earlier (Deshpande & Radhakrishnan 1990 and also DR92) and with those by Phillips & Wolszczan (1989).

6.3 PSR *0943 + 10* (*Fig. 2c*)

Figure 2c shows a high resolution profile obtained by combining the data on two days. Suleimanova & Izvekova (1984) have reported mode changing for this pulsar at 62 and 102 MHz. The pulse profile, obtained by us after averaging many days' data, seems to suggest that only one of the two modes (namely, B and Q) discussed by Suleimanova & Izvekova (1984) becomes prominent at decametric wavelengths. This (B) mode is observed to have two peaks with an intensity ratio of 3.5:1 at 102 MHz. This intensity ratio appears to be about the same at 34.5MHz.However, the separation of the two components has increased to about 80 milliseconds at the present frequency from 31 milliseconds at 102 MHz. This suggests to us that the separation is proportional to $(wavelength)^{0.9}$. It is worth pointing out that at about a meter wavelength this pulsar has a 'conal single' profile (Rankin 1993) suggesting that thesight-line cuts the emission cone tangentially. The fact that no measurements on this pulsar at frequencies above 610 MHz are reported suggests that the sight-line maybemissing the emission beam completely. The profile and the pulse-intensity evolution in the frequency range 0.6–1 GHz is therefore worth investigating. It is also

worth noting that the pulse energy spectrum for this pulsar is seen to be still rising even upto 34.5 MHz (DR92). This happens to be the first case where the spectrum for a long period pulsar does not have a turnover even down to 34.5 MHz. Investigation of the spectrum and pulse profile of this pulsar at frequencies below 34.5MHz would be of interest.

6.4 *PSR 1919 + 21* (*Fig. 2d*)

The pulse profile on this pulsar (Fig. 2d) has the best longitude resolution obtained by us so far. The observed pulse width is about 30 msec implying that the intrinsic pulse width is smaller than that at high frequencies. This is consistent with the spectral behaviour of the pulse width of this pulsar reported by Slee, Bobra & Alurkar (1987) where they find (from the data at and above 80 MHz) that the pulse width decreases at lower frequencies. Again, we do not find any significant interpulse emission in the profiles obtained by us on this pulsar whereas significant interpulse emission had been reported at and below 25 MHz (Brück & Ustimenko 1977, 1979).

7. Summary

In this paper, we have described the swept-frequency dedispersion method adapted for pulsar observations at low radio-frequencies. Using it we have been able to detect finer details in the pulse profiles than were possible earlier at such a low frequency. The dispersion smearing in the worst case (i.e. DM = 34.36 cm^{-3} pc) is only about 9 milliseconds. Such smearing can be further reduced by observing with bands narrower than that (333 KHz) used for the present observations. The subsequent loss in the signal-to-noise ratio, however, should be recovered by observing over longer time spans.

Lastly, regarding the interpulse emission, we notice no significant emission beyond the main pulse window in those cases where significant interpulse emission was claimed to have been detected at and below 25 MHz.

Acknowledgements

We wish to acknowledge the help and cooperation from T. S. Ravishankar, G. N. Rajasekhar and H. A. Ashwathappa during the observations. A. A. D. thanks R. Nityananda, Ch. V. Sastry and N. Udayashankar for many useful discussions.

References

Bruck, Yu. M., Ustimenko, B. Yu. 1976, *Nature,* **260,** 766
Bruck, Yu. M., Ustimenko, B. Yu. 1977, *Astrophys. Space Sci.,* **51**, 225
Bruck, Yu. M., Ustimenko, B. Yu. 1979, *Astr. Astrophys.,* **80**, 170.
Deshpande, A. A. 1987, *Ph. D. Thesis,* Indian Institute of Technology, Bombay.
Deshpande, A. A. 1992,J Astrophys.Astr., **13,** 167.

Deshpande, A. A., Radhakrishnan, V. 1990, '*The Magnetospheric Structure and Emission Mechanisms of Radio Pulsars, Proc. I AU Colloquium* **128**, (eds) T. H. Hankins, J. M. Rankin & J. A. Gil (Poland: Pedagogical University Press).
Deshpande, A. A., Radhakrishnan, V. 1992, *J. Astrophys. Astr.,* **13**, 151.
Deshpande, A. A., Shevgaonkar, R. K., Sastry, Ch. V. 1989, *Journal of I ETE,* **35**, 342.
Izvekova, V. A., Kuzmin, A. D., Malofeev, V. M., Shitov, Yu. P. 1979, *Soviet Astr.,* **23**, 179.
McCulloch, P. M., Taylor, J. H., Weisberg, J. M. 1979, *Astrophys. J.,* **227** L 133.
Phillips, J. A., Wolszczan, A. 1989, *Astrophys. J. Lett.* **344**, L69.
Rankin, J. M. 1993, *Astrophys. J.,* **405**, 285.
Slee, O. B., Bobra, A. D., Alurkar, S. K. 1987, *Austr. J. Phys.,* **40,** 557.
Suleimanova, S. A., Izvekova, V. A. 1984, *Soviet Astr.,* **28,** 32.
Sutton, J. M., Staelin, D. H., Price, R. M., Weiner, R. 1970, *Astrophys.* J., **159,** L89.
Udayashankar, N., Ravishankar, T. S. 1990, *J. Astrophys. Astr.,* **11**, 297.

J. Astrophys. Astr. (1994) **15,** 343–353

A Digital Signal Pre-Processor for Pulsar Search

P. S.Ramkumar,T.Prabu,Madhu Girimaji *Raman Research Institute, Bangalore 560 080*
G. Marker leyulu *National Centre for Radio Astrophysics, TIFR Centre, Poona University Campus, Pune 411 007*

Received 1994 May 20; accepted 1994 July 15

Abstract. A fast digital signal processor has been designed and built for survey and some observations of pulsars. The processor obtains spectral information over a bandwidth of 16 MHz (256 channels) every 25μsecs Wedescribethe design ofthisprocessor and present some test observations made with the Ooty Radio Telescope.

Key words: Pulsars—instrumentation: signal processing.

1. Introduction

During the last twenty seven years since the pulsar was discovered, the number of detected pulsars has risen to about 550. Practically, all of them are observed at radio wavelengths, with the peake mission around 100MHz. Statistical estimates based on the observed population suggest that less than 1% of the galactic population has so far been discovered, and a significant increase in the number of detected pulsars would improve the statistics to a great extent. Millisecond pulsars,, in particular, form a very interesting class, owing to their rich evolutionary history. While the estimated total number of millisecond pulsars in the galaxy exceeds ~ 10,000 (Lorimer 1994), only about 20 of these have so far been found. Not surprisingly, therefore, several major surveys are at present underway in different parts of the globe in an effort to increase the size of the observed population (Bailes 1994; Camilo 1994), in particular of the short period pulsars.

Various selection effects play a major role in restricting the observability of pulsars. At low frequencies, where the emission from pulsars is the strongest, the galactic background radiation limits the detection sensitivity. In addition, dispersion and scattering in the interstellar medium broaden the pulse and thereby limit the distance to which pulsars can be seen, as well as the minimum detectable period. Currently ongoing surveys attempt to optimize data collection methods to keep good sensitivity to as short a period as possible, given the above limitations.

In India, two major radio telescopes offer large collecting area at metre wavelengths, suitable for deep survey of pulsars..These are the recently refurbished Ooty Radio Telescope (ORT) (Selvanayagam *et al.* 1993), a 550 × 30 meter, single polarisation parabolic cylinder working at 327 MHz and the Giant Metre Wave Telescope (GMRT), consisting of 30 dishes of 45 metre diameter, operating at frequencies from 38 MHz to 1.4 GHz, nearing completion at Pune (Swarup *et al.*

1991). In this paper we describe the design and performance of a pulsar search pre-processor we have built, primarily for use at ORT, but based partly on the pulsar instrumentation being built by us for the GMRT (Deshpande 1993). This machine is capable of conducting a survey for millisecond pulsars and being fully digital in construction, is easily programmable to suit different requirements. It has been in use with the ORT since March 1993.

In section 2 we discuss the design considerations for this machine and in section 3 we describe the actual hardware. Section 4 presents some of the results obtained using this machine.

2. Design considerations

Pulsar signals are usually buried in the noise contributed by the galactic background and the receiver. Deep searches for weak pulsars therefore require high-sensitivity receivers. Searches for short-period pulsars also require a high time resolution. Presently known pulsar periods vary from about 1.5 ms to over 5 secs, and the intrinsic pulse duty cycle is typically between 1% to 5%. The observed pulse duty cycle is usually higher due to propagation effects in the intervening medium and the limited bandwidth of the receiver. If the width of time-smearing due to dispersion in the intervening medium is $\Delta\tau_{D,}$ that due to interstellar scattering is $\Delta\tau_s$ and the pre-detection bandwidth is Δf, then the resultant pulse smearing has a width $\Delta\tau_{\text{smear}} = \sqrt{(\Delta\tau_D)^2 + (\Delta f)^{-2} + (\Delta\tau_S)^2}$. When this width is comparable to or greater than the intrinsic pulse width, the apparent peak intensity is reduced.

Many techniques are know for reducing the smearing due to dispersion (e.g. pre-detection (coherent) dedispersion, post-detection (incoherent) dedispersion etc.). In incoherent dedispersion (a method more convenient for pulsar searches), the total band is divided into a large number of narrow channels, outputs from which are 'detected' and combine after appropriate dispersion delay corrections. An optimal choice for channel bandwidth is given by Δf (MHz) = $(10^{-4}/9.1) \times \sqrt{f_0^3(\text{MHz})/DM}$ (Deshpande 1989), i.e., when $(\Delta f)^{-1} = \Delta\tau_D$ (ignoring scattering effects), where f_0 is the centre frequency of observation.

Search observations with high time resolution (as required for millisecond pulsars) result in very high data rates at the output and require massive data storage. Considerable reduction in the effective data rate and size is possible by quantizing the data to a smaller number of bits (1 or 2) per sample. This however, results in some degradation of the search sensitivity (Biggs *et al.* 1989).

The design philosophy adopted in this exercise was aimed at reducing the size, complexity and the cost of the machine while retaining flexibility and operational simplicity. Many extensive, and high-speed computations are achieved through the use of look-up tables at various stages of the machine. At places where the look-up table approach is not appropriate, dedicated logic has been designed, and programmed into 'Erasable Programmable Logic Devices' (EPLDs) which have the advantages mentioned above. In addition, the use of these devices makes it possible to design the entire machine using only 2 layer PCBs and reducing development time substantially. The design has been made modular to facilitate quick replacements in the field and PC based automated test jigs have been developed for quick diagnosis.

With the above points in view, the processor is equipped with hardware capability to generate 256 complex spectral channels over 16 MHz pass-band from two polarization channels. It further detects and sums up the power in these two polarization channels, then performs pre-integration, mean subtraction and gain calibration of data in individual frequency channels. The parameters related to these operations are programmable. The instrument is configured and diagnosed under software control, a few milliseconds before every observation session using a set of PC/AT based parallel I/O ports. During the observation the same PC/AT also computes the running mean and gain calibration factors for the spectral channels besides displaying these on the screen. The data is acquired by a PC/AT based dedicated hardware and is stored on a hard disk. The data is later backed up into a 2.5 GB video cartridge tape. Choice of a PC/AT to setup the configuration of the machine is due to the large software base available under MS-DOS in addition to the hardware flexibility. Similarly the data acquisition hardware is also based on a PC/AT on a MS-DOS platform to allow the use of a variety of I/O devices that are readily available for a PC/AT.

3. Hardware description

The following description of the hardware is based on the block diagram given in Fig. 1.

3.1 *Digital front- end*

The digital front-end for this machine is a pair of A/D converters which sample the baseband signals at the Nyquist rate and feeds them to an FFT engine. The FFT engine uses VLBA FFT chips and produces 256 point complex spectra in each polarization channel, which are then sent out serially. The A/D convertors and the FFT engine were supplied to us by National Center for Radio Astrophysics (NCRA), Pune. To initialize, supply twiddle-factors and run this FFT engine, we developed a controller based on state-machine approach using look-up tables.

3.2 *Search pre-processor*

In the Search Preprocessor (SP), the complex numbers corresponding to the spectrum produced by the FFT are used to compute a power spectrum in each polarization channel using lookup tables. The power terms of the two polarizations are summed in each frequency channel, and the resultant power spectra are pre-integrated over a programmable number of successive spectra for a time span of t_{int}($256\ \mu\text{s} \leqslant t_{\text{int}} \leqslant 4$ ms). The output consists of integrated values in each of the 256 spectral .channels at the chosen output sampling rate. The width of the output word representing the data sample increases with the integration. High speed digital design can be simplified by retaining less number of bits to represent the data with little effect on the signal-to-noise ratio. For this purpose a set of sliding windows are provided before and after the pre-integration to choose the most significant bits of the word and thereby reduce the word widths to manageable sizes. The data at the output of the pre-integrator

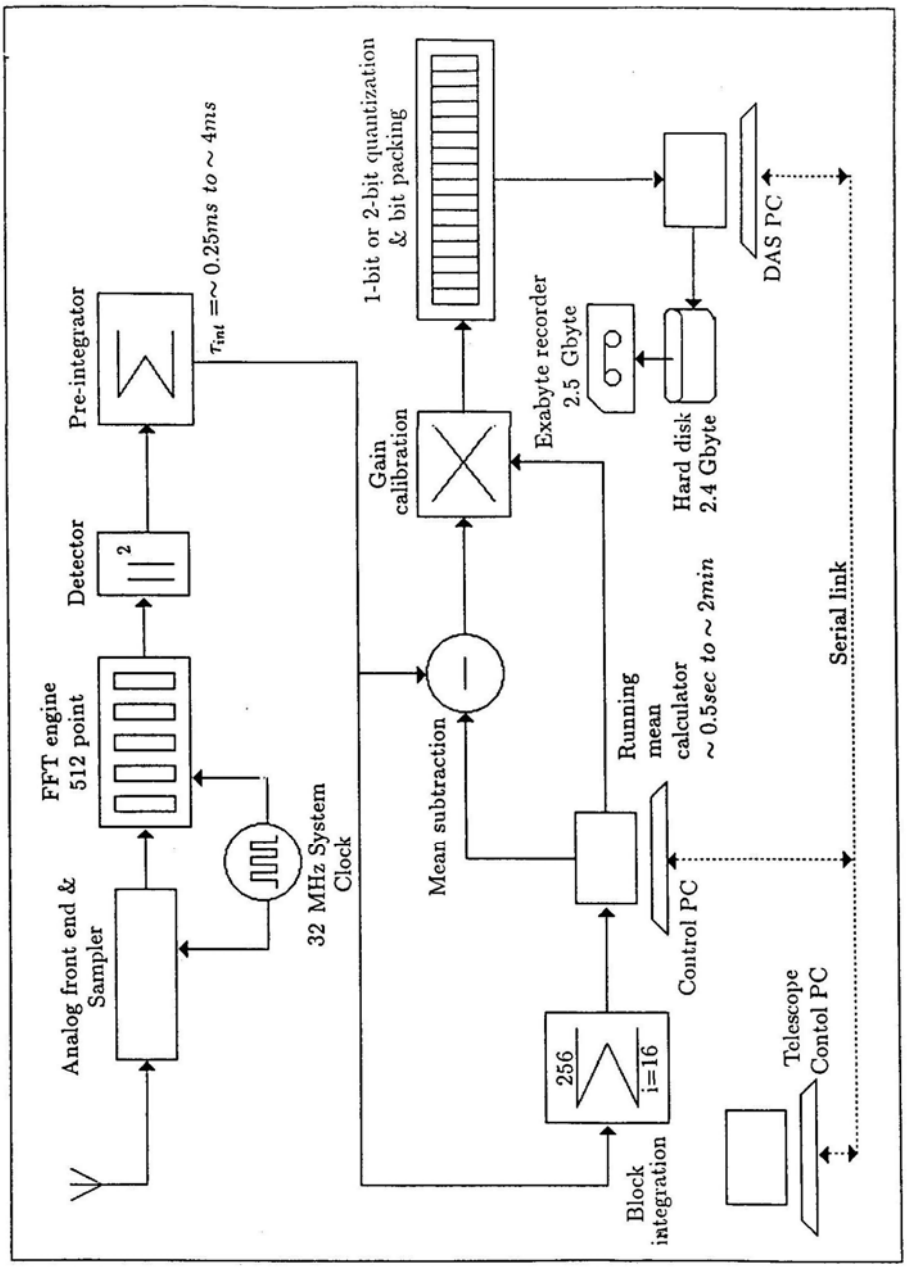

Figure 1. Block diagram showing architecture of the machine.

can be quantized further to a much smaller number of bits after removing its mean value as we are interested mainly in the time variation of the signal rather than its mean value.

The pre-integrated data is sent to a pulsar search preprocessor (PSP) control PC/AT, after block integration over a programmable number of pre-integrated samples (16 to 256 pre-integrated samples) for calculation of the running mean/median for each of the 256 channels. Before the next block-integrated data is ready, the PC/AT computes the running mean over a pre-specified time (0.5 secs to 2 mins) and supplies these values through a dual port RAM (DPRAM) to a mean subtractor (housed in an EPLD) which removes the mean from the pre-integrated data stream. The same PC/AT also computes scale factors to equalize the gains of the spectral channels (only when the output is 2 or more bits per sample) in the pass band and supplied them through another DPRAM that is used as a gain calibration look-up table for correcting the bandshape of the mean subtracted data. In one-bit mode of operation, gain calibration scale factors are set to unity for all channels. This stream of deviation from the mean spectrum is then quantized to one bit two-level or two bit four-level representation per spectral channel. The output bits of consecutive channels are packed to form sets of 16-bit words that are transmitted to the data acquisition system. This logic is programmed into an EPLD.

3.3 *Data acquisition system*

A PC/AT based data acquisition card accepts the data sent by the search preprocessor into a set of First-In-First-Out (FIFO) memories through latches/counters, and their mode of operation can be decided by software: in the counter mode, a deterministic data pattern can be fed to perform self tests to enable easy diagnosis of the acquisition hardware. During observational sessions they work as latches. FIFOs are used as buffers to accommodate the response delays caused by the latency and seek times in the data-storing on the hard disk. The size of the buffer therefore depends on the input data rate, the storage capacity per cylinder of the hard-disk and the seek + latency time. In our case the input rate is about 64 kbytes/sec (in one-bit mode of operation), the capacity is about 36,352 bytes/cylirider and has about 20 msec seek + latency time per cylinder. FIFOs of 8 k × 16 bits are sufficient to handle this data rate. This limit of 64 kB/sec can be enhanced by providing higher density FIFOs which do not alter the external circuitry. Our tests with higher density FIFOs (upto 32 k × 16 bits) indicate that data rate of above 256 kB/s are achievable. Whenever the FIFO is half-filled, the acquisition software transfers the data to a 1.2 Gbyte hard disk drive. A memory mapped I/O protocol is used to enable 16 bit zero watt state data transfer (directly to the hard disk drive controller without the intervention of the microprocessor) to achieve high data throughputs. The PC/AT is equipped with an exabyte recorder to facilitate the backup of the data stored in the hard disk drive to an 8 mm tape cartridge.

The Data Acquisition System (DAS) PC/AT, the PSP PC/AT and a PC/AT controlling the telescope beam direction are linked through serial ports and interact for command and message transfers under software control. The telescope control PC points the antenna beam to a required direction and instructs the PSP PC to start observation. The PSP PC/AT in turn sets up the entire machine, runs preliminary

diagnostics and waits till the running mean stabilizes, before signalling to the DAS PC/AT. Then the DAS initiates data acquisition which is synchronized automatically to the first frequency channel of next time sample and sends a message back to the PSP PC/AT which in turn informs the status to the antenna control PC. During observation the PSP PC/AT continuously displays the running mean of a chosen spectral channel. The power-spectra (i.e., bandshape) at the beginning and at the end of an observation are also recorded in a routine manner.

4. Tests and results

All the modules of the entire machine were independently tested on PC/AT based test jigs with the help of 144-line I/O cards to setup the configuration, provide the clock, to send data to the module and to read back the status and results, and also to help locate errors, under software control The SP module was tested with different pre-integrations, and sliding window positions. The running mean calculation, mean subtraction and gain calibration were checked with data representing different mean values and bandshapes. The DAS was tested at 256kB/sec with both internal and external text patterns. After all these tests proved successful, the modules were integrated and tested with pulse-modulated baseband noise input to simulate a 'zero DM' pulsar signal with various S/N ratios, periods and duty cycles. The system was then used in conjunction with the ORT and initial test observations were made on known pulsars for different combinations of period and flux density. Since the ORT accepts only one polarization, one of the two polarization channels in this receiver was preset to zero. The ORT operates at 327 MHz and the associated RF front end and baseband system provide an 8 MHz passband. This 8 MHz band is sampled at the Nyquist rate and the sampled time sequences are transformed to provide a complex spectrum every 16 μs. The number of points in the frequency spectrum is chosen to provide 256 frequency channels of 32 kHz resolution which is an optimal choice for observation of pulsars with dispersion measure(DM)upto 70 pc cm^{-3} (the total bandwidth would be reduced for search at higher DM).

We have attempted to calibrate the observed profile in flux units considering the architecture of the machine and the statistics of the pulsar signal (development of the procedure used is illustrated in the Appendix). Presently continuum calibration sources and background cold-sky regions have been chosen at the same declination to avoid any declination dependent factor entering into the calculation of sensitivity for a calibration source. Further, to avoid nonlinear quantization effect at FFT and power detection stages, we have chosen sources with flux densities less than a few Jansky. These effects are considered small, and ignored now, but have to be measured for more accurate flux measurements. Also, the observations of the calibration source and the pulsar were spaced many days apart, hence the flux estimates shown in the plots are tentative and may not be accurate.

Results for some combinations observed with sampling interval of 0.5 ms, one-bit, quantization mode are shown in Figs. 2a, 2b and 2c. The rms error due to the noise in the profile is indicated by vertical bars in the respective profiles.

Figure 2a is a profile of PSR1237–41,chosen for it slow flux density (S_{avg} ~ 2.5mJy). It has a DM of 44 pc cm^{-3}, period of ~ 512ms;

Figure 2b is a profile of PSR 0740-28, chosen as a candidate for high flux density

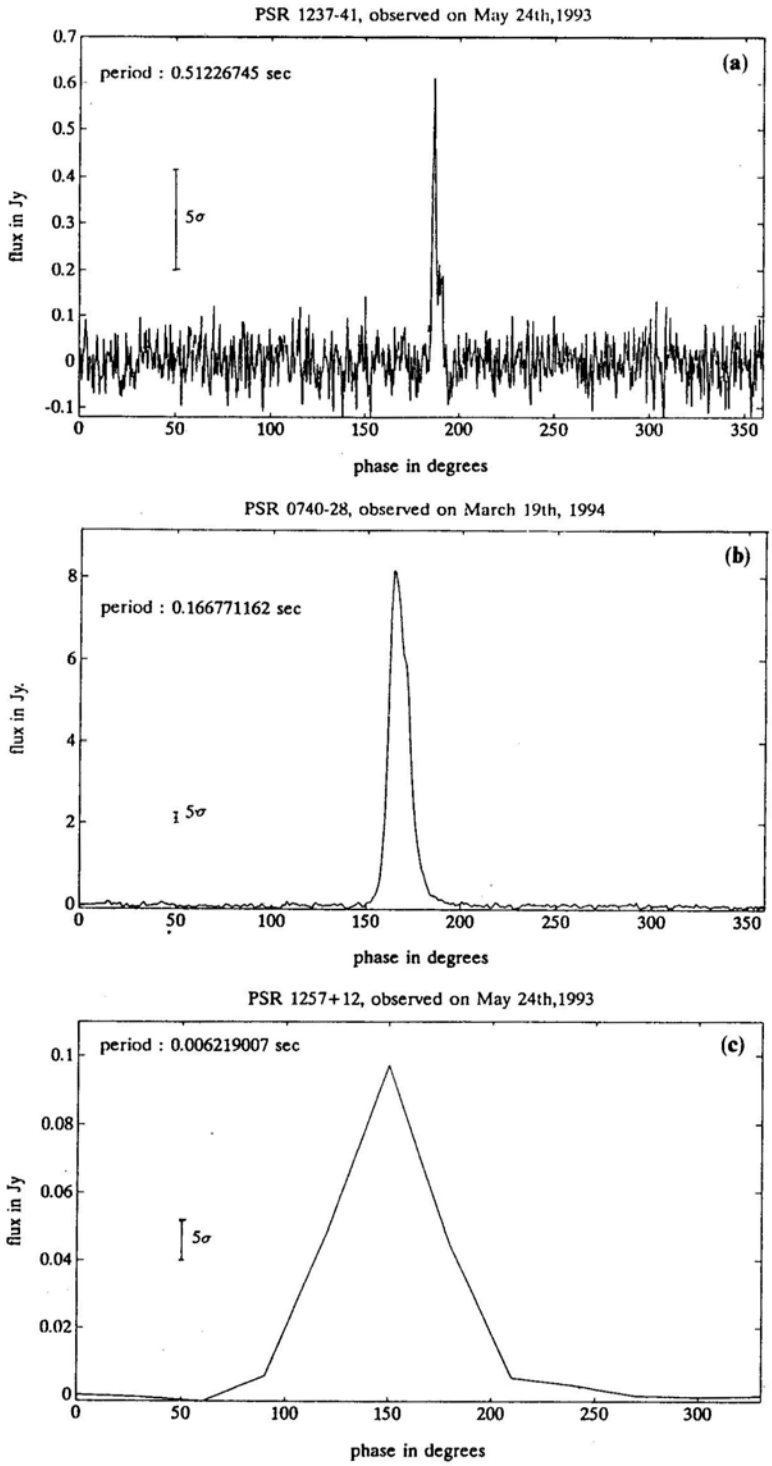

Figure 2. Profiles of observed pulsars: 0.5 ms sampling interval, 9 minutes integration, recording with 1-bit quantization. Flux calibrations was obtained using the. procedure outlined in the Appendix.

($S_{avg} \approx 290$ mJy), DM of 73.6 pc cm $^{-3}$ (for which the smearing within the chosen channel bandwidth will be close to the sampling interval) and period of ~ 166 ms;

Figure 2c shows a profile of PSR 1257 + 12, a candidate with a short period ($p \approx 6$ ms) low flux density ($S_{avg} \approx 15$ mJy), and a low DM of l0 pc cm^{-3}.

Though the intended use of this machine is to search for new pulsars, it can also be used with simple modifications for timing and other studies of known pulsars.

Acknowledgements

We would like to express our sincere thanks to our colleagues Sridhar, Raghavendra, Vijay and Sindhu for all the help they extended in PCB design and wiring of various modules of the machine. We acknowledge with pleasure all the interesting discussions and valuable suggestions from our colleagues D. Bhattacharya, A. A. Deshpande, R. Ramachandran, Yashwant Gupta and S. Upreti. Many thanks to C. R. Subramanya and his colleagues at N.C.R.A., Pune., for providing the sampler and FFT card. Thanks are due again to Yashwant Gupta and D. Bhattacharya for the software which linked our machine to the antenna-control PC/AT through serial ports. Our heartfelt thanks to the staff of RAC, Ooty for providing the telescope time and the analog front-end. Our thanks in particular, to Dr. V. Balasubramanian, for the extensive co-operation we enjoyed at ORT.

APPENDIX

Flux calibration procedure

For a total power receiver with each recorded sample represented by many bits, the flux calibration can be done by pointing to known continuum sources and background cold sky regions by knowing the relation between the deflection in some counts and the actual source flux causing the deflection, as follows

$$\text{Counts/Jansky} = \frac{\mu_{\text{cal}} - \mu_{\text{bsky}}}{S_{\text{source}}}$$

where, μ_{cal}, μ_{bsky} are mean counts when pointed to the calibration source and background sky respectively, S_{source} = flux of the calibration source.

Considering the fact that in our system the data are one-bit samples representing deflections from the mean power, we tap 16-bit data before it goes for mean subtraction and integrate further for about a minute, then record it for a few minutes.

In a given frequency channel, the sensitivity measured from this data can be represented as

$$SNR_{\text{cal}} = \frac{\mu_{\text{cal}} - \mu_{\text{bsky}}}{\sigma_{\text{bsky}}}$$

where, σ_{bsky} is standard deviation of the power received from background sky, in counts.

If there are N_{ch} frequency channels, then the average signal-to-noise ratio is

$$SNR_{calavg} = \frac{1}{N_{ch}} \sum_{i=1}^{N_{ch}} SNR_{cal[i]}$$

In case of a pulsar, the contribution of pulse energy changes the running mean by only a very small amount, hence the threshold set for mean subtraction is about the same as the mean contribution from the background and the receiver.

The 1-bit stream generated from this mean subtracted data represents samples which exceed the mean by 0 and those which are less than the mean by 1s.

Keeping this in mind, we know that after folding N pulses, in the off pulse region (refer Fig. 3 a) we get a mean integrated count (M)

$$M_{offpulse} = N[P(W > \mu_{offpulse}) \times 0 + P(W < \mu_{offpulse}) \times 1]$$
$$= N[P(W < \mu_{offpulse})] = \frac{N}{2}$$

where, W is the power before mean subtraction, $P(W > \mu_{offpulse})$ is the integrated probability of W being greater than $\mu_{offpulse}$, and the threshold for 1-bit quantization is equal to the mean of the distribution of W, $\mu_{off\ pulse}$

For on-pulse locations, the mean count will be (refer Fig. 3b)

$$M_{onpulse} = N[P'(W < \mu_{offpulse})]$$

where, $P'(W > \mu_{off\ pulse})$ is the integrated probability of W being greater than $\mu_{offpulse}$ The mean of the distribution of W is $\mu_{onpulse}$, while the threshold for 1-bit quantization

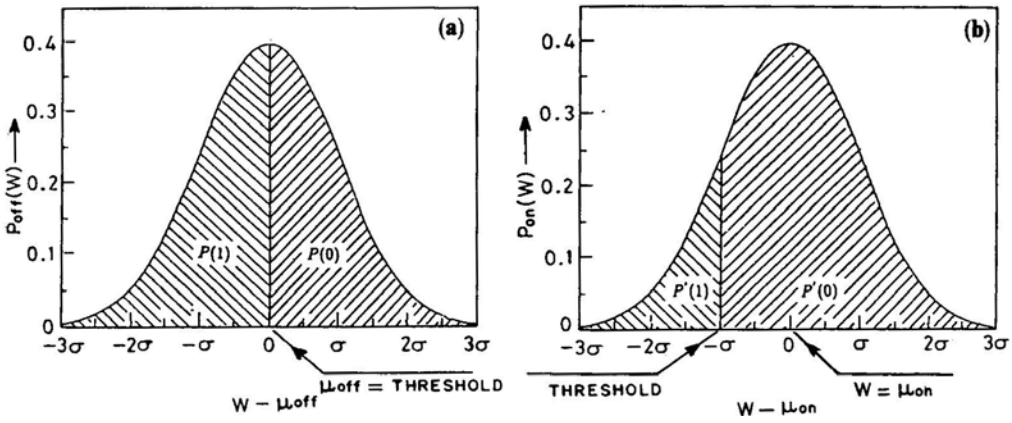

Figure 3a & b. Probability distribution functions of 1-bit data: **a**) In the off-pulse regions, the threshold for 1-bit quantization is equal to the mean $\mu_{offpulse}$, and the probability density is p_{off} (W) **b**) During the on-pulse region, the threshold is still close to the off-pulse mean $\mu_{offpulse}$, while the actual mean has shifted to $\mu_{onpulse}$, and the distribution has a probability density $p_{on}(W)$. The shaded areas indicate the integrated probability when (i) sampled power exceeds the running mean (marked as $P(0)$ [$P'(0)$]), (ii) sampled power is less than the running mean (marked as $P(1)$[$P'(1)$]).

is close to the off-pulse mean μ_{offpulse}. Thus, the change in mean count value is given by

$$\Delta M = \frac{N}{2} - N[P'(W < \mu_{\text{offpulse}})]$$
$$= N[P'(W < \mu_{\text{onpulse}}) - P'(W < \mu_{\text{offpulse}})]$$
$$= N[P'(\mu_{\text{offpulse}} < W < \mu_{\text{onpulse}})]$$
$$\Delta M = \left[\frac{1}{\sqrt{2\pi}\,\sigma_{\text{onpulse}}} \int_{\mu_{\text{offpulse}}}^{\mu_{\text{onpulse}}} e^{-[(W-\mu_{\text{onpulse}})^2/2\sigma^2_{\text{onpulse}}]}\,dW\right]$$

After some manipulation, we get

$$\Delta M = \frac{N}{2}\,\text{erf}\left[\frac{K}{\sqrt{2}}\right]$$

where

$$K = \frac{\mu_{\text{onpulse}} - \mu_{\text{offpulse}}}{\sigma_{\text{onpulse}}}$$

For typical pulsar flux densities, the rms fluctuations are about the same during both off-pulse and on-pulse regions. Hence,

$$K \approx \frac{\mu_{\text{onpulse}} - \mu_{\text{offpulse}}}{\sigma_{\text{offpulse}}}$$

Hence the signal-to-noise power ratio (SNR) after folding over N periods of this 1 bit data stream, is given by

$$SNR_{1\text{bit}} = \frac{\Delta M}{\sigma_{\text{offpulse}}} = \frac{N}{2}\left[\frac{\text{erf}(K/\sqrt{2})}{\sigma_{\text{offpulse}}}\right]$$

Thus, the analog (multibit) sensitivity of this machine 'K' is then given by

$$K = \sqrt{2}\left[\text{erf}^{-1}\left(\frac{2SNR_{1\text{bit}}}{N(\sigma_{\text{offpulse}})}\right)\right]$$

For N_{ch} frequency channels, the average value of K is

$$K_{\text{avg}} = \frac{1}{N_{\text{ch}}}\sum_{i=1}^{N_{\text{ch}}} K_i$$

The ratio of K to the SNR measured on a calibrator source can be used and the deflection in the pulse profile can then be calibrated directly in flux units as

$$S_{\text{PSR}}(\text{Jy}) = S_{\text{cal}}(\text{Jy}) \times \frac{K_{\text{avg}}}{SNR_{\text{calavg}}}$$

References

Bailes, M. 1994, *Proc. 6th Asia Pacific Regional Meeting of the I AU,* Eds. V. K. Kapahi & N. Dadhich (Indian Academy of Sciences) in press.

Biggs, J. D., Lyne, A. G., Johnston, S. 1989, *X-ray binaries, proc. 23rd ESLAB Symposium,* Eds. J. Hunt & B. Battrick, p. 293.

Camilo, F. 1994, *Proc. NATO ASI on Lives of Neutron Stars,* Eds. M. A. Alpar & J. Van Paradijs (Kluwer) in press.

Deshpande, A. A. 1989, *Pulsar Instrumentation for GMRT, Technical report,* Raman Research Institute.

Deshpande, A. A. 1993, *Proc. 6th Asia Pacific Regional Meeting of the IAU,* Eds. V. K. Kapahi & N. Dadhich (Indian Academy of Sciences) in press.s

Lorimer, D. 1994, *Proc. NATO ASI on Lives of Neutron Stars,* Eds. M. A. Alpar & J. Van Paradijs (Kluwer) in press.

Selvanayagam, A. J., Praveenkumar, A., Nandagopal, D., Velusamy, T. 1993,*I.E.T.E. Technical Review,* **10**, 4.

Swarup, G., Ananthakrishnan, S., Kapahi, V. K., Rao, A. P., Subramanya, C. R., Kulkarni, V. K. 1991, *Curr. Sci.* **60,** 2.

J. Astrophys. Astr. (1994) **15,** 355

Preface

A remarkable paper on the formation and properties of speckle patterns was published in the *Proceedings of the Indian Academy of Sciences* in 1943. The author, **G.N. Ramachandran,** was then a research student working with C.V. Raman at the Indian Institute of Science in Bangalore. This paper has been chosen for reproduction in this issue because it brings out, for the first time, many features of speckle patterns which later proved to be of great relevance to ground-based high-resolution optical techniques. These include

(i) The experimental verification of the probability distribution of the intensities

(ii) The fact that individual speckles have a size set by the diffraction limit of the whole aperture

(iii) The demonstration that time averaging produces a pattern whose properties are determined not by the whole aperture but by the individual uncorrelated units which make up the aperture

(iv) The fact that information about the object itself, not just its autocorrelation, is contained in the speckle image.

This last point is made by a plate taken with a triangular source, and one cannot help being struck by the triangular correlations in the image. This picture makes intuitive the idea proposed and exploited by Weigelt and others that the triple correlation contains the full information about the object and can, in particular, distinguish an object from its inverse (i.e., the object rotated by 180 degrees).

Of course, all these features of speckle patterns are now well appreciated by people working in the field of high resolution imaging, but it may be of interest to trace them to one of their original sources in the physics literature, motivated largely by observations of natural phenomena and laboratory experiments. This paper by G.N. Ramachandran certainly deserves wider note than it has received so far.

J. Astrophys. Astr. (1994) **15,** 357–371

Reproduced from *Proceedings of the Indian Academy of Sciences*
Vol. **A2,** 190-200, 1943

FLUCTUATIONS OF LIGHT INTENSITY IN CORON Æ FORMED BY DIFFRACTION

By G.N. RAMACHANDRAN
(From the Department of Physics, Indian Institute of Science, Bangalore)

Received September 22, 1943
(Communicated by Sir C.V. Raman, Kt., F.R.S., N.L.)

1. Introduction

THE problem of determining the resultant of the secondary radiations emitted by a cloud of similar particles under the action of a primary wave is an important one in the field of optics. It might be supposed that when there are a large number, n, of such particles, distributed at random, the resultant intensity is just n times that due to a single particle. The late Lord Rayleigh (1871), however, showed that this is far from being the case, and that the resultant in any particular trial may be anywhere between o and n^2 , and does not show any tendency to close upon the value n. He has also investigated (1880) the probability that the resultant intensity may lie between assigned limits of magnitude, and has derived an expression for the distribution of the resultant intensity.

In a general way, the existence of such fluctuations of intensity is illustrated by the well-known experiment of using a glass plate on which lycopodium powder is dusted as the diffraction screen, and viewing a source of light through it. The effects observed depend greatly on the size of the source and its spectral nature. Even as early as 1877, Exner observed the existence of radial streaks such as those shown in Fig. 3(*a*), Plate I, when the corona is seen in white light. More recently, Laue (1916, 1917) and de Haas (1918) have observed the fluctuations in monochromatic light. In this case, the radial fibres reduce to a "mottled structure" of the

type shown in Fig. 3 (*b*).* Laue's studies led him to suppose that the phenomena could not be completely explained on the basis of classical wave-optics. This contention was disputed by de Haas, who performed further experiments supporting the view that the phenomena are explicable on wave-principles.

In this paper, some theoretical considerations are presented regarding the nature of the fluctuations, and experiments performed with a view to substantiate the theory are also described. It is found, as is shown below, that de Haas's explanation of the phenomena is inadequate, and does not go to the root of the problem. In particular, the Rayleigh statistical law of distribution of intensity has been quantitatively verified for the first time, making use of the fluctuations of intensity in the corona as the basis for measurement.

2. The Nature of the Fluctuations in Monochromatic Light

de Haas's explanation of the mottled structure consists in considering every pair of particles to give rise to a set of interference fringes crossing the field. These are superposed, and produce fluctuations of intensity. This explanation, however, is wholly inadequate. In fact, when the number of particles is very large, one must take the aggregate effect of *all* the particles into account and not merely the effect due to pairs of particles. Each particle gives rise to a corona of its own, and the resultant intensity in any direction is due to the collective action of the wave-fronts diffracted by all the particles in that direction.

The failure of the de Haas point of view may be brought out strikingly by the following analogy. Suppose we are considering the opposite case of a regular square diffraction grating, formed for example by a square mesh of wires. In this case, one may take each pair of meshes in the grating, and imagine it as giving rise to a set of interference fringes of the type imagined by de Haas. But, such a method gives us no idea at all of what the nature

« This will hereafter be referred to also as the "fine-structure" or "structure" of the corona.

of diffraction pattern due to the complete grating would be. The latter could be determined only by taking the waves diffracted by all the meshes simultaneously into account and finding their total effect. In those directions in which all these waves reinforce, we get bright spots, while elsewhere we have dark areas.

In the same way, with the lycopodium powder also, one has to consider the waves diffracted by all the particles together. Each particle becomes the centre of secondary radiation, and in those directions in which the phase relations between the waves diffracted by the particles happen to be such that there is a large co-operative effect, there will be bright spots. Since the positions of the particles on the screen are unknown, one cannot determine the positions of these maxima of intensity; but it is easily seen that there must be a large number of such spots irregularly arranged in the field of view.

We now proceed to show that these spots are in fact as sharply defined as the original image of the source formed by a lens whose aperture is the same as that of the diffracting screen. Consider a point P in the focal plane of the camera where due to the co-operative action of the waves from the various particles, we have a large intensity, say I_P. The amplitude at this point will be *u*p $\sum_1^n e^{ipm}$ where p_m is the phase of the *m*th particle on the screen, and the summation is done for all the *n* particles present, it being assumed that the amplitude due to each particle is unity. Therefore,

$$I_P = \left(\sum_1^n \cos p_m\right)^2 + \left(\sum_1^n \sin p_m\right)^2 = n + \sum_{r=1}^{n} \sum_{s=1}^{n} \cos(p_r - p_s). \tag{1}$$

Consider now a neighbouring point P′. At this point, the phases of the waves from the various particles would be altered. Let the alteration of phase for the *m*th particle be δ_m. Then, the

amplitude at P′ is

$$u_{P'} = \sum_1^n e^{ip_m}\, e^{i\delta_m}, \text{ and the intensity is}$$

$$I_{P'} = \left[\sum_1^n \cos(p_m + \delta_m)\right]^2 + \left[\sum_1^n \sin(p_m + \delta_m)\right]^2 . \quad (2)$$

This can be expressed in the form

$$I_{P'} = n + \sum_r \sum_s \cos(\delta_r - \delta_s)\cos(p_r - p_s) + \sum_r \sum_s \delta_s \sin(p_r - p_s) .$$

If the δ's are small, this can be put in the form

$$I_{P'} = \left[n + \sum_r \sum_s \cos(p_r - p_s)\right] + \sum_r \sum_s \delta_r \delta_s \cos(p_r - p_s) + \sum_r \sum_s \delta_s \sin(p_r - p_s) . \quad (3)$$

The second term is negligible, since it involves second order terms, so that

$$I_{P'} - I_P = \sum_{r=1}^{n} \sum_{s=1}^{n} \delta_s \sin(p_r - p_s) . \quad (4)$$

Now $\sin(p_r - p_s)$ is of the same order of magnitude as $\cos(p_r - p_s)$, so that $\sum \sum \delta_s \sin(p_r - p_s)$ is of a lower order compared with $\sum \sum \cos(p_r - p_s)$ which is the order of I_P. Thus, if δ is small, $(I_{P'} - I_P)$ is small compared with I_P.

Now if we denote by $\delta\phi$ the angular separation of P and P′, then the largest value of δ_r or δ_s is given by $\pi b\ \delta\phi/\lambda$, where b is the width of the diffraction screen, and λ the wave-length of light. It is evident from (4) that $I_{P'}$, does not sensibly differ from I_P over a range of values of $\delta\phi$ within which the largest of the δ's does not exceed a fraction of 2π, and over this range of angles, the large intensity at P will persist. Putting the maximum value of the δ's for this to happen as, say, $\pi/4$ one gets the width of the bright spot as

$$\delta\phi = \frac{1}{4}\frac{\lambda}{b} . \quad (5)$$

Thus, the angular width of the bright spot is of the order of λ/b. Now, it is well known that the diffraction image due to a lens of aperture b also extends over an angle of the order of λ/b, so that the bright spot at P will be of the same sharpness as an image of the source formed by a lens of aperture b.

The argument used in the above discussion is, however, not restricted to the case when the intensity at P is a maximum. Actually, it is true whatever may be the intensity at P, so that one sees that the corona must actually consist of spots whose extension is of the same size as that of the image of the source. We have proved above that these images would not be spread out by an extent more than the aperture of the lens, so that we must expect the fine-structure to consist of sharp and well-defined images of the original source distributed at random. They are in fact the spectra formed by the irregular arrangement of the sources of secondary radiation produced by the particles.

Another interesting result, regarding the number of such spots in the field of view, comes out of the above discussion. As already remarked, the extent of the individual spots is given by the width of the aperture; Thus, we may divide the whole field of view into a number of areas, each of which is occupied by one spot. Now, on increasing the aperture, the area occupied by a spot decreases, so that more spots must appear in the field of view. To observe this phenomenon, the source of light must be small enough, so that the spots do not sensibly overlap. Otherwise, the fluctuations of intensity would all be wiped out by the overlapping, and the individual spots could not be discriminated. Under favourable conditions, however, the argument shows that the density or the number of spots per unit area must depend on the aperture employed, increasing with increase of its dimensions.

3. Experimental Confirmation

The verification of the above two deductions from the theory was done by the following experimental arrangement. The source of light, S (Fig. 1) was a pinhole, or an aperture of any size and

shape as desired, which was illuminated by the filtered mercury radiation of 5461 A. U. At a certain distance from the source was placed a glass plate G, on which lycopodium powder was dusted. The resulting diffraction pattern could be brought to a focus on a plate C by a lens L. An aperture AB was placed in front of the lens, and its size and position could be adjusted. When necessary, the camera could be removed and the pattern directly viewed with the eye.

Initial visual observations using a small circular hole as the source showed that the spots in the corona are also all circular in shape and of the same size as the original source. On increasing or decreasing the size of the pinhole, the spots in the field of view also correspondingly became larger or smaller showing that they are images of the source. But the most convincing proof of this fact was obtained by using a triangular slit as the source, when every one of the spots assumed a triangular shape, and besides had the same size and orientation as the source. Photographs were then taken to illustrate this fact. They are reproduced in Fig. 4 (*a*) and (*b*), Plate I. Fig. 4 (*a*) was taken with a circular pinhole as the source, and Fig. 4 (*b*) with a triangular slit. They show in an unmistakable manner that the spots are in reality images of the source.

The second conclusion from the theory was also verified by observation. On increasing the area of the aperture, it was found that the number of spots in the field of view increased, and *vice* versa as demanded by the theory.

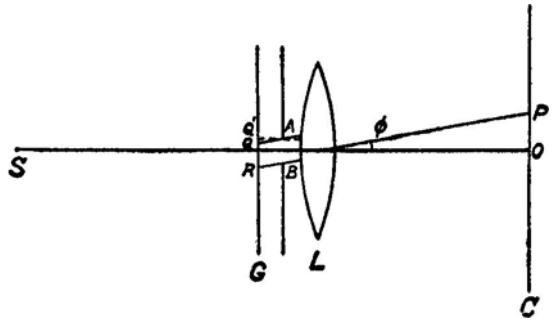

FIG. 1. Experimental Arrangement

During these experiments, a few other interesting phenomena were observed which also find a ready explanation on the idea that the spots are the spectra produced by the collective diffraction by all the particles.

(*a*) If one moves the screen containing the lycopodium powder keeping the eye fixed on the source, then the ring system is not found to undergo any change, but the fine-structure appears to move relative to the pattern of rings in the same direction as the motion of the screen. *Vice versa*, keeping the screen fixed, if one moves the eye, all the while looking at the source, then the fine-structure appears to move in a direction opposite to the motion of the eye. This effect is only the converse of the previous one. Also, if the screen is rotated, the fine-structure appears to rotate in the same direction.

These effects can be explained as being purely due to the geometry of the arrangement. Since the pupil of the eye is small, the whole of the screen does not contribute to the diffraction pattern nor is every portion of the pattern produced by the same portion of the screen. If we consider the corona in a direction ϕ (Fig. 1), the intensity in this direction is due only to the waves diffracted by the region QR of the screen. Hence, if the screen is moved up, the same portion QR is now responsible for the corona in a direction ϕ' parallel to Q′A. This happens for every portion of the screen, so that the fine-structure as a whole appears to move in the same direction as the screen relative to the rings. The effect of rotation is too obvious to need an explanation.

(*b*) During these experiments, it was found that the fine-structure not only moved bodily in the same direction as the motion of the screen, but that there were some internal changes as well. To follow these, the bodily motion was avoided in the following way. The aperture AB was placed in contact with the screen, and the lens L of the camera was large enough so that the whole diffraction pattern was caught by it. In this way, the difficulty of different portions of the screen giving rise to different portions of the corona was overcome. The whole of the screen was always

operative. Now, on moving the screen in its own plane, the fine-structure pattern at the focal plane of the lens did not show any bodily movement; but there was an internal rearrangement of the spots.

This phenomenon could be explained as due to the fact that spherical waves are incident on the screen so that, on moving the screen in its own plane, the phase of the wave falling on each particle is altered. Thus, the phase relations between the waves emitted by different particles are changed, which leads to a change in the pattern of the spectra given by the particles and hence to a random rearrangement of the spots.

It is obvious that these internal changes must vanish if the incident wave is plane, for then a movement of the plate in its own plane should produce no change in the phase relationship between the different particles. This was tested out experimentally and it was found that with parallel light incident on the screen, the fine-structure pattern at the focal plane of the lens was entirely unaffected by moving the screen in its own plane. This shows that the explanation given above for the internal motion of the spots is correct.

(*c*) The phenomenon of the internal rearrangement of the spots can be observed with the eye also, if the aperture AB is made sufficiently small. In this case, on moving the aperture over the screen, different portions of the screen are operative, and since the arrangement of the particles in these are different, the spots in the field of view exhibit a beautiful "dance". The appearance is somewhat similar to that of the field of a spinthariscope, with bright spots appearing and disappearing at random positions.

4. Fluctuations in White Light

We have already shown how, in monochromatic light, the fine-structure consists of a series of images of the source. We now proceed to investigate what happens if white light is used. Suppose that, with monochromatic light of wavelength λ, there is a bright spot at P, in the direction ϕ (Fig. 1). In the diffracting screen,

draw the X-axis parallel to OP, and the Y-axis perpendicular to it, and let (x_m, y_m) be the co-ordinates of the mth particle on the screen with respect to these axes of co-ordinates. Then, (supposing the incident wave to be plane) the intensity in the direction ϕ is equal to

$$\left| \sum_{m=1}^{n} e^{ikx_m \sin \phi} \right|^2 , \tag{6}$$

where k stands for $2\pi/\lambda$. Now, supposing the wavelength of the light to be changed to λ', and that $k' = 2\pi/\lambda'$, then it is readily seen from the above expression that the value of the intensity is unaltered provided we change ϕ to ϕ', such that

$$k \sin \phi = k' \sin \phi', \text{ or } \sin \phi/\lambda = \sin \phi'/\lambda'. \tag{7}$$

Hence, the bright spot, which was formerly at P, would now appear at another point P′ in the direction ϕ' given by expression (7) such that P′ lies along OP. This argument also is not restricted to the case when P is a bright spot, but is quite general. Hence, with an increase in the wavelength of the light, the whole pattern expands radially so that to every point P in the first case there is one, P′, in the second, such that

$$\frac{\mathrm{OP}}{\lambda} = \frac{\mathrm{OP}'}{\lambda'}. \tag{8}$$

If white light is used, there will be a range of wavelengths, so that there will be no discrete spots, but each spot will be spread out into a radial streak, whose colour is violet at the inner end and red at the outer end. The length of every such streak will be directly proportional to its distance from the centre, the streaks further away from the centre being longer.

As already remarked, such radial fibres were actually observed in white light by Exner. The author has observed these carefully and has found that one can actually follow the spectral colours in the order violet to red in any single fibre, as one goes away from the centre. Very close to the centre of the field, however, one can

observe a few white spots, since the dispersion in them is very small on account of their proximity to the centre. The length of the fibres (the distance from the violet to the red end) is found to be proportional to their distance from the centre, and the length of any fibre at a certain distance is found to be a constant, within the limits of the experimental error.

In order to further demonstrate the correlation between the spots in monochromatic light, and the fibres in white light, the following experiment was performed. A pointolite lamp was used to illuminate a fine pinhole, and a mercury green filter supplied by Adam Hilger & Co., was interposed. This transmitted only two bands, one in the green and the other in the red. The fine-structure now presented a beautiful appearance. The pattern was filled with red and green spots; but every green spot was accompanied by a red one, the two being along a radius, and the red spot being the outer one. It was also verified that the ratio of the distances of the red and the green spots from the centre was a constant, and was equal to the ratio of the mean wavelengths of the red and green transmission bands.

5. Verification of the Rayleigh Law of Fluctuations

Lord Rayleigh (1880) derived an expression for the distribution of intensity in the resultant due to n vibrations whose phases are at random. If the amplitude of a vibration is taken as unity, and as a special case, if the phases are assumed to have only either of values 0 or π, then it follows directly from Bernoulli's theorem that the chance of a positive amplitude between x and $x + \delta x$ is $\frac{1}{\sqrt{2\pi n}} e^{-x^2/2n}\, \delta x$. In the more general case of arbitray phase, the probability that the resultant amplitude may lie between r and $r + \delta r$ comes out as

$$\frac{2}{n}\, e^{-r^2/n}\, r\, \delta r \tag{9}$$

From this, it follows that the probability that the intensity may be between I and I + δI is

$$p\,(\mathrm{I})\,\delta\mathrm{I} = \frac{1}{n}\, e^{-\mathrm{I}/n}\, \delta\mathrm{I} \tag{10}$$

We can put this in a more convenient form. Prom (10), it can be shown that the average value of the intensity is n. Expressing I as a fraction f of the average value, *i.e.*, putting $I/n = f$, (10) reduces to

$$p(f)\,\delta f = e^{-f}\delta f. \tag{11}$$

This gives the probability that the resultant intensity may lie between the fractions f and $f + \delta f$ of the average, and is the same function for all values of n. It is a maximum for $f = 0$, and decreases as f increases.

This law can be verified by making use of the fine-structure in the corona. As already said, the fine-structure is produced as a result of the interference of the light diffracted by all the powder grains. The relative phases of these diffracted waves are not known but are distributed at random. Also, for different angles, ϕ, the phase relations are different, so that the whole pattern actually presents the effect of different combinations of these phase relations. Hence, the resultant intensity in the pattern must show the same statistical law of fluctuations as demanded by Rayleigh's theory.

This was verified in the following way. A very fine pinhole illuminated by the mercury green radiation of 5461 Å.U. was used as a source of light, and a picture of the central portion of the corona was taken with an exposure of two hours on a Selochrome plate. To obtain a standard of intensities, a square grating was used instead of the lycopodium screen, and the same exposure was given for the grating also. The grating gave a spectrum, the intensities of whose spots are calculable. The plates for the two photographs were obtained by cutting a single quarter plate into two. Both were developed simultaneously in the same developing bath for the same time. Thus, a strictly comparable scale of intensities was obtained for determining the intensity of the spots in the corona. The photographs of the corona and the standard grating spectra are reproduced in Fig. 5 (*a*) and 5 (*b*), Plate I, respectively.

Now, in the corona, the average intensity falls away from the centre in the proportion $J_1^2(x)/x^2$ where $x = 2\pi a \sin(\phi)/\lambda$, a being the radius of the particle, ϕ the angle of the diffraction, and λ the wavelength of the light. The corona taken in the present case extended upto a value of x = 1.5, for which the average intensity was about half that at the centre. It was therefore divided into annular rings, the widths of which were all equal to x = 0.25, by drawing circles of radii corresponding to x = 0.25, 0.5 etc.. Within each ring, the value of $J_1^2(x)/x^2$ did not vary much, and the average value for a ring was taken to be correct for that ring.

Using the grating spectrum, the intensity of whose spots could be calculated, an arbitrary scale of intensities was obtained. Then, the spots in each ring were classified into this scale, comparing them visually with the standard. The spots having an intensity less than 1 in the arbitrary scale, *i.e.*, those that could not be differentiated with the eye were found by calculating the total number of spots (dividing the area of the ring by the area of a spot) and subtracting from this the number of counted spots. Using this tabulated list, the average intensity (on the arbitrary scale) for that ring could be determined. Thus, the fraction of the total number of spots having an intensity between the fraction f_1 and f_2 of the average could be found. Dividing this by $(f_1 - f_2)$ we get the value of $p(f)$ at $(f_1 + f_2)/2$. Thus, $p(f)$ was evaluated for certain values of f. This was done for four rings, *viz.*, x = 0.25 to 0.50, to 0.50 to 0.75, 0.75 to 1.00, and 1,00 to 1.25. These were plotted in a graph and are reproduced in Fig. 2. The continuous curve represents the theoretical curve calculated from theory, and the experimental values are plotted by points.

A final average of all these four rings was obtained by dividing the intensities of the spots in each by the value of $J_1^2(x)/x^2$ for it, and then determining $p(f)$ and f taking them all into account. These are tabulated in the table below, and are represented by black dots in Fig. 2. It is clearly seen that the experimental points fit the theoretical curve very well, considering

f	$p(f)$	Theoretical	Difference
0.44	0.60	0.62	−0.02
1.29	0.33	0.28	+0.05
2.13	0.14	0.12	+0.02
3.45	0.02	0.03	−0.01
6.25	0.002	0.002	..

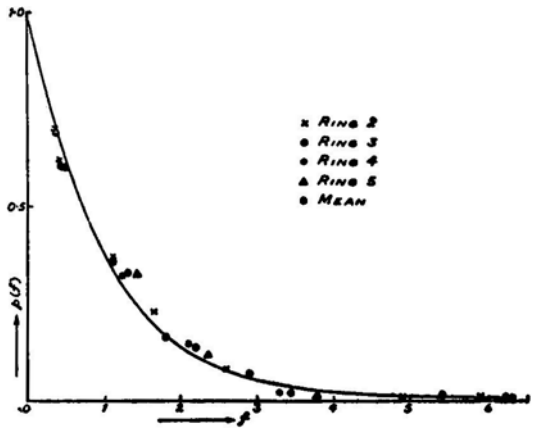

FIG. 2. Verification of Rayleigh's Statistical Law

that the comparison of intensities was done visually. Rayleigh's formula is therefore verified to be true for the distribution of intensity in the corona.

6. Conclusion

The above considerations regarding the fluctuations of intensity are true only for a static diffraction screen, *i.e.*, one in which the phase relations between the various particles is fixed in time. If the particles themselves are in motion, as in a gas or a cloud, then a continuous redistribution of phase takes place, and what one sees is the integrated effect of all these over a definite period. As Lord Rayleigh (1918) has shown, such a redistribution tends

to make the resultant intensity (perceived as an average over a certain period) approach the average value n, this tendency being greater the larger the number of redistributions. Hence, for the light scattered by a gas, or a cloud of particles, one is quite justified in regarding the scattered intensity in inclined directions as equal to n times that due to a single particle.

If the motion of the particles is slow, then the alteration in the position of the spots in the fine-structure will also be slow, and can be observed. Such a slow random motion takes place in Brownian movement, so that it must be capable of detection by this technique. This possibility, which was suggested by Prof. Sir C.V. Raman, is now under investigation.

I wish to express my sincere thanks to Prof. C.V. Raman for suggesting the problem, and for the many helpful hints he gave during the investigation.

7. *Summary*

The fluctuations of light intensity in the diffraction corona produced by a large number of randomly distributed particles are investigated both theoretically and experimentally. The theoretical considerations show that the view put forward by de Haas is inadequate and that really the fluctuations arise owing to the interference of the waves diffracted by *all* the particles, which gives rise to a large number of sharp images of the source in monochromatic light. In white light, these spots must spread out, and produce radial streaks. These deductions from theory are all borne out by experiment.

Making use of the fluctuations of intensity in monochromatic light, verification has been made for the first time of Rayleigh's statistical law of distribution of intensity in the resultant of n vibrations of arbitrary phase. It is shown that the resultant intensity shows no tendency to close upon the average value, n, but that it is distributed over a wide range of values.

REFERENCES

1. de Haas, **W.J.** .. *Proc. K. Akad.*, *Amsterdam*, 1918, **20**, 1278.
2. Exner .. Sitzungsher, Akad. Wien, 1877, **76**, 522.
3. Laue, von .. *Phys. Gesselsch., Züurich*, 1916, 90.
4. ——————— .. *Berichte deutsch. Phys. Gesselsch*, 1917, **19**, 19.
5. Rayleigh, Lord .. *Proc. Lond. Math*. Soc., 1871, **3**, 267.
6. ——————— .. *Phil. Mag.*, 1880, **10**, 73.
7. ——————— .. *Ibid.*, 1918, **36**, 429.

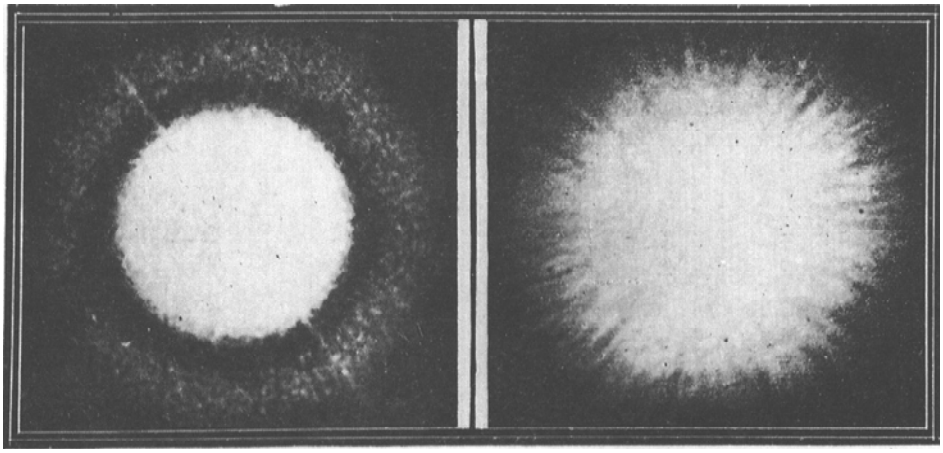

FIG. 3 (*a*) FIG. 3 (*b*)

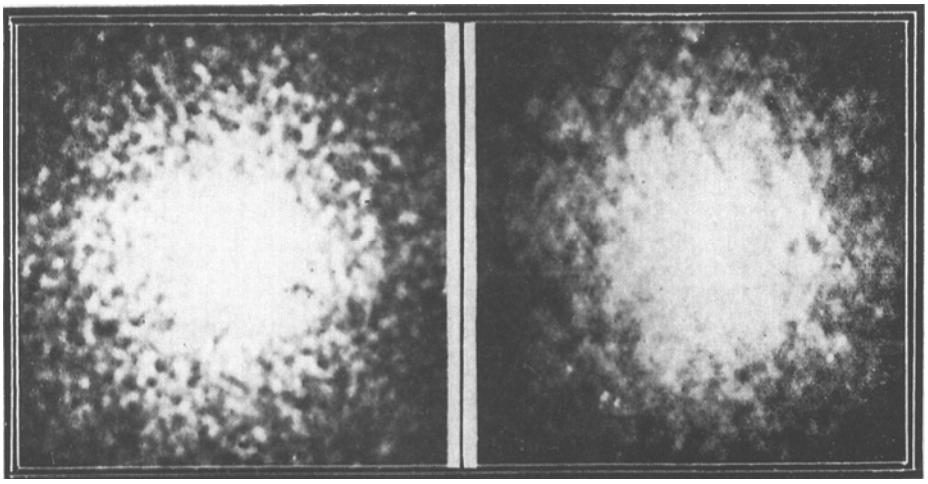

FIG. 4 (*a*) FIG. 4 (*b*)

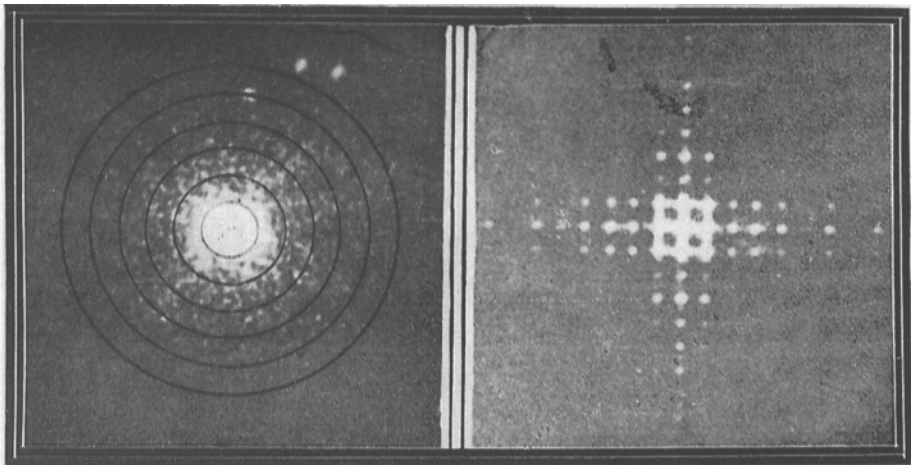

FIG. 5 (*a*) FIG. 5 (*b*)

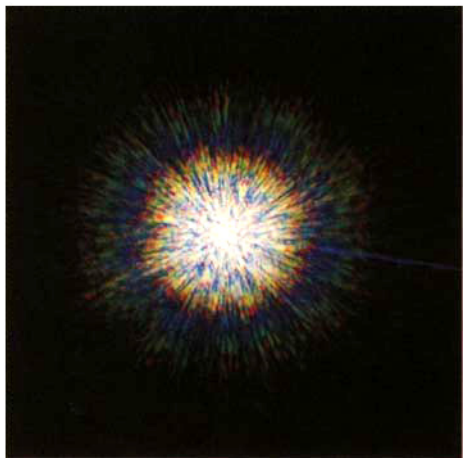

Speckles in monochromatic (*top*) and white light (*bottom*). [Photographs courtesy of Prof. R.P. Riesz]. We refer to a description of the speckle pattern in white light in page 9 and 10 of G.N. Ramachandran's paper.

J. Astrophys. Astr. (1994) **15,** 387–414

Radio Synthesis Imaging of Anisotropic Angular Broadening in the Solar Wind

K. R. Anantharamaiah *Raman Research Institute, Bangalore 560 080, India.*
Pradeep Gothoskar *National Center for Radio Astrophysics, Poona University Campus, Ganeshkhind, Pune 430 001, India*
T. J. Cornwell *National Radio Astronomy Observatory, Very Large Array, Socorro, NM 87801, USA.*

Received 1994 May 24; accepted 1994 September 12

Abstract. We present Very Large Array observations at wavelengths of 2, 3.5, 6, and 20 cm, of angular broadening of radio sources due to the solar wind in the region 2–16 solar radii. Angular broadening is anisotropic with axial ratios in the range 2–16. Larger axial ratios are observed preferentially at smaller solar distances. Assuming that anisotropy is due to scattering blobs elongated along magnetic field lines, the distribution of position angles of the elliptically broadened images indicates that the field lines are non-radial even at the largest heliocentric distances observed here. At $5R_\odot$, the major axis scattering angle is ~ 0.7″ at λ= 6 cm and it varies with heliocentric distance as $R^{-1.6}$. The level of turbulence, characterized by the wave structure function at a scale of 10 km along the major axis, normalized to λ = 20 cm, has a value 20 ± 7 at $5R_\odot$ and varies with heliocentric distance as R^{-3}. Comparison with earlier results suggest that the level of turbulence is higher during solar maximum. Assuming a power-law spectrum of electron density fluctuations, the fitted spectral exponents have values in the range 2.8–3.4 for scale sizes between 2–35 km. The data suggests temporal fluctuations (of up to 10%) in the spectral exponent on a time scale of a few tens of minutes. The observed structure functions at different solar distances do not show any evidence for an inner scale; the upper limits are 1 k m at 2 $R_\odot$ and 4 km at 13 $R_\odot$. These upper limits are in conflict with earlier determinations and may suggest a reduced inner scale during solar maximum.

Key words: Sun: solar wind, scintillations, angular broadening—Methods: observational, radio imaging.

1. Introduction

Scattering of radio waves in an inhomogeneous medium leads to angular broadening of radio sources which can be measured using suitable interferometers. Under certain scattering conditions, the intensity of the radio source fluctuates with time giving rise to the phenomena of scintillations. Interferometric measurements of angular broadening is useful in determining several properties of the scattering medium. The

mutual coherence function, which an interferometer measures, is directly related to the wave structure function of the scattering medium, which, in turn, is related to the spectrum of the density fluctuations (Coles & Harmon 1989). Any anisotropy in the scattering medium, which may be related to the orientation of the magnetic field, is directly obtained by either a radio synthesis image or a model fit to the measured visibilities. In the case of interplanetary scintillations (IPS) the intervening medium is the solar wind, which is an outflowing plasma generated near the sun and accelerated outwards to reach a velocity of ~ 400 km s $^{-1}$ at ~ 30 solar radii ($R_\odot$). Angular broadening of the strong radio source, Crab nebula, due to scattering in the solar wind, has been studied using simple interferometers from as early as 1952 (Machin & Smith 1952; Hewish 1955; Vitkevich 1955; Hewish 1958; Slee 1959; Hogbom 1960; Erickson 1964) and in fact predates the discovery of IPS (Hewish, Scott & Wills 1964). The first two dimensional images of angular broadening of the Crab nebula using aperture synthesis technique was obtained by Blesing & Dennison (1972) using the Culgoora radio heliograph. These early measurements, which were made at low frequencies (< 200 MHz), had already established the anisotropy in the scattering medium as also the variation of scattering angle as a function of solar distance in the range 5-60 $R_\odot$

The Very Large Array (VLA), which has an excellent instantaneous UV coverage with baselines up to 35 km and multiple operating wavelengths (λ = 1.3, 2, 3.5, 6, 20, 90 cm), is well suited for studying the scattering phenomena in the solar wind, especially at small solar elongations (2–20$R_\odot$). The mean electron density in the solar wind varies as ~ R^{-2}, where R is the distance from the Sun, and the magnitude of the scattering angle varies with observing wavelength as λ^2. It is therefore possible to tune the degree of scattering at a given elongation by choosing observing wavelengths appropriately. The high sensitivity of the VLA permits observation of even weak sources (typically < 1 Jy at 20 cm) whose lines of sight pass close to the Sun. Armstrong *et al.* (1986, 1990) were the first to use the VLA to study the angular broadening of the radio source 3C279 and obtain information on the wave structure function, anisotropy and radial dependence of scattering. Subsequently Cornwell, Anantharamaiah & Narayan (1989) used the VLA to obtain high time resolution (tens of milliseconds) images of 3C279 when its line of sight passed close to the Sun. (< 1°) and established the coherence properties of the scattered radiation. Narayan, Anantharamaiah & Cornwell (1990) used longer time-averaged images (~10 s) of 3C279 to show that refractive scintillation occurs in the solar wind and also that the area of the angular broadened image fluctuates in correlation with the total flux as predicted theoretically.

In this paper we present angular broadening observations of three radio sources using the VLA when the elongation of these sources varied between 0.5° to 4°. The motivation for these observations was to study the nature of scattering in the solar wind close to the Sun at many different position angles. At each of the observed position these data provide information on the degree of anisotropy, orientation of the major axis and level of turbulence, which are, in turn, related to the orientation of the magnetic field and the magnitude of the density fluctuations in the solar wind. The measured visibilities (correlations of the electric field) are directly related to the wave structure function of the scattering medium (Coles & Harmon 1989; Armstrong *et al.* 1990) from which we can obtain the spectrum of the density fluctuations which is

assumed to have a power-law form. It may be mentioned here that for the range of elongations observed here there is no direct way of measuring either the magnetic field or the density fluctuations, since the region is too far from the Sun for solar magnetograms and too close to the Sun for space probes.

The integration time of the scatter-broadened images obtained here is typically ~ 10 minutes and therefore correspond to the so called 'ensemble-average' regime as discussed by Narayan *et al.* (1990) and Goodman & Narayan (1989). This regime is obtained when the integration time $t_{\rm int} > t_{\rm ref} = \theta_s D/V$ where θ_s is the scattering angle, D is the distance to the scattering screen (= 1 AU here) and $V$is the transverse velocity of the medium with respect to the observer. $\theta_s D$ (also known as the refractive scale $r_{\rm ref}$) is the largest scale on the screen from which a given point in the observer plane receives the scattered radiation. Other length scales (and corresponding time scales) that come into play when scattering occurs are the Fresnel scale $r_F = \sqrt{\lambda D}$ and diffractive scale $r_{\rm diff} = \lambda/\theta_S$. $r_{\rm diff}$ represents the transverse scale over which the rms phase difference due to the phase changing screen is of the order 1 radian. The demarcation between weak and strong scattering regimes is at $r_{\rm diff} = r_F$. When $r_{\rm diff} < r_F$ scattering is strong and the angular broadening of the source (θ_S) is larger than the Fresnel angle ($\theta_F = r_F/D$). The behaviour of interferometric visibilities in the weak scattering regime has been discussed in detail by Cronyn (1972) and in the strong scattering regime by Narayan & Goodman (1989) and Goodman & Narayan (1989). Cornwell *et al.* (1989) have presented both theoretical and observational study of interferometric imaging in the 'snapshot' regime ($t_{\rm int} < t_{\rm diff} = r_{\rm difi}/V$) under conditions of strong scattering. A summary of the behaviour of scatter-broadened images in different regimes of integration time and scattering strength can be found in Narayan *et al.* (1990).

In the present observations which cover an elongation range of ε = 0.5°– 4°, we find that strong scattering occurs for $\varepsilon \leqslant 1.0°$ at λ = 2 cm, for $\varepsilon \leqslant 1.5°$ at 3.5 cm, for $\varepsilon \leqslant 2.5°$ at 6 cm and for the entire observed range of elongations at λ = 20 cm. The diffractive scales ($r_{\rm diff}$) in these regions of the solar wind range from a few kilometers to several tens of kilometers at these wavelengths (which is very similar to the range of VLA baselines) and the refractive scales ($r_{\rm ref}$) are about a hundred to a few thousand kilometers. The corresponding time scales are $t_{\rm diff}$ ~ 0.01 – 0.5 s and $t_{\rm ref}$ ~ 0.5 – 50s if we assume the solar wind velocity to be ~ 350 km s^{-1}. Notice that the length scales in. the solar wind are comparable to the baselines available in ground based radio interferometers such as the VLA and the VLBA and the time scales are comparable to typical integration times used for visibility and image measurement. Furthermore, anisotropy, which is caused by the relatively strong magnetic field (compared to interstellar conditions) in the solar wind is easily measured with these interferometers. As such, solar wind offers the right conditions for testing many predictions of scattering theories.

This paper is organized as follows. In section 2 we describe the observations and calibration of the data. Section 3 describes imaging and image analysis in which we obtain the angular size and orientation of the major and minor axes of the scatter-broadened images. The measured visibilities are analysed in section 4 in terms of the wave structure function of the scattering medium and also through least squares fit of a scattering model with parameters such as anisotropy, scattering strength, and index of the power law spectrum of density fluctuations in the medium. Finally, the derived parameters are discussed in section 5.

2. Observations

Observations were made using the A-configuration of the VLA during the period 2–6 November 1988. Three sources, 1430–155, 1437–153, and 1443–162, which are considered as VLA calibrators (i.e. they are unresolved over the range of VLA baselines) were observed each day at two or more wavelengths chosen depending on the elongation. These sources have flux densities in the range 0.50–9.0 Jy at our observing wavelengths. In Fig. 1, we show the positions of the three sources with respect to the Sun on different observing dates. Columns 1–3 of Table 1 gives the source name, date of observation, elongation and observing wavelength. Columns 3–5 of Table 2 gives the heliographic latitude, position angle of the line joining the direction of the source and the centre of the Sun measured clockwise from north and the Carrington longitude for the different dates. One of the main problems of observing close to the Sun is that the strong radio flux from the Sun's disk can enter through the side lobes of the primary beam of the antennas and corrupt the visibility measurements of the source. The problem is especially severe at longer wavelengths, where the primary beam is large and the Sun is stronger, and for short baselines, for which delay decorrelation is less. The smallest elongation where useful data could be obtained at our longest observing wavelength (λ = 20 cm) was ~ 1.3° and at the shortest wavelength (λ = 2 cm) it was ~ 0.5°.

Each source was observed for about 10 minutes in the standard VLA continuum mode with a bandwidth of 50 MHz and an integration time of 10 seconds per visibility. At each wavelength, data was recorded from both polarization channels in two intermediate frequency (IF) bands. The instrumental phase and amplitude were calibrated using observations of the source 1354–152 which was > 10° away from the Sun. The amplitude scale was set by observing the source 3C286.

The three sources were again observed on 6 January 1989 when they were > 40° away from the Sun to determine their intrinsic structure. Two of the sources (1430–155 and 1443–162) were found to be point-like and completely unresolved at all wavelengths over the VLA baselines in the A-configuration. However, the third source 1437-153 was found to be a radio galaxy with a strong core and two weak and

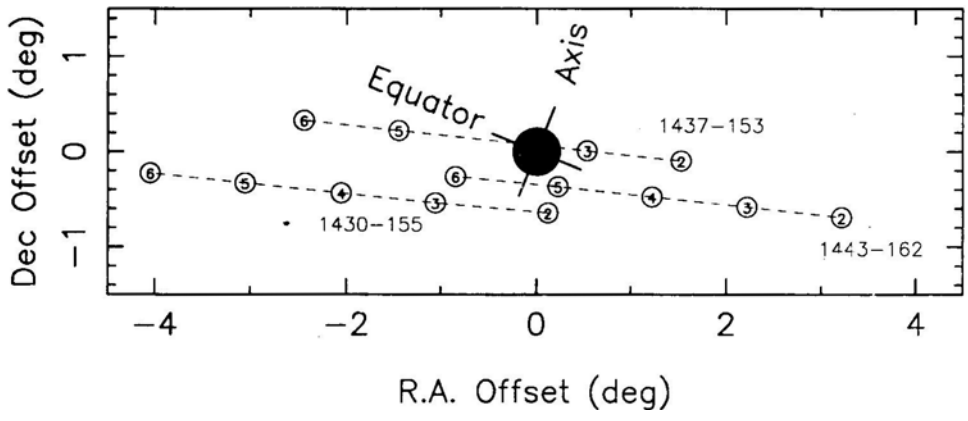

Figure 1. Position of the three observed sources with respect to the Sun on different dates. The number at each position indicates the date of observation in November 1988.

Table 1. Parameters from scatter broadened images.

Date source (1)	ϵ (°) (2)	λ (cm) (3)	Flux (Jy) (4)	θ_{maj} ($''$) (5)	θ_{min} ($''$) (6)	PA (°) (7)	ρ (8)
2 Nov.88	0.66	3.5	0.70	0.163(3)	0.06(1)	82(2)	2.8(5)
1430-155		6	0.62	0.44(1)	0.07(x)	87(9)	6.0(26)
2 Nov.88	1.53	3.5	0.82	0.088(2)	0.031(7)	11(1)	2.8(6)
1437-153		6	0.71	0.297(5)	0.105(5)	17(1)	2.8(1)
2 Nov.88	3.29	3.5	0.62	0.032(1)	0.018(1)	33(2)	1.8(1)
1443-162		6	0.57	0.08(1)	0.04(1)	34(4)	2.0(6)
		20	0.44	1.07(1)	0.39(1)	27(1)	2.7(1)
3 Nov.88	1.19	2	0.74	0.064(1)	0.017(2)	166(1)	3.8(5)
1430-155		3.5	1.04	0.125(1)	0.051(1)	154(1)	2.5(1)
		6	0.75	0.60 (1)	0.18(1)	161(1)	3.3(2)
3 Nov.88	0.54	2	0.76	0.285(7)	0.08(1)	14(1)	3.6(5)
1437-153		3.5	0.64	1.049(1)	0.29(1)	16(1)	3.6(1)
3 Nov.88	2.29	3.5	0.66	0.06(1)	0.025(5)	38(2)	2.4(6)
1443-162		6	0.52	0.205(5)	0.117(5)	23(2)	1.8(1)
		20	0.28	3.6(1)	2.18(4)	17(2)	1.7(1)
4 Nov.88	2.10	6	0.88	0.308(3)	0.08(1)	177(1)	3.7(5)
1430-155		20	0.26	4.26(3)	0.78(1)	179(1)	5.5(1)
4 Nov.88	1.31	3.5	0.61	0.16(1)	0.02(1)	38(x)	6.7(34)
1443-162		6	0.50	0.64(1)	0.16(1)	35(1)	3.9(3)
		20	0.25	9(1)	3(.5)	36(3)	2.9(6)
5 Nov.88	3.07	3.5	0.85	0.042(1)	0.022(1)	1(1)	1.9(1)
1430-155		6	0.88	0.12(1)	0.05(1)	7(2)	2.7(6)
		20	0.33	1.29(1)	0.29(1)	5(1)	4.5(2)
5 Nov.88	1.46	2	0.86	0.096(1)	0.018(5)	23(2)	5.3(15)
1437-153		3.5	0.77	0.35(1)	0.05(1)	24(1)	6.9(14)
		6	0.60	1.43(1)	0.16(1)	22(1)	8.9(6)
		20	0.39	10(1)	3.8(1)	21(3)	2.6(3)
5 Nov.88	0.43	2	0.32	0.79(1)	0.23(1)	47(1)	3.5(2)
1443-162							

Table 1. (continued).

Date source (1)	ϵ (°) (2)	λ (cm) (3)	Flux (Jy) (4)	θ_{maj} ($''$) (5)	θ_{min} ($''$) (6)	PA (°) (7)	ρ (8)
6 Nov.88	4.06	6	0.89	0.074(3)	0.016(4)	1(1)	4.6(12)
1430-155		20	0.38	0.67(3)	0.20(1)	14(1)	3.4(2)
6 Nov.88	2.46	2	1.27	0.025(4)	0.013(5)	19(10)	1.9(8)
1437-153		6	0.71	0.18(1)	0.07(1)	17(3)	2.8(4)
		20	0.54	3.28(5)	1.2(1)	24(1)	2.7(2)
6 Nov.88	0.89	2	0.74	0.245(5)	0.02(5)	175(1)	11(3)
1443-162		3.5	0.60	0.61(1)	0.075(3)	175(1)	8.2(4)
•		6	0.35	2.73(2)	0.286(4)	175(1)	9.6(2)

Notes: (1) Numbers in parenthesis are 1σ errors and apply to the last decimal digit of the value quoted.
(2) (x) indicates that the error could not be estimated.
(3) Formal error on the flux densities (column 3) is < 0.01 Jy.

extended lobes which become stronger at longer wavelengths. Visibility data of this source on short baselines is noticeably affected by its intrinsic structure at λ = 20 cm.

3. Imaging and image analysis

Images of the scatter broadened sources were obtained from the measured visibility data using standard radio synthesis methods as implemented in the software package AIPS (Astronomical Image Processing System) developed by NRAO. A common problem in synthesis imaging with long baselines and short wavelengths is the error introduced in the measured visibility (especially its phase) due to the atmosphere. On the assumption that this error is only dependent on antenna positions, corrections can be derived using the technique of self-calibration (Cornwell & Fomalont 1989). In the present case however, care should be exercised since scintillations themselves will cause fluctuations in the measured visibility phase (and amplitude). In almost all the cases observed here, we expect stable scatter-broadened images since t_{int} (~ 10 minutes) is much greater than t_{ref} (< 0.5 minutes). It several cases, especially at shorter wavelengths, images made without the application of self-calibration showed artifacts indicative of effects due to the atmosphere. In these cases, we found that application of phase corrections obtained from self-calibration with either a point-source model or an initial model obtained from positive 'clean components', vastly improved the quality of the images. During self-calibration, we used a visibility averaging time t_{ave} of one minute which is much larger than the diffractive time scale t_{diff} (< < 1 s) and comparable to the refractive time scale t_{ref}. We therefore expect that the phase variations due to diffractive scintillation to be averaged out and there would be no modification of the scatter-broadened image. Cornwell *et al.* (1989) have discussed the case when $t_{ave} < t_{diff}$, and show that self-calibration in this regime actually removes the angular broadening because of the spatial coherence property of the scattered radiation.

Some examples of scatter-broadened images which are well resolved in the present observations are shown in Figs. 2a and 2b. These images were obtained after applying

phase-corrections from self-calibration as explained above and deconvolving the 'dirty images' (Fourier transform of the measured and corrected visibility function) using conventional 'clean' For each image in Fig. 2, the direction of the line joining the center of the image and the center of the Sun's disk is indicated. Two main results of

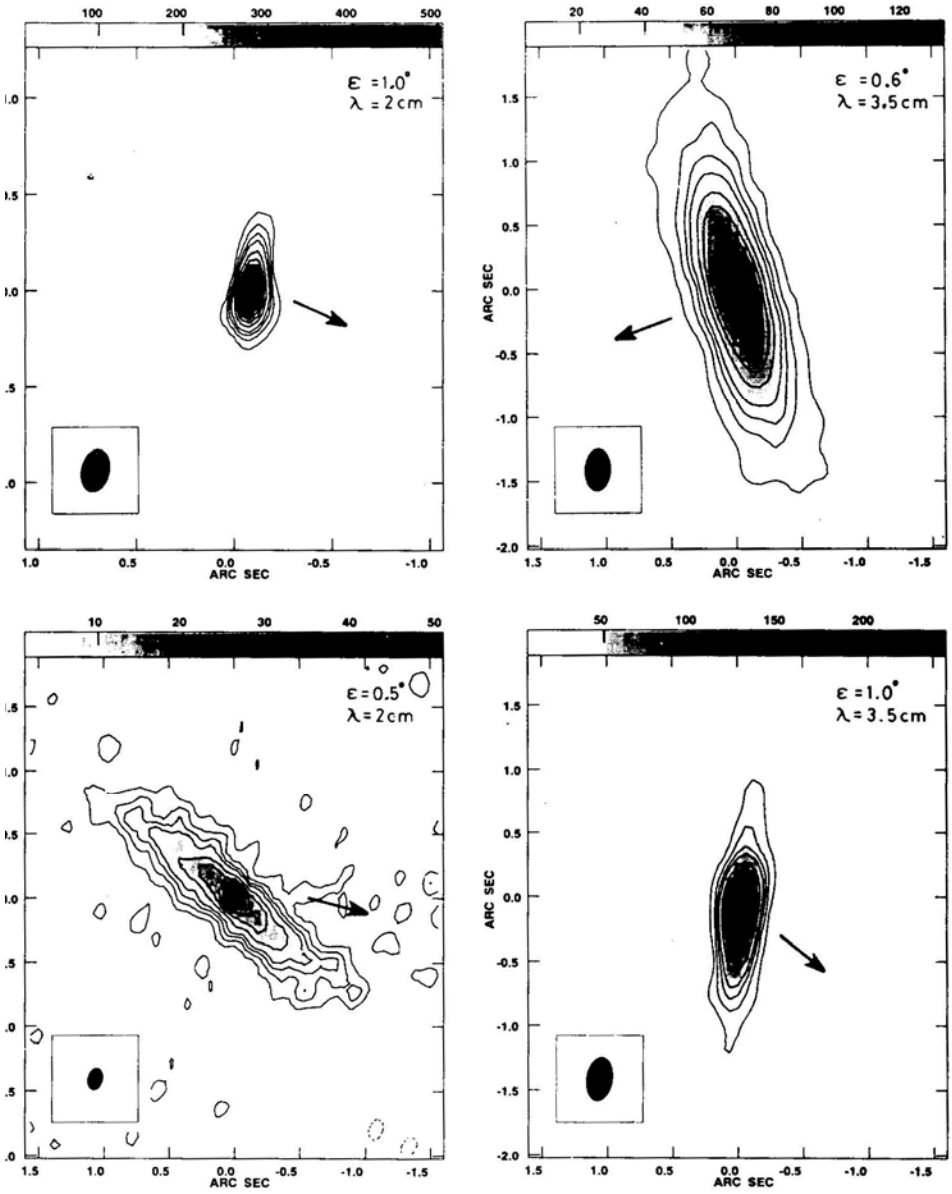

Figure 2a. Examples of scatter-broadened images at wavelengths of 2 and 3.5 cm. Elongation of the source and the wavelength of observation are indicated in each frame. Arrow indicates the direction of the Sun's centre. The contour levels are – 0.5, 0.5, 1, 1.5, 2 to 10 in steps of 1 unit where 1 unit is 43.8 mJy/beam for the top-left frame, 10.5 mJy/beam for the top-right frame, 4.1 mJy/beam for the bottom left frame and 26.7 mJy/beam for bottom-right frame. The restoring beam is shown in the bottom left corner of each image.

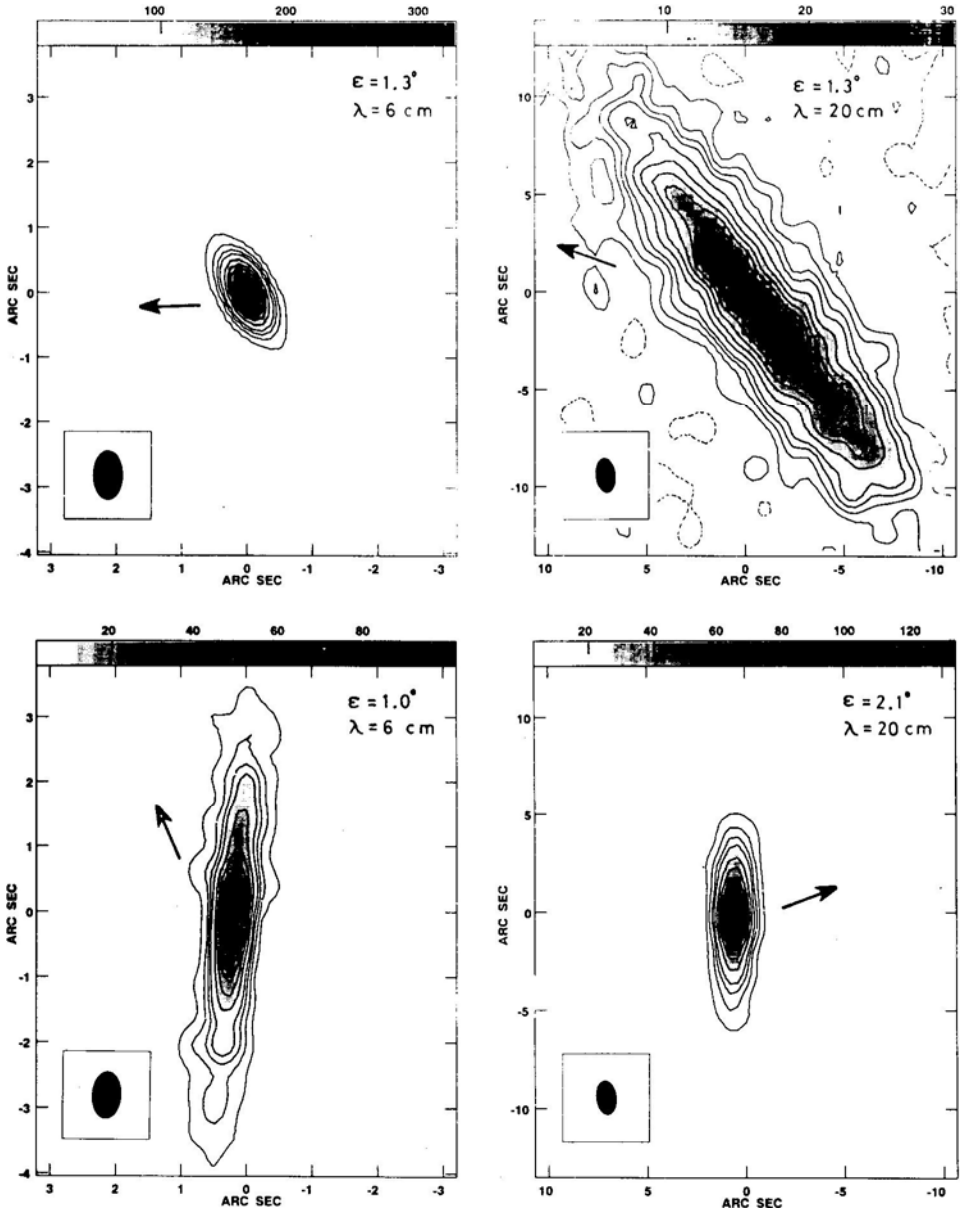

Figure 2b. Examples of scatter-broadened images at wavelengths of 6 and 20 cm. Elongation of the source and the wavelength of observation are indicated in each frame. Arrow indicates the direction of the Sun's centre. The contour levels are – 0.5, 0.5, 1, 1.5, 2 to 10 in steps of 1 unit where 1 unit is 29.1 mJy/beam for the top-left frame, 2.0 mJy/beam for the top-right frame, 8.0 mJy/beam for the bottom left frame and 11.1 mJy/beam for bottom-right frame. The restoring beam is shown at the bottom left corner of each image.

these observations are evident in Fig. 2. First, the scatter-broadening in the solar wind is highly anisotropic at small elongations in. agreement with earlier findings (Hewish 1958; Hogbom I960; Blesing & Dennison 1972; Narayan *et al.* 1989,

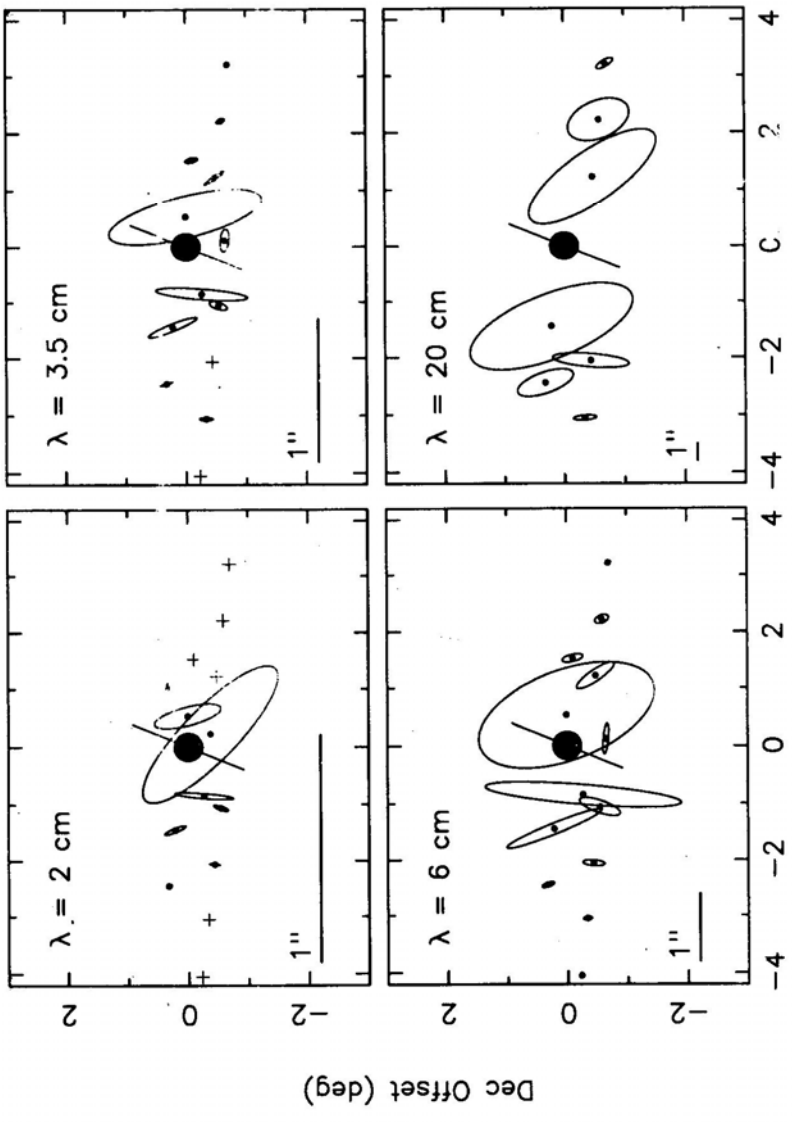

Figure 3. Schematic representation of elliptical shapes of scatter broadened images observed at four wavelengths at various distances from the Sun. The scale for the elliptical images is indicated by a 1 arcsec horizontal line in each frame. A '+' sign at the observed position indicates that the source was unresolved. The direction of the Sun's axis of rotation is indicated in each frame.

Table 2. Parameters from visibility analysis.

Date source	ϵ	Lat.	ϕ_{rad}	Long.	λ	Flux	x_0	y_0	θ(PA)	ρ	D^{20}_{maj}	D^{20}_{min}	β_{fit}	β_{str}
	(°)	(°)	(°)	(°)	(cm)	(Jy)	(km)	(km)	(°)					
(1)	(2)	(3)	(4)	(5)	(6)	(7)	(8)	(9)	(10)	(11)	(12)	(13)	(14)	(15)
2 Nov.88	0.66	−28.3	170	80.8	3.5	0.79	96(x)	27(1)	81(3)	3.6(8)	19(3)	6(5)	3.16(6)	3.16(8)
1430-155					6	0.94	59(x)	11(1)	86(4)	5.3(14)	18(2)	6(3)	2.84(8)	2.83(2)
2 Nov.88	1.53	6.9	94	80.8	3.5	0.86	210(50)	78(8)	13(x)	2.7(7)	7(6)	2.5(18)	3.18(6)	2.98(7)
1437-153					6	0.81	89(7)	26(1)	18(2)	3.5(3)	7.2(5)	1.5(5)	3.00(4)	3.27(10)
2 Nov.88	3.29	0.1	102	80.8	6	0.58	600(100)	250(25)	26(x)	2.4(5)	0.5(5)	0.3(2)	3.10(5)	3.17(11)
1443-162					20	0.48	80(7)	24(1)	28(1)	3.3(3)	0.8(1)	0.3(1)	3.12(4)	3.12(3)
3 Nov.88	1.19	−80.1	243	247.8	3.5	1.10	170(40)	52(4)	153(4)	3.3(8)	–	–	2.98(6)	–
1430-155					6	0.95	44(2)	10.5(2)	159(1)	4.2(8)	20.5(10)	5.5(5)	2.95(4)	2.98(2)
3 Nov.88	0.54	7.5	89	67.8	2	0.93	27(3)	7(.5)	13(2)	4.2(6)	370(49)	77(16)	3.22(8)	3.14(2)
1437-153					3.5	1.13	8(1)	2(.1)	15(2)	4.2(6)	305(52)	93(8)	2.98(4)	2.98(1)
3 Nov.88	2.29	−1.8	105	67.8	3.5	0.69	344(75)	159(15)	31(x)	2.2(5)	5(3)	1.4(13)	2.96(4)	2.96(18)
1443-162					6	0.58	110(8)	55(4)	24(4)	2.0(2)	4.5(6)	2.6(5)	2.90(4)	2.97(3)
					20	0.61	5(.5)	3(.2)	10(5)	1.7(2)	5.0(7)	3.3(2)	2.82(4)	2.87(2)
4 Nov.88	2.10	−31.3	258	234.6	6	0.93	190(4)	29(1)	177(2)	6.5(3)	5.8(9)	0.7(6)	3.24(4)	3.32(6)
1430-155					20	0.48	27(3)	4(.5)	178(1)	6.7(11)	4.2(7)	0.8(1)	3.06(8)	3.04(2)
4 Nov.88	1.31	-5.5	111	54.6	6	0.58	41(3)	9(.2)	36(1)	4.4(3)	23(2)	4(1)	3.28(6)	3.31(4)
1443-162					20	0.56	6(.6)	1.2(.1)	36(1)	5.0(7)	–	–	3.6(2)	3.32(5)

Table 2. (continued).

Date source (1)	ϵ (°) (2)	Lat. (°) (3)	ϕ_{rad} (°) (4)	Long. (°) (5)	λ (cm) (6)	Flux (Jy) (7)	x_0 (km) (8)	y_0 (km) (9)	θ(PA) (°) (10)	ρ (11)	D^{20}_{maj} (12)	D^{20}_{min} (13)	β_{fit} (14)	β_{str} (15)
5 Nov.88	3.07	−14.3	264	221.5	3.5	0.85	934(x)	350(x)	-3(x)	2.7(8)	–	–	3.2(1)	–
1430-155					6	0.88	515(100)	150(10)	9(4)	3.4(7)	0.8(3)	0.3(1)	3.18(4)	3.4(1)
					20	0.43	83(10)	19(1)	5(2)	4.4(6)	0.9(1)	0.2(1)	3.10(6)	3.21(3)
5 Nov.88	1.46	10	279	221.5	2	0.93	219(x)	27(2)	20(3)	8.1(17)	72(14)	–	3.20(8)	3.26(8)
1437-153					3.5	0.86	130(40)	11(.5)	24(1)	11(3)	56(2)	5(2)	3.32(6)	3.14(3)
					6	0.75	49(5)	3.8(.1)	22(1)	13(1)	64(13)	5(2)	3.24(6)	3.01(3)
5 Nov.88	0.43	−15.3	149	41.5	2	1.1	2.5(x)	0.7(.1)	46(4)	3.8(9)	–	560(346)	2.78(6)	3.19(9)
1443-162														
6 Nov.88	4.06	−7.7	267	208.3	20	0.4	211(52)	54(5)	11(4)	3.9(10)	0.2(1)	0.03(1)	3.2(3)	3.49(9)
1430-155														
6 Nov.88	2.46	−7.4	278	208.3	3.5	0.98	598(400)	160(130)	26(50)	3.7(39)	–	–	3.3(3)	–
1437-153					6	0.78	925(500)	243(100)	20(20)	3.8(26)	3.7(6)	1.5(4)	2.6(1)	2.78(5)
					20	0.67	24(10)	6(2)	24(10)	3.8(20)	3.1(3)	0.9(1)	2.9(3)	2.90(3)
6 Nov.88	0.89	−68.9	253	208.3	2	0.85	204(70)	9(.5)	175(1)	22(8)	–	–	3.20(8)	3.20(3)
1443-162					3.5	0.77	86(x)	5.5(.5)	175(1)	16(3)	120(15)	15(6)	3.0(1)	2.92(3)
					6	0.76	15(2)	1.3(.1)	175(1)	11(2)	123(25)	20(5)	2.76(4)	2.83(5)

Notes: (1) Numbers in parenthesis are 1σ errors and apply to the last decimal digit of the value quoted.
(2) (x) indicates that the error could not be estimated.
(3) Formal error on the flux densities (column 7) is < 0.01 Jy.
(4) Column 5 is Carrington longitude for the Carrington rotation number 1808.
(5) Columns 12 and 13 are the structure functions at s = 10 km scaled to $\lambda = 20$ cm.

Armstrong *et al.* 1990). We find that the axial ratios are in the range 2–16 depending on the elongation and position angle. In Fig. 3, we show schematically the elliptical shapes of the scatter-broadened images at different positions with respect to the Sun at four different wavelengths. The second result is that the orientation of the major axis deviates significantly from being normal to the radial from the Sun's center. At some positions, the deviation is in the range 50–75°.

An elliptical gaussian source was fitted (using the procedure JMFIT in AIPS) to each of the observed scatter-broadened image to obtain the angular size of its major and minor axes, the position angle and the total flux. The fitted values along with the formal 1σ errors are given in columns 4–7 of Table 1. Column 8 of Table 1 gives the anisotropy $\rho = \theta_{maj}/\theta_{min}$ obtained from the images.

4. Visibility analysis

Although the images shown in the previous section, which were obtained by Fourier transformation of the measured visibilities, provide a good visual picture of the scatter broadening and give quantitative estimates of the scattering angle and anisotropy, there are likely to be some biases. For example, if the scatter-broadened images are not gaussian in shape (as would be the case for a power-law spectrum of density fluctuations), then the fitted parameters will be biased. However it is possible to directly analyse the measured visibilities in terms of the scattering parameters. The measured visibilities are the time averaged electric field correlations between different points on the ground given by

$$V(\mathrm{s}) = \langle E(\mathrm{r}) E^*(\mathrm{r} + \mathrm{s}) \rangle \tag{1}$$

where s represents the baseline vector. The spatial coherence of the electric field described by the mutual coherence function is simply the normalized visibility given by

$$\Gamma(\mathbf{s}) = \frac{V(\mathbf{s})}{V(0)} \tag{2}$$

The mutual coherence function (equation 2) lends itself to straightforward interpretation in terms of the scattering properties of the medium and also the spatial spectrum of electron density fluctuations in the medium. The relevant theory is discussed by Coles & Harmon (1989) and Armstrong *et al.* (1990). Briefly, the mutual coherence `is related to the wave structure function $D(\mathbf{s}) = \langle [\phi(\mathbf{r}) - \phi(\mathbf{r}+\mathbf{s})]^2 \rangle$ by

$$\Gamma(\mathbf{s}) = \exp\left[-\frac{D(\mathbf{s})}{2} \right] \tag{3}$$

(3) where $\varphi(\mathbf{r})$ is the geometric phase delay on a straight line path from the source to the observer at position **r**. If the scattering medium is characterized by an electron density fluctuation spectrum of power-law form $P_{Ne}(q) \propto q^{-\beta}$ for $q_{out} < q < q_{in}$, where q is the wavenumber, then the wave structure function also has a power law form given by $D(s) \propto s^{\beta-2}$ for $2 < \beta < 4$. Furthermore, at the inner scale sin = $2\pi/q_{in}$ the structure function breaks to the form $\mathrm{D(s)} \propto s^2$. A plot of log$D$(s) versus log($s$) can

therefore be used to obtain the value of β and also the inner scale if it falls within the range of baselines covered by the observations. Note that useful measurements of the structure function can be obtained only over the range of baselines covered by the observations and only when the scatter broadened source is partially resolved by the interferometric array. Since the structure function $D(s)$ scales as λ^2, different wavelengths are effective for different range of scales in the scattering medium. Since the range of scales in our observations are fixed by the range of VLA baselines and since scattering angle increases with decreasing elongation, observations at shorter wavelengths (e.g. 2 cm) provide information at smaller elongations and those at longer wavelengths (e.g. 20 cm) are useful for larger elongations.

Application of the above to the present observations is slightly complicated due to the anisotropy in the scattering medium. Anisotropy implies that the scattering blobs are preferentially elongated in one direction, presumably along the local magnetic field lines. If we assume that the shape of the electron density fluctuation spectrum is independent of direction (i.e. index β has the same value along all directions) then $P_{\mathrm{Ne}}(q) \propto [q_x^2 + (q_y/\rho)^2]^{-\beta/2}$, where ρ is the axial ratio of the blobs and the x-axis is chosen along the direction of elongation in the plane normal to the line of sight. Note that any elongation along the z-direction is projected out. The structure function has the form $D(s) \propto [s_x^2 + (\rho s_y)^2]^{(\beta-2)/2}$. In the present observations, the baselines s are distributed in the xy plane and the orientation of the major axis varies from source to source. A plot of $D(s)$ versus s of all the data will show a lot of scatter since the scattering angle is a function of position angle due to the ellipticity of the image. However for baselines with the same orientation (e.g. baselines lying along one of the arms of the VLA), the mutual coherence function $\Gamma(\mathbf{s})$ and therefore the structure function $D(s)$ will show a simple monotonically increasing behaviour with s.

In Fig. 4, we show plots of log $D(s)$ versus log(s) from one of the observations for five sets of baselines; three corresponding to the three arms of the VLA and the other two to the baselines along the major and minor axis of the scatter-broadened image. To make these plots, the visibilities on each baseline were averaged over the duration of the observations (~ 10 minutes) and therefore correspond to ensemble average visibilities. Within the errors, the slopes of log $D(s)$ versus log(s) plots in Fig. 4, corresponding to the 5 sets of baselines, agree with each other indicating that the value of β is independent of direction. Plots, similar to Fig. 4, were made for all the 36 observations shown in Table 1. Out of these 36, 12 showed well determined structure functions with consistent slopes along the five different position angles. In the remaining 24 cases, 8 each had structure functions well determined along 4, 3, and 2 position angles. In these 24 cases, the structure function was not well determined at other position angles since the source was either resolved or unresolved on the available baselines. The average value of the spectral exponent β obtained from the slopes of log $D(s)$ vs. log(s) plots is given for each case in column 15 of Table 2.

The value of the structure function along the major and minor axis of the image, at s = 10 km and scaled to λ = 20 cm, are given in columns 12 and 13 of Table 2. The values obtained from observations at different frequencies are consistent within the errors. We further examined the consistency of the data obtained at different frequencies at a given elongation by making plots of log $D(s)$ vs log(s) for the same position angle. An example is shown in Fig. 5. For comparison the structure function

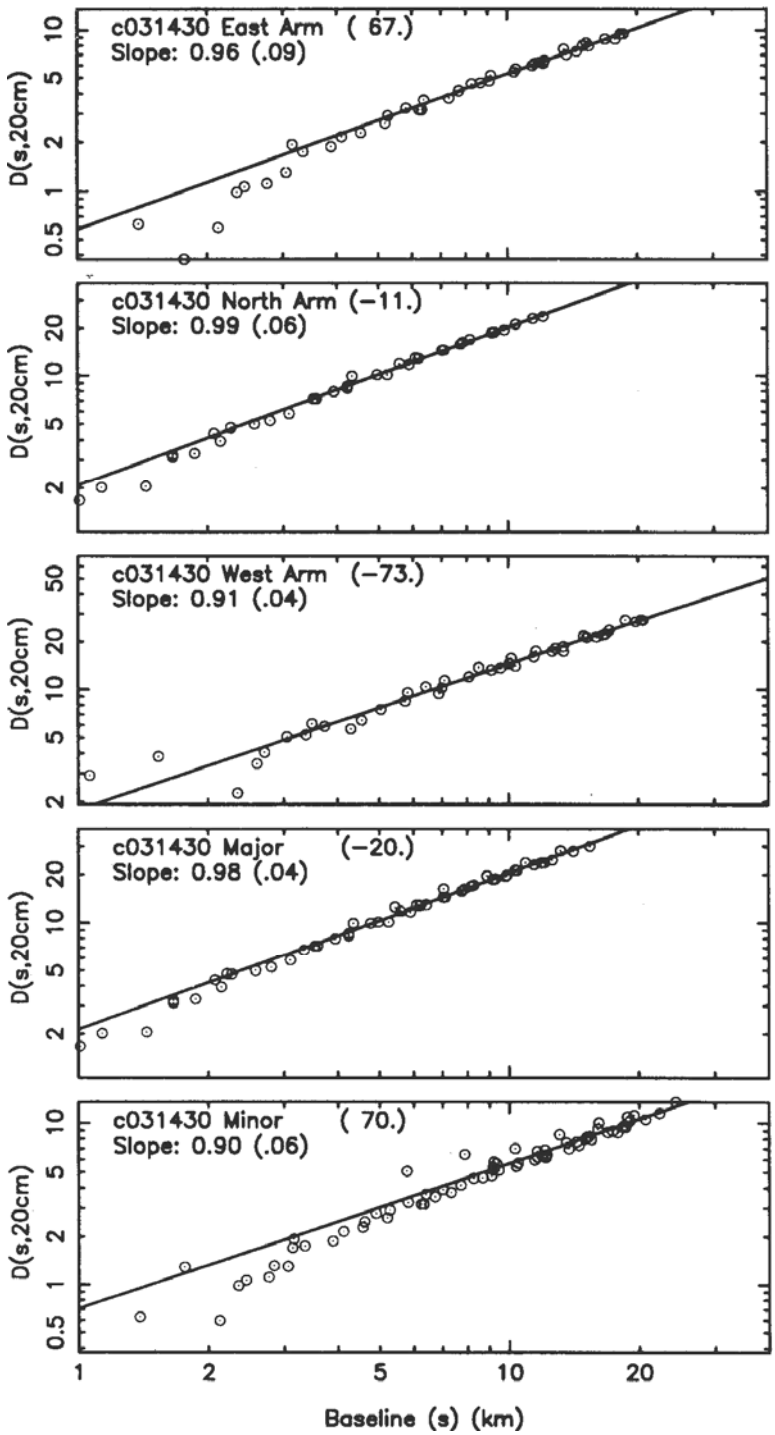

Figure 4. Structure function, scaled to λ = 20 cm, along five position angles for the source 1430155 observed at an elongation of 1.2° and λ = 6 cm. The position angles and the slope of the fitted line are given in each frame. The position angles correspond to the three arms of the VLA and the major and minor axis of the image. The slope of the structure function is equal to β-2 where β is the exponent of the power-law spectrum of electron density fluctuations defined as $P_{Ne}(q) \propto q^{-\beta}$.

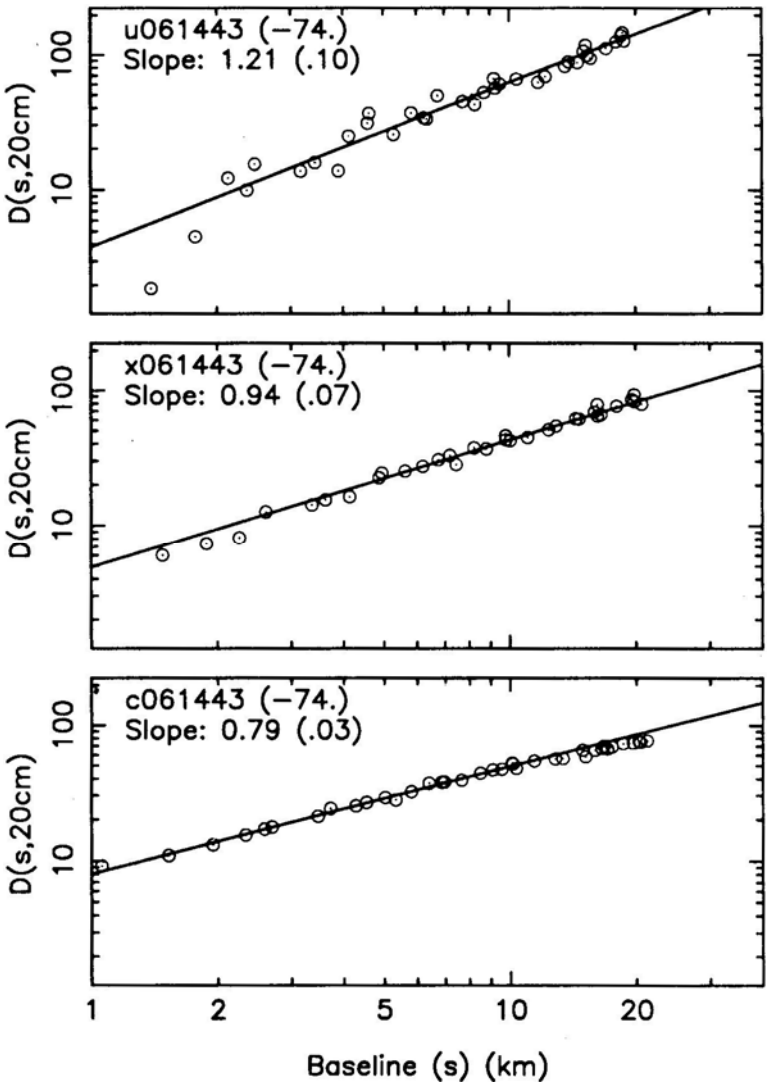

Figure 5. Structure function at 2, 3.5, and 6 cm, each scaled to λ = 20 cm, for the source 1443–162 observed at an elongation of 0.9°. The position angle is – 74° and corresponds to the east arm of the VLA. The slopes of the fitted lines and their errors are also indicated.

at each frequency has been scaled to λ = 20 cm. Fig. 5 shows that, although the magnitude of the structure function is roughly consistent at the three frequencies and follows the expected λ^2 law, the slope of the function decreases systematically with increasing wavelength. Since the range of baselines (s) over which the slopes are determined at the three frequencies are nearly the same, this variation cannot be attributed to any possible change in the spectral exponent with scale size. Presence of any inner scale within these range of baselines is also ruled out since no break is seen in the slope. We examined eleven cases for which well determined structure function (as in Fig. 5) could be obtained at more than one frequency and found no

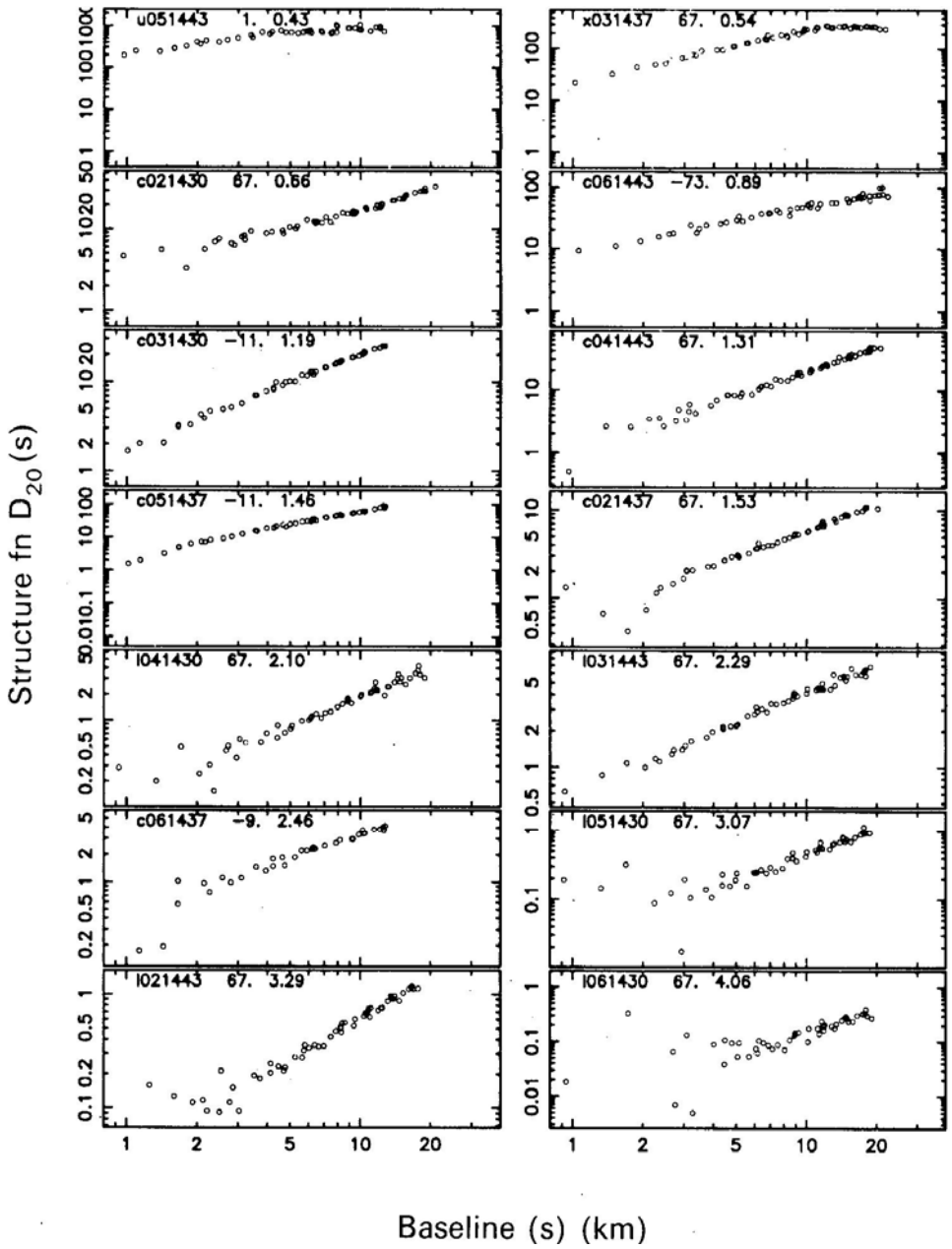

Figure 6. Structure functions, scaled to λ = 20 cm, at all the observed elongations. Wavelength of observation, date, source name, position angle of baselines and the elongation are given for each frame. For example, the top left frame is observation of the source 1443–162 at u band (i.e. λ = 2 cm) on 5th Nov. at an elongation of 0.43°. The position angle chosen is 1°. The nomenclature for the wavelengths are x = 3.5 cm, c = 6 cm and l = 20 cm. For each elongation, we have selected a wavelength and position angle which gives a well determined structure function over a reasonable range of baselines.

clear trend in the behaviour of β with λ; in three cases the exponent decreased with frequency as in Fig. 5, in two cases it increased, in four cases the exponent remained constant within the errors and in two cases the exponent first increased and then decreased. Given this behaviour and the fact that the observations of a given source at different frequencies were separated by 30–35 minutes, we attribute the observed variation in β to temporal fluctuations on a time scale of a few tens of minutes. Such temporal variation in β may be expected since it has been shown (Manoharan *et al.* 1994) that the spectral exponent varies with the velocity of the solar wind which fluctuates on a variety of time scales.

In Fig. 6, we present the structure function obtained at the 14 elongations where observations were made. For this plot, we have chosen, for each case, an observed frequency and a position angle for which the structure function is well determined over a reasonable range of baselines. For comparison, all the structure function values have been scaled to λ = 20 cm. In all the cases shown in Fig. 6, there is no clear indication of an inner scale at which we expect the slope of log $D(s)$ vs. log (s) to change from $\beta - 2$ to 2. In some of the cases, the structure function shows a scatter near the shortest baselines due to the source being unresolved. We estimate upper limits to the inner scale as the shortest baseline down to which log $D(s)$ shows a linear dependence on log (s) in the plots shown in Fig. 6. These limits are given in column 11 of Table 3.

In the above method of analysing the structure functions, only a part of the data is utilized in determining the value of β, since only baselines lying along a selected position angle are used. In order to use all the visibility measurements, we follow the method discussed in Narayan *et al.* (1989) which was based on a theoretical treatment of anisotropic scattering by Narayan & Hubbard (1987). In this method the ensemble average visibilities of the scatter broadened image are predicted on the basis of a five parameter model and compared with the measured visibilities. The five parameters are then optimized using a least-squares fitting algorithm. The model visibilities are given by

$$\langle V_{\text{model}}(u,v) \rangle = F \times \exp[-(au_t^2 + bv_t^2)^{\gamma}] \tag{4}$$

where F is the flux density of the source, $u_t = u \cos\theta + v \sin\theta, v_t = -u \sin\theta + v \cos\theta$, θ is the orientation of the image with respect to the u-axis, $\gamma = (\beta - 2)/2$ where β is the power-law index of electron density fluctuation spectrum and $x_0 = (1/a)^{1/2}$ and $y_0 = (1/b)^{1/2}$ are the scale lengths along the major and minor axis of the scatter broadened image. These scale lengths represent the baseline at which the visibility falls to $1/e$ of its zero-spacing value, $\rho = y_o/x_o$ is the magnitude of anisotropy.

The complex visibility data on each of the 351 baselines, taken with an integration time of 10 seconds, were averaged over the duration of the observations (~ 10 minutes) and over two frequency channels and both polarizations. Self-calibration applied to the visibility data as described in the previous section ensured that the source is at the field centre and since the signal to noise ratio on each visibility measurement is sufficiently large (typically > 10), we fitted the magnitude of the 351 observed visibilities to the model given by equation 4. The five parameters (F, θ, x_o, y_o, and γ) were optimized by minimising χ_v^2 using a conjugate gradient search algorithm, χ_v^2 has the usual definition

$$\chi_v^2 = \frac{\Sigma_{\sigma_{\text{obs}}}^{1/2} (V_{\text{model}} - V_{\text{obs}})^2}{(N - n - 1)} \tag{5}$$

where the summation is over N visibility measurements and n is the number of free parameters. σ_{obs} is the rms noise on individual visibility measurements. If the model chosen is correct and there are no systematic errors, then, χ^2_v will approach unity when the model parameters are optimum. In order to compare the model and the observed visibilities, we define, following equation (3), a structure function at the modified scale s_m

$$D(s_m) = -2.\ln \frac{V(s_m)}{V(0)} \tag{6}$$

where s_m is a modified U V distance given by

$$s_m = (au_t^2 + bv_t^2)^{1/2} \tag{7}$$

and $V(s_m)$ is the observed visibility on the baseline (u, v). The effect of equation (7) is to express the baseline lengths in terms of the fitted scale lengths x_0 and y_0 and the position angle θ. The structure function predicted by the model is also obtained by equation (6) by replacing the observed visibility by the model visibility V_{model} (s_m) given by equation (4). Fig. 7 shows a comparison between the observed and model structure functions (equation 6) for one of the observations. In this plot all the structure

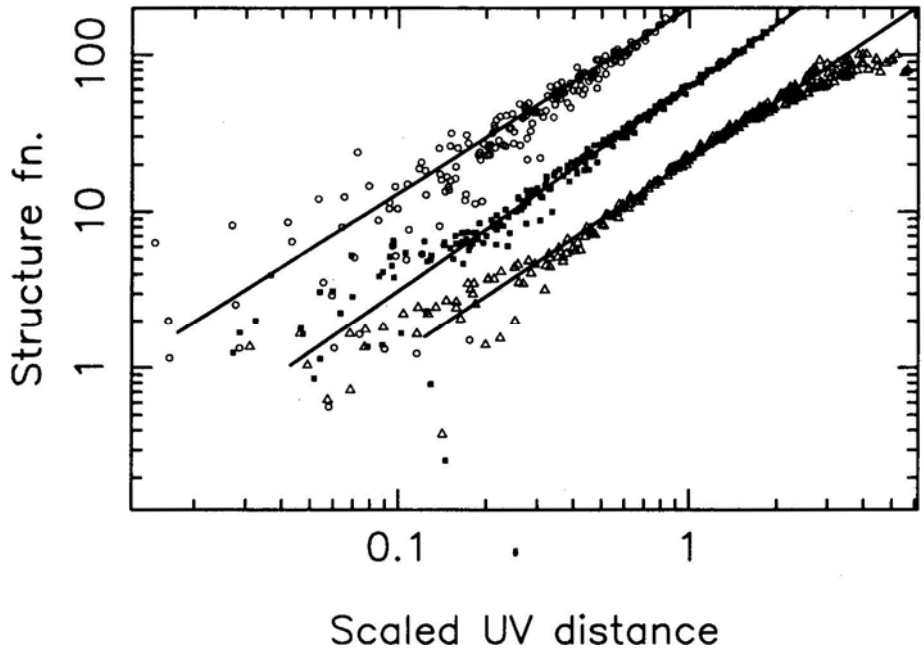

Figure 7. Comparison of observed and model visibilities for the source 1437–143 observed at an elongation of 1.5°. Open circles are observations at λ = 2 cm, solid squares are at 3.5 cm and open triangles are at 6 cm. The observed structure function (equation 6), scaled to λ = 20 cm in each case is plotted against baselines which are scaled and rotated to match the fitted scale lengths along the major and minor axis of the anisotropic image and also its orientation. The scaled baseline lengths are $(au_t^2 + bv_t^2)^{1/2}$ as used in equation (4). The fitted model given by equations (4) and (6) is plotted as a solid line.

functions have been scaled to λ = 20 cm. With the exception pf a few cases, there was good agreement (as in Fig. 7) between the model and the observed values. However, we found that the minimum value of χ^2_ν differed from unity by a factor of 2–10 or even larger in most of the cases. We attribute this to an underestimation of σ_{obs}, which was obtained from the observed fluctuations in the visibility samples with 10 second integration by assuming that these fluctuations are independent in the four IF channels (two frequencies and two polarizations) and that the rms noise goes down

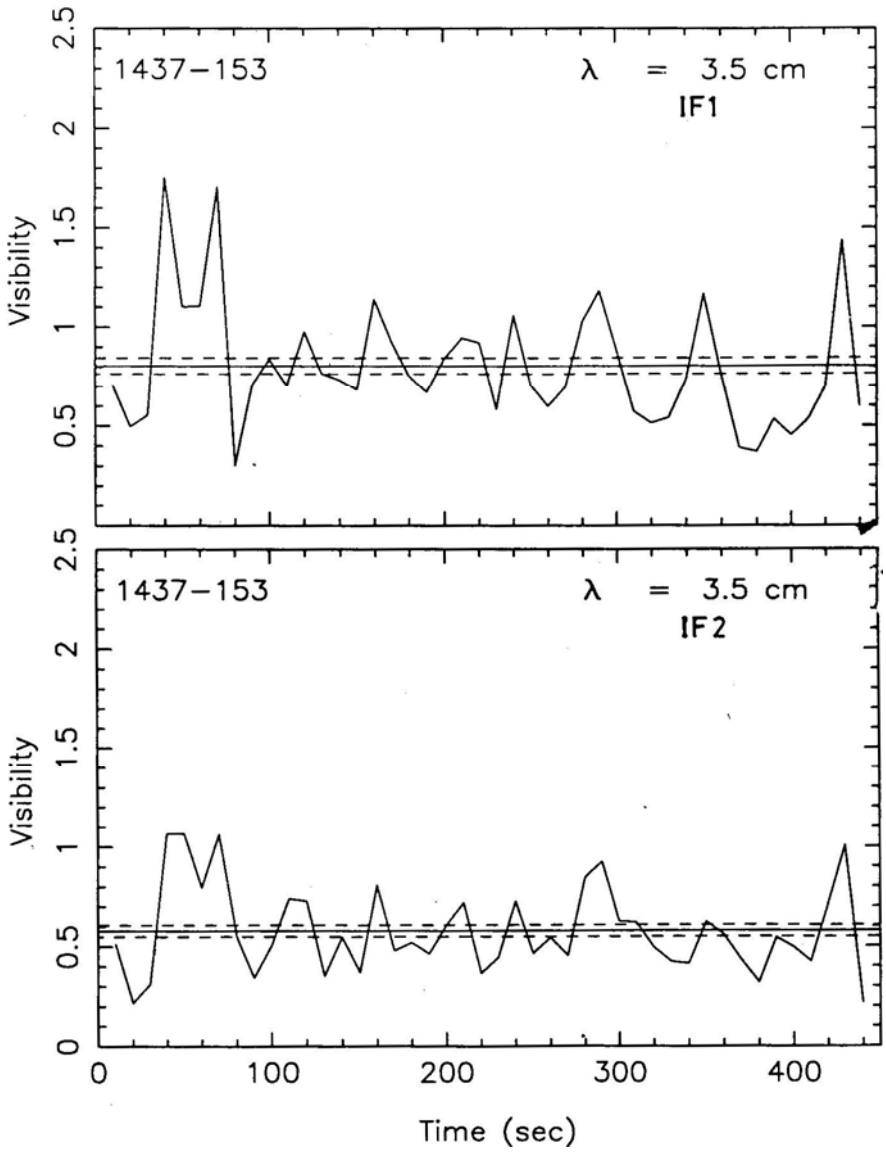

Figure 8. Time variation of the measured visibility in the two IF bands on one of the baselines (Antenna pair 21–27). The pair of dashed lines indicate the expected rms noise level for an integration time of 10 s and a bandwidth of 50 MHz which is used for the observations. The two IF bands are separated by 50 MHz.

by a factor $(1/N_{vis})^{1/2}$ when N_{vis} visibility samples are averaged. Two factors have contributed to an underestimation of σ_{abs}; (i) presence of refractive scintillation with $t_{ref} > 10$s, which introduces partial correlation between many 10 second samples and (ii) the decorrelation bandwidth ($c/d\theta_s^2$, where θ_s is the scattering angle and d is the length of the baseline) is much larger than the separation between the two frequency channels which results in two of the four IFs being not independent for some of the baselines. That this is indeed true can be seen in Fig. 8, where we show, the variation of visibility on one of the baselines as a function of time for two IFs. A high degree of correlation is seen between the two IFs and there are systematic fluctuations in the visibility over a time scale of several tens of seconds. Presence of refractive scintillation in the solar wind with a time scale of few minutes had been established by Narayan *et al.* (1989). A value of χ_v^2 , higher than unity when the model parameters are optimised as described above is consistent with these observations.

The best fit values of F, x_o, y_o, θ and β (= 2γ + 2) along with their corresponding errors are given in columns 7–10 and 14 of Table 2. Statistical error for each parameter was obtained by using the variation of χ_v^2 with the parameter around its best fit value while keeping the other parameters fixed at their optimum values. The fitted values of β are consistent with the values derived from the structure function analysis above (i.e. slope of log $D(s)$versus log (s) plots given in column 15 of Table 2).

5. Discussion

The observations presented here sample the scattering properties of the solar wind in the region 2–16 $R_\odot$ and a range of heliographic latitudes. The parameters obtained are the magnitude of the scattering angle, the level of the structure function, the anisotropy of the scattering blobs, the orientation of the magnetic field lines, the spectral index β of the electron density fluctuation spectrum and upper limits on the inner scale of the density fluctuations. These quantities are summarized in Table 3.

5.1 *Level of turbulence*

Following Armstrong *et al.* (1990), we characterize the level of turbulence by the magnitude of the structure function at a fixed scale of 10 km normalized to λ = 20 cm. This quantity computed along the major and minor axis (denoted by D_{major} and D_{minor}) of the scattered image are given in columns 12 and 13 of Table 2 and the average values for each elongation are given in columns 7 and 8 of Table 3. Fig. 9 shows a plot of D_{major} and D_{minor} as a function of elongation on a log-log scale. The turbulence level shows a power law behaviour; the fitted slopes are – 2.7 ± 0.2 for D_{major} and – 3.0 ± 0.2 for D_{minor}. For a spherically symmetric solar wind having density variance proportional to the square of the mean density, the expected slope is – 3.0. From Fig. 8, the turbulence levels at 5 $R_\odot$ are D_{major} = 20 ± 7 and D_{minor}= 6 ± 3. For comparison, the corresponding values reported by Armstrong *et al.* (1990) (taken from their Fig. 4a) and ~ 7 and ~ 2 from observations in 1983 which is closer to a solar minimum. Our values are about a factor of 3 larger. This may represent the difference in the level of turbulence between solar minimum and maximum, since our observations are closer to a solar maximum. The value of the structure function at

Table 3. Parameters as a function of solar distance.

ϵ (°) (1)	$R/R_\odot$ (2)	Lat (°) (3)	ϕ_{rad} (°) (4)	θ_{maj}^{6cm} ($''$) (5)	ρ (6)	D_{maj}^{20} (7)	D_{min}^{20} (8)	$<\beta>$ (9)	$<PA>$ (°) (10)	s_{in} (km) (11)
0.43	1.72	−15.3	128	9.50 ±0.10†	3.8 ±0.9	–	560 ± 346	2.78 ±0.06	46 ± 4	< 1.5
0.54	2.16	7.5	106	3.55 ±0.04†	4.2 ±0.6	338 ± 35	85 ± 9	3.10 ±0.04	14 ± 2	< 1
0.66	2.64	−28.3	142	0.44 ±0.01	4.5 ±0.1	19 ± 2	6 ± 3	3.00 ±0.07	83 ± 4	< 4
0.89	3.56	−68.9	182	2.73 ±0.02	16.2 ±0.5	122 ± 15	17 ± 4	2.99 ±0.08	175 ± 1	< 1.5
1.19	4.76	−80.1	193	0.60 ±0.01	3.8 ±0.8	21 ± 1	5.5 ± 0.5	2.97 ±0.05	156 ± 3	< 2
1.31	5.24	−05.5	119	0.64 ±0.01	4.7 ±0.5	23 ± 2	4 ± 1	3.44 ±0.15	36 ± 1	< 5
1.46	5.84	10.0	291	1.43 ±0.01	10.6 ±0.2	64 ± 6	5.0 ± 1	3.25 ±0.07	22 ± 2	< 2
1.53	6.12	6.9	106	0.30 ±0.01	3.1 ±0.5	7.2 ± 0.5	2.0 ± 0.7	3.06 ±0.05	15 ± 2	< 4
2.10	8.40	−31.3	250	0.31 ±0.01	6.6 ±0.8	5.0 ± 0.6	0.8 ± 0.3	3.14 ±0.06	178 ± 2	< 4
2.29	9.16	−01.8	115	0.21 ±0.01	2.0 ±0.3	4.8 ± 1.1	2.4 ± 0.5	2.89 ±0.04	22 ± 5	< 2
2.46	9.84	−07.4	289	0.18 ±0.01	3.8 ±0.3	3.4 ± 0.4	1.2 ± 0.2	2.90 ±0.30	23 ± 32	< 3.5
3.07	12.28	−14.3	267	0.12 ±0.01	3.5 ±0.7	0.9 ± 0.3	0.3 ± 0.1	3.16 ±0.07	4 ± 3	< 6
3.29	13.16	0.1	113	0.08 ±0.01	2.9 ±0.4	0.8 ± 0.1	0.3 ± 0.1	3.11 ±0.05	27 ± 1	< 4
4.06	16.24	−07.7	274	0.07 ±0.01	3.9 ±1.0	0.2 ± 0.1	0.03 ± 0.01	3.22 ±0.07	11 ± 4	< 8

Notes: (1) †Extrapolated from higher frequency using $\theta_s \propto \lambda^{2.2}$
(2) Errors quoted are 1σ.

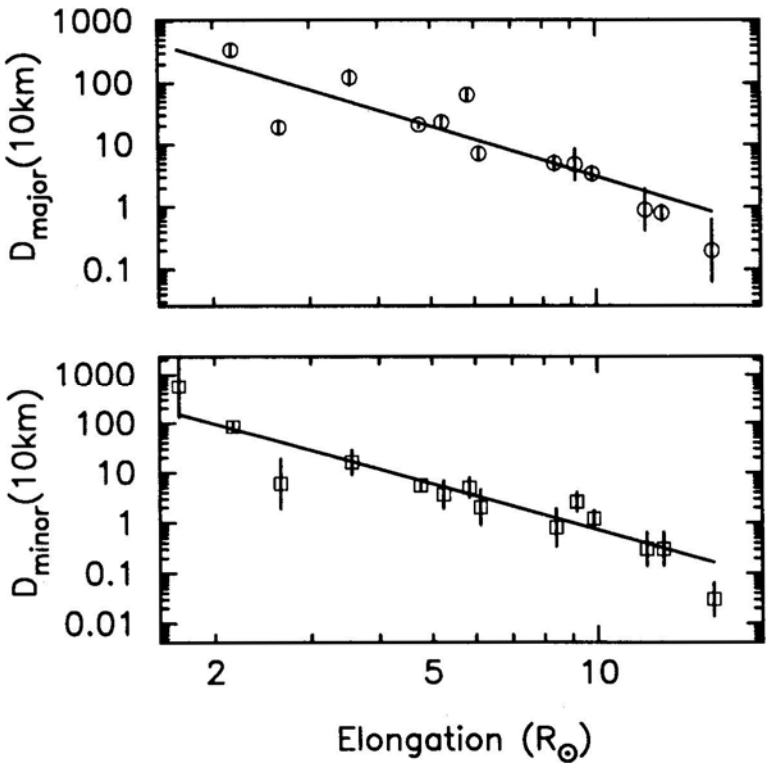

Figure 9. The variation of structure function along the major and minor axis at a scale of 10 km, normalized to λ = 20 cm, as a function of solar distance. The fitted lines have slopes of –2.7 ± 0.2 and – 3.0 ± 0.2 for the top and bottom frames.

$5R_\odot$ (normalized to λ = 20 cm) obtained by Coles & Harmon (1989) (taken from their figure 1), from spectral broadening measurements in 1984, is ~ 13. Since the structure function determination from spectral broadening data requires a knowledge of the solar wind velocity, a direct comparison with $D_{\rm major}$ or $D_{\rm minor}$ obtained from visibility measurements is difficult.

5.2 *Angular broadening*

The magnitude of angular broadening (which, of course is related to the turbulence level discussed above) and its variation with solar distance is of direct interest to observers, for example, to determine the interferometric baselines required to study the scattering phenomena in the solar wind. The observed angular size along the major axis at λ = 6 cm is given in column 5 of Table 3 and plotted as function of solar distance on a log-log scale in Fig. 10a. The angular size of the major axis shows a power law dependence on solar distance R with a slope of – 1.6 ± 0.1 $\theta_{\rm maj} \propto R^{-1.6}$. This type of dependence is also seen in the angular extent of the minor axis and is consistent with earlier findings (Lotova *et al.* 1989, see also compilation by Hollweg 1970 of earlier results). Angular broadening does not seem to depend on heliographic latitude. This is not surprising since these observations are made closer to the solar

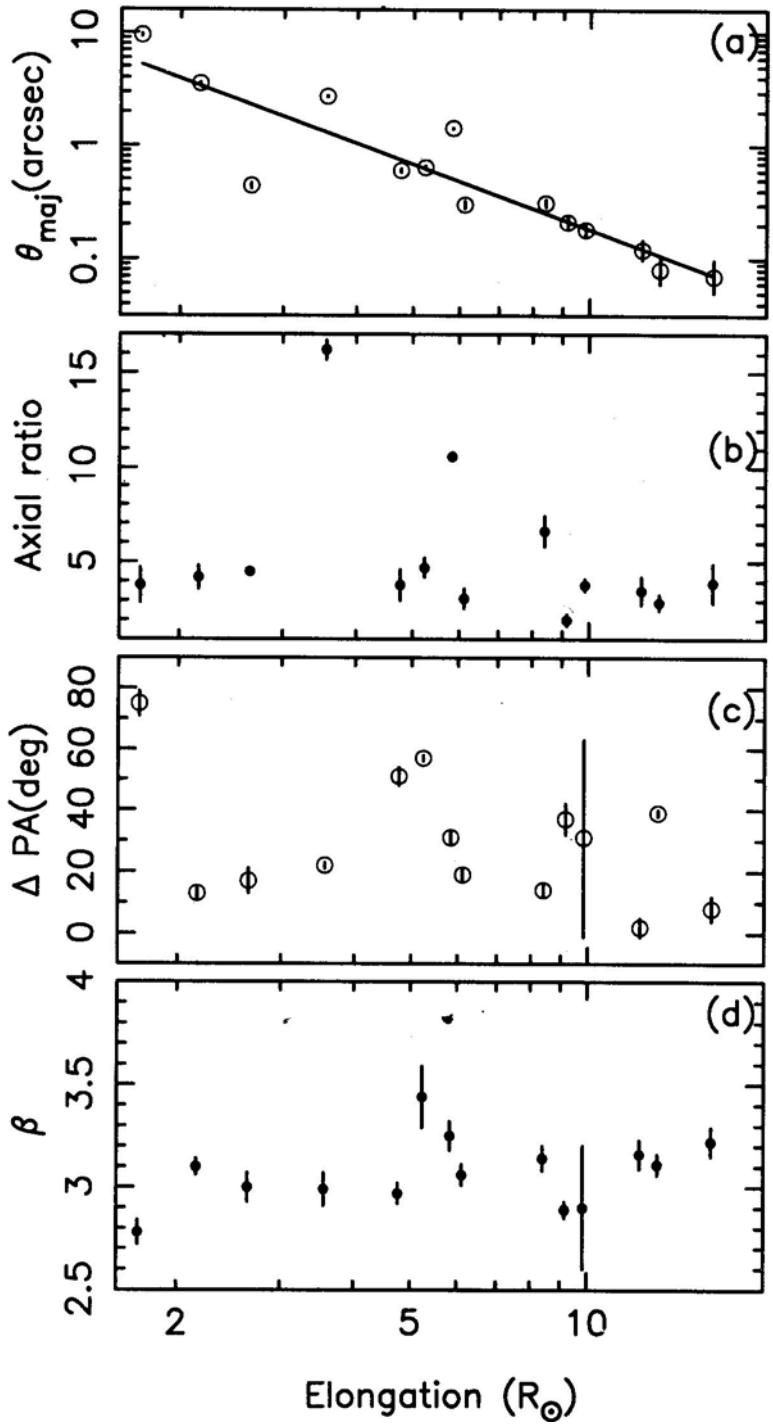

Figure 10. Observed variation of different parameters with solar distance: (a) angular size of the major axis, (b) axis ratio, (c) deviation of position angle of the minor axis from the radial direction and (d) spectral index of the electron density fluctuation spectrum.

maximum when the density fluctuations are expected to be spherically symmetric (Manoharan 1993).

Presence of a transonic region in the solar wind .between 10–20 $R_\odot$ with enhanced scattering properties has been reported by Lotova *et al.* (1985, 1989). It is claimed that in this region, the scattering angles exceed the expected values based on $\theta \propto R^{-1.6}$. In Fig. 10a, there are only 3 data points in the transonic region and they do not show any excess scattering. Further observations are required to confirm the existence of such a region. We note that VLA is well suited to investigate this region using observations at λ = 20 and 90 cm.

5.3 *Anisotropy*

In the elongation range observed here (2–16$R_\odot$), all the scatter-broadened images show anisotropy with the axial ratio ranging from 2 to 16 (Tables 2 and 3). The magnitude of anisotropy does not show any strong dependence on solar distance (Fig. 10b), although larger axial ratios tend to occur only at smaller elongations. Armstrong *et al.* (1990) report marked increase in the axial ratio inside of 6$R_\odot$. However, the difference here is that smaller axial ratios are observed at all elongations and larger axial ratios are observed only at smaller elongations. As seen in Fig. 11a,

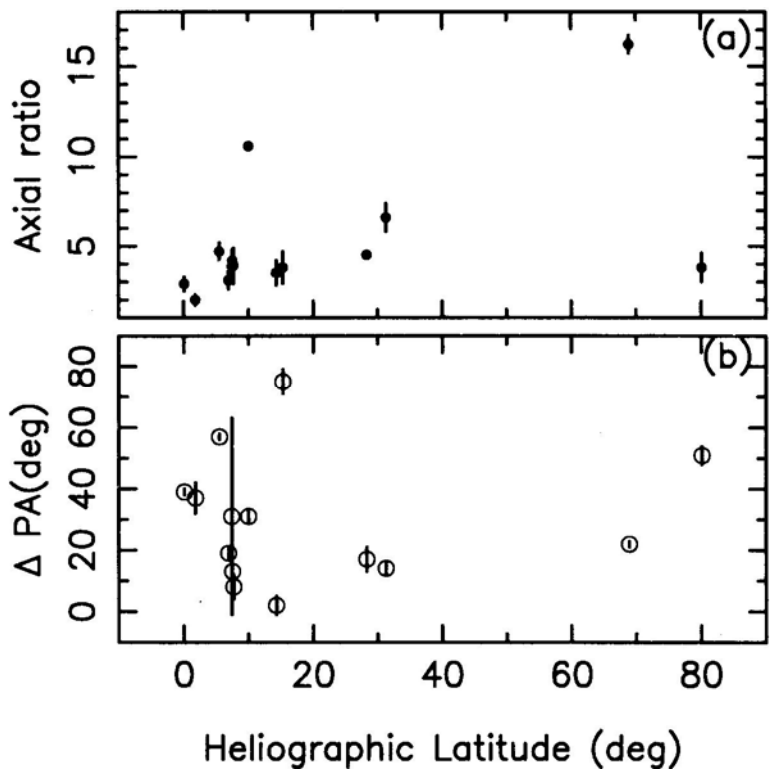

Figure 11. Observed variation of different latitude, of the axial ratio and the deviation of the position angle of the minor axis from radial direction.

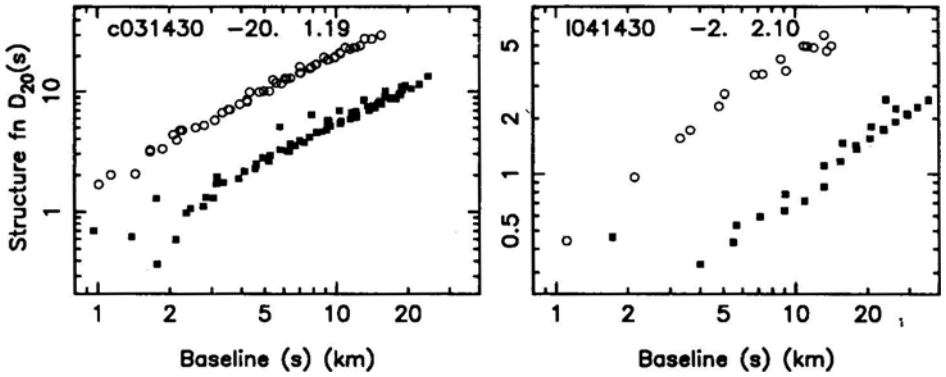

Figure 12. Examples of observe structured function along the major (open circles) and minor (filled squares) axes scaled to $\lambda = 20$ cm. The observed source is 1430–155 at elongations of 1.19ºand 2.10º. The position angles of the major axis are – 20º and – 2º.

there could be a dependence of the axial ratio with heliographic latitute; images in the equatorial region seem to show less anisotropy.

Anisotropy in the scattered image implies anisotropy of the scattering blobs which is perhaps caused due to the blobs being 'stretched' along magnetic field lines. The amount of this 'stretching' may depend on the scale size and the density contrast. It is therefore useful to see whether anisotropy depends on the scale size sampled by these observations (i.e. 1–35 km). In Fig. 12, we show the observed structure functions along the major and minor axis for two of the observations. This figure could be compared with the schematic diagram of Armstrong *et al.* (1990) (their figure 6) which illustrates the expected behaviour when the medium is anisotropic on all scales and when the medium is isotropic near the inner scale. The structure functions in Fig. 12 do not show any inner scale down to 1–2 km and therefore these observations cannot determine whether the inner scale is isotropic or anisotropic. Note that the scatter seen near the shortest baselines in Fig. 12, especially along the minor axis, is due to the source being unresolved and cannot be interpreted as any break in the slope which is expected near the inner scale. Since the structure functions along the major and minor axis, shown in Fig. 12, are essentially parallel to each other in the baseline range 2–35 km, we conclude that the anisotropy is constant over this range of scales.

5.4 *Orientation of the magnetic field lines*

The position angle of the minor axis of the scatter-broadening image indicates the direction along which the scattering blobs are stretched and therefore the local orientation of the magnetic field lines. In Fig. 13, we show the observed position angle of the minor axis at various solar distances. Consistency between the position angles derived from image and visibility analysis indicates that the values are reliable. It is clear that the field lines deviate significantly from the radial direction in many of the positions observed. In contrast, Armstrong *et al.* (1990) have observed that the position angles outside of about 2.5 $R_\odot$ is essentially radial. The difference could be due to our observations being closer to a solar maximum. The observed deviation does not have any strong dependence on radial distance (Fig. 10c) or heliographic

latitude (Fig. lib). When the kinetic energy density exceeds the magnetic energy density, one expects the field lines to be radial. The present data implies that, during solar maximum, the magnetic energy density could be comparable to the kinetic energy density even beyond $10R_{\odot}$.

5.5 *Spectrum of density fluctuations and the inner scale*

On the assumption that the electron density fluctuations in the solar wind has a power law spectrum of the form $P_{Ne}\ (q) \propto q^{-\beta}$ for $q_{\rm out} < q < q_{\rm in}$, where q is the wavenumber, the derived value of the spectral index β is in the range 2.8 to 3.4 with a mean of 3.1 (Tables 2 and 3) which is significantly small compared to the Kolomogorov value of 3.67. No dependence of β is seen either with radial distance from the Sun (Fig. 10d) or heliographic latitude. This value of the exponent applies to scale sizes in the range 2–35 km corresponding to the interferometer baselines used and is consistent with the values obtained by Coles & Harmon (1989) and Manoharan *et al.* (1994) for similar scale sizes using other methods. We have carefully examined the structure function plots (see Fig. 4) for all the sources for baselines along the three arms of the VLA and also along the major and minor axis of the scatter broadened image. We find no instance of any significant change in the value of the exponent with position angles. In most cases the structure function is well sampled in the range 3–30 km and could generally be fitted with a single slope with a value between 0.8 and 1.4.

Upper limits to the inner scale obtained by examining the structure function plots at various solar distances (Fig. 6) are given in column 11 of Table 3. The upper limits range from 1.5 km at 1.7 $R_{\odot}$ to about 4km at 13 $R_{\odot}$. The upper limits to the inner scale at solar distances 8–16 $R_{\odot}$ are more than a factor of two smaller than the inner scale values estimated by Coles & Harmon (1989) using spectral broadening data taken in 1984. If this difference is real, then we could speculate that the inner scales are smaller during a solar maximum.

It is clear that structure function plots such ass presented in Figs. 6 and 12, which can be obtained from interferometric observations are very useful in determining the

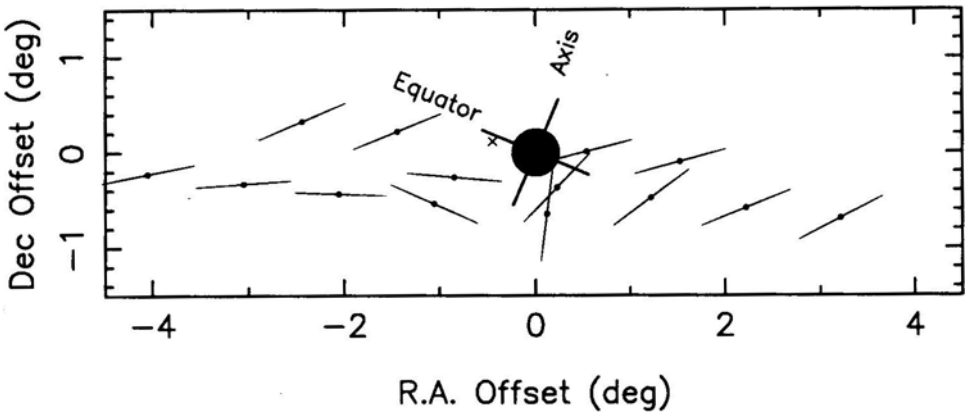

Figure 13. Orientation of the minor axis of scatter-broadened images at the observed positions. The axis of Sun's rotation and the equatorial plane are also indicated.

spectrum of density fluctuations as well as the inner scale. The multiple operating wavelengths of the VLA has been especially useful in selecting the data at the right wavelength to get a well determined structure function at a given solar distance. It would be useful to know, before hand, the right wavelength to choose for the observations if one is interested in making useful structure function measurement at a given scale (i.e. baseline) and a given solar distance. As discussed earlier, useful measurements can be made only if the scatter-broadened source is just or partially resolved by the baselines of interest. Since the angular size of the broadened source (θ_S) scales as λ^2 and the resolution on a given baseline (θ_b) scales as λ/s, the right wavelength of observation at which $\frac{\theta_s}{\theta_b} \sim 1$ is given by $\lambda_{obs} = \lambda_0^2/s\theta_0$ Here θ_0 is the observed angular size at a wavelength λ_0. Using the measured angular size given in column 5 of Table 3 and the power-law fit to θ_{maj} versus solar distance R in Fig. 10a, we get an empirical relation $\lambda_{obs} \simeq 4.5 \frac{R^{1.6}}{s}$, where R is expressed in units of $R_\odot$.

This gives the preferred observing wavelength (within a factor of 1.5), for an interferometric array with baselines ~ s, to make useful structure function measurements at a solar distance R over scale sizes of the order of s.

Acknowledgements

We thank A. Pramesh Rao, R. Narayan, B. J. Rickett and P. K. Manoharan for many illuminating discussions and the referee W. A. Coles whose critical comments and corrections have significantly improved the contents of this paper. The Very Large Array is a part of NRAO which is operated by Associated Universities Inc. under a cooperative agreement with the NSF.

References

Armstrong, J. W., Coles, W. A., Kojima, M., Rickett, B. J. 1986, in *The Sun and the Heliosphere in Three Dimensions*, Ed. R. G. Marsden (Dordrecht: Reidel) p. 59.
Armstrong, J. W., Coles, W. A., Kojima, M., Rickett, B. J. 1990, *Astrophys. J.*, **358**, 692.
Blesing, R. G.,Dennison, P. A.1972, *Proc. Astr. Soc. Aust.*, **2**, 84.
Coles, W. A., Harmon, J. K. 1989, *Astrophys. J.*, **337**, 102.
Cornwell,T. J., Fomalont, E. B. 1989, in *Synthesis Imaging inRadio Astronomy*, Ed. R.A.Perley, F. R. Schwab & A. H. Bridle, ASP (San Francisco: ASP), p. 185
Cornwell, T. J., Anantharamaiah, K. R., Narayan, R. 1989, *J. Opt. Soc. Am. A*, **6**, 977.
Cronyn, W. M. 1972, *Astrophys. J.*, **174**, 181.
Erickson, W. C. 1964, *Astrophys. J.*, **139**, 1290.
Goodman, J., Narayan, R. 1989, *Mon. Not. R. astr. Soc*, **238**, 995.
Hewish, A. 1955, *Proc. R.Soc.*, **228**, 238.
Hewish, A. 1958, *Mon. Not. R. astr. Soc.*, **118**, 534.
Hewish, A, Scott, P. F, Wills, D. 1964, *Nature*, **203**, 1214.
Hogbom, J. A. 1960, *Mon. Not. R. astr. Soc.*, **120**, 530.
Hollweg, J. V. 1970, *J. Geophys. Res.*, *Space Phys.*,**75**, 3715.
Lotova, N. A., Blums, D. F., Vladimirski, K. V. 1985, *Astr. Astrophys.*, **150**, 266.
Lotova, N. A., Medvedeva, O. P., Kazimirskii, P. B., Sololeva, N. S., Naugol'naya, M. N. 1989, *Soviet Astr.*, **33**, 333.
Machin, K. E., Smith, F. G. 1952, *Nature*, **170**, 319.

Manoharan, P. K. 1993, *Solar Phys.*, **148**, 153.
Manoharan, P. K., Kojima, M., Misawa, H. 1994, *J. Geophys. Res.*, (in press).
Narayan, R., Goodman, J. 1989, *Mon. Not. R.astr. Soc.*, **238**, 963.
Narayan, R., Hubbard, W. B. 1987, *Astrophys. J.*, **325**, 503.
Narayan, R., Anantharamaiah, K. R., Cornwell, T. J. 1989, *Mon. Not. R. astr. Soc.*, **241**, 403.
Narayan, R., Cornwell, T. J., Goodman, J., Anantharamaiah, K. R. 1990, in *Radio Astronomical Seeing*, Ed. J. E. Baldwin & W. Shouguan, (Beijing: International Academic Press).
Slee, O. B. 1959, *Aust. J. Phys.*, **12**, No. 2.
Vitkevich, V. V. 1955, *Doklady Akad. N auk SSSR.*, **101**, 42.

J. Astrophys. Astr. (1994) **15,** 415–443

A Study of the Kinematics of the Local Dark Clouds*

B. Ramesh *Raman Research Institute*, *C. V. Raman Avenue*, *Sadashivanagar*, *Bangalore 560 080.*

Received 1994 September 17; accepted 1994 November 5

Abstract. Lack of reliable estimates of distances to most of the local dark clouds has, so far, prevented a quantitative study of their kinematics. Using a statistical approach, we have been able to extract the average spatial distribution as well as the kinematical behaviour of the local dark clouds from their measured radial velocities. For this purpose, we have obtained radial velocities for 115 southern clouds and used the data from the literature for the northern ones. In this paper we present this new data, analyse the combined data and compare our results with those arrived at by earlier studies.

The local clouds are found to be expanding at a speed of ~ 4 kms $^{-1}$ which is in general agreement with the estimates from optical and HI studies. However, it is found that the kinematics of the local clouds is not described by the model proposed for the local HI gas where a ring of gas expanding from a point gets sheared by the galactic rotation. Rather, the observed distribution of their radial velocities is best understood in terms of a model in which the local clouds are participating in circular rotation appropriate to their present positions with a small expansion also superimposed. This possibly implies that cloud-cloud collisions are important. The spatial distribution of clouds derived using such a model is in good agreement with the local dust distribution obtained from measurements of reddening and extinction towards nearby stars. In particular, a region of size ~ 350 pc in diameter enclosing the Sun is found to be devoid of clouds. Intriguingly, most clouds in the longitude range 100° to 145° appear to have negative radial velocities implying that they are approaching us.

Key words: Local ISM structure—Gould's belt—dispersion in cloud velocities.

1. Introduction

OB associations affect substantially the structure, the motion and the evolution of the surrounding interstellar medium over large scales. There are several examples of *shells* and *supershells* in our galaxy as well as in the Large Magellanic Cloud. These

* Carried out under the auspices of the Joint Astronomy Program, Department of Physics, Indian Institute of Science, Bangalore in partial fulfillment of the requirements for the Degree of Doctor of Philosophy.

are regions of low density gas surrounded by denser clouds, actively forming stars and often found to be expanding. Their sizes and energies seem to be consistent with their formation around OB associations due to the combined action of the ionising radiation, stellar winds and Supernovae (Elmegreen 1991). The systematic non-circular motions thus caused will eventually get randomised through cloud-cloud collisions possibly mediated by galactic magnetic fields. These random motions play important roles in cloud-agglomeration (Kwan 1979) and stellar acceleration through gravitational scattering (Stark & Bitz 1978; Spitzer & Schwarzschild 1951). Studies of such regions around OB associations would, therefore, enable one to understand better the processes of large scale energy injection and its eventual redistribution as well as the significance of induced star-formation.

The solar system seems to be inside one such expanding cavity. The reddening measured towards nearby stars indicates that the dust in the solar neighbourhood is distributed in a shell (Lucke 1978) with the surrounding dense clouds harbouring the prominent local OB associations. The local OB stars are apparently confined to a plane inclined to the galactic disc at an angle of ~ 18° forming the *Gould's belt* on the sky. They are found to be expanding with a velocity of ~ 5 kms^{-1} (Cameron & Torra, 1990 and references therein). The local HI gas seems to have the kinematics of a thin ring which expands from a point at ~ 4 kms^{-1} and gets sheared by the galactic rotation (Lindblad *et al*. 1973; Olano 1982). A recent study by Taylor *et al.* (1987) of the nearby dark clouds concluded that while these clouds are also expanding, their kinematics is not described well tjy the above model. The study by Taylor *et al.* was limited to clouds in the northern longitude range of 0° to 220°, especially to those assigned to Gould's belt using a simple proximity criterion. Hence, it was desirable to extend these observations to the rest of the longitude range, i.e. $220° \lesssim l \lesssim 360°$, to make a more complete study of the kinematics of the local clouds. Also, Taylor *et al.* could not estimate the expansion in various directions quantitatively owing to lack of reliable estimates of distances to most nearby clouds. This paper presents our attempt to improve the situation on both counts.

We carried out a CO survey of the southern clouds to obtain their radial velocities. Though the main motivation was to supplement the northern data, there was an additional reason: Whereas Kerr *et al.* (1981) found that the Lindblad'so feature A which delineated *Gould's belt* in the northern sky was also present in the third quadrant upto $l \sim 236°$, May *et al.* (1988) found that there was no evidence for a corresponding feature traced by molecular clouds in the southern CO survey. Thus it was important to make an independent study of the southern dark clouds to confirm whether there was a molecular counterpart to *Gould's belt* and the associated HI gas in the southern galaxy as well. We also undertook a detailed kinematic study of the local population of dark clouds, northern as well as southern. Using a novel approach based on statistical techniques, we have determined the average spatial distribution as well as the kinematical behaviour of the local dark clouds from their measured radial velocities. In this paper, we present the new data, our analysis of the new as well as existing data and compare our, results with those arrived at by earlier studies.

In the next section, details of our observations and the measured velocities are presented. The analysis of the radial velocities of the local dark clouds is presented in section 3 at the end of which the main results are summarised. In section 4 these are discussed in relation to the conclusions of earlier workers.

2. Observations

A survey of the southern dark clouds in $J = 1 \rightarrow 0$ transition of ^{12}CO to obtain their radial velocities was carried out in February–April 1992 using the 10·4 m millimeterwave telescope operated by Raman Research Institute, Bangalore (for a brief description of the telescope, see Patel 1990). A filter–bank spectrometer with 250 kHz (0.65 kms $^{-1}$) resolution covering a total bandwidth of 64 MHz was used. Pointing was checked by beam-switched continuum scans on Jupiter (see Patel 1990 for details). An ambient temperature load was used for calibration. During the observations, the DSB T_{sys} ranged from 600 K to 1100 K. Frequency switching by 15.25 MHz was used for all the observations and the spectra obtained were appropriately combined to recover the loss in S/N due to the switching. Third order polynomials were fitted to the spectra to estimate and remove the curved baselines.

The clouds observed were selected from the catalogue of southern dark clouds compiled by Feitzinger & Stuwe (1984). Their opacity class (mostly > 2) and declination were the criteria used for the selection. Of the 149 clouds observed only 115 were detected in CO. The reason for the non-detection of a large fraction (23%) of the clouds is not entirely clear but may partly be due to our relatively higher detection limit ($3\ \sigma \sim 1$ K). Table 1 (a) and 1 (b) list the coordinates of the clouds detected and their radial velocities obtained by fitting gaussians to the spectral components. The estimated rms error on the velocities is ~ 0.3 kms^{-1}. Table 2 gives a longitudinal sector-wise break-up of the number of dark clouds, with opacity class > 2, listed in the catalogue of Feitzinger and Stuwe, and of those observed and detected by us. Only 30% of the clouds in the longitude range 280° to 320° were accessible from our site.

3. Kinematical analysis and simulations

The kinematical analysis of the local dark clouds presented in this section consists of three parts: (i) The clouds around the four directions 0, 90, 180 and 270 degrees, which we will henceforth refer to as *null* directions, are analysed to estimate the magnitudes of the systematic and random components of their noncircular motions. In general, to estimate these components the contributions due to the circular rotation of the galaxy must be removed first. However, for nearby ($\lesssim 1$ kpc) clouds these contributions are expected to be zero in these four special directions and small for the neighbouring longitudes. So, lack of knowledge of the distances to the clouds around these four directions is not a handicap, (ii) To find if the motions found in (i) are more general, a subset of clouds with reliable estimates of distances and distributed over all longitudes is analysed, (iii) The noncircular motions are quantified independently from an analysis of the radial velocities towards the general population of clouds distributed in all longitudes using statistical techniques and a model for their spatial distribution. Consequently, a *probable* spatial distribution for the clouds is also obtained.

Before describing the three parts of the analysis we wish to make the following remarks:

- The distribution of the clouds in the plane of the sky is shown in Fig. 1a.The *double sinusoidal* behaviour seen in their longitude-velocity plot (Fig. 1b) clearly

Table 1a. Lists the coordinates of the southern dark clouds detected in CO taken from the catalogue of Feitzinger & Stuwe (1984) and their radial velocities obtained by fitting gaussians to the spectra. The serial number in their catalogue is given as the cloud number. The clouds are ordered in galactic longitude and latitude.

Cloud	*l*II	*b*II	V_{lsr}	Cloud	*l*II	*b*II	V_{lsr}
002	237.40	−2.89	25.4	098	270.10	−0.28	1.2
004	237.40	−4.86	20.7	101	270.50	−1.75	4.7
009	239.40	−4.70	23.4	105	270.90	2.48	−3.5
012	247.00	−0.61	20.9	109	271.40	4.89	−3.2
013	247.30	−2.79	−23.4	111	272.50	−3.93	5.4
018	250.30	0.25	12.5	111A	275.30	−1.11	−4.8
024	253.10	−4.28	11.4	114	274.60	0.13	−2.2
025	253.10	−1.37	10.4	116	275.50	2.14	−6.2
026	253.30	3.30	6.7	118	276.30	−0.68	−3.9
030	255.40	−4.88	9.3	142	285.20	9.44	5.7
031	255.50	−4.20	9.8	152	287.80	7.66	4.7
032	255.80	−2.71	9.4	152A	287.80	7.67	10.9
036	258.10	−3.15	−20.4	163	291.00	7.82	8.2
040	259.00	0.96	6.0	163A	291.10	7.85	6.3
041	259.20	3.35	6.9	206	301.70	7.63	13.5
042	259.30	−13.26	4.8	228	304.00	7.37	14.5
044	259.50	−16.54	−21.4	243	307.10	6.54	−13.7
046	259.80	−2.59	9.1	249	308.40	5.81	−2.3
049	260.60	−3.63	6.2	259	311.10	5.79	18.2
050	260.60	−3.70	5.5	262	311.60	−1.18	−1.8
055	262.20	−12.46	5.2	277	315.90	5.90	6.0
056	262.40	3.12	9.0	278	316.10	4.94	−3.1
058	263.10	1.35	6.3	293	319.70	1.53	−17.3
071	265.90	−7.53	3.3	302	323.10	−0.96	−6.0
072	266.00	−7.63	3.3	305	323.80	5.59	−20.2
075	266.70	4.93	2.6	311	326.30	−0.58	−17.3
080	267.30	0.04	4.8	316	331.80	1.82	27.3
081	267.50	4.30	1.0	320	334.30	−1.01	−11.3
082	267.60	−7.35	5.4	321	334.60	18.09	5.8
085	268.10	1.82	−0.5	327	335.30	3.15	3.4
087	268.50	−1.74	1.7	328	335.40	−1.14	−11.8
091	269.40	−7.57	4.8	332	336.10	−2.31	−12.1
093	269.80	4.02	−3.0	333	336.30	3.94	31.5
094	269.80	−11.10	0.1	334	336.40	11.31	6.5
096	270.00	2.88	−2.7	336	336.50	19.14	6.0

Table 1a. (continued)

Cloud	*l*II	*b*II	V_{lsr}	Cloud	*l*II	*b*II	V_{lsr}
337	336.80	−0.96	−21.8	418	354.90	14.97	3.4
339	337.00	4.84	4.1	419	354.90	16.00	2.5
341	337.40	16.68	5.0	429	357.20	4.40	6.4
348	338.90	9.50	6.1	431	357.30	0.90	1.7
349	339.00	16.16	4.9	439	358.60	15.37	2.5
365	342.10	−3.72	−15.7	441	358.90	−3.90	5.2
383	346.70	−9.72	4.9	446	359.80	−18.31	5.3
392	347.90	3.16	−2.9	450	0.22	−18.73	4.7
395	348.80	3.57	2.2	453	1.07	−20.52	4.9
398	350.60	2.60	6.1	456	1.44	9.38	3.5
403	352.00	16.31	3.9	464	3.67	6.35	4.3
406	352.60	1.02	5.5	473	6.11	−1.22	13.4
408	352.80	17.85	2.8	476	6.69	−0.55	−102.5
411	353.60	15.78	4.0	477	6.84	−2.15	10.8
414	354.30	16.35	2.2	479	7.09	−2.32	9.4
415	354.50	−1.70	3.4				

Table 1b, Similar to Table 1a, for lines-of-sight with double components. The velocity of the stronger one is given first followed by that of the weaker one.

Cloud	*l*II	*b*II	$V_{lsr}(1)$	$V_{lsr}(2)$
006	238.40	−4.12	20.5	18.9
007	238.90	−1.57	19.1	27.1
022	251.90	−3.16	13.1	18.3
038	258.60	−2.69	9.5	17.8
052	261.60	0.33	10.9	5.3
053	261.70	−4.36	10.0	13.5
064	265.10	1.43	5.2	8.1
067	265.40	0.41	5.9	0.0
078	267.00	−0.94	4.4	7.7
090	269.40	−1.34	4.0	8.2
099	270.20	−0.98	0.6	6.1
102	270.50	0.53	6.6	−0.2
122	277.10	−2.56	−6.7	−2.0
134	281.60	−0.81	−3.4	3.8
145	286.20	0.10	−20.0	−8.6
149	287.20	−0.21	−18.5	−7.6
342	338.00	16.58	5.2	6.8
372	344.00	−0.41	37.0	33.7

388	347.00	0.51	6.1	−9.8
400	350.80	1.00	5.7	−5.4
406	352.60	1.00	5.5	−1.1
407	352.70	0.90	2.6	5.7
409	352.90	16.93	3.2	2.4
421	355.10	1.60	7.1	−1.9
435	357.90	−2.00	−0.5	4.3
445	359.60	−17.75	6.1	3.6
449	0.21	−4.52	8.7	5.7

Table 2. Observation and detection statistics.

Longitude range	Number of clouds	Observed	Detected	Observed %	Detected %
240°-280°	80	69	53	86.3	76.8
280°-320°	57	17	11	29.8	64.7
320°-360°	99	63	51	63.6	81.0

shows that the contribution of galactic differential rotation is important. We estimate these contributions using the equation

$$V_{\rm rot}\,(l) = Ad \sin\,(2l) \qquad (1)$$

with a value of 14.5 kms $^{-1}$ kpc $^{-1}$ for Oort's constant A. Here d is the distance and l is the longitude of the cloud. We have omitted a factor $\cos^2 b$ in this equation because most of the clouds have latitudes $|b| < 20°$ (Fig. 1a) making the correction unimportant.

- We shall consider each *condensation* of 1.5° extent in longitude and latitude, and 2 kms^{-1} width in velocity, as a *distinct kinematical entity*. The angular size was chosen to be 1.5° because at a distance of 400 pc, the mean distance of these dark clouds as suggested by Feitzinger & Stuwe (1986), the corresponding linear size would be 10 pc which is the upper end of the sizes of these dark clouds under study. Hence we convolved the measured points with a 3-dimensional Gaussian of full width at half maximum in each of the three dimensions equal to the values mentioned above and picked all the local peaks. All points thus obtained are treated as *independent clouds* and used in the following analysis.
- A few clouds with absolute velocities more than 25 kms^{-1} have been excluded from our analysis. As we shall see, the magnitudes of the systematic and peculiar components of non-circular velocities of the local clouds turn out to be ~ 4 kms^{-1}, and hence these few clouds, are likely to be far away and can safely be excluded.

3.1 *Clouds in the null directions*

To get a statistically significant number of clouds around each of the four *null* directions for the present analysis we include all the clouds within a longitude

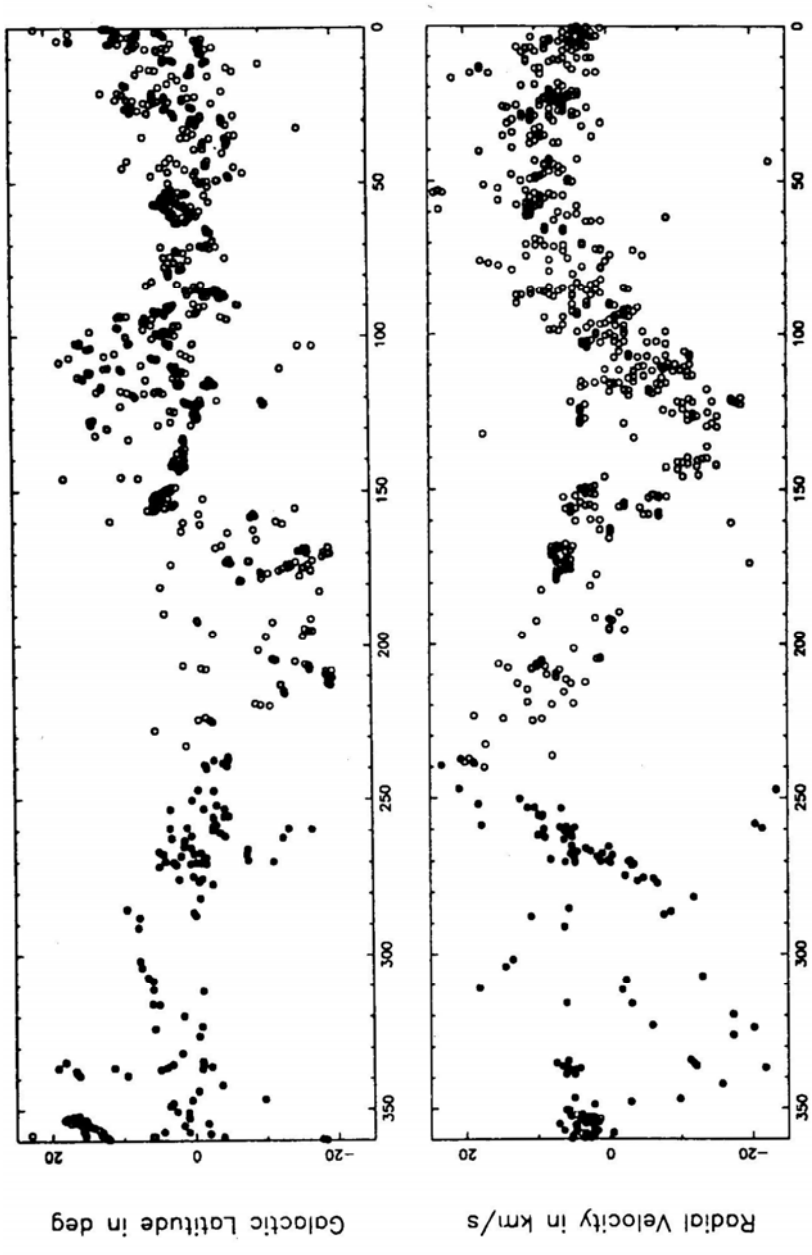

Figure 1. The upper panel (a) shows the latitude vs longitude plot for the entire population of clouds. The lower panel (b) shows the distribution of their radial velocities at different longitudes. In both the plots, the filled circles represent the southern clouds observed by us, while the open ones refer to the northern clouds detected by Taylor *et al.* (1987).

strip of 18° centered around them. We correct for the small contributions to their radial velocities from differential rotation by adopting a mean distance to the clouds in each group. The adopted distances are based on the proximity in the sky and in velocity of these clouds to the reflection nebulae with reasonably good estimates of distances. These distances are also found to be in reasonable agreement with the estimates from the slopes of the distributions of each group of clouds in longitude-velocity plots. The adopted distances for the four groups around the directions 0, 90, 180 and 270 are 180, 500, 140 and 450 pc respectively. We have adopted a distance of 350 pc for a small sub-group of clouds in the 180° direction distinct from the Taurus group of clouds. Similarly, for a sub-group of clouds in the 270° direction that does not trace the Vela IRAS shell found by Sahu (1992) and lies close to the plane coincident with the Vela Molecular Ridge we have adopted a distance of 1.2 kpc. We have also excluded a small sub-group of clouds around the 0° direction lying in the longitude range of 3° to 6° latitude range of – 1° to – 2.5° with a mean velocity of 10.5 kms $^{-1}$ from the analysis. This is because they are likely to be at 900 pc as indicated by their proximity in the sky and in velocity to a reflection nebula at that distance.

After correction for differential rotation on the above basis, the left over errors will be only due to the dispersion in distances. Even if the dispersion in distance about the mean value is as much as the mean distance itself, i.e. ~ 400 pc, the maximum error in the correction at either edge of the strip is ~ 1 kms^{-1} and the average error will be much less. Since this is comparable to the measurement errors in velocity and negligible compared to the dispersion in velocities, including all clouds within a longitude strip of 18° around the *null* directions for the present analysis is justified.

The distribution of residual velocities after these corrections, shown in Fig. 2, were fitted with Gaussians. The mean and the standard deviation give the magnitude of the systematic and the random components of the noncircular motions and are listed in Table 3. In the case of longitudes 180° and 270°, two sets of parameters corresponding to the two distinct groups in each direction are given separately. From these results, we conclude that receding motions of 3 to 6 kms $^{-1}$ are present in all of them. However, in three of the four directions the samples are dominated by specific groups of clouds and hence their receding motions are not necessarily conclusive evidence for general expansion of the local dark clouds. This we proceed to check in the next subsection. The magnitude of the velocity dispersion of clouds is ~ 2 to 5 kms^{-1}, much lower than 7 to 10 kms $^{-1}$ derived by Stark (1984) and we discuss this issue in section 4.

Table 3. Results of *null* direction analysis.

Longitude bins	V_{exp}(kms^{-1})	σ(kms^{-1})	Comments
0	4.6	2.0	Ophiuchus group of clouds.
90	2.7	5.0	
180	6.3	1.3	Taurus group of clouds.
	0.3	3.6	
270	6.5	3.0	Vela IRAS shell.
	0.0	1.5	

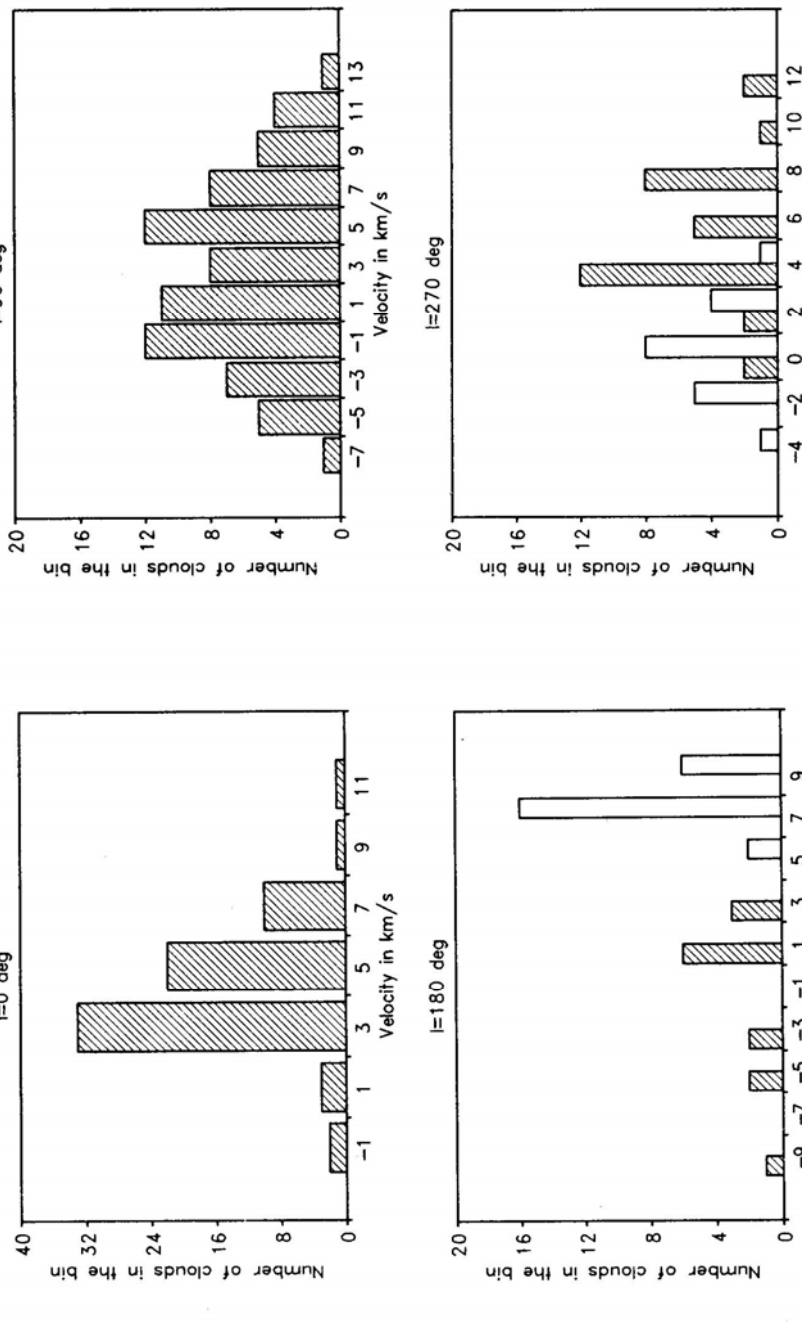

Figure 2. The filled bars in the four panels show the distribution of the residual velocities of the clouds in the four *null* directions. Their LSR velocities have been corrected for adopted distances of 180, 500, 140 and 450 pc respectively. Oort's A constant was taken to be 14·5 $kms^{-1}kpc^{-1}$. The empty bars in the 180° and 270° directions represent clouds associated with the Taurus group at ~150 pc and the Vela Molecular Ridge at ~1200 pc respectively.

Table 4. Reflection nebulae nearer than 500pc.

Cloud	l deg	b deg	Dist kpc	V_{LSR} kms^{-1}	V_{res} kms^{-1}
vdB124	21.0	−0.5	0.17	6.9	5.3
vdB123	31.6	5.2	0.44	7.2	1.5
vdB129	41.6	−18.1	0.04	0.1	−0.5
vdB126	57.0	3.0	0.48	11.7	5.3
vdB135	73.5	−5.1	0.35	12.4	9.6
vdB136	81.4	0.5	0.40	8.5	6.8
vdB147	94.3	−5.3	0.44	6.7	7.7
vdB152	110.3	11.4	0.40	−5.3	−1.5
vdB158	110.6	−12.6	0.48	−8.1	−3.5
vdB150	111.9	14.1	0.50	−4.0	1.0
vdB003	121.4	6.6	0.18	−6.8	−4.5
vdB007	132.9	9.1	0.08	−13.3	−12.1
vdB008	133.9	7.6	0.21	−11.6	−8.6
vdB012	157.4	−20.6	0.17	1.1	2.8
vdB013	158.0	−21.3	0.29	7.0	9.9
vdB017	158.3	−20.4	0.50	7.2	12.2
vdB016	159.2	−21.9	0.14	5.3	6.6
vdB019	160.5	−17.8	0.30	8.6	11.3
vdB032	162.5	1.5	0.30	−2.4	0.1
vdB025	171.4	−19.8	0.11	11.1	11.6
vdB029	172.1	−9.7	0.15	6.4	7.0
vdB034	172.1	−2.3	0.32	6.8	8.1
vdB031	172.5	−0.8	0.12	6.2	6.7
vdB041	182.5	−5.9	0.16	7.7	7.5
vdB056	190.5	−6.9	0.26	8.9	7.5
vdB038	194.6	−15.6	0.32	0.5	−1.8
vdB040	196.8	−15.7	0.24	−5.4	−7.3
vdB043	198.1	−14.6	0.38	−10.3	−13.6
vdB044	207.8	−19.7	0.55	11.1	4.5
vdB055	212.4	−19.0	0.38	2.7	−2.3
vdB087a	221.8	−2.0	0.50	39.8	32.6
vdB086	222.7	−3.4	0.42	11.9	5.8
vdB090a	224.4	−2.7	0.52	14.1	6.6
vdB098	240.4	−2.2	0.38	23.0	18.3
vBH10a	259.3	−3.8	0.48	8.9	6.4
vBH28	265.1	1.4	0.50	5.2	4.0
vBH12	266.2	−7.8	0.48	3.3	2.4
vBH23	267.0	−0.9	0.46	4.5	3.8
vBH63	314.9	−5.1	0.42	4.8	10.9
vdB105	352.9	17.0	0.17	3.6	4.2
vdB108	353.1	15.9	0.14	4.5	5.0
vdB106	353.7	17.7	0.14	2.3	2.7
vdB100a	354.6	22.7	0.15	5.1	5.5
vdB102x	355.5	20.9	0.13	3.3	3.6

Table 4. (Continued) Reflection nebulae farther than 500pc

Cloud	l deg	b deg	Dist kpc	V_{LSR} kms^{-1}	V_{res} kms^{-1}
vdB115	7.4	−1.8	0.91	8.9	5.5
vdB128	69.5	0.4	0.83	−2.2	−10.1
vdB131x	80.5	2.7	1.05	5.0	0.0
vdB142	99.1	3.9	0.72	−8.2	−4.9
vdB155	109.6	2.4	0.58	−9.5	−4.2
vdB001c	117.3	−3.7	0.52	−11.4	−5.3
vdB002	119.0	3.0	0.63	−19.5	−11.8
vdB014	141.5	2.9	0.76	7.6	18.3
vdB039	174.3	−1.7	0.72	7.4	9.5
vdB047	184.0	−4.2	0.87	3.0	1.2
dB075	188.7	3.8	0.55	3.0	0.6
vdB077x	201.9	0.0	1.00	0.0	−10.0
vdB051	206.0	−16.3	0.66	9.8	2.3
vdB057	207.1	−16.2	0.58	9.8	3.0
vdB068x	213.7	−12.4	0.76	9.5	−0.7
vdB080a	219.3	−9.0	0.76	12.6	1.8
vdB093	223.7	−1.9	0.72	17.9	7.5
vdB095	224.7	−1.8	0.79	15.6	4.1
vdB094	225.5	−2.6	0.83	12.4	0.4
vBH05	253.1	−1.4	1.32	10.4	−0.2
vBH03	255.5	−4.2	1.15	9.9	1.8
vBH04	255.6	−3.0	0.87	8.9	2.3
vBH17	260.0	−0.1	0.95	7.8	3.1
vBH27	264.3	1.9	0.91	7.0	4.4
vBH25b	264.4	1.4	0.60	6.3	4.6
vBH29	268.0	1.8	0.79	−0.5	−1.3
vBH30	270.8	0.8	0.95	6.9	7.3
vBH72	336.4	−1.4	1.38	−12.4	2.3
vBH92	358.5	−2.1	1.32	−0.5	0.5

3.2 *Clouds with known distances*

Here, we analyse two sets of clouds: first, those with associated reflection nebulae and second those identified as *individual* by Dame *et al.* (1987) from the composite CO survey.

Reliable estimates of distances to many clouds with associated reflection nebulae already exist. Racine (1968) has obtained the distances to the northern reflection nebulae while van den Bergh & Herbst (1975(have obtained distances for the southern ones. The velocities for the northern clouds have been reported by Kutner *et al.* (1980) and for the southern ones by de Vries *et al.* (1984). For a few clouds for which the data did not exist, we have obtained the radial velocities using the $J = 1 \rightarrow 0$ transition of carbon monoxide. Quantities relevant to our discussion have been taken from the literature and summarized in Table 4. The table lists the clouds with

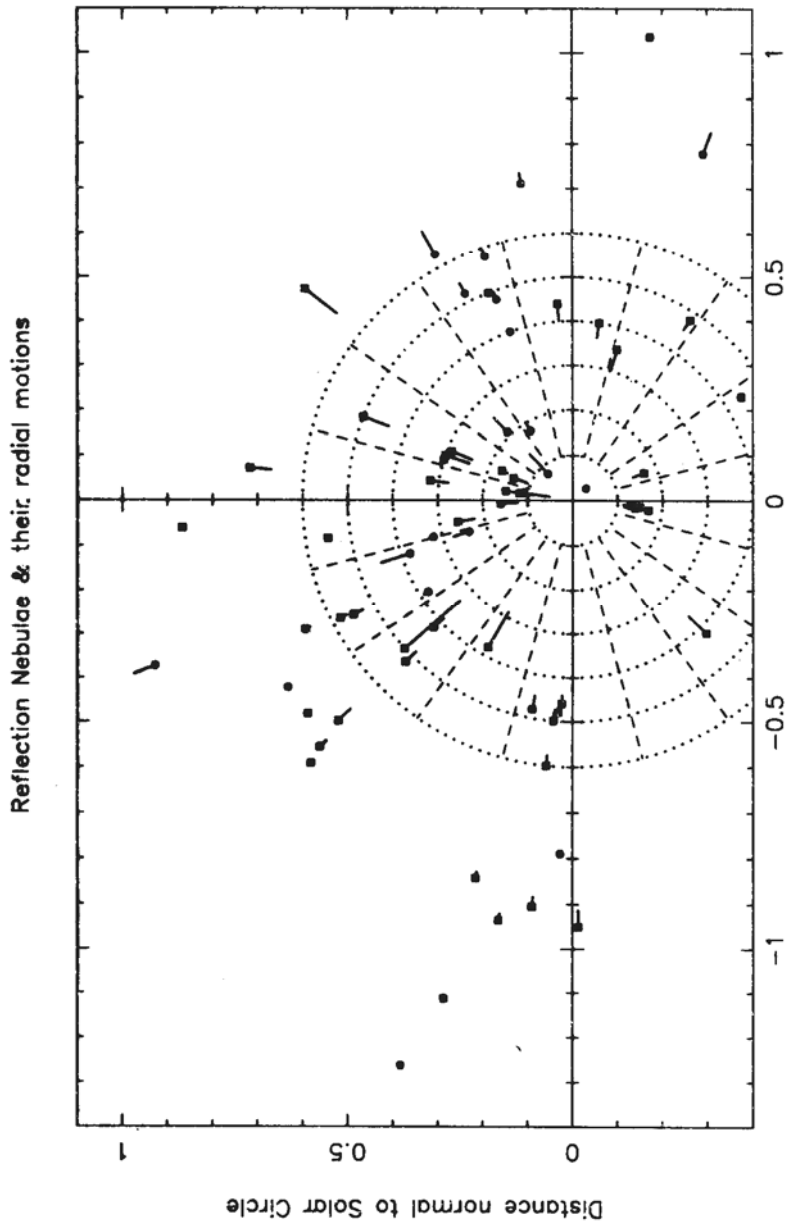

Figure 3. The spatial distribution of clouds with reflection nebulae projected onto the galactic plane. The heads of the *tadpoles* indicate the position of the clouds, while the lengths of the *tails* indicate the magnitude of their residual velocities. Clouds with outward radial velocities are indicated by filled squares, and those coming in by filled circles. The sun is located at the centre of the system of concentric circles. Notice that the clouds in the longitude ranges 100°–145° and 195°–215° are predominantly moving inward.

associated reflection nebulae, both northern (names with 'vdB' as prefix) and southern (names with 'vBH' as prefix), their longitudes, latitudes, distances and LSR and residual velocities.

There are 44 clouds within 500 pc and 29 beyond that have associated reflection nebulae. Fig. 3 shows the spatial distribution of their residual velocities projected onto the plane of the Galaxy with the Sun at the origin and the galactic centre towards the negative Y-axis. The clouds within 500 pc show a clear trend of expansion with a mean velocity of ~ 4.3 kms^{-1} and a dispersion of ~ 7 kms^{-1} while those outside 500 pc show only marginal evidence for expansion. Notice that the clouds in the longitude range 100° to 145° and possibly in the range 195° to 215° form a *distinct kinematical group* with predominantly 'in coming' velocities. They have the effect of reducing the mean expansion velocity and increasing the apparent dispersion. After removing the clouds in these two sectors, there are 33 clouds within 500 pc and 20 beyond. The distribution of their residual velocities is shown in Fig. 4. The filled rectangles represent clouds within 500 pc and the empty ones refer to the clouds beyond. Now, the expansion velocity for the clouds within 500 pc is 7·2 kms^{-1} with a standard deviation for the random velocities of 5.8 kms^{-1}. Clouds outside 500 pc show 2.3 kms^{-1} expansion with 4 kms – 1 random velocity dispersion. One may thus firmly conclude that the clouds within 500 pc show clear evidence of expansion of ~ 7 kms^{-1} in all longitudes except the longitude ranges 100° to 145° and 195° to 215° where most of the clouds have negative velocities. Those outside 500 pc also show expansion, although marginal.

Now we turn to the analysis of the second set of clouds. Dame *et al.* (1987) have identified clouds and cloud complexes within 1 kpc from the composite CO survey. In general, these complexes have large angular extent. In Table 2 of their paper, Dame *et al.* have listed these clouds, their longitude and latitude ranges, their measured radial velocities and their distances compiled from the literature. These distances are

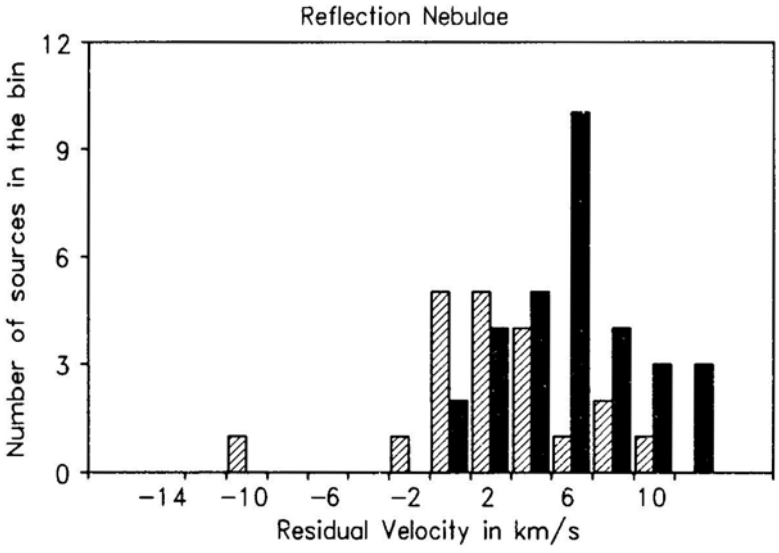

Figure 4. A histogram of the residual velocities of the clouds with associated reflection nebulae excluding those in the longitude ranges 100°–145° and 195°–215°. Filled bars correspond to clouds within 500 pc while those beyond 500 pc are denoted by hatched bars.

Table 5. Composite CO survey clouds.

Cloud	l deg.	b deg.	V_{LSR} kms^{-1}	Dist. kpc	V_{res} kms^{-1}
ρ Ophiuchus	0.5	7.8	3.0	165	3.0
R CrA	0.5	−18.0	6.0	150	6.0
Aquila rift	26.3	2.0	8.0	200	5.7
Aquila rift	39.0	0.0	8.0	200	5.2
Cloud B	49.0	0.5	7.0	300	2.7
Vulpecula rift	58.5	1.0	10.0	400	4.8
Cepheus	110.0	16.5	−5.0	450	−1.1
Lindblad ring	132.0	3.0	1.0	300	5.3
Perseus 2b	158.3	−16.0	5.0	350	8.2
Perseus 2a	167.0	−7.5	−3.0	350	−0.8
Taurus	170.5	−15.8	5.0	140	5.6
Orion B	205.3	−13.5	8.0	450	3.2
Orion A	213.3	−17.8	8.0	450	2.6
Vela sheet	275.5	2.5	3.0	400	4.1
Chamaleon	300.0	−16.0	4.0	215	6.5
Coal sack	303.5	−0.5	−4.0	175	−1.7
G317−4	317.5	−4.0	−6.0	170	−3.6
Lupus	339.5	13.0	5.0	170	6.5
ρ Ophiuchus	356.0	18.5	3.0	165	3.3

based on associated Population I objects or on star counts or on the relation of visual absorption to distance for stars within the cloud boundary. Here we analyze the radial velocities of clouds within 500 pc. The quantities relevant to our discussion are summarized in Table 5. We have used 8 kms^{-1} and 3 kms^{-1} as the velocities of the Orion and Vela clouds respectively. The longitudes and latitudes listed in Table 5 are the averages of the boundary values given by Dame *et al.*, A histogram of the residual velocities is shown in Fig. 5. The mean velocity of expansion is ~ 3·5 kms^{-1}, with a dispersion in the cloud velocities of ~ 3 kms^{-1}. We realise that these *clouds* have large spatial extent and any analysis which assigns a single position, distance and LSR velocity (as done here) is bound to be inaccurate. It is significant that in spite of the possible scatter introduced by this assumption this analysis also leads us to the same conclusions as before, viz. that the local clouds are in a state of expansion.

3.3 *The general population of clouds*

Having found that 'null' direction clouds as well as clouds with known distances and distributed over the entire longitude range show evidence of expansion of ~ 3 to 5 kms^{-1} and a velocity dispersion of 2 to 5 kms^{-1}, we set out to examine whether this apparent expansion about a common centre is true for the entire population of the local clouds. In the process, we have also derived their average spatial distribution. For this analysis, we divided the local cloud population into 10 groups in the following way: In each of the four quadrants in longitude we exclude clouds

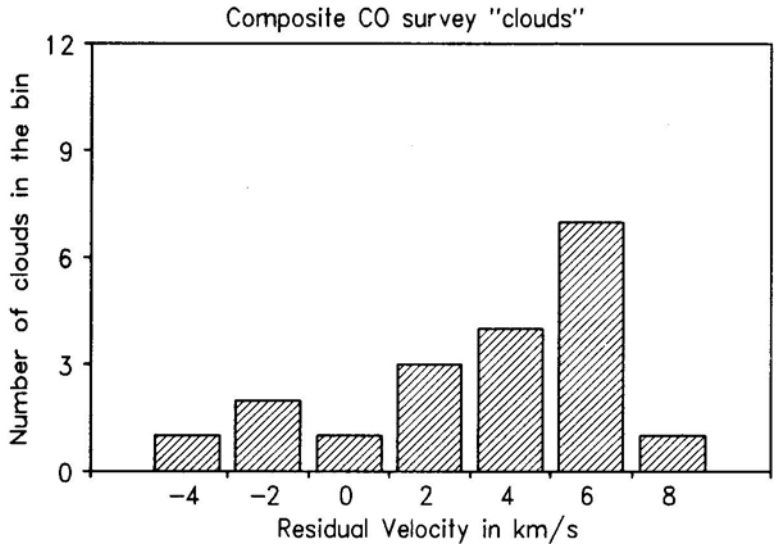

Figure 5. A histogram of the residual velocities of the *CO survey clouds.*

within 15° from the null directions since there is not much distance information that can be derived in these directions. Thus, within each quadrant only clouds within the central 60° are considered. In the first 3 quadrants these 60° segments are further divided into three sectors of 20° each. However, since the total number of clouds in the fourth quadrant is only 25, we analyse them as one single group. Thus the sample included in the present analysis is divided into 10 groups.

Clouds in each group were then subjected to an analysis procedure that involves the following two steps: (1) To generate the positions and radial velocities of pseudo-clouds, same in number as the actual ones, using Monte-Carlo simulations, assuming a model for their spatial distribution (described below). (2) To determine the probability that the simulated cloud velocities and the actually measured cloud velocities are drawn from the same parent distribution using a statistical test. These two steps are repeated for various sets of assumed values for the model parameters. The set of values with highest probability is taken to describe the parent distribution to which the actual set of clouds in that sector belong. This is then repeated for all the sectors. In the following, we describe the model, the statistical test and the results of simulations.

Our basic model is that the spatial distribution of the local clouds can be described by a simple doughnut configuration with well defined inner and outer radii. In the present analysis, we are only concerned with its projection onto the galactic plane. The clouds are assumed to be distributed within this 'annulus' in such a manner that the areal density of clouds is a constant. Our model also assumes that the radial velocity of each cloud in the simulated population can be written as the sum of three components: (1) $V_{\rm rot}$ due to galactic differential rotation, appropriate to its randomly chosen location within the sector (i.e. its distance from us and its specific longitude), (2) $V_{\rm sys}$ due to its systematic motion, and (3) $V_{\rm pec}$ due to peculiar motions, assumed to have a gaussian distribution with a velocity dispersion, σ, i.e. $V_{\rm rad} = V_{\rm rot} + V_{\rm sys} + V_{\rm pec}$ .The facts that the expanding ring model does not fit the molecular data in the northern sector and that the radial velocities of the local clouds show clear signature

of differential rotation suggest this assumption. Although the model is oversimplified, it is not unphysical because the values of the parameters in each sector are estimated independently. To summarize, the various parameters that enter our model are: (i) the inner and outer radii of the annulus: R_1 and R_h (ii) the systematic velocity: V_{sys} (iii) the dispersion in velocity: σ.

For a particular sector, assuming a set of values for these model parameters, the positions and radial velocities of pseudo-clouds, same in number as the actual ones in that sector, are generated using Monte-Carlo simulations. The clouds are distributed at random within the longitude sector keeping the areal density constant. The radial velocity of every pseudo-cloud within this sector is assigned a rotational component arising out of galactic differential rotation, appropriate to its randomly chosen location within the sector (i.e. its distance from us and its specific longitude) and a gaussian distributed random component characterised by the chosen σ. In addition, there will be a contribution to the radial velocity due to its non-circular systematic motion, V_{sys}, also a model parameter. Thus, the radial velocity of any cloud in the simulated population is given by,

$$V_{rad}\,(l) = Ad \sin 2l + V_{sys} + V_{pec} \tag{2}$$

In order to compare the observed population with the synthesised population we construct the cumulative distributions of the *kinematical distances* derived from their radial velocities. *Kinematical distance* is the hypothetical distance at which if the object is placed its radial velocity would be entirely due to galactic differential rotation. It is computed using the expression $V(l) = AD_{kin} \sin (2l)$. Next we construct a cumulative distribution of these kinematical distances i.e. N ($<D_{kin}$) vs D_{kin} for the observed and the synthesised populations. Since the number of clouds in the simulated population is rather small (typically $\sim$ 25 in a given sector) we generate 50 realisations of the synthetic populations for a given set of values for the parameters, using a different seed number each time, and derive an 'ensemble-averaged cumulative distribution'. We then compare this ensemble-averaged cumulative distribution of the synthetic population with the cumulative distribution of the observed population using the Kolomogorov-Smirnov test and obtain the probability that the synthetic and observed populations are drawn from the same parent distribution. As mentioned above, in obtaining the cumulative distribution for the simulated population one has assumed a particular set of values for the expansion velocity, velocity dispersion, and the distances to the inner and outer radii of the annulus in that sector. The procedure is now repeated by assuming different sets of values for these parameters.

Since there are in principle four parameters, we used a partly sequential search. To begin with, the dispersion in peculiar or random velocities (σ) was fixed at a value determined from the earlier analysis of the clouds along the four *null* directions. It may be recalled that the dispersion in the peculiar velocities varied from 2 to 5 kms^{-1} depending on the direction. The velocity dispersion for any particular sector was obtained by interpolation. The expansion velocity, inner and outer radii of the annulus as measured from the sun were varied and the cumulative distributions were compared with that of the observed sample. The best-fit distribution was identified as the one with the highest Kolomogorov-Smirnov probability. Thus, for every given longitude sector the most probable values for V_{exp}, R_1 and R_h were obtained. To illustrate how sensitive the cumulative distributions are to the choice of the parameters, we have summarised the parameters and their KS probabilities for the best and

Table 6a. Parameters for the good fits.

Longitude bins	1	2	3	4	5	6	7	8	9	10
V_{exp} (kms^{-1}) (fixed)	4.5	4.0	4.0	−3.5	−4.0	4.0	2.5	4.5	1.0	10.0
% Probability	100	100	98	100	91	92	100	100	100	100
σ (kms^{-1})	2.5	3.0	4.0	6.0	5.5	5.0	4.5	4.5	4.5	8.0
R_L (pc)	150	250	200	100	250	250	250	300	1300	110
R_H (pc)	400	500	350	450	550	550	550	650	1600	360

Table 6b. Parameters for the poorer fits.

Longitude bins	1	2	3	4	5	6	7	8	9	10
V_{exp} (kms^{-1}) (fixed)	4.5	4.0	4.0	−3.5	−4.0	4.0	2.5	4.5	1.0	10.0
% Probability	64	70	72	76	70	77	72	85	70	70
σ (kms^{-1})	4.0	4.5	6.0	8.0	7.5	7.0	6.5	6.5	6.5	8.0
R_L (pc)	200	250	100	150	200	350	300	150	1300	110
R_H (pc)	400	450	300	450	500	600	550	450	1500	260

somewhat poorer fits for each of the ten sectors in Tables 6a and 6b. For the first two sectors, we have also shown the plots of the corresponding cumulative distributions for the best and poorer fits in Fig. 6. Then, fixing the expansion velocities at the values derived above, the dispersions (σ) in the peculiar velocities, as well as R_l and R_h were varied in the next stage of simulations. This was done mainly to verify the robustness of the conclusions of the previous set of simulations. It turned out that the best fit values for the velocity dispersions agree reasonably well with the values derived earlier from the analysis of the clouds in the *null* directions and the reflection nebulae.

The variation of the K-S probabilities with respect to these parameters is not strongly peaked and therefore the derived parameters could not be estimated more accurately. In summarising the *most probable* values for the parameters in Table 7, we have ascribed errors to take this into account. Having pointed out that the distribution of probabilities has a rather broad maximum, it should also be emphasized, however, that the derived values of the parameters pass various consistency checks. For example, the most probable value for $V_{\rm exp}$ in the various directions derived here agree well with the values obtained from the analysis described in the previous subsections. Also, the derived spatial distribution of the local dark clouds. projected onto the galactic plane, shown in Fig. 7, agrees well with results obtained from various other studies. This is discussed in the next section. Below, we list the main results of the detailed analysis presented in this section.

- The population of the local dark clouds appears to be in a state of expansion about a common centre. Their radial velocity of expansion with respect to us is about 4 kms^{-1}.
- In addition to their systematic motions (i.e. galactic rotation with a superimposed

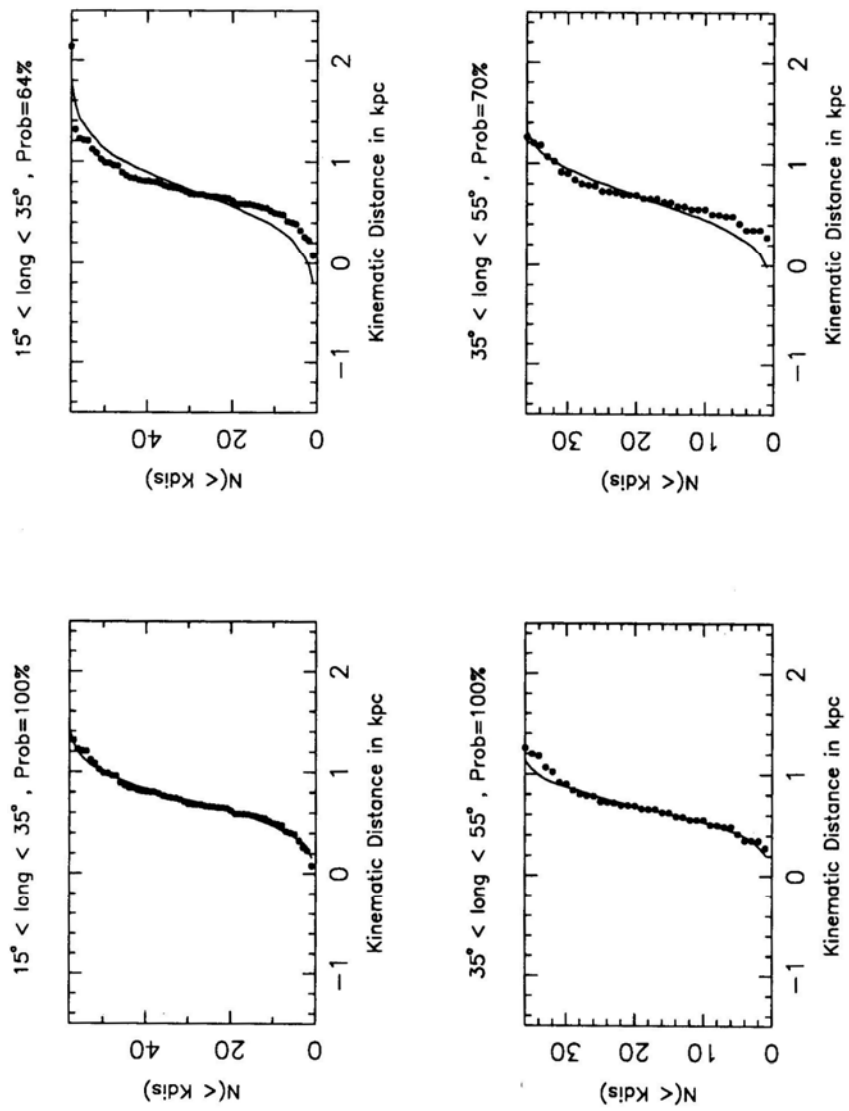

Figure 6. The top and the bottom plots show the cumulative distributions of the *kinematic distances* of the observed clouds and those of simulated populations for the longitude sectors 15°–35° and 35°–55°, respectively. The filled circles represent the observed clouds, and the continuous line is the ensemble-averaged cumulative distribution of the simulated populations. For each of the two longitude directions model fits with two different Kolomogorov-Smirnov probabilities have been shown.

Table 7. Final fit parameters.

Longitude bins	1	2	3	4	5	6	7	8	9	10
$V_{exp}(\mathrm{kms}^{-1})$	4.5	4.0	4.0	−3.5	−4.0	4.0	2.5	4.5	1.0	10.0
$\sigma(\mathrm{kms}^{-1})$	2.5	3.0	4.0	6.0	5.5	5.0	4.5	4.5	4.5	8.0
$R_L(pc)$	150	200	130	150	250	250	250	300	1300	150
$\delta R_L(pc)$	50	50	30	50	50	50	50	100	100	50
$R_H(pc)$	400	500	400	450	550	600	550	650	1600	400
$\delta R_H(pc)$	50	50	50	50	50	50	50	50	100	50

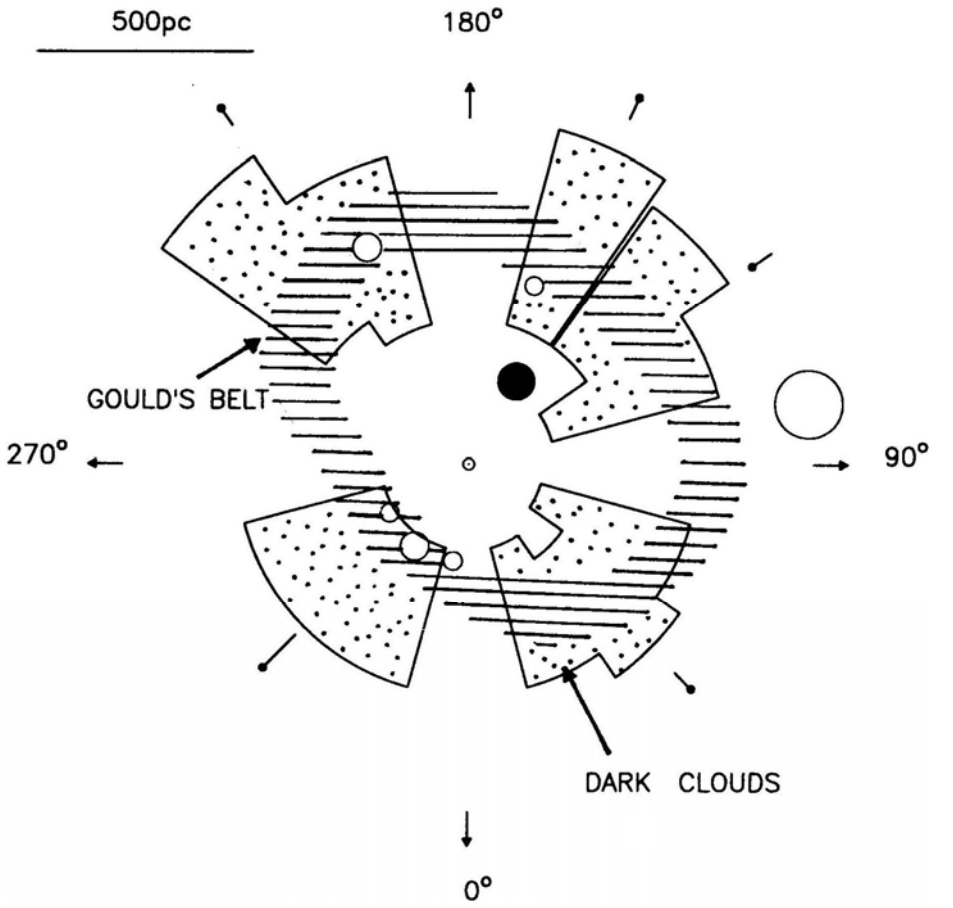

Figure 7. A schematic diagram of the projected spatial distribution of the local dark clouds derived from Table 7. The sun is located at the centre. The open circles indicate the nearby OB associations viz. Orion, Perseus, Lacertae I and Scorpio-Centaurus. The filled circle indicates the position of the Cas-Tau group. The clouds along the four *null* directions are not shown since the estimate of the mean distances to them as derived from the analysis described in section 3.3 are unreliable. The clouds in the longitude range 235º–255º are at a distance of ~ 1.4 kpc and are presumably unrelated to the local system of expanding clouds; hence they too have not been shown. For comparison, Gould's belt is shown by the hatched oval. Except for the clouds in the longitude range 105º–145º which have preominantly negative (inward) velocities, the rest of the clouds are all receding.

expansion velocity about a common centre) the clouds have peculiar or random velocities with a dispersion ~ 3 to 6 kms^{-1}.

- As to their spatial distribution, a model in which they are distributed in an oval-shaped doughnut with the sun offset from the centre fits the data reasonably well. The distance to the inner edge of the doughnut varies from 150 to 300 pc, while that to the outer edge varies from 400 to 600 pc depending upon the longitude. *In our opinion the depletion of clouds in the central region is statistically significant.* A rough estimate suggests that the *morphological centre* of the population of these clouds is at a distance of ~ 160 pc from the sun towards 215° longitude. The mean radius of the doughnut from such an assumed *morphological centre* is ~ 400 pc and the *expansion age* is ~ 100 Myr.
- In the longitude range 235° to 255°, most of the clouds in our sample appear to be unrelated to this system of expanding clouds, and are at a much greater distance of ~ l·4 kpc. (Hence they are not shown in the schematic Fig. 7.)
- An intriguing feature of the local population of the dark clouds is that most of the clouds in the longitude range 100° to 145° have negative radial velocities implying that they are approaching us.

4. Discussion

In this section, we discuss our results in relation with those arrived at by earlier workers and highlight the agreements and disgreements.

4.1 *Expansion*

Our finding that the local population of dark clouds are expanding is in agreement with a similar result arrived at by Taylor *et al.* (1987) from an earlier but limited study. The average expansion velocity of ~ 4 kms^{-1} derived by us is also consistent with the expansion seen in the local population of OB stars (Oort 1927; Cameron & Torra 1990). Optical studies suggest that of the stars within ~ 600 pc only those with ages < 30 Myr show expansion; the older stars within this volume appear to be kinematically inactive. One of our results viz. that there is a depletion of molecular clouds within a distance of $\simeq$ 200 pc from the *morphological centre* is consistent with this.

4.2 *Peculiar velocities*

In addition to the expansion, there is clear evidence for peculiar motions as well. The dispersion in the peculiar velocities is ~ 3 to 6 kms^{-1}. This is consistent with the mean absolute deviation in the peculiar velocities of the nearby OB stars as derived by Blaauw (1956). He found this quantity to be ~ 2 kms^{-1} perpendicular to the line of sight and ~ 3 kms^{-1} along the radial direction. Our values for the dispersion in different directions are likely to be a little higher because of the possible contributions due to improper distance corrections.

Stark (1984) estimates the velocity dispersion of clouds to be ~ 8 kms^{-1} from a study of molecular clouds in the anti-centre direction. This is *larger* than our estimate of 3 to 6 kms^{-1} for the local dark clouds as well as a value of 5 kms^{-1} derived for the

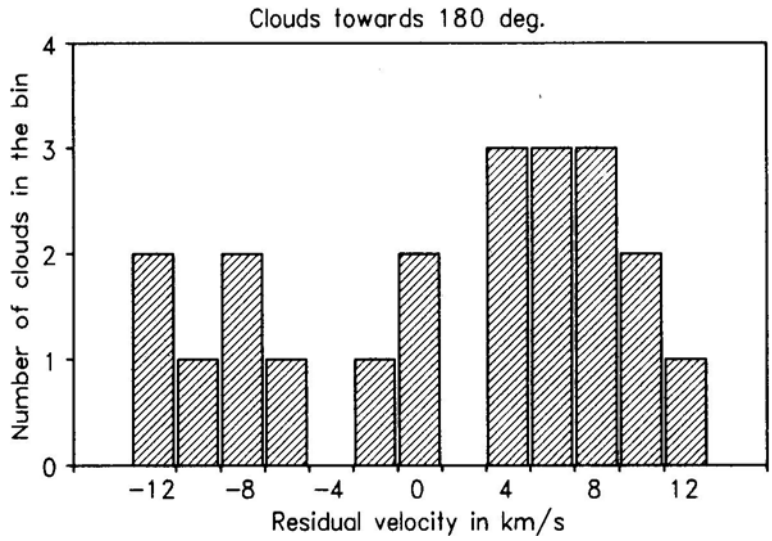

Figure 8. The histogram shows the residual velocities of clouds towards the anticentre direction observed by Stark (1984) after correcting for multiple sampling of the clouds. This was done by requiring that only one cloud occupies a *cell* of dimension 1·5° in longitude as well as latitude, and 2 km/s in velocity. At first sight, this histogram would suggest a very large velocity dispersion for the clouds, but in our opinion, this distribution may consist of more than one group of clouds. Also, any systematic velocity has to be taken out before deducing the true velocity dispersion.

HI clouds in the galactic centre direction (Radhakrishnan & Srinivasan 1980). In this study, we have removed systematic non-circular motions before calculating the dispersion, but Stark's values include such motions. In Fig. 8 we have plotted a histogram of the residual velocities of the clouds discussed by Stark (1984) after identifying distinct kinematical entities as described in the last section. Clearly it is not a *randomised* distribution. In principle, this histogram could be rationalised in terms of two distinct groups of clouds, although we have no way to prove this. Here, we merely wish to point out that the *velocity dispersion* derived from this histogram is bound to be an overestimate.

The kind of estimate made by Stark is, of course, the relevant one if one wishes to study the overall energy in non-circular cloud motions. Our estimate, by removing systematic motions as far as feasible, would correspond to a local dispersion which would be the relevant parameter for modelling the dynamics of a cloud complex i.e. estimating collisions between subclouds and providing for their *heating*.

4.3 *Distribution of the local dark clouds*

In Fig. 7 we have sketched the projected space distribution of the clouds as derived by us. As will be seen, the molecular clouds have a *thicker* distribution than a *thin ring* as conjectured by Lindblad *et al.* (1973). The dimensions of the HI ring in various directions are in general agreement with the inner boundary of the molecular 'annulus' and the O-B associations that define Gould's belt lie well within this annulus. The

spatial distribution is also in good agreement with the distribution of dust in the solar neighbourhood obtained from reddening measurements (Lucke 1978). It is also consistent with the extinction data along various longitudes in the solar neighbourhood. For example, it will be seen that between longitude 235° and 255° most of the dark clouds contained in our sample are at a much greater distance of ~ 1.2 kpc (and therefore not shown in the figure). This is in agreement with the low extinction in this direction upto large distances as found by Westin (1985). The rise of extinction to substantial values even at smaller distances in the first two quadrants is also consistent with smaller values for the inner radius of the annulus in these quadrants.

While the overall distribution is in accord with the optical and the HI studies, there is an important difference. We do not find any evidence for this expanding system of clouds to define a distinct plane or a slab inclined to the galactic plane. In this regard we disagree with the conclusion drawn by Taylor *et al.* (1987) that only the clouds in the Gould's belt plane show significant evidence for expansion. They separated the northern dark clouds into two populations, one belonging to Gould's belt and the other to the galactic plane, using a simple criterion based on proximity on the sky and an iterative procedure. They find that only the clouds in the Gould's belt show significant evidence for expansion. The local clouds in the galactic plane show at best only marginal evidence for expansion. Even this, they attribute to *contamination* of the galactic plane population by the clouds belonging to the Gould's belt in the crossover directions where the separation into two populations is difficult.

In our analysis so far we have made no attempt to separate the clouds in this manner. But in order to verify this conjecture by Taylor *et al.* we separated our sample of clouds (i.e. both the northern and southern clouds) into two distinct planes or slabs following their prescription. It turns out that there are only two longitude sectors (15° – 35° and 55° – 75°) with statistically significant number of clouds belonging to each of the two sub-groups (see Table 8). We subjected the clouds in these two sectors to the analysis procedure outlined in section 33, *but this time keeping the two populations distinct.* The comparison of the simulated cumulative distributions with the observed ones is shown in Fig. 9, and the resultant best fit parameters are given in Table 9. As can be clearly seen, *the two populations i.e. one belonging to Gould's belt plane and the other to the galactic plane show no significant differences in their kinematical behaviour or spatial distribution.* We thus conclude that the clouds in the various longitudes share similar motions regardless of which of the two hypothetical planes they are assigned to.

There are also other reasons why one might consider such a structure with age comparable to the local semi-oscillation period of 30–40 Myr to be apparent rather than real. First of all, even if a set of expanding clouds were initially confined to a thin planar ring inclined with respect to the galactic plane, with the passage of time

Table 8. Distribution of independent clouds in the various longitude bins after separating them into the Galactic and Gould's belt populations.

Longitude bins	1	2	3	4	5	6	7	8	9	10
Galactic plane	33	27	19	61	25	33	4	6	16	2
Gould's plane	25	9	18	10	0	8	22	6	0	23

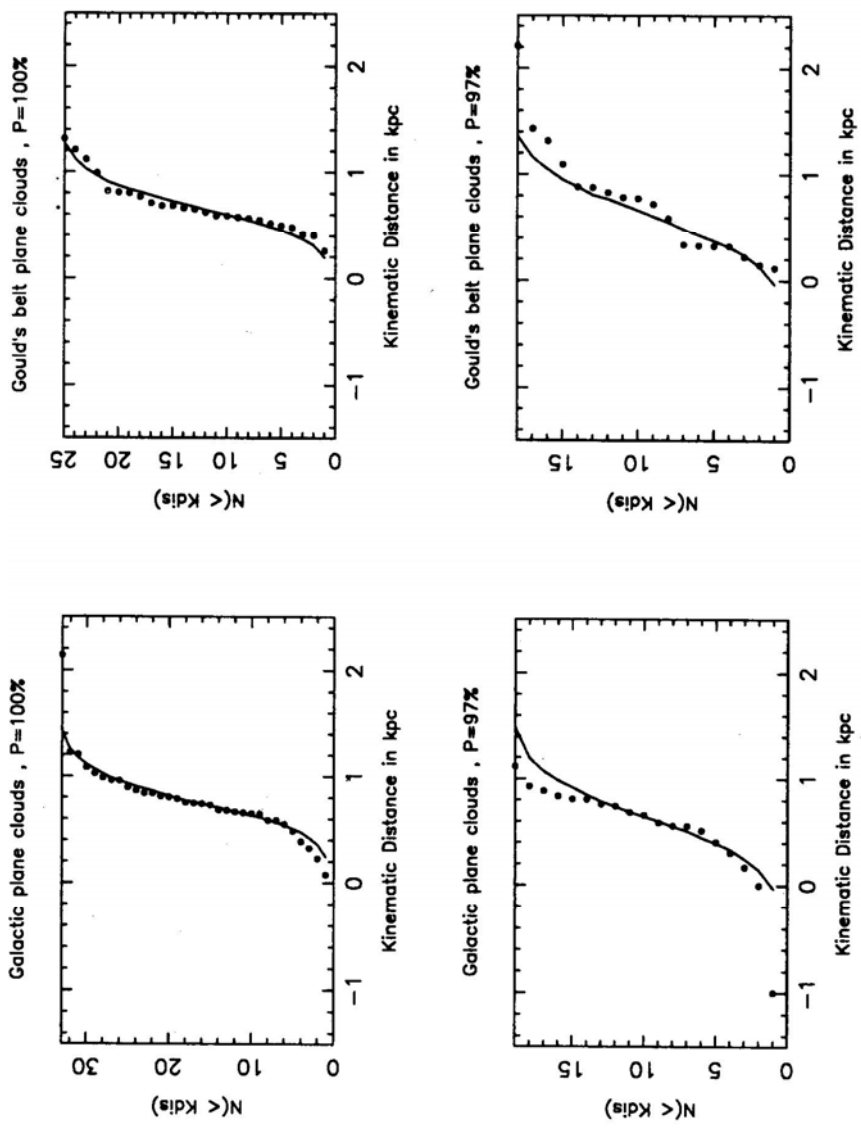

Figure 9. The cumulative distribution of the kinematic distances of the clouds in the longitude ranges 15°–35° and 55°–75°. The panels on the left are for the *galactic plane* clouds while those on the right are for the *Gould's belt plane* clouds. Our main conclusion from this is that both the *galactic plane* clouds and the *Gould's belt plane* clouds show similar kinematics.

Table 9. The best fit values of the four model parameters for the two directions: 15° ≤ / ≤ 35° and 55° ≤ / ≤ 75°. Here V_{exp} is the expansion velocity, σ the velocity, dispersion and R_L and R_H refer to the inner and outer radii of the spatial distribution of the dark clouds.

	V_{exp} kms^{-1}	σ kms^{-1}	R_L pc	R_H pc	V_{exp} kms^{-1}	σ kms^{-1}	R_L pc	R_H pc
Galactic plane	5.5	2.5	150	350	4.0	4.0	150	400
Gould's plane	4.0	2.5	200	400	3.5	4.0	200	400

this distribution will get smeared out and merge with the so called *galactic plane clouds* due to peculiar or random motions. Secondly, creation of such a structure seems to require extremely special conditions. It is difficult to imagine how an inclined structure can be created or if created initially in the plane how the required special distribution of the normal component of the mean velocity can be given. Any deviation from this special distribution would produce warps and wriggles along the belt as it oscillates in the local galactic potential which, given the age of 30–45 Myr, would help in further obliterating its distinct identity from the disk population.

4.4 *Some dark clouds with 'anomalous' motions*

As already mentioned, most of the clouds in the longitude range 100° to 145° are not receding *but coming towards us.* We have no plausible suggestions to make regarding such an apparent streaming motion. It would be worth exploring whether this is due to a velocity reversal induced by some recent stellar explosions or young associations in that region.

Another puzzling feature is the presence of the Taurus molecular clouds near the morphological centre of the expanding population of clouds that we have been considering. Although the radial component of their velocities are positive suggesting that they might be part of the expanding system, their location right near the centre of the system would contradict such an association. The Taurus molecular clouds also differ in two important ways from the Ophiucus and Orion clouds: (1) they do not show evidence of one-sided compression such as one would expect from a set of clouds expanding due to a central energy-momentum source: (2) star formation in these clouds is more or less uniformly distributed (Blaauw 1991). There are two resolutions to this dilemma: either the Taurus molecular clouds have migrated to their present location and therefore are not part of the family of expanding clouds or that they have formed more recently than the expanding system of clouds (Blaauw 1991).

4.5 *Origin of the motions*

Having discussed the expansion and the distribution of the local dark clouds as well as the Gould's belt system of stars, we now turn to a discussion of their possible origin. The two basic facts that need to be explained are the energy and the momentum

in the expansion of the system of stars as well as the clouds, and their presently observed morphology and the nature of their motions.

Energy and momentum: The suggestions that have been made in the literature regarding the source of the energy and momentum responsible for the expansion fall into two categories: according to one hypothesis (see Blaauw 1991 for a review), the observed expansion could be understood in terms of the continued action of the ionising radiation, stellar wind and Supernovae from massive stars belonging to the *Cas-Tau* association located close to the morphological centre of the system. The one-sided star formation in the three major nearby cloud complexes – Orion, Sco-Cen and Perseus – is consistent with this idea. But the *inclination* of the Gould belt system of bright B stars is harder to explain in this picture. An alternative hypothesis due to Franco *et al.* (1988) is that the observed ring-like structure might be understood in terms of the impact of a high-velocity cloud with the galactic disk and the resultant *splash* (Elmegreen 1991). While such an exotic mechanism might explain the location of some of the nearby big molecular cloud complexes (such as Orion) at substantial distances from the galactic plane it is difficult to understand the observed expansion in this picture. In view of this, in the discussion to follow, we will assume that the *Cas-Tau* association is the more likely *central engine* which has powered the expansion. Similar expanding systems of clouds with young OB stars located in the interior – such as the systems of cometary globules and clouds found in Orion, Vela, Cepheus and Rosette regions (Bally *et al.* 1991; Sridharan 1992; Patel *et al*. 1993; Indrani & Sridharan 1994) – lend credibility to this idea. In principle, there are three mechanisms in this scenario that can supply energy and momentum to the clouds: (1) stellar winds, (2) Supernovae, and (3) the rocket effect (Oort & Spitzer 1955). We shall now make simple estimates for the energy and momentum that each of these processes can contribute to see if they can meet the requirements.

The local dark clouds are found to have an average ^{13}CO column density of $\sim 60 \times 1\ 0^{14}$ cm^{-2}. Using $N_{^{13}CO}$ to N_{H_2} conversion factor of 5×10^5 (Dickman 1978) and assuming a mean molecular hydrogen volume density of 500 cm^{-3} the estimated average sizes and masses of the clouds are ~ 2 pc and 600 $M_\odot$, respectively. We estimate that there are ~ 300 such clouds in the first two quadrants alone. Thus the total mass of these clouds would be $\gtrsim 2 \times 10^5\ M_\odot$ and for an average expansion speed of ~ 4 kms^{-1} the total energy would be ~ 10^{50} erg.

Blaauw (1991) has estimated that ~15OB stars would have evaporated from *Cas-Tau* in its lifetime (~ 45Myr). The stellar winds acting over 10 Myr as well as the subsequent Supernovae of massive stars inject similar amounts of mechanical energy and mass which for 10 such stars are ~ 10^{52} erg and ~ 100 $M_\odot$ respectively. Here we have assumed a mass loss rate of ~ $10^{-6}\ M_\odot$ yr^{-1} and a wind velocity of ~ 2000 kms^{-1}. If a reasonable fraction, say 10%, of this energy is intercepted by the clouds the energy requirement can be satisfied but not the momentum. This is because the momentum goes as $\sqrt{2 \times Mass \times Energy}$ and balancing the momentum in the clouds with that in the ejecta requires that the ratio of their kinetic energies is equal to the inverse of the ratio of their masses. In the above cases, while the net mass of the clouds is ~ 1000 times larger than the total ejected mass, even the maximum available mechanical energy in the ejecta is only ~ 100 times larger than that required. This disparity becomes even larger if one assumes some reasonable values for the fraction of mass and energy intercepted. Thus both the stellar winds and the super-

novae from 10 massive stars seem to be unlikely candidates as the primary energy-momentum source. However, it should be noted that a large fraction of the energy goes into *heating* up the matter and the increased internal pressure will push the clouds outward. This is possibly more effective than the direct momentum transfer in the above two mechanisms.

The third mechanism viz. the *rocket effect*, on the other hand, seems to be more probable. When a neutral gas cloud is exposed to the ionising radiation from a star, an ionisation front will be driven into the cloud. The ionised hydrogen produced on the side of the cloud facing the star is at a much higher pressure than the gas outside because of the higher density. Hence this gas expands, producing a recoil on the cloud and thus accelerating it away from the star. This process known as the *rocket effect* (Oort & Spitzer 1955) can accelerate interstellar clouds to high velocities and hence supply the required momentum. However, in the process it leads to the ablation of a significant part of the cloud as well. In fact, the sound velocity in the ionised expanding dense gas is ~ 15 kms^{-1}, and to accelerate a cloud to this velocity half of its initial mass has to be ionised and ablated. It is conceivable that this gas after recombination is now seen as the expanding HI ring.

Morphology and kinematics: There have been two distinct suggestions regarding the origin of the observed clouds and the OB associations:

(a) The clouds were formed due to gravitational collapse of an expanding ring of gas set in motion by the central activity.
(b) The clouds existed close to the center of activity and they were pushed by an expanding ring of gas resulting from the activity at the center.

In both these scenarios, the observed OB associations are to be understood in terms of induced star formation. But there are difficulties with both these scenarios. For example, scenario (b) is inconsistent with the fact that the molecular clouds and associations are located *outside* the expanding HI ring. One would have expected the clouds to have lagged behind the expanding ring which set them in motion. From a kinematical point of view neither of the scenarios mentioned above are able to provide a satisfactory explanation for the observed radial velocities. As already remarked, Taylor *et al.* (1987) had concluded from their analysis that a model in which a ring of clouds expands from a point getting only sheared by the galactic rotation effects in the process does not fit the observed radial velocities of the northern dark clouds. Our analysis of the combined data of both the northern and southern clouds confirms this. As pointed out by Frogel & Stothers (1977) from limited data, the longitude-radial velocity plot (Fig. 1b) clearly shows a double, sinewave behaviour characteristic of galactic differential rotation. The peculiar velocities as well as the distribution of clouds having finite radial thickness can cause the observed scatter. Nevertheless the local dark clouds clearly show an expansion of ~ 4 kms^{-1} as well. Thus, only a model in which the clouds are participating in galactic rotation appropriate to their *present* locations, with a small expansion also super-imposed seems to fit the molecular data. This is at variance with the expanding ring model of Lindblad *et al.* (1973) mentioned above that fits well the velocity data on the local HI gas.

If we were to accept our model to describe the kinematics of the local dark clouds, then it is quite clear that cloud–cloud encounters must be an important ingredient

of any scenario. In this regard, we wish to advance the following suggestion. Let us 'assume that the *Cas-Tau* group of stars formed in a giant molecular cloud. Due to stellar winds and ultraviolet radiation from the massive stars as well as supernova activity, the parent cloud would have fragmented: the denser fragments would have been accelerated through, say, the *rocket effect* (Oort & Spitzer 1955), and in the more diffuse regions the molecular gas would have been dissociated and perhaps even ionised. Due to the continuing action of the stellar winds from the association a large cavity would have been excavated with the more diffuse gas swept into an expanding shell. As the local dark clouds in the vicinity were overtaken by this expanding shell of swept-up gas they too would have been set in motion due to the combined effect of the *Cas-Tau* group of stars and also possibly due to the interaction between the expanding shell of gas and the dark clouds. It is entirely conceivable that during the subsequent 30 to 40 Myr the systematic motions of these clouds could have been degraded through collisions with other clouds in the surrounding interstellar medium. Provided these collisions are sufficient in number, one would expect that the galactic rotational effects would eventually become more important than expansion.

We present a simple estimate to support this conjecture. Let us assume that due to the combined effects of ultraviolet radiation and stellar winds a certain number of clouds are accelerated to a velocity of, say, ~ 20 kms^{-1} which is comparable to the sound speed in the ionised front of the clouds (Spitzer 1978). Let M_1 be the combined mass of these clouds and M_2 be the total mass of the interstellar clouds to which they have imparted energy and momentum. Thus $M_1 + M_2$ will be the mass of the clouds in the doughnut shaped configuration expanding radially with a velocity of ~ 4 kms^{-1}.

Momentum conservation requires $(M_1 + M_2)\ V_2 = M_1\ V_1$. For the assumed values of V_1 ~ 20 kms^{-1}, V_2 ~ 4 kms^{-1}, this implies that M_2/M_1 ~ 4. An inspection of Fig. 7 displaying our derived distribution of the system of expanding clouds shows that the ratio of the projected area of the annulus to that of the centrally depleted region is ~ 5 to 6. Thus the expectation that a certain number of clouds initially accelerated by the *Cas-Tau* group of stars could have imparted radial motions to the remaining clouds is consistent with our derived distribution. Or to put it differently, it is not too difficult to account for the energy and momentum of the system of clouds.

A more arguable point is the following: Does one expect a sufficient number of cloud–cloud collisions to have taken place during the last 30 Myr or so to erase the initial signature of uniform expansion from a common centre? For this to be true the effective cross section for cloud–cloud collisions must be greater than a minimum value given by

$$\sigma_{min} \sim \frac{a^3}{Vt} \tag{3}$$

where α is the mean separation between the clouds, V the relative velocity and t the age of the system. From the geometry of the distribution of clouds given in Fig. 7 and the total number of clouds in the sample we estimate the mean separation to be ~ 60 pc. For an assumed value of V ~ 20 kms^{-1} and t ~ 30 Myr, the effective cross section must be $\geqslant 225$ pc^2 in order for collisions to be important. In other words, the *effective sizes* of the clouds must be ~ 15 pc. Interestingly this is only 3 to 5 times

the mean sizes of the clouds. Thus the importance of cloud–cloud collisions possibly mediated by galactic magnetic fields cannot *a priori* be ruled out (see Elmegreen 1987a, b for a relevant discussion). A detailed investigation of this important and interesting question may be worthwhile but is beyond the scope of this paper. We merely wish to point out the difficulty in understanding the kinematics of the local dark clouds without invoking cloud–cloud collision.

5. Summary

We shall now summarise our main findings. Our objective was to study the kinematics and the spatial distribution of the local dark clouds. Towards this aim the radial velocities towards 115 southern dark clouds were obtained using the $J = 1 \rightarrow 0$ transition of ^{12}CO. Using different methods we analysed these velocities along with those of the northern dark clouds obtained by Taylor *et al.* (1987). We agree with their conclusion that the kinematics of the local clouds is not describable by the expanding ring model proposed for the local HI gas. We find that the observed distribution of the radial velocities is best understood in terms of a model in which the local clouds are participating in circular rotation appropriate to their present positions with a small expansion also super-imposed. This possibly implies that cloud–cloud collisions are important. The 4 kms $^{-1}$ general expansion as well as the spatial distribution derived are in good agreement with those obtained from optical studies. This includes the finding that clouds in the longitude range 235° to 255° are unrelated to the system of expanding clouds, and are at a much greater distance of ~ 1.4 kpc. Intriguingly, most of the clouds in the longitude range 100° to 145°, and some in the range 195° to 215°, appear to have negative radial velocities implying that they are approaching us. The reason for such a streaming motion of a subset of clouds is not clear.

Acknowledgements

I thank the faculty of the Joint Astronomy Program, Department of Physics, Indian Institute of Science, Bangalore for providing me an opportunity to do research in astronomy. My sincere thanks are due to the staff of the Millimeterwave Laboratory and the Observatory at the Raman Research Institute for their help and support during the observations. It gives me great pleasure to thank G. Srinivasan, T. K. Sridharan, A. A. Deshpande and Rajaram Nityananda for their encouragement, helpful discussions and critical comments on the manuscript.

References

Bally, J., Langer, W. D., Wilson, R. W., Stark, A. A., Pound, M. W. 1991, in *IAU Symp. No. 147 on Fragmentation of Molecular Clouds and Star Formation*, Eds. E. Falgarone, F. Boulanger & G. Duvert, (Dordrecht: Kluwer) p. 11.

Blaauw, A. 1991, in *The physics of star formation and the early stellar evolution*, Eds. C. J. Lada & N. D. Kylafis (Kluwer Academic Publ.) p. 125.

Blaauw, A. 1956, *Astrophys. J.*, **123**, 408.
Cameron, F., Torra, J. 1990, *Astr. Astrophys.*, **241**, 57.
Dame, T. M., Ungrechts, H., Cohen, R. S., de Geus, E. J., Grenier, I. A., May, J., Murphy, D. C., Nyman, L. A., Thaddeus, P. 1987, *Astrophys. J.*, **322**, 706.
de Vries, C. P., Brand, J., Israel, F. P., de Graauw, Th., Wouterloot, J. G. A., van de Stadt, H., Habing, H. J. 1984, *Astr. Astrophys. Suppl.* , **56**, 333.
Dickman, R. L. 1978, *Astrophys. J. Suppl.*, **37**, 407.
Elmegreen, B. G. 1991, in *The galactic interstellar medium* Eds. W. B. Burton, B. G. Elmegreen & R. Genzel (SaasFee advanced course 21), 164.
Elmegreen, B. G. 1987a, in *Physical Processes in Interstellar Clouds*, Eds. G. E. Norfill & M. Scholer (NATO ASI C Series Vol. 21), 1.
Elmegreen, B. G. 1987b, in *Physical Processes in Interstellar Clouds*, Eds, G. E. Norfill & M. Scholer (NATO ASI C Series Vol. 21), 105.
Feitzinger,J. V.,Stuwe, J.A.1984, *Astr.Astrophys.Suppl.*, **58**, 365.
Feitzinger, J. V., Stuwe, J. A. 1986, *Astrophys. J.*, **305**, 534.
Franco, J., Tenario-Tagle, G., Bodenheimer, P., Rosyczka, M., Mirabel, I. F. 1988, *Astrophys. J.*, **333**, 826.
Frogel, J. A., Stothers, R. 1977, *Astr. J.*, **82**, 890.
Indrani, C, Sridharan, T. K. 1994, *J. Astrophys. Astr.* **15**, 157.
Kerr, F. J., Bowers, P. F., Hendrson, A. P. 1981, *Astr. Astrophys. Suppl.* , **44**, 63.
Kutner, M. L., Machnik, D. E., Tucker, K. D., Dickman, R. L. 1980, *Astrophys. J.*, **237**, 734.
Kwan, J. 1979, *Astrophys J.*, **229**, 567.
Lucke,xP.xB.1978, *Astr.Astrophys.*, **64**, 367.
Lindblad, P. O., Grape, K., Sandqvist, Aa., Schober, J. 1973, *Astr. Astrophys.*, **24**, 309.
May, J., Murphy, D. C., Thaddeus , P.1988, *Astr. Astrophys. Suppl.*, **73**, 51.
Olano,xC.xA.1982, *Astr.Astrophys.*, **112**, 195.
Oort, J. H. 1927, *Bull. Astr. Inst. Netherlands*, **3**, 275.
Oort, J. H., Spitzer, L. 1955, *Astrophys. J.*, **121**, 6.
Patel, N. A. 1990, Ph. D. thesis, Indian Institute of Science, Bangalore.
Patel, N. A., Xie, T., Goldsmith, P. F. 1993, *Astrophys. J.*, **413**, 593.
Racine, R. 1968, *Astr. J.*, **73**, 223.
Radhakrishnan, V., Srinivasan G. 1980, *J. Astrophys. Astr.*, **1**, 47.
Sahu, M. S. 1992, Ph.D. Thesis, University of Groningen.
Spitzer, L., Schwarzschild, M. 1951, *Astrophys. J.*, **114**, 385.
Spitzer, L. 1978, in *Physical processes in the interstellar medium* (New York: Wiley), pp. 227.
Sridharan, T. K.1992, *J.Astrophys.Astr.*, **13**, 217.
Stark, A. A. 1984, *Astrophys. J.*, **281**, 624.
Stark, A. A., Blitz, L. 1978, *Astrophys. J.* (*Lett*), **225**, L15.
Taylor, D. K., Dickman, R. L., Scoville, N. Z. 1987, *Astrophys. J.*, **315**, 104.
van den Bergh, S., Herbst, W. 1975, *Astr. J.*, **80**, 208.
Westin, T. N. G. 1985, *Astr. Astrophys. Suppl.*, **60**, 99.